An Analysis of Glutathionylation in the Modulation of the Critical Innate Immune Regulators Mal and NEK7

Thesis submitted to the
University of Dublin
for the
Degree of Doctor of Philosophy

By

Mark M. Hughes

School of Biochemistry and Immunology
Trinity College Dublin
Ireland

March 2018

Declaration

This thesis is submitted by the undersigned to the University of Dublin for the examination of Doctor of Philosophy. I declare that this thesis has not been submitted as an exercise for a degree at this or any other university and is entirely my own work with the exception of the following figures:

Figure 4.11
This work was performed by Dylan G. Ryan

Figure 5.8
This work was performed by Alexander Hooftman

Figure 5.15
This work was performed by Dr. Padmaja Tummala

I agree to deposit this thesis in the University's open access institutional repository or allow the library to do so on my behalf, subject to Irish Copyright Legislation and Trinity College Library conditions of use and acknowledgement.

_____

Mark M. Hughes

Acknowledgements

When I started in the lab four years ago, I thought I wouldn't last longer than a week surrounded by such incredible people. I will never forget the beginning of my PhD under my assigned postdoc Becca, who probably thought I would light myself on fire if left unsupervised. I thought I'd play a joke on her, and after scraping cells off plates for an experiment, I added virkon bleach, again jokingly telling her I thought it would help lift the remaining cells off better. She didn't speak to me for a couple of days after that.

Luke, you have been the most incredible supervisor to work for and learn from. I've always felt very proud to be a part of your lab, and I can't thank you enough for seeing potential in me I didn't realise I had. Every meeting I've ever had with you made me feel more confident and able to take on the world. I still remember our first meeting, with slight resentment, when you said, "Ah it'll only be a couple of immunoprecipitations, don't worry". I think I've developed arthritis from this. I also hosted your 50th lab birthday party, so that's serious brownie points.

There's three particularly special lab members I would like to thank. To Anne, Eva and Kathy, I couldn't have done this without you. The constant support, the willingness to answer, "just one small question" and the selflessness in being a supportive friend, I can't put into words how much I appreciate and admire each of you.

To the extended lab family, past and present, Mustafa, Rebecca, Sarah J, Paulina, Mirjam, Sue, Moritz, Danny, Sinéad, Evanna, Raquel, Beth, Cait, Silvia, Sarah C, Dylan, Jamie, Niamh, Zbigniew, Richie, Stefano, Marah, Alex and Ciana. Thanks for all the laughs guys, the constant regimented tea breaks and more importantly, thanks for putting up with me. I genuinely think our nights out have damaged my liver.

To my best friends Jamie, Joy and Nicola. You guys have been such emotional supports that kept me going through my PhD. Funnily enough the support kept a few vineyards in business. I can't thank you enough for the years of friendship, support and banter. Shantay you stay!

To my Mam and Dad, I can't put into words the love I have for you both. Your incredible relationship and devotion for each other made me believe in love. You've kept my head above water more times than I can count, and I would never have reached where I am today without your support. I love you.

To my sisters, Rachael and Ciara, I've finally lived up to the 'brainiac nerd' title you placed on me over the years. I can't thank you enough for your support over the past few years and letting me away with all the late birthday presents because I was "in the lab".

To my grandmother Rita, it's rare to find a woman with such charisma, effervescence for life and to have such a warm and supportive character. You're an inspirational woman and I hope one day to be as courageous and fun as you are.

Finally, but not least, to the one man who has changed my life. To Cathal, I absolutely adore you. We met on the 3rd March 2015. I was exactly one year into the PhD and felt I didn't have what it took to continue any longer. You made me realise I'm good enough. Then you made me realise I can achieve anything. My publications during my PhD are as much yours as they are mine. Who knew three years later I'd finally have written the damned thing you're "sick to death of hearing about". We've been on some fantastic journeys around the world together, and it's only just the beginning. Thank you for everything, I love you.

I dedicate this thesis to my grandparents Matthew and Concepta,

who valued education above all else.

Table of Contents

List of Figures

List of Tables

Abbreviations

AFB1	Aflatoxin B1
AIM2	Absent in Melanoma 2
ALR	AIM2-like receptor
AMPK	AMP-activated protein kinase
APS	Ammonium Persulfate
ASC	Apoptosis-associated speck-like protein containing a CARD
ATP	Adenosine triphosphate
BCAP	B cell adaptor protein
BCR	B cell receptor
BMDM	Bone marrow-derived macrophage
BSA	Bovine serum albumin
Btk	Bruton's tyrosine kinase
CAPS	Cryopyrin-associated periodic syndrome
CARD	Caspase activation and recruitment domain
CD14	Cluster of differentiation 14
cDNA	Complementary DNA
CLR	C-type lectin receptor
CpG	Unmethylated 2'-deoxyribo(cytidine-phosphate-guanosine)
CREB	cAMP response element binding protein
CSE	Cystathionine γ-lyase
Ct	Cycle-threshold
DAMP	Damage associated molecular pattern
DCFDA	2',7' –dichlorofluorescin diacetate
DD	Death domain
DMEM	Dulbecco's modified eagle medium
DMSO	Dimethyl sulfoxide
DNA	Deoxyribonucleic acid
dNTP	Deoxyribonucleotide triphosphate
DP	Dipeptidase
ds	Double stranded
DSS	Dextran sodium sulfate
DTT	Dithiothreitol
ECAR	Extracellular acidification rate
EDTA	Ethylenediaminetetraacetic acid

ELISA	Enzyme-linked immunosorbent assay
EST	Expressed sequence tag
EtOH	Ethanol
FCS	Fetal calf serum
GAPDH	Glyceraldehyde-3-phosphate dehydrogenase
GCL	Glutamate cysteine ligase
GGT	γ-glutamyltranspeptidase
Grx	Glutaredoxin
GSDMD	Gasdermin D
GSH	Glutathione
GSH-EE	Ethyl-ester glutathione
GSNO	S-nitrosoglutathione
GST	Glutathione transferase
GSTO	Glutathione transferase omega
GSTP	Glutathione transferase pi
H_2S	Hydrogen sulfide
HEK	Human embryonic kidney
HIN-200	Hematopoietic expression, IFN-inducible, nuclear localisation domain
HIV	Human immunodeficiency virus
HRP	Horseradish-peroxidase
iBMDM	Immortalised bone marrow-derived macrophage
IFN	Interferon
IKK	IκB kinase IKK
IL	Interleukin
IL-1R	Interleukin-1 receptor
IL-1Ra	Interleukin-1 receptor antagonist
IL-1RAPL	IL-1 receptor accessory protein like-1
IP	Immunoprecipitation
IRAK	Interleukin-1 receptor-associated kinase
IRF	Interferon regulatory factor
IRF3	Interferon regulatory factor 3
ITAM	Immunoreceptor tyrosine-based activation motif
IκB	Inhibitor of NF-κB
JNK	Jun N-terminal kinase
kDa	Kilodalton

KO	Knockout
LB	Lysogeny broth
LBP	LPS binding protein
LDH	Lactate dehydrogenase
LPS	Lipopolysaccharide
LRR	Leucine rich repeat
Mal	MyD88 adaptor-like
MALP2	Macrophage activating lipopeptide-2
MAPK	Mitogen activated protein kinase
MAPPIT	Mammalian protein-protein interaction trap
MD2	Myeloid differentiation factor 2
MFI	Mean fluorescence intensity
MOI	Multiplicity of infection
mRNA	Messenger RNA
MS	Mass spectrometry
MTC	HEK293-MD2-TLR4-CD14
MyD88	Myeloid differentiation factor 88
NACHT	Nucleotide binding and oligomerisation domain
NADPH	Nicotinamide adenine dinucleotide phosphate
NAIP	NLR family apoptosis inhibitory protein
NF-κB	Nuclear factor κB
NK	Natural killer cell
NLR	Nod-like receptor
nm	Nanometer
NMR	Nuclear magnetic resonance
NO	Nitric oxide
NOD	Nucleotide oligomerisation domain
NOX1	NAPDH oxidase 1
NP-40	Nonyl phenoxylpolyethoxyethanol 40
OCR	Oxygen consumption rate
P2X7	Purinergic receptor P2X, ligand-gated ion channel 7
PAGE	Polyacrylamide gel electrophoresis
Pam3CSK4	Pam3Cys-Ser-(Lys)-4
PAMP	Pattern associated molecular pattern
PBS	Phosphate buffered saline

PCR	Polymerase chain reaction
PIP2	Phosphatidylinositol 4,5-bisphosphate
PKC	Protein kinase C
PMSF	Phenylmethanesulfonyl fluoride
Poly (I:C)	Polyinosine-polycytidylic acid
Poly (dA:dT)	Poly(deoxyadenylic-thymidylic) acid
PRR	Pathogen recognition receptor
P/S	Penicillin streptomycin
PS	Phosphatidylserine
PTP1B	Protein tyrosine phosphatase 1B
PVDF	Polyvinylidene fluoride
PYD	Pyrin domain
RA	Rheumatoid arthritis
RLR	RIG-I-like receptor
RNA	Ribonucleic acid
RNS	Reactive nitrogen species
ROS	Reactive oxygen species
RT	Room temperature
RT-PCR	Reverse transcriptase polymerase chain reaction
RyR	Ryanodine receptor
S-4NPG	S-(4-Nitrophenacyl) glutathione
SARM	Sterile alpha and HEAT-armadillo motif
SDS	Sodium dodecyl sulfate
SFM	Serum free medium
SNP	Single nucleotide polymorphism
SOCS1	Suppressor of cytokine signalling 1
SOD1	Superoxide dismutase 1
ss	Single stranded
TAG	TRAM adaptor with GOLD domain
TBS	Tris-buffered saline
TBST	Tris buffered saline tween
TEMED	Tetramethylethylenediamine
TIR	Toll/Interleukin-1 receptor
TIRAP	Toll-interleukin 1 receptor domain containing adaptor protein
TLR	Toll-like receptor

TMED7	Transmembrane P24 Trafficking Protein 7
TNF	Tumour necrosis factor
TRAF	Tumour necrosis factor receptor-associated kinase
TRAM	Trif-related adaptor molecule
TRIF	TIR-domain-containing adaptor-inducing interferon-β
Trx	Thioredoxin
TXNIP	Thioredoxin interacting protein
UTR	Untranslated region
WNV	West Nile virus
WT	Wild-type

Abstract

Macrophages are critical innate immune cells that sense pathogen associated molecular patterns (PAMPs) and host-derived damage associated molecular patterns (DAMPs) through specialized Toll-like receptors (TLRs) to maintain homeostasis. TLR activation drives production of anti-microbial reactive oxygen species (ROS), which bombards invading microbes and must therefore be highly regulated. Overproduction of ROS causes oxidative imbalance, which can be sensed by redox sensitive protein machinery. The main sensor of oxidative insult is the thiol group on cysteine amino acids, which are amenable to redox-induced post-translational modification. Glutathione (GSH), the most abundant cellular antioxidant, regulates ROS levels and directly prevents oxidation of proteins by protecting redox sensitive thiol groups on cysteine amino acids. It is becoming more apparent that GSH not only contributes to cellular integrity, but rather alters protein function by reversibly modifying reactive cysteines.

In this project, I sought to explore the role of GSH in TLR signalling. I focused on the TLR signalling adaptor MyD88-adaptor-like (Mal). The crystal structure of Mal revealed two cysteines, C91 and C157, that crystallised bound to a dithiothreitol (DTT) molecule. The cytosol of the cell is a reducing environment, thereby making these two cysteine residues very interesting potential post-translationally modified targets. Site-directed mutagenesis of C91 and C157 to alanine (C91A, C157A), identified that C91, and not C157, in Mal requires glutathionylation to drive TLR signalling. C91A was unable to interact with MyD88 or IRAK4. C91A also displayed diminished phosphorylation, known to be important for Mal function. Furthermore, positively charged amino acids adjacent to cysteines promote deprotonation of cysteine thiol groups, rendering them more sensitive to glutathionylation. Preventing glutathionylation of C91 by mutation of the positively charged flanking amino acid histidine to proline (H92P) mimicked the effect of C91A. Both C91A Mal and H92P Mal acted as dominant negative inhibitors of TLR4 signalling and were unable to reconstitute TLR4 signalling in Mal-deficient macrophages. Finally, LPS transiently increased the glutathionylation of Mal.

Protein regulation by glutathionylation requires enzymes which can also deglutathionylate substrates as a regulatory mechanism. I also explored the redox enzyme Glutathione transferase omega 1 (GSTO1-1), which has deglutathionylating activity in TLR4 signalling. Using macrophages deficient in GSTO1-1, I identified novel roles for GSTO1-1 in the immunometabolic response to TLR4 activation. I demonstrate that GSTO1-1-deficient macrophages are highly glycolytic, and furthermore that GSTO1-1 deficiency drives

production of the pro-inflammatory cytokine interleukin-1β (IL-1β). Furthermore, using a novel covalent inhibitor of the active site of GSTO1-1 termed C1-27, I identify a role for GSTO1-1 in the regulation of pro-IL-1β processing by the NLRP3 inflammasome, acting via NEK7, and in the induction of Caspase-11, which mediates LPS lethality *in vivo*. I have found that the key NLRP3 regulator NEK7 is glutathionylated on cysteine 79 and cysteine 253 and provide evidence that GSTO1-1 is targeting NEK7 to promote NLRP3 activation. GSTO1-1 therefore also appears to play a role in NLRP3 inflammasome activation.

Overall, this study identifies an important positive role for Mal glutathionylation, a negative role for the deglutathionylating enzyme GSTO1-1 in TLR4 signalling and a regulatory role for GSTO1-1 during inflammasome activation and Caspase-11 induction, highlighting the importance of glutathionylation as a regulator of macrophage activation.

Chapter 1

Introduction

1. Introduction

1.1 The innate immune system

1.1.1 General introduction

The immune system protects against invading pathogens and self-harming malignant cells. It can be subdivided into two categories, the innate immune system and the adaptive immune system. The innate arm of the immune system is the first line of defence against invading pathogens and responds much more rapidly than the adaptive immune response. The innate immune arm uses a general scavenging approach to detect and clear invading pathogens to maintain homeostasis. Innate immune cells utilize an array of antimicrobial factors coupled with phagocytosis to clear infection. This process allows for antigen presentation of the invading pathogen to the adaptive arm of the immune system, leading to antigen-specific effectors and immune memory for rapid response to recurring infection.

In order to mount a response to invading pathogens, the innate immune system must recognise conserved motifs that are present in bacteria, fungi and viruses. These motifs can bind to specific innate immune receptors to drive inflammatory responses. A variety of different cells can express these pattern recognition receptors (PRRs), however they are most common in the professional innate immune phagocytes, monocytes and macrophages. PRRs can bind Pathogen Associated Molecular Patterns (PAMPs) present in the invading pathogen and similarly, endogenous Damage Associated Molecular Patterns (DAMPs) released from damaged or dying host cells. To date, many PRRs have been discovered and characterized in the plasma membrane, endosomal compartments and cytosol and include Toll-like Receptors (TLRs), NOD-like receptors (NLRs), C-type lectin receptors (CLRs), RIG-I-like receptors (RLRs) and AIM2-like receptors (ALRs)/PYHIN-containing proteins. Identification of many PAMP-specific receptors on innate immune cells has challenged the ‘non-specific’ conventional perception of the innate immune response, defining new roles for professional phagocytes in PAMP recognition.

1.1.2 Toll-like receptors

A redefining moment in the field of immunology was the discovery of TLRs. The pioneering work of Charles Janeway greatly contributed to the field of immunology, proposing the idea of PRRs in 1989 [1]. The works of Bruce Beutler and Jules Hoffman, along with Ralph Steinman who discovered the dendritic cell, lead to the discovery of TLRs. This discovery was recognised as one of the most significant findings in immunology in recent years and the Nobel Prize for Physiology or Medicine was awarded to all three in 2011 for their contribution to the field of

immunology [2]. In 1988, the gene encoding the Interleukin-1 receptor type 1 (IL1R1) was cloned. In 1991, the IL1R1 receptor was found to share domain homology with the *Drosophila melanogaster* protein Toll. This finding lead to the discovery by members of Hoffman's lab in 1996 that fungal components can drive inflammatory responses through Toll via upregulation of the anti-fungal peptide Drosomysin. A breakthrough in the field was the discovery of the receptor for lipopolysaccharide (LPS), a PAMP present in gram-negative bacterial cell walls known for a long time to induce sepsis and inflammation, with little understanding into its signalling effects. In 1998, Beutler's group cloned a gene termed '*Lpsd*' [3]. Soon after, research from Danielle Malo's group confirmed the findings that *Lpsd* was TLR4. The following year, Shizuo Akira and colleagues reported that TLR4-deficient mice could not respond to LPS [4], confirming TLR4 as the receptor for LPS. This pioneering research led to the discovery and characterization of TLRs in innate immune cells.

1.1.3 TLR localisation and ligand recognition

TLRs can be found at the plasma membrane and endosomal compartments to detect both PAMPs from pathogens and host-derived sterile DAMPs (Figure 1.1). Both plasma membrane and endosomal TLRs sense a variety of bacterial or viral species to drive an inflammatory response [5, 6]. There are currently 10 human TLRs (13 mouse TLRs) identified which fall into two categories. Cell surface TLRs (TLRs 1, 2, 4, 5, 6, and 11) and intracellular TLRs (TLRs 3, 7, 8 and 9). TLR4 is considered the prototypical TLR and requires accessory proteins to recognise LPS. LPS is a glycolipid that is solubilised by serum protein lipid binding protein (LBP) [7]. LPS-bound LBP will transfer LPS to the leukocyte membrane protein CD14 to enhance LPS sensing by TLR4 [8]. Further characterisation of TLR4 identified another accessory protein, MD-2, involved in LPS sensing [9]. MD-2 belongs to a family of lipid-binding proteins that folds into a β-cup structure, facilitating binding of hydrophobic moieties and interacts with TLR4 [10]. CD14-bound LPS drives TLR4/MD-2 mediated signal transduction. TLR4 has also been found to recognise the plant component taxol [11]. TLR2 can heterodimerize with TLR1 or TLR6 and can recognize triacylated lipopeptides and diacylated lipopeptides respectively from species such as *Mycoplasma* and *Escherichia Coli.* TLR2 can also recognize gram positive lipoproteins and fungal zymozan [12] and has been implicated in viral recognition in inflammatory monocytes [13]. TLR5 can recognize flagellin, a protein monomer utilized by bacteria from a variety of bacterial species, including *Salmonella typhimurium* and *Enterococcus* [14]. TLR11 is expressed by mice, as human TLR11 is a pseudogene which does not code for a functional protein and recognizes profilins from *Toxoplasma gondii* and uropathogenic *E. coli.* TLRs 3, 7, 8 and 9 are exclusively intracellular.

TLR3 recognizes double stranded RNA (dsRNA) from RNA viruses such as West Nile Virus (WNV). TLR7 and TLR8 recognize single stranded RNA (ssRNA) from viruses such as Human immunodeficiency virus (HIV) [15]. TLR9 recognizes DNA which contains unmethylated 2'-deoxyribo(cytidine-phosphate-guanosine) (CpG) motifs from bacteria and viruses and hemozoin, a by-product of malarial infection [16].

1.1.4 Toll-like receptor signalling

Extensive research into TLR structure and TLR signalling pathways has unravelled many complexities of innate immune cells within the past decade. TLRs contain an extracellular leucine-rich repeat domain involved in ligand recognition, forming an 'm' shape structure when dimerized, and an intracellular Toll/interleukin-1 receptor/resistance (TIR) domain, which elicits recruitment of specific adaptor proteins upon receptor ligand recognition and homodimerization (with exception of TLR2, which heterodimerizes with TLRs 1 or 6). There are currently six reported adaptor molecules recruited to the TIR/TIR interface of the dimerized receptors. These are Myeloid differentiation primary response 88 (MyD88), MyD88 adaptor-like (Mal; or TIRAP) [17], sterile-alpha and Armadillo motif containing protein (SARM) [18], TIR-domain-containing adaptor-inducing interferon-β (TRIF) [19], TRIF-related adaptor molecule (TRAM) [20] and B cell adaptor for PI3K (BCAP) [21]. These adaptor molecules signal via the MyD88-dependent or MyD88-independent signalling cascade.

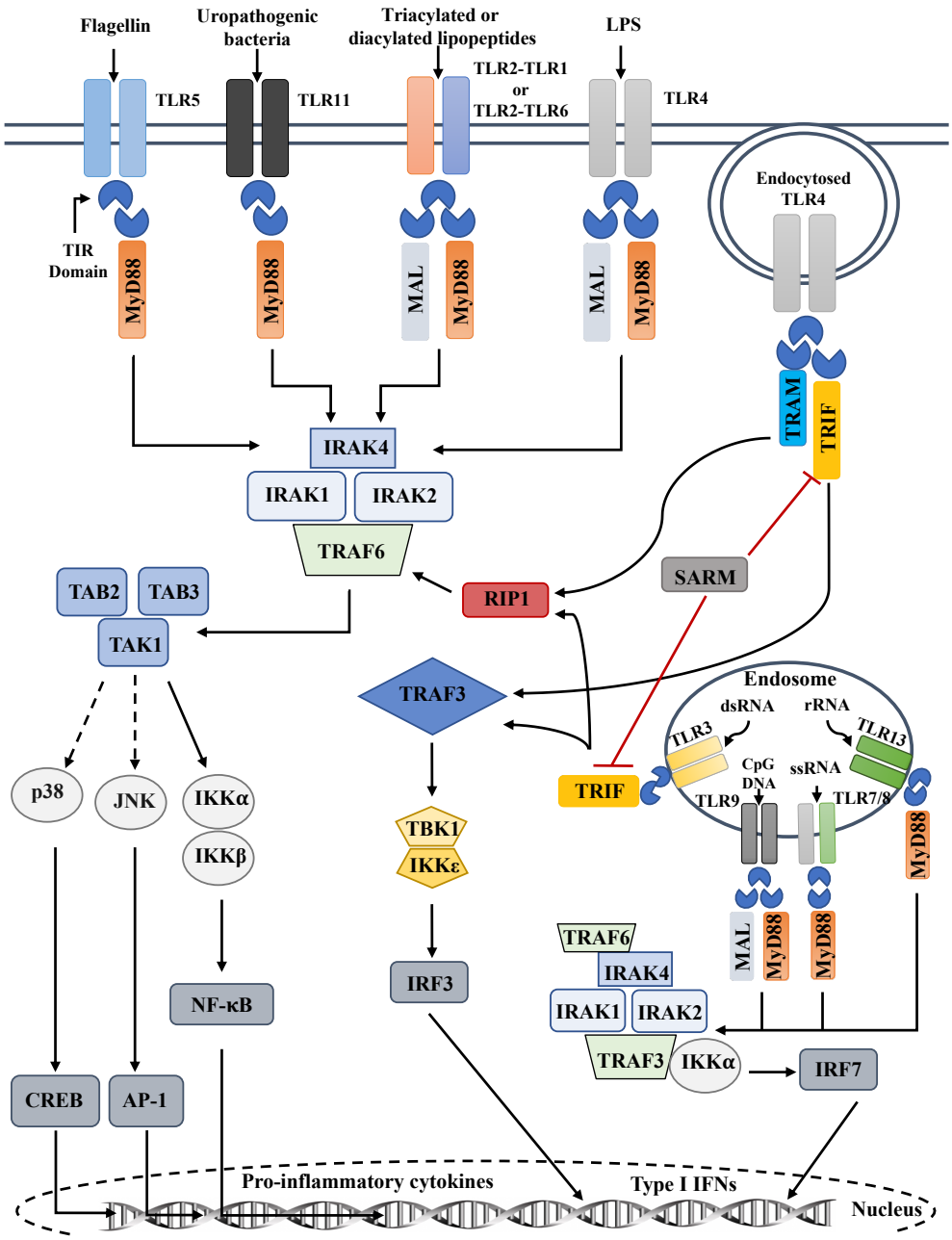

Figure 1.1 TLR pathway signalling schematic

Upon ligand binding, TLRs either homo/heterodimerise and recruit adaptors to their intracellular TIR domains. TLRs 2, 4 and 9 use Mal to recruit MyD88. Each TLR uses MyD88, with exception of TLR3, which recruits TRIF. MyD88 binding initiates assembly of the myddosome, activating TRAF6, leading to activation of TAK1 through ubiquitination, which activates the IKK complex, relieving inhibition of NF-κB subunits through IκBα degradation. TAK1 also drives MAPK signalling and CREB and AP-1 nuclear translocation. Endocytosed TLR4 drives IRF3 and delayed NF-κB activation through dimerization with TLR3, which is limited by SARM. TLRs 7, 8 and 9 drive myddosome assembly to drive anti-viral immunity.

1.1.4.1 MyD88

MyD88 is a canonical adaptor protein utilized by every TLR, with exception of TLR3. MyD88 was discovered in the early 1990's as an accessory molecule that had roles in IL-1R1 signalling [22], and was soon thereafter linked to TLR signalling [23]. MyD88 contains an N-terminal death domain (DD) and a C-terminal TIR domain, which upon TLR receptor dimerization promotes myddosome formation via other DD containing proteins, notably IRAK2 and IRAK4 to allow for formation of an oligomeric signalling complex. MyD88 uses Mal for TLRs 2, 4 and 9, but acts alone in driving TLR5 and TLR7 signalling. MyD88 is highly regulated and has recently been reported to undergo K63-linked polyubiquitination. The deubiquitinase enzyme CYLD was found to negatively regulate MyD88 signalling by removing ubiquitin at lysine 231 in MyD88 [24]. Interestingly, MyD88 can become NEDDylated, a post-translational modification in which a ubiquitin-like NEDD8 protein is conjugated to MyD88, and importantly, NEDDylation of MyD88 antagonises its ubiquitination [25]. IL-1β stimulation promotes MyD88 ubiquitination, and downregulating NEDDylation by the deNEDDylase NEDP1. Furthermore, NEDD8 prevents MyD88 dimerization, inhibiting NF-κB signalling. MyD88 also acts independently of TLR signalling, with roles identified in IFNγ signalling [26], and neuronal mouse models of ischemia/reperfusion [27], highlighting the importance of this adaptor in NF-κB activation.

1.1.4.2 TRIF

Early studies into MyD88 signalling discovered a few anomalies. MyD88-deficient mice were found to still drive delayed LPS-induced NF-κB and MAPK pathways, resulting in activation of interferon regulatory factor 3 (IRF3) and subsequent interferon-inducible genes [28]. This finding indicated that a MyD88-independent pathway must occur that was LPS responsive. TLR3 is localised to endosomes to detect viral dsRNA, and activation leads to upregulation of IRF3, and to a lesser extent, NF-κB to induce IFNβ responses [29]. Early studies identified that TLR3 signalling did not utilize Mal or MyD88, rather another adaptor protein was discovered, termed TRIF. TRIF was found to interact with TLR3 directly through its C-terminal [30]. Under TLR3 activation, TRIF was also shown to mediate the TLR4-dependent but MyD88-independent signalling cascade to promote NF-κB and IFNβ induction [31].

1.1.4.3 TRAM

In addition to interacting with TLR3, TRIF can also directly interact with TRAM through homologous TIR domain interactions. During TLR4 MyD88-independent activation, TRAM is

directly recruited to TLR4 and then promotes TRIF interaction. This interaction is necessary for activation of IRF3 in the MyD88-independent pathway [32]. TLR4 in this context promotes 'biased-signalling' as monophosphoryl lipid A (MPLA), a low toxicity derivative of LPS, preferentially drives TRIF-mediated TLR4 activation [33]. Ligand specificity of TLR4 may thereby directly impact TRAM recruitment. TRAM localises with TLR4 at the plasma membrane and in the Golgi apparatus by myristoylation, as a TRAM variant (TRAM-G2A) with a mutated myristoylation site does not localise in the membrane and is found in the cytosol [34]. TRAM is negatively regulated by transmembrane emp24 domain-containing protein 7 (TMED7), as knockdown of TMED7 increases cytokine RANTES [35]. TMED7 was shown to promote TLR4 trafficking from the ER through the Golgi, forming a stable complex with the ectodomain of TLR4 [36]. Interestingly, TMED7 depletion reduced MyD88-dependent TLR4 activation, however MyD88-independent TLR4 signalling remained functional, indicating a negative role for TMED7 during MyD88-independent TLR4 activation. LPS stimulation co-localises TMED7 with TRAM at late endosomes, where it can inhibit TRAM through the negative regulatory splice variant of TRAM, tram adaptor with GOLD domain (TAG) [37]. TRAM is also phosphorylated by PKCε on serine 16, driving LPS-mediated TRAM activation [38]. TRAM and TRIF have also been recently shown to signal from TLR2. TRIF or TRAM deficient macrophages were found to have decreased production of the chemokine CCL5 upon TLR2 stimulation, and furthermore TRAM co-localised with TLR2 in early endosomes, proposing this signalling event can occur from an intracellular compartment [39].

1.1.4.4 SARM

SARM was initially described as a TLR adaptor protein, however in recent years, many TLR-independent roles of SARM have been described, mainly in neuronal tissues, as mouse SARM plays a role in neuronal morphology and axon degeneration [40], [41]. SARM was discovered to inhibit TRIF in myeloid cells [42], placing SARM on the MyD88-independent pathway. Further myeloid cell roles for SARM have been elucidated, with SARM being required for optimal TLR-induced production of the macrophage chemokine CCL5 [43]. Interestingly, SARM deficient mice are protected from a form of neuronal degeneration termed Wallerian degeneration, whereby axon injury in response to damage or disease promotes localised clearance of damaged axons [44]. Recently, dimerization of the SARM TIR domain has been found to promote NAD^+ consumption, inducing neuronal degeneration [45]. This is the first non-scaffolding example of a TIR domain-containing adaptor protein. Further work is required to link TIR-dependent scaffolding roles of SARM to TLR signalling.

1.1.4.5 BCAP

BCAP is expressed in B cells, macrophages and Natural Killer (NK) cells and can negatively regulate inflammation via TLRs and NK cell receptors. BCAP was initially described as an adaptor protein, linking B cell receptor (BCR) signalling to PI3K-AKT pathway activation [46]. BCAP has been reported to contain a functional N-terminal TIR homology domain, connecting TLRs to PI3K activation. After B-cell activation, BCAP was found to be recruited to the BCR by Nck, a cytoskeleton regulatory protein. Nck bound to the BCR via the non-immunoreceptor tyrosine-based activation motif (ITAM) phosphorylated tyrosine residue at position 204. Ablation of Nck resulted in decreased B cell survival and antibody responses *in vivo* [47]. BCAP can also negatively regulate cytokine expression, and furthermore BCAP deficiency *in vivo* worsens dextran sodium sulphate (DSS)-induced colitis [48].

1.1.5 Mal

A major focus of this thesis is Mal, which was discovered independently in the early 2000's by Horng et al. [49] and Fitzgerald et al. [17]. Mal is also known as TIR-domain containing TLR adaptor protein (TIRAP), however it shall be referred to as Mal in this text. Following its initial discovery, Mal was quickly identified as a bridging adaptor between TLR4 and MyD88 [50], [51]. Mal also bridges TLR2 to MyD88 and has been recently shown to signal from TLR7 and TLR9, revealing a broader role for Mal in TLR signalling [52] [53].

1.1.5.1 Mal structure

The crystal structure of the Mal-TIR domain was resolved in 2011 to 3.0 Å, highlighting differences between previously crystallised TIR-domains of MyD88 [54], IL-1 receptor accessory protein-like 1 (IL-1RAPL) [55], TLR1, TLR2 and TLR10 [56]. Mal-TIR does not contain the canonical BB loop found in each TIR domain, instead Mal contains an AB loop that is structurally distinct (Figure 1.2) [57]. The Mal-TIR domain was further resolved in 2012 by Lin et al. to 2.4 Å, confirming the extended AB loop and furthermore, the extending AB loop of a Mal homodimer binds both TIR domains of TLR4 and MyD88 simultaneously [58]. Further analysis into the structure of Mal by Bovjin et al. identified the AB loop as the binding interface for TLR4 and MyD88 binding, using MAPPIT (mammalian protein-protein interaction trap), a mammalian yeast two hybrid method [59]. These studies have highlighted a crucial scaffolding role of Mal in bridging both TIR domains of TLR4 and MyD88 for signal transduction and furthermore the atypical AB loop as a critical interface for Mal activity. Recently, Mal has also been found to form filaments *in vitro* and furthermore, Mal filaments co-form with filaments

from the TIR domains of TLR4 and MyD88, identifying a highly conserved interaction complex [60].

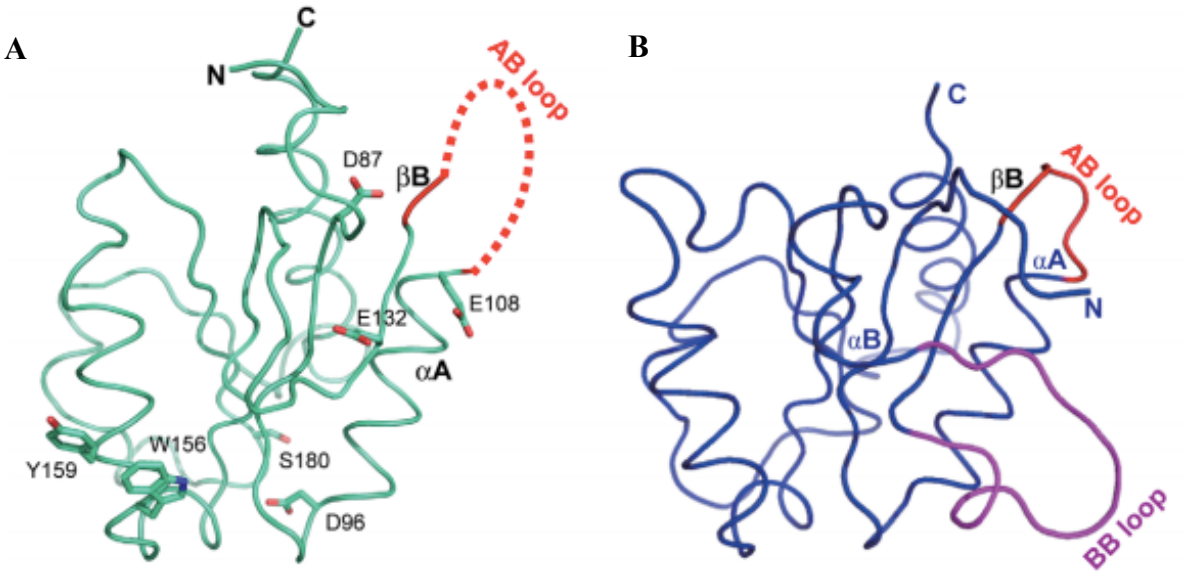

Figure 1.2 Comparison of the TIR domains of Mal and MyD88 determined by X-ray crystallography

The TIR domain of Mal (A) contains an extended loop between the αA and βB region. In comparison, the TIR domain of MyD88 (B) contains a short canonical AB loop between αA and βB as seen in other TIR-containing adaptors. MyD88 also has a BB loop, which is seen in the X-ray crystallography structure. This image was modified from [58].

1.1.5.2 Mal signalling

Insight into the structure of Mal has elucidated the mechanism by which Mal can simultaneously bridge both TLR4 and MyD88. Mal however, has also recently been identified as an endosomal adaptor, associating with TLR9 by altering its lipid binding specificity [53]. Mal contains a phosphatidylinositol 4,5-bisphosphate (PIP2) binding domain, which upon TLR stimulation can associate with the cell membrane to promote TLR4 signalling. This anchoring effect spatially localises Mal with the TIR domains of TLR4. Mal can also interact with the PI3K class 1A p110δ isoform, which converts PIP2 to PIP3, thereby causing Mal to dissociate from the membrane [61]. To link Mal to TLR9 activation, Bonham et al. cleverly created Mal mutants with variable PI binding domains. Using this approach, they discovered the PI specificity required for Mal signalling from either TLR4 or TLR9. [53]. By replacing the endogenous lipid-binding domain of Mal with a pleckstrin homology domain specific to binding to PI(4,5)P2, they identified that Mal co-localised at the plasma membrane exclusively. Similarly, they also generated a PI(3)P-specific Mal which contains the localization domain of p40-phox, which binds exclusively to PI(3)P on endosomes [62] and SLP2a-Mal, which binds phosphatidylserine (PS). PS is generally found in both cell surface and endosomal membrane compartments and aids trafficking through endosomes [63]. PI(3)P-Mal and SLP2a-Mal were TLR9 responsive with CpG and bound exclusively to endosomes, however PI(4,5)P2-Mal signalled from TLR4 when stimulated with LPS and was exclusively plasma membrane bound. Complementing this finding, Zhao et al. linked the mechanism of Mal membrane dissociation to the PI binding domain (PBM). Phosphorylation of the PBM on Thr28 induced disorder in the helical region of Mal, distorting membrane interactions to limit TLR4 activation [64].

Interestingly, the requirement for Mal in TLR2 signalling remains questioned. Kenny et al. identified that Mal was not required for TLR2 signalling at high ligand concentrations, and furthermore inhibited TLR3 responses [65]. Using synthetic TLR2 agonists Pam3CSK4 (TLR1/2) and macrophage-activating lipopeptide-2 (Malp-2) (TLR2/6), Mal deficient cells had no impairment in signalling. Mal may however, be utilized by TLR2 at low ligand concentrations, as Kenny et al. showed TLR2 stimulation at low ligand concentrations drove the cytokine IL-6 and NF-κB induction in a Mal-dependent manner. This finding was validated by Cole et al. demonstrating Mal-independent TLR2 responses to *Francisella tularaemia* through phagosomal retention [66]. TLR4-driven Mal can also interact with TRAF6 to activate cAMP response element binding protein (CREB) upon LPS stimulation, driving IL-10 production via signalling through Pellino3, p38, MAPK and MK2, independently of NF-κB [67].

A decoy peptide generated from helix D of the TLR2 TIR domain, termed 2R9, has also been found to have potent anti-inflammatory effects through negative targeting of Mal. 2R9 was found to specifically bind to Mal, limiting signalling from TLRs 2, 4, 7 and 9, firmly placing Mal on the TLR9 pathway [52].

TLR-independent roles for Mal have also been studied. Mal has recently been reported to interact with the IFNγ receptor and is required for IFNγ signalling. A well-characterized single nucleotide polymorphism (SNP) which converts serine at position 180 to leucine (S180L) in Mal has been found to promote susceptibility to bacterial infection and decreased cytokine production in response to TLR2 activation. The S180L variant was unable to interact with the IFNγ receptor [68]. Mal promiscuity is summarised in Figure 1.3.

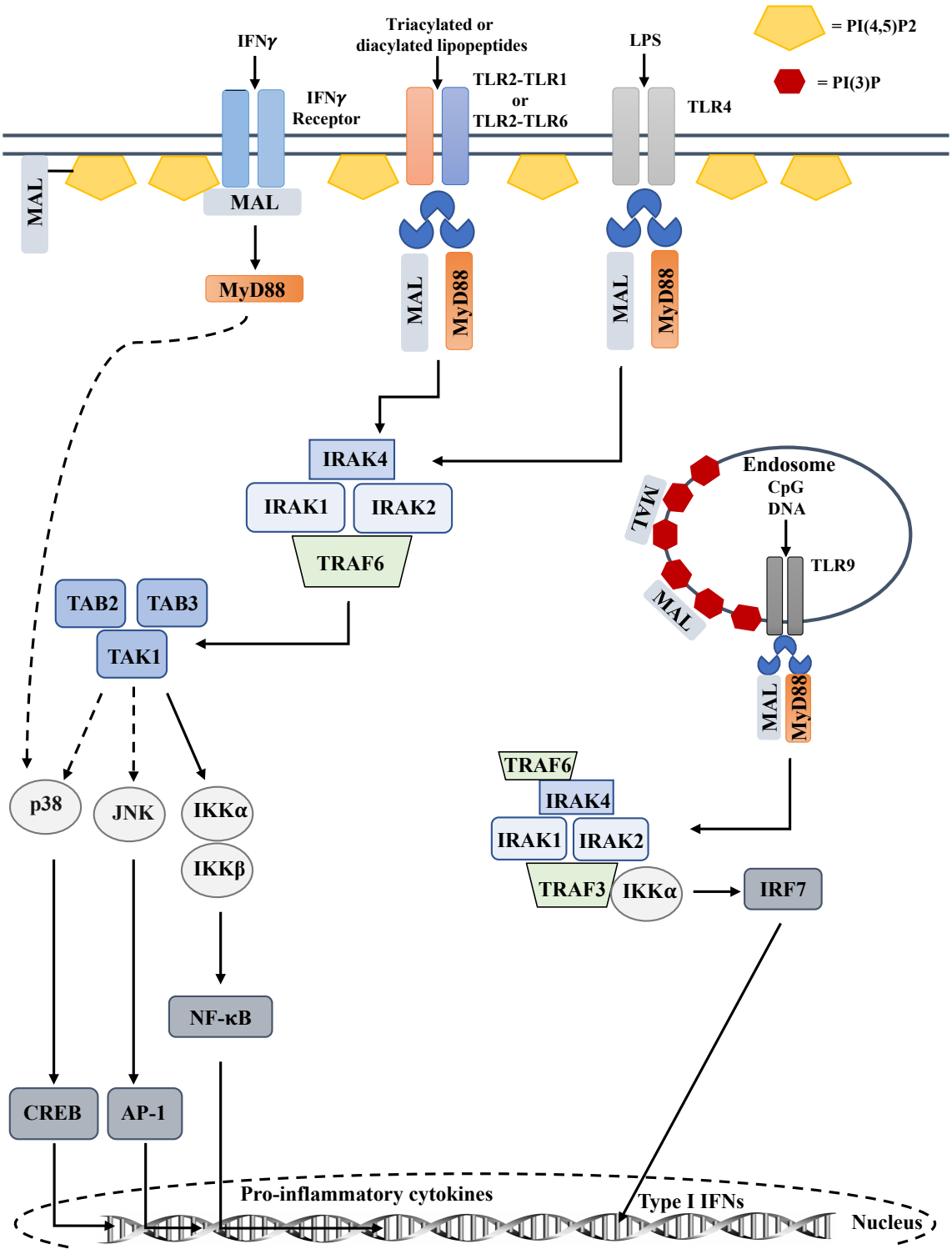

Figure 1.3 Promiscuity of TLR adaptor Mal

Mal can signal from the IFNγ receptor to drive p38 activation, which can drive responses to *Mycobacterium tuberculosis* infection [53]. Mal is used by TLRs 2, 4 and has recently been shown to signal from TLR9. Mal signals from the cell membrane when bound to PI(4,5)P2 phospholipid motifs. Mal can also signal from TLR9 when bound to endosomal-rich PI(3)P motifs to drive myddosome assembly for anti-viral responses.

1.1.5.3 Post-translational regulation of Mal

Post-translational modifications of Mal have been well-studied. Mal requires phosphorylation by Bruton's tyrosine kinase (Btk) on tyrosine 86, 106 and 187 to elicit TLR2 and TLR4 downstream signalling [69]. Both IRAK1 and IRAK4 have been found to phosphorylate Mal on threonine 28, resulting in Mal polyubiquitination and proteasomal degradation [70]. Negative regulation of Mal also occurs by suppressor of cytokine signalling 1 (SOCS1), which mediates polyubiquitination of Mal [71]. Further, cytoplasmic linker protein 170 (CLIP170) has been recently identified as a novel Mal regulator. CLIP170 induces Mal polyubiquitination and subsequent degradation, limiting production of IL-6 and TNFα [72].

Caspase-1 is the executioner Caspase involved in processing of the pro-inflammatory cytokines pro-IL-1β and pro-IL-18 to mature cytokines to drive inflammation [73]. Caspase-1 has been reported to cleave Mal at position D198, resulting in release of a 4kDa fragment that may open a binding domain for MyD88 [74]. The requirement for Mal cleavage however, remains disputed. In 2010, Ulrichts et al. confirmed Mal and Caspase-1 interaction, however the cleavage event does not promote NF-κB signalling, rather inhibits Mal function [75]. Mal is thereby highly regulated to prevent aberrant TLR activation, possibly to dampen cytokine production (Figure 1.4).

Bacterial infection employs complex mechanisms to subvert host defences for colonization and dissemination. Targeting TLR components using protein mimics to the Mal TIR domain have been reported to promote Mal polyubiquitination [76] and degradation [77], promoting bacterial colonization [78]. *Brucella* has been shown to produce a protein mimic, TcpB, which binds to the TIR domain of Mal, resulting in Mal degradation, subverting TLR signalling. Mal is essential for bacterial clearance, as Mal-deficient mice have higher bacterial burden in the lung, and are unable to clear *E. coli*, *Klebsiella pneumoniae* and *Bordetella pertussis* infection [79], [80] resulting in bacterial dissemination to the spleen and premature mortality. Interestingly, Mal was not required for host defence in a model involving intraperitoneal infection with *Salmonella typhimurium*. However, Mal-deficient mice had an increased susceptibility to orally-given *S. typhimurium* [81]. Mal was shown to be required for intestinal barrier integrity, as Mal-deficient mice have increased mucosa blood permeability and altered expression of occludins and claudin-3. Mal can also interact with several protein kinase C (PKC) isoforms, and inhibition of PKC or Mal promoted bacterial invasion due to increased permeability. A global PKC inhibitor was also shown to increase susceptibility to orally given bacteria in mice.

Interestingly, a link between Mal deficiency and adaptive immune response compensation has been identified in a small family of seven individuals. This family presented with a missense mutation in Mal, limiting TLR2 and TLR4 responses, however only one family member presented with a high susceptibility to *Staphylococcus aureus* infection [82]. Israel et al. were able to restore IL-6 production from whole blood of the healthy Mal-deficient individuals using lipoteichoic acid (LTA), the staphylococcal TLR2 agonist. This finding suggested a plasma component could restore TLR2 signalling in response to *S. aureus* infection. The six-healthy patients were found to produce an anti-LTA antibody in their serum. Similar to the effects observed by Kenny et al. [83], TLR2 signalling was restored in the initial unhealthy Mal-deficient patient, using an anti-LTA antibody, allowing prolonged exposure of high ligand concentrations to circumvent the requirement for Mal in TLR2 signalling. Whilst the mechanism for why the individual with Mal deficiency who had chronic *S. aureus* infection remained unanswered, this finding highlights how the adaptive immune system can rescue Mal deficiency through production of sustained ligand concentrations to restore cytokine production, circumventing Mal deficiency. Mal is thereby highly regulated by many distinct pathways and can be subverted during infection.

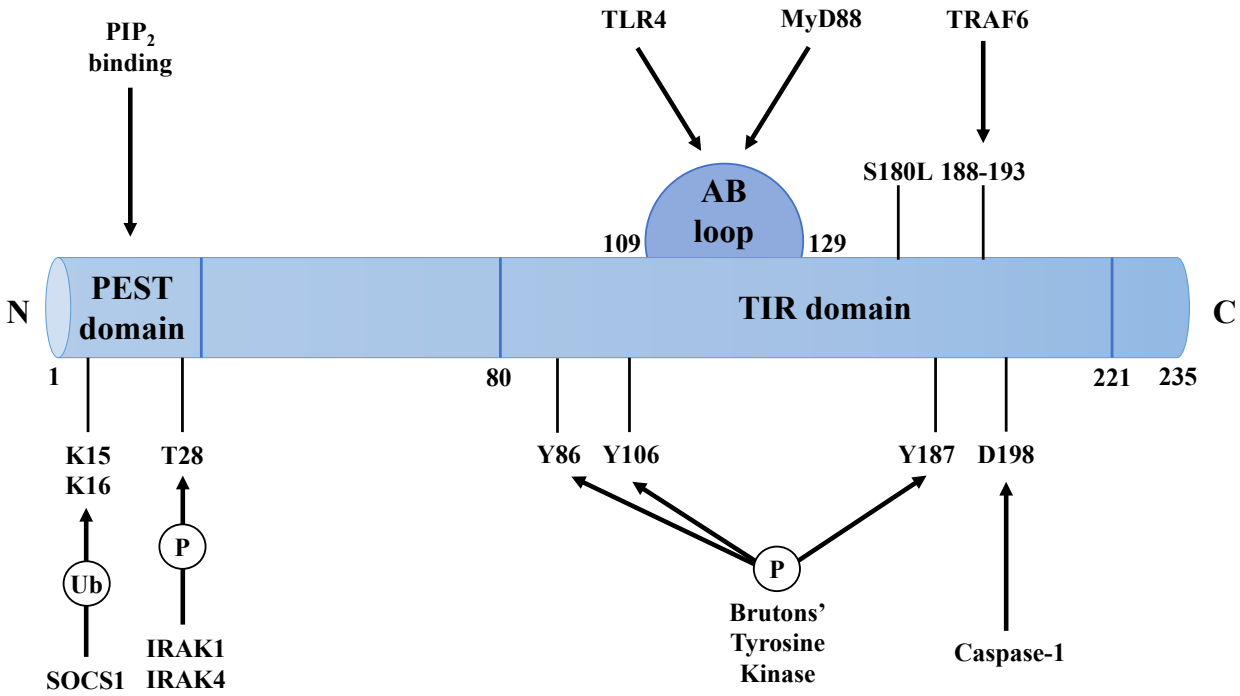

Figure 1.4 Post-translational regulation of Mal

Mal contains an N-terminal PEST (proline, glutamate, serine threonine) motif, and N-terminal PIP_2 binding. Mal is negatively polyubiquitinated by SOCS1 on K15 and K16. IRAK1 and IRAK4 phosphorylate Mal on T28, promoting membrane dissociation and polyubiquitination. Bruton's tyrosine kinase positively phosphorylates Mal on Y86, Y106 and Y187. Caspase-1 cleaves Mal on D198, producing a 4kDa fragment. Mal contains an atypical 'AB' loop motif and binds MyD88 and TLR4. TRAF6 also binds to Mal between position 188-193. This schematic is adapted from [84].

2.1 Redox biology

This project concerns the redox regulation of Mal during TLR4 signalling and I will now give an overview of how reactive oxygen species (ROS) impact on protein function, via modification of cysteines as well as the enzymes that control this process. The cytoplasm of an activated phagocytic cell is a dangerous place due to the accumulation of reactive molecules, such as ROS and reactive nitrogen species (RNS), which can perturb cytoplasmic oxidative balance and confer damaging post-translational modifications on cellular machinery [85]. ROS and RNS are physiologically relevant molecules, being produced as a by-product of cellular metabolism and from professional ROS generators, such as the NAPDH oxidases [86]. Due to the constant presence of these molecules intracellularly, they are continuously scavenged and eliminated by our antioxidant defence system. Oxidative stress occurs when the balance between generation and elimination of endogenous ROS is disturbed, thereby overwhelming our cellular antioxidant defence system, promoting oxidation of protein machinery, leading to cell dysregulation [87]. Thiol groups on cysteine amino acids are the most susceptible amino acids to oxidation and can be post-translationally modified by ROS [88]. Our cells therefore have many safeguards to prevent aberrant oxidation of cellular machinery. Constant monitoring of the redox environment involves glutathione and redox sensitive enzymes such as glutathione transferases (GSTs), superoxide dismutases, peroxidases and catalases [89].

2.1.1 Irreversible redox post-translational modifications

2.1.1.1 Oxidation and Sulfenylation

Due to the presence of a thiol group side chain, cysteine amino acids are the most susceptible to oxidative damage and can thereby act as intracellular ‘sensors’ to oxidative insults. The cysteine thiol has a net charge of –II, which is termed its oxidation state [90]. Thiol groups are influenced by the pKa of neighbouring amino acids and their own thiol group is usually in equilibrium with its own deprotonated thiolate form ($Cys\text{-}S^-$) [91]. Cysteines are also structurally important in proteins as they form disulphide bonds to maintain protein tertiary structure [92]. Due to the presence of a thiol group, cysteine is readily oxidized to cystine, a cysteine dimer. Excessive ROS can promote the formation of thiol intermediates on cysteines, termed sulfenic acid, sulfinic acid and sulfonic acid in proteins [93]. Over-oxidation of cysteine residues to sulfonic acid is irreversible and will promote proteasomal degradation. Glutathione can reverse the formation of sulfenic and sulfinic acid in conjunction with reductase (sulfenic) or sulfiredoxin (sulfinic) enzymes resulting in regeneration of native protein structure and generation of nontoxic intermediates as a by-product, such as H_2O. Sulfenic acids are initially formed on cysteine thiols due to direct interaction with predominantly hydrogen peroxide [94].

Not all thiols however, are susceptible to sulfenic acid formation, as this is dictated on the thiolate form of cysteine, which is more nucleophilic and thereby more susceptible to oxidation [91]. GSH is thereby a key player in maintaining cysteine redox homeostasis, preventing over-oxidation of protein thiols. A representation of redox modifications discussed below is shown in Figure 1.5.

2.1.2 Reversible redox post-translational modifications

2.1.2.1 Sulfenylamide

A less well known post-translational modification of cysteine thiols is sulfenylamidation, or the formation of a sulfenylamide intermediate. One of the best characterized examples of sulfenylamide formation is on Protein Tyrosine Phosphatase 1B (PTP1B), a cysteine-dependent highly redox sensitive enzyme that negatively regulates insulin signalling. PTP1B is directly inhibited by hydrogen peroxide, promoting insulin secretion [95], [96]. After sulfenic acid formation on PTP1B, the newly formed sulfenic acid was shown to further react with a neighbouring amide nitrogen, yielding a cyclic sulfenylamide. This formation is considered a 'redox switch', as the newly formed sulfenylamide can be rapidly reversed back to the catalytically active thiol form of PTP1B via interaction with other biological thiols. Notably, this modification has been observed for other proteins, indicating that this process may occur in cells as a redox switch [97], [98].

2.1.2.2 Sulfhydration

Hydrogen sulphide (H_2S) is an organic molecule found in the body attributed as the most physiological vasorelaxant [99], [100]. Interestingly, mice deficient in the enzyme that produces H_2S, cystathionine γ-lyase (CSE), are hypertensive [101]. H_2S is reported to form a persulphide bond (R-SSH) on cysteines, and some proteins have been identified to be sulfhydrated, including GAPDH and actin [102]. Mice deficient in CSE have an imbalanced oxidative stress environment, due to reduction in the levels of cellular glutathione [103], and CSE is depleted in Huntington's Disease tissues, suggesting CSE depletion as a pathological mechanism [104]. H_2S has also been reported to affect the DNA binding ability of NF-κB. Sulfhydration of cysteine 38 in the p65 subunit of NF-κB increased the anti-apoptotic activity of NF-κB in mice treated with TNFα, as TNF drives H_2S formation [105]. Interestingly, GAPDH sulfhydration was shown to play a role in the response of neurons to IL-1β treatment. IL-1β promotes neuronal damage and memory impairment, and H_2S was found to promote this effect. An increase in CSE-mediated H_2S production promoted GAPDH sulfhydration, causing

GAPDH to interact with an E3 ubiquitin ligase, Siah [106]. The GAPDH-Siah complex interacted with PSD95, a synaptic scaffolding protein, causing E3-linked polyubiquitination, resulting in PSD95 proteasomal degradation. The decrease in PSD95 in mice promoted IL-1β mediated neuronal damage.

2.1.2.3 Nitrosylation

Cysteine thiols are also susceptible to post-translational modification by RNS, modifying thiol groups to nitrosothiol (-SNO). Little is known about the mechanism by which RNS regulates proteins. RNS has been linked to regulation of ion channels, enzymatic modulation of kinases, oxidoreductases and phosphatases in inflammatory conditions [107], [108]. The removal of the nitrosylated group from thiols has been predominantly shown to be catalysed by the thioredoxin reductase system of enzymes. Interestingly, exogenous compounds, such as S-nitrosoglutathione (GSNO) can promote nitrosylation or glutathionylation of thiol groups. Many factors can influence the possibility of the thiol group being either nitrosylated or glutathionylated, including pKa differences and neighbouring amino acid charges [109]. The parameters which can promote thiol post-translational modifications will be discussed in detail later.

2.1.3 Glutathionylation

Glutathione (γ-L-glutamyl-L-cysteinyl-glycine; GSH) is the fundamental non-protein tripeptide redox agent that detoxifies ROS. Composed of the amino acids glutamate, cysteine and glycine, GSH is utilized within the cell to maintain redox homeostasis [110]. Overproduction of ROS can target the thiol group of cysteine amino acids on proteins. GSH can prevent oxidation of proteins via formation of mixed disulphides to redox-sensitive cysteine amino acids in proteins [111]. Cells contain a variety of redox enzymes, such as glutathione transferases and glutaredoxins, which utilize GSH to detoxify ROS and maintain protein integrity. GSH is predominantly found in the thiol-reduced form, reaching intracellular concentrations of up to 10mM [112], and the ratio of reduced GSH to oxidized GSH (termed GSSG) can be used as a measure of cellular oxidative imbalance [113]. GSH may however not be limited to antioxidant defence, with post-translational modifications placing GSH as both a positive and negative regulator of protein function. GSH is ubiquitously expressed in all cell types and tissues. Aside from cellular detoxification, GSH is also a source of readily accessible cysteine, a rate-limiting amino acid for many cellular processes, including synthesis of GSH itself. The amino acid cysteine is also crucial for maintaining protein tertiary structure via disulphide bond formation [114], [115] and depending on the environment it is in, is highly

redox sensitive. High levels of GSH may thereby have a dual role in acting as a cysteine storage pool for physiological use as well as oxidative defence.

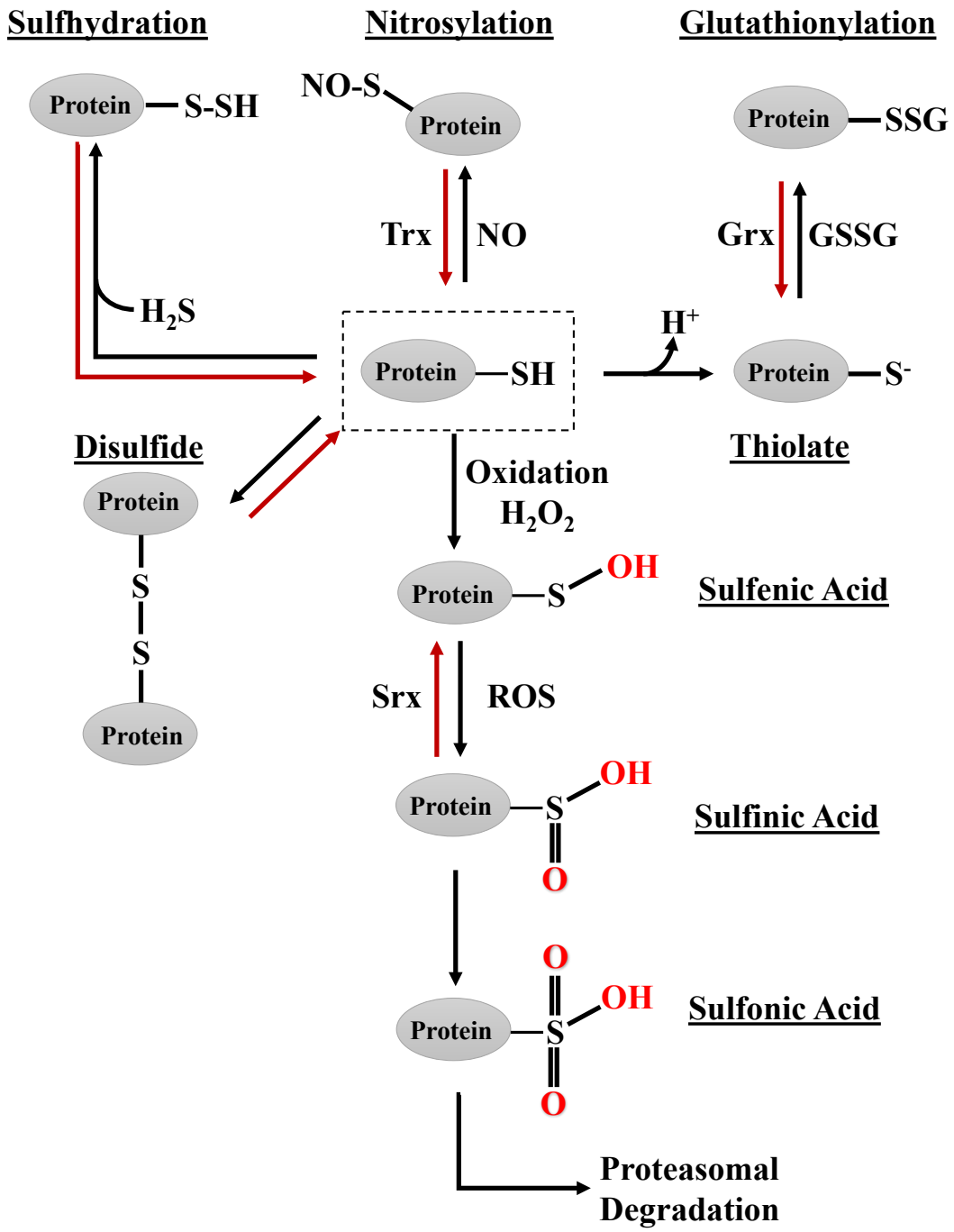

Figure 1.5 Redox mechanisms controlling protein oxidation

Proteins containing solvent accessible thiols are susceptible to oxidative stress. Thiol groups can become sulfhydrated (H_2S), nitrosylated (NO), or glutathionylated (SSG) in response to oxidative stress. Oxidation can also induce disulfide bond formation. Over-oxidation of proteins can lead to reversible forms of thiol oxidation states. Sulfenic and sulfinic acid formation can be reversed by redox enzymes including reductase and sulfiredoxins, respectively. Over-oxidation to sulfonic acid is irreversible and leads to proteasomal degradation.

2.1.3.1 Glutathione synthesis

GSH is synthesized in a two-step enzymatic process requiring ATP at each step to generate GSH from the amino acids glutamate, cysteine and glycine. The chemistry of GSH is interesting to note, as GSH is resistant to proteolytic cleavage due to the bond between glutamate and cysteine. Departing from the conventional α-carbonyl group bond between amino acids, glutamate and cysteine form a γ-carbonyl group bond. This minor bonding change prevents GSH degradation by conventional mechanisms. Surprisingly, only one enzyme can hydrolyse such a bond, called γ-glutamyltranspeptidase (GGT), which exists extracellularly and cleaves GSH into γ-glutamylamino acid and cysteinylglycine. Cysteinylglycine is further hydrolysed by dipeptidase (DP) into cysteine and glycine and can be imported back into the cytoplasm via amino acid transporters. Before GSH can be regenerated however, γ-glutamylamino acid must be converted to 5-oxoproline, a glutamate precursor. 5-oxoprolinase can subsequently convert 5-oxoproline to glutamate. The rate-limiting step in GSH synthesis occurs via the enzyme glutamate cysteine ligase (GCL), which reacts glutamate with cysteine to form γ-glutamylcysteine. Cysteine is the rate-limiting amino acid in this process and can prevent GSH synthesis if relative abundance is low. Lastly, GSH synthase catalyses the formation of GSH in the cytosol via bonding of γ-glutamylcysteine and glycine. Upon exposure to oxidative stressors such as superoxide or hydrogen peroxide, GSH scavenges ROS and forms GSSG, which can be recycled in the cytoplasm to reduced GSH by glutathione reductase (Figure 1.6).

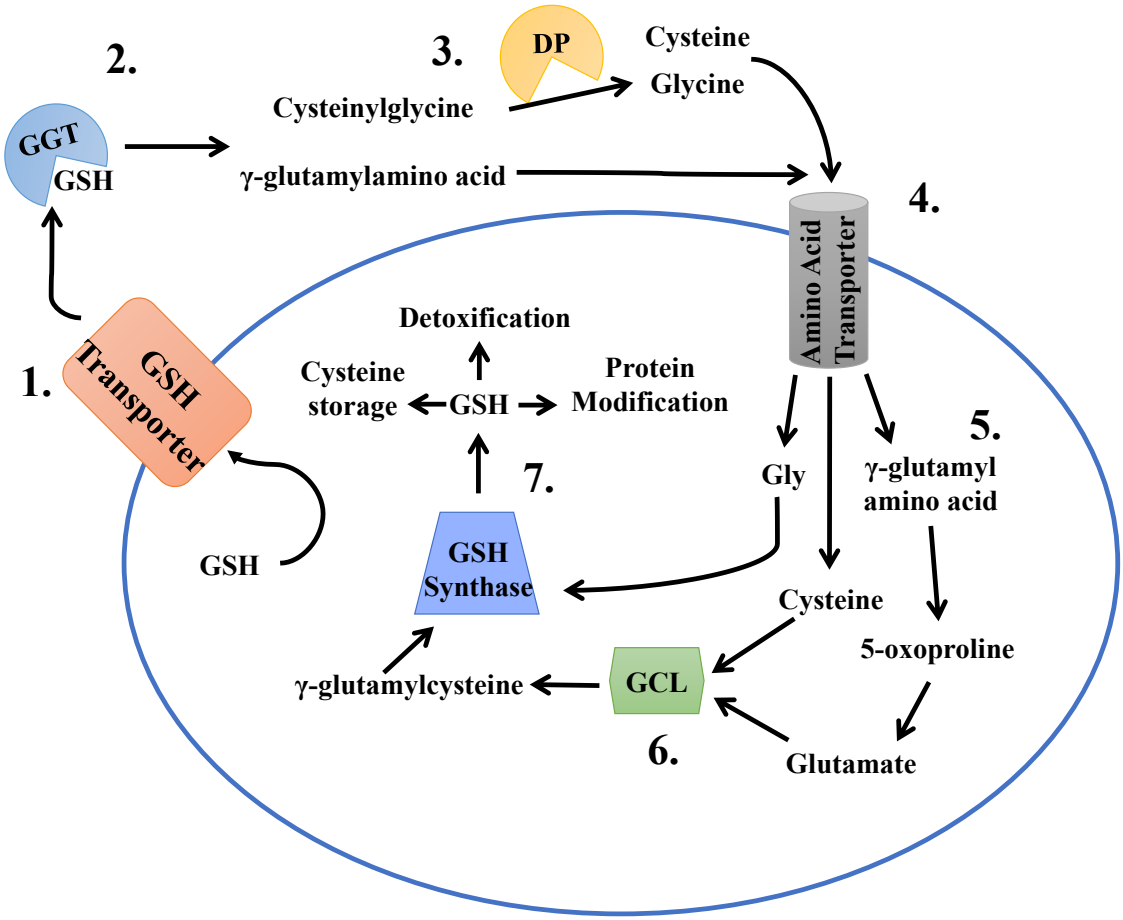

Figure 1.6 GSH synthesis

GSH is exported from the cell to the extracellular environment via a glutathione transporter (1). Extracellular GSH is targeted by γ-glutamylpeptidase (GGT), transferring the γ-glutamyl component of GSH to an amino acid, forming γ-glutamylamino acid and cysteinylglycine (2). Cysteinylglycine is further cleaved by dipeptidase (DP) into the amino acids cysteine and glycine (3). Transport of the GSH breakdown products re-enters the cell via an amino acid transporter (4). Release of the amino acid component of γ-glutamylamino acid forms 5-oxoproline, which is further converted to glutamate in an ATP-dependent process (5). Newly formed glutamate and cysteine are ligated into γ-glutamylcysteine via glutamate cysteine ligase (GCL) in an ATP-dependent process (6). γ-glutamylcysteine and glycine are ligated via GSH synthase to reform GSH (7).

2.1.4 Enzymes involved in glutathionylation

2.1.4.1 Glutaredoxin

The glutaredoxins are a small family of enzymes consisting of one hundred amino acids involved in glutathione conjugation reactions. Considered to be a part of the thioredoxin family, which will be discussed later, due to the presence of a canonical thioredoxin fold domain, they contain structural elements unique to the glutaredoxins. Glutaredoxins can catalyse 'monothiol' or 'dithiol' reactions based on their active site motif 'CXXS' or 'CXXC', respectively [116]. Monothiol reactions are commonly used by glutaredoxins to deglutathionylate substrates. The N-terminal region of glutaredoxins containing the thiol group attacks the substrate in a nucleophilic attack, deglutathionylating the substrate of interest and results in the formation of glutaredoxin-GSH intermediate (Figure 1.7). Glutaredoxin differs from thioredoxins in that glutaredoxins can then be recycled non-enzymatically by one molecule of GSH to GSSG [117]. Dithiol reactions are not as efficient as monothiol reactions, due to the presence of a second cysteine active site residue, which can form a disulphide bond and decrease enzymatic efficiency of glutaredoxin [118].

2.1.4.2 Thioredoxin

Thioredoxins are a highly conserved class of small thermostable enzymes consisting of an active site 'CXXC' motif. Thioredoxins retain structural similarity to glutaredoxins, however their substrate specificity is highly variable [119]. Interestingly, thioredoxin has been reported to have anti-inflammatory properties owing to its role in detoxification, and a truncated version of thioredoxin, (Trx-80), has been reported to drive pro-inflammatory M1 macrophage polarization, enhancing atherosclerosis [120]. This class of enzymes shares up to 69% sequence similarity with *E. coli* thioredoxin [121], however each thioredoxin has been reported to differ in activity, owing to the variation in their 'thioredoxin-fold'. Indeed, many enzymes have been reported to contain the thioredoxin-fold, including the Glutathione Transferases (GSTs).

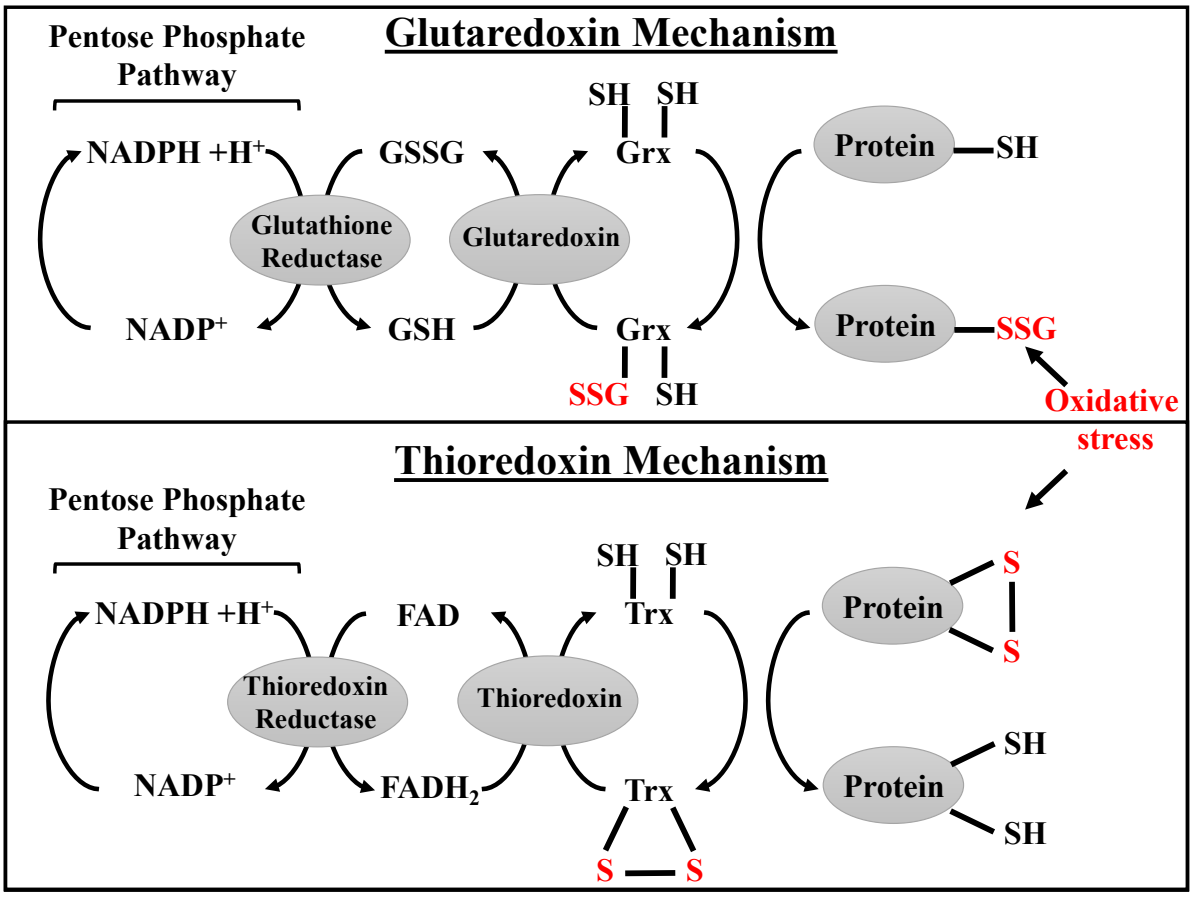

Figure 1.7 Regulation of glutaredoxin and thioredoxin mechanisms

Oxidative stress on proteins promotes glutathionylation and disulfide bond formation. Glutaredoxins catalyse the removal of –SSG in a monothiol mechanism, which can be converted to GSSG. GSSG can be further converted back to two molecules of GSH by Glutathione reductase, utilizing NADPH produced from the Pentose Phosphate Pathway. Similarly, thioredoxins can revert oxidative stress on proteins using $FADH_2$ as a cofactor. Thioredoxin reductase also uses NAPDH generated from the Pentose Phosphate Pathway to regenerate $FADH_2$.

2.1.5 Glutathione transferases

Glutathione transferases (previously termed Glutathione-S-transferases) play a critical role in the regulation of cellular responses as phase II detoxification enzymes expressed in many organisms. Seven classes of GST have been identified, termed alpha (α), mu (μ), pi (π), sigma (σ), theta (θ), omega (ω) and zeta (ζ), each class containing up to several isoforms [122]. GSTs can be further categorised into three classes, cytosolic, mitochondrial and microsomal (termed MAPEGs). Each class of GST can form functional dimers, by either homo- or heterodimerising. Each GST contains a similar structure, with an N-terminal site that binds glutathione (G-site) and a hydrophobic C-terminal site (H-site) that binds hydrophobic substrate [123]. Two GST classes of enzymes have been studied extensively in cancer and inflammation, namely GST pi and GST omega.

2.1.5.1 Glutathione transferase pi

GSTP has been found to be overexpressed in many drug-resistant cancer cell lines, and is therefore an interesting target in chemotherapy treatment [124]. Indeed, GSTP1 has recently been identified as an inducer of triple-negative breast cancer by regulating glycolytic metabolism by interaction with glyceraldehyde-3-phosphate dehydrogenase (GAPDH) activity. Pharmacological inhibition of GSTP in these cells impairs tumorigenesis, highlighting the importance of a glutathionylating enzyme in disease progression [125]. GSTP contains an active site tyrosine residue, which deprotonates GSH into the thiolate form, promoting interaction with an electrophilic substrate [126] . Interestingly, GSTP auto-glutathionylates itself on two cysteines, C47 and C101 [127], which influences the monomeric structure of GSTP, further altering the tertiary structure. This alteration may thereby promote protein interactions with GSTP, as GSTP has been shown to regulate JNK by associating with JNK in unstressed cells. It is conceivable that glutathione can limit this interaction, as Adler et al. identified that UV irradiation or H_2O_2 treatment dissociated GSTP from JNK, which may possibly recruit glutathione to GSTP, altering its tertiary structure by binding C47 and C101, releasing JNK [128]. GSTP has also been shown to play a role in macrophages. LPS treatment has been reported to upregulate GSTP in Raw267.4 cells, inhibiting MAPK, JNK and NF-κB signalling [129]. Further work is required to fully elucidate the role of GSTP in signalling.

2.1.5.2 Glutathione transferase omega

Board et al. originally discovered GSTO1-1 through the Expressed Sequence Tag (EST) database. GSTO1-1 is a particular focus of this study. GSTO1-1 was subsequently cloned and structurally resolved to 2Å [130]. This initial study identified that GSTO1-1 had key variances

from the other characterized GST classes. Most notable, was the effector functions of GSTO1-1 that include thiol transferase activity and dehydroascorbate reductase activity, both of which are characteristic of glutaredoxins. GSTO1-1 contains structural elements separate to the canonical GST fold (Figure 1.8). The active site cysteine residue C32 is found in the N-terminal extension in the α1 region, a placement that has been identified as a motif for glutaredoxins and thioredoxins. These different enzymatic activities make the GSTO class of GSTs interesting targets for enzymatic inhibition, as the GSTO class has been linked to pathogenesis of neurodegenerative disorders, including Alzheimer's Disease [131].

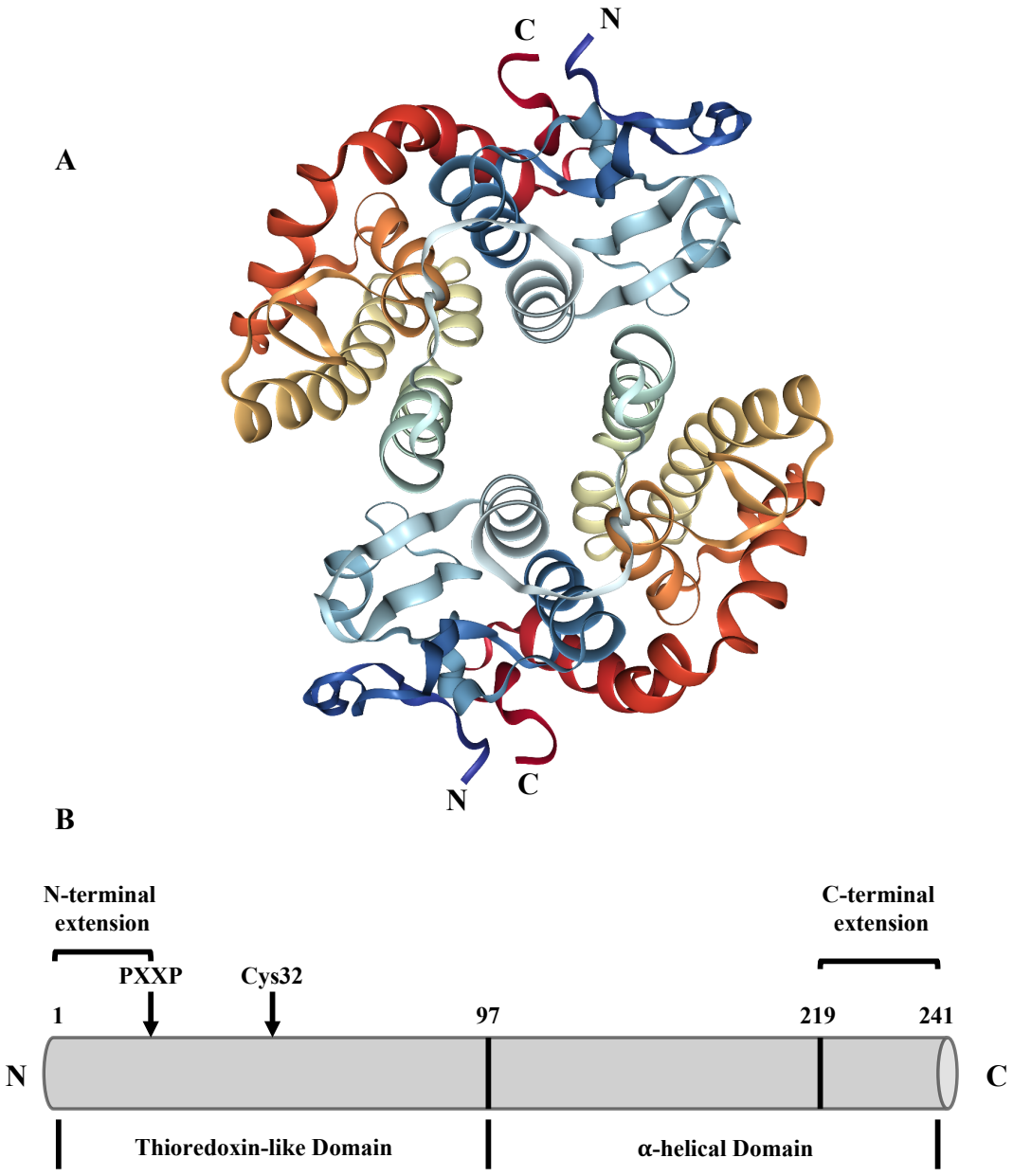

Figure 1.8 GSTO1-1 structure

Structure of GSTO1-1 homodimer. N-terminal regions are highlighted in navy blue and C-terminal regions are highlighted in red. Helices are shown as cylindrical structures and β-strands are shown as curved arrows. Helices and β-strands are variable in colour for differentiation (A). A simplified diagram of GSTO1-1, highlighting the thioredoxin-like domain containing the PXXP motif and active site C32 residue, and the α-helical domain (B). The structure of GSTO1-1 was modified from [130]; PBD: 1EEM.

2.1.5.3 GSTO1-1 structure and function

There are three GSTO genes, GSTO1 and GSTO2 are expressed on chromosome 10, whereas the third gene on chromosome 3 is a pseudogene. GSTO1-1 denotes the functional homodimer and will be referred to as GSTO1-1 hereon. GSTO1-1 has two structural domains, a GSH-binding domain termed G site, which binds glutathione, and a substrate-binding domain, termed the H-site [130]. GSTO1-1 was also found to have an atypical opening, forming a V-shape that is more exposed than other GSTs. This opening is considered relatively large, which could potentially facilitate interacting proteins and allow for substrate specificity. GSTO1-1 does not reduce model substrates of other GST family members and therefore despite its name does not appear to have typical GST enzymatic activity. Experiments testing the activity of GSTO1-1 identified that, bar some relatively minor activity towards the substrate 1-chloro-2, 4-dinitrobenzene, GSTO1-1 had little affinity to process a wide range of characteristic GST substrates from the alpha, mu, pi and theta classes [130]. Due to the lack of compatibility of GSTO1-1 with known substrates of GSTs, *in vitro* analyses identified that GSTO1-1 catalyses the reduction of phenacyl glutathione to acetophenones, the first specific reaction linked to GSTO1-1 [132], and recognized 4-nitrophenacyl glutathione (S-4NPG) as a specific substrate, with no reactivity towards GSTO2-2 [133]. A proposed mechanism of GSTO1-1 catalysis would thereby involve a glutathionylated substrate binding to the H-site, exposing substrate-bound GSH to GSTO1-1, allowing formation of a mixed disulphide through transfer of substrate GSH to Cys32, which could then be recycled from GSTO1-1 to release reduced GSH and reform active GSTO1-1. GSTO1-1 would therefore appear to deglutathionylate substrates, acting as a glutaredoxin.

GSTO1-1 was shown to catalyse the deglutathionylation of thiol-containing peptide *in vitro*. A C32A mutant GSTO1-1 was inactive [134]. Further evidence for deglutathionylation activity of GSTO1-1 stemmed from the use of T47-D cells, which are naturally deficient in GSTO1-1. By plasmid-mediated overexpression of GSTO1-1 and catalytically inactive C32A GSTO1-1, they identified a significant reduction in levels of total glutathionylation, measured as nanomoles of GSH/mg of protein, by GSTO1-1 and not C32A GSTO1-1. In the same study, due to the large difference in glutathionylation status of the cell, mass spectrometry was then employed to identify specific proteins that undergo deglutathionylation in the presence of GSTO1-1. Of which, β-actin was one of the highest hits for deglutathionylation. The glutathionylation status of β-actin affects its physiological activity [134]. Deglutathionylation of β-actin was shown to affect the globular to filamentous (G/F) ratio of β-actin, with GSTO1-1 presence resulting in decreased levels of G-actin, linking GSTO1-1 to cytoskeletal

rearrangement. The removal of GSH from proteins thereby highlights a dynamic role of GSH in cellular function (Figure 1.9). The high levels of GSH within the cytosol may keep β-actin basally glutathionylated as G-actin, and upon stimulation with agents such as LPS, macrophages might remodel G-actin into F-actin through the activity of GSTO1-1 deglutathionylation.

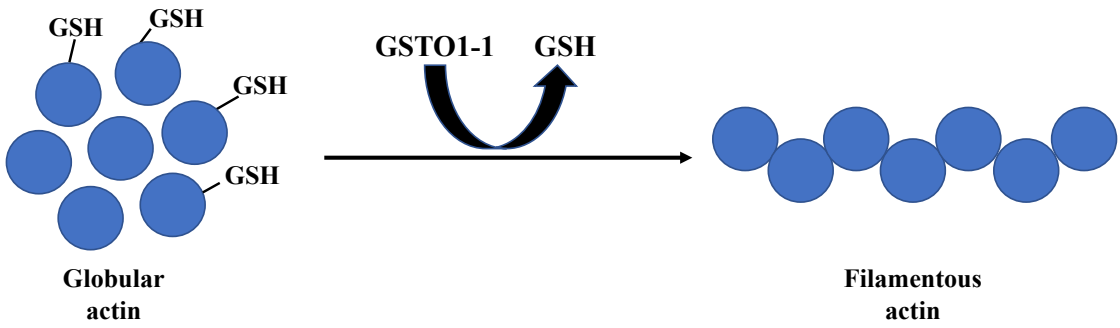

Figure 1.9 GSTO1-1 Regulates Actin Rearrangement

Globular actin (G-actin) is glutathionylated basally. Upon stimulation or oxidative stress, GSTO1-1 catalyses the removal of GSH from G-actin, promoting oligomerisation of G-actin to filamentous actin (F-actin).

Caspase-1 is another possible substrate for GSTO1-1 due to glutathionylation being known to inhibit its activity [135]. GSTO1-1 might remove the GSH to activate Caspase-1, leading to processing of pro-IL-1β, pro-IL-18 and pyroptosis via inflammasomes (Figure 1.10).

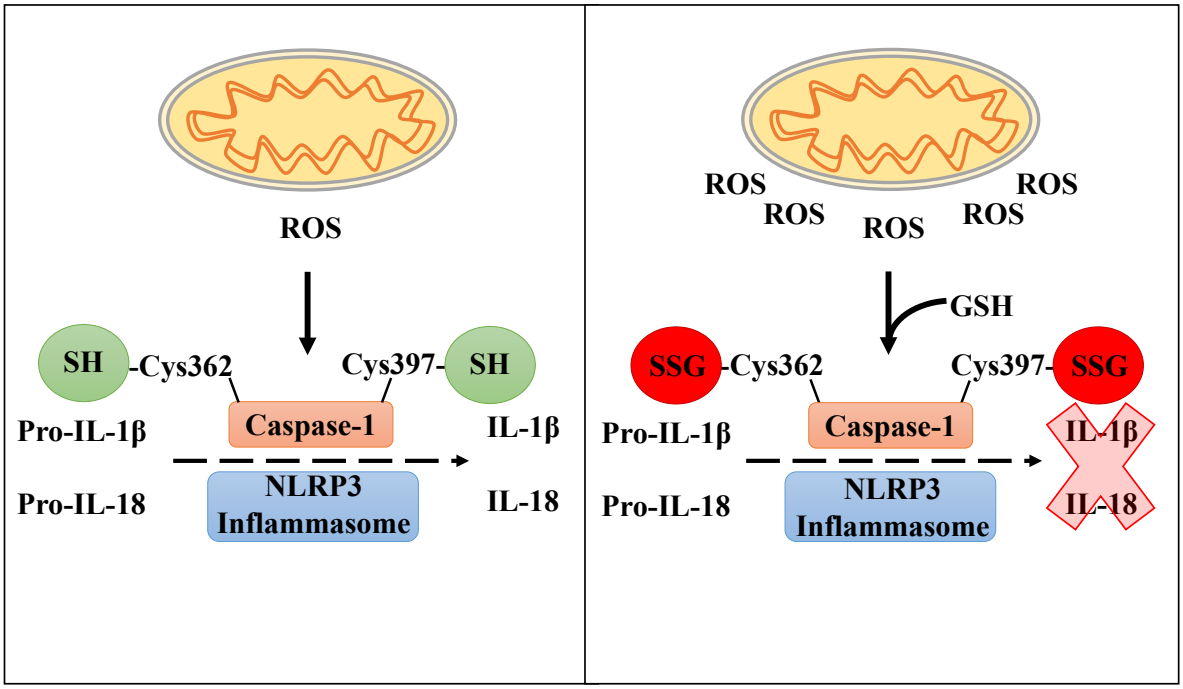

Figure 1.10 GSH-dependent inhibition of Caspase-1 activity

(Left) Production of ROS from mitochondria drives NLRP3 inflammasome activation, producing mature IL-1β and IL-18 via Caspase-1 activity. (Right) Over time, ROS accumulation leads to GSH binding to Cys362 and Cys397 on Caspase-1, inhibiting Caspase-1 catalytic activity. Oxidizing agents, such as superoxide and hydrogen peroxide, can induce glutathionylation of Caspase-1, preventing cleavage of pro-IL-1β and pro-IL-18.

2.1.5.4 GSTO1-1 and NF-κB translocation

NF-κB, one of the most widely characterized transcription factors that up-regulates a plethora of inflammatory genes, has been shown to require GSTO1-1 for nuclear translocation in macrophages. NF-κB has previously been reported as a redox sensitive protein. Oxidation of cys38 in the p-65 subunit of NF-κB and cys62 in the p-50 subunit will prevent DNA binding [136]. Menon et al. examining the effect of GSTO1-1 deficiency via knockdown approaches in macrophages discovered that the absence of GSTO1-1 prevented nuclear translocation of NF-κB upon LPS stimulation [137]. This indicates that NF-κB may require GSTO1-1 for dissociation from IκBα, possibly by deglutathionylation. This would place GSTO1-1 as a potential downstream effector of TLR4 signalling. However, components of the TLR4 signalling pathway are possibly deglutathionylated by GSTO1-1 allowing them to become active, which would promote NF-κB activation.

2.1.5.5 GSTO1-1 as an autophagy gatekeeper

GSTO1-1 has been recently reported to play a key role in cell survival following Aflatoxin B1 (AFB1) treatment of macrophages, a mycotoxin considered to be the most potent carcinogen found in contaminated food, with powerful immunosuppressive effects [138]. GSTO1-1 has previously been linked to apoptosis regulation, preventing apoptosis via the activity of JNK1 [139]. Interestingly, Paul et al. have identified a cytoprotective role for GSTO1-1 in AFB1-treated macrophages. A 6hr treatment of AFB1 was reported to induce an elevation in ROS levels from mitochondria, resulting in loss of mitochondrial membrane potential and subsequent JNK mediated Caspase-dependent cell death [140]. GSTO1-1 was identified as the causative link between autophagy and apoptosis, as siRNA mediated knockdown of GSTO1-1 mimicked 6hr AFB1 treatment results, promoting apoptosis. This suggests inhibiting GSTO1-1 increases ROS production, which may lead to cytotoxic effects. These data indicate that GSTO1-1 plays a role in cell survival via autophagy induction by agents such as AFB1, however the exact mechanism by which GSTO1-1 exerts cytoprotective effects remains unclear. Increased ROS and NF-κB activity was found to promote mitochondrial fission in hepatocellular carcinoma, enhancing autophagy and preventing apoptosis [141]. GSTO1-1 activity in response to xenobiotics may therefore result in GSTO1-1 mediated NF-κB translocation and may thereby promote autophagy. Further studies will be required to verify the role of GSTO1-1 in autophagy induction and if other xenobiotics could induce similar autophagy-related cell responses.

2.1.5.6 GSTO1-1 and metabolic reprogramming in macrophages

The knockdown of GSTO1-1 in J774.1A cells decreased expression of NADPH oxidase 1 (NOX1) after LPS stimulation. NOX1 is one of the main producers of ROS along with mitochondria, and similar results were obtained utilizing the GSTO1-1 inhibitor ML175. The authors suggested that GSTO1-1 acts upstream of NOX1 on the TLR4 pathway [137], and further studies published by the same authors identified a critical role for GSTO1-1 in the modulation of macrophage metabolism via LPS. Indeed, LPS activation will skew the phenotype of macrophages towards a pro-glycolytic state [142], however this switch is significantly attenuated in GSTO1-1 deficient cells. In addition to the effect on NOX1, GSTO1-1 deficient cells did not increase mitochondrial ROS generation with LPS treatment compared to a significant ROS enhancement in control cells, implicating GSTO1-1 in mitochondrial ROS production [143]. Assessing the oxidative tone of stressed cells can give insight into the effect of ROS by measuring the flux between reduced and oxidized glutathione (GSH/GSSG) [144]. Control cells had a significant drop in GSH:GSSG ratio compared to GSTO1-1 deficient cells, which is suggestive of a lack of oxidative stress in the GSTO1-1 deficient cells. Furthermore, The JC-1 ratio, a measurement of mitochondrial membrane potential, remained unchanged in GSTO1-1-deficient cells compared to control cells which exhibited decreased mitochondrial membrane potential with LPS treatment. The alteration in mitochondrial membrane potential has an associated relationship with the imbalance of the AMP:ATP ratio, a major readout of intracellular energy status, which is controlled by AMP-activated protein kinase (AMPK) [145]. AMPK phosphorylation is indicative of an activation signal, and LPS treatment of non-silencing controls diminished p-AMPK in comparison to GSTO1-1 deficient cells. This indication of altered energy metabolism could have a direct impact on the glycolytic phenotype of GSTO1-1 deficient cells. Indeed, the extracellular acidification rate (ECAR) and oxygen consumption rate (OCR) of LPS-treated GSTO1-1 deficient cells and control cells were examined as markers for altered glycolysis or oxidative phosphorylation respectively. Interestingly, GSTO1-1 deficient cells did not observe the steady increase in ECAR, which is representative of increased glycolysis. Contrastingly, the reported decrease of OCR observed in LPS-treated macrophages was abrogated in GSTO1-1 deficient cells, implying that these cells do not respond to LPS treatment. Succinate accumulates in LPS-treated macrophages, which stabilizes HIF1α to promote IL-1β levels [146]. The build-up of succinate and citrate was abolished in GSTO1-1 deficient cells, concomitant with decreased HIF1α production. These data clearly place GSTO1-1 as a key modulator of LPS-responsiveness within macrophages. GSTO1-1 was also found to be essential for macrophage phagocytosis, with GSTO1-1 deficient cells having lower efficacy in ingestion of fluorescently labelled pathogenic

particles. The many defects in GSTO1-1 deficient macrophages suggest that it is targeting an early or global event in TLR4 signalling, since it affects all TLR4 responses, be they NF-κB activation, induction of NOX1, or metabolic programming impairment in the absence of GSTO1-1. The varied roles of GSTO1-1 are summarised in Figure 1.11.

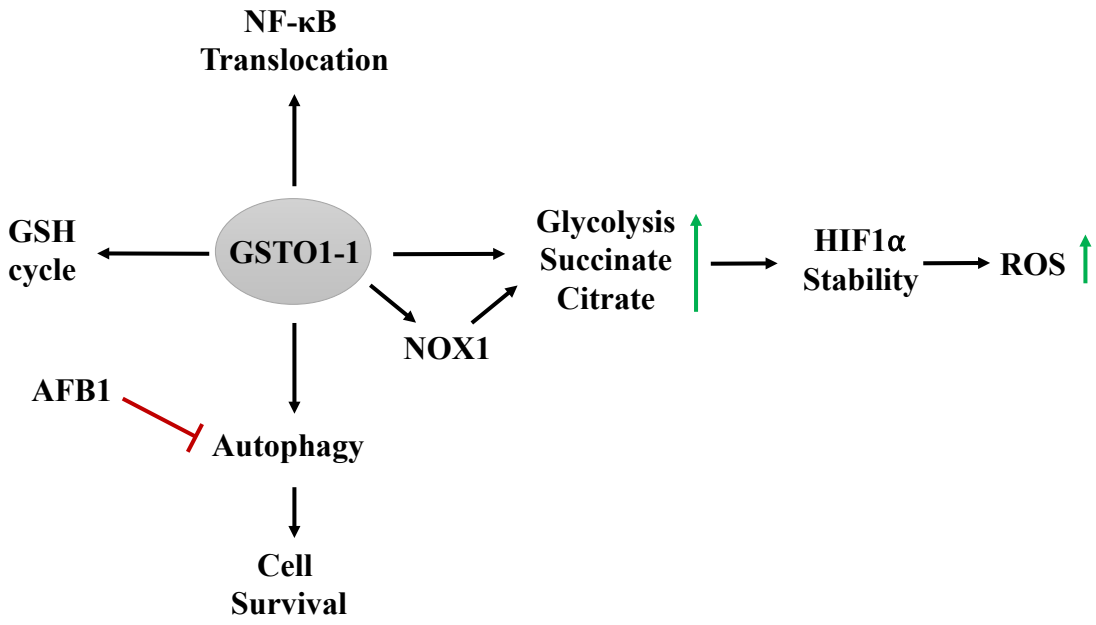

Figure 1.11 A GSTO1-1 axis in macrophage signalling

GSTO1-1 protects macrophages from Aflatoxin B1-induced apoptosis. GSTO1-1 is also essential for LPS action in macrophages, including translocation of NF-κB to the nucleus, increased glycolysis, elevated TCA cycle intermediate succinate levels, NOX-1 activation, and subsequent ROS induction. GSTO1-1 is therefore likely to regulate components in the TLR4 signalling pathway.

2.1.6 Cytokine release inhibitory drugs target GSTO1-1

In 2003, Laliberte et al. identified sulfonurea containing compounds called cytokine release inhibitory drugs (CRIDs) as potential inhibitors of the omega class GSTs. Initially, CRIDs were found to limit processing of IL-1β in human monocytes and interestingly, mice given oral CRID had attenuated production of IL-1β in response to LPS and ATP, with no effect on IL-6 or TNFα [147]. Further studies identified GSTO1-1 as a potential CRID target by affinity labelling of radioactive CRID1 and CRID2. Recombinant GSTO1-1 had incorporated radiolabelled CRID2 and mutagenesis of the active site cysteine 32 in GSTO1-1 abolished CRID2 interaction. GSTO1-1 was therefore considered a potential target for the class of CRID compounds. A definitive role for GSTO1-1 in the processing of IL-1β still remains unexplored. GSTO1-1-deficient mice were recently shown to have reduced serum IL-1β production in response to LPS challenge *in vivo*, possibly indicating a role for GSTO1-1 in IL-1β activation and secretion [148]. Recently, a derivative of CRIDs, termed MCC950, has been found to potently block the activation of the oligomeric IL-1β processing complex, termed the inflammasome [149]. Since this discovery, many stressors and DAMPs have been linked to activation of the inflammasome. The inflammasome and its regulation by redox mechanisms will now be discussed.

2.1.6.1 The Inflammasome

Activation of macrophage TLRs drives assembly of signalling competent platforms termed inflammasomes, which all share core proteins to drive processing of IL-1β and IL-18. The NLRP3 (NLR family, pyrin domain containing 3) inflammasome is a multi-component assembly of adaptor and effector proteins highly expressed in myeloid cells, consisting of NLRP3, adaptor protein apoptosis-related speck-like protein (ASC), NIMA related kinase 7 (NEK7) and Caspase-1 [150] [151, 152].

The discovery of the NLRP3 inflammasome in 2002 by Jürg Tschopp identified the mechanism of IL-1β and IL-18 cleavage [153]. In this seminal study, they identified the components of the inflammasome in a cell free system and further linked NLRP3 to the autoimmune disease Muckle-Wells syndrome [154]. The NLRP3 inflammasome is the best characterised inflammasome and has also been linked to metabolic disorders, as NLRP3-deficient mice are hypersensitive to insulin when given a high-fat diet [155], and furthermore insulin sensitivity is increased in obese type 2 diabetic patients who undergo calorie restriction and exercise due to decreased levels of NLRP3 [156].

NLRP3 senses an array of DAMPs including ATP, the pore forming ionophore Nigericin and crystalline substances. Activation of the NLRP3 inflammasome will drive pro-IL-1β and pro-IL-18 processing to further drive inflammation and promote a form of cell death termed pyroptosis. NLRP3 assembly primes Caspase-1 auto-catalytic activation. Further, Caspase-1 activation has been linked to activation of the recently described 'non-canonical inflammasome', which will be discussed.

Owing to the complexity of inflammasome sensing and regulation, NLRP3 can be considered an intracellular safeguard to sense and limit altered metabolite production. The range of activators of NLRP3 appears broad, however distinct inflammasomes have since been discovered to respond to other cellular insults. The absent in melanoma (AIM2) inflammasome senses intracellular bacterial and viral DNA [157]. The NLRC4 inflammasome senses intracellular flagellin and the type III secretion system (T3SS) [158], a needle complex 60-80nm in length from gram-negative bacterial species via NLR family apoptosis inhibitory proteins (NAIPs) [159] to trigger IL-1β production. NAIP1 recognises the T3SS needle protein [160], NAIP2 recognises the T3SS inner rod protein, and NAIP5 and NAIP6 recognise flagellin to drive NLRC4 activation [161]. A graphical representation of the best characterised inflammasomes is shown in Figure 1.12.

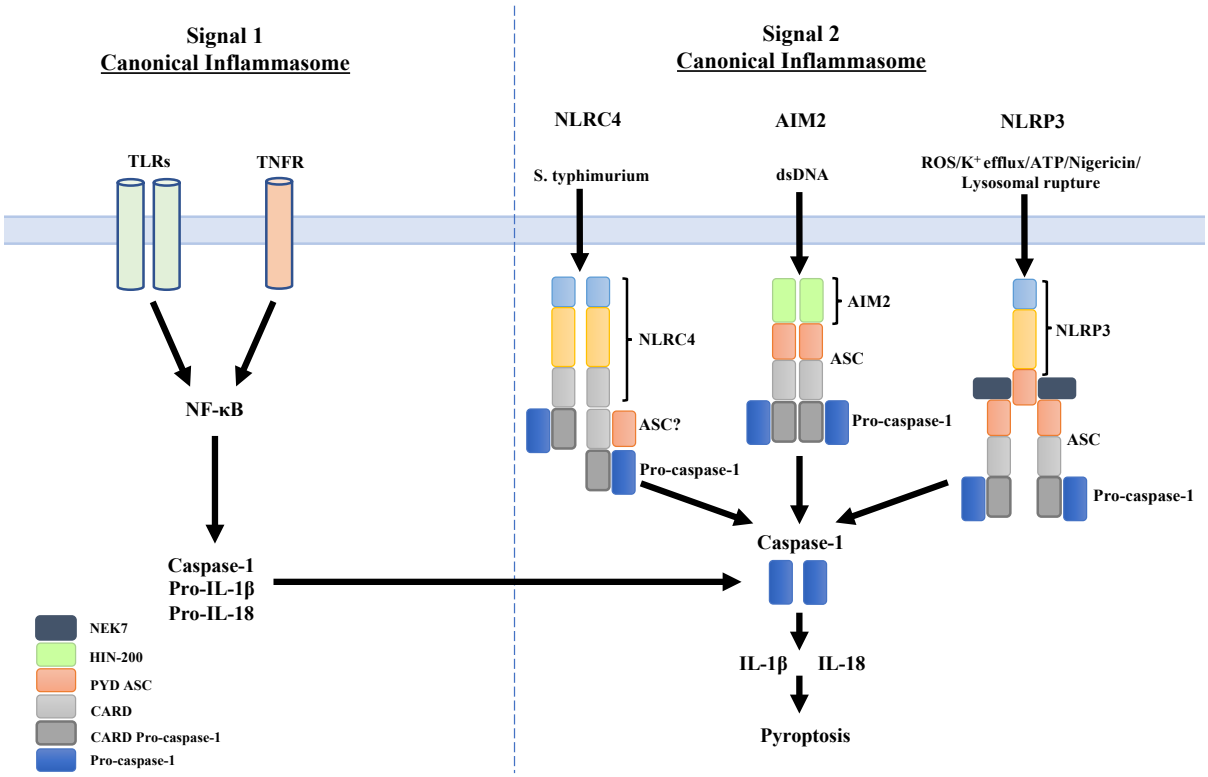

Figure 1.12 The NLRC4, AIM2 and NLRP3 Inflammasomes

Activation of TLR or TNF receptor signalling or 'Signal 1' drives translocation of NF-κB to the nucleus to transcribe inflammasome components and inflammatory cytokines pro-IL-1β and pro-IL-18. Direct sensing of flagellated bacteria, dsDNA or DAMPs drive activation of the NLRC4, AIM2 and NLRP3 inflammasomes, respectively, driving Caspase-1 activation.

2.1.6.2 The Non-Canonical Inflammasome

Whilst the canonical inflammasomes have been extensively characterised, a recent discovery has indicated a non-canonical inflammasome exists to directly sense LPS from gram-negative bacteria. LPS is well-characterised to induce septic shock *in vivo* via Caspase-1-dependent IL-1β secretion. Recently however, Caspase-11 was identified as the key executioner Caspase in LPS-induced septic shock models *in vivo*, as a mouse strain 129S6, which harbours a polymorphism in the Caspase-11 gene locus, is much more resistant to LPS-induced septic shock [162]. Broz et al. generated Caspase-1- and Caspase-11-deficient mice and identified that Caspase-1 deficiency renders mice more susceptible to *S. typhimurium* infection, indicating that Caspase-11 activation drives the inflammatory phenotype associated with infection *in vivo* [163].

Further studies have confirmed a role for Caspase-11 during endotoxin shock and found that the Caspase-11 CARD domain binds to the lipid A moiety of LPS to trigger non-canonical inflammasome activation [164]. Caspase-11 activation ultimately results in cleavage of the pore forming protein Gasdermin D (GSDMD), inducing pyroptosis. Further, Caspase-11 has been reported to act upstream of NLRP3 activation during intracellular LPS sensing, promoting Caspase-11-dependent NLRP3 activation and IL-1β secretion [165].

Caspase-11 can be induced by both TLR4 and Interferon signalling [166]. Two recent studies have identified a TLR4-independent but Caspase-11-dependent role during septic shock. Both studies concluded that TLR4 is utilised to induce Caspase-11 gene expression, as Caspase-11-deficient mice were resistant to LPS-induced septic shock when primed with TLR3 agonist Poly I:C and further treated with excessive LPS. TLR4-deficient mice primed with Poly I:C however, were highly susceptible to LPS challenge, resulting in mortality. These findings importantly place Caspase-11 as an executioner of septic shock, independent of TLR4 activation [167, 168]. The NLRP3 inflammasome is a particular focus of this thesis and the crosstalk between NLRP3 and Caspase-11 will be explored.

2.1.6.3 Endogenous regulators of NLRP3

As mentioned above, NLRP3 senses an array of DAMPs to trigger Caspase-1 activation and IL-1β processing. Due to the ability of NLRP3 to drive systemic inflammation, NLRP3 must be highly regulated. Fatty acids such as palmitate have been shown to activate NLRP3 [169]. This may be one reason why obesity drives inflammation. More recently, the ketone body β-hydroxybutyrate (BHB) has been shown to suppress the activation of the NLRP3

inflammasome when stimulated with urate crystals, lipotoxic lipids and ATP in macrophages. Ketone bodies are made from free fatty acids during starvation. BHB was shown to specifically target the NLRP3 inflammasome. BHB had no impact on canonical Caspase-1 activation from AIM2 and NLRC4 inflammasomes, nor the non-canonical Caspase-11 inflammasome [170]. BHB targeted potassium (K^+) efflux, resulting in reduced ASC oligomerisation and reduced NLRP3 inflammasome stability. A ketogenic diet, which would increase BHB levels endogenously, also attenuated NLRP3-mediated Caspase-1 activation and pro-IL-1β processing in *in vivo* mouse models of Muckle-Wells syndrome, urate crystal-induced peritonitis and familial cold auto-inflammatory syndrome [170]. A ketone diet was also shown to upregulate antioxidant pathways and limit ROS generation thereby limiting NLRP3-mediated inflammation [171] (Figure 1.13).

Interestingly, a ketogenic diet has been reported to alleviate gout-induced inflammation, (which is driven by uric acid, a product of purine metabolism), without impacting on bacterial clearance during infection. BHB blocked both mouse and human gout in neutrophils and macrophages. BHB plays a dual role by limiting the priming and assembly of NLRP3 in neutrophils, as BHB decreased phosphorylation of NF-κB, decreasing inflammasome assembly components [172]. Overall, there may be a balance between fatty acids as activators and ketone bodies as inhibitors of NLRP3, with obesity promoting and starvation limiting inflammation via its effects on NLRP3.

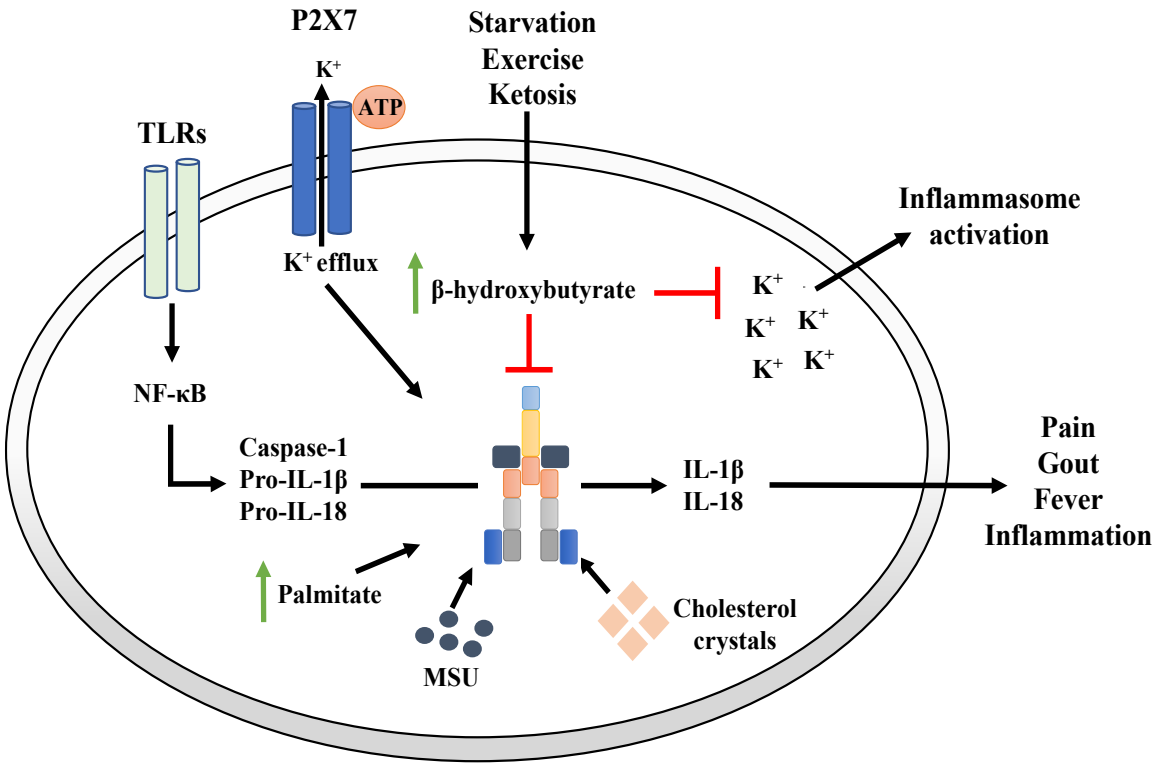

Figure 1.13 Dietary metabolites regulate NLRP3 activation via K+ efflux

TLRs drive the transcription of NLRP3 inflammasome components via NF-κB nuclear translocation and promotes NLRP3 inflammasome assembly. Extracellular ATP, sensed by the P2X7 receptor, and MSU crystals trigger NLRP3 inflammasome activation. The ketone body β-hydroxybutyrate produced during starvation periods limits NLRP3 inflammasome activation, blocking ATP and MSU-mediated pro-IL-1β and pro-IL-18 processing. β-hydroxybutyrate targeted K^+ efflux, decreasing ASC oligomerisation with NLRP3.

Recent data have further emphasised the link between NLRP3 and obesity. NLRP3-deficient mice are resistant to diet-induced metabolic syndrome symptoms and nephropathy, further highlighting a connection between inflammasome activation and lipid metabolism [173]. Cholesterol catabolism results in the production of amphipathic bile acids, which function as detergents to promote intestinal nutrient absorption and homeostasis [174]. A new role for bile acids in the regulation of the NLRP3 inflammasome has been described. Bile acids specifically target NLRP3 and inhibit inflammasome activation through a TGR5-cAMP-PKA axis [175]. TGR5 activation by bile acids triggered NLRP3 ubiquitination via PKA-mediated phosphorylation of Ser291 on NLRP3. Bile acids also suppressed LPS-induced septic shock *in vivo*. In tandem with other studies targeting NLRP3 in type 2 diabetes, a high fat diet model which induces NLRP3-dependent insulin resistance and type 2 diabetes was abolished with bile acid treatment (Figure 1.14).

Prostaglandin E_2 (PGE_2) is a widely characterised bioactive lipid derived from arachidonic acid with potent pro-inflammatory effects [176-178]. PGE_2 has been identified to regulate NLRP3-mediated IL-1β maturation endogenously. In human macrophages, PGE_2 inhibits NLRP3 activation through the EP4 receptor, increasing intracellular cAMP levels [179]. In a more recent study in murine macrophages, PGE_2 has been identified to promote pro-IL-1β processing. PGE_2 can signal through the EP2 receptor, and ablation of the EP2 receptor decreases IL-1β maturation in an NLRP3-dependent manner [180]. Furthermore, in primary human monocytes, PGE_2 was shown to boost processing of pro-IL-1β by NLRP3. The role of PGE_2-mediated PKA activation on NLRP3 activity however, is not fully elucidated. It would be interesting to examine the effects of PGE_2-mediated PKA activation on potential phosphorylation of NLRP3 as seen with bile acids. Overall, the evidence suggests that PGE_2 will limit NLRP3 and this may be part of its anti-inflammatory tissue protective effects.

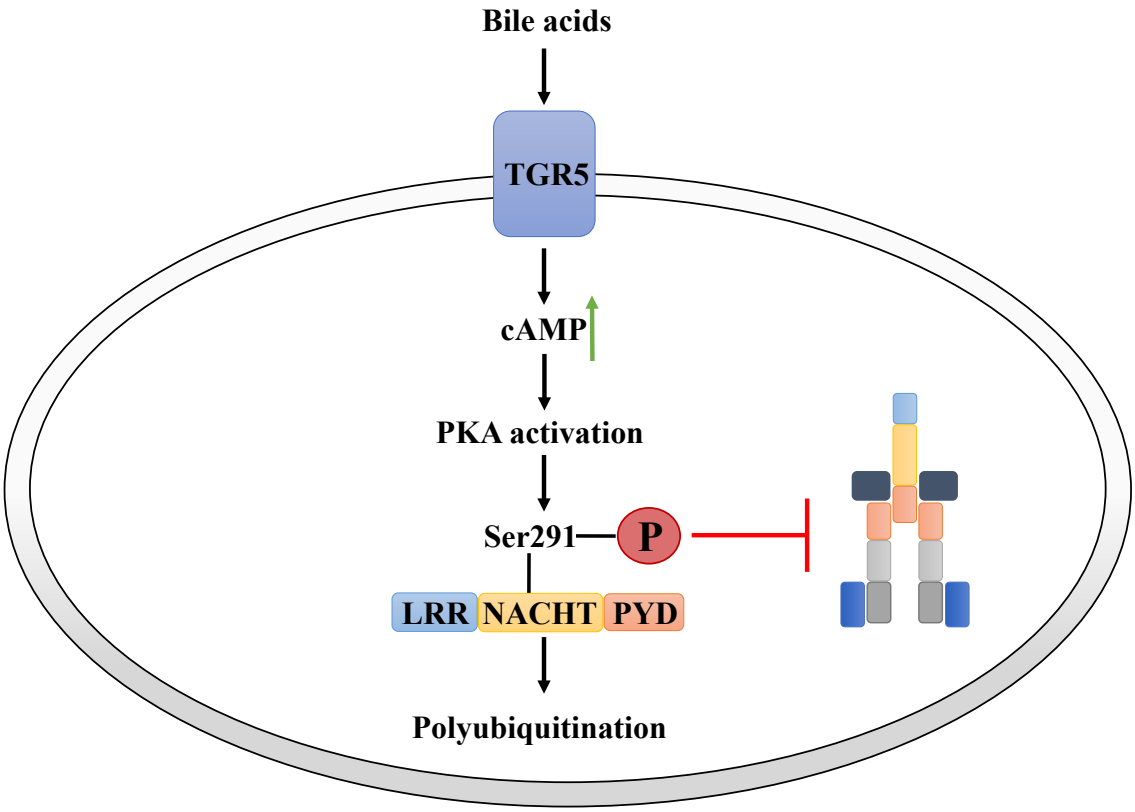

Figure 1.14 Bile acids promote NLRP3 phosphorylation and degradation

Bile acids produced from cholesterol catabolism are sensed by the TGR5 receptor, increasing intracellular cAMP levels, mediating PKA activation. PKA phosphorylates NLRP3 in the NACHT domain on Ser291. Phosphorylation of NLRP3 on Ser291 promotes K48 and K63-linked polyubiquitination and NLRP3 degradation, limiting NLRP3 inflammasome activation.

2.1.6.4 Redox regulation of the NLRP3 inflammasome

As stated above, glutathionylation has been linked to negative regulation of Caspases. Both Caspase-1 and Caspase-3 are negatively regulated by GSH, limiting their proteolytic capabilities [181, 182]. Glutathionylation of NLRP3 has recently been identified in macrophages co-treated with LPS and curcumin, an anti-inflammatory compound [183]. Interestingly, the deglutathionylation of NLRP3 was associated with increased interaction of glutathionylated Caspase-1, suggesting the NLRP3 inflammasome assembles in tandem with enzymatically inhibited caspase-1, possibly to prevent activation of the NLRP3 inflammasome. This finding warrants further research, as GSH may itself limit inflammasome activation. Oxidative stress could thereby induce NLRP3 activation, triggering deglutathionylation of Caspase-1 to promote IL-1β processing.

Recent evidence has identified a new component of the inflammasome, NEK7, a serine-threonine kinase previously associated with mitosis [152]. Mice deficient in NEK7 could not form competent NLRP3 inflammasomes *in vivo*. NEK7 bound to the LRR of NLRP3, dependent on generation of mitochondrial ROS. This finding presents NEK7 as a potential ROS-sensing inflammasome stimulus, which may detect increasing ROS levels to trigger inflammasome assembly. It would be interesting to elucidate if ROS generated from mitochondrial-independent sources could also act as a NEK7 trigger, or if NEK7 is exclusively sensing mitochondrial ROS. Concurrently, NEK7 was also identified by He et al. to drive NLRP3 activation, and further attributed NEK7 activation to K^+ efflux, suggesting NEK7 acts as both an ion and ROS sensor [151].

The efflux of cytosolic K^+ is a known trigger for NLRP3 inflammasome activation [184], and furthermore the chloride intracellular channel (CLIC) proteins CLIC1 and CLIC4 have been shown to impact on *Il1β* transcription and NLRP3 inflammasome activation [185]. CLICs have been shown to be activated downstream of K^+ efflux and ROS. Mitochondrial ROS has been shown to drive translocation of CLICs to the plasma membrane where they cause chloride efflux. The chloride efflux was then shown to drive NEK7-NLRP3 activation [186]. This study therefore provides a new insight into ROS as a driver of NLRP3. Interestingly, a known activating NLRP3 variant in cryopyrin-associated periodic syndrome (CAPS)-associated macrophages, R258W, also required NEK7 for chronic activation, independent of K^+ efflux [151].

Mechanisms to regulate NLRP3 post-transcriptionally have also been described. Tristetraprolin (TTP), an RNA-binding protein, binds to the 3'-untranslated region (UTR) of NLRP3 in human macrophages, repressing NLRP3 expression. Knockdown of TTP increased NLRP3 activation, but not AIM2 or NLRC4 activation, and subsequently increased Caspase-1 activation and IL-1β cleavage [187]. Regulation of NLRP3 by TTP may also be impacted by levels of ROS produced by the metabolic shift in macrophages upon PAMP recognition. TTP contains redox-reactive cysteines which, when oxidised, result in inhibition of TTP RNA-binding capacity [188]. Thus, TTP oxidation may act as a feedback mechanism, linking increased ROS levels produced during metabolic reprogramming to rapid NLRP3 transcription.

Ugonin U, a natural flavonoid derived from *Helminthostachys zeylanica* has been shown to drive superoxide generation via the activity of Phospholipase C (PLC) [189]. In human monocytes, Ugonin U stimulated NLRP3 activation by triggering mitochondrial ROS generation. Ugonin U-mediated activation of PLC was found to trigger release of intracellular calcium (Ca^{2+}), and negative targeting of Ca^{2+} release inhibited the inflammatory effects of Ugonin U [190]. Furthermore, scavenging of mitochondrial ROS by the tool compound MitoTEMPO limited the effects of Ugonin U, firmly placing mitochondrial ROS as a determinant in NLRP3 inflammasome activation.

Lipid metabolism has also been linked to NLRP3. Moon *et al.* identified a role for the uncoupling protein-2 (UCP2) in NLRP3 activation. UCP2-deficient mice were found to have overall improved survival in sepsis models, concomitant with impaired fatty acid synthesis, and decreased IL-1β and IL-18 levels. UCP2 was identified as a driver of fatty acid synthase (FASN), a key enzyme involved in fatty acid synthesis. UCP2-deficient mice had reduced lipid synthesis, concomitant with decreased NLRP3-mediated Caspase-1 activation. Inhibition of FASN by chemical inhibitors also suppressed NLRP3 activation and *NLRP3* and *IL1β* transcription, linking fatty acid synthesis as a key driver of both inflammatory gene transcription and NLRP3 activation [191]. In a separate and somewhat contradicting study, Moon *et al.* also identified the ROS producer NADPH Oxidase 4 (NOX4), an enzyme involved in superoxide anion formation, as an NLRP3 activator through fatty acid oxidation. NOX4-deficient mice had reduced levels of the mitochondrial fatty acid oxidation enzyme carnitine palmitoyltransferase 1A (CPT1A), resulting in decreased NLRP3 inflammasome activation, with no effect on NLRC4 or AIM2 inflammasomes. Inhibition of fatty acid oxidation by the drug etoxomir also limited NLRP3 activation, identifying another prominent role of an altered oxidative environment inducing NLRP3 activation [192]. Production of ROS is crucial as a

microbicidal mechanism, however the consequences of producing an oxidative environment lies firmly on antioxidant capacity, the lack of which can damage cell machinery, driving inflammation through mechanisms which can activate the NLRP3 inflammasome.

2.1.6.5 Glycolysis and NLRP3 activation

Activation of TLRs will alter metabolism in macrophages causing a shift to aerobic glycolysis. Inhibition of glycolysis by a glucose analogue, 2-deoxyglucose, was shown to suppress LPS-induced IL-1β mRNA production in macrophages, with a strong increase in the Krebs cycle intermediate succinate [146]. Limiting glucose uptake can trigger glycolytic stress, decreasing the amount of reducing equivalents required for homeostasis. Interestingly, a compound termed GB111-NH_2, induces NLRP3 inflammasome formation by inhibiting glycolytic enzymes GAPDH and α-enolase, impairing NADH production and driving mitochondrial ROS production [193]. This provides a curious contradiction. Inhibition of glycolysis with 2-deoxyglucose appears to block induction of IL-1β mRNA, whereas targeting of GAPDH and α-enolase increases NLRP3 activation and IL-1β secretion. The biological significance of this is not clear but warrants further investigation.

Energy metabolism is under constant surveillance by redox/nutrient sensor mammalian target of rapamycin complex I (mTORC1) to regulate protein synthesis. However, unlike the study with GB111-NH_2, mTORC1-mediated glycolysis was shown to drive NLRP3 inflammasome activation. Inhibiting mTORC1 by torin1, a selective mTOR inhibitor, suppressed NLRP3 activation both *in vitro* and *in vivo* [194]. Furthermore, deficiency of Raptor, an mTORC1 binding partner, suppressed Caspase-1 activation and glycolysis during NLRP3 inflammasome activation, with mTORC2 deficiency having no effect observed on NLRP3 activation. Hexokinase-1, the first enzyme in glycolysis which converts glucose to glucose-6-phosphate, provided a mechanistic link between mTORC1 and NLRP3 activation, as depletion of glucose in the media of respiring macrophages blocked Caspase-1 activation during NLRP3 inflammasome activation. Interestingly, Hexokinase-1 knockdown also suppressed NLRP3 activation by extracellular ATP, linking energy sensing and active glycolysis as pre-requisites for NLRP3 inflammasome activation [194]. Inhibition of glycolysis by 2-deoxyglucose however, also triggers a decrease in intracellular ATP levels, which is sensed by NLRP3, and drives inflammasome activation. 2-deoxyglucose dose-dependently decreased intracellular ATP, with a concomitant increase in IL-1β secretion [195]. One possible explanation to this ATP and 2-deoxyglucose paradox may be due to imbalanced energy sensing as a trigger for inflammasome activation. Under resting conditions, hexokinase is tethered to the mitochondria

via Akt activity [196]. Hexokinase may also play a role in ATP depletion-mediated NLRP3 activation, as Akt activity decreases during ATP starvation [197], which may promote untethering of hexokinase from the mitochondria, without need for signal 2 to drive NLRP3 activation.

A more recent study has identified hexokinase as an intracellular PRR for N-acetylglucosamine, a glucose-derivative peptidoglycan utilised by gram positive bacterial cell walls. Hexokinase binding to N-acetylglucosamine was sufficient to induce dissociation of hexokinase from mitochondria, promoting NLRP3 inflammasome activation [198] (Figure 1.15).

2.1.6.6 Redox regulation of NLRP3 via mitochondrial reprogramming

The Krebs cycle has garnered much excitement in the field of immunology in recent years as Krebs cycle intermediates directly impact on cytokine production, including the production of pro-IL-1β through succinate accumulation [146], targeting of complex I of the mitochondrial electron transport chain to boost IL-10 [199], and targeting complex II to prevent succinate oxidation, limiting ROS-induced pro-IL-1β [200]. (Figure 1.15). Oxidised mitochondrial DNA itself acts as a second signal to drive NLRP3 inflammasome activation [201]. Succinate has been a focus, being shown to stabilise HIF1α to promote NLRP3 activation. Such activation of NLRP3 exacerbated tissue damage and promoted inflammation, indicating a possible prominent role of NLRP3 hyper-activation specifically in the context of joint inflammation in rheumatoid arthritis (RA) [202]. Under normoxic conditions Succinate dehydrogenase (SDH) converts succinate to fumarate, another Krebs cycle intermediate. A role for fumarate in NLRP3 regulation has also been described. Dimethyl fumarate (DMF) limits NLRP3 activation in a model of Dextran sulfate sodium (DSS) colitis. Administration of DMF prevented intestinal shortening, promoting weight gain comparable to control levels. Furthermore, DMF reduced both production and activation of NLRP3 [203]. Further work is required to examine the role of fumarate in inflammatory signalling. It is intriguing that succinate and fumarate can have profound inflammatory and anti-inflammatory activities, respectively.

S. typhimurium infection is sensed by the NLRC4 inflammasome through recognition of flagellin [204], triggering inflammasome activation via phosphorylation of NLRC4 [205], with delayed activation of NLRP3 [206], suggesting a mechanism of NLRP3 evasion. Indeed, upon infection *S. typhimurium* downregulates flagellin expression to avoid NLRC4 entirely. During infection with *S. typhimurium*, the bacteria's own Krebs cycle enzymes aconitase, isocitrate lyase and isocitrate dehydrogenase have been shown to inhibit NLRP3 activation. *S.*

typhimurium deficient in these enzymes induced NLRP3 activation rapidly in macrophages [207]. Aconitase-deficient *S. typhimurium* were unable to drive acute systemic virulence and failed to persist in chronic infection. Each mutant was identified to require a ROS signal to drive NLRP3 activation, as mice overexpressing a mitochondrial-located human catalase, which degrades mitochondrial H_2O_2 thereby limiting ROS, failed to induce NLRP3 activation upon *S. typhimurium* infection. However, mitochondrial ROS is not the only inducible source of ROS. Macrophages infected with the protozoan parasite *Leishmania amazonensis* also trigger NLRP3 inflammasome activation via ROS induced by the professional ROS generator NADPH oxidase [208], as NADPH oxidase inhibition prolonged *L. amazonensis* infection, adding further complexity into the source of ROS and disease outcomes.

Conflicting evidence arises when mitochondrial ROS is considered an NLRP3 inflammasome stimulus. Some researchers identify ROS as a regulatory signal [209, 210], whereas others indicate ROS itself as a weak signal to drive inflammasome activation and instead stems from mitochondrial dysfunction, triggering cardiolipin interaction with NLRP3 due to translocation from the inner to outer mitochondrial membrane, independent of ROS (Figure 1.15) [211]. Proximity of NLRP3 to mitochondria is also considered a determinant in inflammasome activation. The mitochondrial antiviral signalling protein MAVS has been shown to directly interact with NLRP3 and promote its oligomerisation, which may facilitate ROS activation by mitochondrial localisation [212]. Activation of Caspase-1 by both NLRP3 and AIM2 inflammasomes has been identified to promote mitochondrial damage and limit mitophagy through cleavage of Parkin, increasing the levels of intracellular ROS, which may in turn act as a positive feedback mechanism to promote inflammasome activation and pyroptosis [213].

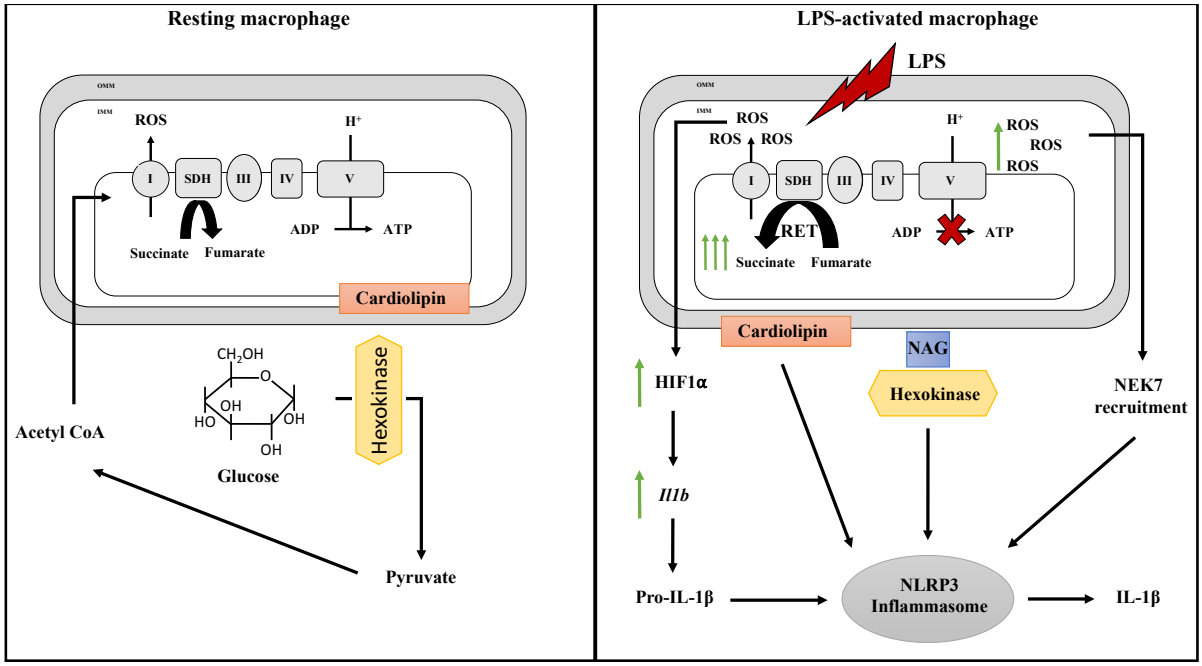

Figure 1.15 Altered mitochondrial dynamics impact NLRP3 activation

Under resting conditions (Left), macrophages utilize glucose via glycolysis to produce pyruvate in the cytosol. Pyruvate undergoes a series of decarboxylation reactions to form Acetyl CoA, which is used as fuel to drive the Krebs cycle and ATP production. Hexokinase remains tethered to the mitochondrial membrane and cardiolipin is retained in the inner mitochondrial membrane. LPS activated macrophages (Right), undergo metabolic reprogramming, promoting succinate oxidation by succinate dehydrogenase, generating ROS which promotes HIF1α stability and transcription of IL-1β mRNA. Damaged mitochondria also transport cardiolipin to the outer mitochondrial membrane, which promoting NLRP3 inflammasome activation. N-acetylglucosamine sensing promotes Hexokinase untethering and drives NLRP3 activation. Increased levels of mitochondrial ROS (mROS) also drives recruitment of NEK7 to activate the NLRP3 inflammasome.

2.2 Aims

The overall aim of this project is to explore the role of glutathionylation in the regulation of the critical TLR adaptor Mal, and via studies on GSTO1-1, the key inflammasome components NLRP3 and Caspase-11.

The specific aims are as follows:

- Test if the adaptor protein Mal is a glutathionylated protein.
- To determine if glutathionylation of Mal promotes or inhibits TLR4 signalling.
- To examine whether antioxidant imbalance promotes Mal post-translational modification.
- To test whether GSTO1-1 plays a role upstream of NF-κB signalling in macrophages.
- To establish if GSTO1-1 affects macrophage cytokine production.
- To investigate whether GSTO1-1 can affect Caspase-11 and NEK7 activation.

I have found that glutathionylation of Mal on C91 is required for Mal to interact with MyD88 and IRAK4 and generate a signal. I have also found that GSTO1-1 inhibits metabolic reprogramming in LPS-treated macrophages and regulates NLRP3 inflammasome activation via NEK7 deglutathionylation and Caspase-11 induction.

The characterisation of GSH as a novel regulator of TLR signalling via effects on Mal, and the mechanisms by which the enzyme GSTO1-1 might impact on TLR4 signalling and NLRP3 inflammasome activation could provide new therapeutic targets for the treatment of inflammatory conditions which involve TLRs and the NLRP3 inflammasome.

Chapter 2

Materials and Methods

2 Materials and Methods

2.1 Materials

2.1.1 Buffers

Table 2.1 Buffer compositions

Buffer Name	Buffer Composition
PBS (10X)	1.45 M NaCl, 39 mM NaH_2PO_4, 22.7 mM Na_2HPO_4
Sample Lysis Buffer (5X)	10% (w/v) glycerol, 2% (w/v) sodium dodecyl sulphate (SDS), 215 mM Tris pH 6.8, 200 µg/mL bromophenol blue. 50 µL of 1 M dithiothreitol (DTT) is added to 950 µL 5X sample buffer immediately before use.
SDS-PAGE Running Buffer (10X)	144 g 192 mM glycine, 30.3 g 25 mM Tris, 10 g 0.1% SDS. Diluted to 1 L with dH2O.
SDS-PAGE Transfer Buffer	1.9 M glycine, 35 mM SDS, 0.25 M Trizma base
Tris-buffered saline (TBS) Tween (TBST) 10X	87.6 g NaCl, 10 mL Tween-20, 12.11 g Tris. Diluted to 1 L with dH_2O.
Low Stringency Lysis Buffer (500mL)	50mM HEPES, 100mM NaCl, 1 mM EDTA, 10% glycerol, 1% NP-40. pH to 7.5.
ELISA Wash Buffer	0.05% Tween in PBS, pH 7.2-7.4

2.1.2 Cell culture media

DMEM (Dulbecco's Modified Eagle Medium) was obtained from Gibco Biosciences. Fetal calf serum (FCS) was obtained from Biosera. Penicillin/Streptomycin and Trypsin-EDTA were sourced from Sigma Aldrich. Blasticidin, Normocin and Hygrogold were from Invivogen.

2.1.3 Animals

C57/Bl6 mice obtained from Harlan UK were maintained under pathogen-free conditions in line with Irish and European Union regulations. Use of animals received ethical approval by the universities' ethics committees in accordance with the personal licence approved by the

HPRA. GSTO1-1 deficient mice were generated by Taconic and hind legs were generously donated by Professor Philip Board (Australian National University, Canberra, Australia).

2.1.4 Cell lines

HEK293T, 293-TLR4/MD2/CD14 (MTC), 293T-TLR2 cell lines were from Invivogen. Murine bone marrow-derived macrophages (BMDMs) were differentiated from bone marrow. L929 cells were obtained from Sigma. Control and Mal-deficient immortalized BMDMs (iBMDMs) were a kind gift from Professor Doug Golenbock (UMass Medical School, Massachusetts).

2.1.5 TLR stimuli

Ultrapure rough LPS for *in vitro* experiments (from *E. Coli,* serotype EH100) was purchased from Alexis. Pam3CSK4, Poly (I:C) and R848 were purchased from Invitrogen. *S. typhimurium* UK-1 strain was obtained from Dr. Sinéad Corr (TCD).

2.1.6 Antibodies

Anti-IκBα, p-ERK1/2, p-P65, p-JNK, p-P38 and Mal antibodies were purchased from Cell Signalling. Anti-β-actin, FLAG-tag, Caspase-11 and Myc-tag were purchased from Sigma Aldrich. Anti-Caspase-1 p20 and NLRP3 were purchased from Adipogen International. Anti-ASC and IRAK4 were purchased from Santa Cruz. Anti-HIF1α and GAPDH were purchased from Novus Biologicals. Anti-GSTO1 was purchased from Genetex. Anti-IL-1β was purchased from Biolegend. Anti-NEK7 was purchasesd from Abcam. Anti-HA tag was purchased from Cambridge Biosciences. Anti-GSH was purchased from Virogen. Anti-mouse, rabbit, rat and goat IgG were purchased from Jackson ImmunoResearch.

2.1.7 General lab chemicals

Standard suppliers Sigma Aldrich or Fisher Scientific were used to obtain all general laboratory chemicals unless otherwise stated. Genejuice was purchased from Novagen. Plasmid purification maxiprep kits were purchased from Qiagen. TNFα, IL-1β, IL-6 and IL-10 ELISA Duoset kits were purchased from R&D Systems. CytoTox96 non-radioactive cytotoxicity assay and FuGene transfection reagent were purchased from Promega. StrataClean Resin was purchased from Agilent Technologies. CellROX was purchased from Molecular Probes. DCFDA was purchased from Abcam. ATP, Nigericin and Poly (dA:dT) were purchased from Invitrogen. Spectra multicolour broad range protein ladder, RNAiMAX Lipofectamine reagent, scramble and GSTO1-1 siRNA were purchased from Thermo Fisher Scientific.

2.1.8 Luciferase assay reagents

5X Passive Lysis buffer was obtained from Promega. Coelenterazine, the *Renilla* luciferase substrate, was purchased from Biotium (1mg/mL in 100% EtOH) and stored at -20°C. 2X Firefly luciferase assay mix was generated (Table 2.2) and diluted to 1X with deionized water before use.

Table 2.2 2X Firefly assay mix composition

Reagent	Amount	Concentration
ATP	24mL of 10mM	530µM
DTT	2.34g	33.3mM
EDTA	91.2µL from 0.5M pH8	0.1mM
Tricine	1.634g	20mM
D-Luciferin	60mg	470µM
$MgSO_4 \cdot 7H_2O$	2.42mL from 500mM	2.67mM
Acetyl Coenzyme A	3.79mL from 25mg/mL	270µM

2.1.9 Plasmids

The following plasmids were generated in the Luke O'Neill lab: HA-Empty Vector (pcDNA3.1) and HA-Mal (pcDNA3.1). FLAG-IRAK4 (pcDNA3.4) and FLAG-IRAK4 KD (pcDNA3.4) were from Amgen. Myc-MyD88 (pcDNA3.1) was a gift from Marta Muzio (Mario Negri Institute, Milan, Italy). TK-Renilla (pGL4) and NF-κB luciferase (pGL4) were purchased from Promega. GSTO1-1 was purchased from Origene (pCMV6; MC208607). The following plasmids were purchased from Addgene: FLAG-NLRP3 (pcDNA3; 75127), FLAG-Pro-caspase-1 (pcDNA3; 75128), HA-ASC (pCI; 41553), FLAG-pro-IL-1β (pCMV; 75131) and HA-NEK7 (pcDNA3; 75142).

2.1.10 Site directed mutagenesis (SDM)

Generating primers using QuikChange Primer Design Tool was performed (Table 2.3 and 2.4) and site directed mutagenesis of Mal and NEK7 plasmids was undertaken using the QuikChange II Lightning kit (Agilent Technologies). Primers were ordered from Eurofins MWG Operon. The following Mal mutants were created from site directed mutagenesis (Table 2.3). The following NEK7 mutants were created from site directed mutagenesis (Table 2.4).

Table 2.3 Site Directed Mutagenesis primers for Mal mutants

Primer	Sense	Antisense
C89A	5' cctcactgtggcacacggcgacgtcatagtctttgc 3'	5' gcaaagactatgacgtcgccgtgtgcaacagtgagg 3'
C91A	5' ctatgacgtctgcgtggcccacagtgaggaagac 3'	5' gtcttcctcactgtgggccacgcagacgtcatag 3'
C116A	5' ggagttgcaggaaggcgcgcaggctggcag 3'	5' ctgccagcctgcgcgccttcctgcaactcc 3'
C134A	5' ctgctcagtgcctgggccagctcggacactat 3'	5' atagtgtccgagctggcccaggcactgagcag 3'
C142A	5' atgagcagcacccgggcgtgactactgctcag 3'	5' ctgagcagtagtcacgcccgggtgctgctcat 3'
C157A	5' ccttcaggacccctgggccaagtaccagatgctg 3'	5' cagcatctggtacttggcccaggggtcctgaagg 3'
C174A	5' agggggatggtggcgccctcggcccc 3'	5' ggggccgagggcgccaccatcccct 3'

Table 2.4 Site Directed Mutagenesis primers for NEK7 mutants

Primer	Sense	Antisense
C53A	5' cggcactccatccaagagagcggatgctctataaacttca 3'	5' tgaagtttatagagcatccgctctcttggatggagtgccg 3'
C79A	5' ggaggtctatttctttgatagcatcagcacgtgctttggca 3'	5' tgccaaagcacgtgctgatgctatcaaagaaatagacctcc 3'
C146A	5' catgtggtccagtgcactggcgagctgaacgaagtatttc 3'	5' gaaatacttcgttcagctcgccagtgcactggaccacatg 3'
C224A	5' gccatctcatatagcagagcgccaagagaccagatgtc 3'	5' gacatctggtctcttggcgctctgctatatgagatggc 3'
C247A	5' gtcacactgctctatcttcttagccagagaatacaagttcatcttg 3'	5' caagatgaacttgtattctctggctaagaagatagagcagtgtgac 3'
C253A	5' ggagaggcgggtagtcagcctgctctatcttcttac 3'	5' gtaagaagatagagcaggctgactacccgcctctcc 3'
C274A	5' ggatctgggttgatggctatattaactagctgtcgtagctcc 3'	5' ggagctacgacagctagttaatatagccatcaacccagatcc 3'
C298A	5' gtgcttgcggtagctgcatgcatcctctttgccac 3'	5' gtggcaaagaggatgcatgcagctaccgcaagcac 3'

2.1.11 Seahorse reagents

XF assay buffer, Seahorse cell culture plates, utility plates and calibrant solution were obtained from Agilent Technologies. Glucose and oligomycin were purchased from Sigma.

2.2 Methods

2.2.1 Cell culture and cell line maintenance

HEK293T, MTC, HEK293-TLR2, iBMDM and L929 cells were cultured in DMEM medium containing 10% FCS (v/v) and 1% penicillin/streptomycin (P/S) (v/v). Cells were cultured at 37°C in 5% CO_2 to maintain optimum growth conditions. iBMDMs and L929 cells were removed from flasks by a cell scraper in 10mL PBS. HEK293Ts, MTCs and HEK293-TLR2s were removed from the flask by incubation with 5mL trypsin-ethylenediaminetetraacetic acid (EDTA). 5mL complete medium was added to dilute trypsin-EDTA to prevent further catalysis. Cells were centrifuged at 300 x g for 5min before resuspending the pellet in fresh media. Cell viability was assessed by Trypan Blue dye, which can only permeate non-viable cells. Cells were counted using a haemocytometer and a bright light microscope before being plated for experiments.

2.2.2 Cell line cryopreservation

To maintain stocks of cell lines, cells were grown to ~60% confluency and were harvested as previously described. Cells were centrifuged at 300 x g for 5min and resuspended in 90% FCS and 10% DMSO before being placed into 1.5mL cryovials. Each cryovial was placed into a cryo-freezing container containing isopropanol at -80°C overnight before being transferred to liquid nitrogen for long-time storage.

2.2.3 Generation of bone marrow-derived macrophages

Healthy C57/Bl6 mice were euthanized in a CO_2 chamber. A laminar flow hood and all utensils were sterilized with ethanol before use. The mice were sprayed with 70% ethanol before dissection. An incision was made in the centre of the abdomen and the skin was pulled backward over the hind legs. The femur was cut just below the hip joint to remove the leg. Muscle was removed from the femur and tibia. The knee joint was repeatedly extended to break it carefully, to avoid exposing the bone marrow. The foot was then removed from the tibia above the ankle joint, and both femur and tibia were placed into ice-cold DMEM containing 1% P/S. The bones were then flushed through the bone cavity with pre-warmed DMEM using a 25G needle and 10mL syringe. The bone marrow was collected in a 50mL tube and centrifuged at 300 x g for 5min. Cells were resuspended in 3mL red blood cell lysis buffer for 5min, before adding 7mL DMEM and centrifuged as described previously. Cells were resuspended in 30mL DMEM containing 20% M-CSF containing L929 media, 10% FCS and 1% P/S. 10mL of suspended cells were plated in three non-cell culture coated 10cm dishes.

Cells were incubated in standard cell culture conditions for 6 days, with cells receiving 1mL M-CSF-containing L929 media on day 3. After 6 days, cells were scraped in ice-cold PBS, resuspended and counted as described previously. Cells were then plated for experiments in DMEM containing 10% M-CSF-containing L929 media, 10% FCS and 1% P/S.

2.2.4 Enzyme-linked immunosorbent assay (ELISA)

Supernatants from treated cells were removed and cytokine levels present were colourimetrically measured using Duoset ELISA kits according to manufacturer's instructions for the cytokines TNFα, IL-1β, IL-6 and IL-10. The optical density values were measured using a 96-well plate reader set to 450nm and concentrations of cytokines were determined using a standard curve.

2.2.5 Plasmid DNA preparation

2.2.5.1 Plasmid transformation

Plasmid DNA was transformed into competent *E. coli* DH5α strain. 50ng of DNA was transformed into 20μL DH5α in a micro-centrifuge tube and incubated on ice for 30min. Cells were then placed in an incubator at 42°C for 45 seconds before immediately placing back on ice for 2min to allow for DH5α recovery. Cells were resuspended in 200μL S.O.C medium and plated on ampicillin agar plates. Agar plates were incubated at 37°C overnight.

2.2.5.2 Plasmid purification

After transformation on agar plates, a single colony was selected using a sterile micropipette tip and added to 5mL lysogeny broth (LB) medium without antibiotics for 4-6h at 37°C and 250rpm shaking. 100μL of this starter culture was transferred into 100mL of pre-warmed LB broth containing ampicillin and left shaking at 250rpm overnight at 37°C. The bacterial cell culture was harvested the next day by centrifugation at 4000rpm for 30min at 4°C. LB broth was removed and cell pellets were used to extract plasmid DNA using a maxiprep kit according to the manufacturer's instructions, or frozen for future extraction. Mal cysteine to alanine mutants were assessed for correct folding by collaborators. All Mal mutants, except C157A, fold correctly [214]. NEK7 cysteine to alanine mutants were not assessed for correct folding.

2.2.6 Luciferase assay

HEK293T, MTC and HEK293-TLR2 cells were seeded at $2x10^5$ cells/mL in 96-well plates 24h prior to transfection. Cells were transfected with 20-100ng of plasmids depending on plasmid

expression efficiency. 60ng NF-κB luciferase plasmid and 20ng TK *Renilla* plasmid was used to control for cell death and cell transfection efficiency. Plasmid levels were kept constant using a relevant empty vector control to a total of 200ng. For transfection, 9.2μL Serum free media (SFM) was vortexed with the 0.8μL of the transfection reagent Genejuice and incubated for 5min. Plasmid DNA was then added to the SFM/Genejuice mix and incubated for 15min at room temperature. This mixture was then added dropwise to the cells and left for 24h. For the luciferase assay, cells were either untreated, or treated for 6h with 100ng/mL LPS for MTC or 100ng/mL Pam3CSK4 for HEK293-TLR2 responses. Supernatant was gently removed and cells were lysed with 60μL 5X passive lysis buffer diluted to 1X in water for 15min gently rocking. 20μL of cell lysate was added to two white 96-well plates. 2X firefly assay mix was diluted in PBS to 1X. The remaining 20μL from the cell lysate was pooled from triplicate samples and transferred to a new eppendorf. 10μL of 5X sample loading buffer with DTT was added to examine protein levels of each plasmid. 40μL of 1X firefly assay mix was added to one white 96-well plate, and 40μL of a 1:500 dilution of coelenterazine in PBS was added to the second white 96-well plate. Both plates were examined for luminescence using a plate reader. NF-κB readings were normalized to TK *Renilla* internal control.

2.2.7 Co-immunoprecipitation assay

HEK293Ts and MTCs were seeded at $2.5x10^5$ cells/mL in 10cm dishes for 24h prior to transfection. BMDMs were seeded at $1x10^6$ cells/mL in 10cm dishes for 24h prior to stimulation. Cells were transfected as described previously with varying concentrations of 2-5μg of plasmid. In all cases, the amount of plasmid DNA was kept constant in each transfection by using the appropriate amount of empty vector control. 24h post transfection supernatant was removed and cells were washed with 5mL ice-cold PBS before being transferred directly to ice. Cells were harvested by lysis in 700μL of low stringency lysis buffer (50mM HEPES pH 7.5, 100mM NaCl, 1mM EDTA, 10% glycerol, 0.5% Nonident P40 (NP-40), 1mM phenylmethylsulphonyl fluoride (PMSF), 11.5μg/mL aprotinin, 1μg/mL leupeptin and 1mM sodium orthovanadate) for 15min on ice. For non-reducing immunoprecipitations, 50mM N-ethylmaleimide was added. Plates were scraped with a cell scraper and lysate transferred into microcentrifuge tubes. Tubes were centrifuged at 20,000 x g for 10min at 4°C. Microcentrifuge tubes were prepared with 30μL A/G bead slurry with 1μg of the relevant antibody or IgG control. 650μL of lysate was then incubated with antibody coated A/G beads for 2h rotating at 4°C. The remaining 50μL of lysate was boiled with 10μL 5X sample loading buffer with DTT. For non-reducing immunoprecipitations, DTT was omitted from sample loading buffer. After

2h the cell lysate/bead microcentrifuge tubes were centrifuged at 300 x g for 2min at 4°C, supernatant removed and beads washed three times with 1mL low stringency lysis buffer. The immune complexes were eluted by addition of 50µL 5X sample loading buffer, boiled for 5min and analysed by SDS-PAGE and western blotting.

2.2.8 Western blotting

2.2.8.1 SDS lysis for total protein

Prior to lysis, media was removed from cells. Cells were lysed directly using 50µL 5X sample loading buffer containing DTT (50µL was added to 950µL sample loading buffer before use). The lysates were transferred to microcentrifuge tubes and boiled for 5min. Protein samples were frozen at -20°C.

2.2.8.2 SDS polyacrylamide gel electrophoresis (SDS-PAGE)

Protein samples were resolved using a BioRad apparatus. An 8% or 10% acrylamide resolving gel was poured first. After polymerization, a 5% stacking gel was poured on top of the resolving gel and lanes were formed using a BioRad comb. The polymerized gel plate was placed in a BioRad tank filled with 1X SDS-running buffer. The protein samples and a protein standard of known molecular weights were loaded onto the gel to allow determination of the sizes of proteins from protein lysates. Gels were electrophoresed at 25mA per gel, until the dye front from the sample loading buffer ran to the end of the gel. Gel compositions are summarized in Table 2.5.

Table 2.5 Composition of acrylamide gels

Components for 2 Gels	8% Resolving Gel	10% Resolving Gel	15% Resolving Gel	5% Stacking Gel
dH_2O	7 mL	5.9 mL	3.4 mL	4.1 mL
30% Protogel	4 mL	5 mL	7.5 mL	1 mL
Tris pH 8.8	3.8 mL	3.8 mL	3.8 mL	-
Tris pH 6.8	-	-		750 µL
10% SDS	150 µL	150 µL	150 µL	60 µL
10% APS	150 µL	150 µL	150 µL	60 µL
TEMED	6 µL	6 µL	6 µL	6 µL

2.2.8.3 Electrophoretic transfer of protein to membranes

Once proteins were resolved, proteins were transferred to polyvinylidene fluoride (PVDF) membranes using a wet transfer apparatus. A piece of PVDF was initially soaked in 100% methanol to activate the membrane. All other components of the wet transfer were soaked in 1X transfer buffer before use. The transfer apparatus was assembled as follows, from cathode to anode: sponge, two layers of filter paper, PVDF activated with methanol, gel, two layers of filter paper and sponge. This assembly was sealed in a plastic cassette and placed in a transfer cassette within a transfer tank containing 1X transfer buffer and a cooling pack. A constant current of 200mA was used for transfer of 2 gels for 2h, or 30mA for overnight transfer.

2.2.8.4 Membrane blocking, antibody probing and visualization

Once transferred, PVDF membrane was blocked for non-specific antibody binding using 5% (w/v) non-fat milk powder (Marvel) reconstituted in 1X TBST for 1h at room temperature. The membrane was incubated with 1:1000 dilution of primary antibody and left to incubate for 2h at room temperature or overnight at 4°C. After incubation, the membrane was washed four times with 1X TBST for 40min on a roller, replacing TBST after every 10min. The membrane was then incubated with a species-specific secondary IgG antibody (anti-goat, anti-rabbit, anti-mouse) conjugated to a horseradish peroxidase (HRP) at 1:2000 for 1h room temperature or overnight at 4°C. The membrane was washed four times with 1X TBST every 5min, changing the TBST between each wash. For protein visualization, a chemiluminescent substrate was prepared according to the manufacturer's instructions (Thermo Scientific). The membranes were incubated in chemiluminescent substrate for 1min and visualized using a BioRad GelDoc.

2.2.9 RNA analysis

2.2.9.1 RNA extraction

Cell supernatant was removed and cells were lysed in 350µL lysis buffer (Ambion). The cell lysates were immediately frozen at -80°C and thawed gently prior to RNA extraction. Upon thawing, 350µL of 70% EtOH was added to the cell lysate for 2min to allow for RNA precipitation before transferring to Ambion RNA spin columns. The purification was followed as per manufacturer's instructions. The eluted RNA was quantified using a Nanodrop 2000 micro-volume UV-vis spectrophotometer and each RNA sample was diluted to the lowest yield.

2.2.9.2 Reverse transcription polymerase chain reaction

After RNA extraction and quantification, reverse transcription polymerase chain reaction (RT-PCR) was used to convert RNA to complementary DNA (cDNA) using a high capacity cDNA reverse transcription kit. 10µL of RNA was added to 10µL of reaction mix as described in Table 2.6. 20µL RNA/RT-PCR mix was transferred to 200µL micro tubes and placed in a thermal cycler programmed to: 10min 25°C, 120min 37°C, 15min 85°C and final holding stage of 4°C. Samples were diluted to 80µL in dH_2O and stored at -20°C.

Table 2.6 RT-PCR of RNA to cDNA

Component	Volume (µL)
10X RT Buffer	2
10X Random Primers	2
100mM deoxyribonucleotide triphosphates (dNTPs)	1
Multiscribe Reverse Transcriptase	1
Nuclease-free water	3.5
RNA (50-100ng/µL)	10

2.2.9.3 Real-time quantitative PCR

Real-time quantitative PCR (qPCR) was performed on cDNA generated from RT-PCR. qPCR was used to examine the expression levels of mouse IL-6, TNFα, IL-1β, IL-10, iNOS, Arginase-1, Mrc1, IL-12p40, PHD3, GLUT1, LDHa, IL1-RA, GSTO1-1, NLRP3, Caspase-11 and RPS18 (Table 2.7). qPCR was performed using SYBR Green reagents using the following reaction mix listed in Table 2.8. Relative fold values were calculated using the cycle-threshold (C_t) method and normalized to RPS18 housekeeping gene.

Table 2.7 SYBR Primers

Primer	Sense		Antisense	
IL-1β	5' GGAAGCAGCCCTTCATCTTT	3'	5' TGGCAACTGTTCCTGAACTC	3'
IL-6	5' ACGATGATGCACTTGCAG	3'	5' ACTCCAGAAGACCAGAGGAA	3'
IL-10	5' AGGCGCTGTCATCGATTT	3'	5' CACCTTGGTCTTGGAGCTTAT	3'
TNFα	5' GCCTCTTCTCATTCCTGCTT	3'	5' TGGGAACTTCTCATCCCTTTG	3'
IL-12p40	5' GTCCTCAGAAGCTAACCATCTC	3'	5' AGTCCAGTCCACCTCTACAA	3'
iNOS	5' GTGGTCCTCACTGACACCCT	3'	5' GGTGCGGACATCTTCTGACT	3'
ARG1	5' GGCAGAGGTCCAGAAGAATG	3'	5' TCCACCCAAATGACACATAGG	3'
MRC1	5' CTGGCGAGCATCAAGAGTAA	3'	5' CATAGGTCAGTCCCAACCAAA	3'
PHD3	5' TGCTGAAGAAAGGGCAGAAG	3'	5' GCACACCACAGTCAGTCTTTA	3'
GLUT1	5' GATCACTGCAGTTCGGCTATAA	3'	5' GTAGCGGTGGTTCCATGTT	3'
LDHa	5' ATCTTGACCTACGTGGCTTGGA	3'	5' CCATACAGGCACACTGGAATCTC	3'
IL-1RA	5' TTGTGCCAAGTCTGGAGA	3'	5' CTCAGAGCGGATGAAGGTAAAG	3'
GSTO1	5' CAAGAAGGCACGTCAGAAGA	3'	5' TTCCCTTAGGTTCGGAGAGT	3'
Caspase 11	5' CCTGAAGAGTTCACAAGGCTT	3'	5' CCTTTCGTGTACGGCCATTG	3'
NLRP3	5' CTCCCGCATCTCCATTTGT	3'	5' GCGTTCCTGTCCTTGATAGAG	3'
RPS18	5' GGATGTGAAGGATGGGAAGT	3'	5' CCCTCTATGGGCTCGAATTT	3'

Table 2.8 SYBR Green qPCR Reaction Mix

Component	Volume (μL)
Kapa SYBR mix	5μL
Primer Pair mixed (10μM final)	0.3μL
Nuclease-free H_2O	0.7μL
cDNA	4μL

2.2.10 Electroporation of Mal deficient iBMDMs

Mal deficient iBMDMs were harvested and counted as described previously. $1x10^6$ cells/mL were used for each reconstitution with 5μg of plasmid electroporated per sample. Cells were reconstituted using the NEON electroporation system. Briefly, cells were centrifuged and resuspended in 100μL buffer R. 5μg of plasmid was immediately added to the resuspended cells and placed in a 100μL NEON tip. The NEON tip was gently placed into the NEON electroporation machine in 3mL buffer E. A current was briefly applied to the tip consisting of 1680V, 1 pulse for 20ms. Electroporated cells were immediately transferred to 900μL antibiotic free DMEM media and incubated overnight at 37°C in 5% CO_2 incubator. Cells were treated with 100ng/mL LPS for the times indicated and then harvested as previously described.

2.2.11 Inflammasome assays

BMDMs were harvested and counted as previously described. $5x10^5$ cells/mL were seeded on 12-well plates and left overnight at 37°C in 5% CO_2 incubator. Cells were treated with 100ng/mL LPS for 3h. After 3h, media was removed and replaced with serum free DMEM. The GSTO1-1 inhibitor C1-27 was added for 45 min. Cells were treated with 5mM ATP or 10μM Nigericin for 45min for the NLRP3 inflammasome. 1μg Poly (dA:dT) was transfected for 2h using Lipofectamine 2000 for activation of the AIM2 inflammasome. To assess NLRC4 inflammasome activation, *Salmonella typhimurium* UK1 was grown in LB broth at 37°C shaking overnight, and subsequently sub-cultured until OD1. Bacterial innocula were prepared by centrifugation and washed with PBS, followed by reconstitution in DMEM to M.O.I. 20 for an infection assay. On the day of the assay, BMDMs were treated with 100ng/mL LPS for 3h. Medium was removed and replaced with serum free DMEM containing 5μM C1-27 for 45min followed by infection with *S. typhimurium* at M.O.I 20 for 15min. After 15 min, gentamicin (50 μg/mL; Sigma) was added to kill extracellular bacteria for a further 105min. Supernatants were collected for ELISA analysis, monolayers were washed with PBS and cells lysed with 5X sample loading buffer prior to western blotting. The remaining supernatant was incubated with 5μL of StrataClean Resin beads, briefly vortexed for 1 min and centrifuged at 300 x g for 2min at 4°C. The supernatant was removed, and beads were resuspended in 30μL 5X sample loading buffer. Cells were lysed in 50μL 5X sample loading buffer and analysed by SDS-PAGE.

2.2.12 FACS analysis of cellular reactive oxygen species

BMDMs were seeded at $5x10^5$ cells/mL on 12-well plates and left overnight at 37°C in 5% CO_2 incubator. Cells were treated as normal. Staining commenced 1h prior to completion of cell stimulations. CellROX or DCFDA stain was prepared by thawing on ice. CellROX or DCFDA was added directly into cell culture plates (2μL/mL) and incubated at 37°C covered with tinfoil for 30 min. After 40min incubation, the supernatant was removed and was replaced with 1mL PBS. Cells were detached using a cell scraper and transferred into polypropylene FACS tubes. Cells were pelleted by centrifugation at 650 x *g* for 3 min at room temperature. Cell pellets were washed 3 times with PBS (1mL) and resuspended in 500μL PBS and vortexed. Cells were then analysed using a Dako CyAn flow cytometer, and data was analysed using FlowJo software.

2.2.13 Seahorse analysis of lactate production

Cells were plated at $2x10^5$ cells/well (250µL) of a Seahorse plate in DMEM containing 10% FCS and 1% P/S. One well per row of the culture plate contained only supplemented media without cells. This controlled for background measurements. Cells were treated and stimulated as normal. The day prior to stimulations, the Seahorse XF24 analyser was turned on to warm up. A utility plate containing calibrant solution (1mL/well) together with the plates containing the injector ports and probes was placed in a CO_2-free incubator at 37°C overnight. The day of the experiment Seahorse medium supplemented with 25mM glucose was prepared in XF assay buffer. This involved preparing a 1M glucose solution by addition of 1.8g glucose to 10mL XF assay buffer, which was diluted 1:40 to obtain 25mM final concentration. This medium was adjusted to pH 7.4 and filter-sterilized. The supernatant from cell culture plates was removed and replaced with 500µL XF media containing glucose and the cell culture plate was placed in a CO_2-free incubator for at least 30min.

During this time, the inhibitor oligomycin was prepared in glucose-supplemented medium (16µL in 1984µL media) and 70µL of this solution was added to the respective injector plate port. Similarly, 100ng LPS was prepared in glucose-supplemented medium and 70µL of this solution was added to the respective injector plate port. This plate, together with the utility plate was run on the Seahorse for calibration. Once complete, the utility plate was replaced with the cell culture plate and run on the Seahorse.

2.2.14 ASC Speck formation assay

To analyse ASC speck formation by crosslinking, disuccinimidyl suberate (DSS) was used. BMDMs were seeded at $1.5x10^6$cell/mL in 6-well plates in technical duplicate and incubated at 37°C 5% CO_2 overnight. Cells were pre-treated with 100ng/mL LPS for 3h. After 3h of LPS stimulation, media was removed and replaced with 1mL DMEM containing 5µM C1-27 for 45 min. After 45 min, cells were treated with 5mM ATP for 45 min. Supernatant was removed and cells were washed twice with 200µL ice cold 50mM HEPES. Cells were lysed on ice for 15min in 200µL lysis solution (0.5% Triton X-100, 50mM HEPES, protease and phosphatase inhibitors). Duplicate samples were pooled and centrifuged at 6000 x g for 15 min at 4°C. The Triton X-100 soluble fraction (supernatant) was removed and stored at -20°C. The Triton X-100 insoluble fraction (pellet) was washed twice with 50mM HEPES and centrifuged at 6000 x g for 15 min at 4°C. During the washing step, DSS-crosslinking buffer was made (50mM HEPES, 150mM NaCl pH 8). DSS was allowed to reach RT prior to resuspension in anhydrous

DMSO (54.3µL DMSO to 2mg DSS for 100mM stock). The Triton X-100 insoluble pellet was resuspended in 490µL DSS-crosslinking buffer and incubated with 10µL rehydrated DSS (2mM final concentration), mixed immediately and incubated for 45min at 37°C. After 45min, samples were centrifuged at 6000 x g for 15 min at 4°C. The supernatant was removed gently, and the remaining DSS-crosslinked pellet was resuspended in 50µL sample loading buffer containing DTT. Samples were analysed by SDS-PAGE.

2.2.15 Endogenous knockdown of GSTO1-1

BMDMs were seeded at $5x10^5$ cells/mL on 12-well plates and left overnight at 37°C in 5% CO_2 incubator. Cell medium was removed and cells were washed briefly with PBS. 500µL Opti-MEM reduced serum medium was added to cells. 10nmol scramble or GSTO1-1 siRNA (Ambion) was incubated with 5µL RNAiMAX Lipofectamine reagent in 500µL Opti-MEM for 10min. After incubation, 500µL siRNA-lipofectamine mix was added to cells to yield 1mL of Opti-MEM medium containing 5nmol siRNA final concentration. Cells were left for 36-48h before treatment.

2.2.16 LPS Transfection and LDH assay

BMDMs were seeded at $5x10^5$ cells/mL on 12-well plates and left overnight at 37°C in 5% CO_2 incubator. Cells were treated with 100ng/mL LPS for 4h to induce Caspase-11 expression. After 4h, medium was removed and cells were washed with PBS. 1mL of complete medium was added to cells. 2µL of 1mg/mL LPS was added to 45.5µL Opti-MEM medium and vortexed immediately. 2.5µL RT FuGene transfection reagent was added to the LPS/Opti-MEM, mixed gently and left for 10min RT. 50µL was added per well and left for 16h before harvesting supernatant for ELISA and LDH assays. LDH assay was performed as per manufacturer's instructions. Briefly, 50µL of cell supernatant was added to a 96-well plate with 50µL of LDH assay buffer and left for 30min in the dark. 50µL stop solution (CH_3COOH) was added to the plate and absorbance measured at 490nm.

2.2.17 *In vivo* sepsis model

Seven-week-old C57BL/6 control and C57BL/6 GSTO1-1-deficient mice were injected with 100µL 10mg/kg LPS or 100µL PBS for 90min. Mice were sacrificed, whole blood was harvested and left to coagulate for 30 min at RT. Serum was removed and analysed for cytokines by Quantikine ELISA.

2.2.18 Mass Spectrometry of NEK7

HEK293T cells were reverse transfected with HA-tagged NEK7. HEK293T cells were seeded at $7.5x10^5$ cells/mL in 10mL in 10cm dishes. During the plating, 10µg NEK7 was transiently transfected into the HEK293T cells using GeneJuice and left overnight at 37°C in 5% CO_2 incubator. Cell medium was removed, cells were washed gently with PBS and cells were immediately lysed in low stringency lysis buffer containing protease and phosphatase inhibitors. An immunoprecipitation was performed as section 2.2.7 using an anti-HA antibody conjugated to A/G beads. After 2h rotating at 4°C, A/G beads were washed three times with low stringency lysis buffer. After the third wash, the A/G beads were dried and incubated with 250µL of 200µg HA peptide (I2149) for 30min at 37°C at 300rpm. Beads were agitated every 5min to prevent sedimentation of A/G beads. A/G beads were centrifuged at 300 x g for 2min. Supernatant was removed and stored on ice. A/G beads were subsequently incubated with a further 250µL of 200µg HA peptide for 30min at 37°C at 300rpm and centrifuged at 300 x g for 2min. Both 250µL supernatants were combined and concentrated using an Amicon Ultra 10K concentrating column. The concentrated eluate was incubated with 5mM GSSG pH 8 for 1h at RT prior to loading on an 8% acrylamide gel. The 8% gel was fixed in coomassie blue fixing solution (50% MeOH, 10% HoAC, 40% ultrapure H_2O) in a clear container for 30min on an orbital shaker at RT. Fixing solution was removed and replaced with Coomassie Blue R-250 for 1h at RT with gentle agitation. The gel was washed overnight at 4°C with de-staining solution (5% MeOH, 7.5% HoAC and 87.5% ultrapure H_2O). The gel bands were excised in a laminar flow hood and placed in sterile eppendorfs. 500µL band wash solution was added (50% MeOH, 5% HoAC and 45% ultrapure H_2O) to eppendorfs and mixed at 1300rpm at RT for 2h, with wash solution changed every 30min to remove Coomassie stain. Gel bands were stored in 500µL band wash solution on dry ice. Gel fragments were digested using Trypsin and analysed by 1D nLC-MS/MS by a 4000QTRAP mass spectrometer. The resulting data was processed using the Mascot search engine.

2.2.19 Peritoneal exudate cell isolation and culture

Peritoneal exudate cells (PECs) were isolated from mice by sterile PBS gavage of the peritoneal cavity post-sacrifice. Injected mice were gently agitated for 1min and PBS syringed from the left flank was placed in a sterile falcon tube placed on ice. Cells were centrifuged at 300 x g for 5min and resuspended in RPMI medium containing 10% FCS and 1% P/S. Cells were plated on 12-well plates at $5x10^5$ cells/mL. After 3h, medium was removed and replaced with complete RPMI. Cells were stimulated for 3h with LPS, medium removed and stimulated with 10µM

Nigericin for 1h. Supernatant was removed for ELISA and samples were lysed in 5X sample loading buffer for western blot analysis.

2.2.20 Statistical Analysis

P-values were calculated by two-tailed unpaired Students t-test or one-way ANOVA in GraphPad Prism version 5.0. * signifies a P-value of ≤0.05, ** signifies a P-value of ≤0.01 and *** signifies a P-value of ≤0.001.

Chapter 3

Glutathionylation of Mal on Cysteine 91 regulates TLR4 activation

Investigation into the role of glutathione as a post-translational modification in Mal

3.1 Introduction

Macrophages respond to bacterial or viral infection by triggering a complex inflammatory cascade, potentiating cytokine release and inflammation for effective host responses for pathogen clearance. In order for macrophages to effectively propagate such signals, they utilize highly specialized transmembrane receptors termed TLRs. Each TLR has an affinity for certain PAMPs, resulting in activation of signalling cascades via activation and recruitment of adaptor proteins intracellularly. Mal is one such adaptor protein shared by TLRs 2, 4 and 9. Mal also has a TLR-independent role as an adaptor for the IFN-γ receptor. Mal must therefore be regulated post-translationally to prevent aberrant cytokine production and inflammation.

Studies have identified a critical role for Mal in response to *Staphylococcal* infections. In families harbouring a missense mutation, Mal deficiency renders such individuals highly susceptible to chronic infection. Polymorphisms of Mal also exist within human populations. One such polymorphism, S180L, is unusual in that it can confer susceptibility if homozygous to bacterial infection, including *M. tuberculosis* infection, or resistance if heterozygous. Indeed, S180L appears to be a Goldilocks' variant, which is present in 26.9% of a UK cohort [215].

Post-translational modifications of the TLR adaptor Mal have been studied extensively prior to this project, however researchers failed to consider the redox environment as a potential regulator of Mal activation. This study examined the regulation of TLR adaptor Mal by GSH, and whether glutathionylation of Mal could have a positive or negative effect on the regulation of TLR responses. We have discovered that Mal is a glutathionylated protein, and furthermore that glutathionylation of Mal on cysteine 91 is crucial for TLR responses. We have found functional importance for Mal glutathionylation, as a Mal mutant (C91A), which fails to bind GSH, acts as a dominant negative mutation and is unable to interact with downstream partners MyD88 or IRAK4. Interestingly, supplementation of cells with the antioxidant N-acetylcysteine limited LPS-induced Mal glutathionylation, indicating a potential early ROS signal in activation of TLR signalling.

3.1.1 Identification of conserved cysteine amino acids in Mal

The first aim of this project was to identify which cysteines in Mal were conserved across species. Using the bioinformatics software Uniprot, I aligned FASTA sequences from human, mouse, rat, chicken, panther, bovine, pig, guinea pig, cat, orangutan and canine Mal (Fig 3.1). Cysteines 89, 91, 116, 134, 142 and 157 were highly conserved across all species. Cysteine 174 was less conserved but was conserved in human and mouse Mal. Crystallization of Mal by Valkov et al. [43] identified that cysteines 91 and 157 cannot form a disulphide bond, due to being 5Å apart. We next sought to assess if cysteines were potential glutathionylation targets.

3.1.2 Mal is endogenously glutathionylated and glutathionylation is increased in response to LPS treatment

I next examined if Mal was glutathionylated endogenously and used an immunoprecipitation approach, isolating Mal from murine BMDMs. Using a highly specific antibody that recognises –SSG modified proteins, Mal was found to be endogenously glutathionylated basally without stimulation, and with 1h LPS treatment the glutathionylation status of Mal was decreased (Figure 3.2A). Mal appeared to immunoprecipitate as a dimer, with a clear band observed at 50kDa. A non-specific band is observable at 260kDa, which may potentially be due to the non-reducing properties of the gel.

I next performed a time course with LPS. LPS treatment increased Mal glutathionylation at 5 and 15 min relative to unstimulated Mal with a decrease occurring at 60 min LPS treatment (Figure 3.2 B Lane 4). The decrease in Mal glutathionylation with LPS treatment in Figure 3.2 A is more pronounced than in Figure 3.2 B lane 4.

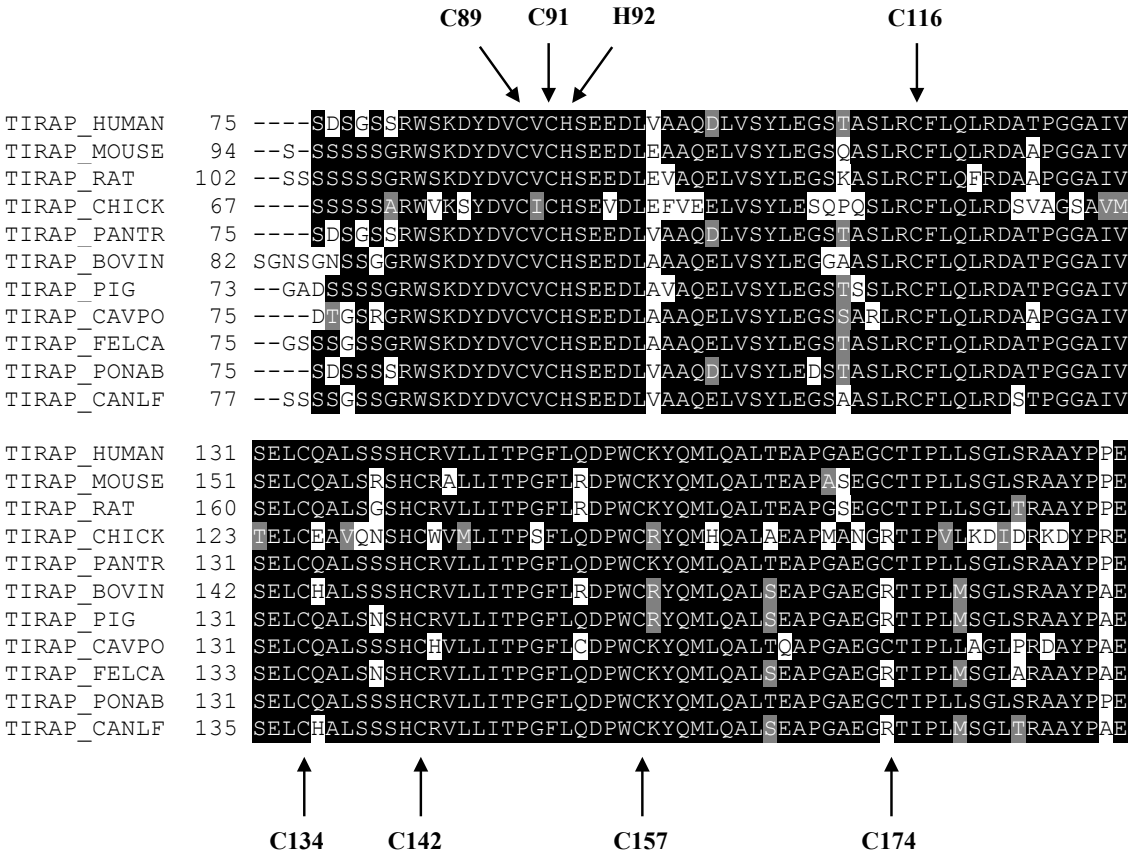

Figure 3.1 Conservation of Mal cysteine amino acids

Conservation of Mal cysteines was assessed using bioinformatics software Uniprot. FASTA sequences were aligned and examined conservation against human, mouse, rat, chicken, panther, bovine, pig, guinea pig, cat, orangutan and canine Mal. Cysteines 89, 91, 116, 134, 142 and 157 were highly conserved. Cysteine 174 was conserved between human, mouse, rat, panther, guinea pig and orangutan Mal. The flanking amino acid to Cysteine 91, Histidine 92, was conserved across all species.

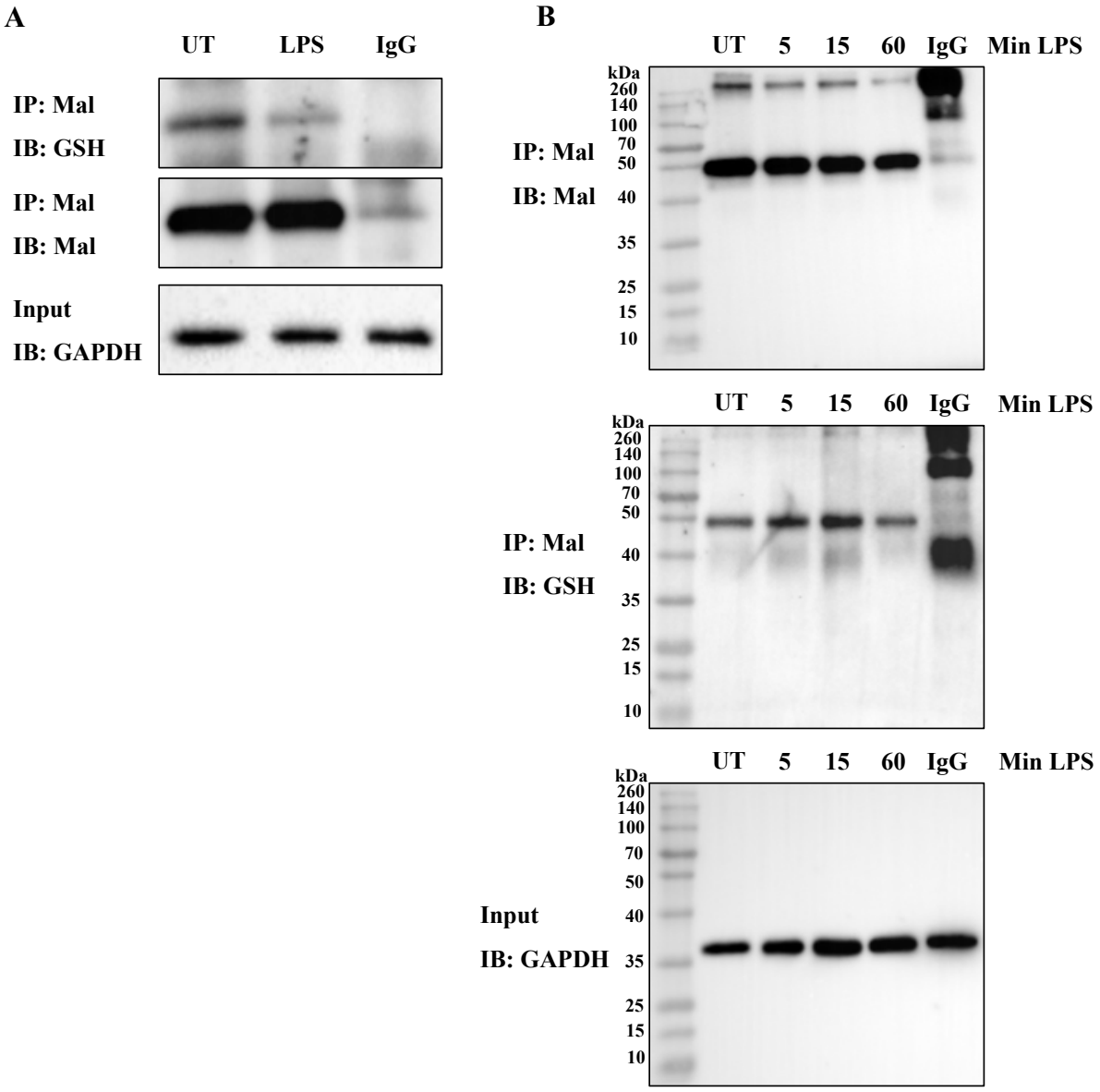

Figure 3.2 Endogenous Mal glutathionylation in LPS-activated macrophages

(A) Murine bone marrow derived macrophages (BMDMs) were seeded at 1x10^6 cells/mL in 10cm dishes and left at 37°C 5% CO2 overnight. Cells were treated with 100ng/mL LPS for 60min and lysed using low stringency lysis buffer supplemented with protease inhibitors and 50mM N-ethylmaleimide. The lysate was immunoprecipitated on A/G beads and subjected to non-reducing SDS-PAGE. Samples were blotted for anti-SSG, anti-Mal or anti-GAPDH. (B) BMDMs treated as above were treated with 100ng/mL LPS for the times indicated and subjected to immunoprecipitation and non-reducing SDS-PAGE as above. Each blot is representative of three independent experiments. Samples were blotted for anti-SSG, anti-Mal or anti-GAPDH.

3.1.3 Mal Cysteine 91 is a glutathionylation target

I next examined the cysteine residues that might be potential glutathionylation targets. As stated above, the structure of Mal identified C91 and C157 as two cysteines which could not form a disulphide bond. Previous work from collaborators had found that C157 mutation to Alanine disrupted Mal structure (B. Kobe, personal communication), therefore we decided to examine the effect of cysteine to alanine mutation of C91. As shown in the upper panel, overexpressed WT Mal was basally glutathionylated (Figure 3.3 Top panel Lane 2) and LPS treatment caused an increase in glutathionylation (Lane 4) The C91A form of Mal displayed reduced glutathionylation (Lane 3) and LPS addition had no effect on C91A glutathionylation (Lane 5). These results indicate that C91 can undergo glutathionylation.

3.1.4 Histidine 92 promotes Mal glutathionylation

Glutathionylation of cysteine amino acids has been reported to be influenced by positively charged neighbouring amino acids. The neighbouring amino acid to C91 is a histidine residue, H92. Having previously detected decreased glutathionylation of C91A, we mutagenized Histidine 92 to examine its potential effect on C91 glutathionylation. H92 was substituted with a proline amino acid, which is structurally similar to histidine (H92P). As shown in Figure 3.4 Top panel, overexpressed WT Mal was basally glutathionylated (Lane 2) and, in contrast to Figure 3.3, LPS treatment caused a decrease in glutathionylation (Lane 4), possibly due to overexpression of Mal. The H92P form of Mal was not glutathionylated (Lane 3) and LPS addition had no effect on H92P glutathionylation (Lane 5). Overexpressed WT Mal also displays a prominent doublet band (Lane 2), which is noticeably absent in H92P Mal (Lane 3) These results suggest that mutating Histidine 92 to Proline prevents glutathionylation of C91, most likely due to the lack of positive charge.

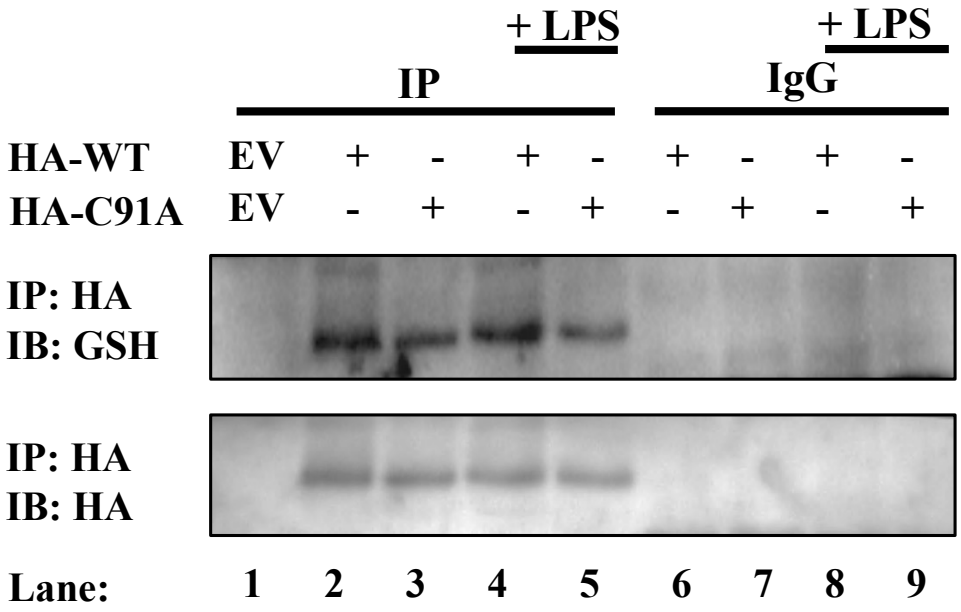

Figure 3.3 Mal C91A has impaired glutathionylation

HEK293-MD2-TLR4-CD14 cells were seeded at 2x10^5 cells/mL in 10cm dishes and incubated at 37°C 5% CO2 overnight. The following day cells were transfected with 5μg empty vector (EV), 2μg WT HA-Mal plasmid with 3μg HA-EV or 3μg C91A HA-Mal plasmid and 2μg HA-EV. 24h post transfection, cells were treated with 100ng/mL LPS for 60min and lysed using low stringency lysis buffer supplemented with protease inhibitors and 50mM N-ethylmaleimide. Mal was immunoprecipitated on A/G beads coated with 1μg HA-tag antibody for 2h at 4°C. Beads were washed three times and boiled in 5X sample loading buffer and subjected to non-reducing SDS PAGE. Samples were blotted for –SSG (upper panel) or the HA-tag (bottom panel for immunoprecipitated Mal). Each blot is representative of three independent experiments.

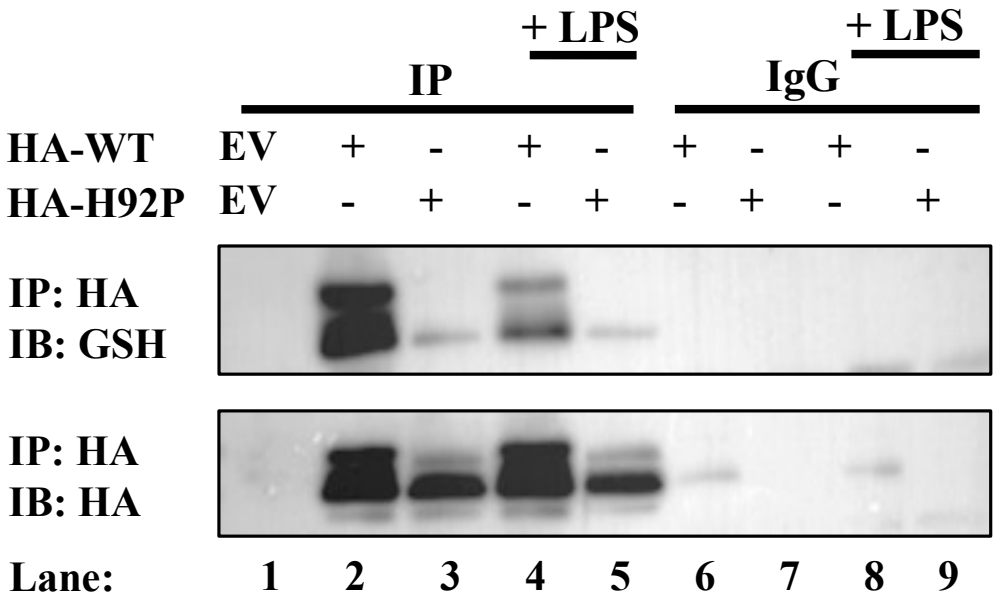

Figure 3.4 Mal H92P has impaired glutathionylation

HEK293-MD2-TLR4-CD14 cells were seeded at $2x10^5$ cells/mL in 10cm dishes and incubated at 37°C 5% CO2 overnight. The following day cells were transfected with 5μg EV, 2μg WT HA-Mal plasmid with 3μg HA-EV or 3μg C91A HA-Mal plasmid and 2μg HA-EV. 24h post transfection, cells were treated with 100ng/mL LPS for 60min and lysed using low stringency lysis buffer supplemented with protease inhibitors and 50mM N-ethylmaleimide. Mal was immunoprecipitated on A/G beads coated with 1μg HA-tag antibody for 2h at 4°C. Beads were washed three times and boiled in 5X sample loading buffer and subjected to non-reducing SDS PAGE. Samples were blotted for –SSG (upper panel) or the HA-tag (bottom panel for immunoprecipitated Mal). Each blot is representative of three independent experiments.

3.1.5 C91A and H92P cannot drive NF-κB luciferase activation

After determining that Mal C91 could be glutathionylated, I next tested whether Mal C91A was functionally impaired using activation of NF-κB luciferase as an assay. As shown in Figure 3.5 A, C91A Mal was unable to drive NF-κB activity. The P125H mutant was inactive as expected (this mutant is a dominant negative form of Mal). Overexpression of C157A and a double C91A/C157A mutant yielded similar results. C91A and C91A/C157A had attenuated NF-κB activity in this luciferase assay, however C157A was still able to generate a signal, although attenuated. I attributed the inability of C91A/C157A to drive NF-κB activation to C91A as C157A was still able to drive NF-κB activation.

I next tested the H92P mutant of Mal. As shown in Figure 3.5 B, similar to C91A, H92P was unable to drive NF-κB activity in a luciferase assay compared to WT Mal. Western blots confirmed expression of each form of Mal (bottom panel).

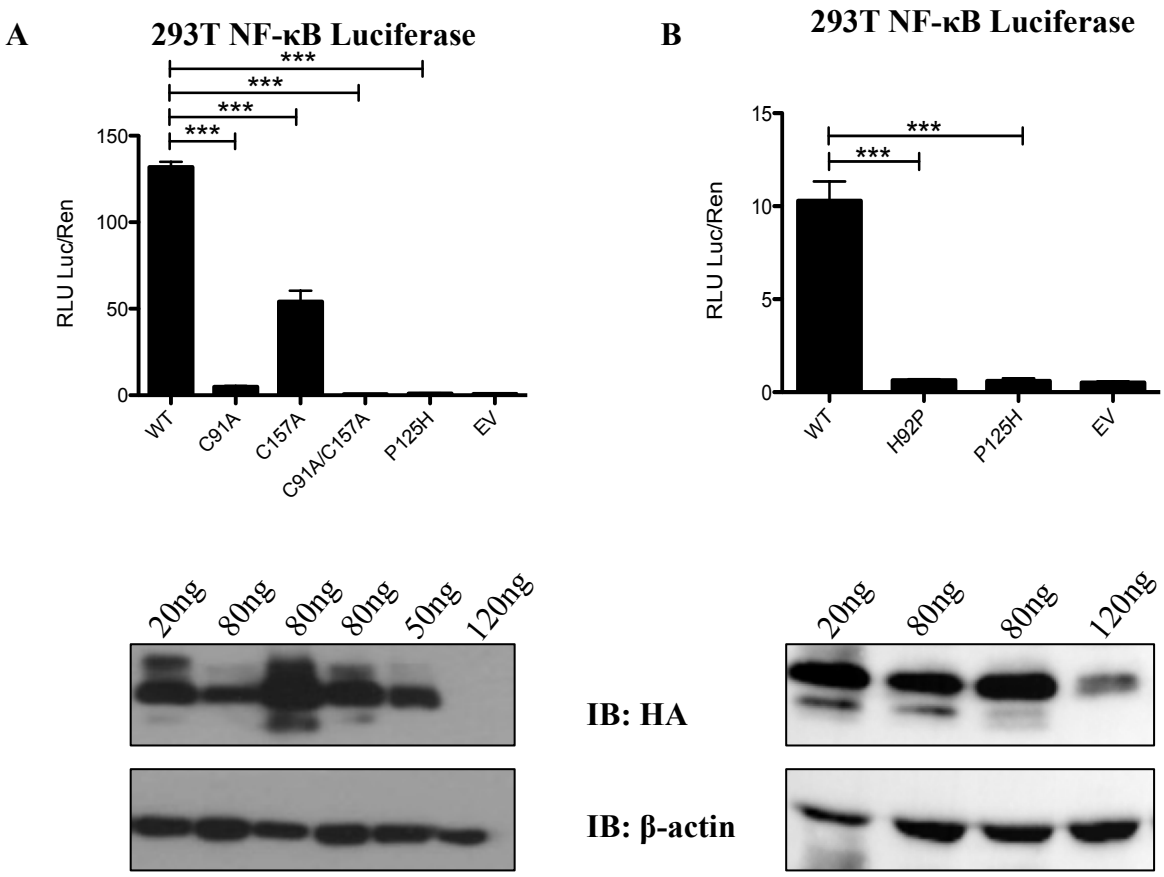

Figure 3.5 C91A and H92P cannot drive NF-κB activation and display decreased phosphorylation

(A) HEK293T cells were seeded at $2x10^5$ cells/mL in a 96-well plate and incubated at 37°C 5% CO2 overnight. Cells were transfected with WT HA-Mal, C91A HA-Mal, C157A HA-Mal, C91A/C157A HA-Mal, P125H HA-Mal or HA-EV for 24h. Luciferase activity was determined and control *Renilla* reading normalized to Firefly luciferase activity to control for transfection efficiency. Mal protein level was assessed by western blot. (B) HEK293T cells were treated as above and transfected with WT HA-Mal, H92P HA-Mal, P125H HA-Mal and HA-EV. Luciferase activity was determined and *Renilla* reading normalized to Firefly luciferase activity. Mean expression ± S.E.M of three independent experiments carried out in triplicate is shown. *** $P \leq 0.001$

3.1.6 C91A and H92P are dominant negative mutants in TLR4 signalling

I next sought to examine if the overexpressed plasmids could have an impact on TLR4 signalling. MTC cell lines are readily transfectable and stably express TLR4 and the accessory components MD2 and CD14. In Figure 3.6 A, I overexpressed WT Mal or each cysteine to alanine Mal mutant and then treated the transfected cells with LPS. The C91A Mal mutant displayed a dominant negative effect on TLR4 signalling, with impaired NF-κB activation compared to WT Mal. Mal P125H completely abrogated TLR4 responses as expected. As shown in Figure 3.6 B, H92P Mal had a dominant negative impact on TLR4 signalling, with decreased NF-κB activity after LPS treatment. Western blots of the protein lysate were assessed for equal protein expression (lower panels).

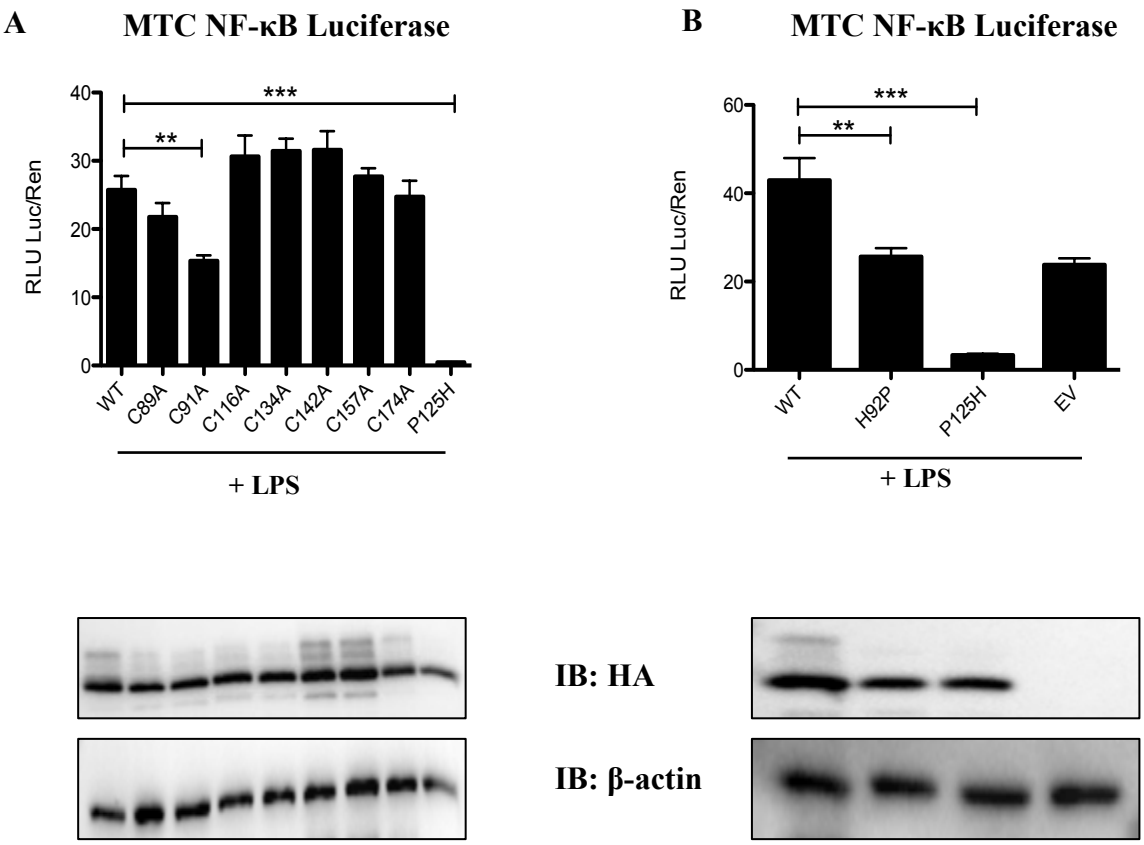

Figure 3.6 C91A and H92P are dominant negative mutations for TLR4 signalling

(A) 293T-MD2-TLR4-CD14 cells were seeded at $2x10^5$ cells/mL in a 96-well plate and incubated at 37°C 5% CO2 overnight. Cells were transfected with WT HA-Mal, cysteine to alanine HA-Mal mutants, P125H HA-Mal or HA-EV for 24h. 100ng/mL LPS was added to the cells 6h prior to luciferase assay. Luciferase activity was determined and *Renilla* reading normalized to Firefly luciferase activity. Mal protein level was assessed by western blot. (B) 293T-MD2-TLR4-CD14 cells were treated as above and transfected with Mal WT, H92P, P125H and EV. Luciferase activity was determined and *Renilla* reading normalized to Firefly luciferase activity. Mean expression ± S.E.M of three independent experiments carried out in triplicate is shown. ** $P \leq 0.01$, *** $P \leq 0.001$

3.1.7 C91A and H92P are dominant negative mutants in TLR2 signalling

I next sought to examine if the overexpressed plasmids could have an impact on TLR2 signalling. HEK293-TLR2 express TLR2, which can be stimulated with the TLR2 agonist Pam3CSK4. As shown in Figure 3.7 A, comparable to LPS treatments, C91A Mal displayed a dominant negative effect on TLR2 signalling, with impaired NF-κB activation compared to WT Mal. The dominant negative effect was less pronounced than the TLR4 response. Mal P125H completely abrogated TLR2 responses. Similarly, in Figure 3.8 B, H92P Mal had a dominant negative impact on TLR2 signalling, with decreased NF-κB activity. This observed dominant negative effect was stronger compared to C91A Mal. Western blots of the protein lysate were assessed for equal protein expression (lower panel).

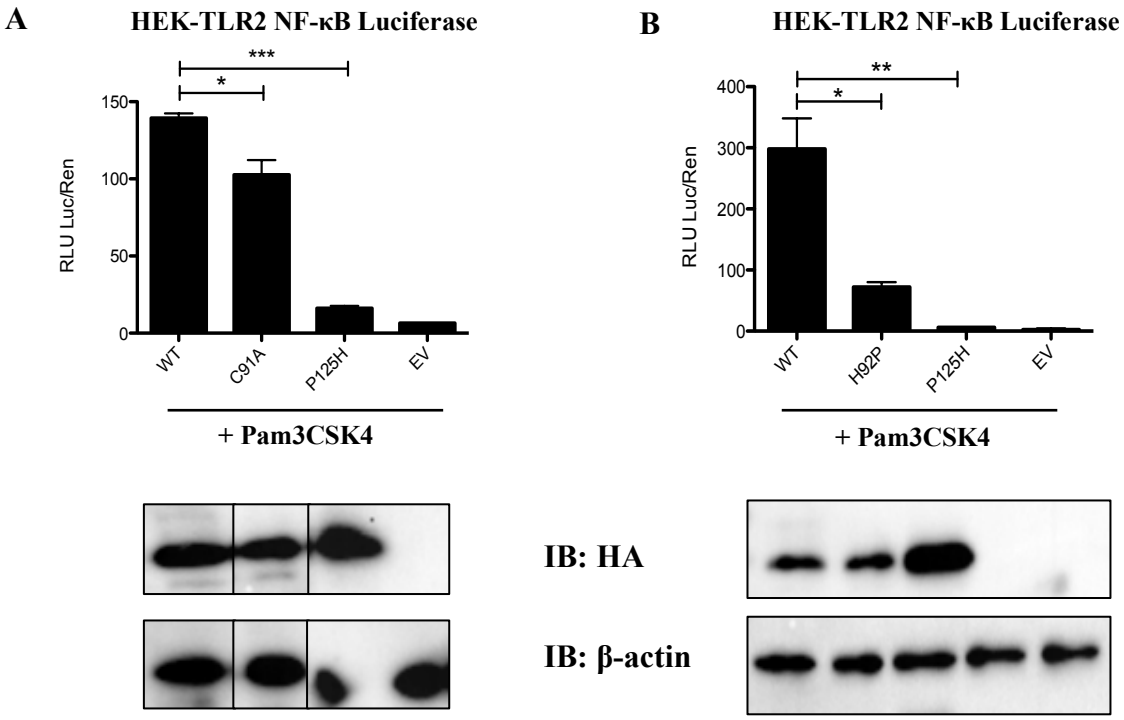

Figure 3.7 C91A and H92P are dominant negative mutations for TLR2 signalling

(A) HEK293-TLR2 cells were seeded at $2x10^5$ cells/mL in a 96-well plate and incubated at 37°C 5% CO2 overnight. Cells were transfected with WT HA-Mal, HA-C91A Mal, HA-P125H Mal or HA-EV for 24h. 100ng/mL Pam3CSK4 was used to stimulate cells for 6h prior to luciferase assay. Luciferase activity was determined and *Renilla* reading normalized to Firefly luciferase activity. Mal protein level was assessed by western blot. (B) HEK293-TLR2 cells were treated as above and transfected with Mal WT, H92P, P125H and EV. Luciferase activity was determined and *Renilla* reading normalized to Firefly luciferase activity. Mean expression ± S.E.M of three independent experiments carried out in triplicate is shown. * $P \leq 0.05$, *** $P \leq 0.001$

3.1.8 C91A and H92P cannot reconstitute TLR4 signalling in Mal-deficient iBMDMs

I next examined whether Mal C91A or H92P could reconstitute LPS signalling in Mal-deficient immortalised bone marrow-derived macrophage (iBMDM) cells. IκBα degradation was used as a signal for NF-κB activation. As shown in Figure 3.8 A, WT Mal transfection rendered iBMDMs sensitive to LPS, with IκBα degradation being evident at 60 and 90 minutes treatment. The level of degradation reached 56% when normalized to control β-actin levels by densitometry. Transfection of cells with plasmids encoding C91A Mal (Figure 3.8 B) or H92P Mal (Figure 3.8 C) did not reconstitute the response to LPS, confirming their lack of activity.

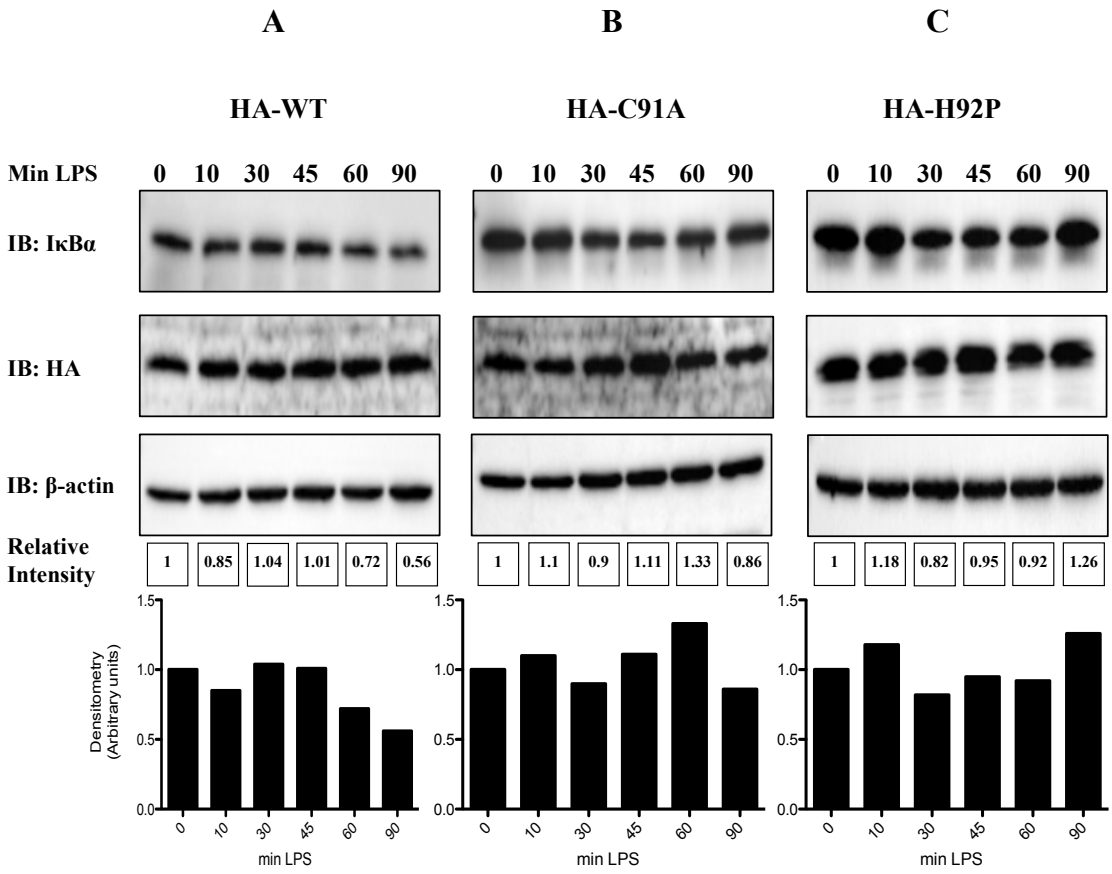

Figure 3.8 C91A and H92P do not reconstitute the TLR4 signalling pathway

(A) Mal-deficient iBMDMs were reconstituted with 5μg of WT HA-Mal plasmid, (B) 5μg C91A HA-Mal or (C) 5μg H92P HA-Mal using the NEON electroporation system. $1x10^6$ cells/mL were resuspended in 100μL buffer R and incubated briefly with 5μg of Mal plasmids. iBMDMs were immediately loaded to a 100μL NEON tip and electroporated at 1680V for 20ms and 1 pulse. Electroporated cells were placed in 900μL pre-warmed antibiotic free media and incubated at 37°C 5% CO2 overnight. Immediately the next morning cells were treated with LPS for the times indicated, lysed and subjected to SDS-PAGE. IκBα, HA-tag and β-actin were assessed by western blot. Blots are representative of three independent experiments each.

3.1.9 C91A cannot interact with MyD88 in a co-immunoprecipitation assay

I next examined whether C91A Mal might be impaired in its ability to interact with MyD88. As shown in Figure 3.9 there is an interaction between WT Mal and Myc-MyD88 (Upper panel Lane 5). This interaction is absent with C91A Mal (Lane 6). The pulldown of both WT Mal and C91A Mal was equal for the immunoprecipitation bait (second uppermost panel compare Lanes 5 and 6). Mal C91A expressed poorly when transfected alone compared to WT Mal (second uppermost panel compare Lanes 2 and 3). C91A Mal expressed better when co-transfected with Myc-MyD88. Input blots of Mal and Myc-MyD88 (lower panels) indicate Mal and MyD88 were sufficiently overexpressed before immunoprecipitation. Lane 1 appeared to contain a smeared band, possibly due to the development of the blot.

3.1.10 H92P cannot interact with MyD88 in a co-immunoprecipitation assay

I next tested whether the H92P form of Mal might be similarly impaired in its ability to interact with MyD88. As shown in Figure 3.10, there is an interaction between WT Mal and Myc-MyD88 (Upper panel Lane 5). This interaction is reduced with H92P Mal (Lane 6). The pulldown of both WT Mal and H92P Mal was equal for the immunoprecipitation bait (second uppermost panel compare Lanes 5 and 6). Similar to C91A, Mal H92P expressed poorly when transfected alone compared to WT Mal (second uppermost panel compare Lanes 2 and 3). H92P Mal expressed better when co-transfected with Myc-MyD88. Input blots of Mal and Myc-MyD88 (lower panels) indicate Mal and MyD88 were sufficiently overexpressed before immunoprecipitation.

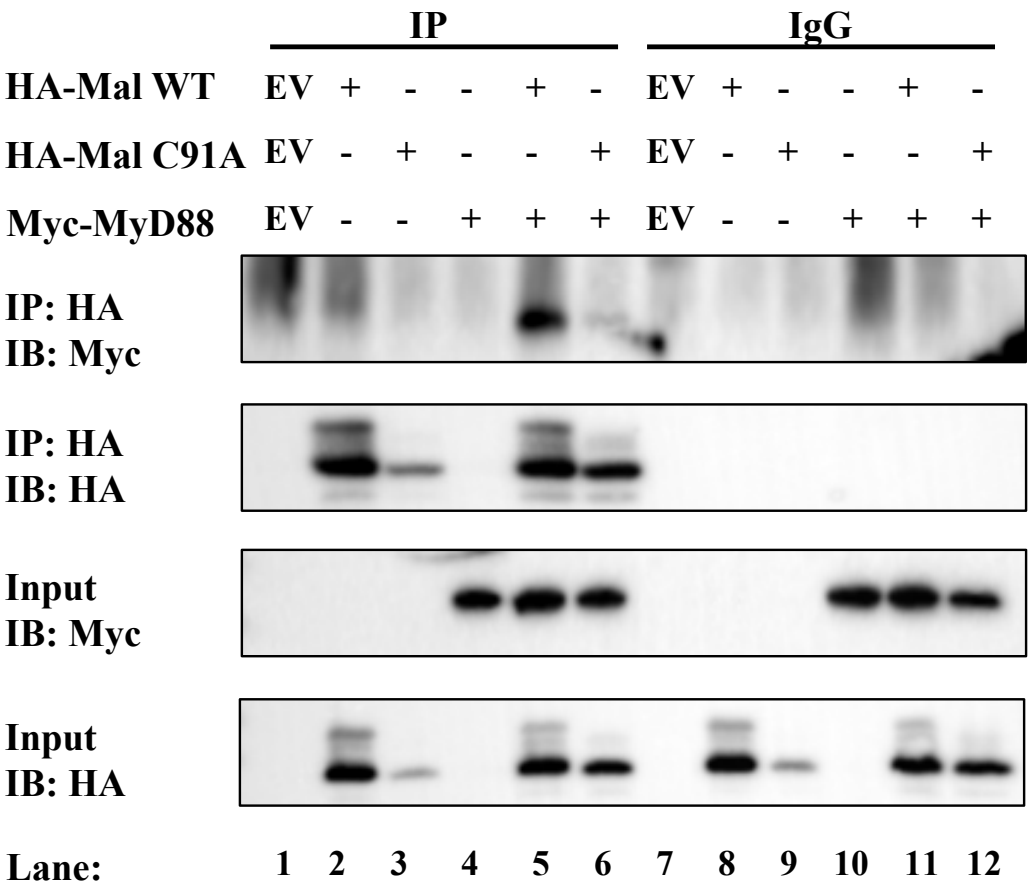

Figure 3.9 C91A does not immunoprecipitate with MyD88

HEK293T cells were seeded at 2.5x10^5 cells/mL in 10cm dishes and incubated at 37°C 5% CO_2 overnight. Cells were transfected with WT HA-Mal, C91A HA-Mal, Myc-MyD88 or HA-EV. In each transfection, the total concentration of plasmid DNA was kept constant by addition of relevant EV control. 48h post transfection cells were lysed in low stringency lysis buffer. 50µL of lysate was kept for analysis while the remaining lysate was added to protein A/G beads coated with 1µg of anti-HA antibody or 1µg mouse-IgG control antibody for 2h rotating at 4°C. Samples were washed three times in 1mL low stringency lysis buffer and resuspended in 50µL sample loading buffer. Whole cell lysates and immunoprecipitated samples were analysed by western blotting using anti-Myc and anti-HA antibodies. The results shown are representative of four independent experiments.

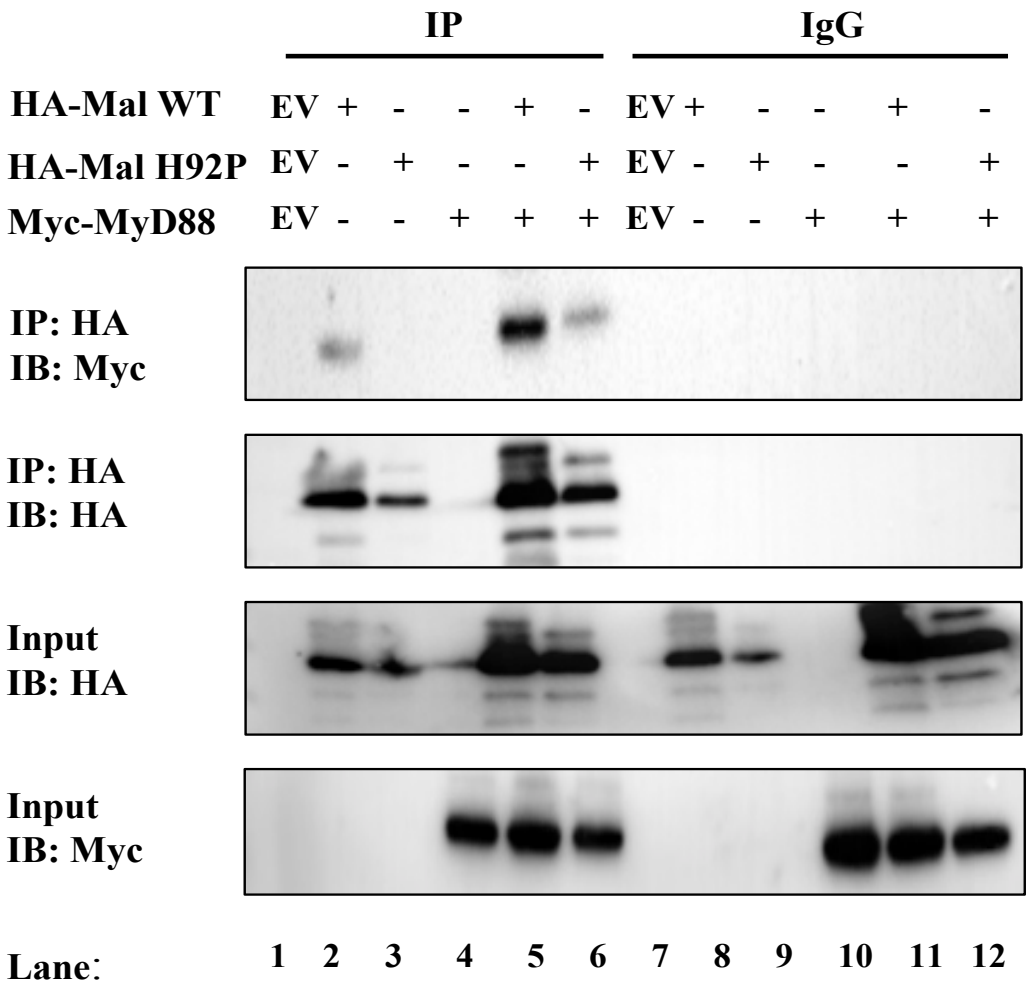

Figure 3.10 H92P does not immunoprecipitate with MyD88

HEK293T cells were seeded at 2.5x10^5 cells/mL in 10cm dishes and incubated at 37°C 5% CO_2 overnight. Cells were transfected with WT HA-Mal, HA-H92P Mal, Myc-MyD88 or HA-EV. In each transfection, the total concentration of plasmid DNA was kept constant by addition of relevant EV control. 48h post transfection cells were lysed in low stringency lysis buffer. 50µL of lysate was kept for analysis while the remaining lysate was added to protein A/G beads coated with 1µg of anti-HA antibody or 1µg mouse-IgG control antibody for 2h rotating at 4°C. Samples were washed three times in 1mL low stringency lysis buffer and resuspended in 50µL sample loading buffer. Whole cell lysates and immunoprecipitated samples were analysed by western blotting using anti-Myc and anti-HA antibodies. The results shown are representative of three independent experiments.

3.1.11 IRAK4 cannot induce degradation of C91A or H92P

Previous literature has identified that IRAK4 can phosphorylate Mal, resulting in polyubiquitination and degradation by the proteasome [216]. I next tested whether Mal C91A and H92P might be resistant to IRAK4-mediated degradation. As shown in Figure 3.11 A, transfection of HEK293T cells with increasing concentrations of a plasmid encoding IRAK4 induced degradation of Mal, as determined by densitometry, with Mal levels reducing to 28% with the highest protein concentration of IRAK4. As shown in Figure 3.11 B, overexpression of IRAK4 did not induce degradation of C91A. Densitometry confirms no degradation of C91A relative to loading control. Similarly, in Figure 3.11 C, overexpression of IRAK4 did not induce H92P degradation. Overall, these results suggest that IRAK4 cannot phosphorylate and promote degradation of C91A or H92P Mal.

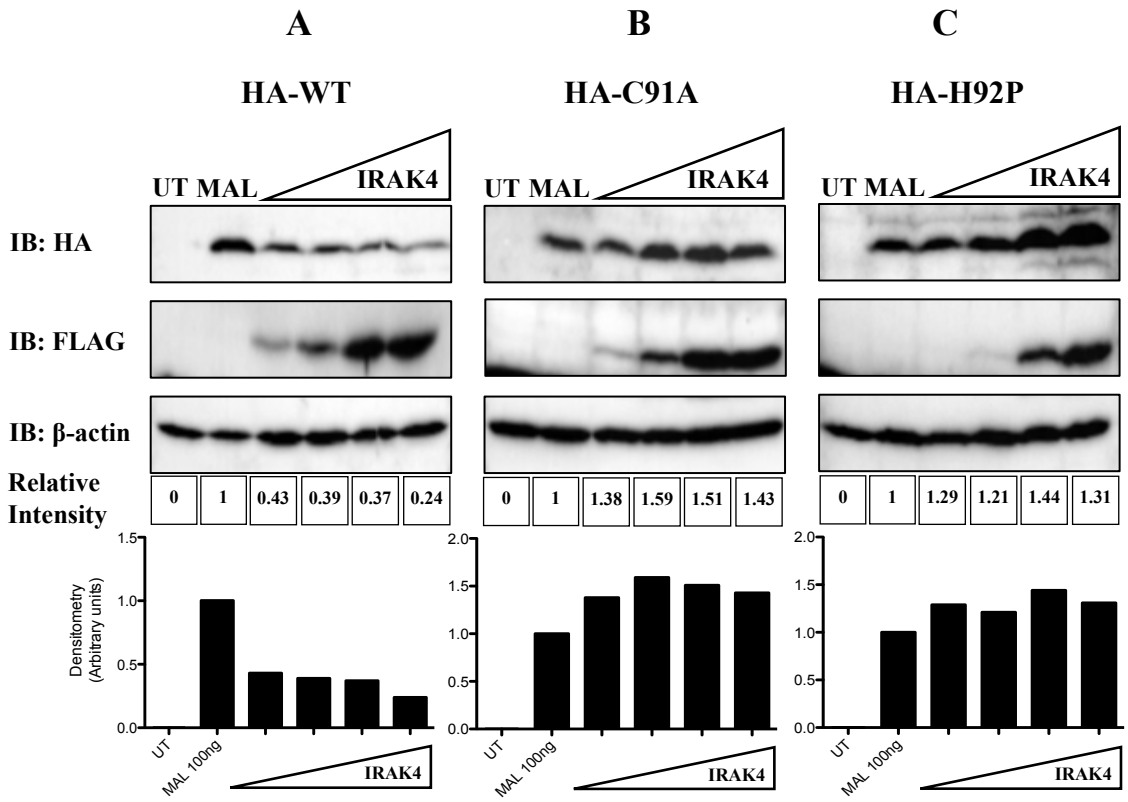

Figure 3.11 IRAK4 does not induce degradation of Mal C91A or H92P

HEK293T cells were seeded at $2x10^5$ cells/mL in 12-well plates and incubated at 37°C 5% CO_2 overnight. Cells were transfected with WT HA-Mal, C91A HA-Mal, H92P HA-Mal, FLAG-IRAK4 or mock transfected. In each transfection, the total concentration of plasmid DNA was kept constant by addition of relevant EV control. 24hr post transfection cells were lysed in 50μL sample loading buffer. Cell lysates were analysed by western blotting using anti-HA, anti-FLAG and anti-β-actin antibodies. Densitometry was performed using ImageLab5 software using β-actin as a loading control. The results shown are representative of three independent experiments.

3.1.12 IRAK4 cannot co-immunoprecipitate with C91A or H92P

I next sought to examine if IRAK4 would co-immunoprecipitate with WT Mal, C91A Mal or H92P Mal since as stated above, IRAK4 activation will lead to Mal degradation [216]. We used an IRAK4 kinase dead (IRAK4-KD) version whereby the ATP binding site is mutagenized to prevent kinase activity of IRAK4 and WT IRAK4 as a control. IRAK4-KD interacts with Mal. As shown in Figure 3.12, IRAK4 did not interact with WT Mal (Top panel Lane 2), as previously reported [216]. Similarly, C91A and H92P could not interact with IRAK4 (Top panel Lane 3 and 4 respectively). IRAK4-KD interacted with WT Mal (Top panel Lane 5). However, IRAK4-KD displayed reduced interaction with C91A or H92P (Top panel Lanes 6 and 7 respectively). To test for Mal expression, we immunoblotted for HA-tag from the lysate collected before co-immunoprecipitation. In the third panel WT Mal, C91A and H92P are expressed, with decreased expression of Mal in lane 2 due to IRAK4 kinase activity promoting degradation of Mal. C91A Mal (Third panel Lane 3) or H92P Mal (Third panel Lane 4) did not undergo degradation in response to IRAK4. The pulldown of IRAK4 and IRAK4-KD was relatively even (Second Panel Lanes 2-7). Overall, these results suggest that IRAK4 cannot interact with Mal when the glutathionylation site of Mal is mutagenized, as C91A and H92P could not interact with either IRAK4 or the kinase dead version. Mal glutathionylation may therefore be required for interaction with IRAK4.

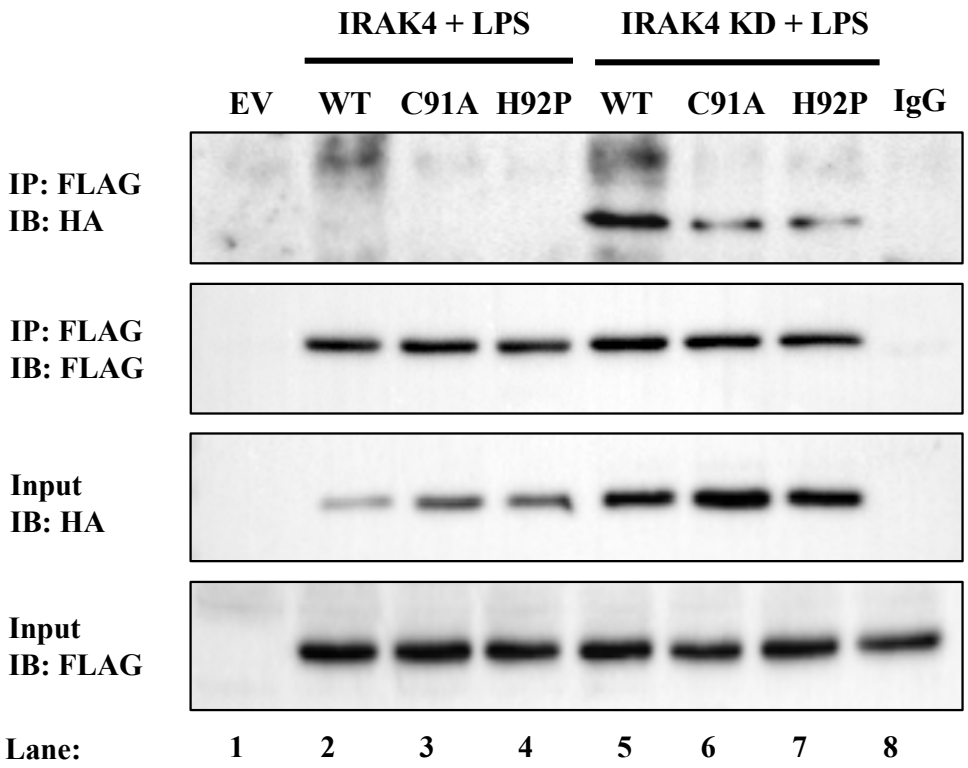

Figure 3.12 IRAK4 does not immunoprecipitate with Mal C91A or H92P

MTCs were seeded at $2.5x10^5$ cells/mL in 10cm dishes and incubated at 37°C 5% CO_2 overnight. Cells were transfected with WT HA-Mal, HA-C91A Mal, HA-H92P Mal, FLAG-IRAK4 or FLAG-IRAK4 KD or mock transfected. In each transfection, the total concentration of plasmid DNA was kept constant by addition of relevant EV control. 48h post transfection cells were lysed in low stringency lysis buffer. 50μL of lysate was kept for analysis while the remaining lysate was added to protein A/G beads coated with 1μg of anti-FLAG antibody or 1μg mouse-IgG control antibody for 2hr rotating at 4°C. Samples were washed three times in 1mL low stringency lysis buffer and resuspended in 50μL sample loading buffer. Whole cell lysates and immunoprecipitated samples were analysed by western blotting using anti-HA and anti-FLAG antibodies. The results shown are representative of three independent experiments.

3.1.13 Mal glutathionylation can be prevented using the antioxidant NAC

We next sought to identify if the glutathionylation of Mal was dependent on ROS production in response to LPS stimulation. Pre-treatment of iBMDMs with N-acetylcysteine (NAC), a ROS scavenger, prevented Mal glutathionylation in response to LPS (Top panel compare Lane 8 to 3). The pulldown of Mal was relatively even (Middle panel lanes 1-4, 6-9). GAPDH served as a loading control (Bottom panel). This suggests that ROS may mediate the glutathionylation of Mal. The band for GSH in lane 3 is very strong compared to Fig 3.2 and may be due to differences between primary cell and immortalised cell line immunoprecipitation.

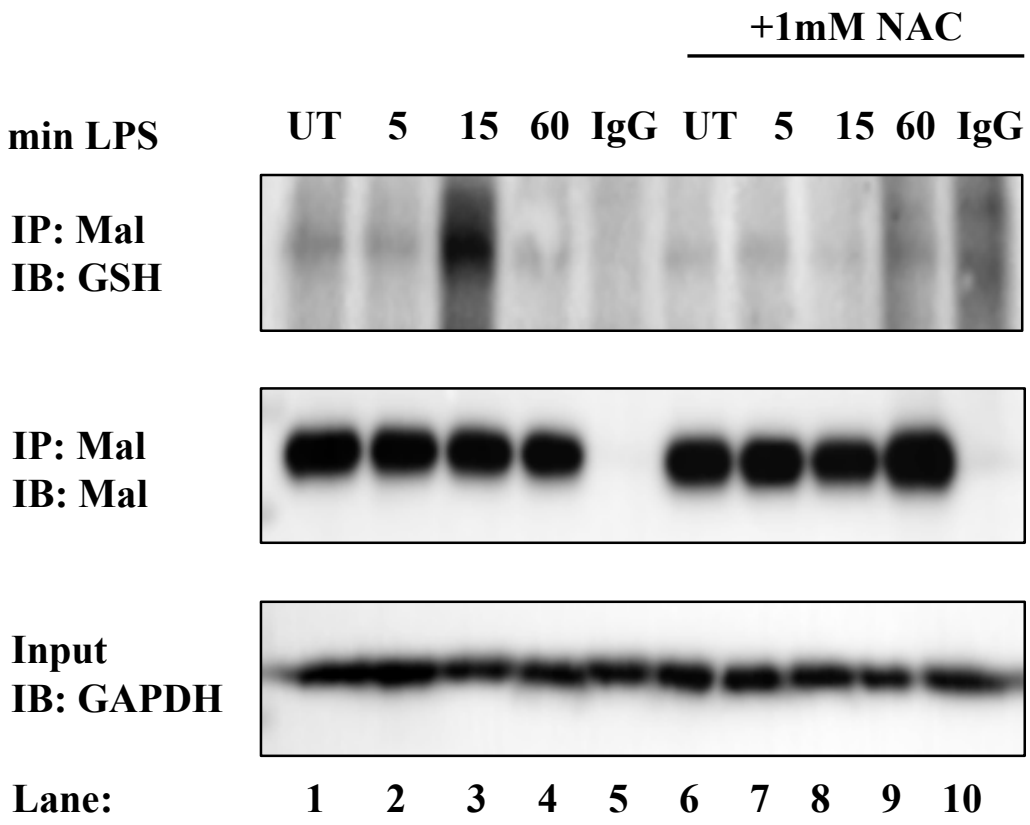

Figure 3.13 Glutathionylation of Mal is prevented with N-acetylcysteine pre-treatment
iBMDMs were seeded at $2.5x10^5$ cells/mL in 10cm dishes and incubated at 37°C 5% CO_2 overnight. Once cells reached 80% confluency, cells were pre-treated with 1mM NAC for 60min. Cells were then treated with 100ng/mL LPS for the times indicated. Cells were lysed in low stringency lysis buffer with 50mM N-ethylmaleimide. 50µL of lysate was kept for analysis while the remaining lysate was added to protein A/G beads coated with 1µg of anti-Mal antibody or 1µg mouse-IgG control antibody for 2h rotating at 4°C. Samples were washed three times in 1mL low stringency lysis buffer and resuspended in 50µL sample loading buffer without DTT added. Whole cell lysates and immunoprecipitated samples were analysed by western blotting using anti-Mal, anti-GSH and anti-GAPDH antibodies. The results shown are representative of three independent experiments.

3.2 Discussion

The first line of investigation into this project employed bioinformatics to assess whether Mal contained cysteines that could potentially be targeted as a site for post-translational modification. As stated previously, Mal has been shown to be regulated by several modifications. Glutathionylation of redox-sensitive cysteines has been shown to regulate many enzymes, including inhibition of Caspase-1 [181], succinyl-coA transferase and ATP synthase (F_1 complex, α-subunit) [217], and also promotes stability of HIF1α [218]. We hypothesised that Mal may be regulated by glutathione, possibly through direct binding to a cysteine that is solvent accessible.

I first examined C91 and C157 as they were reported to be more than 5Å apart and could therefore not form a structural disulphide bond [57].To examine the potential for Mal to be glutathionylated, I first performed an endogenous immunoprecipitation under non-reducing conditions to prevent disruption of the potential glutathionylation site using BMDMs as my primary cell of interest. We hypothesized that if glutathionylation of Mal was essential for function, then addition of LPS may affect Mal glutathionylation. Mal was basally glutathionylated, and addition of LPS for 1h promoted deglutathionylation of Mal. This result implied that Mal glutathionylation was transient and could possibly be induced by LPS. I then sought to further elucidate if an LPS time-course could affect Mal glutathionylation. Addition of LPS at 5min and 15min increased Mal glutathionylation, and this increased glutathionylation was reduced to comparable levels of basal glutathionylation at 60min LPS treatment. Once TLR4 is activated, a multimeric assembly composed of MyD88, IRAK4, IRAK2 and IRAK1, termed the myddosome, promotes IκBα degradation. TLR4 activation has been shown to be a transient process, with degradation of the NF-κB inhibitory protein IκBα occurring rapidly with LPS treatment [219]. Our initial findings indicated that Mal glutathionylation may promote TLR4 activation, possibly through myddosome assembly to allow for MyD88 recruitment. Our finding that Mal glutathionylation was reduced at 60min LPS treatment led us to hypothesize that the deglutathionylation of Mal may act as an inhibitory feedback mechanism to limit TLR4 activation. We therefore sought to expand upon our findings by limiting Mal glutathionylation.

I next examined which cysteines in Mal are required for GSH binding. Using site directed mutagenesis, I designed primers which would introduce a mutation into wild-type Mal. I primarily generated three cysteine to alanine mutants, C91A and C157A and a double C91A/C157A mutant. Initial overexpression studies identified that C157A frequently resulted in incorrectly folded protein and did not express relative to C91A. For this reason, I used C91A

for our initial experiments. Mal C91A was not glutathionylated when overexpressed and immunoprecipitated compared to wild-type Mal. Pre-treatment of LPS did not induce C91A glutathionylation. The glutathionylation of wild-type Mal was increased however with LPS. Previous reports suggested that neighbouring amino acids which have a positive charge, such as lysine, histidine and arginine, can directly impact on the ability for cysteine thiol groups to become more prone to glutathionylation [220]. Bioinformatic alignment of the amino acid sequence of Mal indicated that a conserved histidine, H92, neighboured C91. I next mutagenized H92 to a structurally similar amino acid, proline, which does not have a positive charge. Like C91A, H92P was not glutathionylated when overexpressed and immunoprecipitated. LPS pre-treatment did not induce glutathionylation of H92P. Immunoprecipitation, followed by blotting of C91A and H92P also indicated the absence of an upper band on Mal, which is interpreted as the phosphorylation band.

I next examined if C91 was the main functional glutathionylation target, as Mal contains 7 cysteines, C89, C91, C116, C134, C142, C157 and C174. I examined if each mutant could successfully drive NF-κB activation via luciferase assay as a functional readout, as each cysteine except C91 and C157 have been reported to be in disulphide bond formation and would be occluded from GSH in tertiary structure [57]. C91A and C157A were unable to drive NF-κB activation as anticipated. I decided to use a higher plasmid concentration of C157A and used an NF-κB luciferase assay as a readout to assess if C157A was structurally unstable at lower concentrations. C157A could drive NF-κB activation, albeit at an attenuated level and appeared to have the upper phosphorylation band seen in wild-type Mal. C91A however could not drive NF-κB activation. The double mutant C91A/C157A had attenuated NF-κB reporter activity, and this was attributed to C91A, as C157A could drive NF-κB. Similarly, H92P could not drive NF-κB activation compared to wild-type Mal. Overexpression of plasmids in HEK293T cells however relies on the expression of the plasmid to drive NF-κB activation and does not require a stimulus. I overexpressed each cysteine mutant in MTCs, which are LPS responsive and used an NF-κB luciferase assay to assess TLR4 activation. Notably, only C91A had a dominant negative effect, with significantly attenuated NF-κB activation. Likewise, H92P attenuated NF-κB activation with LPS treatment. Mal is also utilized by TLR2 as an adaptor protein. I next assessed if TLR2 would be impaired similar to TLR4 with C91A and H92P. Both mutants attenuated NF-κB activation in HEK293-TLR2 cells treated with Pam3CSK4, however C91A did not have as significant an impact as a dominant negative mutant towards TLR2 activation. Kenny et al. reported that Mal is not required by TLR2 to signal using high

ligand concentrations [65], which may explain why the dominant negative effect observed during TLR4 signal activation is limited under TLR2 stimulation with Pam3CSK4.

Having gathered data on numerous NF-κB luciferase assays, I decided to examine if C91A and H92P could reconstitute iBMDMs deficient in Mal. Wild-type Mal successfully reconstituted TLR4 signalling, with degradation of IκBα used as the readout for TLR4 activation. Both C91A and H92P mutants failed to reconstitute TLR4 signalling, with protein expression comparable to wild-type Mal. Glutathionylation of Mal on C91 must therefore be required for TLR4 activation to drive assembly of the myddosome to activate NF-κB.

TLR4 activation is initiated by Mal dimerization to allow for myddosome assembly [221]. Mal dimerization promotes MyD88 recruitment, through interaction via homologous TIR domains. It has been well established that Mal can interact with MyD88 and IRAK4, two components of the myddosome. The results I obtained indicated that both C91A and H92P function as dominant negative mutations, preventing activation of NF-κB. The binding of GSH may therefore promote Mal interaction with TLR components. To assess this, I performed co-immunoprecipitations of C91A with MyD88. The results of the co-immunoprecipitation experiments indicated that C91A and MyD88 did not interact. Similarly, co-immunoprecipitation of H92P with MyD88 failed to interact. This experiment suggests that glutathionylation of C91 is critical for interaction with MyD88. Preventing glutathionylation by mutating the positively charged H92 abrogated Mal-MyD88 interaction, which compliments the previously described immunoprecipitations indicating H92P negatively affects C91 glutathionylation.

Due to the lack of interaction with MyD88, I hypothesized that the dominant negative effects of C91A and H92P may limit myddosome assembly. IRAK4 has been previously reported to induce phosphorylation of Mal on threonine 28, inducing polyubiquitination and subsequent proteasomal degradation of Mal [70]. IRAK4 is also a component of the myddosome [222]. IRAK4-induced degradation of WT Mal may therefore be limited when Mal is unable to become glutathionylated. IRAK4 induced Mal degradation, however both C91A and H92P Mal failed to degrade with increasing concentrations of IRAK4. This data suggests that Mal glutathionylation can promote IRAK4-mediated phosphorylation and Mal degradation as the mutants are unaffected by IRAK4. The kinase dead version of IRAK4 immunoprecipitated with wild-type Mal, however this interaction was attenuated by both C91A and H92P. This data contrasts previous reports of GSH limiting phosphorylation, as GSH has been shown to

negatively regulate the phosphorylation of STAT3 [223]. This data suggests that GSH binding to Mal may promote a conformational change to allow for interaction with MyD88. It may also open threonine 28 to allow for phosphorylation of Mal by IRAK4. Both Mal mutants cannot be glutathionylated, and may thereby occlude threonine 28 from IRAK4, preventing the interaction with IRAK4.

Having established that Mal is glutathionylated, I considered how LPS can induce glutathionylation, as GSH can be compartmentalized to varying concentrations [112], that may not respond rapidly to TLR4 activation. There is an abundant literature that LPS drives ROS [199], [200], so I decided to examine if an antioxidant pre-treatment would prevent Mal glutathionylation in response to LPS. Using N-acetylcysteine, Mal glutathionylation was prevented, pointing to a mechanism whereby LPS binding to TLR4 can conceivably initiate a rapid localized ROS microenvironment, promoting Mal glutathionylation for myddosome assembly. Previous evidence using L929 cells treated with the anticancer agent curcumin has demonstrated a rapid induction of ROS detectable from 5min, coupled with a decrease in total free-GSH pools. The decrease in total GSH was linked to induction of Caspase-3-independent apoptosis and cytochrome c release from the mitochondria. Interestingly pre-treatment with GSH prevented curcumin-induced cell death [224]. This finding may point to a mechanism whereby GSH is rapidly sequestered by redox-sensitive cysteines upon TLR activation, reducing the overall GSH pool transiently to promote signalling. Further work is required to confirm the impact of antioxidants on Mal glutathionylation.

3.3 Final conclusion

Overall, I have characterised a novel post-translational modification in the TLR signalling adaptor Mal. Mal is the first reported adaptor protein to undergo glutathionylation and therefore glutathionylation of other adaptor proteins warrants investigation. Mal C91 is the main glutathionylated cysteine, and alteration of C91 limits Mal activation. I have further characterized the functional relevance of Mal glutathionylation, as Mal C91A cannot interact with MyD88 or IRAK4, limiting the capacity for TLR activation. As glutathionylation is a redox sensitive event, the mechanisms driving Mal glutathionylation warrant further investigation. The main findings from this chapter are summarised in Figure 3.14.

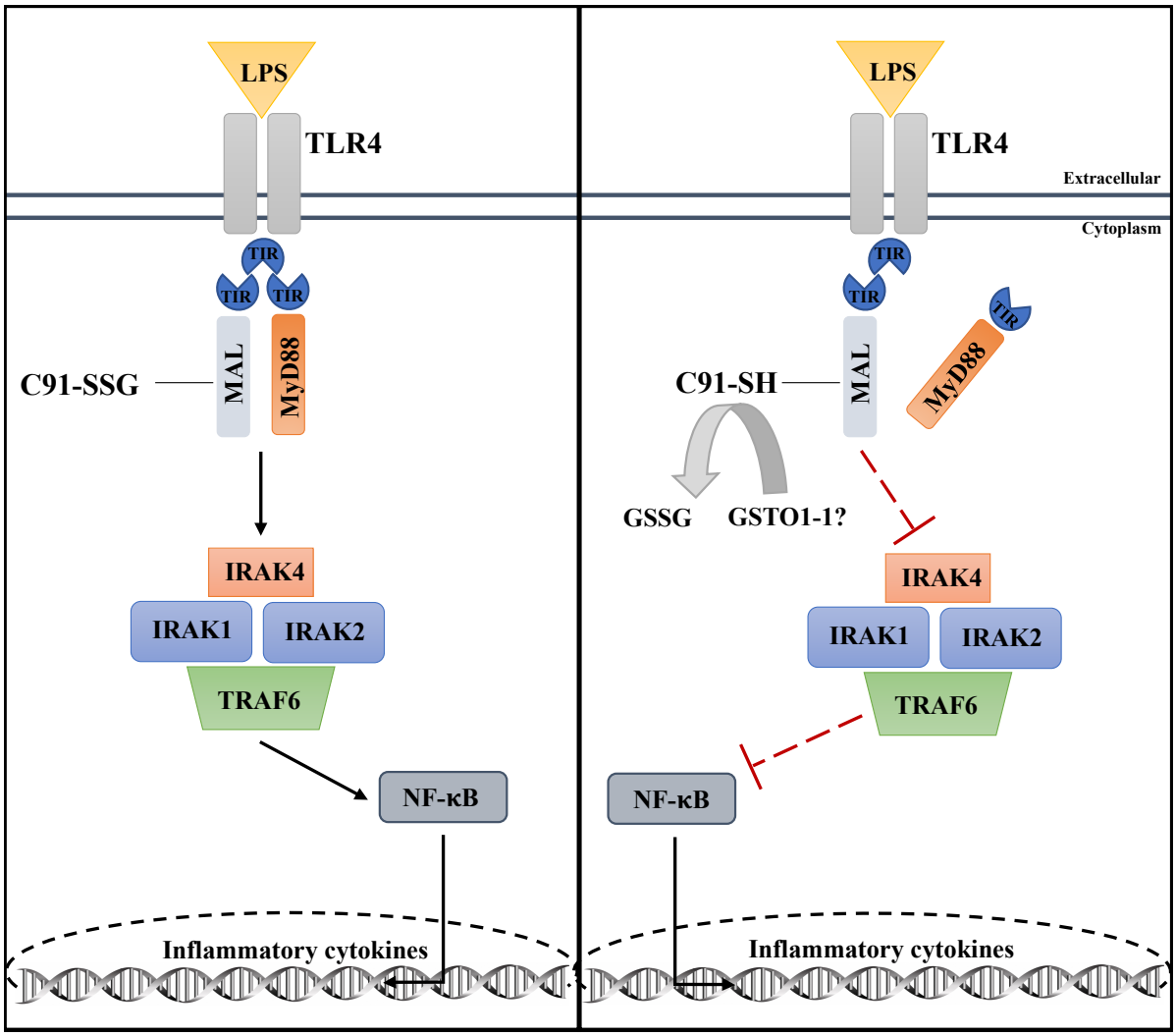

Figure 3.14 Schematic summary of results from Chapter 3

LPS-binding to TLR4 induces an intracellular conformation change to allow for TIR domain interactions and subsequent recruitment of TIR domain-containing adaptors Mal and MyD88. Glutathionylation of Mal (left) promotes Mal-MyD88 interaction to drive assembly of the myddosome containing IRAKs 1, 2 and 4 and TRAF6, ultimately leading to activation and translocation of NF-κB to the nucleus to upregulate inflammatory gene transcription. Deglutathionylation of Mal (right), results in Mal inactivation and failure to interact with MyD88, limiting activation of NF-κB.

Chapter 4

GSTO1-1 acts as an anti-inflammatory enzyme in macrophages

Characterisation of GSTO1-1 function in macrophages

4.1 Introduction

Macrophages responding to PAMPs require a system to effectively and efficiently remove insults, the most robust of which is generation of ROS to clear pathogens. ROS generation can be a relatively slow process, due to molecular remodelling of macrophages to a pro-oxidant environment. Such remodelling is known to affect mitochondrial dynamics, resulting in induction of pro-inflammatory factors including the transcription factor HIF1α and the cytokine pro-IL-1β [146, 225]. Utilization of ROS is however, a tipping point scenario, whereby under-production can reduce efficacy of pathogen clearance, or over-production, which can result in indiscriminate protein oxidation and degradation. Macrophages thereby rely on the tripeptide GSH as a fail-safe mechanism to prevent unwanted damage to proteins during infection.

Glutathionylation or deglutathionylation of proteins can have profound effects on their signalling capacity, as evidenced by the effects of glutathionylation of Mal discussed in Chapter 3. Professional redox enzymes, such as the glutaredoxins, have been known for many years to catalyse such reactions however the specificity of glutathionylation reactions in macrophages remains poorly defined. Research by Menon et al. identified a glutathione transferase, GSTO1-1, as a potential deglutathionylating enzyme involved in innate immune signalling [137, 226]. Owing to its structural similarity to glutaredoxins, and an atypical active site cysteine residue, GSTO1-1 can function in the glutathionylation cycle. Structural studies of GSTO1-1 identified a large V-shaped cleft, potentially allowing docking of proteins to promote glutathionylation reactions. Furthermore, GSTO1-1-deficient J774A.1 macrophages have impaired responses to LPS, placing GSTO1-1 as a regulatory enzyme upstream of NF-κB in TLR4 signalling.

Cell lines are known to have altered metabolic requirements, and as such, we decided to examine the role of GSTO1-1 in primary murine macrophages. In contrast to previously published reports, we find GSTO1-1 deficiency does not impair TLR activation, thereby eliminating GSTO1-1 as the regulator of Mal glutathionylation. Furthermore, we identify GSTO1-1 as a regulator of HIF1α and pro-IL-1β production, with ROS production significantly greater in GSTO1-1-deficient BMDMs. Interestingly these findings implicate GSTO1-1 as an endogenous anti-inflammatory enzyme and warrant further examination.

To further understand the importance of the catalytic activity of GSTO1-1, a small molecule inhibitor of GSTO1-1, termed C1-27, was utilized. Importantly, we find that C1-27 can also increase HIF1α and pro-IL-1β production, placing the enzymatic function of GSTO1-1 as a critical determinant of its anti-inflammatory responses.

4.1.1 GSTO1-1 does not limit TLR4 responses to LPS

Previous investigations into the role of the deglutathionylating enzyme GSTO1-1 in macrophages have identified that GSTO1-1 is required for TLR4 signalling, as GSTO1-1-deficient J774.1A macrophages have decreased LPS responses [118]. Using GSTO1-1-deficient BMDMs, I therefore next examined the potential broad effect of GSTO1-1 deficiency on general TLR responses, to confirm whether GSTO1-1 deficiency might limit TLR signalling. If a role for GSTO1-1 could be found, I then planned to test glutathionylated Mal as a substrate for GSTO1-1. GSTO1-1-deficient BMDMs used in this chapter were obtained from Prof. Philip Board from the University of Canberra and required 48h shipment. I first compared WT BMDMs with GSTO1-1-deficient BMDMs for TLR4 responses using an IκBα degradation time-course as a readout. As shown in Figure 4.1 top panel, LPS induced degradation of IκBα from 15min, with IκBα beginning to return to basal levels at 60min LPS treatment (Top panel left-hand side). GSTO1-1 deficiency had no effect on IκBα degradation (Top panel right-hand side), with similar effects compared to WT BMDMs. In the second panel, phosphorylation of p38 is also similar between WT and GSTO1-1-deficient BMDMs, with phosphorylation increased from 5min LPS treatment. In the third panel, phosphorylation of JNK is also evident, similar between WT and GSTO1-1-deficient cells, however the signal was weaker. In the lowest panel, β-actin served as a loading control. GSTO1-1 deficiency was confirmed by qPCR as depicted in the histogram.

4.1.2 Effect of GSTO1-1 deficiency on TLR3 responses to Poly I:C

I next examined if GSTO1-1 deficiency could affect TLR3 signalling. As shown in Figure 4.2, GSTO1-1-deficient BMDMs may have delayed IκBα degradation compared to WT BMDMs (Top panel left-hand side vs right-hand side). Phosphorylation of p38 (Second panel left-hand side vs right-hand side), or JNK (Third panel) was similar in both WT and GSTO1-1-deficient BMDMs. Detection of phospho-JNK was very weak again. β-actin was used as a loading control (Lowest panel).

4.1.3 Effect of GSTO1-1 deficiency on TLR1/2 responses to Pam3CSK4

I next examined if GSTO1-1 deficiency could affect TLR2 signalling. As shown in Figure 4.3 top panel, GSTO1-1-deficient BMDMs appeared to have differences in IκBα degradation when treated with Pam3CSK4 (Top panel left-hand side vs right-hand side), however this difference was attributed to uneven loading of protein sample, as the loading control GAPDH protein bands are much weaker in the GSTO1-1-deficient cells (Lower panel left-hand side vs right-

hand side). The β-actin loading control used at the time of sample processing was unreliable and I had to use GAPDH for optimal detection purposes. Similarly, at 30min and 45min Pam3CSK4 treatment, phosphorylation of p38 is similar in both WT and GSTO1-1-deficient BMDMs (Second panel left-hand side vs right-hand side). In the third panel, phosphorylation of JNK also appeared to have negligible differences between WT and GSTO1-1-deficient BMDMs. This experiment would need to be re-examined with GSTO1-1-deficient BMDMs to account for error in sample loading.

4.1.4 GSTO1-1 does not limit TLR 7/8 responses to R848

I also examined if GSTO1-1 deficiency affected TLR7/8 responses. As shown in Figure 4.4, GSTO1-1-deficient BMDMs had no observable differences in IκBα degradation compared to WT BMDMs (Top panel left-hand side vs right-hand side). Phosphorylation of p38 (Second panel) or JNK (Third panel) was comparable between WT and GSTO1-1-deficient BMDMs. GAPDH served as a loading control (Lowest panel). There appears to be less GAPDH detected in WT BMDMs compared to GSTO1-1-deficient BMDMs, due to inaccurate loading.

4.1.5 GSTO1-1 does not limit TNFα receptor signalling

GSTO1-1 appeared to have no role in early TLR signalling. I therefore decided to examine TNFα signalling. As shown in Figure 4.5 top panel, GSTO1-1 deficiency had no comparable difference in IκBα degradation to WT BMDMs (Upper panel). Phosphorylation of p38 (Second panel) was comparable between WT and GSTO1-1-deficient BMDMs. GAPDH served as a loading control (Lowest panel). JNK phosphorylation was not detectable in response to TNFα treatment, as the signal was too weak. Overall, canonical TLR and TNFα receptor activation appears to be independent of GSTO1-1 activity, as there are no discernible differences in IκBα degradation and p38 phosphorylation.

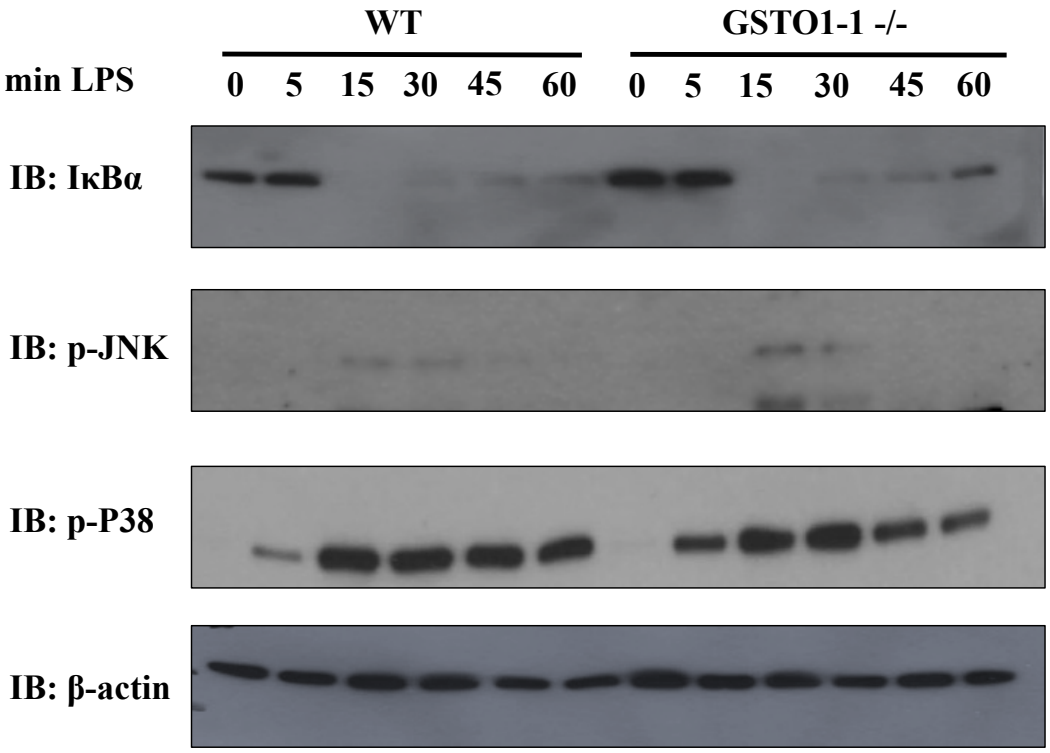

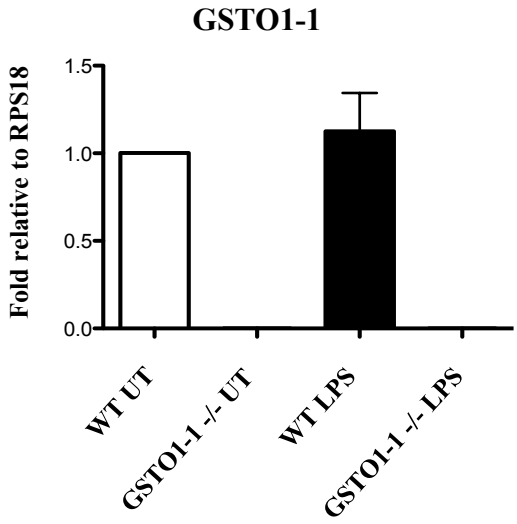

Figure 4.1 GSTO1-1 deficiency does not inhibit TLR4 signalling

Wild-type and GSTO1-1-deficient BMDMs were seeded at $5x10^5$ cells/mL in 12-well plates and incubated at 37°C 5% CO_2 overnight. Cells were treated with 100ng/mL LPS for the times indicated and lysed in 50μL sample loading buffer. Samples were analysed by western blotting using anti-IκBα, anti-pP38, anti-pJNK and anti-β-actin antibodies. GSTO1-1 deficiency was confirmed by qPCR. The results shown are representative of three independent experiments.

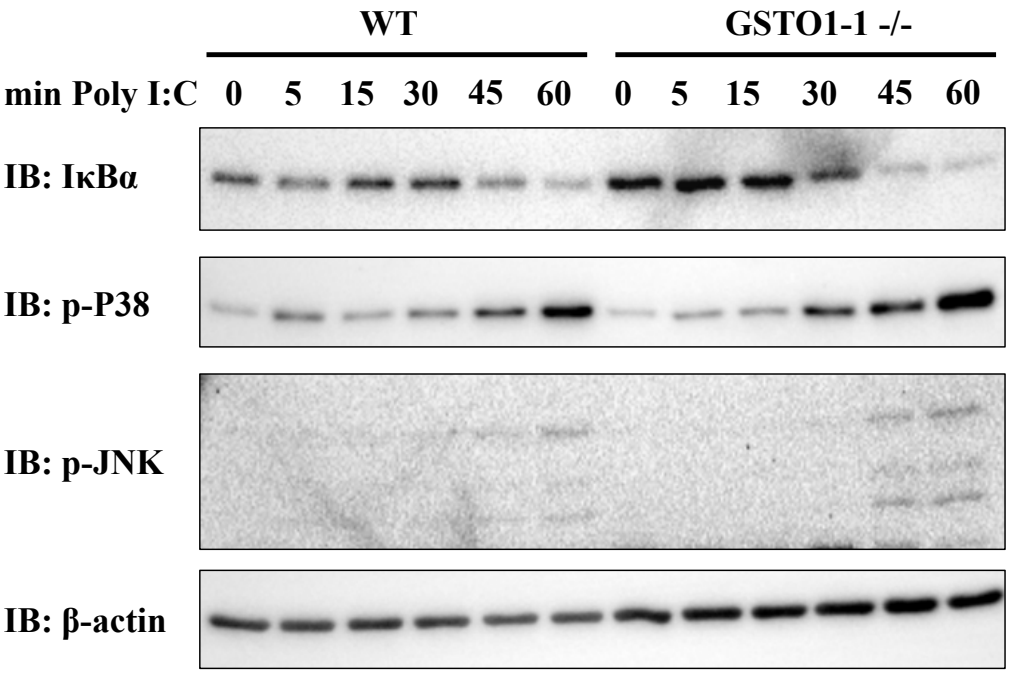

Figure 4.2 Effect of GSTO1-1 deficiency during TLR3 signalling

Wild-type and GSTO1-1-deficient BMDMs were seeded at $5x10^5$ cells/mL in 12-well plates and incubated at 37°C 5% CO_2 overnight. Cells were treated with 10μg/mL Poly I:C for the times indicated and lysed in 50μL sample loading buffer. Samples were analysed by western blotting using anti-IκBα, anti-pP38, anti-pJNK and anti-β-actin antibodies. GSTO1-1 deficiency was confirmed by qPCR in Figure 4.1. The results shown are representative of three independent experiments.

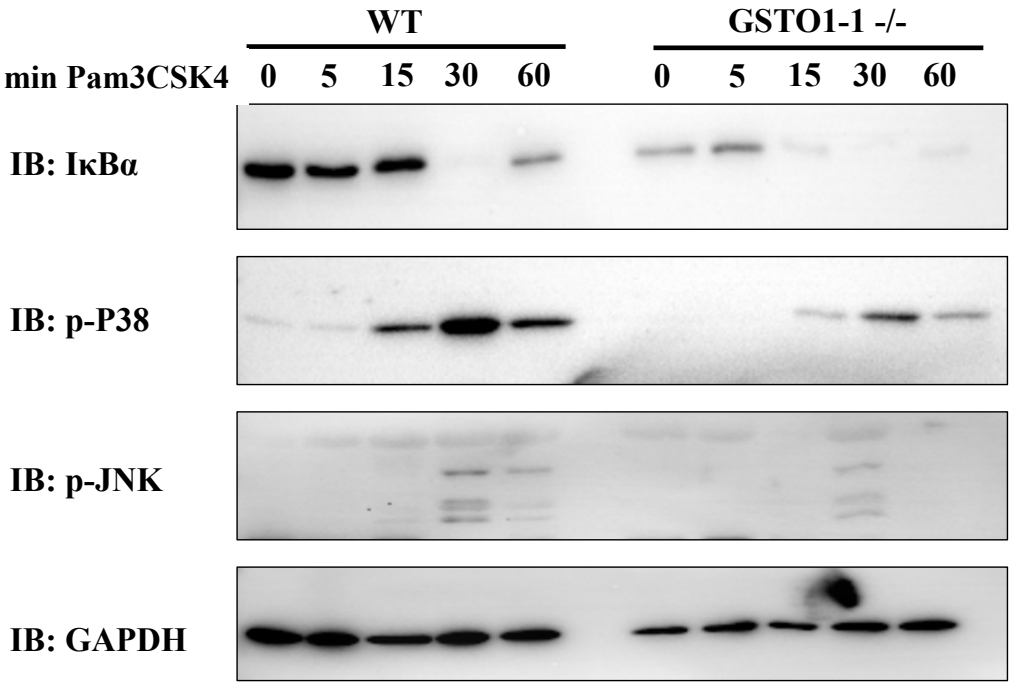

Figure 4.3 Effect of GSTO1-1 deficiency during TLR1/2 signalling

Wild-type and GSTO1-1-deficient BMDMs were seeded at $5x10^5$ cells/mL in 12-well plates and incubated at 37°C 5% CO_2 overnight. Cells were treated with 100ng/mL Pam3CSK4 for the times indicated and lysed in 50μL sample loading buffer. Samples were analysed by western blotting using anti-IκBα, anti-pP38, anti-pJNK and anti-GAPDH antibodies. GSTO1-1 deficiency was confirmed by qPCR in Figure 4.1. The results shown are representative of three independent experiments.

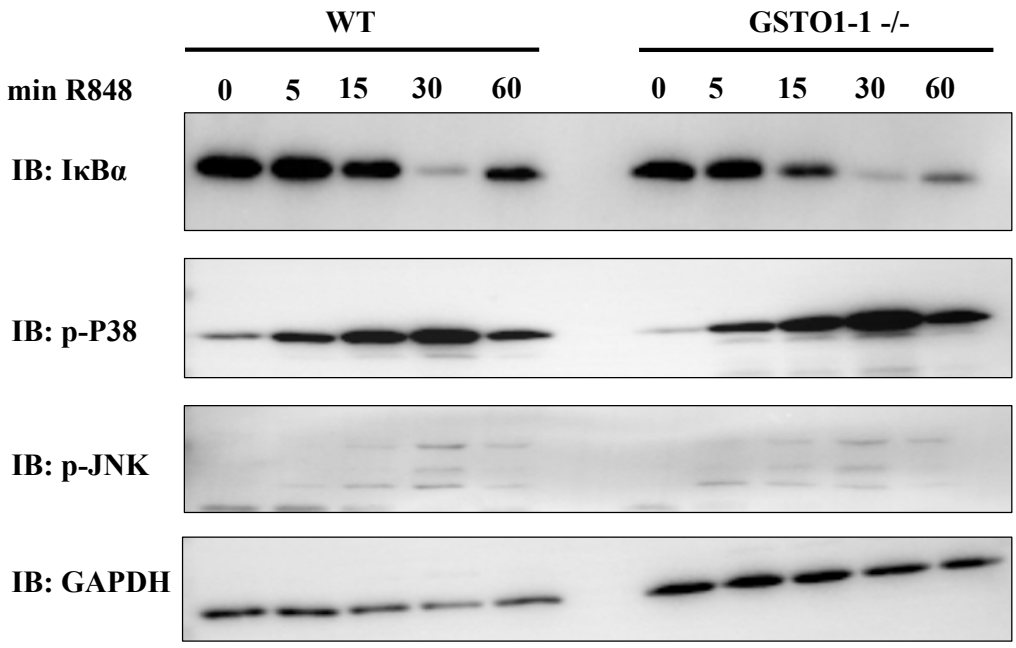

Figure 4.4 GSTO1-1 deficiency does not inhibit TLR7/8 signalling

Wild-type and GSTO1-1-deficient BMDMs were seeded at $5x10^5$ cells/mL in 12-well plates and incubated at 37°C 5% CO_2 overnight. Cells were treated with 10μg/mL R848 for the times indicated and lysed in 50μL sample loading buffer. Samples were analysed by western blotting using anti-IκBα, anti-pP38, anti-pJNK and anti-GAPDH antibodies. GSTO1-1 deficiency was confirmed by qPCR in Figure 4.1. The results shown are representative of three independent experiments.

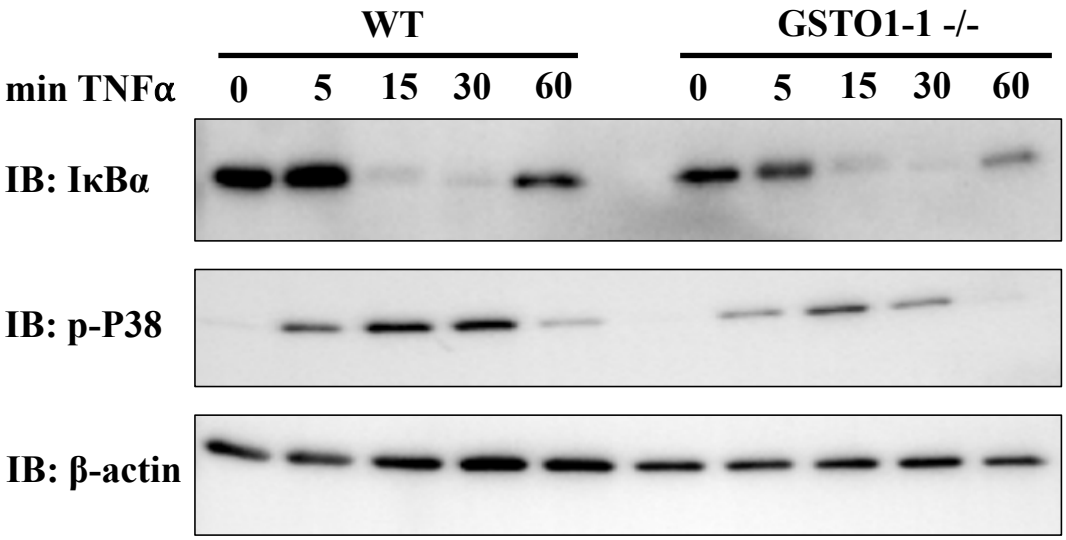

Figure 4.5 GSTO1-1 deficiency does not inhibit TNFα signalling

Wild-type and GSTO1-1-deficient BMDMs were seeded at $5x10^5$ cells/mL in 12-well plates and incubated at 37°C 5% CO_2 overnight. Cells were treated with 20ng/mL recombinant TNFα for the times indicated and lysed in 50μL sample loading buffer. Samples were analysed by western blotting using anti-IκBα, anti-pP38, anti-pJNK and anti-GAPDH antibodies. GSTO1-1 deficiency was confirmed by qPCR in Figure 4.1. The results shown are representative of three independent experiments.

4.1.6 GSTO1-1-deficient BMDMs produce more IL-10

I next assessed whether GSTO1-1 deficiency would impact on cytokine production in response to LPS treatment. As shown in Figure 4.6 A, LPS-treated GSTO1-1-deficient BMDMs had no significant difference in IL-6 protein production, however the RNA level appeared to be significantly decreased (Figure 4.6 B). GSTO1-1-deficient BMDMs produced significantly more IL-10 in response to LPS, both in terms of protein (Figure 4.6 C) and mRNA (Figure 4.6 D). GSTO1-1 deficiency had no effect on TNFα protein (Figure 4.6 E) and mRNA (Figure 4.6 F). GSTO1-1 deficiency was confirmed by qPCR (Figure 4.6 G).

4.1.7 GSTO1-1-deficient BMDMs are not classically M1 or M2 polarised

As shown in Figure 4.7, GSTO1-1-deficient macrophages also had an altered polarisation compared to WT BMDMs, as the expression of a common M2 macrophage marker Arginase-1 was attenuated in IL-4 treated GSTO1-1-deficient BMDMs (Figure 4.7 A). GSTO1-1-deficient BMDMs also expressed less iNOS when treated with LPS (Figure 4.7 B). Another common M2 macrophage marker, Mrc1, had no observable differences between WT and GSTO1-1-deficient BMDMs (Figure 4.7 C). Again, in this experiment GSTO1-1-deficient BMDMs expressed higher levels of IL-10 transcript compared to WT BMDMs (Figure 4.7 D). IL-12p40, another M1 marker, was attenuated compared to WT BMDMs with LPS treatment (Figure 4.7 E). GSTO1-1 deficiency was confirmed by qPCR (Figure 4.7 F).

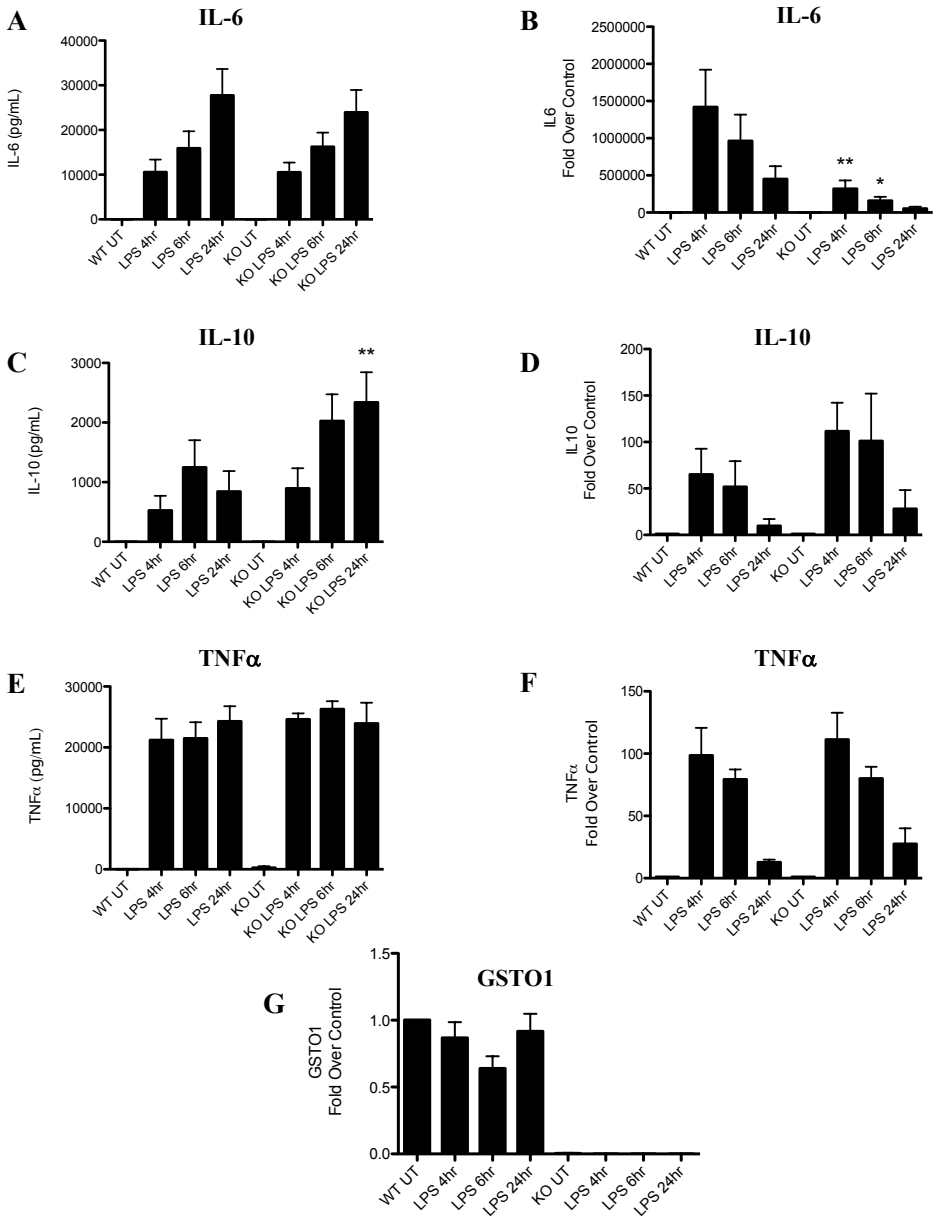

Figure 4.6 ELISA and RNA profile of LPS-treated GSTO1-1-deficient BMDMs

Wild-type and GSTO1-1-deficient BMDMs were seeded at $5x10^5$ cells/mL in 12-well plates and incubated at 37°C 5% CO_2 overnight. Cells were treated with 100ng/mL LPS for 4h, 6h and 24h. Supernatant was harvested for ELISA for IL-6 (A), IL-10 (C) and TNFα (E). Cells were lysed in 350μL RNA lysis buffer and RNA isolated using Ambion RNA extraction kit. RNA was reverse transcribed and cDNA was used for qPCR with SYBR Green components. cDNA was analysed using the cycle-threshold (Ct) value normalized to RPS18 control gene for IL-6 (B), IL-10 (D), TNFα (F) and GSTO1 (G). Mean ± S.E.M of three independent experiments each carried out in triplicate is shown. * $P \leq 0.05$, ** $P \leq 0.005$.

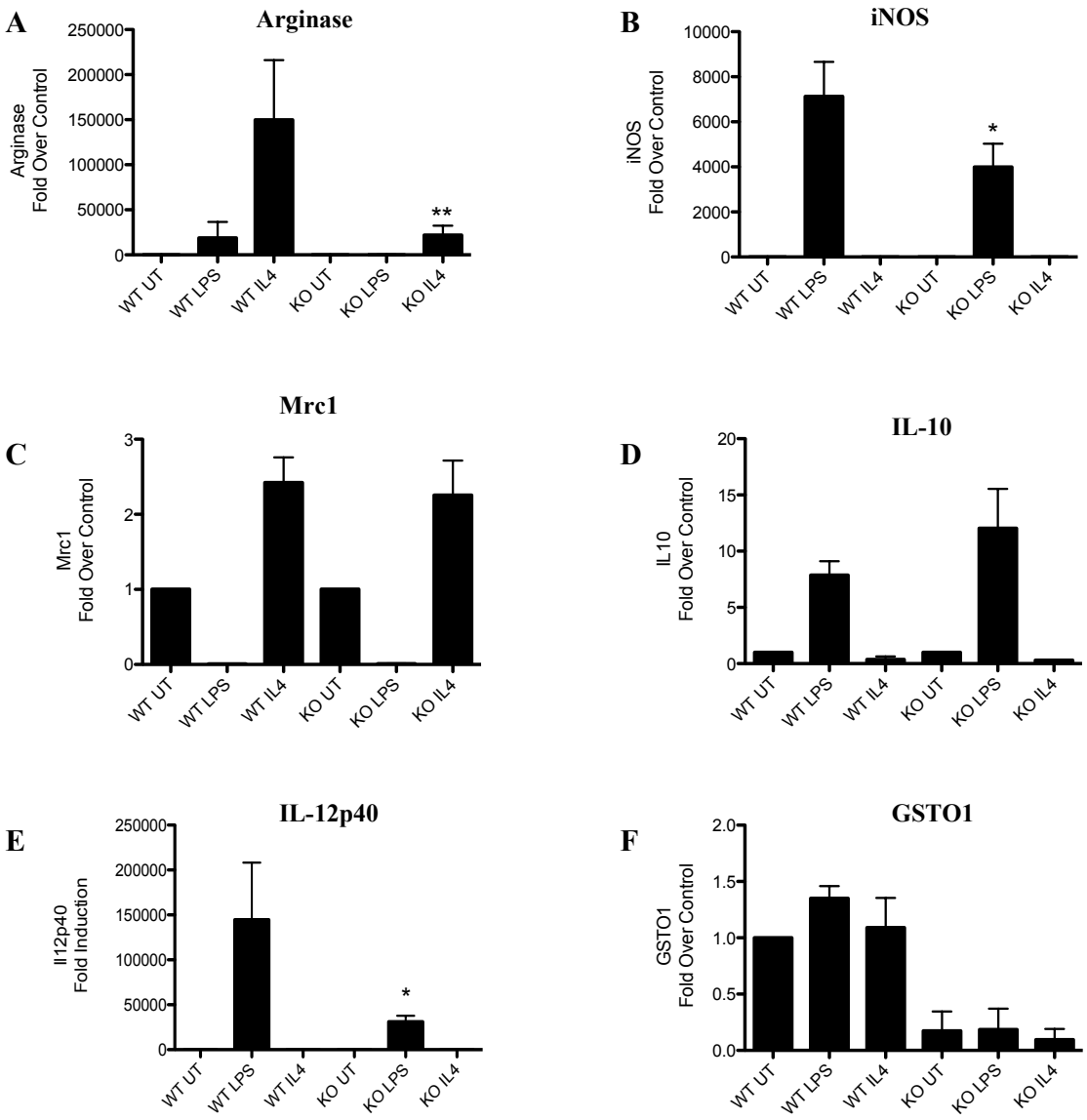

Figure 4.7 GSTO1-1-deficient BMDMs have altered M1/M2 polarization

Wild-type and GSTO1-1-deficient BMDMs were seeded at $5x10^5$ cells/mL in 12-well plates and incubated at 37°C 5% CO_2 overnight. Cells were treated with 100ng/mL LPS or 20ng/mL IL-4 for 24h. Cells were lysed in 350µL RNA lysis buffer and RNA isolated using Ambion RNA extraction kit. RNA was reverse transcribed and cDNA was used for qPCR with SYBR Green components. cDNA was analysed using the cycle-threshold (Ct) value normalized to RPS18 control gene for Arginase (A), iNOS (B), Mrc1 (C), IL-10 (D), IL-12p40 (E) and GSTO1 (F). Mean ± S.E.M of three independent experiments each carried out in triplicate is shown. * $P \leq 0.05$, ** $P \leq 0.005$

4.1.8 GSTO1-1-deficient BMDMs produce more ROS

I next measured ROS levels in GSTO1-1-deficient BMDMs. As shown in Figure 4.8 GSTO1-1-deficient cells have basally higher ROS levels compared to WT BMDMs. LPS addition increased ROS levels in WT BMDMs however this increase was much higher in the GSTO1-1-deficient cells. ROS levels may have been variable due to shipment of legs.

4.1.9 GSTO1-1-deficient BMDMs have increased HIF1α and IL-1β protein levels

Because of the increase in ROS evident in the GSTO1-1-deficient BMDMs, I next measured HIF1α and pro-IL-1β production, which are driven by ROS in LPS-treated macrophages [146, 227]. In Figure 4.9 GSTO1-1-deficient BMDMs produced higher levels of HIF1α protein compared to WT BMDMs in response to LPS treatment (Figure 4.9 Top panel left-hand side vs right-hand side). Similarly, GSTO1-1-deficient BMDMs produced higher levels of pro-IL-1β (Figure 4.9 Middle panel left-hand side vs right-hand side). β-actin served as a loading control (Figure 4.9 Lowest panel).

4.1.10 GSTO1-1-deficient BMDMs have increased IL-1β and HIF1α gene target expression

Due to the observed increase in HIF1α protein, I next examined whether the expression of HIF1α target genes would be increased. In Figure 4.10 A, GSTO1-1-deficient BMDMs had a significantly higher expression level of prolyl hydroxylase domain-containing protein 3 (PHD3) at 24h LPS treatment compared to WT BMDMs. The expression of lactate dehydrogenase a (LDHa) was also significantly increased at 24h LPS treatment compared to WT BMDMs (Figure 4.10 B). The expression of glucose transporter type 1 (GLUT1) was also increased at 24h LPS compared to WT BMDMs (Figure 4.10 C). Again, compared to WT BMDMs, the induction of IL-1β was significantly increased with 24h LPS treatment (Figure 4.10 D), correlating with the western blot in Figure 4.9, potentially due to increased HIF1α production. GSTO1-1 deficiency was confirmed by qPCR (Figure 4.10 E).

4.1.11 GSTO1-1-deficient BMDMs have a higher rate of glycolysis

Macrophages treated with LPS skew their phenotype towards a pro-glycolytic environment, with increased levels of HIF1α [121]. As HIF1α levels were higher in the GSTO1-1-deficient BMDMs, I measured the initial glycolytic flux caused by LPS. As shown in Figure 4.11, GSTO1-1-deficient BMDMs have a higher rate of basal glycolysis compared to WT BMDMs, as measured by the extracellular acidification rate (ECAR). Addition of LPS greatly enhanced

GSTO1-1-deficient BMDM glycolytic flux, however the LPS-treated WT BMDMs did not respond to LPS. This data requires further investigation, however the basal ECAR suggests that GSTO1-1-deficient BMDMs are more glycolytic.

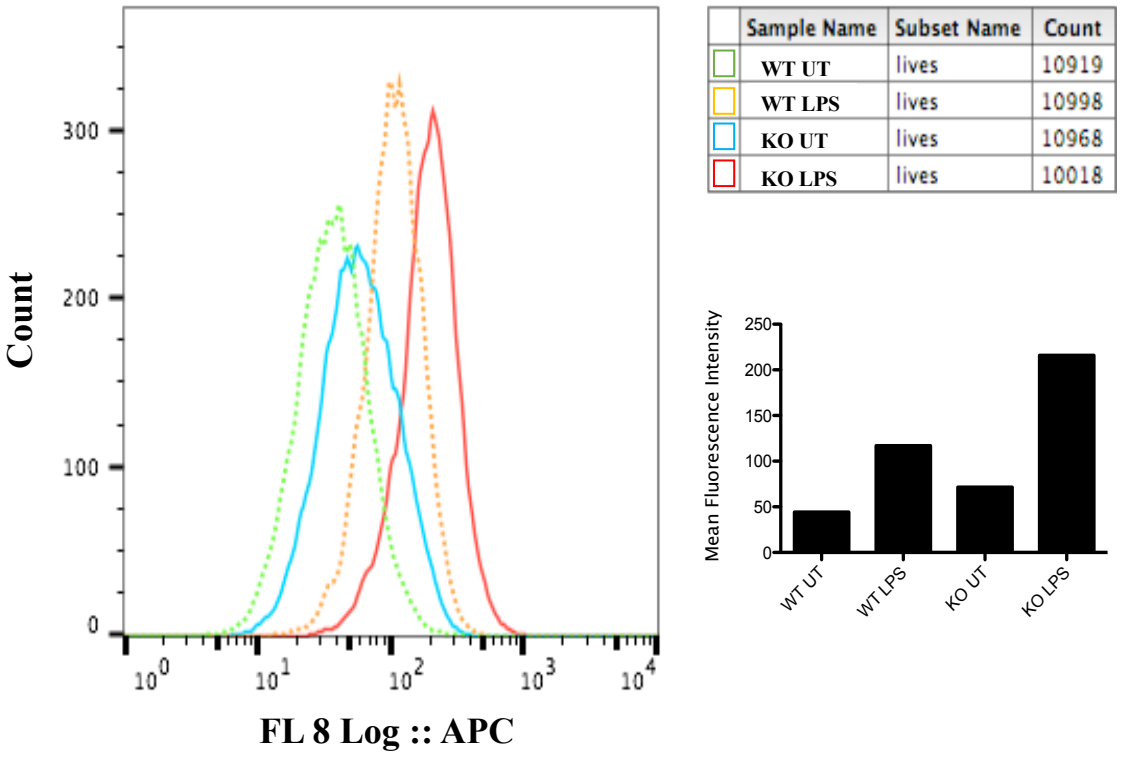

Figure 4.8 GSTO1-1-deficient BMDMs have increased ROS production

Wild-type and GSTO1-1-deficient BMDMs were seeded at 5x10^5 cells/mL in 12-well plates and incubated at 37°C 5% CO_2 overnight. Cells were treated with 100ng/mL LPS for 24hr prior to treatment with cellular ROS stain MitoROS dye for 1hr with minimal light. Live cells were analysed by Flow cytometry for ROS production, and mean fluorescence intensity (MFI) was quantified. Data shown is representative of three pooled WT and GSTO1-1-deficient BMDMs.

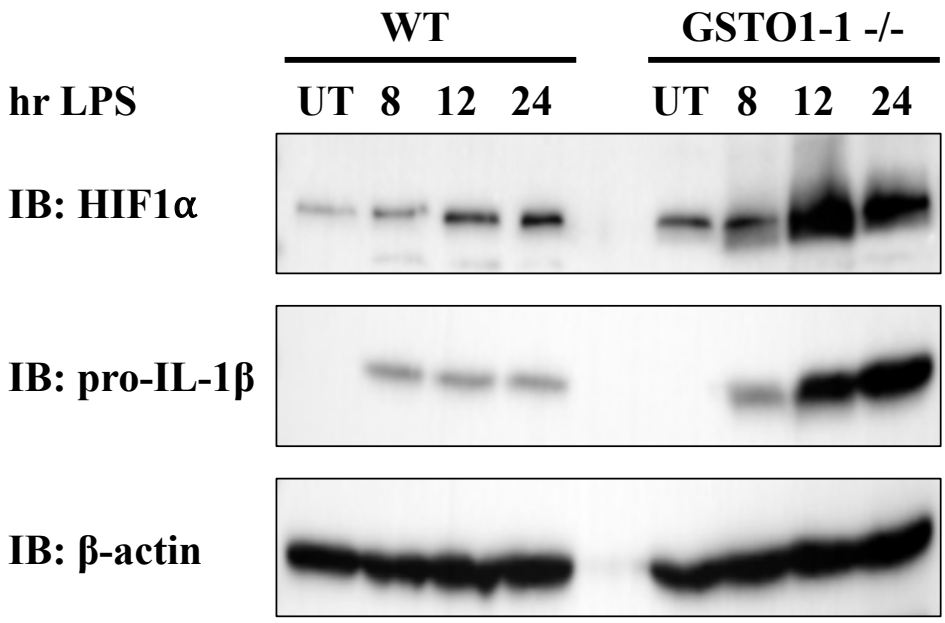

Figure 4.9 GSTO1-1-deficient BMDMs have increased HIF1α and IL-1β levels

Wild-type and GSTO1-1-deficient BMDMs were seeded at $5x10^5$ cells/mL in 12-well plates and incubated at 37°C 5% CO_2 overnight. Cells were treated with 100ng/mL LPS for the times indicated and lysed in 50μL sample loading buffer. Samples were analysed by western blotting using anti-HIF1α, anti-IL-1β and anti-β-actin antibodies. GSTO1-1 deficiency was confirmed by qPCR in Figure 4.10. The results shown are representative of three independent experiments.

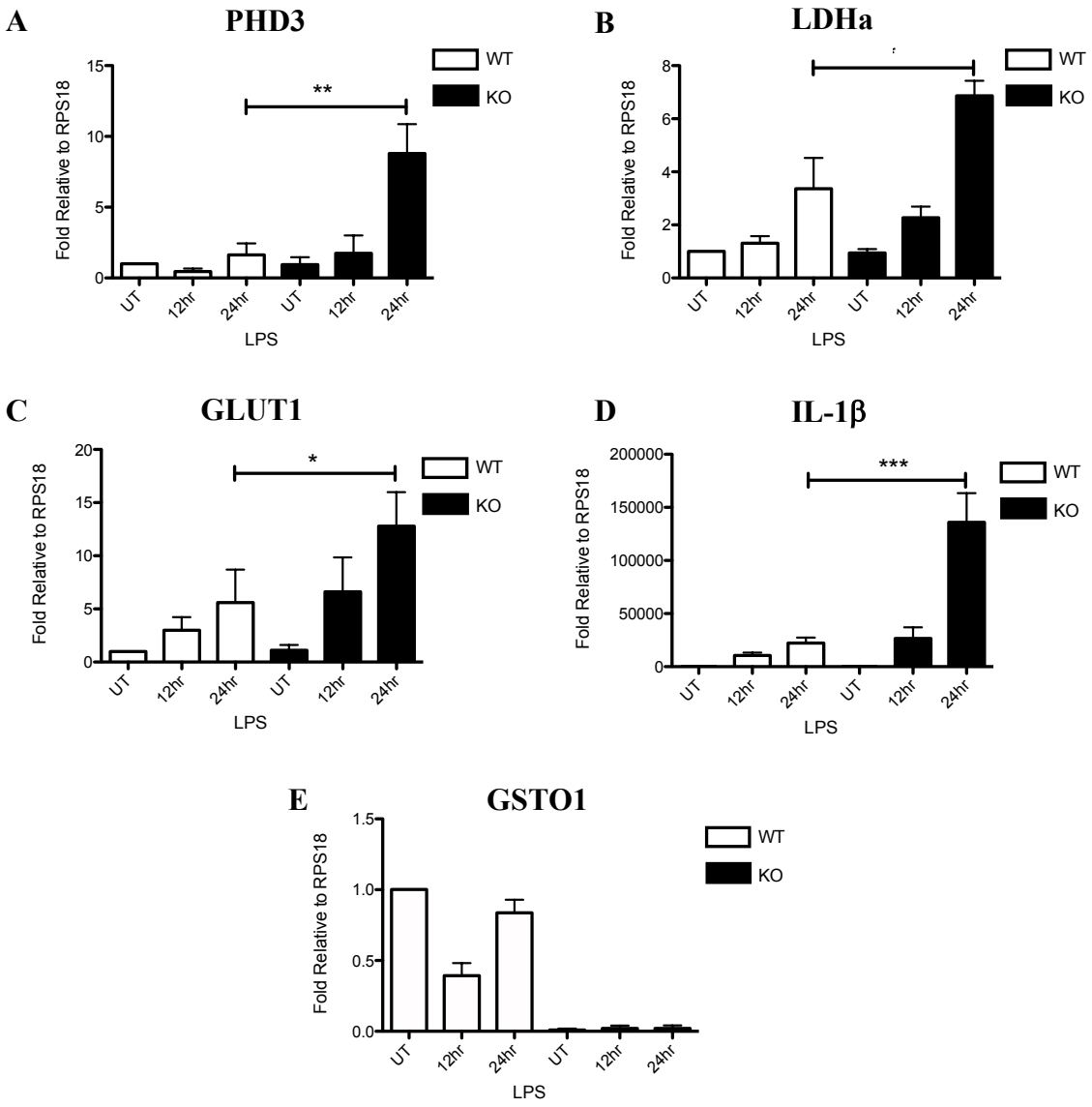

Figure 4.10 GSTO1-1 deficiency Increases HIF1α target gene transcription

Wild-type and GSTO1-1-deficient BMDMs were seeded at $5x10^5$ cells/mL in 12-well plates and incubated at 37°C 5% CO_2 overnight. Cells were treated with 100ng/mL LPS for 12hr and 24hr. Cells were lysed in 350µL RNA lysis buffer and RNA isolated using Ambion RNA extraction kit. RNA was reverse transcribed and cDNA was used for qPCR with SYBR Green components. cDNA was analysed using the cycle-threshold (Ct) value normalized to RPS18 control gene. Mean ± S.E.M of three independent experiments each carried out in triplicate is shown. * $P \leq 0.05$, ** $P \leq 0.005$, *** $P \leq 0.001$

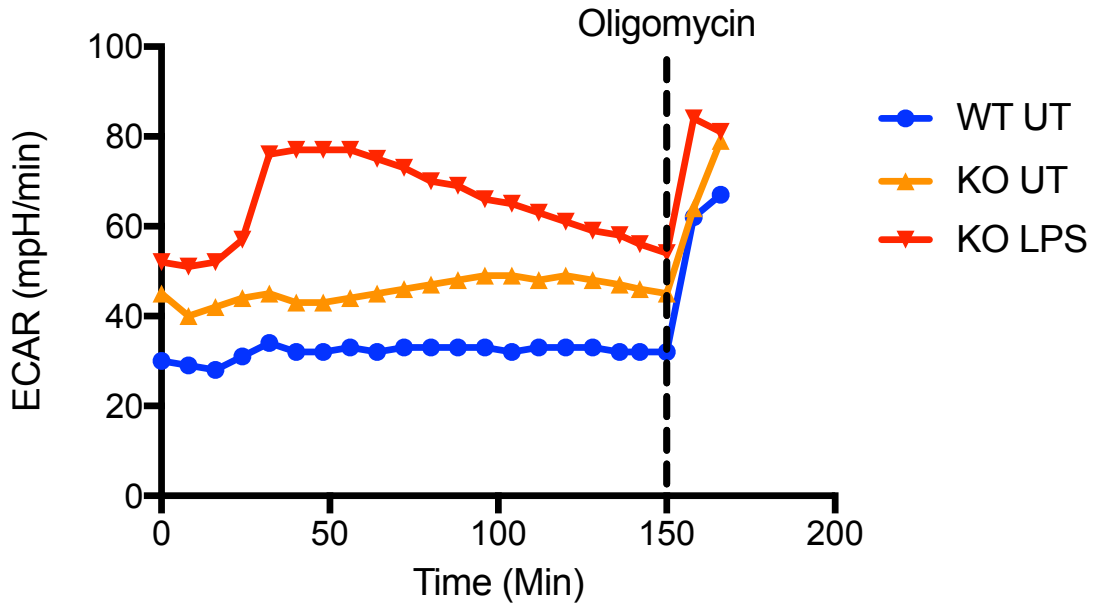

Figure 4.11 GSTO1-1-deficient BMDMs have an altered basal glycolytic rate

Wild-type and GSTO1-1-deficient BMDMs were seeded at $2x10^5$ cells/mL in a Seahorse cell culture plate incubated at 37°C 5% CO_2 overnight. A calibration plate was also prepared containing calibrant solution (1mL/well). The following day Seahorse medium supplemented with 25mM glucose was prepared and adjusted to pH7.4. Media was removed from cells and replaced with 500µL glucose-supplemented Seahorse medium. The cell culture plate was placed in a CO_2-free incubator for at least 30min. LPS (100ng/mL) and Oligomycin was added to respective ports on the injector plate and placed on the cell culture plate and analysed by the Seahorse Analyser. Data shown is representative of three pooled WT and GSTO1-1-deficient BMDMs.

4.2. Inhibition of GSTO1-1 by C1-27

4.2.1 C1-27 does not limit TLR4 activation

To assess the relevance of the catalytic activity of GSTO1-1, I used a recently described small molecule inhibitor of GSTO1-1, termed C1-27, which binds to the active site C32 to limit GSTO1-1 catalytic activity [228]. I first examined the potential cytotoxic effects of C1-27. Pre-treatment with C1-27 prior to 24h LPS stimulation had no discernible effects on LDH release, and the highest dose tested, 5μM was used unless otherwise stated (Figure 4.12 A). As shown in Figure 4.15 B, pre-treatment of BMDMs with C1-27 had no effect on TLR4 signalling. In the upper panel the degradation of IκBα was unaffected compared to LPS treatment, nor was there any discernible difference between phosphorylation of P38 or P65 (second and third panel). C1-27 pre-treatment appeared to increase phosphorylation of pERK1/2 (fourth panel), however this effect was only observed once. In the lowest panel, β-actin served as loading control.

4.2.2 C1-27 increases HIF1α and pro-IL-1β Production

I next examined if C1-27 could mimic the pro-inflammatory effects of GSTO1-1 deficiency by examining the production of HIF1α and pro-IL-1β production. Similar to Figure 4.9, enzymatic inhibition of GSTO1-1 markedly increases HIF1α production (Figure 4.13 top panel) and boosts pro-IL-1β production at three doses compared to LPS control. β-actin served as a loading control.

4.2.3 C1-27 Promotes IL-1β and HIF1α-dependent gene transcription

GSTO1-1-deficient BMDMs displayed an increased glycolytic phenotype in response to LPS treatment, with a significant increase in HIF1α production. As shown in Figure 4.14, C1-27 pre-treatment somewhat increased HIF1α transcription factor activity, as a trend towards increased pro-IL-1β transcription was observed (Figure 4.14 A), with no effect on TNFα mRNA levels (Figure 4.14 B). The IL1-receptor antagonist (IL1-RA) was also examined. C1-27 treatment significantly decreased the transcript of IL1-RA (Figure 4.14 C) and dose-dependently increased transcription of HIF1α-dependent PHD3 (Figure 4.14 D).

4.2.4 IL-10 production is impaired by C1-27

I next examined the effect of C1-27 on cytokine production from TLR4 activation. In comparison to the observed boost in IL-10 production from GSTO1-1-deficient BMDMs, C1-

27 dose-dependently decreased IL-10 production from BMDMs stimulated with LPS (Figure 4.15 A). C1-27 had no effect on IL-6 (Figure 4.15 B) or TNFα production (Figure 4.15 C).

4.2.5 C1-27 decreases ROS production

I next measured ROS production in C1-27-treated BMDMs. In comparison to Figure 4.8, pre-treatment with C1-27 dose-dependently decreased the production of ROS as measured by 2',7' –dichlorofluorescin diacetate (DCFDA) staining after 24h LPS treatment (Figure 4.16).

4.2.6 Endogenous knockdown of GSTO1-1 ablates IL-10 production

In order to separate the observed differences in cytokine production between the GSTO1-1-deficient BMDMs and C1-27 treated cells, I employed the use of siRNA to endogenously knockdown GSTO1-1 from BMDMs. In response to LPS treatment, IL-10 production was ablated in GSTO1-1 knockdown BMDMs compared to scramble siRNA control (Figure 4.17 B), with no significant differences between IL-6 (Figure 4.17 A) and TNFα production (Figure 4.17 C). GSTO1-1 knockdown was confirmed by western blot (Figure 4.17 D).

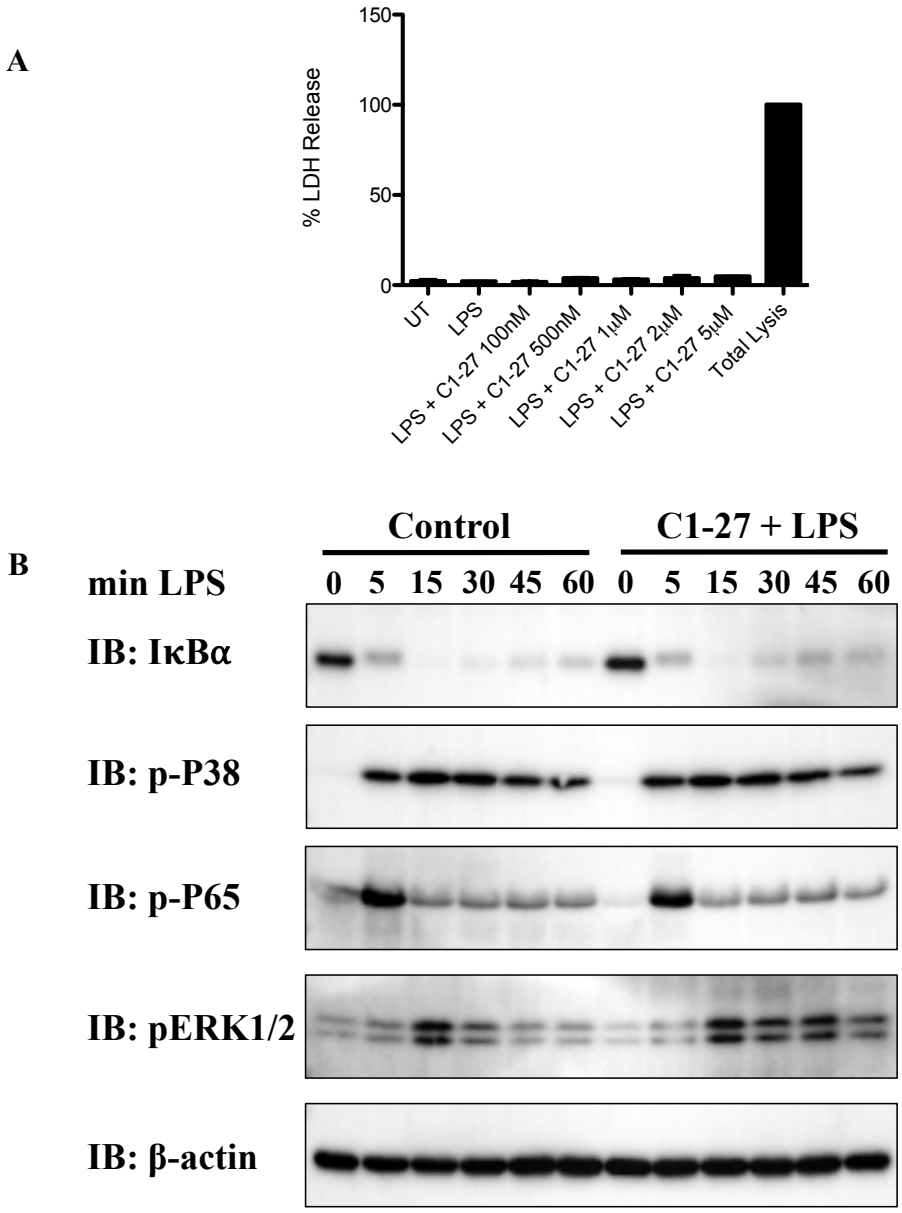

Figure 4.12 C1-27 does not limit TLR4 signalling upstream of NF-κB activation

Wild-type BMDMs were seeded at 5x10^5 cells/mL in 12-well plates and incubated at 37°C 5% CO_2 overnight. (A) Cells were pre-treated with indicated doses of C1-27 2h prior to 24h LPS treatment. 10X lysis solution was added to an untreated well for total cell lysis control. Supernatants were removed and 50μL was added to 50μL Promega Cytotox-96 substrate buffer for 30min at RT. 25μL stop solution was added and absorbance was measured at 492nm. (B) Cells were pre-treated with 5μM C1-27 for 2h and then stimulated with 100ng/mL LPS for the times indicated and lysed in 50μL sample loading buffer. Samples were analysed by western blotting using anti-IκBα, anti-pP38, anti-pP65, anti-pERK1/2 and anti-β-actin antibodies. The results shown are representative of three independent experiments.

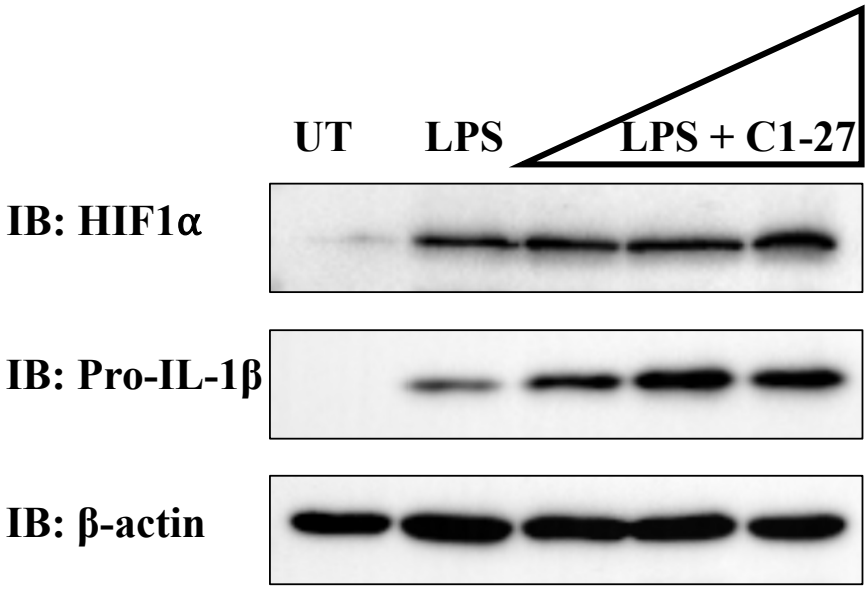

Figure 4.13 Effect of C1-27 on HIF1α and pro-IL-1β protein levels

BMDMs were seeded at $5x10^5$cell/mL in 12-well plates and incubated at 37°C 5% CO_2 overnight. Cells were pre-treated with a dose range of 5 μM C1-27 for 2h and treated with 100ng/mL LPS for 24h. Cells were lysed in sample loading buffer and analysed by western blotting using anti-IL-1β, anti-HIF1α and anti-β-actin antibodies. Data shown is representative of three independent experiments.

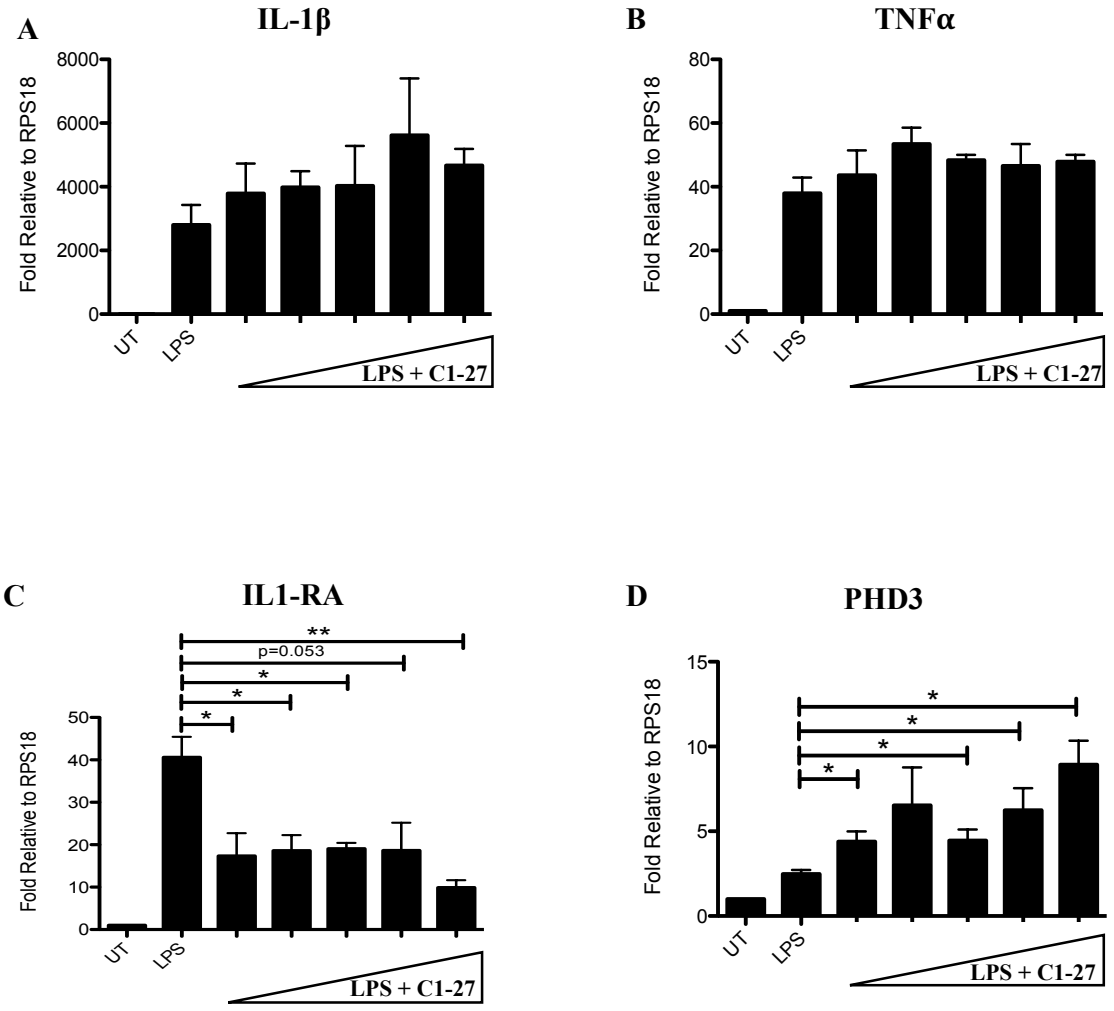

Figure 4.14 C1-27 Promotes IL-1β and HIF1α-dependent gene transcription

BMDMs were seeded at $5x10^5$ cell/mL in 12-well plates and incubated at 37°C 5% CO_2 overnight. Cells were pre-treated with a dose range of 1-10 μM C1-27 for 2h, prior to treatment with 100ng/mL LPS for 24h. Cells were lysed in 350μL RNA lysis buffer and RNA isolated using Ambion RNA extraction kit. RNA was reverse transcribed and cDNA was used for qPCR with SYBR Green components. cDNA was analysed using the cycle-threshold (Ct) value normalized to RPS18 control gene for IL-1β (A), TNFα (B), IL1-RA (C) and PHD3 (D). Mean ± S.E.M of three independent experiments each carried out in triplicate is shown. * $P \leq 0.05$, ** $P \leq 0.005$.

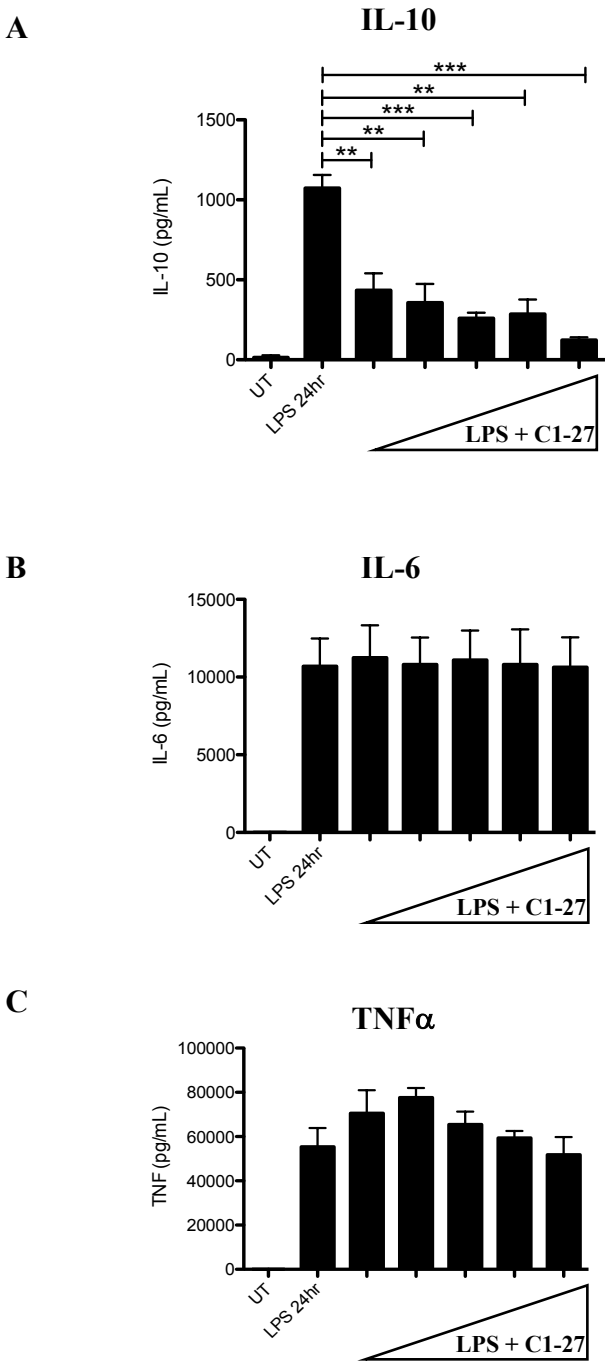

Figure 4.15 Enzymatic inhibition of GSTO1-1 by the catalytic inhibitor C1-27 attenuates IL-10 production in BMDMs

BMDMs were seeded at $5x10^5$cell/mL in 12-well plates and incubated at 37°C 5% CO_2 overnight. Cells were pre-treated with a dose range of 1-10μM C1-27 for 2h and treated with 100ng/mL LPS for 24h. Supernatant was harvested for ELISA for IL-10 (A), IL-6 (B) and TNFα (C). Mean ±S.E.M of three independent experiments each carried out in triplicate is shown. ** P ≤0.005, *** P ≤0.001

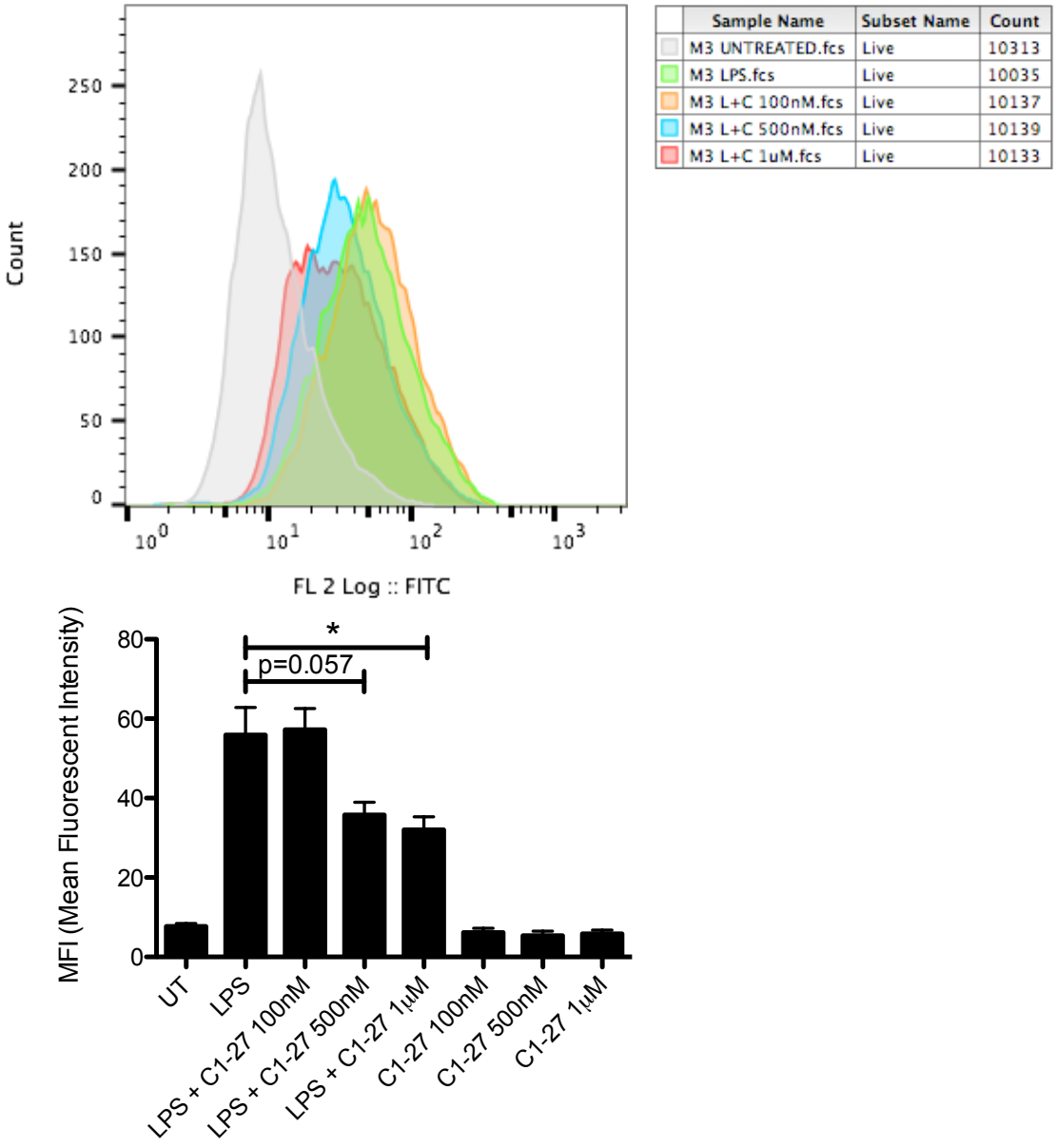

Figure 4.16 C1-27 decreases ROS production

BMDMs were seeded at 5x10^5 cells/mL in 12-well plates and incubated at 37°C 5% CO_2 overnight. Cells were pre-treated with indicated doses of C1-27 2h prior to treatment with 100ng/mL LPS for 24h. The cellular ROS stain DCFDA was added to each well for 45min with minimal light. Live cells were analysed by Flow cytometry for ROS production, and mean fluorescence intensity (MFI) was quantified. Mean ± S.E.M of three independent experiments is shown. * $P \leq 0.05$

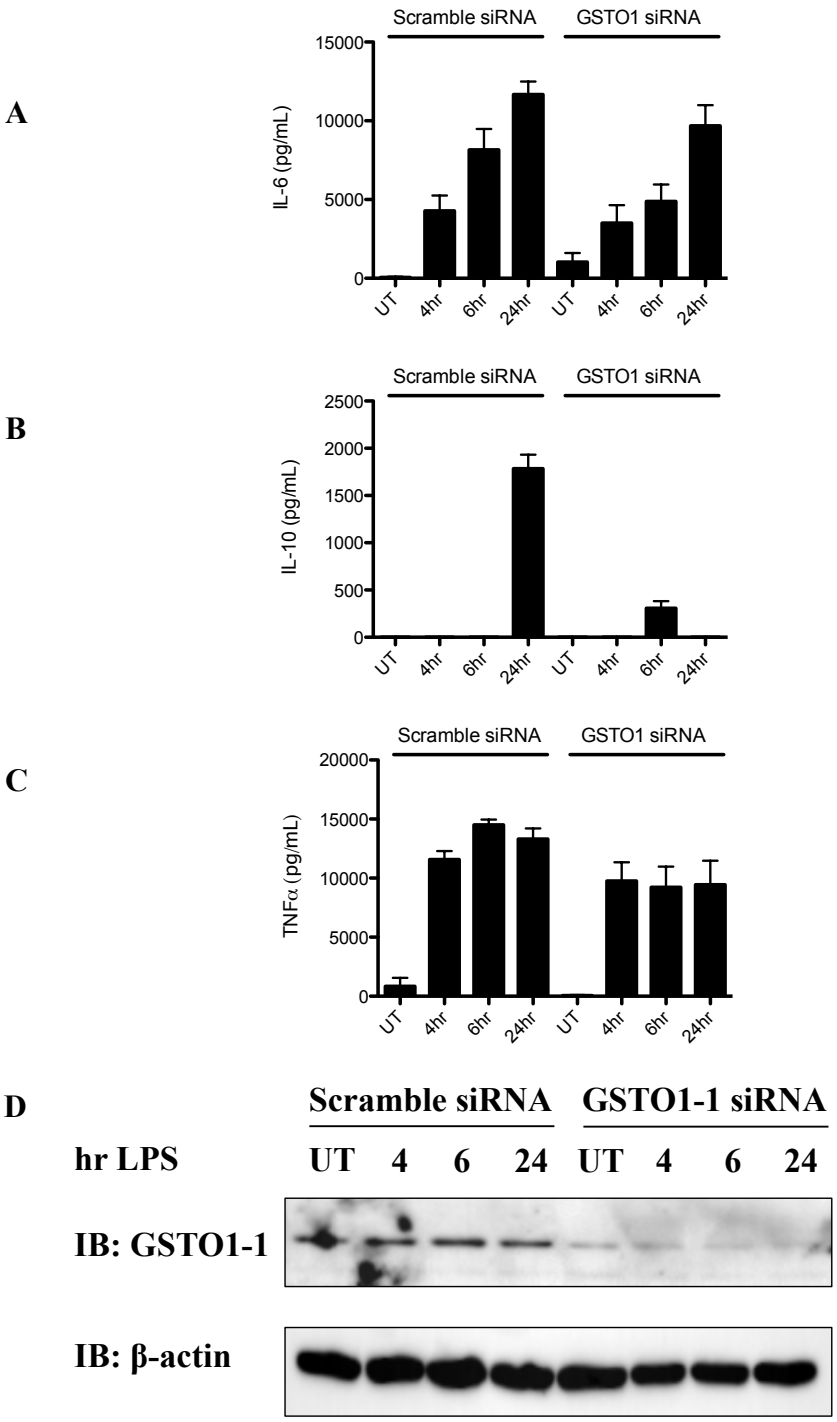

Figure 4.17 siRNA knockdown of GSTO1-1 limits IL-10 production

BMDMs were seeded at 5x10^5 cells/mL in 12-well plates and incubated at 37°C 5% CO_2 overnight. Cells were transfected with 5nmol scramble siRNA (Ambion) or GSTO1 siRNA in OptiMEM media for 36h using RNAiMAX lipofectamine. Cells were treated with 100ng/mL LPS for times indicated. Supernatant was harvested for ELISA for IL-6 (A), IL-10 (B) and TNFα (C). Cells were lysed in sample loading buffer and analysed by western blotting using anti-GSTO1 and anti-β-actin antibodies (D). Representative of three independent western blot experiments is shown.

4.3 Discussion

The role of the glutathionylation system in regulation of human health is poorly characterized. The levels of GSH alter drastically as we age, and such decreases are correlated to increased susceptibility to neurodegenerative diseases including Parkinson's Disease [229] and Alzheimer's Disease [230]. Furthermore, altered redox metabolism is directly linked to effective pathogen clearance and cancer progression [231]. The glutathione transferase class of enzymes are able to interact with a wide variety of substrates, and catalyse reactions from deglutathionylation to prostaglandin synthesis [122]. Whilst all glutathione transferases contain canonical features, such as the GST fold and an active site serine or tyrosine residue, only one GST termed GSTO1-1 contains an active site cysteine residue, increasing the capacity for GSTO1-1 to regulate redox signalling.

My interest in GSTO1-1 came from reports placing GSTO1-1 as a potential regulatory enzyme upstream of NF-κB, however the precise target was unknown. J774.A1 cells deficient in GSTO1-1 were shown to block translocation of NF-κB to the nucleus, potentially identifying an enzyme proximally located at the beginning of TLR4 activation [137]. I hypothesised that GSTO1-1 may act as a regulatory switch for Mal activation, as Mal glutathionylation is critical for TLR4 activation, seen in Chapter 3. Whilst predominantly reported as a deglutathionylating enzyme, GSTO1-1 has also been reported to glutathionylate residues *in vitro* with weaker affinity [232]. The enzymatic activity of GSTO1-1 towards Mal could result in two potential consequences. GSTO1-1 may act to glutathionylate Mal to drive TLR4 activation, or GSTO1-1 could potentially deglutathionylate Mal as an 'off-switch' to limit excessive TLR signalling. If deficiency in GSTO1-1 results in TLR4 inhibition, I would hypothesise that GSTO1-1 serves to glutathionylate Mal to promote NF-κB nuclear translocation.

My studies began using GSTO1-1-deficient mice generously donated by Prof. Philip Board to examine if TLR activation was impaired. Previous reports have identified that components of TLR signalling, such as MyD88, TRAF6 and NF-κB, are affected by the redox environment, which impacts their signalling capacity [233], [234], [235]. We hypothesised that GSTO1-1 must regulate either Mal or a component of the myddosome to limit NF-κB activation.

I began by examining activation of TLRs 1/2, 3, 4, 7/8 and the TNFα receptor in order to identify a possible role for GSTO1-1 in IκBα degradation as a readout of NF-κB activation. When tested, GSTO1-1-deficient BMDMs did not have impaired responses to TLR ligands or TNFα stimulation, with degradation of IκBα present in response to each ligand examined.

Although the characterisation of GSTO1-1 is not exhaustive upstream of NF-κB due to limitations in the availability of GSTO1-1-deficient mice, the data does suggest that GSTO1-1 is not limiting the phosphorylation of TLR components that lead to NF-κB activation or transcription of NF-κB-dependent genes. This finding contrasts previous reports that GSTO1-1 is required for translocation of NF-κB to the nucleus [137].

I next decided to examine if cytokine production was impaired in GSTO1-1-deficient BMDMs. Interestingly, GSTO1-1-deficient BMDMs produced higher levels of the anti-inflammatory cytokine IL-10 in response to LPS, with no significant differences in protein level of cytokines IL-6 and TNFα, measured by ELISA. Whilst the RNA levels of IL-6 were significantly reduced, no statistical differences were observed between production of IL-6 measured by ELISA in control and GSTO1-1-deficient BMDMs. Due to the higher level of IL-10, we speculated if the absence of GSTO1-1 would further promote an M2, or pro-resolution, macrophage. In order to assess this, LPS or IL-4 was used to polarise the macrophages into classically activated 'M1' or alternatively activated 'M2' macrophages, respectively and looked at expression of specific subsets of either M1 or M2 genes. GSTO1-1-deficient BMDMs had reduced expression of iNOS, an M1 marker, however they also had significantly decreased expression of Arginase, an M2 marker in response to IL4. Another commonly used M2 marker, Mrc1, had no significant differences between wild-type and GSTO1-1-deficient BMDMs. This finding indicated that GSTO1-1-deficient BMDMs are not classically M1 or M2 polarized. Interestingly LPS-induced IL-12p40 production was significantly reduced in GSTO1-1-deficient BMDMs. IL-12p40 functions as a regulator of the adaptive immune system, specifically driving T-helper 1 (Th1) activation [236, 237]. It would be interesting to examine the deficiency of GSTO1-1 on the pathogenicity of the mouse model of experimental autoimmune encephalomyelitis (EAE), as Th1 activation by IL-12p40 is known to be pathogenic in EAE [238].

The second major aim of this chapter was to assess if GSTO1-1 deficiency had an impact on the energetic demands of the cell, as redox signalling is closely linked to glycolysis and oxidative phosphorylation in macrophages, with recent discoveries identifying a critical role for the TCA cycle intermediate succinate in inflammation. Glycolysis has come to the forefront in recent years as a key metabolic reprogramming event in macrophage biology, as macrophages shift from oxidative phosphorylation to a glycolytic phenotype upon LPS treatment. Metabolic reprogramming of macrophages promotes microbial clearance, due to

higher ROS production and accumulation of TCA cycle intermediate succinate [146], which can stabilize HIF1α to further promote IL-1β transcription.

GSTO1-1 functions predominantly as a deglutathionylating enzyme, removing GSH from mixed disulphides to protect against oxidative damage. In order to assess if metabolic reprogramming was occurring in GSTO1-1-deficient cells, I firstly examined ROS production in response to LPS treatment in GSTO1-1 deficient BMDMs. Interestingly, GSTO1-1-deficient BMDMs produced higher levels of ROS basally, and considerably higher ROS production with LPS compared to WT cells. This finding poses a paradox, as increased IL-10 has been reported to limit ROS production in a model of DSS-induced colitis [239]. The observed differences in ROS production lead us to hypothesise that GSTO1-1 must play an anti-inflammatory role in macrophages. In a tumour micro-environment, cells have been shown to switch from oxidative-phosphorylation to glycolysis to promote rapid energy production. This 'metabolic switch', also known as the Warburg effect, is exploited by tumour cells and occurs in macrophages [142]. Interestingly, GSTO1-1-deficient BMDMs also have a high level of basal glycolysis compared to wild-type control BMDMs, generating ROS as a by-product of metabolic reprogramming. Increased ROS production leads to HIF1α stabilisation through degradation of the PHDs, leading to HIF1α activation and metabolic switching towards sustained glycolysis as seen in the GSTO1-1-deficient BMDMs. HIF1α stabilisation subsequently promotes transcription of genes containing hypoxia response elements (HREs). The IL-1β promoter contains a HRE, and GSTO1-1-deficient BMDMs also produce higher levels of pro-IL-1β when treated with LPS. Furthermore, HIF1α target genes are also increased in GSTO1-1-deficient BMDMs, including GLUT1, which transports glucose into the cell [240], further fuelling glycolytic demand.
I have shown that GSTO1-1-deficient macrophages are highly glycolytic and produce increased pro-inflammatory mediators in response to LPS treatment. Interestingly, *Gsto1* has recently been reported to be a HIF1α-dependent gene, and ablation of GSTO1-1 or inhibition of HIF1α is linked to overall reduction in metastasis and cancer progression [241]. From my data, GSTO1-1 may serve to negatively regulate HIF1α under basal conditions. Further work is required to confirm a role for GSTO1-1 in HIF1α signalling.

GSTO1-1-deficient mice were a limiting factor in these experiments, and I utilized a recently described covalent GSTO1-1 inhibitor, termed C1-27, to further place GSTO1-1 as a regulator of HIF1α and pro-IL-1β. C1-27-mediated GSTO1-1 inhibition mimicked most of the results obtained from GSTO1-1-deficient BMDMs. C1-27 dose-dependently increased pro-IL-1β and

HIF1α levels and increased PHD3 expression, whilst having no effect on degradation of IκBα or phosphorylation of P38. Interestingly, C1-27 decreased the production of the IL-1 receptor antagonist (IL1-RA), highlighting the potential anti-inflammatory effects of GSTO1-1. In contrast to the GSTO1-1-deficient BMDMs, C1-27 dose-dependently decreased IL-10 production. Furthermore, use of C1-27 dose-dependently decreased the production of ROS in contrast to GSTO1-1-deficient BMDMs. Due to the differences observed between the inhibitor-treated and GSTO1-1-deficient BMDMs I tested endogenous knockdown of GSTO1-1 using siRNA in BMDMs. Similar to C1-27, endogenous knockdown of GSTO1-1 attenuated IL-10 production. I have yet to test siRNA-mediated knockdown of GSTO1-1 and ROS production. These differences observed in IL-10 production require further investigation, as a link between GSTO1-1-mediated deglutathionylation and the production of IL-10 is unexplored. Perhaps GSTO1-1 may play a role in deglutathionylating the transcription factor CREB, which is known to drive IL-10 production [242], as my data suggests inhibition or removal of GSTO1-1 does not affect NF-κB activation, another known IL-10 producer. There are significant differences observed between the GSTO1-1-deficient mice, C1-27 treated BMDMs and siRNA-mediated GSTO1-1 knockdown BMDMs, however this may be potentially due to compensation by other GST family members. Menon et al. reported other GST class family members had increased expression in the GSTO1-1-deficient mice [148], which could impact the interpretation of the inhibitor-treated and siRNA-knockdown cells. The main differences between the GSTO1-1-deficient mice, GSTO1-1 siRNA mediated knockdown and C1-27 treated macrophages are summarised in Table 4.1.

Table 4.1 Variation between GSTO1-1-deficient mice, GSTO1-1 siRNA knockdown and C1-27 treated macrophages

	GSTO1-1-deficient mice	GSTO1-1 siRNA	C1-27
IL-6	N.D	N.D	N.D
IL-10	↑	↓	↓
TNFα	N.D	N.D	N.D
IL-1β	↑	?	↑
HIF1α	↑	?	↑
ROS	↑	?	↓
IL-1RA	?	?	↓
PHD3	↑	?	↑
LDHa	↑	?	?
GLUT1	↑	?	?
Arginase	↓	?	?
iNOS	↓	?	?
IL-12p40	↓	?	?

N.D = No difference

? = Not tested

Although the physiological role of GSTO1-1 is poorly understood, Menon et al. has identified that GSTO1-1-deficient mice are resistant to LPS-induced lethality *in vivo* [148], suggesting that GSTO1-1 may also regulate Caspase-1 or Caspase-11 activation. In addition, GSTO1-1 has been previously shown to interact with the inflammasome adaptor protein ASC. I therefore decided to next characterise a potential role for GSTO1-1 in the processing of pro-IL-1β due to the potential scope of GSTO1-1 substrate range and the availability of C1-27 as a tool to probe inflammasome activation. Recently IL-1β has been identified as a glutathionylated cytokine, which directly impacts on its pro-inflammatory activity [243] and GSTO1-1 could thereby play a role in IL-1β processing.

4.4 Final Conclusion

Overall, I have identified a potential regulatory role of GSTO1-1 in the production of HIF1α and IL-1β. HIF1α has been reported to undergo glutathionylation, stabilising HIF1α protein in response to ischemia reperfusion (IR) injury, promoting its angiogenic functions [218]. GSTO1-1 may serve to negatively regulate HIF1α via deglutathionylation to potentially promote its hydroxylation by the PHDs and subsequent degradation. Whether GSTO1-1-deficient mice would be protected from IR remains to be examined but warrants investigation. It would be interesting to examine if other redox enzymes, such as the glutaredoxins, phenocopy the observed differences in GSTO1-1-deficient mice. I have also identified GSTO1-1 as a potential novel regulator of IL-10. Examination of IL-10 production in GSTO1-1-deficient BMDMs requires further experiments to confirm the paradoxical increase in IL-10 production compared to C1-27 and siRNA-mediated IL-10 ablation. Nevertheless, the potential role of GSTO1-1 regulating HIF1α and IL-10 is intriguing. The main findings of this chapter have been graphically summarised in Figure 4.18.

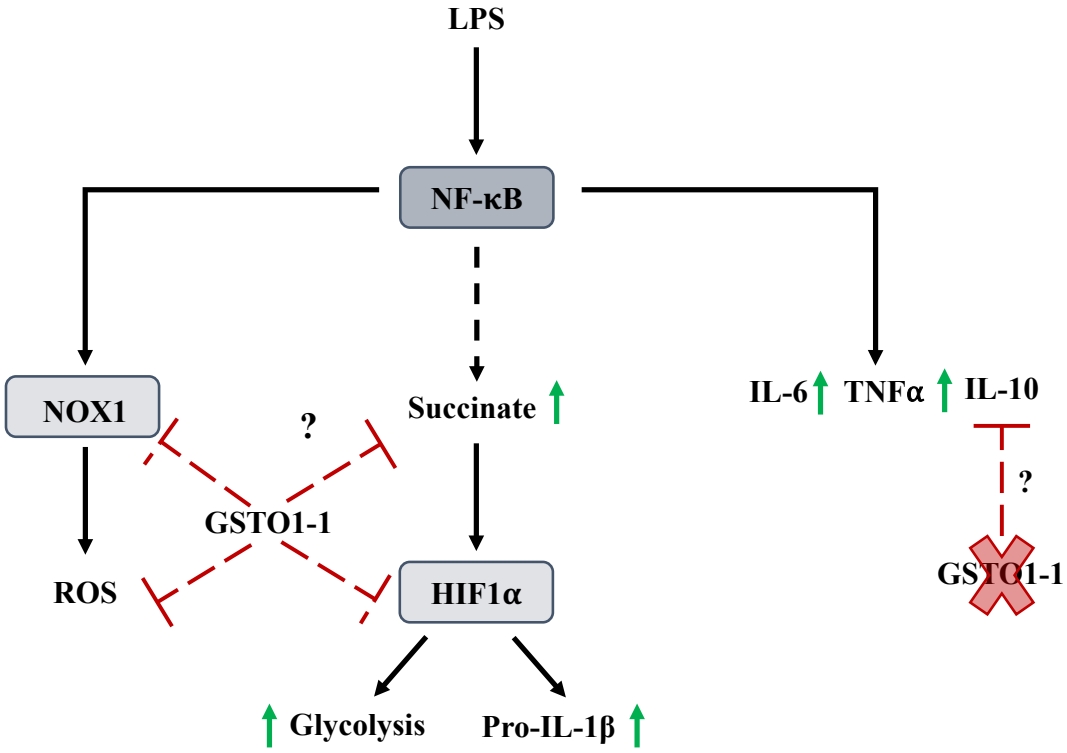

Figure 4.18 Schematic summary of results from Chapter 4

GSTO1-1 does not act upstream of NF-κB activation in murine BMDMs. GSTO1-1-deficiency results in increased levels of ROS, HIF1α, pro-IL-1β and glycolytic flux, suggesting a potential negative regulation of inflammation by GSTO1-1. Enzymatic inhibition of GSTO1-1 or endogenous knockdown ablates IL-10 production, possibly through a NF-κB independent mechanism.

Chapter 5

GSTO1-1 regulates the NLRP3 Inflammasome

GSTO1-1 is a novel component of the NLRP3 Inflammasome

5.1 Introduction

Inflammation has long been identified as the driving factor of many chronic inflammatory conditions and autoimmunity, including atherosclerosis [244], type 2 diabetes [245], ageing [246], obesity [247] and rheumatoid arthritis [248]. Macrophages of the innate immune system have been extensively examined in inflammatory phenotypes to elucidate the molecular mechanism of chronic low-grade inflammation. Once activated, TLRs drive assembly of inflammasomes, multimeric molecular signalling platforms. The NLRP3 (NLR family, pyrin domain containing 3) inflammasome is a multi-component assembly of adaptor and effector proteins highly expressed in myeloid cells, consisting of NLRP3, ASC, NEK7 and Caspase-1.

The discovery of the NLRP3 inflammasome in 2002 identified the mechanism of IL-1β and IL-18 cleavage[153], and further identified the components of the inflammasome in a cell free system, linking NLRP3 to the autoimmune disease Muckle-Wells syndrome [154]. Further inflammasomes have since been identified and characterised, including the NACHT, LRR and PYD domains-containing protein 1 (NLRP1), NLR family CARD domain-containing protein 4 (NLRC4) and the AIM2 inflammasome.

Murine inflammasomes require a two-step activation, requiring a 'priming' signal via NF-κB activation to generate inflammasome components, including pro-IL-1β and pro-IL-18, via TLRs. The second driving signal in NLRP3 inflammasome activation is sensing of DAMPs, such as extracellular ATP, the pore-forming ionophore Nigericin, and crystalline substances. In contrast, human monocytes circumvent the requirement for DAMP recognition, and drive NLRP3 inflammasome activation through an alternate TLR4-dependent mechanism [249].

NLRP3 can mediate pyroptotic cell death by priming Caspase-1 auto-catalytic activation, driving non-canonical inflammasome cleavage of the pore-forming protein GSDMD [162, 250]. Owing to the complexity of inflammasome sensing and regulation, NLRP3 can be considered an intracellular safeguard to sense and limit infection.

I became interested in NLRP3 due to previous reports of a potential role for GSTO1-1 in the regulation of inflammasome activation. GSTO1-1 was previously shown to interact with the adaptor protein ASC [251], however the enzymatic function of GSTO1-1 on inflammasome

activation remained unexplored. GSTO1-1-deficient mice have impaired IL-1β secretion in response to LPS treatment *in vivo*, which may also be Caspase-11 dependent [148]. The NLRP3 inflammasome is potently inhibited by a recently described small molecule inhibitor termed MCC950. MCC950 was synthesised from a parent compound termed CRID2 [147], which was found to bind to GSTO1-1 by affinity labelling and could implicate GSTO1-1 as the target for MCC950. There are many potential substrates for GSTO1-1 in inflammasome activation. Caspase-1 glutathionylation on cysteine 362 and cysteine 397 is inhibitory towards pro-IL-1β processing [181]. NLRP3 has also been identified as a glutathionylated protein by immunoprecipitation [183], which may be potentially regulated by GSTO1-1.

Here, using a small molecule inhibitor, endogenous knockdown approaches and GSTO1-1-deficient mice, we identify that GSTO1-1 regulates the NLRP3 inflammasome and Caspase-11-mediated NLRP3 inflammasome activation. Targeting of GSTO1-1 during NLRC4 or AIM2 inflammasome activation has no effect on pro-IL-1β processing. We identify that GSTO1-1 interacts with the novel inflammasome component NEK7. Using mass spectrometry and site directed mutagenesis, we confirm that NEK7 is glutathionylated on Cysteine 253 and furthermore, glutathionylation of Cysteine 253 negatively regulates NLRP3 inflammasome activation. GSTO1-1-deficient mice also have impaired inflammatory responses *in vivo*. Overall, we have characterised a novel NLRP3 inflammasome component, which may act as the ROS sensor for NLRP3 inflammasome activation.

5.1.1 The GSTO1-1 inhibitor C1-27 limits NLRP3 inflammasome activation

I began by testing activation of the NLRP3 inflammasome using LPS for 3h as a priming signal for inflammasome assembly in BMDMs, changing the cell medium to SFM medium and then treated BMDMs with C1-27 for 45min. I then added 'signal 2' using ATP for 45min to drive NLRP3 activation. As shown in Figure 5.1 A, enzymatic inhibition of GSTO1-1 inhibited the secretion of processed IL-1β into the supernatant compared to controls, with no effect on TNFα secretion identifying specificity in IL-1β processing (Figure 5.1 B). I also examined the levels of Pro-IL-1β and Pro-caspase-1 from the lysate of treated BMDMs. As shown in Figure 5.1 C, processing of pro-IL-1β is reduced in C1-27-treated BMDMs compared to controls (lysate blot middle panel, compare lanes 4 and 7). The supernatants were also concentrated using StrataClean Resin to examine secretion of processed Caspase-1 p20 subunit and the IL-1β p17 subunit (supernatant blot Figure 5.1 C, compare lanes 4 and 7) and C1-27 reduced the processing of both subunits.

5.1.2 C1-27 reduces the cell death associated with NLRP3 activation

The NLRP3 inflammasome senses a variety of stimuli, however the pore forming ionophore Nigericin is especially potent at inducing NLRP3-mediated pyroptosis [252]. I next decided to examine if the level of death associated with NLRP3 activation would be reduced by C1-27 treatment. In Figure 5.2 A, C1-27 significantly reduced the levels of cell death associated with NLRP3 activation, as measured by LDH release into the supernatant. C1-27 also reduced pro-IL-1β processing (Figure 5.2 B), had no effect on TNFα release (Figure 5.2 C) and also blocked release of Caspase-1 p20 subunit and IL-1β p17 subunit into the supernatant similar to ATP stimulation (Figure 5.2 D, compare lanes 4 and 7).

5.1.3 C1-27 has no effect on NLRC4 inflammasome activation

In order to confer specificity to C1-27, I next decided to examine the NLRC4 inflammasome, with senses intracellular flagellin to drive NLRC4 inflammasome activation [204]. NLRC4 activation is similar to NLRP3, and both complexes use Caspase-1 and ASC. BMDMs treated with LPS and C1-27 as described were infected with a MOI 20 of *S. typhimurium* UK-1 for 15min and treated with 50μg/mL gentamicin to kill remaining bacteria for 105min before analysis. As shown in Figure 5.3 A, C1-27 pre-treatment prior to infection had no effect on IL-1β processing, and also had no effect on TNFα secretion (Figure 5.3 B). It is unusual that TNFα secretion was reduced in response to LPS and *S. typhimurium* infection compared to LPS control. Pro-IL-1β was cleaved similar to controls (Lysate blot Figure 5.3 C middle panel,

compare lanes 4 and 7), with no differences observed between processing of Caspase-1 p20 subunit or IL-1β p17 subunit (Supernatant blot Figure 5.3 C, compare lanes 4 and 7).

5.1.4 C1-27 has no effect on AIM2 inflammasome activation

The NLRC4 inflammasome can be activated independent of the adaptor protein ASC, which is shared with NLRP3 and AIM2. I next decided to test C1-27 in AIM2 inflammasome activation using a synthetic double stranded DNA (dsDNA) termed Poly (dA:dT). As shown in Figure 5.4 A, C1-27 pre-treatment had no effect on IL-1β secretion into the supernatant, with no effect on TNFα production (Figure 5.4 B). Similar to the NLRC4 inflammasome, C1-27 was unable to block cleavage of Pro-IL-1β (Lysate blot Figure 5.4 C, middle panel, compare lanes 4 and 7), and had no effect on secretion of Caspase-1 p20 subunit or IL-1β p17 subunit (Supernatant blot Figure 5.4 C, compare lanes 4 and 7).

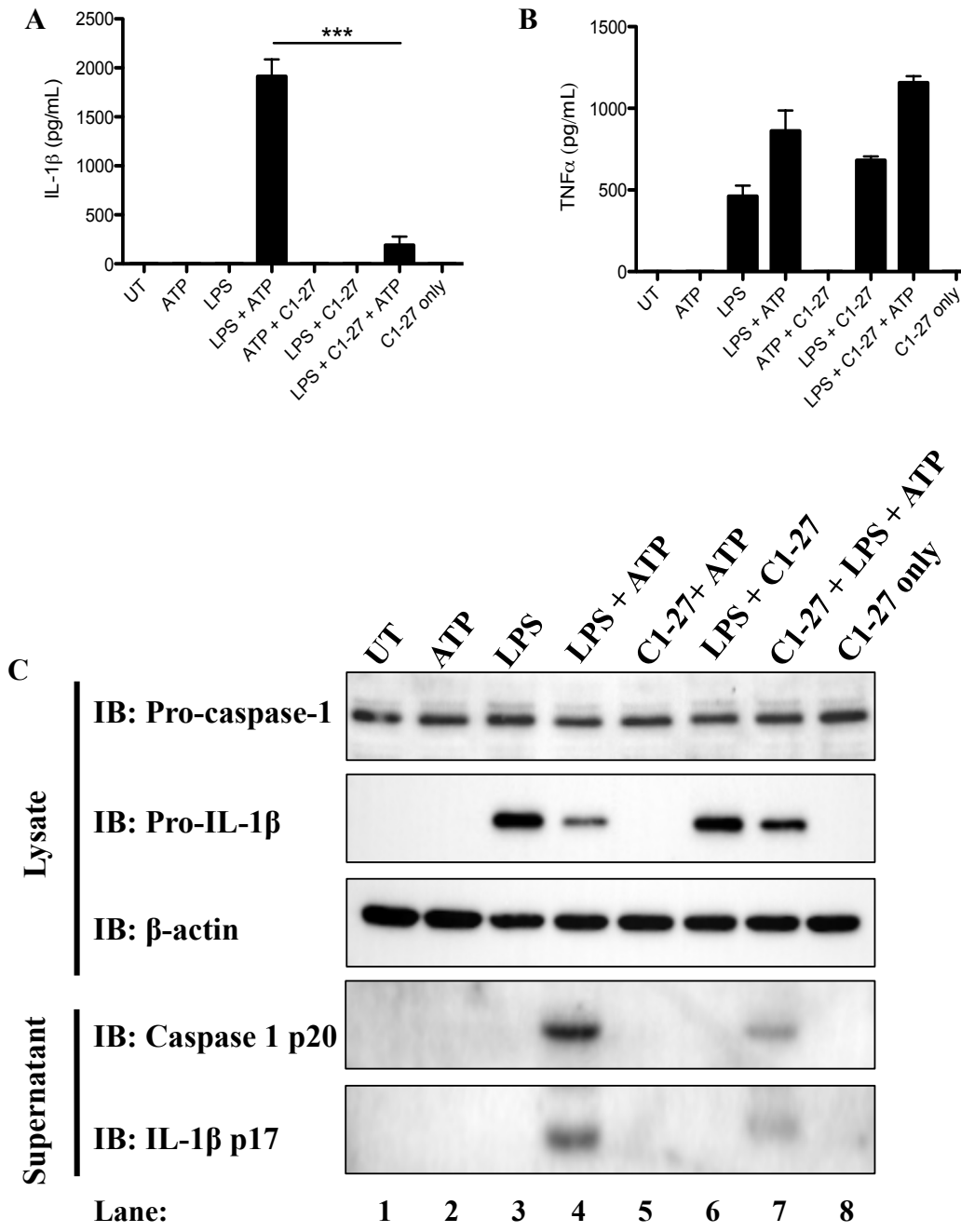

Figure 5.1 C1-27 limits ATP-mediated IL-1β processing

BMDMs were seeded at 5x10^{5}cell/mL in 12-well plates and incubated at 37°C 5% CO_2 overnight. Cells were pre-treated with 100ng/mL LPS for 3h. After 3h of LPS stimulation, media was removed and replaced with 1mL complete DMEM containing 5μM C1-27 for 45min. After 45min, cells were treated with 5mM ATP for 45min. Supernatant was harvested for ELISA and supernatant blots. Cells were lysed in sample loading buffer and analysed by western blotting using anti-IL-1β, anti-Caspase 1 p20 and anti-β-actin antibodies. Mean ± S.E.M of three independent experiments is shown.

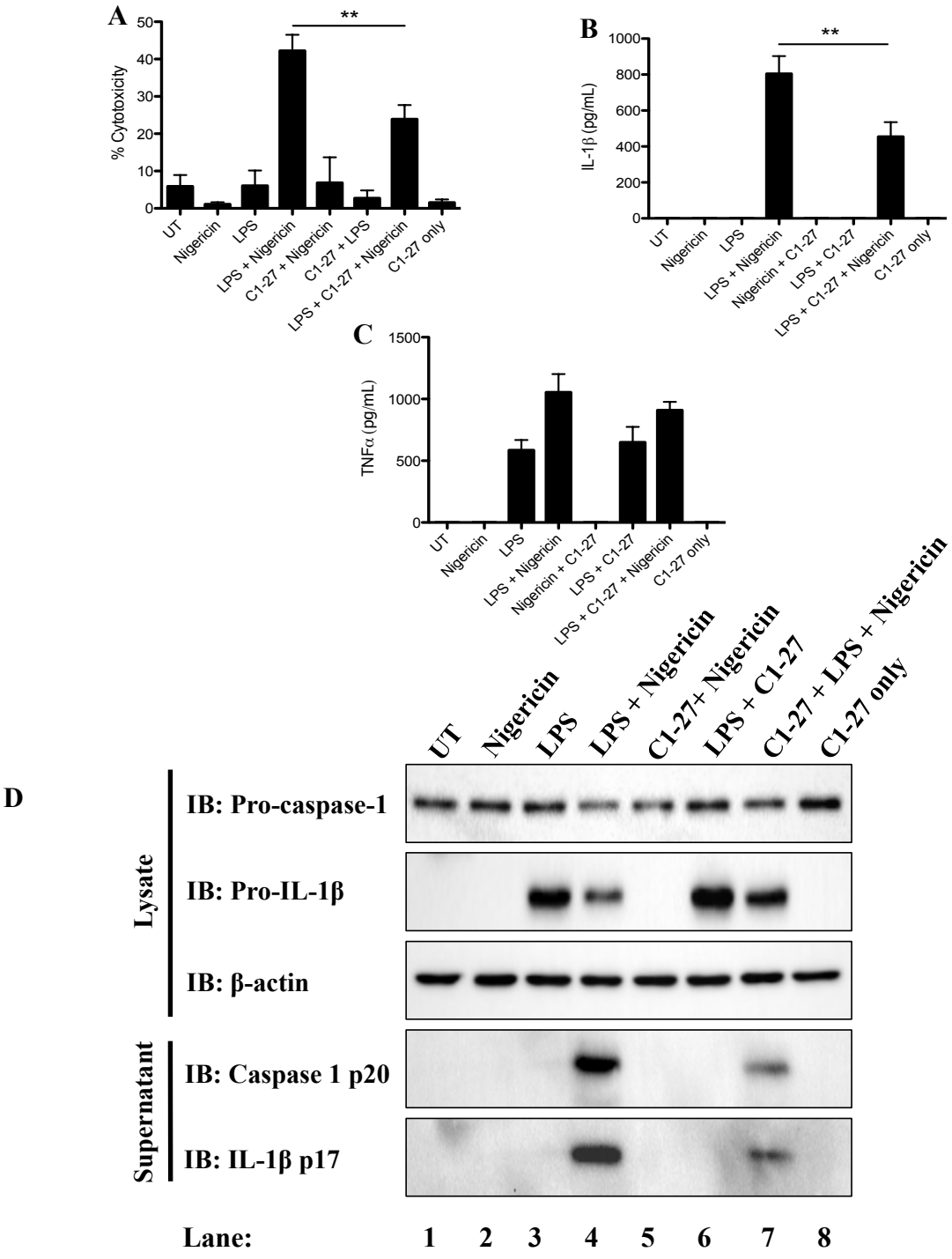

Figure 5.2 C1-27 limits Nigericin-mediated IL-1β processing

BMDMs were seeded at 5x10^{5}cell/mL in 12-well plates and incubated at 37°C 5% CO_2 overnight. Cells were pre-treated with 100ng/mL LPS for 3h. After 3h of LPS stimulation, media was removed and replaced with 1mL complete DMEM containing 5μM C1-27 for 45min. After 45min, cells were treated with 10μM Nigericin for 1h. Supernatant was harvested for LDH cytotoxicity assay, ELISA and supernatant blots. Cells were lysed in sample loading buffer and analysed by western blotting using anti-IL-1β, anti-Caspase 1 p20 and anti-β-actin antibodies. Mean ± S.E.M of three independent experiments is shown.

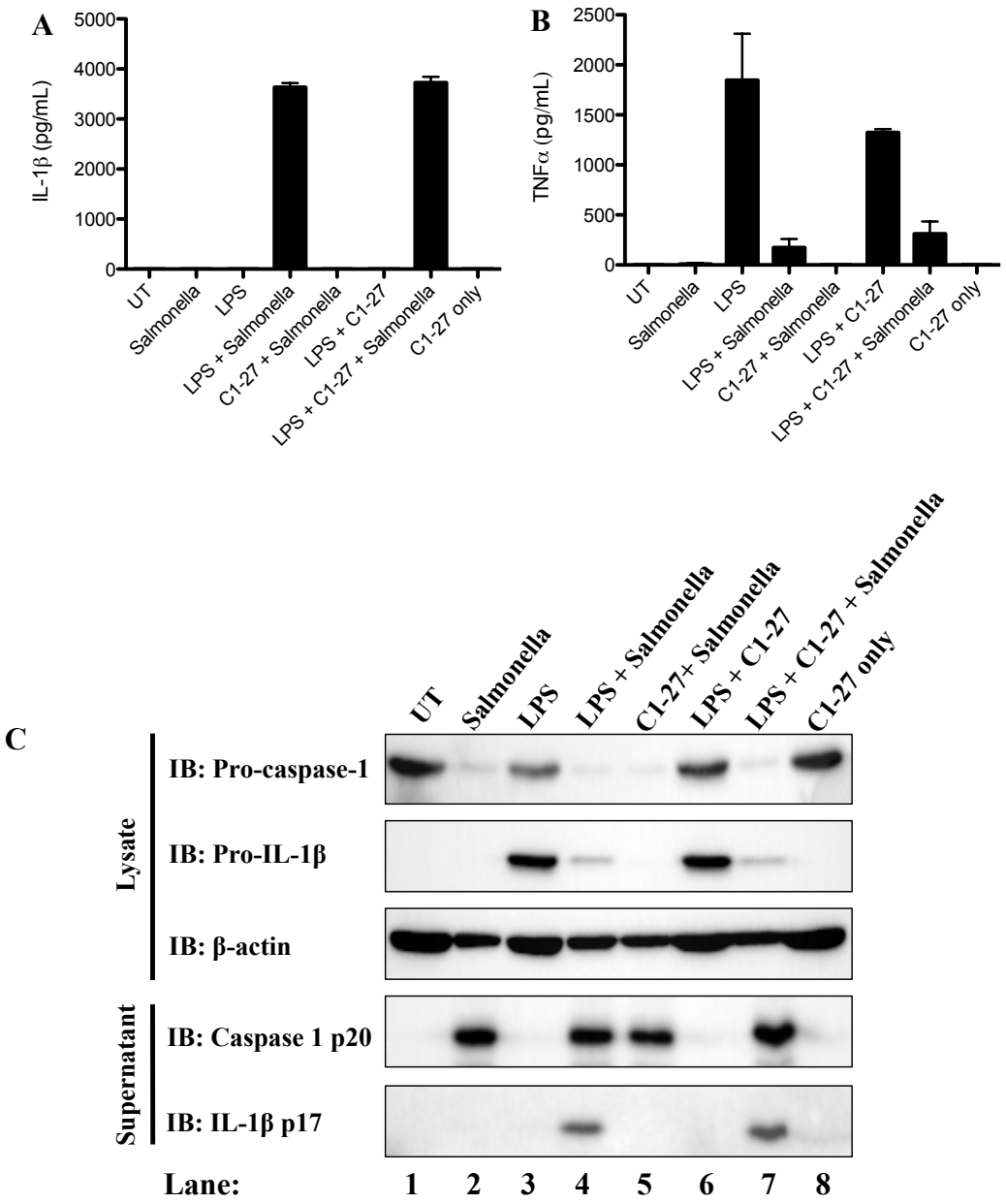

Figure 5.3 C1-27 does not limit *Salmonella typhimurium*-mediated IL-1β processing

BMDMs were seeded at 5x10^{5}cell/mL in 12-well plates and incubated at 37°C 5% CO_2 overnight. Cells were pre-treated with 100ng/mL LPS for 3h. After 3h of LPS stimulation, media was removed and replaced with 1mL complete DMEM containing 5μM C1-27 for 45min. After 45min, cells were infected with MOI 20 *S. typhimurium*. After 15min, gentamycin was added to the supernatant and left for 2h. Supernatant was harvested for ELISA and supernatant blots. Cells were lysed in sample loading buffer and analysed by western blotting using anti-IL-1β, anti-Caspase 1 p20 and anti-β-actin antibodies. Mean ± S.E.M of three independent experiments is shown.

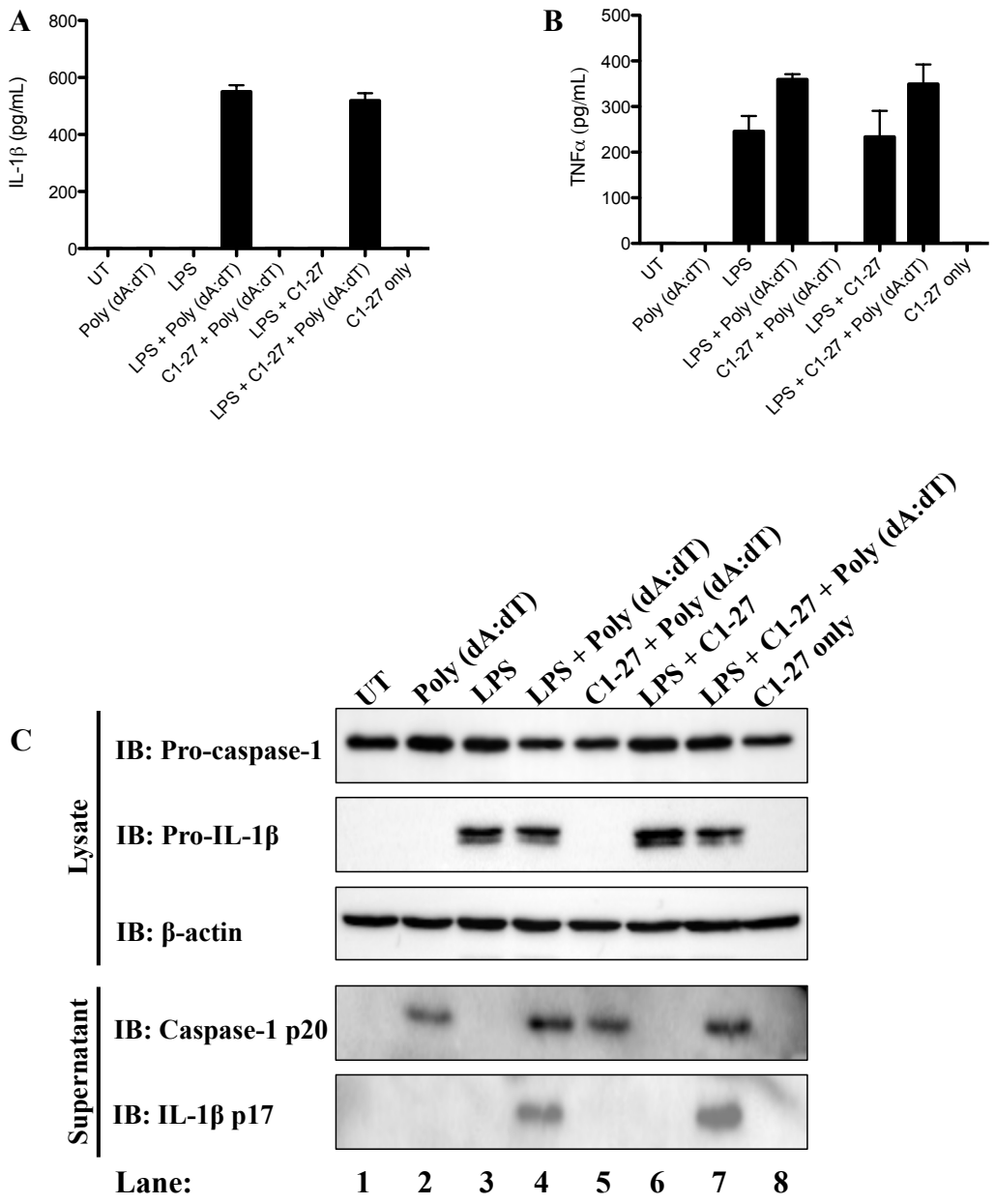

Figure 5.4 C1-27 does not limit AIM2 inflammasome activation

BMDMs were seeded at 5x10^{5}cell/mL in 12-well plates and incubated at 37°C 5% CO_2 overnight. Cells were pre-treated with 100ng/mL LPS for 3h. After 3h of LPS stimulation, media was removed and replaced with 1mL DMEM containing 5μM C1-27 for 45min. After 45min, cells were transfected with 1μg Poly (dA:dT) using Lipofectamine 2000 as the transfection reagent for 2h. Supernatant was harvested for ELISA and supernatant blots. Cells were lysed in sample loading buffer and analysed by western blotting using anti-IL-1β, anti-Caspase 1 p20 and anti-β-actin antibodies. Mean ± S.E.M of three independent experiments is shown.

5.1.5 C1-27 limits ASC oligomerisation

Activation of the NLRP3 inflammasome results in assembly of an oligomeric complex composed of Caspase-1, NLRP3 and the adaptor protein ASC. ASC is a ubiquitously expressed protein, however ASC forms multimers upon inflammasome activation which can be detected by chemical crosslinking [253]. As shown in Figure 5.5, C1-27 pre-treatment reduced the levels of ASC multimers. C1-27 reduced DSS-crosslinked ASC speck formation in the Triton X-100 insoluble fraction (Figure 5.5 Top panel). ASC was depleted in the LPS and ATP Triton X-100 soluble fraction, however ASC was increased in the C1-27 pre-treatment before ATP addition (Figure 5.5 Middle panel), indicating C1-27 limits assembly of the NLRP3 inflammasome, upstream of Caspase-1 activation.

5.1.6 Endogenous knockdown of GSTO1-1 boosts Pro-IL-1β at 24h LPS treatment

I next decided to endogenously knockdown GSTO1-1 from LPS-stimulated BMDMs to assess the relevance of GSTO1-1 on NLRP3 components, independent of a small molecule inhibitor. As shown in Figure 5.6 A, siRNA specific to GSTO1-1 efficiently reduced the levels of GSTO1-1 (Second panel). I examined ASC expression in response to GSTO1-1 knockdown and found no difference in ASC levels between control and GSTO1-1 siRNA knockdown (Top panel). Pro-IL-1β production was increased at 24h in GSTO1-1 siRNA treatments compared to control siRNA (Third panel), in agreement with the GSTO1-1-deficient mice and C1-27 treated BMDMs. GSTO1-1 knockdown had no effect on transcription of NLRP3 (Figure 5.6 B) however, a trend of increased IL-1β mRNA was observed at 24h compared to control (Figure 5.6 C). No effect on TNFα transcription was observed (Figure 5.6 D). GSTO1-1 was also efficiently knocked down at the mRNA level (Figure 5.6 E).

5.1.7 GSTO1-1 knockdown limits NLRP3 activation

Due to the observed effects of C1-27, I decided to endogenously knockdown GSTO1-1 to assess if GSTO1-1 affected NLRP3 activation. GSTO1-1 knockdown resulted in a modest decrease in IL-1β secretion (Figure 5.7 A), with no effect on TNFα (Figure 5.7 B). GSTO1-1 was efficiently knocked down by siRNA compared to control siRNA (Figure 5.7 C, third panel). GSTO1-1 knockdown resulted in a decrease in pro-IL-1β processing, similar to C1-27 pre-treatment (Figure 5.7 C, second panel, compare lanes 4 and 8). GSTO1-1 knockdown decreased cleavage of the Caspase-1 p20 subunit and IL-1β p17 subunit into the supernatant similar to ATP stimulation (Figure 5.7 C lowest panels, compare lanes 4 and 8).

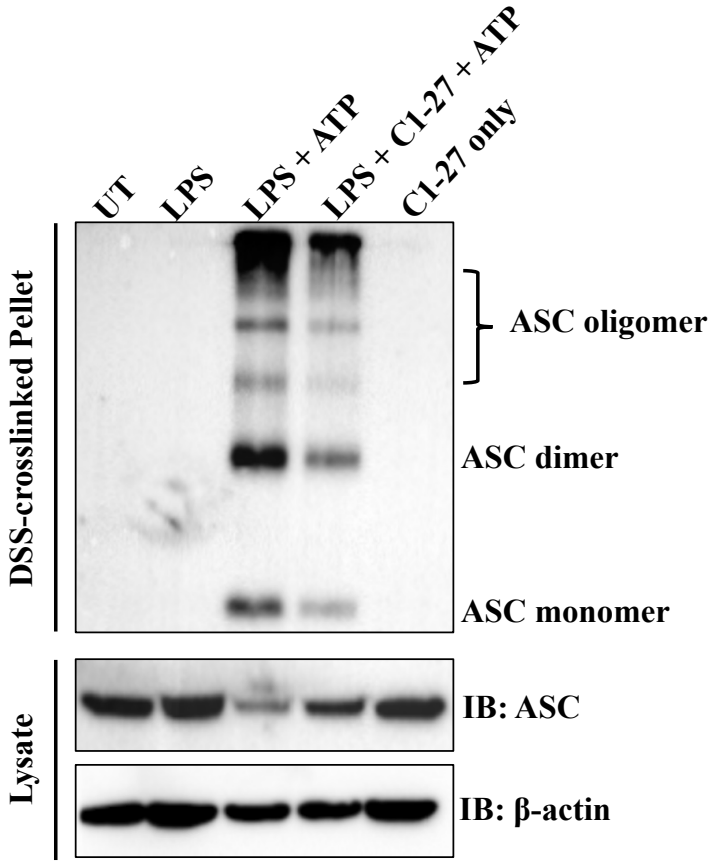

Figure 5.5 C1-27 reduces ASC speck formation

BMDMs were seeded at 3x10^{6}cells/mL in 6-well plates 37°C 5% CO_2 overnight. Cells were treated as described in (A). Cells were washed in 200µL 50mM HEPES and lysed in lysis buffer (0.5% Triton X-100, 50mM HEPES). Samples were centrifuged at 6000 x g for 15min at 4°C. Supernatant (lysate) was stored in -20°C. The pellet was crosslinked in crosslinking buffer (50mM HEPES, 150mM NaCl pH 8) and 2mM DSS. Samples were incubated at 37°C for 45min and centrifuged at 6000 x g for 15min at 4°C. Supernatant was discarded and pellet was resuspended in sample loading buffer and analysed by SDS-PAGE using anti-ASC and anti-β-actin antibodies. The results shown are representative of three independent experiments.

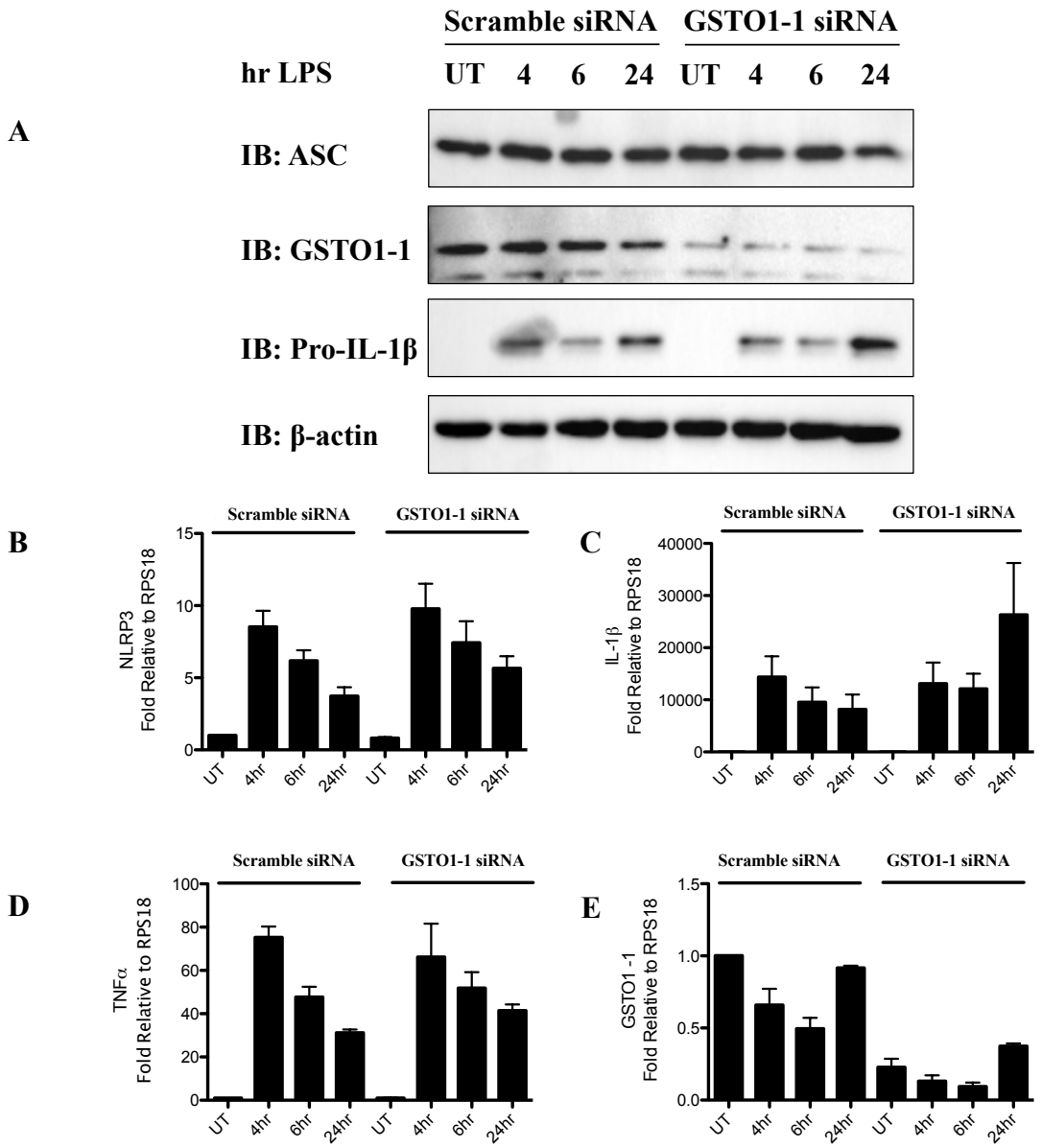

Figure 5.6 Endogenous knockdown of GSTO1-1 does not affect NLRP3 expression

BMDMs were seeded at 5x10^{5}cell/mL in 12-well plates and incubated at 37°C 5% CO_2 overnight. Cells were transfected with 20nmol scramble siRNA (Ambion) or GSTO1 siRNA in OptiMEM media for 36h using RNAiMAX lipofectamine. Cells were treated with 100ng/mL LPS for times indicated. Cells were lysed in sample loading buffer and analysed by western blotting using anti-NLRP3, anti-ASC, anti-GSTO1, anti-IL-1β and anti-β-actin antibodies. Representative of three independent western blot experiments is shown. Identical treatment was performed for RNA samples before harvesting. Cells were lysed in 350μL RNA lysis buffer and RNA isolated using Ambion RNA extraction kit. RNA was reverse transcribed and cDNA was used for qPCR with SYBR Green components. cDNA was analysed using the cycle-threshold (Ct) value normalized to RPS18 control gene. Mean ± S.E.M of three independent experiments each carried out in triplicate is shown.

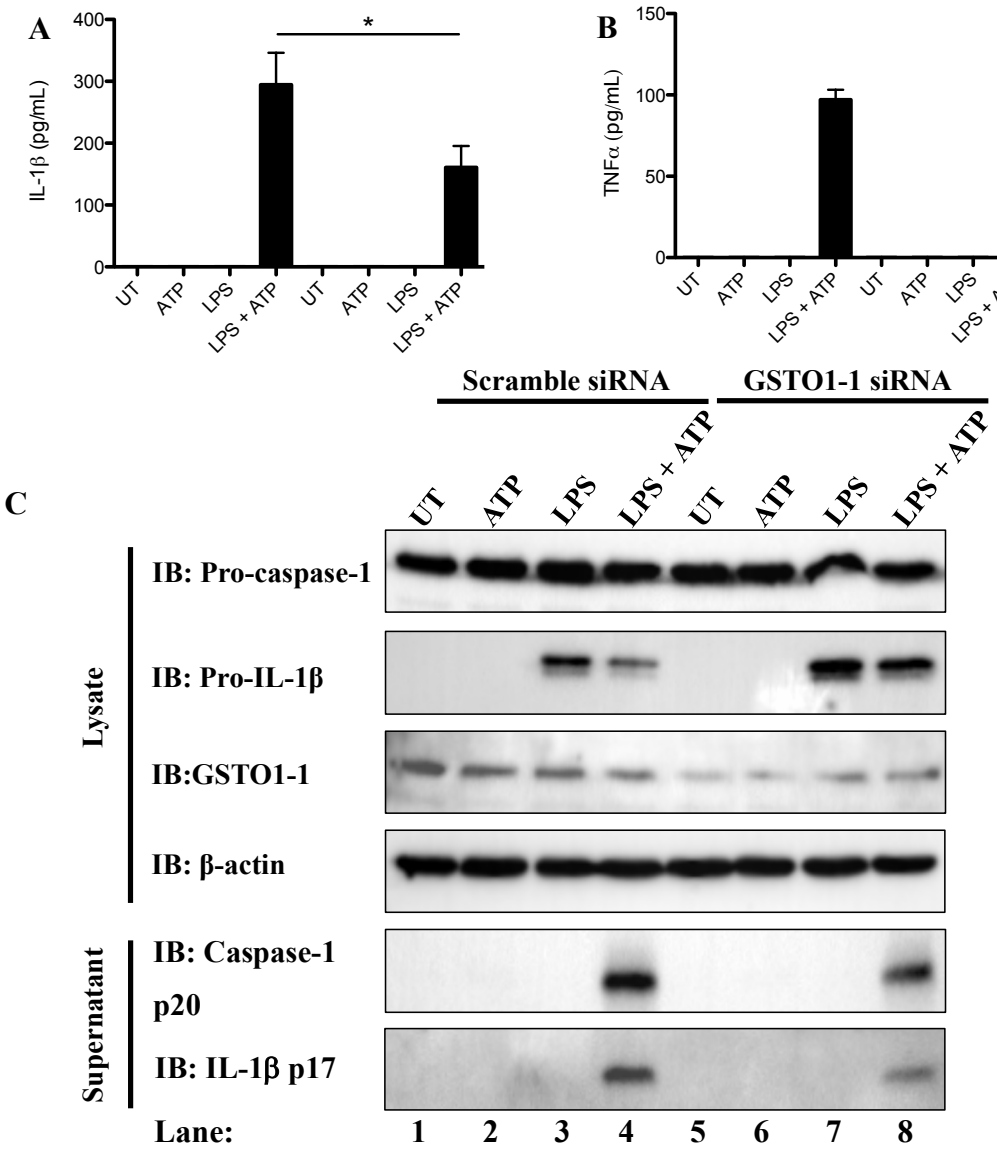

Figure 5.7 Endogenous knockdown of GSTO1-1 limits NLRP3 inflammasome activation

BMDMs were seeded at 5x10^{5}cell/mL in 12-well plates and incubated at 37°C 5% CO_2 overnight. Cells were transfected with 20nmol scramble siRNA (Ambion) or GSTO1 siRNA in OptiMEM media for 36h. Cells were pre-treated with 100ng/mL LPS for 3h. After 3h, the medium was removed and replaced with serum free DMEM. Cells were treated with 5mM ATP for 45min. Supernatant was harvested for ELISA and supernatant blots. Cells were lysed in sample loading buffer and analysed by western blotting using anti-Caspase 1, anti-GSTO1, anti-IL-1β, and anti-β-actin antibodies. Mean ± S.E.M of ELISA data is shown. Representative of three independent western blot experiments is shown.

5.1.8 Ethyl-ester glutathione (GSH-EE) reduces NLRP3 inflammasome activation

I hypothesised that glutathionylation of the inflammasome would limit NLRP3 activation, as GSTO1-1 functions as a deglutathionylating enzyme. I therefore assessed if a cell permeable version of glutathione (GSH-EE) would efficiently reduce inflammasome activation. As shown in Figure 5.8 A, GSH-EE dose dependently decreased IL-1β cleavage as measured by ELISA. Further, GSH-EE dose dependently increased the levels of Pro-caspase-1 and Pro-IL-1β (Figure 5.8 B, First and second panel, compare lanes 3 and 6). Increasing doses of GSH-EE also limited secretion of mature IL-1β into the supernatant (Figure 5.8 B, bottom panel, compare lanes 3 and 6).

5.1.9 GSTO1-1 boosts Pro-IL-1β Processing in NLRP3 Inflammasome Reconstituted 293T Cells

Murine inflammasomes can be reconstituted in 293T cells to assess cleavage of Pro-IL-1β into the supernatant [254]. 293T cells were reconstituted with ASC, NLRP3, Pro-caspase-1, NEK7 and Pro-IL-1β and treated with Nigericin to induce IL-1β cleavage. In Figure 5.9 A, reconstitution of the NLRP3 inflammasome induced IL-1β secretion into the supernatant, as measured by ELISA. Addition of GSTO1-1 further promoted IL-1β secretion into the supernatant. Pro-caspase-1 was omitted as a negative control. The levels of GSTO1-1 and Pro-caspase-1 are confirmed by western blot (Figure 5.9 B). β-actin served as a loading control.

5.1.10 GSTO1-1 interacts with ASC and NEK7

GSTO1-1 has previously been reported to interact with the adaptor protein ASC. Furthermore, a recently described inflammasome component, NEK7, has been reported to act as the intracellular ROS sensor for NLRP3 activation [151, 152]. I hypothesised that the ROS sensing capacity of NEK7 may be mistaken with the activity of GSTO1-1 and decided to both confirm the ASC interaction with GSTO1-1 and further assess if GSTO1-1 could interact with NEK7. As shown in Figure 5.9, overexpression of untagged GSTO1-1, HA-tagged ASC and HA-tagged NEK7 in HEK293T cells resulted in an interaction between all three components. The interaction between GSTO1-1 and ASC is very evident (Figure 5.10, Top panel Lane 2), and a weaker interaction is observed for NEK7 (Figure 5.10, Top panel Lane 3). GSTO1-1 may be interacting with ASC indirectly through proximity with NEK7, as C1-27 has no effect on the AIM2 inflammasome (Figure 5.4). I used an anti-HA antibody to pulldown ASC and NEK7 (Second panel) as bait for GSTO1-1.

5.1.11 NEK7 interacts with GSTO1-1 endogenously

To confirm a role for GSTO1-1 in NEK7 glutathionylation, I next assessed if NEK7 could interact with GSTO1-1 endogenously. As shown in Figure 5.11, NEK7 was successfully pulled down in primary macrophages stimulated with LPS or LPS and ATP treatment (Figure 5.11 Second panel). GSTO1-1 interacts with NEK7 in response to LPS treatment and interaction is enhanced in response to LPS and ATP treatment (Compare Figure 5.11 Top panel Lanes 1 and 2). Addition of C1-27 prior to ATP stimulation reduced GSTO1-1 interaction with NEK7 (Figure 5.11 Top panel Lane 3). No band was observed in the IgG control (Figure 5.11 Second panel Lane 4). GSTO1-1 and NEK7 expression was detected in whole cell lysates (Figure 5.11 Third and Fourth panel). β-actin served as loading control (Figure 5.11 Bottom panel).

5.1.12 NEK7 is a glutathionylated protein

In order to assess potential targets for GSTO1-1, I assessed whether NEK7 could be glutathionylated. As shown in Figure 5.11, overexpression of NEK7 in 293T cells resulted in glutathionylation of NEK7 (Figure 5.12 Top panel, middle lane). A non-specific band is observable in the EV control lane, however the band intensity is weak compared to NEK7. A small shift of 5kDa was observed for the glutathionylated band. NEK7 was successfully immunoprecipitated (Figure 5.12 Middle panel, middle lane). No bands were detectable in the IgG control (Figure 5.12 Top panel, third lane), indicating specificity of the glutathionylation.

5.1.13 Mass Spectrometry of NEK7 identifies Cysteine 79 and Cysteine 253 glutathionylation

To verify the glutathionylation status of NEK7, mass spectrometry was performed to characterise which cysteines potentially undergo glutathionylation. NEK7 was immunoprecipitated and incubated with GSSG to induce glutathionylation of solvent accessible cysteines. Figure 5.13 shows a summary diagram of the observed modifications detected on NEK7 by mass spectrometry (See appendix for full list of modified peptides). Glutathionylation of NEK7 was detected on cysteines 79 and 253 when incubated with 5mM GSSG prior to trypsin digest.

5.1.14 Cysteine 253 in NEK7 is negatively regulated by glutathionylation

In order to elucidate the functional consequences of glutathionylation in NEK7, I mutagenized each cysteine in NEK7 to alanine and reconstituted the inflammasome in HEK293T cells with WT NEK7 or NEK7 mutants. As shown in Figure 5.14, the inflammasome was successfully reconstituted, and IL-1β production was boosted in the presence of GSTO1-1 transfection.

There was no significant difference in inflammasome activation by the NEK7 mutants with exception of C253A, which boosted IL-1β production relative to the WT condition co-transfected with GSTO1-1, indicating that C253 may be the target site for GSTO1-1 deglutathionylation.

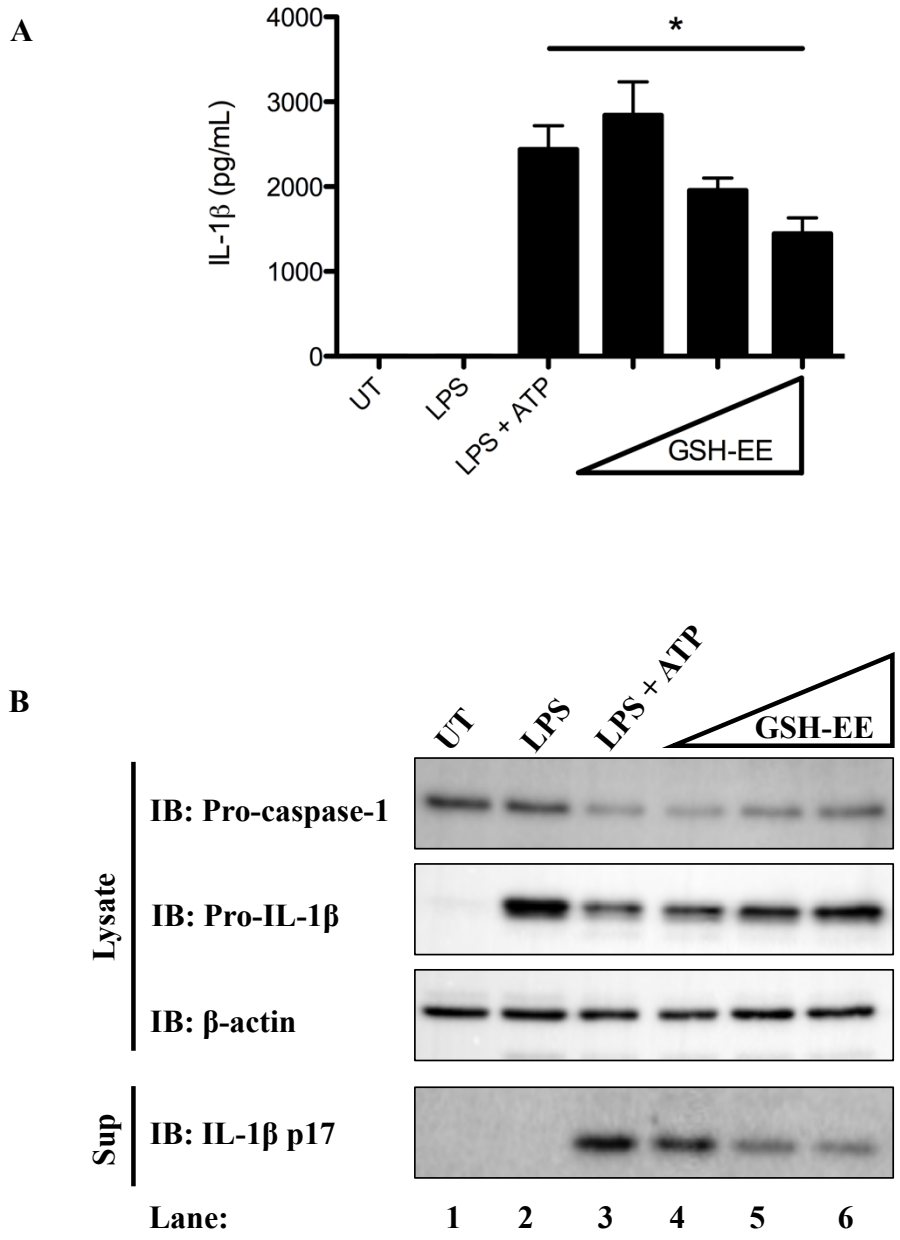

Figure 5.8 Exogenous ethyl-ester GSH attenuates NLRP3 inflammasome pro-IL-1β processing

BMDMs were seeded at $5x10^5$cell/mL in 12-well plates and incubated at 37°C 5% CO_2 overnight. Cells were pre-treated with 100ng/mL LPS for 3h. After 3h, cells were treated with a dose range of GSH-EE for 45min. After 45min cells were treated with 5mM ATP for 45min. Supernatant was harvested for ELISA. Cells were lysed in sample loading buffer and analysed by western blotting using anti-Caspase 1, anti-IL-1β, and anti-β-actin antibodies. Mean ± S.E.M of three independent experiments is shown.

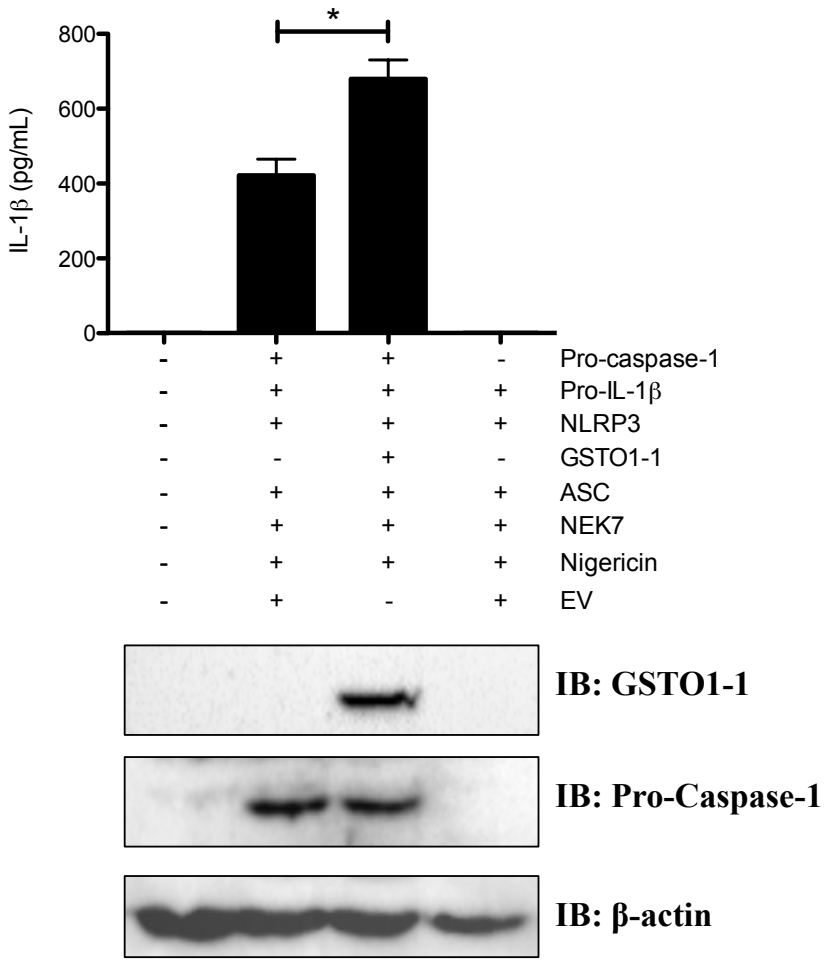

Figure 5.9 GSTO1-1 boosts IL-1β processing in 293T Cells

HEK293T cells were seeded at $2x10^5$ cells/mL and incubated at 37°C 5% CO_2 overnight. Cells were transfected with EV, HA-ASC, HA-NEK7, FLAG-Pro-caspase-1, Pro-IL-1β, FLAG-NLRP3 or GSTO1-1. In each transfection, the total concentration of plasmid DNA was kept constant by addition of relevant EV control. 24h post transfection, the cell medium was removed and replaced with complete DMEM medium. Cells were left for 6h, with 10μM Nigericin added 1h prior to harvesting. Supernatant was harvested for ELISA. Cells were lysed in sample loading buffer and analysed by western blotting using anti-Caspase 1, anti-GSTO1, and anti-β-actin antibodies. Mean ± S.E.M of three independent experiments is shown.

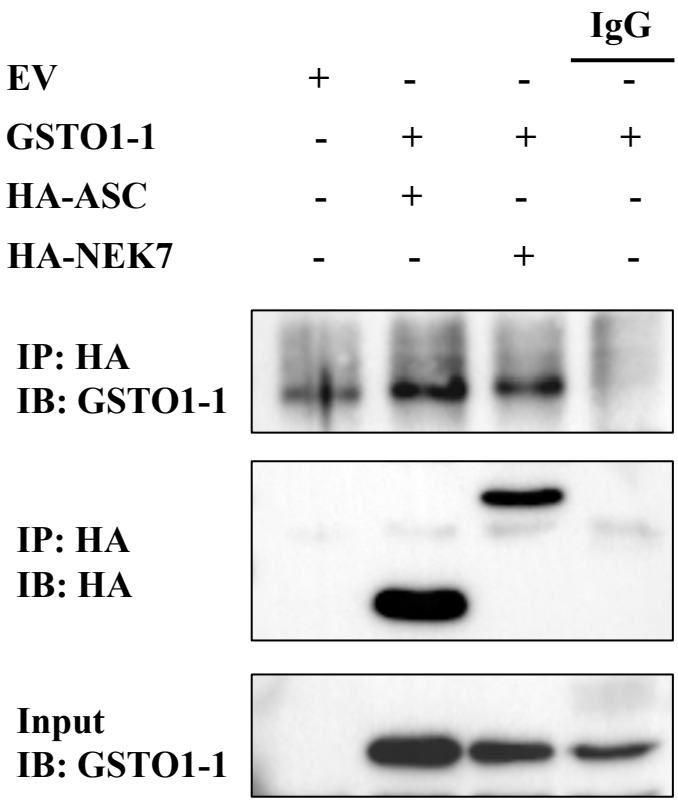

Figure 5.10 GSTO1-1 interacts with ASC and NEK7 when overexpressed

HEK293T cells were seeded at 2.5x10^5 cells/mL in 10cm dishes and incubated at 37°C 5% CO_2 overnight. Cells were transfected with EV, GSTO1-1, HA-ASC or HA-NEK7. In each transfection, the total concentration of plasmid DNA was kept constant by addition of relevant EV control. 48h post transfection cells were lysed in low stringency lysis buffer. 50µL of lysate was kept for analysis while the remaining lysate was added to protein A/G beads coated with 1µg of anti-HA antibody or 1µg mouse-IgG control antibody for 2h rotating at 4°C. Samples were washed three times in 1mL low stringency lysis buffer and resuspended in 50µL sample loading buffer. Whole cell lysates and immunoprecipitated samples were analysed by western blotting using anti-HA and anti-GSTO1-1 antibodies. The results shown are representative of three independent experiments.

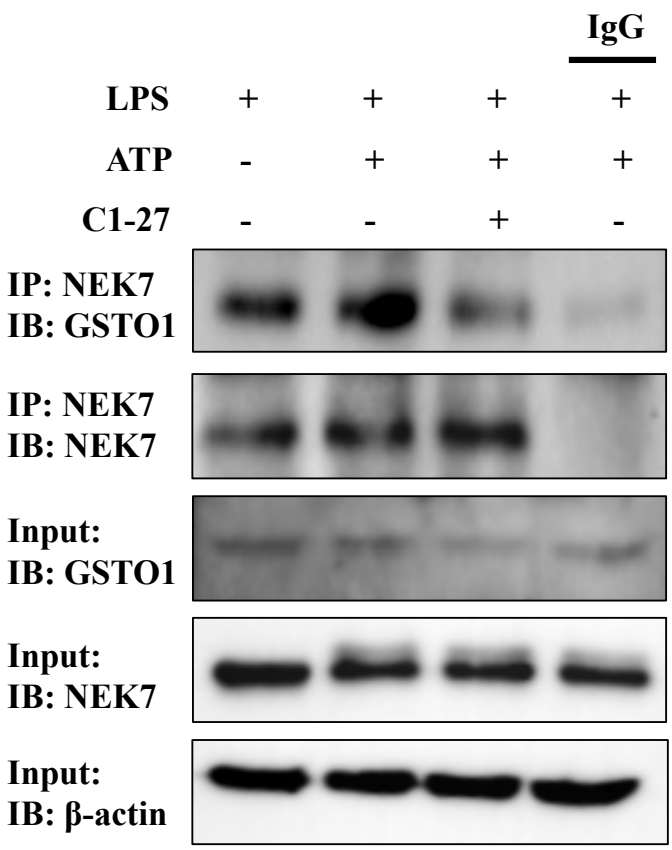

Figure 5.11 NEK7 interacts with GSTO1-1 endogenously during an NLRP3 inflammasome assay

BMDMs were seeded at 1x10^6 cells/mL in 10cm dishes and left at 37°C 5% CO2 overnight. Cells were treated with 100ng/mL LPS for 3h, media removed and replaced with serum free medium. 5μM C1-27 was added for 45min to indicated samples and then treated with 5mM ATP for 30min. Samples were lysed using low stringency lysis buffer supplemented with protease inhibitors. The lysate was immunoprecipitated on A/G beads and subjected to SDS-PAGE. Samples were blotted for anti-NEK7, anti-GSTO1-1 or anti-β-actin. Each blot is representative of two independent experiments.

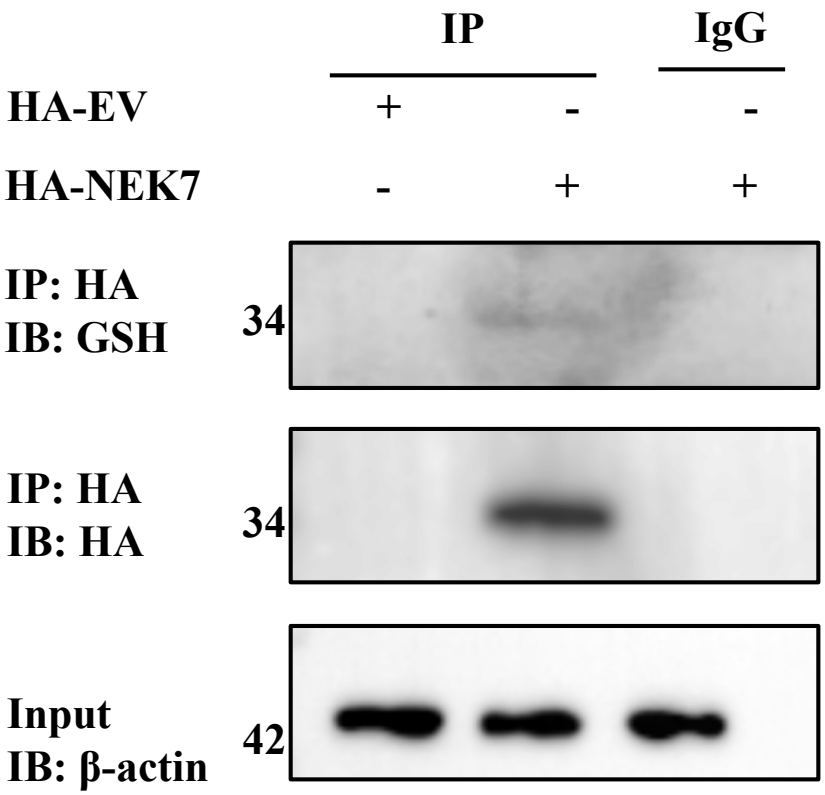

Figure 5.12 NEK7 is glutathionylated when overexpressed in 293T cells

HEK293Ts were seeded at 2.5x10^5 cells/mL in 10cm dishes and incubated at 37°C 5% CO_2 overnight. Cells were transfected with 5μg HA-EV or 5μg HA-NEK7. 24h post transfection cells were lysed in low stringency lysis buffer with 50mM N-ethylmaleimide. 50μL of lysate was kept for analysis while the remaining lysate was added to protein A/G beads coated with 1μg of anti-HA antibody or 1μg mouse-IgG control antibody for 2h rotating at 4°C. Samples were washed three times in 1mL low stringency lysis buffer and resuspended in 50μL sample loading buffer without DTT added. Whole cell lysates and immunoprecipitated samples were analysed by western blotting using anti-HA, anti-GSH and anti-β-actin antibodies. The results shown are representative of three independent experiments.

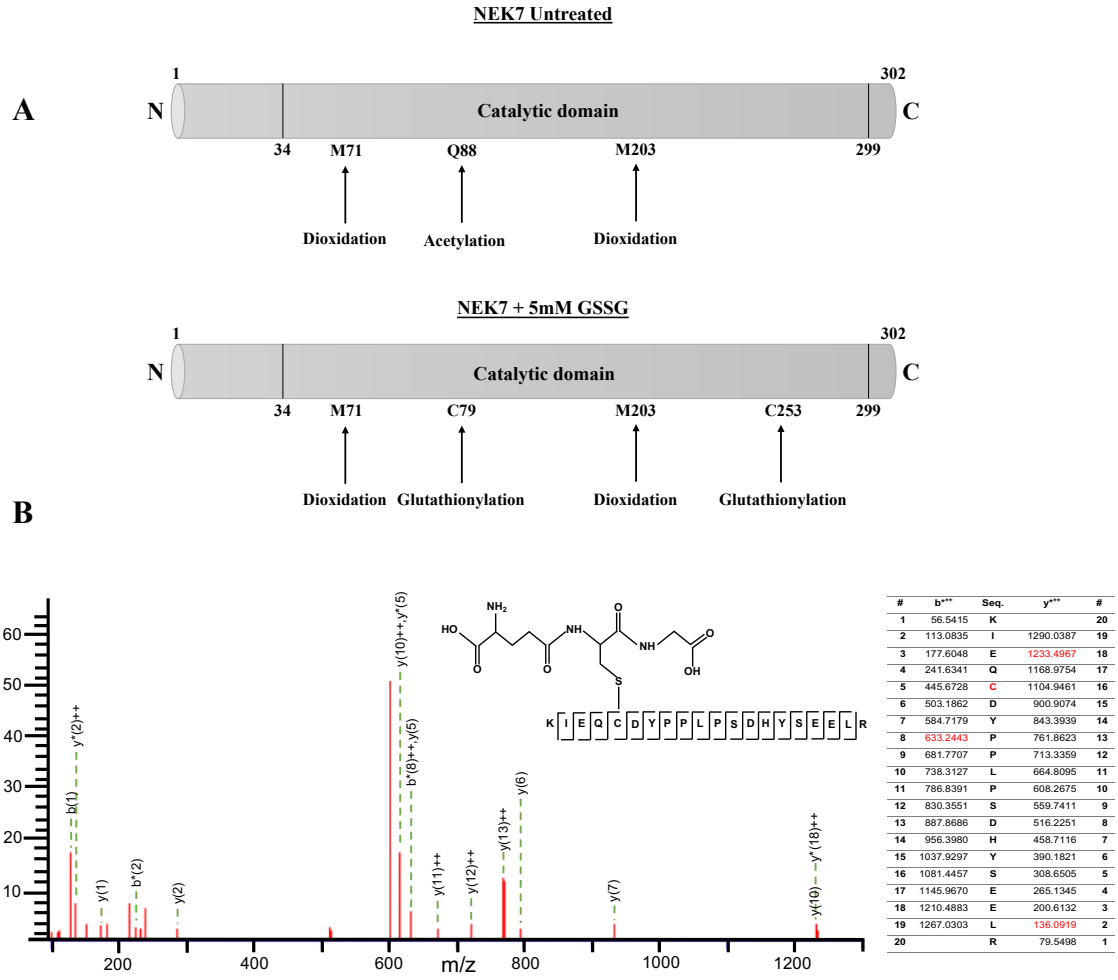

#	b***	Seq.	y***	#
1	56.5415	K		20
2	113.0835	I	1290.0387	19
3	177.6048	E	1233.4967	18
4	241.6341	Q	1168.9754	17
5	445.6728	C	1104.9461	16
6	503.1862	D	900.9074	15
7	584.7179	Y	843.3939	14
8	633.2443	P	761.8623	13
9	681.7707	P	713.3359	12
10	738.3127	L	664.8095	11
11	786.8391	P	608.2675	10
12	830.3551	S	559.7411	9
13	887.8686	D	516.2251	8
14	956.3980	H	458.7116	7
15	1037.9297	Y	390.1821	6
16	1081.4457	S	308.6505	5
17	1145.9670	E	265.1345	4
18	1210.4883	E	200.6132	3
19	1267.0303	L	136.0919	2
20		R	79.5498	1

Figure 5.13 Mass Spectrometry of NEK7 identifies Cysteine 79 and Cysteine 253 glutathionylation

HEK293Ts were seeded at 7.5x10^5 cells/mL in 10cm dishes and reverse transfected with 10µg HA-NEK7 and incubated at 37°C 5% CO_2 overnight. Cells were lysed in low stringency lysis buffer. 30µL of lysate was kept for analysis while the remaining lysate was added to protein A/G beads coated with 2µg of anti-HA antibody or 2µg mouse-IgG control antibody for 2h rotating at 4°C. Samples were washed three times in 1mL low stringency lysis buffer and dried A/G beads were incubated with 200µg HA peptide to elute bound NEK7. The eluate was concentrated using Amicon Ultra 10K columns. NEK7 was incubated with 5mM GSSG (pH 8) or H_2O if untreated for 1h at RT. Samples were ran on a non-reducing SDS-PAGE gel, fixed with fixing solution for 30min RT, stained with Coomassie R-250 for 1h RT and washed with detain solution overnight at 4°C. Bands were excised for 1D nLC-MS/MS (4000 QTRAP) mass spectrometry analysis using trypsin digest and analysed using Mascot software. (A) Schematic diagram of detected modifications on NEK7. (B) Mass spectrum of Cysteine 253 with GSH adducts detected.

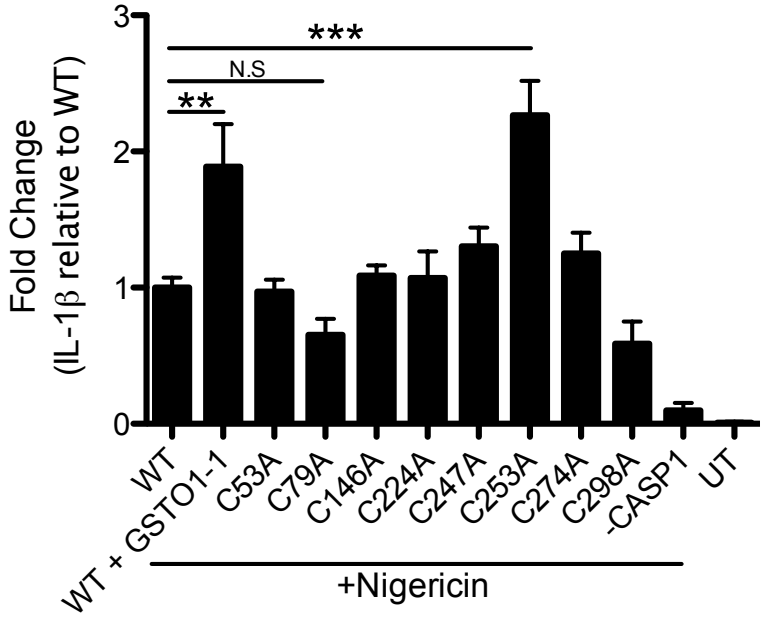

Figure 5.14 C253A boosts IL-1β production in Inflammasome-reconstituted 293Ts

HEK293T cells were seeded at $2x10^5$ cells/mL and incubated at 37°C 5% CO_2 overnight. Cells were transfected with EV, HA-ASC, HA-NEK7 or HA-NEK7 mutants, FLAG-Pro-caspase-1, Pro-IL-1β, FLAG-NLRP3 or GSTO1-1 (WT + GSTO1-1). In each transfection, the total concentration of plasmid DNA was kept constant by addition of relevant EV control. 24h post transfection, the cell medium was removed and replaced with complete DMEM medium. Cells were left for 6h, with 10μM Nigericin added 1h prior to harvesting. Supernatant was harvested for ELISA. Mean ± S.E.M of three independent experiments is shown.

5.1.15 MCC950 does not limit the enzymatic activity of GSTO1-1

Due to the similarities in IL-1β inhibition by MCC950 and C1-27, we next assessed if MCC950 could limit the enzymatic activity of GSTO1-1. The enzymatic activity of GSTO1-1 in the presence of MCC950 or C1-27 was measured by Dr. Padmaja Tummala (John Curtin School of Medical Research, Australia). GSTO1-1 specifically catalyses the reduction of S-(4-nitrophenacyl)glutathione (4NPG) and the enzymatic rate can be measured spectrophotometrically [133]. C1-27 potently inhibited GSTO1-1, with an IC_{50} of 44nM (Figure 5.15). MCC950 was unable to effectively inhibit GSTO1-1, with an IC_{50} of 124.8μM (Figure 5.15).

5.1.16 GSTO1-1 deficient peritoneal exudate cells have impaired NLRP3 inflammasome activation

A GSTO1-1-deficient mouse colony was successfully bred at the end of this project for experimental use. To confirm a role for GSTO1-1 in the NLRP3 inflammasome, peritoneal exudate cells (PECs) from WT and GSTO1-1-deficient mice were tested for NLRP3 inflammasome activation. As shown in Figure 5.16 A, GSTO1-1-deficient PECs primed with LPS and stimulated with Nigericin have impaired mature IL-1β secretion in the supernatant compared to WT PECs (Second lysate panel, compare lanes 3 and 6). Mature IL-1β p17 and Caspase-1-p20 cleavage are also decreased in the supernatant of GSTO1-1-deficient mice (Figure 5.16 B, Lower panels, compare lanes 3 and 6).

5.1.17 GSTO1-1-deficient BMDMs have impaired NLRP3 inflammasome activation

In order to compare the effects of C1-27 on the NLRP3 inflammasome, BMDMs from GSTO1-1-deficient mice were tested for NLRP3 inflammasome activation. GSTO1-1-deficiency was confirmed by western blot (Figure 5.17 A). In Figure 5.17 B, GSTO1-1-deficient mice have impaired pro-IL-1β processing in response to LPS and Nigericin, with no significant differences observed in TNFα secretion (Figure 5.17 C). Similarly, both mature IL-1β p17 and mature Caspase-1 p20 were decreased in the supernatants of GSTO1-1-deficient mice (Figure 5.17 D, Lower panels, compare lanes 4 and 8).

5.1.18 GSTO1-1-deficient mice have impaired inflammatory responses *in vivo*

To further implicate a role for GSTO1-1 during the inflammatory response, seven-week-old C57BL/6 control and C57BL/6 GSTO1-1-deficient mice were injected with 10mg/kg LPS or PBS for 90min to assess serum cytokine production. As shown in Figure 5.18 A, GSTO1-1-

deficient mice produce less secreted IL-1β into the blood compared to controls. GSTO1-1-deficient mice had significantly increased IL-10 production in response to LPS treatment (Figure 5.18 B). No differences were observed in TNFα production between control and GSTO1-1-deficient mice (Figure 5.18 C).

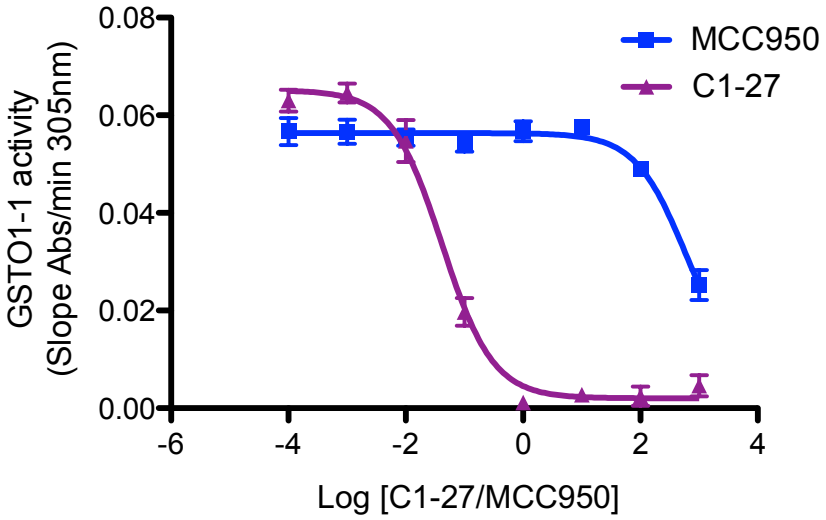

Figure 5.15 MCC950 does not limit GSTO1-1 enzymatic activity

GSTO1-1 enzymatic activity was measured by measuring the reduction of 4-NPG to 4-nitroacetophenone. 5 µg ml^{-1} recombinant GSTO1-1 in reaction buffer (100 mM Tris (pH 8.0), 1.5 mM EDTA and 1 mM DTT) was incubated with DMSO or different concentrations of inhibitors for 30 min at 37 °C. A dose range of C1-27 or MCC950 was added to the reaction and decrease in absorbance at 305 nm was recorded.

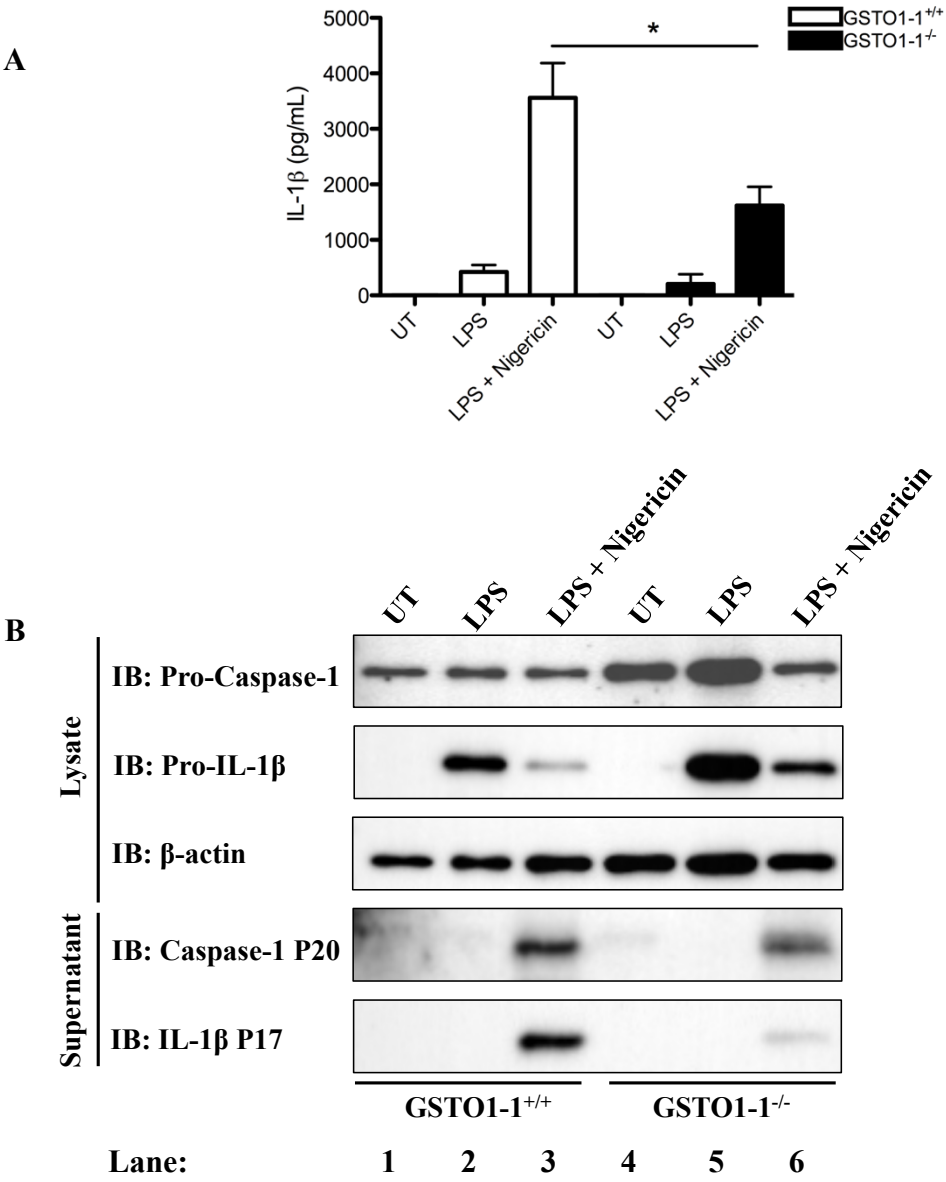

Figure 5.16 GSTO1-1-deficient PECs have impaired NLRP3 inflammasome activation

Peritoneal cells were obtained from WT and GSTO1-1-deficient mice. 5mL of sterile PBS was injected into the peritoneum and agitated briefly before draining. Peritoneal cells were centrifuged at 1500rpm for 5min and diluted to $5x10^5$ cells/mL in complete RPMI. Cells were left to adhere to 24-well tissue culture plates for 2h at 37°C 5% CO_2. Cells were stimulated with 100ng/mL LPS for 3h. After 3h medium was removed and replaced with SFM RPMI. 10μM Nigericin was added for 45min. Supernatant was harvested for ELISA and western blot. Cells were lysed in sample loading buffer and analysed by western blotting using anti-Caspase 1, anti-IL-1β, and anti-β-actin antibodies. Mean ± S.E.M of three independent experiments is shown.

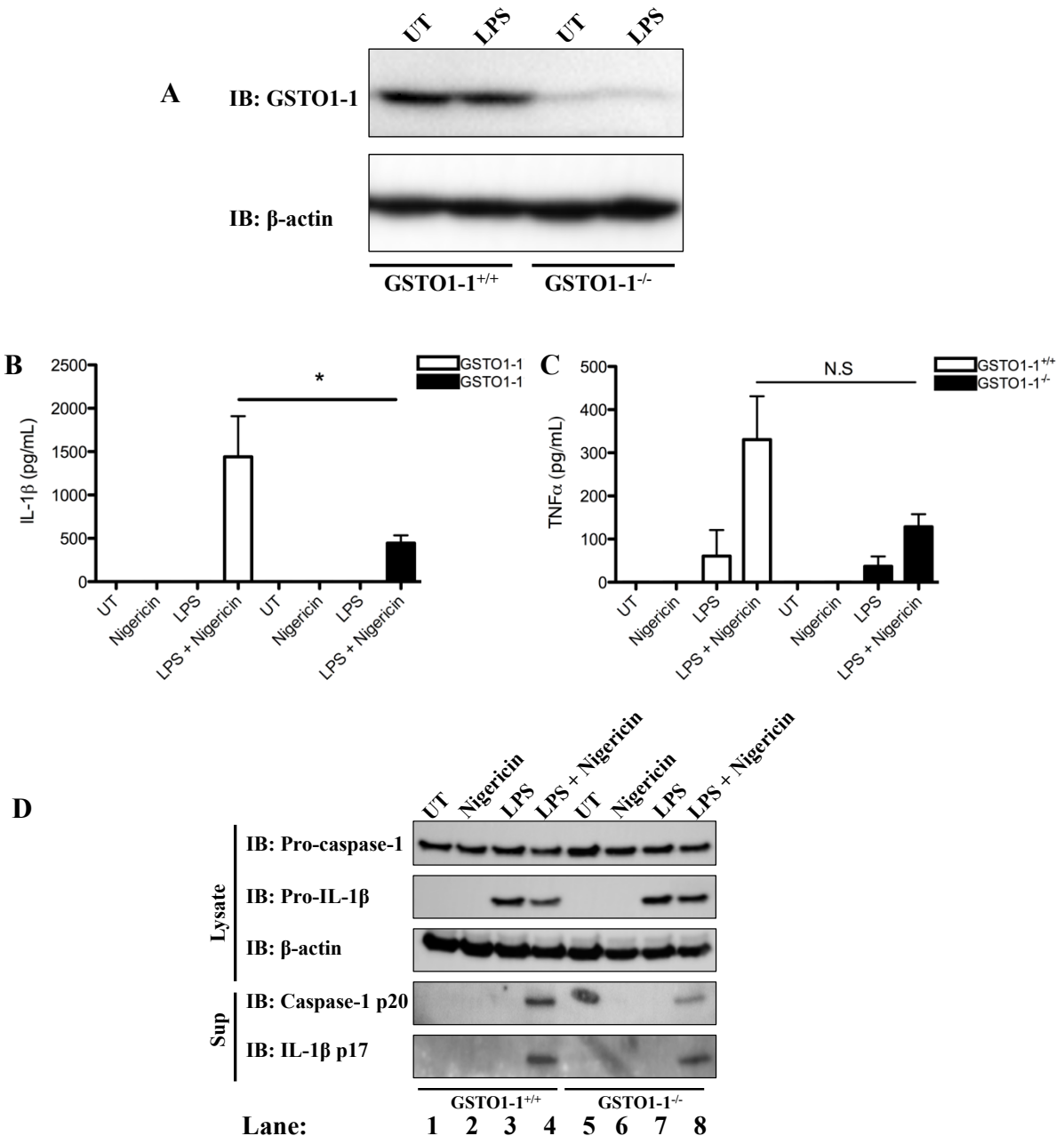

Figure 5.17 GSTO1-1-deficient BMDMs have impaired NLRP3 inflammasome activation

WT and GSTO1-1-deficient BMDMs were seeded at $5x10^5$cell/mL in 12-well plates and incubated at 37°C 5% CO_2 overnight. Cells were pre-treated with 100ng/mL LPS for 3h. After 3h of LPS stimulation, media was removed and replaced with 1mL complete DMEM containing 10μM Nigericin for 1h. Supernatant was harvested for ELISA and supernatant blots. Cells were lysed in sample loading buffer and analysed by western blotting using anti-IL-1β, anti-Caspase 1 p20 and anti-β-actin antibodies. Mean ± S.E.M of three independent experiments is shown.

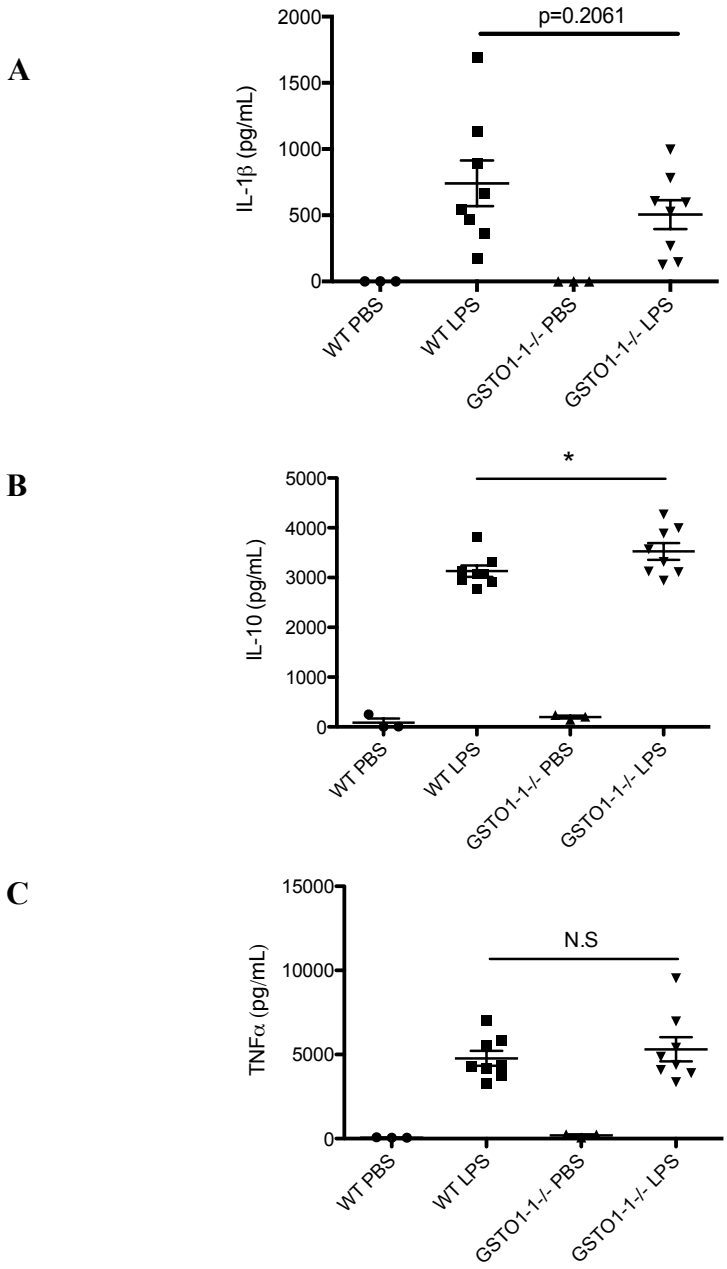

Figure 5.18 GSTO1-1-deficient mice have an impaired inflammatory response *in vivo*

Seven-week-old C57BL/6 control and C57BL/6 GSTO1-1-deficient mice were injected with 100μL 10mg/kg LPS or 100μL PBS for 90min. Mice were sacrificed, whole blood was harvested and left to coagulate for 30 min at RT. Serum was removed and analysed for cytokines by Quantikine ELISA. Mean ± S.E.M is shown (WT and GSTO1-1-deficient PBS n=3 per group; WT and GSTO1-1-deficient LPS n=8 per group).

5.2 GSTO1-1 regulates LPS-induced Caspase-11 expression

Due to the observed protection C1-27 conferred against pyroptotic cell death in Figure 5.2, and the recently described role for GSTO1-1 in LPS-mediated endotoxemia [148], I decided to examine if GSTO1-1 played a role in regulation of Caspase-11. As shown in Figure 5.19 A, pre-treatment with C1-27 blocked the production of Caspase-11 in BMDMs. C1-27 dose dependently decreased Caspase-11 production (Figure 5.19 B) and had no effect on the induction of Caspase-11 mRNA (Figure 5.19 C).

5.2.1 GSTO1-1 regulates Interferon β (IFN-β)-induced Caspase-11 expression

Caspase-11 has been shown to be an interferon-inducible gene [255]. I decided to test an LPS-independent system to examine the effects of C1-27 on Caspase-11 production. Similar to Figure 5.19, C1-27 pre-treatment blocked the production of IFNβ-mediated Caspase-11 at both 4h and 6h treatment (Figure 5.20 A). C1-27 had no effect on induction of Caspase-11 mRNA by IFN-β treatment (Figure 5.20 B).

5.2.2 GSTO1-1 knockdown by siRNA reduces Caspase-11 production

Due to the strong effect of inhibition of GSTO1-1 on Caspase-11 induction, an inhibitor-independent siRNA knockdown of GSTO1-1 was performed to rule out any off-target effects of C1-27. As shown in Figure 5.21, siRNA-mediated knockdown of GSTO1-1 ablated Caspase-11 production (Figure 5.21 Top panel), similar to C1-27, indicating the enzymatic activity of GSTO1-1 is required for Caspase-11 production. GSTO1-1 knockdown was confirmed by western blot (Figure 5.21 Middle panel).

5.2.3 C1-27 blocks IL-1β release and limits Caspase-11 mediated pyroptosis

Caspase-11 activation via direct binding of intracellular LPS results in induction of pyroptosis, inducing cleavage of the pore-forming protein GSDMD, and further can activate the inflammasome via Caspase-1 cleavage to promote IL-1β secretion [256, 257]. The activation of Caspase-11 was therefore examined using C1-27. As shown in Figure 5.22 A, IL-1β production was assessed by ELISA to confirm activation of pyroptosis by intracellular LPS transfection (Tf). LPS priming to induce Caspase-11, followed by LPS transfection resulted in IL-1β secretion. Pre-treatment with C1-27 prior to LPS priming, or C1-27 treatment after LPS priming reduced IL-1β secretion. LPS-primed and LPS-transfected cells had significant levels of cell death, however pre-treatment with C1-27 significantly reduced cell death (Figure 5.22

B). C1-27 treatment after LPS priming could not reduce cell death associated with Caspase-11 activation (Figure 5.22 B), however IL-1β release in this condition was also blocked.

5.2.4 MCC950 does not limit Caspase-11 induction by LPS

Due to the observed similarities between MCC950 and C1-27, I decided to examine if MCC950 could limit pyroptotic cell death similar to C1-27. As shown in Figure 5.15, MCC950 did not effectively inhibit GSTO1-1 enzymatic activity. To confirm this effect functionally, BMDMs were pre-treated with a dose range of C1-27 and MCC950 prior to LPS treatment. C1-27 was able to reduce Caspase-11 expression at the highest dose tested, whereas MCC950 had no effect on Caspase-11 expression (Figure 5.23 A, Top panel). C1-27 or MCC950 pre-treatment prior to LPS stimulation limited IL-1β production in response to LPS transfection (Figure 5.23 B). C1-27 pre-treatment was also able to reduce pyroptosis associated with LPS transfection (Figure 5.23 C) however, MCC950 pre- or post-LPS treatment was unable to limit pyroptosis associated with LPS transfection.

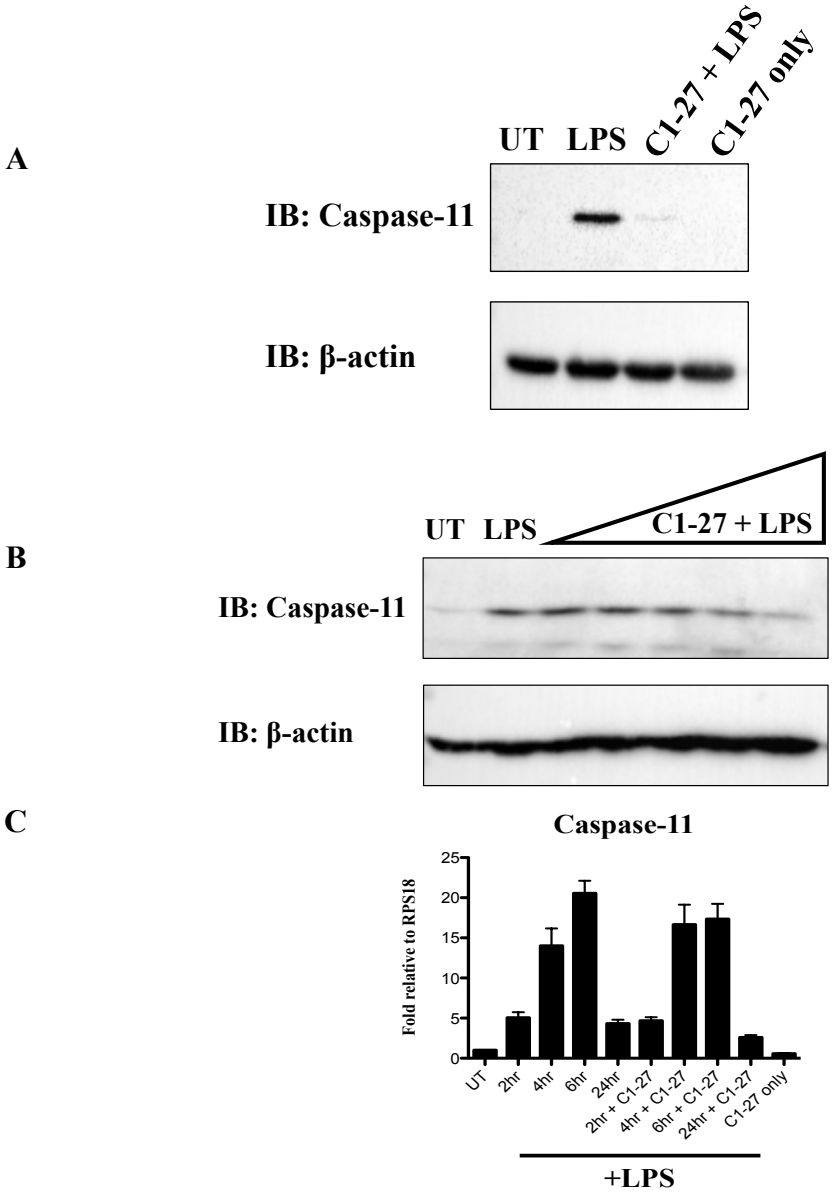

Figure 5.19 GSTO1-1 is required for post-translational Caspase-11 induction by LPS

BMDMs were seeded at 5x10^{5}cell/mL in 12-well plates and incubated at 37°C 5% CO_2 overnight. Cells were pre-treated with C1-27 before treatment with 100ng/mL LPS for times indicated. Cells were lysed in sample loading buffer and analysed by western blotting using anti-Caspase-11 and anti-β-actin antibodies. Representative of three independent western blot experiments is shown (A and B). RNA was extracted from C1-27 pre-treated LPS-stimulated BMDMs for times indicated (C). Cells were lysed in 350μL RNA lysis buffer and RNA isolated using Ambion RNA extraction kit. RNA was reverse transcribed, and cDNA was used for qPCR with SYBR Green components. cDNA was analysed using the cycle-threshold (Ct) value normalized to RPS18 control gene. Mean ± S.E.M of three independent experiments each carried out in triplicate is shown.

A

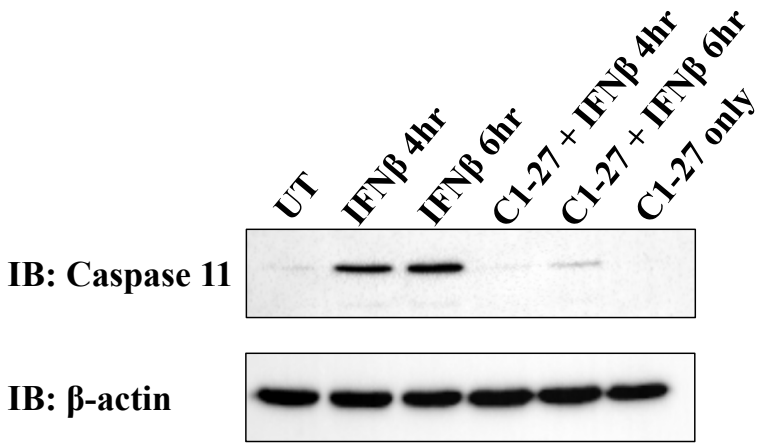

B

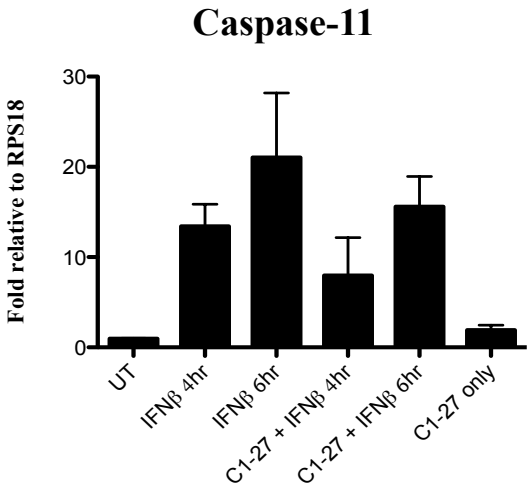

Figure 5.20 GSTO1-1 is required for post-translational Caspase-11 induction by IFNβ

BMDMs were seeded at 5x10^{5}cell/mL in 12-well plates and incubated at 37°C 5% CO_2 overnight. Cells were pre-treated with C1-27 before treatment with 100ng/mL IFN-β for times indicated. Cells were lysed in sample loading buffer and analysed by western blotting using anti-Caspase-11 and anti-β-actin antibodies. Representative of three independent western blot experiments is shown (A). RNA was extracted from C1-27 pre-treated LPS-stimulated BMDMs for times indicated (B). Cells were lysed in 350μL RNA lysis buffer and RNA isolated using Ambion RNA extraction kit. RNA was reverse transcribed, and cDNA was used for qPCR with SYBR Green components. cDNA was analysed using the cycle-threshold (Ct) value normalized to RPS18 control gene. Mean ± S.E.M of three independent experiments each carried out in triplicate is shown.

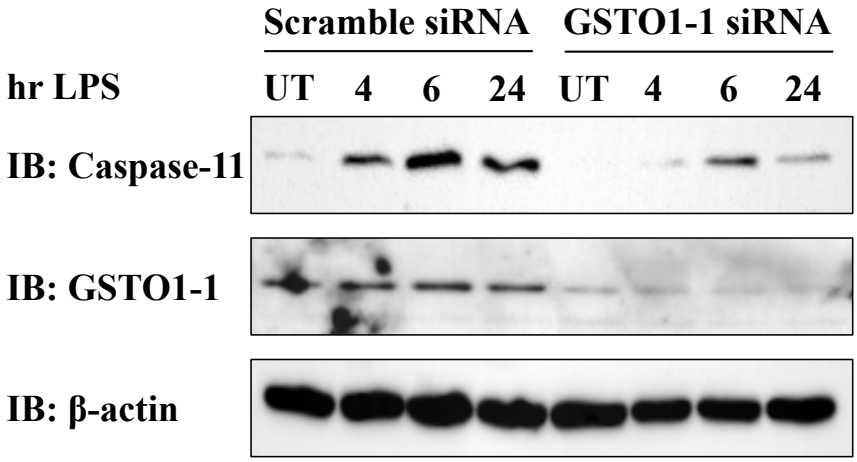

Figure 5.21 GSTO1-1 knockdown by siRNA reduces Caspase-11 production

BMDMs were seeded at $5x10^5$cell/mL in 12-well plates and incubated at 37°C 5% CO_2 overnight. Cells were transfected with 5nmol scramble siRNA (Ambion) or GSTO1 siRNA in OptiMEM media for 36h. Cells were treated with 100ng/mL LPS for times indicated. Cells were lysed in sample loading buffer and analysed by western blotting using anti-Caspase-11, anti-GSTO1 and anti-β-actin antibodies. Representative of three independent western blot experiments is shown.

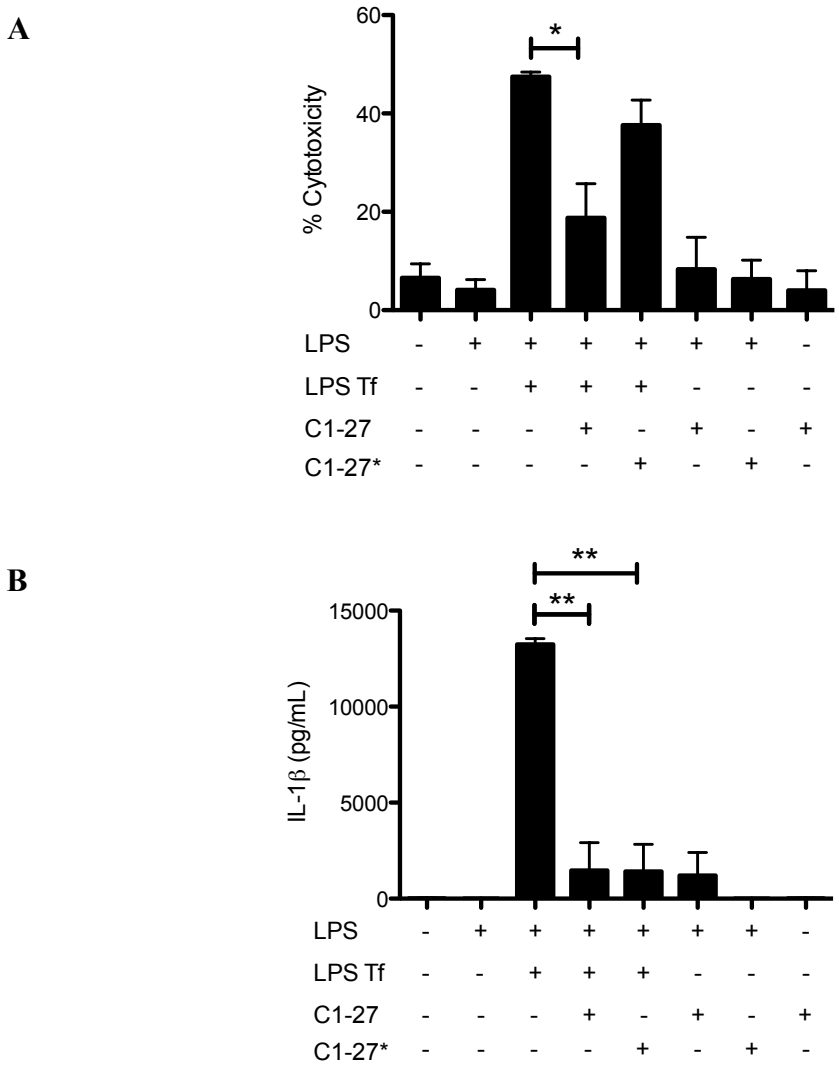

Figure 5.22 C1-27 limits Caspase-11-mediated IL-1β secretion and pyroptotic LDH release

BMDMs were seeded at 5x10^{5}cell/mL in 12-well plates and incubated at 37°C 5% CO_2 overnight. Cells were pre-treated with C1-27 for 2h before treatment with 100ng/mL LPS for 4h. C1-27* indicates C1-27 treatment post-LPS stimulation. 1μg/mL LPS was transfected using FuGene transfection reagent (labelled Tf) for 16h. The next day the supernatant was removed, IL-1β release was examined by ELISA (A) and LDH release was quantified using Promega Cytotox 96 assay (B).

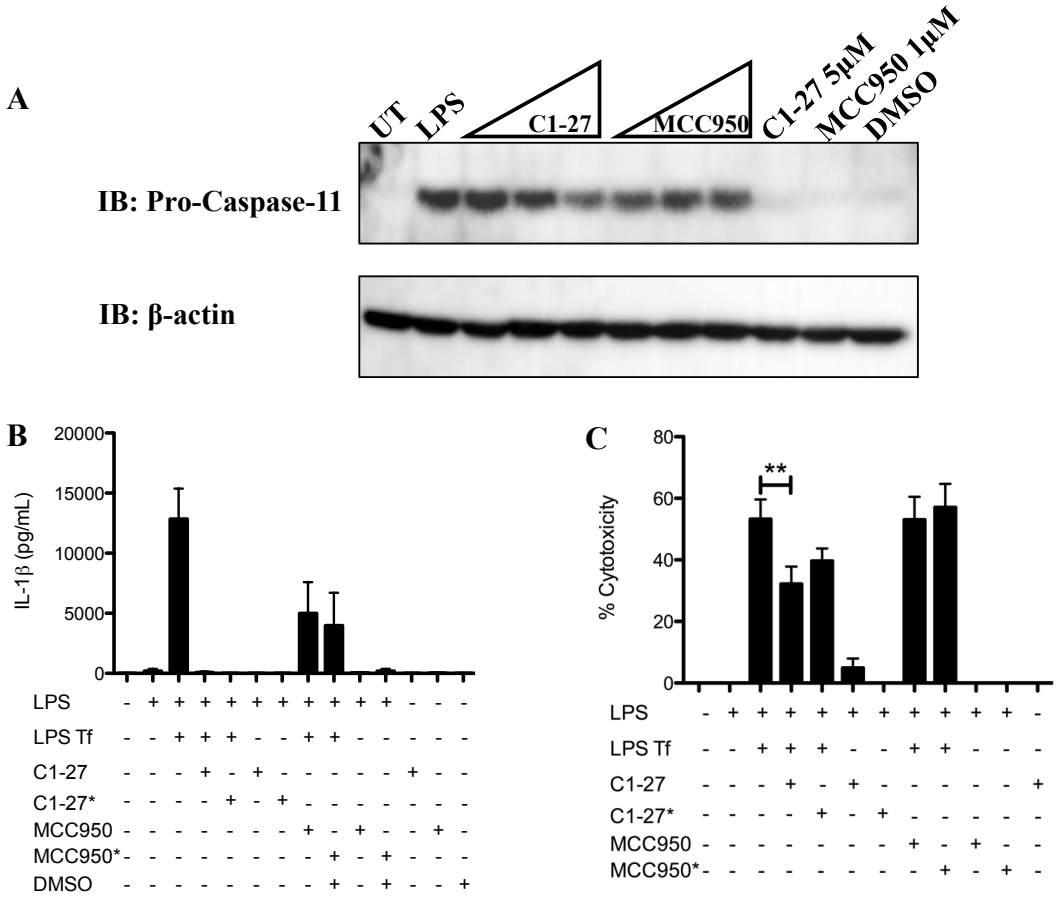

Figure 5.23 MCC950 does not limit Pro-caspase-11 induction or limit Caspase-11-induced pyroptosis

BMDMs were seeded at 5x10^{5}cell/mL in 12-well plates and incubated at 37°C 5% CO_2 overnight. Cells were pre-treated with C1-27 or MCC950 for 2h before treatment with 100ng/mL LPS for 4h. Cells were lysed in sample loading buffer and analysed by western blotting using anti-Caspase-11 and anti-β-actin antibodies. Representative of three independent western blot experiments is shown (A). BMDMs were seeded at 5x10^{5}cell/mL in 12-well plates and incubated at 37°C 5% CO_2 overnight (B, C). Cells were pre-treated with C1-27 or MCC950 for 2h before treatment with 100ng/mL LPS for 4h. C1-27* and MCC950* indicates C1-27 and MCC950 treatment post-LPS stimulation, respectively. 1μg/mL LPS was transfected using FuGene transfection reagent (labelled Tf) for 16h. The next day the supernatant was removed, IL-1β release was examined by ELISA (B) and LDH release was quantified using Promega Cytotox 96 assay (C).

5.3 Discussion

In this chapter I have investigated the effect of GSTO1-1 during inflammasome activation and pyroptosis. I originally hypothesised that GSTO1-1 may regulate Mal activation, however as seen in Chapter 4, GSTO1-1-deficient mice displayed no overall phenotypic variance in TLR activation. The levels of Pro-IL-1β however, were consistently higher in GSTO1-1-deficient BMDMs. Further, GSTO1-1 has previously been shown to interact with the inflammasome adaptor protein ASC by overexpression [251], potentially placing GSTO1-1 as an inflammasome component. I hypothesised that the enzymatic activity of GSTO1-1 would be required to regulate inflammasome activation, with potential substrates including Caspase-1 and NLRP3. Caspase-1 glutathionylation limits Pro-IL-1β cleavage, via glutathionylation of cysteines 362 and 397 [181]. NLRP3 has also been identified as a glutathionylated protein by immunoprecipitation [183], however western blotting for post-translational modifications can give false-positive results and mass spectrometry would be required to confirm this effect. A previous study identified that C1-27 can limit IL-1β secretion by the NLRP3 inflammasome in THP-1 cells [228], however the role of GSTO1-1 in primary macrophage inflammasome activation remained unexplored. From this evidence, I therefore began by assessing the role of GSTO1-1 in inflammasome activation using C1-27 as a tool compound.

I began by assessing how C1-27 affected the activation of the NLRP3 inflammasome. In response to LPS and ATP, C1-27 was able to potently block the processing of Pro-IL-1β into mature IL-1β. The observed inhibition by C1-27 was specific, as TNFα remained unaffected. Western blotting of the cell lysates and supernatants confirmed that C1-27 potently blocked processing of Pro-IL-1β and Pro-caspase-1. Having observed similar effects to Ramkumar et al., I decided to examine the effect of Nigericin, the pore forming ionophore, on NLRP3 activation. Nigericin drives NLRP3 activation and induces pyroptosis very potently. C1-27 was also able to significantly reduce IL-1β cleavage and cell death, similar to the effects of ATP.

The observation that C1-27 limited NLRP3 inflammasome activation indicated that GSTO1-1 does exert a role in inflammasome activation. The NLRP3 inflammasome however, shares Caspase-1 with the NLRC4 and AIM2 inflammasomes. Further, the NLRP3 inflammasome also shares ASC with the NLRC4 and AIM2 inflammasomes. I therefore decided to narrow down potential substrates for GSTO1-1 by assessing C1-27 in both the NLRC4 and AIM2 inflammasomes. I first assessed the activation of the NLRC4 inflammasome.

Intracellular flagellin drives a robust activation of the NLRC4 inflammasome. NLRC4 activation is critical in regulating *S. typhimurium* infection, and *S. typhimurium* has developed strategies to evade host machinery by downregulating flagellin expression to avoid inflammasome activation [207]. Using *S. typhimurium*, we found that C1-27 was unable to block activation of the NLRC4 inflammasome, with IL-1β secretion comparable to control cells. TNFα secretion was comparable between treatments however *S. typhimurium* infection did not robustly drive TNFα secretion and should be re-examined. Processing of Pro-caspase-1 and Pro-IL-1β was unaffected by C1-27. Whilst this evaluation is not exhaustive, it does indicate that GSTO1-1 does not regulate the activation of Caspase-1. It would be important to test a dose range of C1-27 to fully assess the effects of GSTO1-1 on NLRC4 activation.

In order to further limit the observed effects of C1-27, the AIM2 inflammasome was assessed. AIM2 senses intracellular dsDNA, and I used the synthetic dsDNA Poly (dA:dT) to trigger AIM2 activation by transfection. If an effect on AIM2 activation was observed, GSTO1-1 could potentially be regulating ASC. Similar to the NLRC4 inflammasome, treatment with C1-27 prior to Poly (dA:dT) transfection had no observed effect on pro-IL-1β processing and Caspase-1 activation. Western blotting also confirmed cleavage of Caspase-1 and IL-1β was unaffected by C1-27.

Having assessed the function of C1-27 during NLRP3, NLRC4 and AIM2 inflammasome activation, I concluded that GSTO1-1 was exerting its enzymatic function on NLRP3 or NEK7. C1-27 could therefore be a potential novel drug candidate for inflammasome regulation. Previous reports have identified potent inflammasome inhibitors, MCC950 [149] and CY-09 [258], however neither compounds are generated on an α-chloroacetamide backbone like C1-27, which could potentially allow for generation of a new class of GSTO1-1 inhibitors that regulate the NLRP3 inflammasome. A current limitation in this study is the effect of C1-27 *in vivo*. NLRP3 mutations are well characterised to induce a family of diseases termed cryopyrin-associated periodic syndrome (CAPS), including Muckle-Wells syndrome. Individuals suffering from Muckle-Wells syndrome suffer episodic IL-1β-mediated inflammation, commonly affecting the skin and joints [154]. It would therefore be crucial to examine the effects of C1-27 *in vivo* in a mouse model of CAPS.

Inflammasome activation results in recruitment of adaptor proteins which oligomerize to form a competent signalling platform. During NLRP3 inflammasome activation, the prion-like protein ASC oligmerizes into a punctate speck, termed the ASC speck, which can be easily

quantified by flow cytometry, or via western blotting by crosslinking. I therefore examined if C1-27 could impact the assembly of the NLRP3 inflammasome. C1-27 treatment reduced both the percentage of ASC speck positive cells by flow cytometry and crosslinked ASC by western blotting, indicating that GSTO1-1 is critical for NLRP3 inflammasome assembly. This places GSTO1-1 upstream of Caspase-1 activation. Perhaps the glutathionylation status of inflammasome components regulates correct assembly and stoichiometry for aggregation into the inflammasome.

I next decided to assess if endogenous knockdown of GSTO1-1 in primary BMDMs could affect NLRP3 inflammasome components. No effect was observed on the protein levels of the adaptor ASC. As a control, I also confirmed that GSTO1-1 knockdown increased pro-IL-1β production as previously seen in the GSTO1-1-deficient mice at 24h LPS treatment. No effect was observed on NLRP3 transcriptionally, and I also observed a trend towards increased IL-1β transcription at 24h LPS. There is a disparity between GSTO1-1 acting as a negative regulator of Pro-IL-1β induction, whilst also required for Pro-IL-1β processing during NLRP3 inflammasome activation. GSTO1-1-deficient cells and C1-27 treated BMDMs have increased levels of HIF1α and may thereby explain the observed boost in IL-1β production.

Further, if GSTO1-1 was required for NLRP3 inflammasome activation, knockdown of GSTO1-1 should attenuate pro-IL-1β cleavage. I assessed NLRP3 inflammasome activation in GSTO1-1 siRNA-knockdown primary BMDMs. GSTO1-1 knockdown attenuated mature IL-1β and Caspase-1 secretion into the supernatant, further indicating that GSTO1-1 regulates NLRP3 inflammasome activation.

Having observed a strong reduction in IL-1β processing by targeting GSTO1-1, I decided to test if exogenous GSH could mimic inhibition of GSTO1-1. GSH was previously reported to have no effect on NLRP3 inflammasome activation [181], however the addition of cell-permeable GSH-EE was prior to LPS stimulation, and is therefore not specific to inflammasome activation. I hypothesised that GSTO1-1 would serve to deglutathionylate an NLRP3 inflammasome component, driving inflammasome activation. Therefore, an exogenous increase in cell-permeable GSH-EE would potentially negate NLRP3 inflammasome activation similar to C1-27. Interestingly, GSH-EE added after LPS stimulation dose dependently decreased processing of pro-IL-1β and limited mature IL-1β secretion into the supernatant at the highest dose tested. Whilst addition of GSH-EE is in no way specific to regulating the NLRP3 inflammasome, as GSH-EE could simply be limiting the ROS component reported for

inflammasome activation, it certainly does indicate that glutathionylation limits activation. It would be interesting to assess if GSH-EE limited ASC speck formation.

The NLRP3 inflammasome can be reconstituted in HEK293T cells using plasmids encoding NLRP3 inflammasome components [254]. Due to the negative regulation of IL-1β processing by C1-27, I examined if overexpression of GSTO1-1 would boost IL-1β processing. Interestingly, IL-1β processing, in the presence of GSTO1-1, was enhanced compared to control, placing GSTO1-1 as a key regulator of IL-1β processing in the NLRP3 inflammasome.

I next decided to examine the potential interaction of GSTO1-1 with inflammasome components to narrow down GSTO1-1 substrates. As mentioned previously, GSTO1-1 has been shown to interact with ASC [251]. A new ROS-sensing component of the inflammasome, NEK7, has also been reported [152]. I sought to determine if I could confirm the GSTO1-1-ASC interaction, and furthermore, if GSTO1-1 could interact with NEK7. I hypothesised that GSTO1-1 should interact with NEK7 and could potentially indicate that GSTO1-1 is the ROS sensor regulating inflammasome activation. I was able to co-immunoprecipitate GSTO1-1 with both ASC and NEK7. I was unable to detect an interaction of GSTO1-1 with NLRP3, suggesting GSTO1-1 may directly regulate NEK7. I was able to co-immunoprecipitate NEK7 with GSTO1-1 endogenously in response to both LPS and LPS and ATP stimulation. Interestingly, C1-27 treatment prior to ATP stimulation reduced the interaction between GSTO1-1 and NEK7, however this finding requires further replicates to confirm the interaction.

Due to the interaction observed between GSTO1-1 and NEK7, I assessed if NEK7 is a glutathionylated protein. Overexpression of NEK7 identified glutathionylation by western blot. To confirm this finding, I generated samples to detect GSH adducts on NEK7 by mass spectrometry in response to GSSG pre-treatment. NEK7 contains 8 cysteines and interestingly, two cysteines, cysteine 79 and cysteine 253, were identified as glutathionylated by mass spectrometry. I tested the functional relevance of glutathionylation on NEK7 by performing site directed mutagenesis to generate cysteine to alanine mutants, which were then transfected into a reconstituted NLRP3 inflammasome to assess IL-1β production. Glutathionylation of cysteine 79 had no functional effect on NEK7, however C253A significantly boosted IL-1β production similar to the overexpression of GSTO1-1 in the WT reconstituted inflammasome. This finding indicates that GSTO1-1 may deglutathionylate NEK7 on cysteine 253 to facilitate NLRP3 inflammasome activation and IL-1β processing.

GSTO1-1 was originally identified as a target for CRID inhibitors, which limit IL-1β production [147]. I therefore decided to assess if MCC950, a CRID2 derivative, was exerting its inhibitory effects on IL-1β processing through binding to GSTO1-1. Dr. Padmaja Tummala from Prof. Philip Boards laboratory performed an enzyme assay using a specific GSTO1-1 substrate, 4NPG [133], to assess if MCC950 inhibited GSTO1-1-mediated reduction of 4NPG. MCC950 was a poor inhibitor of GSTO1-1, with an IC_{50} of 124.8μM, compared to C1-27 with an IC_{50} of 44nM. This finding highlights that MCC950 does not affect GSTO1-1 and furthermore, C1-27 is a potent and specific GSTO1-1 inhibitor.

At the end of this project, a GSTO1-1-deficient mouse colony was successfully re-derived and bred for use in Trinity College Dublin. I first assessed if GSTO1-1 deficiency would mimic C1-27 and GSTO1-1 knockdown. PECs from GSTO1-1-deficient mice had impaired IL-1β production in response to LPS and Nigericin. GSTO1-1-deficient BMDMs also displayed impaired NLRP3 inflammasome activation, confirming the findings of C1-27. Interestingly, GSTO1-1-deficient mice had decreased serum IL-1β production in response to LPS treatment *in vivo*. In contrast to Menon et al., TNFα production in response to LPS was unaffected in the GSTO1-1-deficient mice, with TNFα production comparable to control mice. It is important to note that the TNFα measurement reported by Menon et al. was at 30min LPS treatment, which may be too early to detect TNFα in the serum. Further, IL-10 production was significantly increased in the GSTO1-1-deficient mice in contrast to C1-27, indicating that GSTO1-1-deficiency limits inflammatory responses *in vivo*.

Activation of the NLRP3 inflammasome is closely linked to induction of pyroptosis. In recent years, Caspase-11 has been shown to be the intracellular receptor for LPS, and furthermore drives cleavage of the pore-forming protein GSDMD via 'non-canonical' signalling. Recently GSDMD activation has been identified as the main channel for secretion of processed IL-1β [259]. Due to the close link between inflammasome activation and pyroptosis, and the resistance of GSTO1-1-deficient mice to LPS-induced lethality, I decided to examine the role of GSTO1-1 during activation of Caspase-11.

I employed the use of C1-27 to assess if the enzymatic activity of GSTO1-1 regulated Caspase-11. C1-27 treatment ablated expression of Caspase-11 when assessed by western blot. Due to the strong ablation of Caspase-11, I tested a dose range of C1-27 in BMDMs and Caspase-11 was dose-dependently decreased in response to increasing concentrations of C1-27. My results

compliment the finding that GSTO1-1-deficient mice are resistant to LPS-induced lethality [148], as Caspase-1 is no longer considered the main effector in LPS-induced lethality, rather Caspase-11 activity is the main effector [257]. Interestingly, C1-27 had no effect on Caspase-11 mRNA induction, indicating GSTO1-1 regulates Caspase-11 post-transcriptionally.

Due to the strong effect of C1-27 on Caspase-11 expression I decided to test an LPS-independent system. Type I interferon signalling requires activation of the Interferon α/β receptor (IFNAR) receptor by interferons IFN-α and IFN-β [260]. IFN-β has been shown to strongly induce expression of Caspase-11. C1-27 pre-treatment prior to IFN-β stimulation also ablated Caspase-11 expression, with no effect on Caspase-11 mRNA induction. The use of small molecule inhibitors can however lead to off-target effects and I decided to examine endogenous knockdown of GSTO1-1 to confirm if Caspase-11 expression was affected. Similar to C1-27, endogenous knockdown of GSTO1-1 limited expression of Caspase-11.

My results suggested that GSTO1-1 is a critical regulator of Caspase-11 activation. However, to confirm the functional effects of C1-27, I examined the induction of pyroptosis through transfection of LPS into LPS-primed BMDMs. Interestingly, C1-27 treatment prior to or post-LPS priming limited processing of IL-1β, identifying the importance for GSTO1-1 during inflammasome activation. C1-27 treatment prior to LPS priming resulted in a significant decrease in overall cell death, however C1-27 treatment post LPS priming could not rescue the associated death. Interestingly, MCC950 was unable to block the death associated with LPS transfection in this assay, indicating GSTO1-1 functions independently of MCC950 inhibition. This finding confirms a role for GSTO1-1 in both inflammasome and Caspase-11 regulation. It is unusual that C1-27 pre-treatment limits Caspase-11 expression, with no effect on mRNA induction, however C1-27 treatment post LPS priming has no effect. If GSTO1-1 served to glutathionylate/deglutathionylate Caspase-11, enzymatic inhibition pre- or post-LPS priming should affect Caspase-11 activity. The enzymatic function of GSTO1-1 may serve to destabilise Caspase-11 post-transcriptionally. This finding is difficult to interpret however, it does suggest a potential translational regulation of Caspase-11 by GSTO1-1 and warrants further investigation.

5.4 Final Conclusion

In summary, I have identified that C1-27 potently limits activation of the NLRP3 inflammasome. C1-27 was unable to limit activation of the AIM2 or NLRC4 inflammasomes, indicating specificity in GSTO1-1 regulating NLRP3 inflammasome activation. C1-27 further

limits inflammasome activation at the level of ASC speck formation. NEK7 is glutathionylated on cysteines 79 and 253, and mutagenesis of C253A boosts IL-1β production, indicating negative regulation of C253 by glutathionylation. GSTO1-1 may serve to deglutathionylate NEK7 to potentially promote interaction with Caspase-1 or ASC. GSTO1-1 may also serve to act as the intracellular ROS sensor for inflammasome activation, driving NEK7 activation. Further, GSTO1-1-deficient mice have decreased NLRP3 inflammasome activation. I have also identified GSTO1-1 as a potential novel regulator of Caspase-11. GSTO1-1 may serve to positively regulate Caspase-11 function, however this finding warrants further investigation. The main findings of this chapter have been graphically summarised in Figure 5.24.

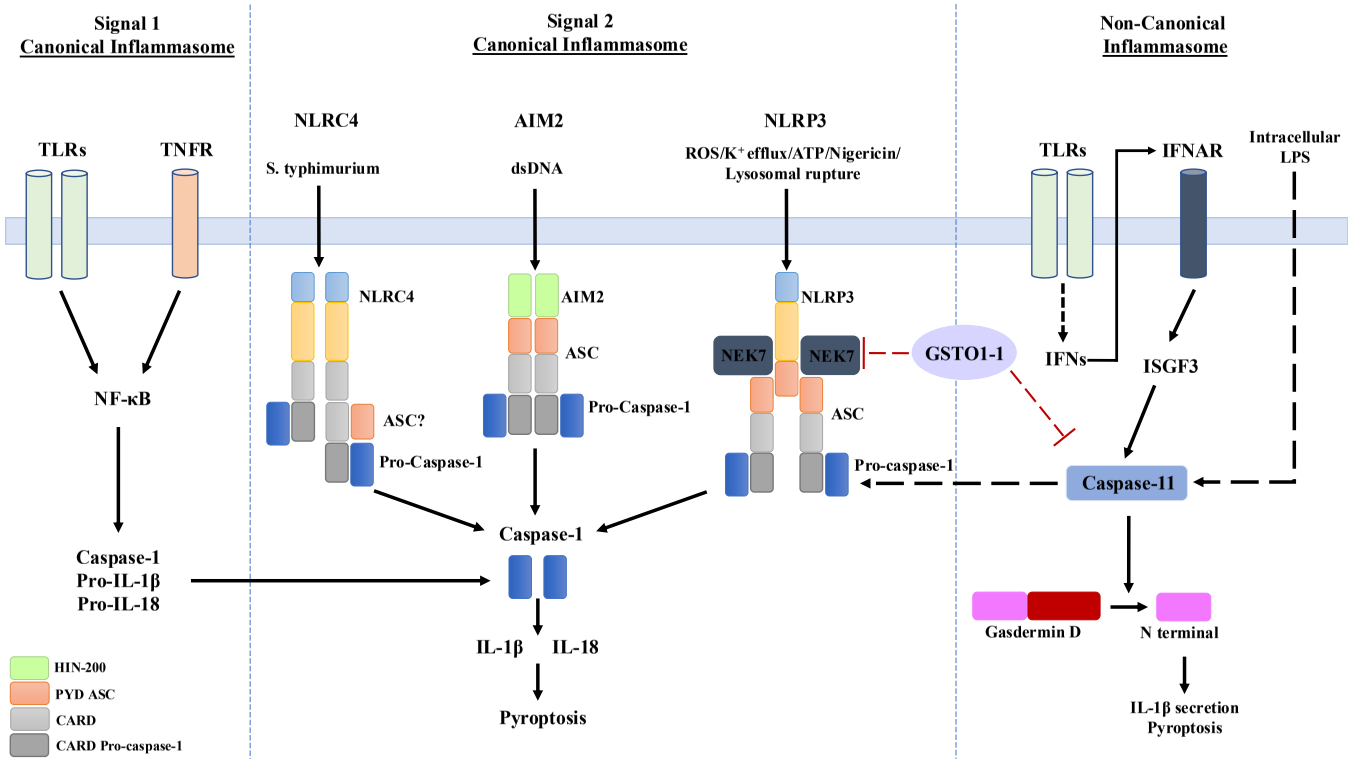

Figure 5.24 Schematic summary of results from Chapter 5

Activation of TLR or TNF receptor signalling or 'Signal 1' drives translocation of NF-κB to the nucleus to transcribe inflammasome components and inflammatory cytokines pro-IL-1β and pro-IL-18. Caspase-11 is also transcribed by TLR or IFNAR activation. Direct sensing of flagellated bacteria, dsDNA or DAMPs drive activation of the NLRC4, AIM2 and NLRP3 inflammasomes, respectively, driving Caspase-1 activation. LPS bound to intracellular bacteria can be directly sensed by Caspase-11, triggering cleavage of Gasdermin D and pyroptosis. Enzymatic inhibition of GSTO1-1 on Cys32 by C1-27 ablates NLRP3 inflammasome activation and pyroptotic cell death mediated by Caspase-11.

Chapter 6

Final discussion and future perspectives

Final discussion and future perspectives

Macrophage activation in response to bacterial and viral infection is known to drive metabolic reprogramming, generating ROS to limit pathogenicity and protect the host. Many diseases have identified a dysregulated redox component influencing pathogenesis, including Alzheimer's disease, Parkinson's Disease and Cancer [229-231, 261]. Further, fibrosing of tissues, which is mediated by macrophage-produced transforming growth factor-β (TGF-β), is a redox dependent mechanism driving increased levels of H_2O_2 and NO, promoting fibrotic tissue deposition [262]. Post-translational modifications have long been considered important regulatory mechanisms to activate or limit pathway activation, such as phosphorylation, ubiquitination and acetylation. Cysteine amino acids are amenable to oxidation and as such, act as receptors for altered oxidation imbalance. Oxidation of cysteines alters function and can promote redox-dependent post-translational modification, however the impact of redox signalling on immune pathway activation is only recently garnering significant attention. Redox regulatory mechanisms governing macrophage activation during TLR engagement with adaptor proteins has however, remained unexplored. The first chapter of this thesis examined the potential effect of redox signalling on the function of the TLR adaptor Mal.

In my studies, I identified that the TLR adaptor protein Mal is a glutathionylated protein. Mal contains seven cysteine residues which could be potentially glutathionylated. The structure of Mal was identified in 2011 by Valkov et al., and during the crystallisation process they identified two cysteines, C91 and C157 not in disulphide bond formation, making these two cysteines attractive post-translational targets. Valkov et al. identified that Mal contained a structural motif uncommon with other canonical TIR domain-containing adaptor proteins. Canonical TIR domains contain a BB loop, however Mal instead contained a structurally unique long AB loop, providing the first example of heterogeneity in TIR domain adaptors (Figure 6.1). Using site directed mutagenesis, I was able to identify C91 as the functionally relevant glutathionylation target and furthermore, mutagenesis of C91 to alanine abrogated Mal function, limiting assembly of the oligomeric adaptor assembly termed the myddosome, and acted as a dominant negative mutation, preventing TLR4 activation in Mal C91A-reconstituted Mal-deficient iBMDMs. Further, Mal C91A was unable to interact with downstream effector IRAK4 or the kinase-dead version, indicating that glutathionylation of C91 promotes structural reassembly of Mal to allow for IRAK4-mediated phosphorylation.

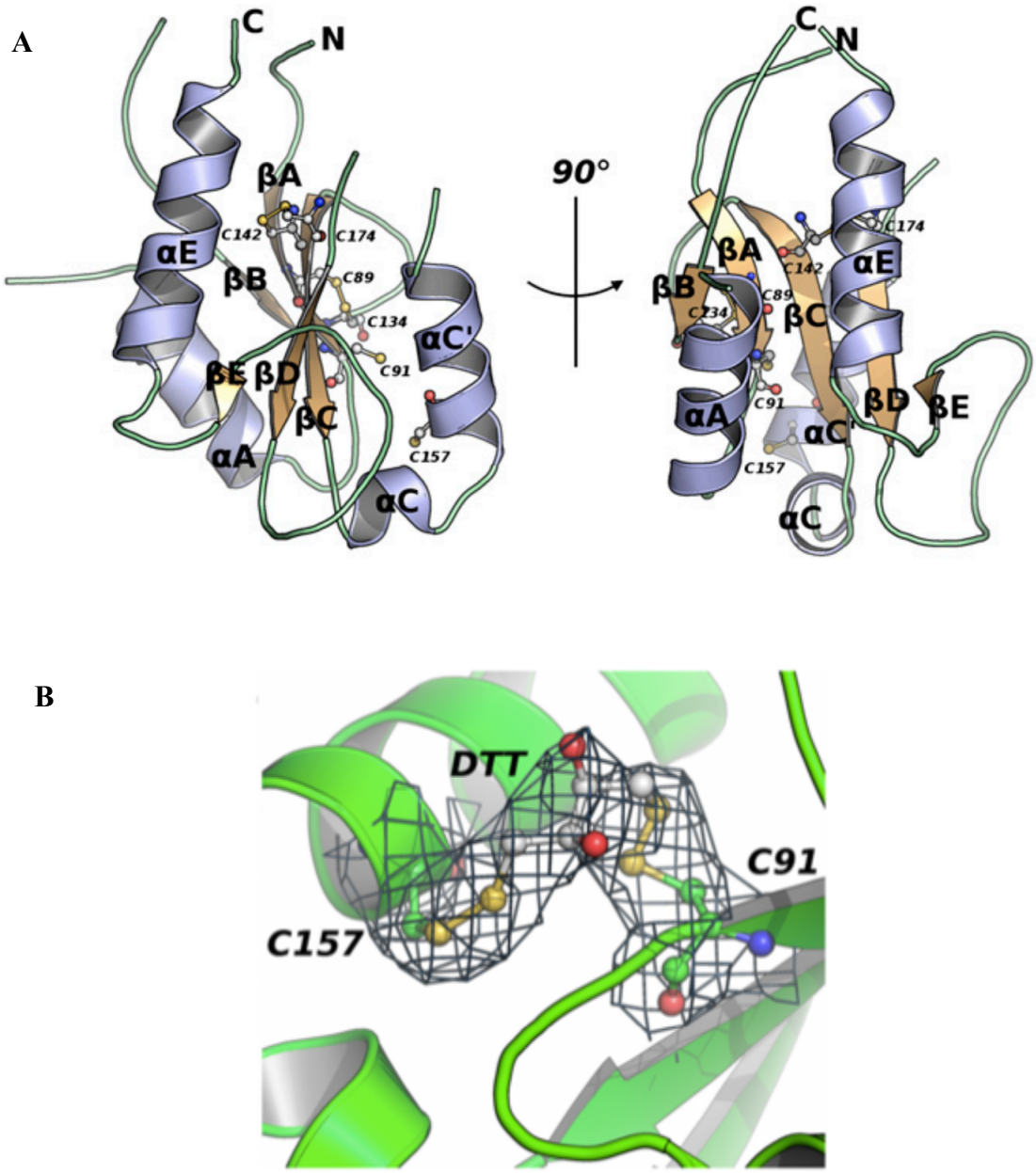

Figure 6.1 Crystal structure of Mal TIR domain identifies C91 and C157 as redox targets
The crystal structure of the human Mal-TIR domain taken from [57] identified a structural rearrangement termed the AB-loop (A). This structural cartoon representation highlights secondary elements in the Mal-TIR. The α-helices are shaded in cerulean, the β-helices are shaded in canary and the cysteine amino acids are highlighted in ball-and-stick representation. Cysteine 91 and 157 are proximally located 5Å apart and crystallised bound to a DTT molecule (B).

Positively charged amino acids, such as lysine, arginine and histidine, have been reported in the literature to aid deprotonation of cysteines, rendering the amino acid more susceptible to oxidation-induced stress. Using bioinformatics, I identified that C91 was flanked by the positively charged amino acid Histidine 92. Using mutagenesis of H92 to proline, I was able to recapitulate the effects of C91A, experimentally providing one of the first examples of positively charged amino acids promoting glutathionylation in macrophage TLR signalling.

During the course of this project, in collaboration with Prof. Bostjan Kobe from the University of Queensland, we identified that the previous crystal structure of Mal was incorrect [214]. Mal was incorrectly identified as an AB loop-containing adaptor, but instead harbours the canonical BB-loop motif seen in TIR domains [214] (Figure 6.2). These findings question the validity of previous studies using the crystal structures of Mal for computational interaction studies. Complementary to my experiments, Mal was also shown to be glutathionylated by MS and that glutathionylation of C91 induced a large redox shift in Mal structure measured by solution structure NMR. This structure therefore confirmed my finding of glutathionylation of Mal on C91. The redox shift may explain why IRAK4 had reduced interaction with the mutant versions of Mal. Mal glutathionylation is likely to be a positive regulatory event, inducing TLR activation. TLRs however, require a mechanism to limit aberrant activation, and IRAK4-mediated phosphorylation of Mal promotes membrane dissociation and polyubiquitination [70]. In future work, it would be important to assess if the membrane-binding capacity of Mal was affected by deglutathionylation. Mal appears to be inherently flexible and glutathionylation could promote a structural rearrangement that allows IRAK4 to phosphorylate threonine 28. This finding is exciting, as bacteria such as *Brucella spp*. subvert host immune responses by secreting TcpB, a Mal TIR mimetic, competing with Mal-TLR4 interactions to limit TLR activation entirely [76, 77, 263]. I have confirmed that Mal glutathionylation promotes TLR activation, and alignment of Mal with TcpB identified a serine instead of a cysteine at position C91 in TcpB, which may explain its ability to subvert host inflammation by acting as a competitive dominant negative inhibitor of TLR activation (Figure 6.3).

Specific targeting of Mal C91 holds promise therapeutically. I identified that pre-treatment with the oxidant scavenger N-acetylcysteine limited Mal glutathionylation. N-acetylcysteine has also been reported to limit cytokine production in macrophages [264], and indicates that tailored redox targeting of C91 could reduce over-activation of TLR signalling. Mal is also utilised by the IFNγ receptor [68], and glutathionylation status of Mal could also dictate IFNγ signalling. As mentioned previously, Mal SNPs are present in the population, with S180L being the best

characterised. Whether glutathionylation of Mal is altered in S180L Mal remains to be explored but could identify a further important role for C91 in Mal activation.

Future experiments will continue to elucidate the relevance of Mal glutathionylation in inflammation. An observation was the absence of an upper band in Mal C91A compared to Mal WT, which is indicative of phosphorylation. I would further characterise whether Mal glutathionylation is a critical mediator of Mal activity, or whether glutathionylation is simply a precursor signal for phosphorylation. It would be very interesting to delineate the requirement of either post-translational modification or whether these events are independent. Finally, I would confirm if glutathionylation of Mal affects membrane binding or TLR4 interaction.

Overall, I have therefore attributed another regulator of Mal activation, via glutathionylation of C91 to drive TLR activation (Figure 6.4).

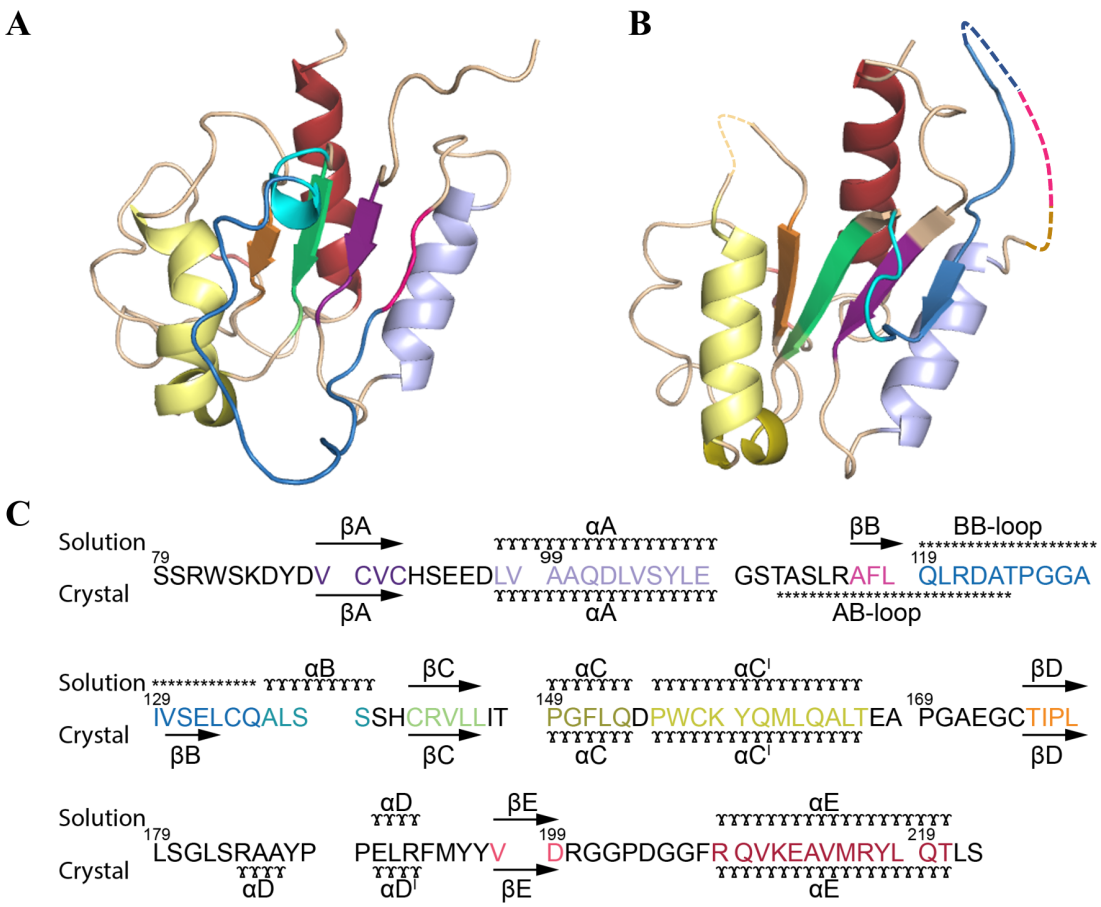

Figure 6.2 Comparison of the solution and crystal structures of MAL-TIR

(A) Solution structure of MAL-TIR-C116A, shown in cartoon representation. (B) Crystal structure of MALTIR [57]. Regions in the crystal structure comprising residues 112–123 (AB loop) and 168–171 do not have interpretable electron density and are not included in the crystal structure model; they are shown here for illustration purposes by dotted lines. (C) Structure-based sequence alignment, showing the elements of secondary structure. (ɤ) α-helix, (→) β-strand, (***) loop.

Figure 6.3 Sequence alignment of TIR-containing adaptors with TcpB

Sequence alignment of TcpB with the homolog TcpC, and TIR-domains from TLR2, TLR4, MyD88, Mal, SARM, TRIF and TRAM. Homologous regions are highlighted by boxes. Mal contains a cysteine at position 91, which is replaced by a serine in TcpB. This image is adapted from [77].

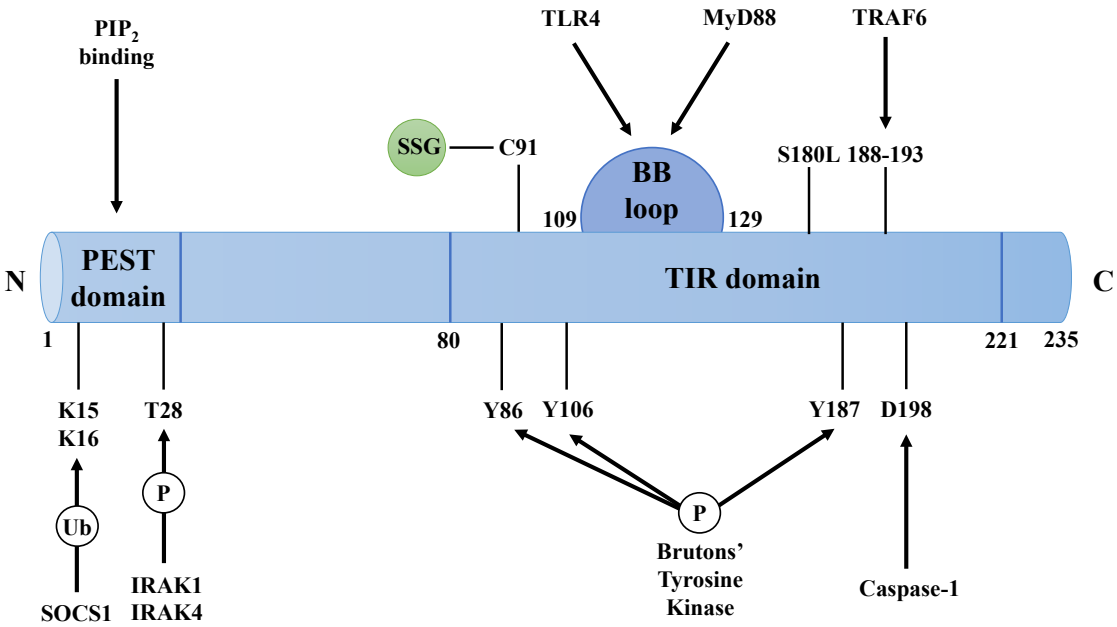

Figure 6.4 An updated model of the regulators of Mal activation

Mal contains an N-terminal PEST (proline, glutamate, serine threonine) motif, and N-terminal PIP_2 binding region. Mal is negatively polyubiquitinated by SOCS1 on K15 and K16. IRAK1 and IRAK4 phosphorylate Mal on T28, promoting membrane dissociation and polyubiquitination. Bruton's tyrosine kinase positively phosphorylates Mal on Y86, Y106 and Y187. Caspase-1 cleaves Mal on D198, producing a 4kDa fragment. Mal contains a typical BB loop motif and binds MyD88 and TLR4. TRAF6 also binds to Mal between position 188-193. Glutathionylation of Mal on C91 positively regulates Mal activation. This schematic is adapted from [84].

The second major focus of this thesis was to characterize the role of the deglutathionylating enzyme GSTO1-1 during TLR activation in macrophages. Previous reports placed GSTO1-1 upstream of NF-κB activation during TLR4 activation [226, 265], potentially indicating that GSTO1-1 may be the redox regulatory switch that controls Mal glutathionylation. Unpublished work from our lab also indicated that shRNA-mediated knockdown of GSTO1-1 in J774A.1 cells blocked TLR4 activation. It is important to note that the J774A.1 cells used by Menon et al. were generated in the Prof. Luke O'Neill lab, and their metabolic energy demands and redox environment may vary compared to primary cells. In collaboration with Prof. Philip Board from the University of Canberra, GSTO1-1-deficient mice were generated. I obtained legs from the GSTO1-1-deficient mice to assess the role of GSTO1-1 during Mal activation.

The initial experiments I performed indicated that GSTO1-1 did not function upstream of NF-κB activation, although this characterisation was not exhaustive, due to limitation in the availability of GSTO1-1-deficient mice, it did indicate that the main phenotype observed in the J774A.1 cells was incorrect. Although GSTO1-1 was proposed to be the Mal regulatory enzyme, we decided to further examine the role of GSTO1-1 in a broad context of TLR signalling. My most robust finding was that GSTO1-1 deficiency affected the production of pro-IL-1β and HIF1α. Both IL-1β and HIF1α are glutathionylated proteins [218, 243], and GSTO1-1 may serve to negatively regulate them. Whether glutathionylation of proteins affects stability however, remains uncharacterised. HIF1α stability is promoted by glutathionylation, so it would be important to co-immunoprecipitate HIF1α and GSTO1-1. This finding also places GSTO1-1 into the expanding field of immunometabolism, as GSTO1-1-deficient mice also displayed increased baseline glycolysis compared to controls, which was probably due to enhanced HIF1α activation.

An inhibitor of GSTO1-1 was recently published, termed C1-27 [228]. Due to the limitation in GSTO1-1-deficient mice, and the variability between the J774A.1 cell line, I decided to characterise the effect of GSTO1-1 inhibition. Interestingly, C1-27 increased Pro-IL-1β and HIF1α production, similar to that seen in the GSTO1-1-deficient mice. Production of ROS however, was decreased in contrast to the GSTO1-1-deficient cells, which could possibly be due to off-target effects of C1-27. Similarly, I found increased production of IL-10 in GSTO1-1-deficient mice, however IL-10 production was abrogated using C1-27. In order to delineate this disparity, I also endogenously knocked down GSTO1-1 in BMDMs to confirm the role of GSTO1-1 during IL-10 production. Similar to C1-27, GSTO1-1 knockdown ablated IL-10 production. This finding warrants further investigation, and IL-10 production should be re-

examined in the GSTO1-1-deficient mice. Although differences still remain when comparing knockdown versus inhibitor-treated cells, the most robust finding is an altered immunometabolic profile in the inhibitor-treated and GSTO1-1-deficient mice. The GSTO1-1-deficient mice also displayed altered M1/M2 polarisation, indicating the cells are not classically polarised. An unbiased non-reducing proteomic screen would be useful to help identify possible substrates for GSTO1-1 in response to LPS and IL-4 treatment. McGarry et al., using this approach, quantified GSTP-mediated glutathionylation in mouse liver by comparing GSTP-deficient mice to controls [266]. A HIF1α-GSTO1-1 axis has been recently described in breast cancer stem cells [241]. In particular, Lu et al. identified an enrichment of breast cancer stem cells in response to chemotherapeutic agents by triggering HIF1α-dependent *Gsto1* transcription. Inhibiting HIF1α in this context limited enrichment, proposing a HIF1α-dependent GSTO1-1-mediated resistance to chemotherapy. It would be interesting to quantify the metabolic profile of GSTO1-1-deficient mice to identify if metabolites such as succinate, which drives HIF1α , are also altered, however this is beyond the scope of this project.

During the course of this project, personal correspondence with Prof. Philip Board indicated that GSTO1-1-deficient mice were resistant to LPS-induced lethality. I therefore decided to examine GSTO1-1 in the context of inflammasome activation. GSTO1-1 does interact with the inflammasome adaptor protein ASC and furthermore, GSTO1-1 shares structural homology with the CLICs, which are characterised as family members in the extended GST superfamily [267]. CLIC1 and CLIC4 have been found to regulate inflammasome activation both transcriptionally and during inflammasome activation [185, 186]. Furthermore, Caspase-1, the effector Caspase during inflammasome activation that drives pro-IL-1β and pro-IL-18 processing, is also negatively redox regulated by glutathionylation [181]. NLRP3 is also redox regulated and has been reported to drive inflammasome activation in response to H_2O_2 [268].

Using C1-27, I found a specific role for GSTO1-1 during NLRP3 inflammasome activation. C1-27 was able to potently block NLRP3, but not NLRC4 or AIM2 inflammasomes, indicating GSTO1-1 functions to regulate either NLRP3 or NEK7, and not Caspase-1, ASC, NLRC4 or AIM2. NLRP3 has been shown to be glutathionylated by immunoprecipitation, and the deglutathionylation of NLRP3 enhances interaction with Caspase-1 [183], however this finding requires further validation, as I was unable to detect glutathionylation of NLRP3 by overexpression. Interestingly, exogenous GSH-EE addition also limited NLRP3 inflammasome activation, indicating that glutathionylation of an NLRP3 inflammasome component may limit IL-1β processing. Furthermore, reconstitution of the NLRP3 inflammasome in HEK293T cells

with GSTO1-1 boosted IL-1β secretion, firmly placing GSTO1-1 as an NLRP3 inflammasome regulator during inflammasome activation.

A recent NLRP3 inflammasome interactor was also described, NEK7 [151, 152]. NEK7 is proposed to sense redox stress to trigger the inflammasome. By co-immunoprecipitation I identified that GSTO1-1 does interact with NEK7. I was able to detect glutathionylation of NEK7 by overexpression. This finding was validated by MS, with GSH adducts detected on cysteines 79 and 253. Through site directed mutagenesis, I identified that NEK7 C253A boosted IL-1β secretion comparable to the observed boost by GSTO1-1 during NLRP3 inflammasome reconstitution in HEK293Ts, indicating that GSTO1-1 may deglutathionylate C253 to drive inflammasome activation.

A screen for IL-1β limiting inhibitors identified the sulfonurea-containing CRIDs in the early 2000's. Affinity labelling identified CRID2 bound to GSTO1-1 [147]. Derivatives of CRID2 were produced and one compound, termed MCC950, was found to limit NLRP3 inflammasome activation with nanomolar potency. MCC950 also reduced chronic activation of NLRP3 in CAPS-patients and is currently being tested in clinical trials. The target for MCC950 however, remains elusive. Compared to Coll et al., C1-27 appears to phenocopy the effects of MCC950. C1-27 also contains a sulfonurea group, similar to MCC950 (Figure 6.5). MCC950 was unable to effectively limit GSTO1-1 enzymatic activity *in vitro* compared to C1-27, indicating MCC950 inhibits the NLRP3 inflammasome independent of GSTO1-1. In future studies, it would also be important to assess the efficacy of C1-27 *in vivo* in animal models of NLRP3-mediated inflammation. GSTO1-1-deficient mice became available in Trinity College Dublin at the end of this project, and serum cytokine analysis from LPS-treated WT and GSTO1-1-deficient mice indicated that GSTO1-1-deficient mice had impaired inflammatory responses *in vivo*. Interestingly, IL-10 production was significantly increased in the GSTO1-1-deficient mice and warrants further investigation. Further, PECs and BMDMs from GSTO1-1-deficient mice had impaired NLRP3 inflammasome activation. It is unusual that GSTO1-1 can serve to positively regulate NLRP3 inflammasome activation, but also negatively regulate Pro-IL-1β production at 24h, however this could be explained by the increased production of HIF1α, which drives IL-1β production [146].

Further work is required to elucidate the precise function of GSTO1-1 in TLR4 signalling. During the course of this project I had limited availability of GSTO1-1-deficient BMDMs, and C1-27 was only recently available to further probe the function of GSTO1-1. We have

generated GSTO1-1-deficient mice and will be able to study the metabolic reprogramming that occurs in GSTO1-1-deficient cells via Seahorse metabolic flux analysis. Due to the increase in ROS production, it would be interesting to examine the oxygen consumption rate (OCAR) and mitochondrial integrity of these cells. I would also like to examine if a hypoxic environment would limit the enzymatic function of GSTO1-1, due to the potential negative regulation of HIF1α by GSTO1-1. The role of GSTO1-1 in the production of IL-10 should also be explored. The potential broad substrate specificity of GSTO1-1 poses a challenge in terms of conferring specificity, and I would therefore aim to quantify the differences in protein glutathionylation in GSTO1-1-deficient BMDMs compared to control by mass spectrometry, potentially highlighting the components in various pathways that GSTO1-1 may deglutathionylate.

A

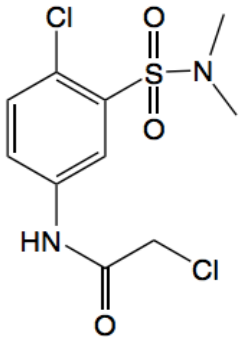

B

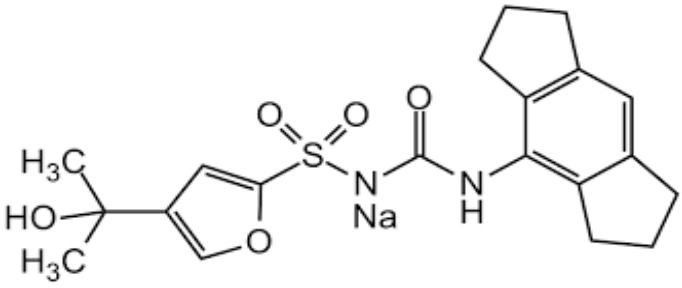

Figure 6.5 The structures of C1-27 and MCC950

Chemical structural representation of C1-27 (A) and MCC950 (B). C1-27 and MCC950 share the sulfonurea function group. C1-27 covalently binds GSTO1-1 on C32, inhibiting enzymatic function. CRID2, the initial compound MCC950 is based on, also bound to GSTO1-1.

Activation of the NLRP3 inflammasome induces pyroptotic cell death [269]. Recently, the 'non-canonical' inflammasome has been identified. During infection, LPS present on intracellular bacteria can be directly sensed by Caspase-11, triggering Caspase-11-mediated cleavage of GSDMD. The N-terminal of GSDMD oligomerises to form a pore, promoting pyroptosis. The GSDMD pore is also the main secretory mechanism for bioactive IL-1β [259]. Due to the strong effect of GSTO1-1 inhibition on NLRP3 inflammasome activation and the resistance to LPS-induced lethality reported in the GSTO1-1-deficient mice, I decided to assess whether Caspase-11 is differentially activated by GSTO1-1.

Using C1-27, I identified that GSTO1-1 is critical for the production of Caspase-11 protein, however no effect was observed on the transcription of Caspase-11 mRNA. C1-27 also blocked Caspase-11-mediated IL-1β processing and limited pyroptotic cell death in response to LPS transfection. Similar effects were observed with IFN-β treatment. Interestingly, MCC950 could not limit pyroptosis associated with Caspase-11 activation, further emphasising GSTO1-1 is not the target for MCC950. Importantly, siRNA-mediated knockdown of GSTO1-1 in primary BMDMs also confirmed a decrease in Caspase-11 protein in response to LPS stimulation. Further work is required to confirm the role of GSTO1-1 during Caspase-11 activation, however it is apparent that GSTO1-1 appears to have a critical role during Caspase-11 signalling. Caspase-11 activation in response to intracellular LPS also triggers Caspase-1 activation [165], and may explain why IL-1β processing is blocked by C1-27 treatment during Caspase-11 activation (Figure 6.6). The lack of effect on Caspase-11 transcription indicates that GSTO1-1 is exerting its function post-transcriptionally. The 3'-untranslated region (3'UTR) contains AU-rich elements which are known target sites to regulate mRNA stability [270]. GAPDH has been shown to bind AU-rich elements of endothelin-1, resulting in mRNA destabilisation. Interestingly, glutathionylation of GAPDH on C152 prevented endothelin-1 mRNA destabilisation [271]. An RNA immunoprecipitation of GSTO1-1 with Caspase-11 mRNA would informatively indicate a role for GSTO1-1 post-transcriptionally in Caspase-11 regulation.

The identification of GSTO1-1 as a novel NLRP3 inflammasome regulator is an exciting concept and warrants further investigation. My evidence suggests GSTO1-1 specifically regulates NEK7 deglutathionylation during NLPR3 inflammasome activation. NEK7 was originally discovered by similarity to a fungal mitosis regulator, termed NIMA [272], and has since been well-characterised as a centrosome regulating protein, aiding mitotic spindle formation and subsequent microtubule instability, driving cell division [273-276]. NEK7 is a

kinase and has been shown to respond to oxidative insults during telomere replication by phosphorylating TRF1, a telomere maintenance enzyme to protect telomere integrity [277]. NEK7 has been shown to either function as a mitotic component or an NLRP3 inflammasome interactor, but not concurrently [152]. It would be interesting to assess if NEK7 glutathionylation promotes mitosis, as deglutathionylation of C253 enhances NLRP3 inflammasome activation. The ablation of Caspase-11 by enzymatic inhibition or knockdown of GSTO1-1 also warrants further investigation, however the precise role of GSTO1-1 in Caspase-11 regulation is elusive. Researchers are now able to quantify the 'translatome' [278], and it would be interesting to examine if GSTO1-1 regulated Caspase-11 post-transcriptionally or Caspase-11 mRNA stability. Additionally, the cleavage and regulation of GSDMD should also be examined.

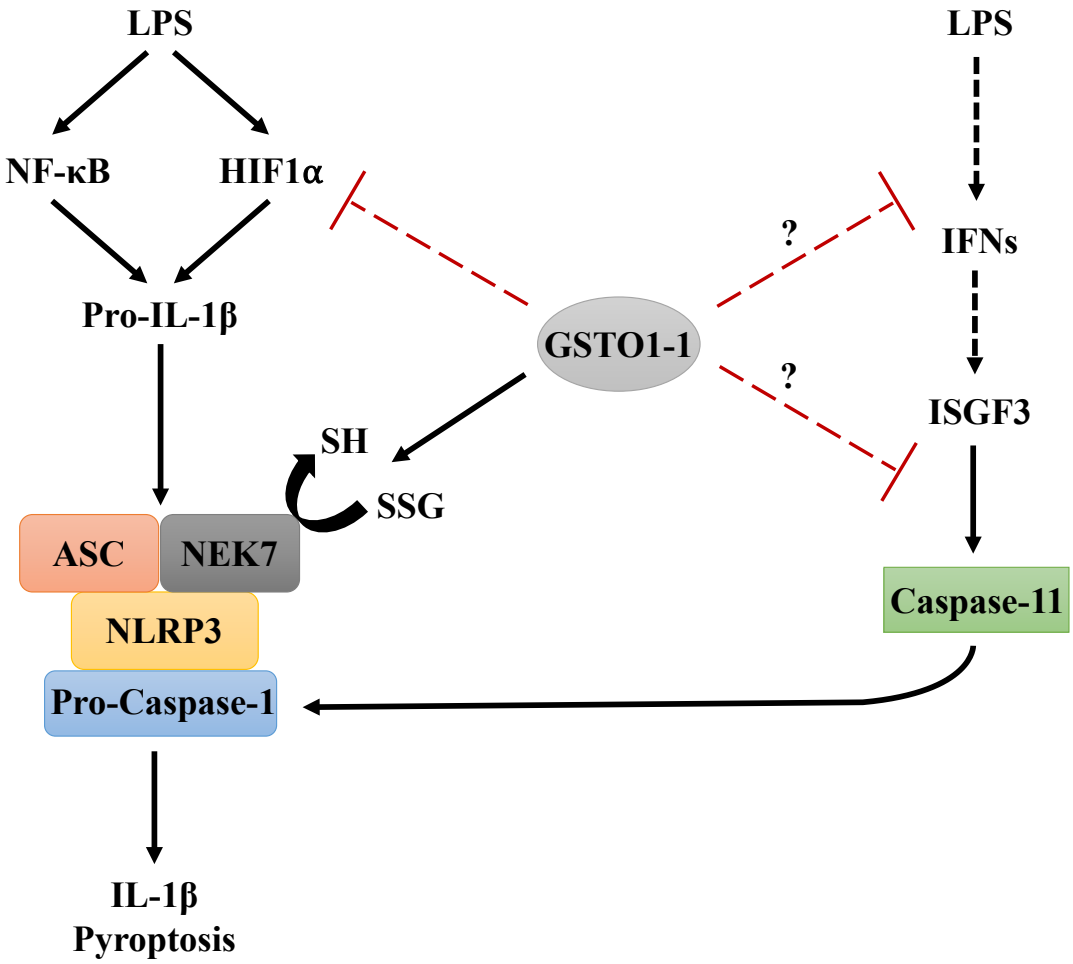

Figure 6.6 GSTO1-1 regulates canonical and non-canonical inflammasome activation

LPS drives the stabilisation of HIF1α and activation of NF-κB, which promotes transcription of IL-1β. GSTO1-1 serves to negatively regulate HIF1α, as GSTO1-1 deficiency results in increased HIF1α production. Pro-IL-1β is processed by the NLRP3 inflammasome, and GSTO1-1 increases Pro-IL-1β cleavage, possibly through NEK7 deglutathionylation of cysteine 253. LPS also drives transcription of Pro-caspase-11 through an IFN-β-dependent manner. GSTO1-1 inhibition or deficiency limits Pro-caspase-11 production and pyroptosis.

My thesis has examined a broad range of pathways; however, a common theme emerges surrounding redox regulation. Although it is convenient to think that ROS acts as a bactericidal mechanism, ROS generation can affect multiple pathways concurrently, dependent on the solvent accessibility of cysteines present in proteins which may become perturbed, and the physiological quantity of ROS produced. Glutathionylation of proteins is known to affect function, however it is only recently that technological advancements can quantify glutathionylation of proteins by MS [279, 280]. I have characterised a novel redox regulatory mechanism during TLR4 activation. Mal glutathionylation is critical for TLR4-mediated responses. I have also examined the function of GSTO1-1 during macrophage activation, identifying roles for GSTO1-1 in immunometabolism and NLRP3 inflammasome activation. IL-1 therapeutics also hold promise clinically, with recent findings by Ridker et al. reporting specific IL-1β targeting with Canakinumab, a monoclonal anti-IL-1β antibody, reduced cardiovascular events in a cohort of over 10,000 patients over 48 months, placing NLRP3 regulation as a critical mediator of inflammation [281]. My thesis suggests GSTO1-1 targeting during inflammasome activation may be beneficial for the development of anti-inflammatory therapies. Generation of C1-27 derivatives with nanomolar potency could prove useful in the treatment of inflammatory diseases. This work provides new insights into the complexities surrounding the redox regulation of innate immune signalling pathways.

Chapter 7

References

References

1. Janeway, C.A., Jr., *Approaching the asymptote? Evolution and revolution in immunology.* Cold Spring Harb Symp Quant Biol, 1989. **54 Pt 1**: p. 1-13.
2. O'Neill, L.A., D. Golenbock, and A.G. Bowie, *The history of Toll-like receptors - redefining innate immunity.* Nat Rev Immunol, 2013. **13**(6): p. 453-60.
3. Poltorak, A., et al., *Genetic and physical mapping of the Lps locus: identification of the toll-4 receptor as a candidate gene in the critical region.* Blood Cells Mol Dis, 1998. **24**(3): p. 340-55.
4. Hoshino, K., et al., *Cutting edge: Toll-like receptor 4 (TLR4)-deficient mice are hyporesponsive to lipopolysaccharide: evidence for TLR4 as the Lps gene product.* J Immunol, 1999. **162**(7): p. 3749-52.
5. Modhiran, N., et al., *Dengue virus NS1 protein activates immune cells via TLR4 but not TLR2 or TLR6.* Immunol Cell Biol, 2017. **95**(5): p. 491-495.
6. Carty, M. and A.G. Bowie, *Recent insights into the role of Toll-like receptors in viral infection.* Clin Exp Immunol, 2010. **161**(3): p. 397-406.
7. Schumann, R.R., et al., *Structure and function of lipopolysaccharide binding protein.* Science, 1990. **249**(4975): p. 1429-31.
8. Wright, S.D., et al., *CD14, a receptor for complexes of lipopolysaccharide (LPS) and LPS binding protein.* Science, 1990. **249**(4975): p. 1431-3.
9. Gioannini, T.L., et al., *Isolation of an endotoxin-MD-2 complex that produces Toll-like receptor 4-dependent cell activation at picomolar concentrations.* Proc Natl Acad Sci U S A, 2004. **101**(12): p. 4186-91.
10. Park, B.S., et al., *The structural basis of lipopolysaccharide recognition by the TLR4-MD-2 complex.* Nature, 2009. **458**(7242): p. 1191-5.
11. Kawasaki, K., et al., *Mouse toll-like receptor 4.MD-2 complex mediates lipopolysaccharide-mimetic signal transduction by Taxol.* J Biol Chem, 2000. **275**(4): p. 2251-4.
12. Sato, M., et al., *Direct binding of Toll-like receptor 2 to zymosan, and zymosan-induced NF-kappa B activation and TNF-alpha secretion are down-regulated by lung collectin surfactant protein A.* J Immunol, 2003. **171**(1): p. 417-25.
13. Barbalat, R., et al., *Toll-like receptor 2 on inflammatory monocytes induces type I interferon in response to viral but not bacterial ligands.* Nat Immunol, 2009. **10**(11): p. 1200-7.
14. Kinnebrew, M.A., et al., *Bacterial flagellin stimulates TLR5-dependent defense against vancomycin-resistant Enterococcus infection.* The Journal of infectious diseases, 2010. **201**(4): p. 534-543.
15. Beignon, A.S., et al., *Endocytosis of HIV-1 activates plasmacytoid dendritic cells via Toll-like receptor-viral RNA interactions.* J Clin Invest, 2005. **115**(11): p. 3265-75.
16. Coban, C., et al., *Immunogenicity of whole-parasite vaccines against Plasmodium falciparum involves malarial hemozoin and host TLR9.* Cell Host Microbe, 2010. **7**(1): p. 50-61.
17. Fitzgerald, K.A., et al., *Mal (MyD88-adapter-like) is required for Toll-like receptor-4 signal transduction.* Nature, 2001. **413**(6851): p. 78-83.
18. Mink, M., et al., *A novel human gene (SARM) at chromosome 17q11 encodes a protein with a SAM motif and structural similarity to Armadillo/beta-catenin that is conserved in mouse, Drosophila, and Caenorhabditis elegans.* Genomics, 2001. **74**(2): p. 234-44.
19. Yamamoto, M., et al., *Role of adaptor TRIF in the MyD88-independent toll-like receptor signaling pathway.* Science, 2003. **301**(5633): p. 640-3.
20. Yamamoto, M., et al., *TRAM is specifically involved in the Toll-like receptor 4-mediated MyD88-independent signaling pathway.* Nat Immunol, 2003. **4**(11): p. 1144-50.

21. Ni, M., et al., *B-cell adaptor for PI3K (BCAP) negatively regulates Toll-like receptor signaling through activation of PI3K.* Proc Natl Acad Sci U S A, 2012. **109**(1): p. 267-72.
22. Muzio, M., et al., *IRAK (Pelle) family member IRAK-2 and MyD88 as proximal mediators of IL-1 signaling.* Science, 1997. **278**(5343): p. 1612-5.
23. Medzhitov, R., et al., *MyD88 is an adaptor protein in the hToll/IL-1 receptor family signaling pathways.* Mol Cell, 1998. **2**(2): p. 253-8.
24. Lee, B.C., et al., *Deubiquitinase CYLD acts as a negative regulator for bacterium NTHi-induced inflammation by suppressing K63-linked ubiquitination of MyD88.* Proc Natl Acad Sci U S A, 2016. **113**(2): p. E165-71.
25. Yan, F., et al., *MyD88 NEDDylation negatively regulates MyD88-dependent NF-kappaB signaling through antagonizing its ubiquitination.* Biochem Biophys Res Commun, 2016.
26. Sun, D. and A. Ding, *MyD88-mediated stabilization of interferon-gamma-induced cytokine and chemokine mRNA.* Nat Immunol, 2006. **7**(4): p. 375-81.
27. Ye, X., et al., *MyD88 contributes to neuroinflammatory responses induced by cerebral ischemia/reperfusion in mice.* Biochem Biophys Res Commun, 2016. **480**(1): p. 69-74.
28. Kawai, T., et al., *Lipopolysaccharide stimulates the MyD88-independent pathway and results in activation of IFN-regulatory factor 3 and the expression of a subset of lipopolysaccharide-inducible genes.* J Immunol, 2001. **167**(10): p. 5887-94.
29. Matsumoto, M., et al., *Establishment of a monoclonal antibody against human Toll-like receptor 3 that blocks double-stranded RNA-mediated signaling.* Biochem Biophys Res Commun, 2002. **293**(5): p. 1364-9.
30. Oshiumi, H., et al., *TICAM-1, an adaptor molecule that participates in Toll-like receptor 3-mediated interferon-beta induction.* Nat Immunol, 2003. **4**(2): p. 161-7.
31. Hoebe, K., et al., *Identification of Lps2 as a key transducer of MyD88-independent TIR signalling.* Nature, 2003. **424**(6950): p. 743-8.
32. Kagan, J.C., et al., *TRAM couples endocytosis of Toll-like receptor 4 to the induction of interferon-beta.* Nat Immunol, 2008. **9**(4): p. 361-8.
33. Mata-Haro, V., et al., *The vaccine adjuvant monophosphoryl lipid A as a TRIF-biased agonist of TLR4.* Science, 2007. **316**(5831): p. 1628-32.
34. Rowe, D.C., et al., *The myristoylation of TRIF-related adaptor molecule is essential for Toll-like receptor 4 signal transduction.* Proc Natl Acad Sci U S A, 2006. **103**(16): p. 6299-304.
35. Doyle, S.L., et al., *The GOLD domain-containing protein TMED7 inhibits TLR4 signalling from the endosome upon LPS stimulation.* Nat Commun, 2012. **3**: p. 707.
36. Liaunardy-Jopeace, A., C.E. Bryant, and N.J. Gay, *The COP II adaptor protein TMED7 is required to initiate and mediate the delivery of TLR4 to the plasma membrane.* Sci Signal, 2014. **7**(336): p. ra70.
37. Palsson-McDermott, E.M., et al., *TAG, a splice variant of the adaptor TRAM, negatively regulates the adaptor MyD88-independent TLR4 pathway.* Nat Immunol, 2009. **10**(6): p. 579-86.
38. McGettrick, A.F., et al., *Trif-related adapter molecule is phosphorylated by PKC{epsilon} during Toll-like receptor 4 signaling.* Proc Natl Acad Sci U S A, 2006. **103**(24): p. 9196-201.
39. Nilsen, N.J., et al., *A role for the adaptor proteins TRAM and TRIF in toll-like receptor 2 signaling.* J Biol Chem, 2015. **290**(6): p. 3209-22.
40. Chen, C.Y., et al., *Sarm1, a negative regulator of innate immunity, interacts with syndecan-2 and regulates neuronal morphology.* J Cell Biol, 2011. **193**(4): p. 769-84.
41. Gerdts, J., et al., *Sarm1-mediated axon degeneration requires both SAM and TIR interactions.* J Neurosci, 2013. **33**(33): p. 13569-80.

42. Carty, M., et al., *The human adaptor SARM negatively regulates adaptor protein TRIF-dependent Toll-like receptor signaling.* Nat Immunol, 2006. **7**(10): p. 1074-81.
43. Gurtler, C., et al., *SARM regulates CCL5 production in macrophages by promoting the recruitment of transcription factors and RNA polymerase II to the Ccl5 promoter.* J Immunol, 2014. **192**(10): p. 4821-32.
44. Osterloh, J.M., et al., *dSarm/Sarm1 is required for activation of an injury-induced axon death pathway.* Science, 2012. **337**(6093): p. 481-4.
45. Summers, D.W., et al., *SARM1-specific motifs in the TIR domain enable NAD+ loss and regulate injury-induced SARM1 activation.* Proc Natl Acad Sci U S A, 2016. **113**(41): p. E6271-e6280.
46. Okada, T., et al., *BCAP: the tyrosine kinase substrate that connects B cell receptor to phosphoinositide 3-kinase activation.* Immunity, 2000. **13**(6): p. 817-27.
47. Castello, A., et al., *Nck-mediated recruitment of BCAP to the BCR regulates the PI(3)K-Akt pathway in B cells.* Nat Immunol, 2013. **14**(9): p. 966-75.
48. Troutman, T.D., et al., *Role for B-cell adapter for PI3K (BCAP) as a signaling adapter linking Toll-like receptors (TLRs) to serine/threonine kinases PI3K/Akt.* Proc Natl Acad Sci U S A, 2012. **109**(1): p. 273-8.
49. Horng, T., G.M. Barton, and R. Medzhitov, *TIRAP: an adapter molecule in the Toll signaling pathway.* Nat Immunol, 2001. **2**(9): p. 835-41.
50. Horng, T., et al., *The adaptor molecule TIRAP provides signalling specificity for Toll-like receptors.* Nature, 2002. **420**(6913): p. 329-333.
51. Yamamoto, M., et al., *Essential role for TIRAP in activation of the signalling cascade shared by TLR2 and TLR4.* Nature, 2002. **420**(6913): p. 324-329.
52. Piao, W., et al., *A Decoy Peptide that Disrupts TIRAP Recruitment to TLRs Is Protective in a Murine Model of Influenza.* Cell Rep, 2015. **11**(12): p. 1941-52.
53. Bonham, K.S., et al., *A promiscuous lipid-binding protein diversifies the subcellular sites of toll-like receptor signal transduction.* Cell, 2014. **156**(4): p. 705-716.
54. Ohnishi, H., et al., *Structural basis for the multiple interactions of the MyD88 TIR domain in TLR4 signaling.* Proc Natl Acad Sci U S A, 2009. **106**(25): p. 10260-5.
55. Khan, J.A., et al., *Crystal structure of the Toll/interleukin-1 receptor domain of human IL-1RAPL.* J Biol Chem, 2004. **279**(30): p. 31664-70.
56. Nyman, T., et al., *The crystal structure of the human toll-like receptor 10 cytoplasmic domain reveals a putative signaling dimer.* J Biol Chem, 2008. **283**(18): p. 11861-5.
57. Valkov, E., et al., *Crystal structure of toll-like receptor adaptor MAL/TIRAP reveals the molecular basis for signal transduction and disease protection.* Proceedings of the National Academy of Sciences of the United States of America, 2011. **108**(36): p. 14879-14884.
58. Lin, Z., et al., *Structural insights into TIR domain specificity of the bridging adaptor Mal in TLR4 signaling.* PLoS One, 2012. **7**(4): p. e34202.
59. Bovijn, C., et al., *Identification of binding sites for myeloid differentiation primary response gene 88 (MyD88) and Toll-like receptor 4 in MyD88 adapter-like (Mal).* J Biol Chem, 2013. **288**(17): p. 12054-66.
60. Ve, T., et al., *Structural basis of TIR-domain-assembly formation in MAL- and MyD88-dependent TLR4 signaling.* Nat Struct Mol Biol, 2017. **24**(9): p. 743-751.
61. Aksoy, E., et al., *The p110delta isoform of the kinase PI(3)K controls the subcellular compartmentalization of TLR4 signaling and protects from endotoxic shock.* Nat Immunol, 2012. **13**(11): p. 1045-54.
62. Kagan, J.C. and R. Medzhitov, *Phosphoinositide-Mediated Adaptor Recruitment Controls Toll-like Receptor Signaling.* Cell, 2006. **125**(5): p. 943-955.
63. Uchida, Y., et al., *Intracellular phosphatidylserine is essential for retrograde membrane traffic through endosomes.* Proc Natl Acad Sci U S A, 2011. **108**(38): p. 15846-51.

64. Zhao, X., et al., *Membrane targeting of TIRAP is negatively regulated by phosphorylation in its phosphoinositide-binding motif.* Sci Rep, 2017. **7**: p. 43043.
65. Kenny, E.F., et al., *MyD88 adaptor-like is not essential for TLR2 signaling and inhibits signaling by TLR3.* J Immunol, 2009. **183**(6): p. 3642-51.
66. Cole, L.E., et al., *Phagosomal retention of Francisella tularensis results in TIRAP/Mal-independent TLR2 signaling.* J Leukoc Biol, 2010. **87**(2): p. 275-81.
67. Mellett, M., et al., *Mal mediates TLR-induced activation of CREB and expression of IL-10.* J Immunol, 2011. **186**(8): p. 4925-35.
68. Ni Cheallaigh, C., et al., *A Common Variant in the Adaptor Mal Regulates Interferon Gamma Signaling.* Immunity, 2016. **44**(2): p. 368-79.
69. Gray, P., et al., *MyD88 adapter-like (Mal) is phosphorylated by Bruton's tyrosine kinase during TLR2 and TLR4 signal transduction.* J Biol Chem, 2006. **281**(15): p. 10489-95.
70. Dunne, A., et al., *IRAK1 and IRAK4 promote phosphorylation, ubiquitination, and degradation of MyD88 adaptor-like (Mal).* J Biol Chem, 2010. **285**(24): p. 18276-82.
71. Mansell, A., et al., *Suppressor of cytokine signaling 1 negatively regulates Toll-like receptor signaling by mediating Mal degradation.* Nat Immunol, 2006. **7**(2): p. 148-55.
72. Jakka, P., et al., *Cytoplasmic Linker Protein CLIP170 Negatively Regulates TLR4 Signaling by Targeting the TLR Adaptor Protein TIRAP.* J Immunol, 2017.
73. McGettrick, A.F. and L.A. O'Neill, *NLRP3 and IL-1beta in macrophages as critical regulators of metabolic diseases.* Diabetes Obes Metab, 2013. **15 Suppl 3**: p. 19-25.
74. Miggin, S.M., et al., *NF-kappaB activation by the Toll-IL-1 receptor domain protein MyD88 adapter-like is regulated by caspase-1.* Proc Natl Acad Sci U S A, 2007. **104**(9): p. 3372-7.
75. Ulrichts, P., et al., *Caspase-1 targets the TLR adaptor Mal at a crucial TIR-domain interaction site.* J Cell Sci, 2010. **123**(Pt 2): p. 256-65.
76. Sengupta, D., et al., *Subversion of innate immune responses by Brucella through the targeted degradation of the TLR signaling adapter, MAL.* J Immunol, 2010. **184**(2): p. 956-64.
77. Radhakrishnan, G.K., et al., *Brucella TIR Domain-containing Protein Mimics Properties of the Toll-like Receptor Adaptor Protein TIRAP.* J Biol Chem, 2009. **284**(15): p. 9892-8.
78. Li, W., et al., *Brucella TIR-like protein TcpB/Btp1 specifically targets the host adaptor protein MAL/TIRAP to promote infection.* Biochem Biophys Res Commun, 2016. **477**(3): p. 509-14.
79. Jeyaseelan, S., et al., *Toll-IL-1 receptor domain-containing adaptor protein is critical for early lung immune responses against Escherichia coli lipopolysaccharide and viable Escherichia coli.* J Immunol, 2005. **175**(11): p. 7484-95.
80. Jeyaseelan, S., et al., *Toll/IL-1R domain-containing adaptor protein (TIRAP) is a critical mediator of antibacterial defense in the lung against Klebsiella pneumoniae but not Pseudomonas aeruginosa.* J Immunol, 2006. **177**(1): p. 538-47.
81. Corr, S.C., et al., *MyD88 adaptor-like (Mal) functions in the epithelial barrier and contributes to intestinal integrity via protein kinase C.* Mucosal Immunol, 2014. **7**(1): p. 57-67.
82. Israel, L., et al., *Human Adaptive Immunity Rescues an Inborn Error of Innate Immunity.* Cell, 2017. **168**(5): p. 789-800.e10.
83. Kenny, E.F., et al., *MyD88 adaptor-like is not essential for TLR2 signaling and inhibits signaling by TLR3.* Journal of Immunology, 2009. **183**(6): p. 3642-3651.
84. Bernard, N.J. and L.A. O'Neill, *Mal, more than a bridge to MyD88.* IUBMB Life, 2013. **65**(9): p. 777-86.
85. Hughes, M.M., A.F. McGettrick, and L.A.J. O'Neill, *Glutathione and Glutathione Transferase Omega 1 as Key Posttranslational Regulators in Macrophages.* Microbiol Spectr, 2017. **5**(1).

86. Szanto, I., et al., *Expression of NOX1, a superoxide-generating NADPH oxidase, in colon cancer and inflammatory bowel disease.* J Pathol, 2005. **207**(2): p. 164-76.
87. Vaziri, N.D. and B. Rodriguez-Iturbe, *Mechanisms of disease: oxidative stress and inflammation in the pathogenesis of hypertension.* Nat Clin Pract Nephrol, 2006. **2**(10): p. 582-93.
88. Grek, C.L., et al., *Causes and Consequences of Cysteine S-Glutathionylation.* Journal of Biological Chemistry, 2013. **288**(37): p. 26497-26504.
89. Gostner, J.M., et al., *Redox regulation of the immune response.* Redox Rep, 2013. **18**(3): p. 88-94.
90. Poole, L.B., *The Basics of Thiols and Cysteines in Redox Biology and Chemistry.* Free Radic Biol Med, 2015. **0**: p. 148-57.
91. Roos, G. and J. Messens, *Protein sulfenic acid formation: from cellular damage to redox regulation.* Free Radic Biol Med, 2011. **51**(2): p. 314-26.
92. Yen, T.Y., et al., *Characterization of cysteine residues and disulfide bonds in proteins by liquid chromatography/electrospray ionization tandem mass spectrometry.* J Mass Spectrom, 2000. **35**(8): p. 990-1002.
93. Paulech, J., et al., *Global analysis of myocardial peptides containing cysteines with irreversible sulfinic and sulfonic acid post-translational modifications.* Mol Cell Proteomics, 2015. **14**(3): p. 609-20.
94. Lo Conte, M. and K.S. Carroll, *The redox biochemistry of protein sulfenylation and sulfinylation.* J Biol Chem, 2013. **288**(37): p. 26480-8.
95. Mahadev, K., et al., *Insulin-stimulated hydrogen peroxide reversibly inhibits protein-tyrosine phosphatase 1b in vivo and enhances the early insulin action cascade.* J Biol Chem, 2001. **276**(24): p. 21938-42.
96. Meng, T.C., et al., *Regulation of insulin signaling through reversible oxidation of the protein-tyrosine phosphatases TC45 and PTP1B.* J Biol Chem, 2004. **279**(36): p. 37716-25.
97. Yang, J., et al., *Reversible oxidation of the membrane distal domain of receptor PTPalpha is mediated by a cyclic sulfenamide.* Biochemistry, 2007. **46**(3): p. 709-19.
98. Lee, J.W., S. Soonsanga, and J.D. Helmann, *A complex thiolate switch regulates the Bacillus subtilis organic peroxide sensor OhrR.* Proc Natl Acad Sci U S A, 2007. **104**(21): p. 8743-8.
99. Hosoki, R., N. Matsuki, and H. Kimura, *The possible role of hydrogen sulfide as an endogenous smooth muscle relaxant in synergy with nitric oxide.* Biochem Biophys Res Commun, 1997. **237**(3): p. 527-31.
100. Zhao, W., et al., *The vasorelaxant effect of H(2)S as a novel endogenous gaseous K(ATP) channel opener.* Embo j, 2001. **20**(21): p. 6008-16.
101. Yang, G., et al., *H2S as a physiologic vasorelaxant: hypertension in mice with deletion of cystathionine gamma-lyase.* Science, 2008. **322**(5901): p. 587-90.
102. Mustafa, A.K., et al., *H2S signals through protein S-sulfhydration.* Sci Signal, 2009. **2**(96): p. ra72.
103. Lee, Z.W., et al., *The cystathionine gamma-lyase/hydrogen sulfide system maintains cellular glutathione status.* Biochem J, 2014. **460**(3): p. 425-35.
104. Paul, B.D., et al., *Cystathionine gamma-lyase deficiency mediates neurodegeneration in Huntington's disease.* Nature, 2014. **509**(7498): p. 96-100.
105. Sen, N., et al., *Hydrogen sulfide-linked sulfhydration of NF-kappaB mediates its antiapoptotic actions.* Mol Cell, 2012. **45**(1): p. 13-24.
106. Mir, S., T. Sen, and N. Sen, *Cytokine-induced GAPDH sulfhydration affects PSD95 degradation and memory.* Mol Cell, 2014. **56**(6): p. 786-95.
107. Hess, D.T., et al., *Protein S-nitrosylation: purview and parameters.* Nat Rev Mol Cell Biol, 2005. **6**(2): p. 150-66.

108. Altaany, Z., et al., *The coordination of S-sulfhydration, S-nitrosylation, and phosphorylation of endothelial nitric oxide synthase by hydrogen sulfide.* Sci Signal, 2014. **7**(342): p. ra87.
109. Giustarini, D., et al., *S-nitrosation versus S-glutathionylation of protein sulfhydryl groups by S-nitrosoglutathione.* Antioxid Redox Signal, 2005. **7**(7-8): p. 930-9.
110. Morris, D., et al., *Glutathione and infection.* Biochim Biophys Acta, 2013. **1830**(5): p. 3329-49.
111. Alanazi, A.M., G.A. Mostafa, and A.A. Al-Badr, *Glutathione.* Profiles Drug Subst Excip Relat Methodol, 2015. **40**: p. 43-158.
112. Montero, D., et al., *Intracellular glutathione pools are heterogeneously concentrated().* Redox Biol, 2013. **1**(1): p. 508-13.
113. Zhou, Y., et al., *Genetic analysis of tissue glutathione concentrations and redox balance.* Free Radic Biol Med, 2014. **71**: p. 157-64.
114. Perlman, J.H., et al., *A disulfide bond between conserved extracellular cysteines in the thyrotropin-releasing hormone receptor is critical for binding.* J Biol Chem, 1995. **270**(42): p. 24682-5.
115. Patil, N.A., et al., *Cellular disulfide bond formation in bioactive peptides and proteins.* Int J Mol Sci, 2015. **16**(1): p. 1791-805.
116. Stroher, E. and A.H. Millar, *The biological roles of glutaredoxins.* Biochem J, 2012. **446**(3): p. 333-48.
117. Holmgren, A., et al., *Thiol redox control via thioredoxin and glutaredoxin systems.* Biochem Soc Trans, 2005. **33**(Pt 6): p. 1375-7.
118. Lillig, C.H. and C. Berndt, *Glutaredoxins in thiol/disulfide exchange.* Antioxid Redox Signal, 2013. **18**(13): p. 1654-65.
119. Holmgren, A., *Thioredoxin and glutaredoxin systems.* J Biol Chem, 1989. **264**(24): p. 13963-6.
120. Mahmood, D.F., et al., *Truncated thioredoxin (Trx-80) promotes pro-inflammatory macrophages of the M1 phenotype and enhances atherosclerosis.* J Cell Physiol, 2013. **228**(7): p. 1577-83.
121. Arnér, E.S.J. and A. Holmgren, *Physiological functions of thioredoxin and thioredoxin reductase.* European Journal of Biochemistry, 2000. **267**(20): p. 6102-6109.
122. Board, P.G. and D. Menon, *Glutathione transferases, regulators of cellular metabolism and physiology.* Biochim Biophys Acta, 2013. **1830**(5): p. 3267-88.
123. Dourado, D.F., P.A. Fernandes, and M.J. Ramos, *Mammalian cytosolic glutathione transferases.* Curr Protein Pept Sci, 2008. **9**(4): p. 325-37.
124. Laborde, E., *Glutathione transferases as mediators of signaling pathways involved in cell proliferation and cell death.* Cell Death Differ, 2010. **17**(9): p. 1373-80.
125. Louie, S.M., et al., *GSTP1 Is a Driver of Triple-Negative Breast Cancer Cell Metabolism and Pathogenicity.* Cell Chem Biol, 2016. **23**(5): p. 567-78.
126. Tew, K.D. and D.M. Townsend, *Regulatory functions of glutathione S-transferase P1-1 unrelated to detoxification.* Drug Metab Rev, 2011. **43**(2): p. 179-93.
127. Tew, K.D., et al., *The role of glutathione S-transferase P in signaling pathways and S-glutathionylation in cancer.* Free Radic Biol Med, 2011. **51**(2): p. 299-313.
128. Adler, V., et al., *Regulation of JNK signaling by GSTp.* Embo j, 1999. **18**(5): p. 1321-34.
129. Xue, B., et al., *Regulation of lipopolysaccharide-induced inflammatory response by glutathione S-transferase P1 in RAW264.7 cells.* FEBS Lett, 2005. **579**(19): p. 4081-7.
130. Board, P.G., et al., *Identification, Characterization, and Crystal Structure of the Omega Class Glutathione Transferases.* Journal of Biological Chemistry, 2000. **275**(32): p. 24798-24806.
131. Li, Y.J., et al., *Glutathione S-transferase omega-1 modifies age-at-onset of Alzheimer disease and Parkinson disease.* Hum Mol Genet, 2003. **12**(24): p. 3259-67.

132. Board, P.G. and M.W. Anders, *Glutathione transferase omega 1 catalyzes the reduction of S-(phenacyl)glutathiones to acetophenones.* Chem Res Toxicol, 2007. **20**(1): p. 149-54.
133. Board, P.G., et al., *S-(4-Nitrophenacyl)glutathione is a specific substrate for glutathione transferase omega 1-1.* Anal Biochem, 2008. **374**(1): p. 25-30.
134. Menon, D. and P.G. Board, *A role for glutathione transferase Omega 1 (GSTO1-1) in the glutathionylation cycle.* J Biol Chem, 2013. **288**(36): p. 25769-79.
135. Meissner, F., K. Molawi, and A. Zychlinsky, *Superoxide dismutase 1 regulates caspase-1 and endotoxic shock.* Nat Immunol, 2008. **9**(8): p. 866-872.
136. Toledano, M.B. and W.J. Leonard, *Modulation of transcription factor NF-kappa B binding activity by oxidation-reduction in vitro.* Proc Natl Acad Sci U S A, 1991. **88**(10): p. 4328-32.
137. Menon, D., et al., *Glutathione transferase omega 1 is required for the lipopolysaccharide-stimulated induction of NADPH oxidase 1 and the production of reactive oxygen species in macrophages.* Free Radic Biol Med, 2014. **73**: p. 318-27.
138. Meissonnier, G.M., et al., *Immunotoxicity of aflatoxin B1: impairment of the cell-mediated response to vaccine antigen and modulation of cytokine expression.* Toxicol Appl Pharmacol, 2008. **231**(2): p. 142-9.
139. Piaggi, S., et al., *Glutathione transferase omega 1-1 (GSTO1-1) plays an anti-apoptotic role in cell resistance to cisplatin toxicity.* Carcinogenesis, 2010. **31**(5): p. 804-811.
140. Paul, S., et al., *Glutathione-S-transferase omega 1 (GSTO1-1) acts as mediator of signaling pathways involved in aflatoxin B1-induced apoptosis–autophagy crosstalk in macrophages.* Free Radical Biology and Medicine, 2015. **89**: p. 1218-1230.
141. Huang, Q., et al., *Increased mitochondrial fission promotes autophagy and hepatocellular carcinoma cell survival through the ROS-modulated coordinated regulation of the NFKB and TP53 pathways.* Autophagy, 2016. **12**(6): p. 999-1014.
142. Palsson-McDermott, E.M., et al., *Pyruvate kinase M2 regulates Hif-1alpha activity and IL-1beta induction and is a critical determinant of the warburg effect in LPS-activated macrophages.* Cell Metab, 2015. **21**(1): p. 65-80.
143. Menon, D., et al., *GSTO1-1 modulates metabolism in macrophages activated through the LPS and TLR4 pathway.* J Cell Sci, 2015. **128**(10): p. 1982-90.
144. Sentellas, S., et al., *GSSG/GSH ratios in cryopreserved rat and human hepatocytes as a biomarker for drug induced oxidative stress.* Toxicol In Vitro, 2014. **28**(5): p. 1006-15.
145. Mo, C., et al., *The crosstalk between Nrf2 and AMPK signal pathways is important for the anti-inflammatory effect of berberine in LPS-stimulated macrophages and endotoxin-shocked mice.* Antioxid Redox Signal, 2014. **20**(4): p. 574-88.
146. Tannahill, G.M., et al., *Succinate is an inflammatory signal that induces IL-1beta through HIF-1alpha.* Nature, 2013. **496**(7444): p. 238-42.
147. Laliberte, R.E., et al., *Glutathione s-transferase omega 1-1 is a target of cytokine release inhibitory drugs and may be responsible for their effect on interleukin-1beta posttranslational processing.* J Biol Chem, 2003. **278**(19): p. 16567-78.
148. Menon, D., et al., *GSTO1-1 plays a pro-inflammatory role in models of inflammation, colitis and obesity.* Sci Rep, 2017. **7**(1): p. 17832.
149. Coll, R.C., et al., *A small-molecule inhibitor of the NLRP3 inflammasome for the treatment of inflammatory diseases.* Nat Med, 2015. **21**(3): p. 248-55.
150. Lu, A., et al., *Unified Polymerization Mechanism for the Assembly of ASC-dependent Inflammasomes.* Cell, 2014. **156**(6): p. 1193-206.
151. He, Y., et al., *NEK7 is an essential mediator of NLRP3 activation downstream of potassium efflux.* Nature, 2016. **530**(7590): p. 354-7.
152. Shi, H., et al., *NLRP3 activation and mitosis are mutually exclusive events coordinated by NEK7, a new inflammasome component.* Nat Immunol, 2016. **17**(3): p. 250-8.

153. Martinon, F., K. Burns, and J. Tschopp, *The inflammasome: a molecular platform triggering activation of inflammatory caspases and processing of proIL-beta.* Mol Cell, 2002. **10**(2): p. 417-26.
154. Agostini, L., et al., *NALP3 forms an IL-1beta-processing inflammasome with increased activity in Muckle-Wells autoinflammatory disorder.* Immunity, 2004. **20**(3): p. 319-25.
155. Zhou, R., et al., *Thioredoxin-interacting protein links oxidative stress to inflammasome activation.* Nat Immunol, 2010. **11**(2): p. 136-40.
156. Vandanmagsar, B., et al., *The NLRP3 inflammasome instigates obesity-induced inflammation and insulin resistance.* Nat Med, 2011. **17**(2): p. 179-88.
157. Hornung, V., et al., *AIM2 recognizes cytosolic dsDNA and forms a caspase-1-activating inflammasome with ASC.* Nature, 2009. **458**(7237): p. 514-8.
158. Miao, E.A., et al., *Innate immune detection of the type III secretion apparatus through the NLRC4 inflammasome.* Proc Natl Acad Sci U S A, 2010. **107**(7): p. 3076-80.
159. Reyes Ruiz, V.M., et al., *Broad detection of bacterial type III secretion system and flagellin proteins by the human NAIP/NLRC4 inflammasome.* Proc Natl Acad Sci U S A, 2017. **114**(50): p. 13242-13247.
160. Yang, J., et al., *Human NAIP and mouse NAIP1 recognize bacterial type III secretion needle protein for inflammasome activation.* Proc Natl Acad Sci U S A, 2013. **110**(35): p. 14408-13.
161. Rauch, I., et al., *NAIP proteins are required for cytosolic detection of specific bacterial ligands in vivo.* J Exp Med, 2016. **213**(5): p. 657-65.
162. Kayagaki, N., et al., *Non-canonical inflammasome activation targets caspase-11.* Nature, 2011. **479**(7371): p. 117-21.
163. Broz, P., et al., *Caspase-11 increases susceptibility to Salmonella infection in the absence of caspase-1.* Nature, 2012. **490**(7419): p. 288-91.
164. Shi, J., et al., *Inflammatory caspases are innate immune receptors for intracellular LPS.* Nature, 2014. **514**(7521): p. 187-92.
165. Ruhl, S. and P. Broz, *Caspase-11 activates a canonical NLRP3 inflammasome by promoting K(+) efflux.* Eur J Immunol, 2015. **45**(10): p. 2927-36.
166. Schauvliege, R., et al., *Caspase-11 gene expression in response to lipopolysaccharide and interferon-gamma requires nuclear factor-kappa B and signal transducer and activator of transcription (STAT) 1.* J Biol Chem, 2002. **277**(44): p. 41624-30.
167. Hagar, J.A., et al., *Cytoplasmic LPS activates caspase-11: implications in TLR4-independent endotoxic shock.* Science, 2013. **341**(6151): p. 1250-3.
168. Kayagaki, N., et al., *Noncanonical inflammasome activation by intracellular LPS independent of TLR4.* Science, 2013. **341**(6151): p. 1246-9.
169. Wen, H., et al., *Fatty acid-induced NLRP3-ASC inflammasome activation interferes with insulin signaling.* Nat Immunol, 2011. **12**(5): p. 408-15.
170. Youm, Y.H., et al., *The ketone metabolite beta-hydroxybutyrate blocks NLRP3 inflammasome-mediated inflammatory disease.* Nat Med, 2015. **21**(3): p. 263-9.
171. Zhu, Q., et al., *The ketone metabolite beta-hydroxybutyrate attenuates oxidative stress in spinal cord injury by suppression of class I histone deacetylases.* J Neurotrauma, 2017.
172. Goldberg, E.L., et al., *beta-Hydroxybutyrate Deactivates Neutrophil NLRP3 Inflammasome to Relieve Gout Flares.* Cell Rep, 2017. **18**(9): p. 2077-2087.
173. Bakker, P.J., et al., *Nlrp3 is a key modulator of diet-induced nephropathy and renal cholesterol accumulation.* Kidney Int, 2014. **85**(5): p. 1112-22.
174. Chiang, J.Y., *Regulation of bile acid synthesis: pathways, nuclear receptors, and mechanisms.* J Hepatol, 2004. **40**(3): p. 539-51.
175. Guo, C., et al., *Bile Acids Control Inflammation and Metabolic Disorder through Inhibition of NLRP3 Inflammasome.* Immunity, 2016. **45**(4): p. 944.

176. Ricciotti, E. and G.A. FitzGerald, *Prostaglandins and Inflammation.* Arterioscler Thromb Vasc Biol, 2011. **31**(5): p. 986-1000.
177. Coulombe, F., et al., *Targeted prostaglandin E2 inhibition enhances antiviral immunity through induction of type I interferon and apoptosis in macrophages.* Immunity, 2014. **40**(4): p. 554-68.
178. Hooper, K.M., et al., *Prostaglandin E2 Inhibition of IL-27 Production in Murine Dendritic Cells: A Novel Mechanism That Involves IRF1.* J Immunol, 2017. **198**(4): p. 1521-1530.
179. Sokolowska, M., et al., *Prostaglandin E2 Inhibits NLRP3 Inflammasome Activation through EP4 Receptor and Intracellular Cyclic AMP in Human Macrophages.* J Immunol, 2015. **194**(11): p. 5472-5487.
180. Zaslona, Z., et al., *The Induction of Pro-IL-1beta by Lipopolysaccharide Requires Endogenous Prostaglandin E2 Production.* J Immunol, 2017. **198**(9): p. 3558-3564.
181. Meissner, F., K. Molawi, and A. Zychlinsky, *Superoxide dismutase 1 regulates caspase-1 and endotoxic shock.* Nat Immunol, 2008. **9**(8): p. 866-72.
182. Huang, Z., et al., *Inhibition of caspase-3 activity and activation by protein glutathionylation.* Biochem Pharmacol, 2008. **75**(11): p. 2234-44.
183. Guglielmo, A., et al., *A mechanistic insight into curcumin modulation of the IL-1beta secretion and NLRP3 S-glutathionylation induced by needle-like cationic cellulose nanocrystals in myeloid cells.* Chem Biol Interact, 2017. **274**: p. 1-12.
184. Munoz-Planillo, R., et al., *K(+) efflux is the common trigger of NLRP3 inflammasome activation by bacterial toxins and particulate matter.* Immunity, 2013. **38**(6): p. 1142-53.
185. Domingo-Fernandez, R., et al., *The intracellular chloride channel proteins CLIC1 and CLIC4 induce IL-1beta transcription and activate the NLRP3 inflammasome.* J Biol Chem, 2017. **292**(29): p. 12077-12087.
186. Tang, T., et al., *CLICs-dependent chloride efflux is an essential and proximal upstream event for NLRP3 inflammasome activation.* Nat Commun, 2017. **8**(1): p. 202.
187. Haneklaus, M., et al., *The RNA-binding protein Tristetraprolin (TTP) is a critical negative regulator of the NLRP3 inflammasome.* J Biol Chem, 2017. **292**(17): p. 6869-6881.
188. Lee, S.J. and S.L. Michel, *Cysteine oxidation enhanced by iron in tristetraprolin, a zinc finger peptide.* Inorg Chem, 2010. **49**(3): p. 1211-9.
189. Chen, C.Y., et al., *A novel immunomodulatory effect of ugonin U in human neutrophils via stimulation of phospholipase C.* Free Radic Biol Med, 2014. **72**: p. 222-31.
190. Chen, C.Y., et al., *Ugonin U stimulates NLRP3 inflammasome activation and enhances inflammasome-mediated pathogen clearance.* Redox Biol, 2017. **11**: p. 263-274.
191. Moon, J.S., et al., *UCP2-induced fatty acid synthase promotes NLRP3 inflammasome activation during sepsis.* J Clin Invest, 2015. **125**(2): p. 665-80.
192. Moon, J.S., et al., *NOX4-dependent fatty acid oxidation promotes NLRP3 inflammasome activation in macrophages.* Nat Med, 2016. **22**(9): p. 1002-12.
193. Sanman, L.E., et al., *Disruption of glycolytic flux is a signal for inflammasome signaling and pyroptotic cell death.* Elife, 2016. **5**: p. e13663.
194. Moon, J.S., et al., *mTORC1-Induced HK1-Dependent Glycolysis Regulates NLRP3 Inflammasome Activation.* Cell Rep, 2015. **12**(1): p. 102-15.
195. Nomura, J., et al., *Intracellular ATP Decrease Mediates NLRP3 Inflammasome Activation upon Nigericin and Crystal Stimulation.* J Immunol, 2015. **195**(12): p. 5718-24.
196. Majewski, N., et al., *Hexokinase-mitochondria interaction mediated by Akt is required to inhibit apoptosis in the presence or absence of Bax and Bak.* Mol Cell, 2004. **16**(5): p. 819-30.

197. Hahn-Windgassen, A., et al., *Akt activates the mammalian target of rapamycin by regulating cellular ATP level and AMPK activity.* J Biol Chem, 2005. **280**(37): p. 32081-9.
198. Wolf, A.J., et al., *Hexokinase Is an Innate Immune Receptor for the Detection of Bacterial Peptidoglycan.* Cell, 2016. **166**(3): p. 624-36.
199. Kelly, B., et al., *Metformin Inhibits the Production of Reactive Oxygen Species from NADH:Ubiquinone Oxidoreductase to Limit Induction of Interleukin-1beta (IL-1beta) and Boosts Interleukin-10 (IL-10) in Lipopolysaccharide (LPS)-activated Macrophages.* J Biol Chem, 2015. **290**(33): p. 20348-59.
200. Mills, E.L., et al., *Succinate Dehydrogenase Supports Metabolic Repurposing of Mitochondria to Drive Inflammatory Macrophages.* Cell, 2016.
201. Shimada, K., et al., *Oxidized mitochondrial DNA activates the NLRP3 inflammasome during apoptosis.* Immunity, 2012. **36**(3): p. 401-14.
202. Li, Y., et al., *Succinate/NLRP3 Inflammasome Induces Synovial Fibroblast Activation: Therapeutical Effects of Clematichinenoside AR on Arthritis.* Front Immunol, 2016. **7**: p. 532.
203. Liu, X., et al., *Dimethyl fumarate ameliorates dextran sulfate sodium-induced murine experimental colitis by activating Nrf2 and suppressing NLRP3 inflammasome activation.* Biochem Pharmacol, 2016. **112**: p. 37-49.
204. Zhao, Y., et al., *The NLRC4 inflammasome receptors for bacterial flagellin and type III secretion apparatus.* Nature, 2011. **477**(7366): p. 596-600.
205. Matusiak, M., et al., *Flagellin-induced NLRC4 phosphorylation primes the inflammasome for activation by NAIP5.* Proc Natl Acad Sci U S A, 2015. **112**(5): p. 1541-6.
206. Broz, P., et al., *Redundant roles for inflammasome receptors NLRP3 and NLRC4 in host defense against Salmonella.* J Exp Med, 2010. **207**(8): p. 1745-55.
207. Wynosky-Dolfi, M.A., et al., *Oxidative metabolism enables Salmonella evasion of the NLRP3 inflammasome.* J Exp Med, 2014. **211**(4): p. 653-68.
208. Lima-Junior, D.S., et al., *Dectin-1 Activation during Leishmania amazonensis Phagocytosis Prompts Syk-Dependent Reactive Oxygen Species Production To Trigger Inflammasome Assembly and Restriction of Parasite Replication.* J Immunol, 2017.
209. Dostert, C., et al., *Innate immune activation through Nalp3 inflammasome sensing of asbestos and silica.* Science, 2008. **320**(5876): p. 674-7.
210. Zhou, R., et al., *A role for mitochondria in NLRP3 inflammasome activation.* Nature, 2011. **469**(7329): p. 221-5.
211. Iyer, S.S., et al., *Mitochondrial cardiolipin is required for Nlrp3 inflammasome activation.* Immunity, 2013. **39**(2): p. 311-323.
212. Park, S., et al., *The mitochondrial antiviral protein MAVS associates with NLRP3 and regulates its inflammasome activity.* J Immunol, 2013. **191**(8): p. 4358-66.
213. Yu, J., et al., *Inflammasome activation leads to Caspase-1-dependent mitochondrial damage and block of mitophagy.* Proc Natl Acad Sci U S A, 2014. **111**(43): p. 15514-9.
214. Hughes, M.M., et al., *Solution structure of the TLR adaptor MAL/TIRAP reveals an intact BB loop and supports MAL Cys91 glutathionylation for signaling.* Proc Natl Acad Sci U S A, 2017.
215. Khor, C.C., et al., *A Mal functional variant is associated with protection against invasive pneumococcal disease, bacteremia, malaria and tuberculosis.* Nature Genetics, 2007. **39**(4): p. 523-528.
216. Dunne, A., et al., *IRAK1 and IRAK4 Promote Phosphorylation, Ubiquitination, and Degradation of MyD88 Adaptor-like (Mal).* Journal of Biological Chemistry, 2010. **285**(24): p. 18276-18282.

217. Garcia, J., et al., *Regulation of mitochondrial glutathione redox status and protein glutathionylation by respiratory substrates.* J Biol Chem, 2010. **285**(51): p. 39646-54.
218. Watanabe, Y., et al., *Glutathione adducts induced by ischemia and deletion of glutaredoxin-1 stabilize HIF-1alpha and improve limb revascularization.* Proc Natl Acad Sci U S A, 2016. **113**(21): p. 6011-6.
219. Verma, I.M., et al., *Rel/NF-kappa B/I kappa B family: intimate tales of association and dissociation.* Genes Dev, 1995. **9**(22): p. 2723-35.
220. Forman, H.J., J.M. Fukuto, and M. Torres, *Redox signaling: thiol chemistry defines which reactive oxygen and nitrogen species can act as second messengers.* Am J Physiol Cell Physiol, 2004. **287**(2): p. C246-56.
221. Bryant, C.E., M. Symmons, and N.J. Gay, *Toll-like receptor signalling through macromolecular protein complexes.* Mol Immunol, 2015. **63**(2): p. 162-5.
222. Motshwene, P.G., et al., *An oligomeric signaling platform formed by the Toll-like receptor signal transducers MyD88 and IRAK-4.* J Biol Chem, 2009. **284**(37): p. 25404-11.
223. Butturini, E., et al., *S-Glutathionylation at Cys328 and Cys542 impairs STAT3 phosphorylation.* ACS Chem Biol, 2014. **9**(8): p. 1885-93.
224. Thayyullathil, F., et al., *Rapid reactive oxygen species (ROS) generation induced by curcumin leads to caspase-dependent and -independent apoptosis in L929 cells.* Free Radical Biology and Medicine, 2008. **45**(10): p. 1403-1412.
225. Krawczyk, C.M., et al., *Toll-like receptor-induced changes in glycolytic metabolism regulate dendritic cell activation.* Blood, 2010. **115**(23): p. 4742-9.
226. Menon, D., et al., *GSTO1-1 modulates metabolism in macrophages activated through the LPS and TLR4 pathway.* J Cell Sci, 2015. **128**(10): p. 1982-1990.
227. Jung, S.N., et al., *Reactive oxygen species stabilize hypoxia-inducible factor-1 alpha protein and stimulate transcriptional activity via AMP-activated protein kinase in DU145 human prostate cancer cells.* Carcinogenesis, 2008. **29**(4): p. 713-21.
228. Ramkumar, K., et al., *Mechanistic evaluation and transcriptional signature of a glutathione S-transferase omega 1 inhibitor.* Nature Communications, 2016. **7**: p. 13084.
229. Smeyne, M. and R.J. Smeyne, *Glutathione metabolism and Parkinson's disease.* Free Radic Biol Med, 2013. **62**: p. 13-25.
230. Mandal, P.K., et al., *Brain glutathione levels--a novel biomarker for mild cognitive impairment and Alzheimer's disease.* Biol Psychiatry, 2015. **78**(10): p. 702-10.
231. Panieri, E. and M.M. Santoro, *ROS homeostasis and metabolism: a dangerous liason in cancer cells.* Cell Death Dis, 2016. **7**(6): p. e2253.
232. Menon, D. and P.G. Board, *A Role for Glutathione Transferase Omega 1 (GSTO1-1) in the Glutathionylation Cycle.* Journal of Biological Chemistry, 2013. **288**(36): p. 25769-25779.
233. Stottmeier, B. and T.P. Dick, *Redox sensitivity of the MyD88 immune signaling adapter.* Free Radic Biol Med, 2016. **101**: p. 93-101.
234. Chantzoura, E., et al., *Glutaredoxin-1 regulates TRAF6 activation and the IL-1 receptor/TLR4 signalling.* Biochem Biophys Res Commun, 2010. **403**(3-4): p. 335-9.
235. Kabe, Y., et al., *Redox regulation of NF-kappaB activation: distinct redox regulation between the cytoplasm and the nucleus.* Antioxid Redox Signal, 2005. **7**(3-4): p. 395-403.
236. Heufler, C., et al., *Interleukin-12 is produced by dendritic cells and mediates T helper 1 development as well as interferon-gamma production by T helper 1 cells.* Eur J Immunol, 1996. **26**(3): p. 659-68.
237. Athie-Morales, V., et al., *Sustained IL-12 signaling is required for Th1 development.* J Immunol, 2004. **172**(1): p. 61-9.

238. Mondal, S., A. Roy, and K. Pahan, *Functional Blocking Monoclonal Antibodies against IL-12p40 Homodimer Inhibit Adoptive Transfer of Experimental Allergic Encephalomyelitis.* J Immunol, 2009. **182**(8): p. 5013-23.
239. Li, B., et al., *IL-10 modulates DSS-induced colitis through a macrophage-ROS-NO axis.* Mucosal Immunol, 2014. **7**(4): p. 869-78.
240. Freemerman, A.J., et al., *Metabolic Reprogramming of Macrophages: GLUCOSE TRANSPORTER 1 (GLUT1)-MEDIATED GLUCOSE METABOLISM DRIVES A PROINFLAMMATORY PHENOTYPE.* J Biol Chem, 2014. **289**(11): p. 7884-96.
241. Lu, H., et al., *Chemotherapy-Induced Ca(2+) Release Stimulates Breast Cancer Stem Cell Enrichment.* Cell Rep, 2017. **18**(8): p. 1946-1957.
242. Sanin, D.E., C.T. Prendergast, and A.P. Mountford, *IL-10 Production in Macrophages Is Regulated by a TLR-Driven CREB-Mediated Mechanism That Is Linked to Genes Involved in Cell Metabolism.* J Immunol, 2015. **195**(3): p. 1218-32.
243. Zhang, X., et al., *Positive Regulation of Interleukin-1beta Bioactivity by Physiological ROS-Mediated Cysteine S-Glutathionylation.* Cell Rep, 2017. **20**(1): p. 224-235.
244. Chavez-Sanchez, L., et al., *Innate immune system cells in atherosclerosis.* Arch Med Res, 2014. **45**(1): p. 1-14.
245. Lee, J., *Adipose tissue macrophages in the development of obesity-induced inflammation, insulin resistance and type 2 diabetes.* Arch Pharm Res, 2013. **36**(2): p. 208-22.
246. Minciullo, P.L., et al., *Inflammaging and Anti-Inflammaging: The Role of Cytokines in Extreme Longevity.* Arch Immunol Ther Exp (Warsz), 2016. **64**(2): p. 111-26.
247. Johnson, A.R., J.J. Milner, and L. Makowski, *The inflammation highway: metabolism accelerates inflammatory traffic in obesity.* Immunol Rev, 2012. **249**(1): p. 218-38.
248. Chimenti, M.S., et al., *The interplay between inflammation and metabolism in rheumatoid arthritis.* Cell Death Dis, 2015. **6**: p. e1887.
249. Gaidt, M.M., et al., *Human Monocytes Engage an Alternative Inflammasome Pathway.* Immunity, 2016. **44**(4): p. 833-46.
250. Kayagaki, N., et al., *Caspase-11 cleaves gasdermin D for non-canonical inflammasome signalling.* Nature, 2015. **526**(7575): p. 666-71.
251. Coll, R.C. and L.A.J. O'Neill, *The Cytokine Release Inhibitory Drug CRID3 Targets ASC Oligomerisation in the NLRP3 and AIM2 Inflammasomes.* PLoS ONE, 2011. **6**(12): p. e29539.
252. Mariathasan, S., et al., *Cryopyrin activates the inflammasome in response to toxins and ATP.* Nature, 2006. **440**(7081): p. 228-32.
253. Hoss, F., et al., *Detection of ASC Speck Formation by Flow Cytometry and Chemical Cross-linking.* Methods Mol Biol, 2018. **1714**: p. 149-165.
254. Shi, H., A. Murray, and B. Beutler, *Reconstruction of the Mouse Inflammasome System in HEK293T Cells.* Bio Protoc, 2016. **6**(21).
255. Yen, J.H. and D. Ganea, *Interferon β induces mature dendritic cell apoptosis through caspase-11/caspase-3 activation.* Blood, 2009. **114**(7): p. 1344-54.
256. Kang, S.J., et al., *Dual Role of Caspase-11 in Mediating Activation of Caspase-1 and Caspase-3 under Pathological Conditions.* J Cell Biol, 2000. **149**(3): p. 613-22.
257. Man, S.M., et al., *Differential roles of caspase-1 and caspase-11 in infection and inflammation.* Sci Rep, 2017. **7**: p. 45126.
258. Jiang, H., et al., *Identification of a selective and direct NLRP3 inhibitor to treat inflammatory disorders.* J Exp Med, 2017. **214**(11): p. 3219-3238.
259. Evavold, C.L., et al., *The Pore-Forming Protein Gasdermin D Regulates Interleukin-1 Secretion from Living Macrophages.* Immunity, 2017.
260. Ivashkiv, L.B. and L.T. Donlin, *Regulation of type I interferon responses.* Nat Rev Immunol, 2014. **14**(1): p. 36-49.

261. Li, Y.J., et al., *Revealing the role of glutathione S-transferase omega in age-at-onset of Alzheimer and Parkinson diseases.* Neurobiol Aging, 2006. **27**(8): p. 1087-93.
262. Sampson, N., P. Berger, and C. Zenzmaier, *Redox signaling as a therapeutic target to inhibit myofibroblast activation in degenerative fibrotic disease.* Biomed Res Int, 2014. **2014**: p. 131737.
263. Snyder, G.A., et al., *Crystal structures of the Toll/Interleukin-1 receptor (TIR) domains from the Brucella protein TcpB and host adaptor TIRAP reveal mechanisms of molecular mimicry.* J Biol Chem, 2014. **289**(2): p. 669-79.
264. Raza, H., A. John, and J. Shafarin, *NAC attenuates LPS-induced toxicity in aspirin-sensitized mouse macrophages via suppression of oxidative stress and mitochondrial dysfunction.* PLoS One, 2014. **9**(7): p. e103379.
265. Menon, D., et al., *Glutathione transferase Omega 1 is required for the lipopolysaccharide-stimulated induction of NADPH oxidase 1 and the production of reactive oxygen species in macrophages.* Free Radical Biology and Medicine, 2014. **73**: p. 318-327.
266. McGarry, D.J., et al., *Proteome-wide identification and quantification of S-glutathionylation targets in mouse liver.* Biochem J, 2015. **469**(1): p. 25-32.
267. Dulhunty, A., et al., *The glutathione transferase structural family includes a nuclear chloride channel and a ryanodine receptor calcium release channel modulator.* J Biol Chem, 2001. **276**(5): p. 3319-23.
268. Bai, H., et al., *Cathepsin B links oxidative stress to the activation of NLRP3 inflammasome.* Exp Cell Res, 2018. **362**(1): p. 180-187.
269. Shi, J., et al., *Cleavage of GSDMD by inflammatory caspases determines pyroptotic cell death.* Nature, 2015. **526**(7575): p. 660-5.
270. Mayr, C., *Evolution and Biological Roles of Alternative 3'UTRs.* Trends Cell Biol, 2016. **26**(3): p. 227-237.
271. Rodriguez-Pascual, F., et al., *Glyceraldehyde-3-phosphate dehydrogenase regulates endothelin-1 expression by a novel, redox-sensitive mechanism involving mRNA stability.* Mol Cell Biol, 2008. **28**(23): p. 7139-55.
272. Kandli, M., et al., *Isolation and characterization of two evolutionarily conserved murine kinases (Nek6 and nek7) related to the fungal mitotic regulator, NIMA.* Genomics, 2000. **68**(2): p. 187-96.
273. Yissachar, N., et al., *Nek7 kinase is enriched at the centrosome, and is required for proper spindle assembly and mitotic progression.* FEBS Lett, 2006. **580**(27): p. 6489-95.
274. O'Regan, L. and A.M. Fry, *The Nek6 and Nek7 protein kinases are required for robust mitotic spindle formation and cytokinesis.* Mol Cell Biol, 2009. **29**(14): p. 3975-90.
275. Kim, S., S. Kim, and K. Rhee, *NEK7 is essential for centriole duplication and centrosomal accumulation of pericentriolar material proteins in interphase cells.* J Cell Sci, 2011. **124**(Pt 22): p. 3760-70.
276. Cohen, S., et al., *Nek7 kinase accelerates microtubule dynamic instability.* Biochim Biophys Acta, 2013. **1833**(5): p. 1104-13.
277. Tan, R., et al., *Nek7 Protects Telomeres from Oxidative DNA Damage by Phosphorylation and Stabilization of TRF1.* Mol Cell, 2017. **65**(5): p. 818-831.e5.
278. King, H.A. and A.P. Gerber, *Translatome profiling: methods for genome-scale analysis of mRNA translation.* Brief Funct Genomics, 2016. **15**(1): p. 22-31.
279. Yu, J., et al., *Mass spectrometry based detection of glutathione with sensitivity for single-cell analysis.* Rapid Commun Mass Spectrom, 2015. **29**(7): p. 681-9.
280. Bukowski, M.R., C. Bucklin, and M.J. Picklo, *Quantitation of protein S-glutathionylation by liquid chromatography-tandem mass spectrometry: correction for contaminating glutathione and glutathione disulfide.* Anal Biochem, 2015. **469**: p. 54-64.

281. Ridker, P.M., et al., *Antiinflammatory Therapy with Canakinumab for Atherosclerotic Disease.* N Engl J Med, 2017. **377**(12): p. 1119-1131.

Chapter 8

Appendix

8.1 NEK7 Glutathionylated peptides identified by Mass Spectrometry

Description	Score	Coverage	# Proteins	# Unique Peptides	# Peptides	# PSMs	# AAs	MW [kDa]	calc. pI					
NEK7	2903.41	70.86	1	26	26	127	302	34.5	8.25					
A2	Sequence	# PSMs	# Proteins	# Protein Groups	Protein Group Accessions	Modifications	ΔCn	IonScore	Exp Value	Charge	MH+ [Da]	ΔM [ppm]	RT [min]	# Missed Cleavages
High	KVQIFDLmDAK	8	1	1	NEK7	M8(Oxidation)	0.0000	74	7.12782E-07	2	1323.69780	0.02	39.14	1
High	TTAAHSLVGTPYYmSPER	12	1	1	NEK7	M14(Oxidation)	0.0000	63	9.0773E-06	3	1996.94510	0.87	33.52	0
High	KVQIFDLMDAK	1	1	1	NEK7		0.0000	63	1.06649E-05	3	1307.70371	0.65	45.81	1
High	ALRPDmGYNTLANFR	5	1	1	NEK7	M6(Oxidation)	0.0000	58	3.45109E-05	3	1754.86612	1.01	39.37	1
High	TTAAHSLVGTPYYMSPER	6	1	1	NEK7		0.0000	56	5.38216E-05	3	1960.95047	1.02	36.28	0
High	VQIFDLmDAKAR	1	1	1	NEK7	M7(Dioxidation)	0.0000	55	5.90142E-05	3	1438.73618	0.15	39.32	1
High	VQIFDLmDAKAR	7	1	1	NEK7	M7(Oxidation)	0.0000	55	6.47078E-05	3	1422.74063	-0.29	40.97	1
High	VQIFDLmDAK	10	1	1	NEK7	M7(Oxidation)	0.0000	54	7.31066E-05	2	1195.60320	0.33	50.60	0
High	ALRPDMGYNTLANFR	2	1	1	NEK7		0.0000	53	8.97339E-05	3	1738.87076	0.77	42.77	1
High	LGDLGLGR	3	1	1	NEK7		0.0000	52	0.000134883	2	800.46233	-0.25	35.06	0
High	RPDIAYYYDVAK	7	1	1	NEK7		0.0000	51	0.000153446	2	1409.74590	2.49	37.22	1
High	VQIFDLMDAK	2	1	1	NEK7		0.0000	48	0.000323561	2	1179.60832	0.37	54.73	0
High	VQIFDLMDAKAR	2	1	1	NEK7		0.0000	44	0.000770826	3	1406.74656	0.30	46.31	1
High	GQFSEVYR	7	1	1	NEK7		0.0000	42	0.001191123	2	985.47411	0.31	27.46	0
High	RPDIAYYYDVAKR	3	1	1	NEK7		0.0000	41	0.001428751	3	1565.84507	0.99	34.02	2
High	TTAAHSLVGTPYYmSPER	1	1	1	NEK7	M14(Dioxidation)	0.0000	41	0.001678636	3	2012.93991	0.81	32.35	0
High	DIKPANWFTATGVVK	3	1	1	NEK7		0.0000	40	0.002233349	3	1672.96415	0.49	49.81	1
High	ALRPDmGYNTLANFRIEK	2	1	1	NEK7	M6(Oxidation)	0.0000	38	0.003483025	4	2125.08803	0.96	39.49	2
High	EIDLLK	4	1	1	NEK7		0.0000	37	0.003697912	2	730.43450	-0.10	37.43	0
High	qLNHPNVIK	3	1	1	NEK7	N-Term(Gln->pyro-Glu)	0.0000	35	0.006222381	2	1045.57976	0.78	29.63	0
High	IHENGYNPK	12	1	1	NEK7	N4(Deamidated)	0.0000	35	0.006698176	3	1122.51935	-1.89	22.49	0
High	IHENGYNPK	3	1	1	NEK7		0.0000	34	0.007761695	2	1121.53752	0.06	18.91	0
High	KVQIFDLmDAKAR	1	1	1	NEK7	M8(Oxidation)	0.0000	34	0.008451943	4	1550.83474	-0.82	32.37	2
High	VQIFDLmDAK	1	1	1	NEK7	M7(Dioxidation)	0.0000	33	0.008994076	2	1211.59795	0.19	46.66	0
High	ARADCIKEIDLLK	1	1	1	NEK7		0.0000	33	0.00933161	3	1487.82273	-1.60	40.53	2
High	mNLYSLCK	1	1	1	NEK7	M1(Oxidation)	0.0000	33	0.009461425	2	987.46391	0.08	40.86	0
High	IGRGQFSEVYR	4	1	1	NEK7		0.0000	33	0.010542815	3	1311.68103	0.44	27.71	1
High	KIEQcDYPPLPSDHYSEELR	1	1	1	NEK7	C5(Glutathione)	0.0000	31	0.017456476	4	2724.20107	3.44	36.51	1
High	QLNHPNVIK	2	1	1	NEK7		0.0000	28	0.031185777	2	1062.60637	0.83	17.67	0
High	RLIPER	1	1	1	NEK7		0.0000	27	0.03749355	2	783.48326	-0.42	18.40	1
High	qLNHPnVIK	3	1	1	NEK7	N-Term(Gln->pyro-Glu); M6(Deamic	0.0000	27	0.044152629	2	1046.56426	1.24	31.61	0
High	LGDLGLGRFFSSK	1	1	1	NEK7		0.0000	26	0.049540065	3	1396.75751	-0.64	50.90	1
High	ADcIKEIDLLK	1	1	1	NEK7	C3(Glutathione)	0.0000	24	0.073275125	4	1565.75405	-0.62	40.00	1
High	ARADcIKEIDLLK	1	1	1	NEK7	C5(Glutathione)	0.0000	21	0.143534588	4	1792.89272	-0.30	36.12	2
High	VmHRDIKPANVFITATGVVK	1	1	1	NEK7	M2(Oxidation)	0.0000	19	0.261792119	4	2212.23134	1.88	41.84	2
High	DEQSQGmQGPPVTQFQPQK	2	1	1	NEK7	M7(Oxidation)	0.0000	18	0.343523592	3	2145.98417	-1.35	35.89	0
High	qLVNICTNPDPEKR	1	1	1	NEK7	N-Term(Gln->pyro-Glu)	0.0000	14	0.779752128	2	1621.82390	-7.91	56.58	1
Medium	ASCLLDGVPVALK	1	1	1	NEK7		0.0000	14	0.816500713	2	1285.71465	-3.01	62.37	0

8.2 Conference Abstracts

Irish Society for Immunology, Cork, Ireland 2016

Title: Glutathionylation of Mal is critical for LPS-induced TLR4 Signalling

Mark M. Hughes and Luke A.J. O'Neill

Poster presentation

Glutathione, the most abundant cellular antioxidant, which binds to cysteine residues on proteins, has been recently linked as an inhibitory post-translational modification of caspase-1 and STAT3 function. MyD88 adapter-like (Mal) is the first protein to interact with Toll-like receptor (TLR) 2/4 to drive inflammatory cytokines within macrophages. We have identified that glutathionylation of cysteine 91 (C91) in Mal promotes Mal-MyD88 interaction, driving LPS-induced NFκB activation. Mutating C91 to alanine (C91A) inhibits Mal glutathionylation and acts as a dominant negative mutation, with compromised ability to interact with MyD88. The C91A mutation also displays diminished phosphorylation, known to be important for Mal function. Furthermore, positively charged amino acids adjacent to cysteines have been linked to increased glutathionylation. Preventing glutathionylation of C91 by mutation of the positively charged flanking amino acid histidine to proline (H92P) mimics the effects of C91A. Glutathione is thereby a novel positive regulator of Mal activity and shows the importance of this post-translational modification on TLR signalling.

Irish Society for Immunology, Dublin, Ireland 2017

Title: Glutathione Transferase Omega-1 is involved in LPS-induced Lethality: Evidence for a Role in Caspase-11 Regulation

Mark M. Hughes, Deepthi Menon, Philip G. Board and Luke A.J. O'Neill

Poster presentation

Recent evidence identified Caspase-11 as the key Caspase involved in sepsis. Macrophages require extreme precision when controlling their responses to extracellular ligands, such as microbial pattern associated molecular patterns (PAMPs), to prevent aberrant tissue damage and a hyper-inflammatory response. Toll-like receptors (TLRs) on macrophages recognize PAMPs and drive inflammation using reactive oxygen species (ROS) as a bactericidal mechanism. Glutathione (GSH) is the most abundant antioxidant in cells that supplies reducing equivalents to neutralize ROS. Without GSH, toxic levels of ROS can accumulate in tissues and blood, potentially amplifying tissue damage. Continued exposure can result in septic shock.

GSH conjugation to cysteine amino acids (termed glutathionylation) has been found to profoundly affect protein function. Caspase-1, which processes the major pro-inflammatory cytokine pro-IL-1β, has been found to be inhibited by glutathionylation. Glutathione transferase omega 1 (GSTO1-1), a deglutathionylating enzyme, has previously been implicated upstream of NF-κB on the TLR4 signalling pathway and is known for its role in poor cancer prognosis.

We have found that GSTO1-1 deficient mice are resistant to LPS lethality *in vivo*. An analysis of possible targets for GSTO1-1 revealed that GSTO1-1 is required for induction of caspase-11 and pyroptosis. We find that Caspase-11 is a glutathionylated enzyme. A novel enzymatic inhibitor of GSTO1-1 limited intracellular LPS-mediated pyroptosis. These findings extend our understanding of GSH as a regulatory modification in macrophage function and highlight GSTO1-1 as a novel regulator of cell death, making GSTO1-1 a promising therapeutic target.

8.3 Record of Publication

First author publications

Hughes, M.M., et al., Solution structure of the TLR adaptor MAL/TIRAP reveals an intact BB loop and supports MAL Cys91 glutathionylation for signaling. Proceedings of the National Academy of Sciences, 2017. 114(32): p. E6480-e6489.

Review publications

Hughes, M.M. and L.A.J. O'Neill, Metabolic regulation of NLRP3. Immunological Reviews, 2018. 281(1): p. 88-98.

Hughes, M.M., A.F. McGettrick, and L.A. O'Neill, Glutathione and Glutathione Transferase Omega 1 as Key Posttranslational Regulators in Macrophages. Microbiology Spectrum, 2017. 5(1).

Other publications

Mills, E.L., et al., Itaconate is an anti-inflammatory metabolite that activates Nrf2 via alkylation of KEAP1. Nature, 2018. 556(7699): p. 113-117.

Ní Cheallaigh, C., et al., A Common Variant in the Adaptor Mal Regulates Interferon Gamma Signaling. Immunity, 2016. 44(2): p. 368-379.

Solution structure of the TLR adaptor MAL/TIRAP reveals an intact BB loop and supports MAL Cys91 glutathionylation for signaling

Mark M. Hughes[a,1], Peter Lavrencic[b,c,d,1], Rebecca C. Coll[a,c], Thomas Ve[b,c,e], Dylan G. Ryan[a], Niamh C. Williams[a], Deepthi Menon[a,f], Ashley Mansell[g], Philip G. Board[f], Mehdi Mobli[d,2], Bostjan Kobe[b,c,2], and Luke A. J. O'Neill[a,2]

[a]School of Biochemistry and Immunology, Trinity Biomedical Sciences Institute, Trinity College Dublin, Dublin 2, Ireland; [b]School of Chemistry and Molecular Biosciences, Australian Infectious Diseases Research Centre, The University of Queensland, Brisbane, QLD 4072, Australia; [c]Institute for Molecular Bioscience, The University of Queensland, Brisbane QLD 4072, Australia; [d]Centre for Advanced Imaging, The University of Queensland, Brisbane QLD 4072, Australia; [e]Institute for Glycomics, Griffith University, Southport, QLD 4222, Australia; [f]John Curtin School of Medical Research, Australian National University, Canberra, ACT 2601, Australia; and [g]Centre for Innate Immunity and Infectious Diseases, Hudson Institute of Medical Research, Monash University, Melbourne, VIC, 3168, Australia

Edited by Jonathan C. Kagan, Children's Hospital Boston, Boston, MA, and accepted by Editorial Board Member Ruslan Medzhitov June 28, 2017 (received for review February 2, 2017)

MyD88 adaptor-like (MAL) is a critical protein in innate immunity, involved in signaling by several Toll-like receptors (TLRs), key pattern recognition receptors (PRRs). Crystal structures of MAL revealed a nontypical Toll/interleukin-1 receptor (TIR)-domain fold stabilized by two disulfide bridges. We therefore undertook a structural and functional analysis of the role of reactive cysteine residues in the protein. Under reducing conditions, the cysteines do not form disulfides, but under oxidizing conditions they are highly amenable to modification. The solution structure of the reduced form of the MAL TIR domain, determined by NMR spectroscopy, reveals a remarkable structural rearrangement compared with the disulfide-bonded structure, which includes the relocation of a β-strand and repositioning of the functionally important "BB-loop" region to a location more typical for TIR domains. Redox measurements by NMR further reveal that C91 has the highest redox potential of all cysteines in MAL. Indeed, mass spectrometry revealed that C91 undergoes glutathionylation in macrophages activated with the TLR4 ligand lipopolysaccharide (LPS). The C91A mutation limits MAL glutathionylation and acts as a dominant negative, blocking the interaction of MAL with its downstream target MyD88. The H92P mutation mimics the dominant-negative effects of the C91A mutation, presumably by preventing C91 glutathionylation. The MAL C91A and H92P mutants also display diminished degradation and interaction with interleukin-1 receptor-associated kinase 4 (IRAK4). We conclude that in the cell, MAL is not disulfide-bonded and requires glutathionylation of C91 for signaling.

MAL/TIRAP | glutathione | Toll-like receptor | NMR spectrometry | inflammation

Toll-like receptors (TLRs) are an important class of pattern recognition receptors. Upon recognition of pattern-associated molecular patterns, TLRs undergo dimerization. The consequent dimerization of the cytoplasmic Toll/interleukin-1 receptor (IL-1R)/resistance protein (TIR) domains leads to the recruitment of TIR domain-containing adaptor proteins, such as MyD88 and MyD88 adaptor-like (MAL; or TIRAP). MAL is required to recruit MyD88 to multiple TLRs, including TLR2 (1, 2), TLR4 (3), and TLR9 (4). The assembly culminates in an oligomeric assembly of kinases, including IRAK2 and IRAK4 (5, 6), termed the Myddosome, leading to NF-κB activation and inflammatory gene expression.

The crystal structures of the TIR domain of MAL (7–10) showed significant differences from the structures of other TIR domains, including MyD88 (11), IL-1 receptor accessory protein-like 1 (IL-1RAPL) (12), TLR1, TLR2 (13), and TLR10 (14). In particular, the MAL TIR-domain structures lack helix αB and feature a long AB loop situated between helix αA and β-strand βB, which includes the conserved and functionally important BB-loop proline-containing motif (15–17). Furthermore, these crystal structures contain two disulfide bonds involving residues C89–C134 and C142–C174, respectively. The presence of disulfides is unusual for a cytosolic protein and poses an intriguing possibility of redox control of MAL-mediated signaling.

Posttranslational modifications of MAL have been studied extensively (18–22); however, redox mechanisms affecting MAL have not been characterized. Glutathione (γ-L-glutamyl-L-cysteinyl-glycine; GSH), a tripeptide composed of the amino acids glutamic acid, cysteine, and glycine, is the most abundant nonprotein tripeptide and is used by the cell to maintain redox homeostasis and prevent overoxidation of cytoplasmic components (23). The cysteine thiol group (-SH) forms a mixed disulfide with GSH, which can be spontaneously or enzymatically catalyzed. GSH, however, does not act solely as an antioxidant. Recent evidence has identified that GSH can act as both a positive and negative regulator of proteins, regulating STAT3 phosphorylation (24),

Significance

Toll-like receptor (TLR) signaling pathways are targeted to limit inflammation in immune cells. TLRs use adaptor proteins to drive inflammatory signaling platforms for effective microbial clearance. Here we show that MyD88 adaptor-like (MAL), an adaptor protein in TLR signaling, undergoes glutathionylation in response to LPS, driving macrophage responses to proinflammatory stimuli. We also determined the solution structure of MAL in the reduced form without disulfides, revealing a typical BB loop observed in adaptor proteins, in contrast to previously reported crystal structures. This alternate solution structure reveals the inherent flexibility of MAL, supporting the hypothesis that glutathionylation may reposition the MAL BB loop for MyD88 interaction to drive inflammation. This discovery could lead to novel approaches to target MAL glutathionylation in dysregulated TLR signaling, limiting inflammation.

Author contributions: M.M.H., P.L., R.C.C., T.V., M.M., B.K., and L.A.J.O. designed research; M.M.H., P.L., T.V., D.G.R., and N.C.W. performed research; M.M.H., P.L., R.C.C., T.V., D.M., A.M., P.G.B., M.M., B.K., and L.A.J.O. analyzed data; and M.M.H., P.L., M.M., B.K., and L.A.J.O. wrote the paper.

The authors declare no conflict of interest.

This article is a PNAS Direct Submission. J.C.K. is a guest editor invited by the Editorial Board.

Data deposition: The sequences reported in this paper have been deposited in the Protein Data Bank [(PDB ID code 2Y92 (MAL crystal structure) and PDB ID code 2NDH (MAL solution NMR structure)].

[1]M.M.H. and P.L contributed equally to this work.

[2]To whom correspondence may be addressed. Email: m.mobli@uq.edu.au, b.kobe@uq.edu.au, or laoneill@tcd.ie.

This article contains supporting information online at www.pnas.org/lookup/suppl/doi:10.1073/pnas.1701868114/-/DCSupplemental.

caspase-1 activity (25), and the anion carrier proteins mitochondrial uncoupling proteins 2 and 3 (UCP2 and UCP3) (26). GSH has also been linked to stabilization of hypoxia-inducible factor 1-α (HIF1α) under ischemic conditions (27).

Here, we present the structural and functional characterization of the role of reactive cysteine residues in MAL. We determined the solution structure of the C116A mutant of TIR domain of MAL, observing remarkable structural differences compared with the disulfide-bonded structure, including the relocation of a β-strand and repositioning of the BB-loop region to a location more typical for TIR domains. C91 is found to be the most reactive cysteine in the protein, and indeed is shown to undergo glutathionylation in macrophages. This glutathionylation is required for the interaction of MAL with MyD88 and subsequent phosphorylation and degradation by IRAK4. Jointly, our data show that the disulfide-bonded form of MAL is unlikely to be the signaling-competent form in the cell, but that modification of reactive cysteines is functionally important, in particular glutathionylation of C91 during signaling.

Results

Redox States of Cysteines in *Escherichia-coli*-Expressed MAL^{TIR}. The crystal structures of the TIR domain of MAL (7–10) revealed two disulfide bonds involving residues C89–C134 and C142–C174, respectively. To analyze the redox states of cysteine residues under different redox conditions, we expressed the protein corresponding to its TIR domain (residues 79–221; MAL^{TIR}) in three different *Escherichia coli* (*E. coli*) cell types (BL-21, SHuffle, and Origami). BL-21 cells contain a reducing cytosolic environment, similar to eukaryotic cells. On the other hand, SHuffle and Origami are strains that have been engineered so that cytoplasmic reductive pathways are impaired, resulting in an oxidative cytosolic environment that promotes the formation of cytoplasmic disulfide bonds (28). MAL^{TIR} produced in all three bacterial strains yielded a similar elution profile by size-exclusion chromatography (*SI Appendix*, Fig. S1). Ellman's reagent was used to estimate the average percentage of reduced cysteine residues in MAL^{TIR} (*SI Appendix*, Table S1). These results indicate that the cysteine residues in MAL^{TIR} are in the reduced form under reducing conditions, but are sensitive to redox modifications. The intact mass of MAL^{TIR}-expressed *E. coli* BL-21 cells was further analyzed using mass spectrometry, revealing the possible presence of one disulfide bond.

To analyze the role of individual cysteine residues in MAL^{TIR}, single-cysteine mutants were produced in both BL-21 and SHuffle cells (*SI Appendix*, Fig. S1). The results show that some cysteine residues are more prone to oxidation than others (*SI Appendix*, Table S2). Exposure of MAL^{TIR} to 5 mM oxidized glutathione (GSSG) resulted in a number of modifications including *S*-glutathionylation, dioxidation and dehydroalanine formation (*SI Appendix*, Table S3 and Fig. S2). Taken together, our results show that the cysteine residues of MAL are susceptible to modifications in solution.

NMR Solution Structure of MAL^{TIRC116A} Reveals Remarkable Structural Differences from the Crystal Structures. We used NMR spectroscopy to characterize MAL^{TIR} structurally. To identify the best experimental conditions for such studies, the effects of temperature and protein concentration on the stability of MAL^{TIR} and its single-cysteine mutants were examined. The protein was less prone to precipitation at lower temperatures and lower concentrations. Remarkably, precipitated protein could be resolubilized by incubation on ice. The cysteine mutations had varying effects on the MAL^{TIR} structure, with several mutants including C91A showing very few differences and the C157A mutant showing the highest differences from the wild-type protein (*SI Appendix*, Tables S4 and S5 and Fig. S3). The C116A mutant protein (designated here as MAL^{TIRC116A}) was chosen for further structural studies due to high protein expression levels and as it remained monomeric for ∼12 h in solution at high concentrations. The NMR data were acquired as multiple parts that were coassembled for processing [details reported elsewhere (29)]. For the MAL^{TIRC116A} protein, 72% of all atoms could be assigned; the unassigned 28% were mostly in the disordered regions of the proteins. The calculations yielded an ensemble of 20 structures with a heavy-atom amide-backbone (NH, C_α, C′) rmsd of 1.28 Å (*SI Appendix*, Table S6 and Fig. S4).

Typical TIR-domain structures feature a central five-stranded parallel β-sheet (strands βA–βE) surrounded by five α-helices (αA–αE) on both sides of the sheet (30). By contrast, the crystal structures of MAL^{TIR} (7–10) revealed an absence of helix αB; the sequence corresponding to strand βB in typical TIR domain structures is instead located in the long and flexible AB loop. The solution structure of the reduced form of MAL^{TIRC116A} reveals that the secondary-structure arrangement is more consistent with a typical TIR-domain fold than with the crystal structures of MAL^{TIR} (Fig. 1, *SI Appendix*, Figs. S4 and S5, and Movie S1). The AB loop connecting αA and βB is short, comprising only 7 residues (109–115). This loop is followed by the strand βB (residues 116–119), as supported by a large number of short- to medium-range interresidue NOEs (*SI Appendix*, Fig. S6). Because resonance assignments of the backbone residues of wild-type MAL^{TIR} could be made in this region, we were able to confirm that the secondary structures of these residues (116–119) in both the MAL^{TIRC116A} and the wild-type MAL^{TIR} protein were consistent with the formation of a β-strand. This arrangement allows for the formation of a long flexible BB loop between the strand βB and the helix αB; the loop corresponds to residues 120–134. This loop contains many unassigned atoms, and those assigned show few long-range NOEs, suggesting inherent flexibility. The helix αB is short (comprising 5 residues), similar to MyD88^{TIR}; for comparison, it comprises 11 residues in TLR1^{TIR} and 9 residues in TcpB^{TIR}, a bacterial MAL mimetic which disrupts TLR signaling.

The chemical shifts of the C_β atoms of the six cysteine residues in MAL^{TIRC116A} range from 25.8 to 31.4 ppm, which indicates they are all reduced. The solution structure contains one pair of cysteine residues (C142 and C174) in close-enough proximity (5.4–6.9 Å) for possible disulfide-bond formation; however, chemical shifts of cysteine C_β atoms indicate that they are both reduced. The comparison of NMR spectra of MAL^{TIRC116A} at pH values 7.5, 8.0, or 8.6 (*SI Appendix*, Table S7 and Fig. S7) suggests that the structure remains unchanged over the tested pH conditions.

MAL^{TIR} Is Sensitive to Redox Change. Exposure of the wild-type MAL^{TIR} to redox conditions that ranged from "fully reducing" (GSH only) to "fully oxidizing" (GSSG only) and included three physiological conditions (31) of −225 mV, −199 mV, and ,190 mV, indicated that cysteines varied in reactivity. Major changes in chemical shifts were observed for the fully oxidizing condition containing only GSSG, especially for cysteine residues 89, 91, and 157 (*SI Appendix*, Fig. S8). Cysteine residue 91 was the most reactive, with 45% signal loss at −190 mV, compared with −225 mV, indicating that this residue had undergone oxidation to a large extent. The data suggest that the redox potential of C91 is close to −190 mV, whereas cysteines C89, 134, 142, and 172 have a redox potential <−190 mV and that C116 and C157 have redox potentials <<−190 mV. Cysteines are prone to modifications in an oxidative environment induced by inflammatory stimuli and the modifications have been shown to act as signals, for example in peroxiredoxin secretion from exosomes (32).

MAL Is Glutathionylated Endogenously. Bioinformatic analyses of MAL identified conservation of cysteine residues across most species, including human, mouse, and rabbit, except for C174, which is variable in these species (Fig. 2*A*). Given the reactive cysteines in MAL, we wished to test if it was glutathionylated endogenously. MAL was indeed glutathionylated basally and glutathionylation increased after 5 and 15 min of LPS treatment, and

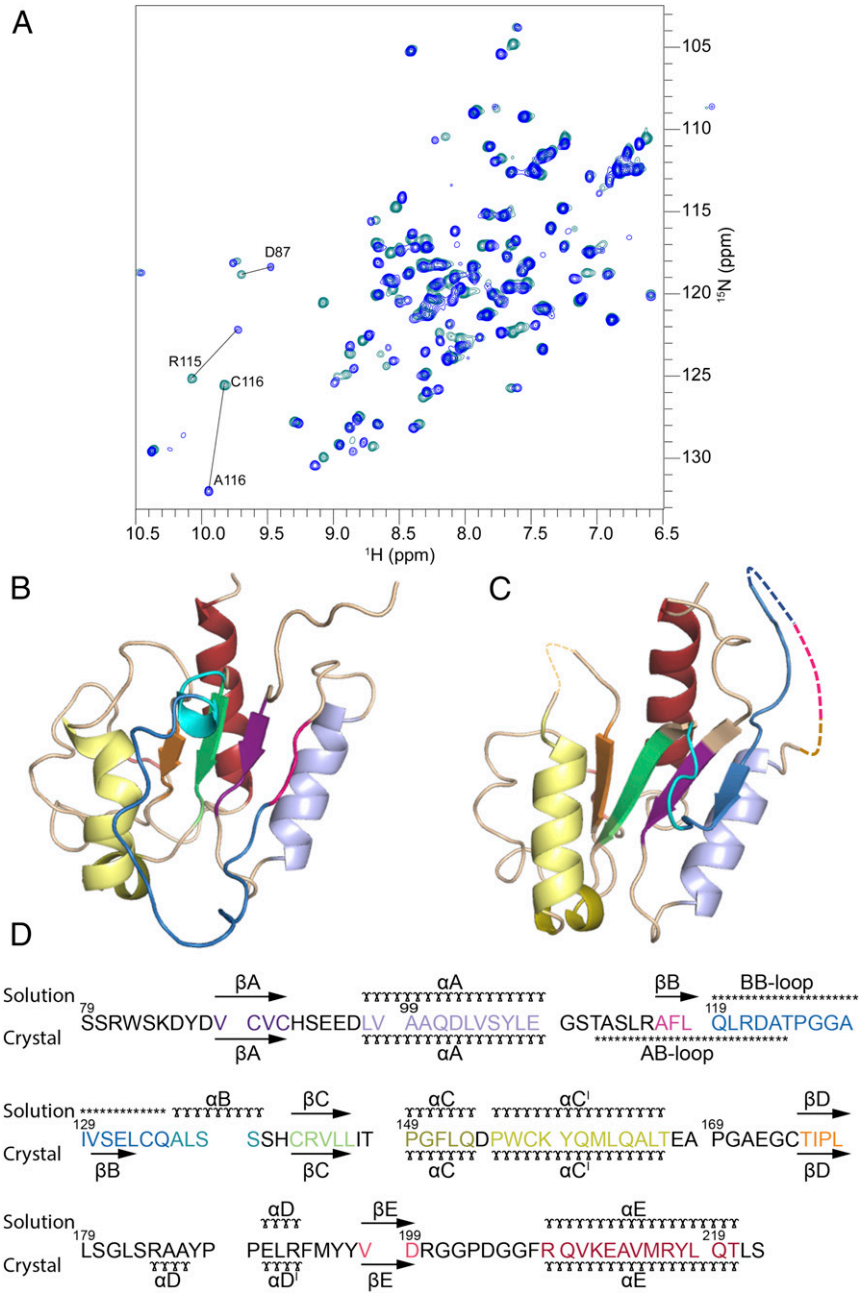

Fig. 1. Comparison of the solution and crystal structures of MAL^{TIR}. (*A*) Overlay of ^{1}H-^{15}*N*-HSQC spectra from MAL^{TIRC116A} (blue) and wild-type MAL^{TIR} (cyan). Most chemical shifts of ^{1}H and ^{15}N are conserved between the spectra, with large shifts detected only for the mutated C116 residue, the neighboring residue R115, and additionally, residue D87. (*B*) Solution structure of MAL^{TIRC116A}, shown in cartoon representation. (*C*) Crystal structure of MAL^{TIR} (7) (PDB ID Code 2Y92) shown as in *B*. Regions in the crystal structure comprising residues 112–123 (AB loop) and 168–171 do not have interpretable electron density and are not included in the crystal structure model; they are shown here for illustration purposes by dotted lines. (*D*) Structure-based sequence alignment, showing the elements of secondary structure. The solution secondary structure is based on the CYANA calculations (60). (↿) α-helix, (→) β-strand, (***) loop.

reverted to basal levels after 60 min of LPS treatment (Fig. 2*B*). To assess the glutathionylation site of MAL, we used cysteine-to-alanine mutants of MAL. Based on the evidence that cysteine 91 is the most reactive thiol, we chose the C91A mutant for initial functional studies. Overexpression of wild-type MAL and its C91A mutant (MAL^{C91A}) in HEK293 TLR4-MD2-CD14 cells (MTCs), followed by immunoprecipitation of MAL under non-reducing conditions, was performed to examine glutathionylation as a potential modification. To prevent deglutathionylation, we used the alkylating compound *N*-ethylmaleimide to modify free sulfhydryl groups. We also sought to identify if induction of TLR4 signaling by LPS would affect the potential glutathionylation status of MAL. Overexpressed wild-type MAL was found to be variably glutathionylated and underwent increased glutathionylation in response to LPS (Fig. 2*C*; compare lane 2 to lane 4), whereas MAL^{C91A} displayed decreased glutathionylation (Fig. 2C; compare lane 3 to lane 2), identifying that C91 is the main glutathione target in MAL.

Positively charged amino acids are known to influence cysteine susceptibility to glutathionylation. This occurs via deprotonation of neighboring cysteines, promoting cysteine thiolate anion formation, which would promote recruitment of glutathione to prevent further

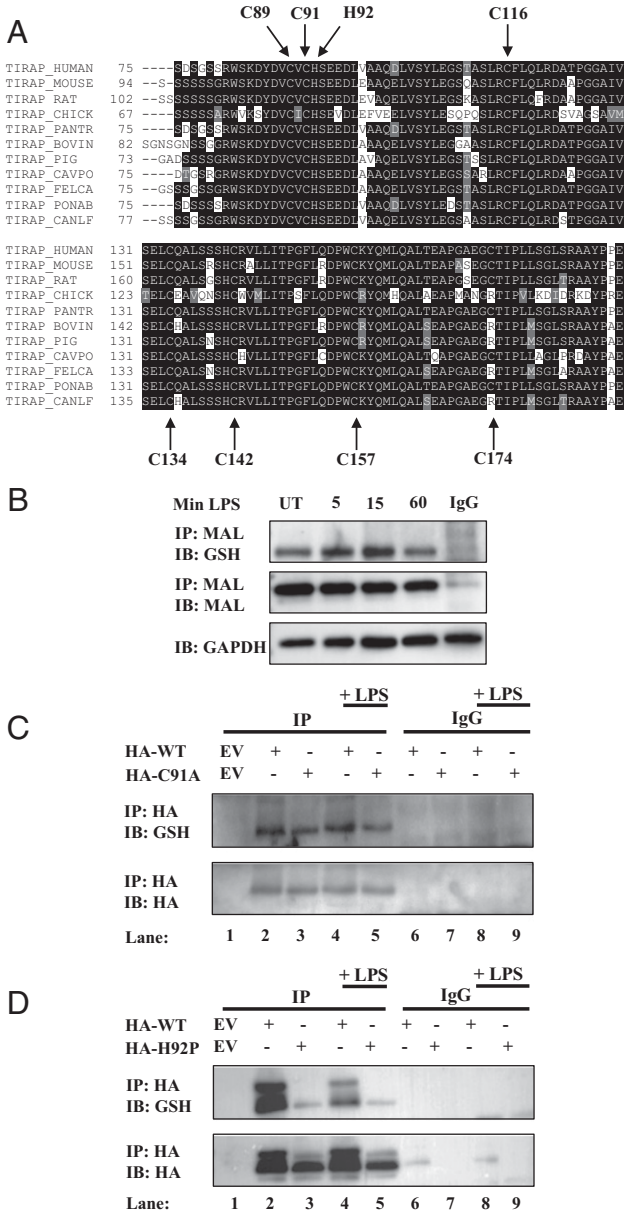

Fig. 2. MAL is glutathionylated on cysteine 91. (*A*) Sequence alignment highlighting MAL cysteine conservation across species. (*B*) BMDMs were treated with LPS (100 ng/mL) for 5, 15, or 60 min. Cells were lysed in low-stringency lysis buffer containing 50 mM *N*-ethylmaleimide. MAL was immunoprecipitated from lysate on A/G beads coated with MAL antibody and subjected to nonreducing SDS/PAGE. (*C* and *D*) MTC cells were transfected with empty vector, HA-tagged wild-type MAL, MAL^{C91A} (*C*), or MAL^{H92P} (*D*). Cells were treated with LPS (100 ng/mL) for 45 min. Cells were lysed in low-stringency lysis buffer containing 50 mM *N*-ethylmaleimide. MAL was immunoprecipitated from lysate on A/G beads coated with anti-HA antibody and subjected to nonreducing SDS/PAGE. The blots in *B*, *C*, and *D* are representative of three independent experiments.

oxidation (33). The flanking amino acid to C91, histidine 92, was mutated to proline (H92P) to eliminate the possible positive charge, which could in turn affect C91 glutathionylation. Indeed, MAL could not be glutathionylated in MAL^{H92P} (Fig. 2*D*).

MAL Mutations Limit TLR2 and TLR4 Signaling. TLR pathway activation can be measured using overexpressed MAL and an NF-κB luciferase reporter construct. We initially examined the effect of each cysteine mutant on LPS-treated MTC cells. NF-κB activation was not affected in cells transfected with most cysteine-to-alanine mutants, the notable exception being MAL^{C91A}, the overexpression of which had a dominant-negative effect (Fig. 3*A*). MAL^{C116A} could drive NF-κB activation similar to wild-type MAL, supporting the suggestion that this mutation had no significant effect on MAL structure and function, consistent with the NMR data. To confirm the dominant-negative effect of the C91A mutation, we overexpressed MAL^{C91A} in HEK293T cells. MAL^{C91A} overexpression could not drive NF-κB activation in HEK293T cells (Fig. 3*B*). Transfection of MAL^{C91A} into HEK293-TLR2 cells treated with TLR2 agonist Pam3Csk4 yielded similar results to TLR4-driven NF-κB activation; however, the dominant-negative effects of MAL^{C91A} are less pronounced (Fig. 3*C*). Transfection with MAL^{H92P} was also unable to drive NF-κB (Fig. 3*D*), and acted as a dominant-negative mutant against LPS (Fig. 3*E*) and Pam3Csk4 (Fig. 3*F*). MAL P125H, which is known to act as a dominant-negative mutant, served as a control, inhibiting NF-κB activation.

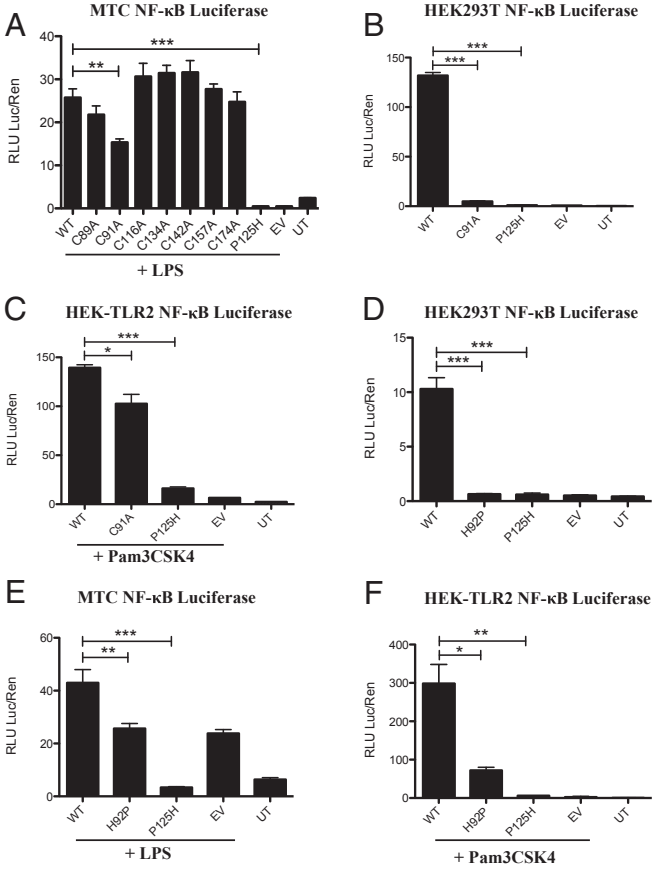

Fig. 3. Overexpression of MAL mutants limits NF-κB activation. MTC cells (*A* and *E*), HEK293T cells (*B* and *D*), and HEK-TLR2 cells (*C* and *F*) were transfected with wild-type MAL, MAL mutants, NF-κB reporter, and TK Renilla plasmids. Cells were lysed in 1× passive lysis buffer and lysates were used for NF-κB reporter assays. NF-κB activity was assayed using 1× Luciferase Assay Mix. TK Renilla fold was assayed using 1:500 dilution of coelenterazine in PBS. (*A* and *E*) MTC cells were treated with LPS (100 ng/mL) for 6 h before lysis with 1× passive lysis buffer. (*C* and *F*) HEK-TLR2 treated with Pam3Csk4 (100 ng/mL) for 6 h before lysis with 1× passive lysis buffer. Fluorescence was measured using FLUOstar Optima plate reader and gain adjustment was used to control for fluorescence. The data in *A*–*F* represent mean ± SEM of three individual experiments, each carried out in triplicate. $*P < 0.05$, $**P < 0.01$, $***P < 0.001$.

C91A and H92P MAL Mutants Cannot Reconstitute TLR4-Mediated IκBα Degradation. To further confirm impaired signaling by both MAL^{C91A} and MAL^{H92P}, we reconstituted MAL-deficient immortalized bone-marrow-derived macrophages (iBMDMs) and examined the degradation of the NF-κB inhibitory protein IκBα as a readout for NF-κB activation by TLR4 stimulation with LPS. The reconstitution of wild-type MAL yielded degradation of IκBα, with degradation reaching 50% at 90 min (Fig. 4*A*). Reconstitution of MAL-deficient iBMDMs with MAL^{C91A} failed to reconstitute TLR4 signaling, with no degradation of IκBα detected (Fig. 4*B*). Similarly, MAL^{H92P} did not reconstitute TLR4 signaling, with minimal degradation of IκBα (Fig. 4*C*).

C91A and H92P MAL Mutants Cannot Interact with MyD88. TLR stimulation induces MAL recruitment and interaction with MyD88 to drive formation of the Myddosome (4). We therefore sought to examine if MAL^{C91A} and MAL^{H92P} would be impaired in their ability to interact with MyD88. Wild-type MAL, when overexpressed, interacted with overexpressed MyD88 (Fig. 5*A*, lane 5, *Top*). MAL^{C91A}, however, did not interact with MyD88 (Fig. 5*A*, lane 6; compare with lane 5, *Top*). Lysates were examined to confirm the expression of each protein before immunoprecipitation (Fig. 5*A*, third and fourth panels). MAL^{C91A} appeared to express poorly when transfected (Fig. 5*A*, lane 3, fourth panel); however, cotransfection of MyD88 appeared to drive MAL^{C91A} expression to equal levels as wild-type MAL (Fig. 5*A*, lanes 5 and 6; compare with lane 2, *Bottom*). Similarly, when MAL^{H92P} was overexpressed, it failed to interact with MyD88, whereas wild-type MAL interacted with MyD88 (Fig. 5*B*, lane 6; compare with lane 5, *Top*). As above, lysates were examined for expression of plasmids before immunoprecipitation (Fig. 5*B*, third and fourth panels). These findings indicate that the C91A and H92P mutations prevent the interaction of MAL with MyD88, explaining the dominant-negative effect of these mutants.

IRAK4 Cannot Degrade or Interact with C91A and H92P MAL Mutants. It has been shown previously that IRAK1 and IRAK4 phosphorylate MAL on threonine 28, promoting MAL degradation (18, 22). We therefore sought to examine if the dominant-negative effects of MAL^{C91A} and MAL^{H92P} would affect IRAK1/4-mediated degradation of MAL. Overexpression of wild-type MAL with increasing concentrations of a plasmid encoding IRAK4 decreased MAL protein expression dose-dependently (Fig. 6*A*, *Top*). Overexpression of IRAK4 was unable to cause the degradation of MAL^{C91A} (Fig. 6*B*, *Top*). Correspondingly, overexpression of IRAK4 failed to induce degradation of MAL^{H92P} with increasing IRAK4 concentrations (Fig. 6C, *Top*).

As shown previously, the kinase-dead form (KD), but not kinase-active form of IRAK4, interacts with MAL (18). We therefore examined whether IRAK4-KD could interact with MAL mutants. As shown in Fig. 6*D*, wild-type MAL did not interact with IRAK4 when overexpressed (*Top*, lane 2), as expected, nor did the MAL^{C91A} or MAL^{H92P} mutants (*Top*, lanes 3 and 4, respectively). Wild-type MAL interacted strongly with IRAK4-KD (*Top*, lane 5); however, this interaction was attenuated with MAL^{C91A} and MAL^{H92P} (*Top*, lanes 6 and 7). Wild-type MAL was considerably depleted in lysates from IRAK4-transfected cells as opposed to cells transfected with IRAK4-KD (compare lane 2 to lane 5, third panel). However, the level of expression of the MAL^{C91A} and MAL^{H92P} mutants was similar between IRAK4 and IRAK4-KD (third panel; compare lanes 3 and 4 to lanes 6 and 7). Comparable levels of IRAK4 and IRAK4-KD were present before immunoprecipitation (*Bottom*).

Discussion

The crystal structures of the TIR domain of MAL (7–10) all show unusual features compared with other TIR-domain structures, in particular the presence of two disulfide bridges and the presence of a long flexible AB loop. We therefore aimed to characterize the TIR domain of MAL and its cysteine mutants in solution. Based

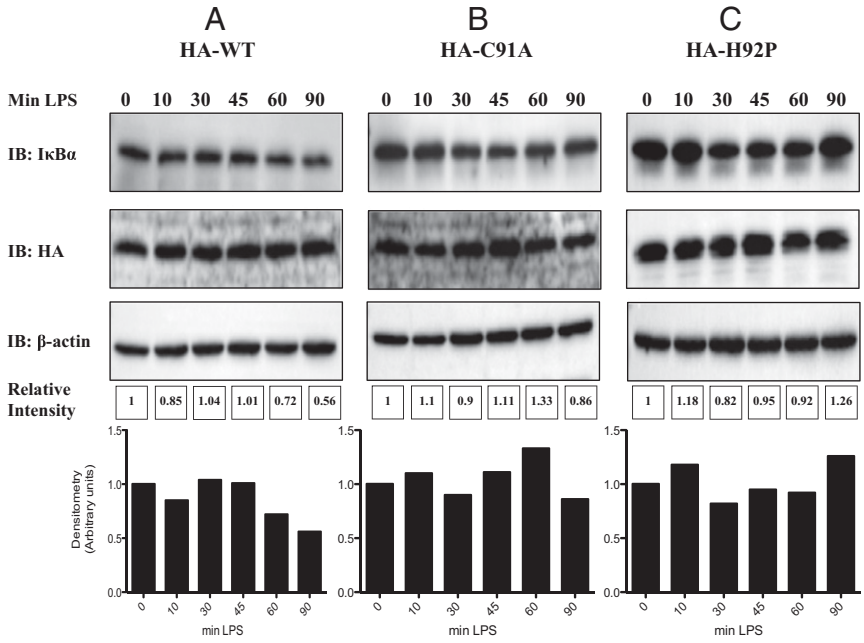

Fig. 4. C91A and H92P MAL mutants fail to reconstitute TLR4 signaling in MAL-deficient iBMDMs. (*A*) MAL-deficient iBMDMs were reconstituted with 5 μg of MAL wild-type plasmid, (*B*) 5 μg MAL^{C91A}, or (C) 5 μg MAL^{H92P} using the Neon electroporation system. MAL-deficient iBMDMs (1.1×10^6 cells/mL) were resuspended in 110 μL buffer R and 5 μg of wild-type MAL, MAL^{C91A}, or MAL^{H92P}. iBMDMs were immediately loaded to a 100 μL Neon tip and electroporated at 1,680 V for 20 ms and one pulse. Electroporated cells (100 μL) were placed directly into 900 μL prewarmed antibiotic-free media and incubated at 37 °C and 5% CO_2 overnight. Immediately the next morning, the cells were washed with PBS, media replaced with fresh DMEM containing 10% FCS, and treated with LPS for the times indicated. Cells were lysed in 5× sample-loading buffer and subjected to SDS/PAGE. IκBα, HA-tag, and β-actin were assessed by Western blot. The blots in *A*–*C* are representative of three independent experiments. Densitometry was performed using ImageLab 5.0 using β-actin as a loading control.

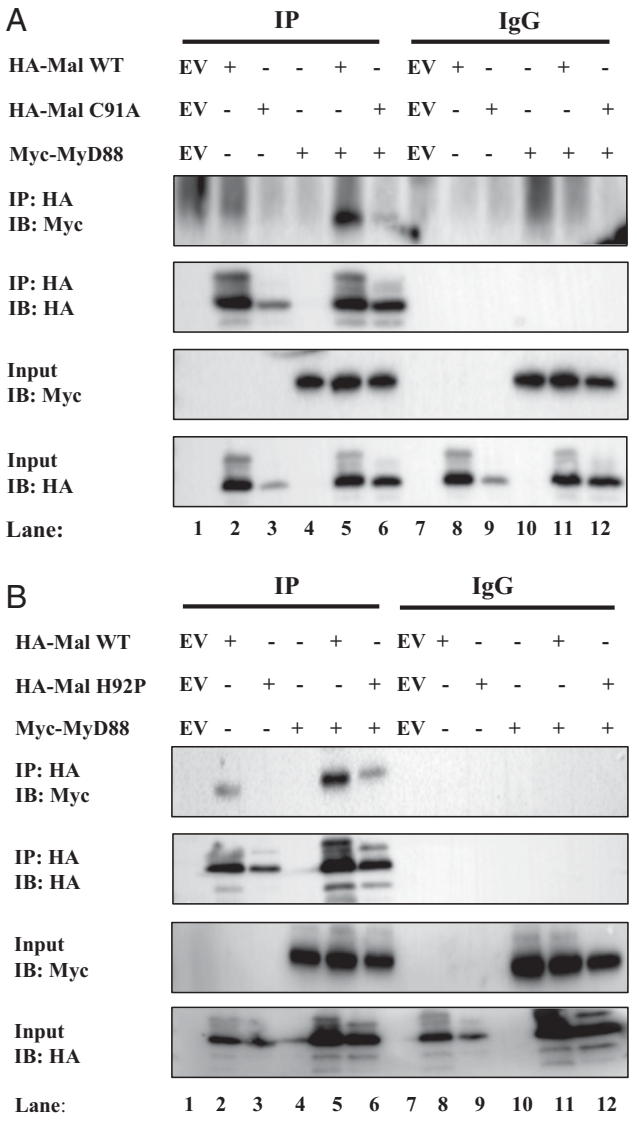

Fig. 5. MAL mutants C91A and H92P cannot interact with MyD88. (*A* and *B*) HEK293T cells were transfected with wild-type MAL, Myc-MyD88, EV, and (*A*) MAL^{C91A} or (*B*) MAL^{H92P}. In each transfection, the total concentration of plasmid DNA was kept constant by addition of relevant EV control. Post-transfection (48 h), the cells were lysed in low-stringency lysis buffer. Fifty μL of lysate was kept for analysis, while the remaining lysate was added to protein A/G beads coated with 1 μg of anti-HA antibody or 1 μg mouse-IgG control antibody for 2 h rotating at 4 °C. Samples were washed three times in 1 mL low-stringency lysis buffer and dried A/G beads were resuspended in 50 μL sample-loading buffer. Whole cell lysates and immunoprecipitated samples were analyzed by SDS/PAGE. Proteins were detected by immunoblot using anti-Myc and anti-HA antibodies. The results shown are representative of three independent experiments.

on the available MAL crystal structures, the construct comprising residues 79–221 (designated here as MAL^{TIR}) was selected for structural studies by solution NMR spectroscopy. The C116A mutant ($MAL^{TIRC116A}$) was found to have superior stability and behaved as a stable monomer, compared with the wild-type protein and other cysteine-to-alanine mutants. The $MAL^{TIRC116A}$ structure was found to be representative of the wild-type MAL^{TIR} protein, based on the comparison of chemical shifts and secondary structure analysis. The structure was solved at a pH of 8.6 in a high ionic strength of 200 mM sodium chloride. However, the comparison of spectra of ^{15}N-labeled MAL^{TIR} in the pH range of 8.6–7.5 shows that the structure is representative of a more physiological pH (*SI Appendix*, Fig. S6). The extreme conditions of high salt and pH yielded suitable sample concentrations for NMR analysis. These conditions, however, result in a loss of signals at rapidly exchanging backbone amide NHs and poor signal-to-noise ratio of the NMR resonances. To overcome these difficulties, an unconventional data acquisition strategy and advanced processing methods at ultrahigh fields had to be used to produce a medium-to-low-resolution solution structure of MAL^{TIR} (29).

The solution structure shows a structural rearrangement in the protein compared with the crystal structures (Fig. 1, *SI Appendix*, Fig. S5, and Movie S1). Consistent with other "typical" TIR-domain structures, the solution structure contains a long BB loop (residues 120–134) situated between strand βB and helix αB. The BB loop is a conserved feature among TIR domains and a number of studies have identified it to be important for mediating homotypic TIR-domain interactions (15–17, 34, 35). The striking structural differences are the result of the secondary structure arrangement between residues 111 and 139 (Fig. 1, *SI Appendix*, Fig. S5, and Movie S1). The crystal structures contain a flexible AB loop corresponding to residues 111–124, linking helix αB and strand βB. This rearrangement is caused by cysteine residues 89 and 134 forming a disulfide bond and shifting the location of strand βB. In the solution structure, the C_α atoms of these two cysteine residues are 11 Å apart, making disulfide-bond formation unlikely (36). The second disulfide bond found in the crystal structures involves the pair C142 and C174. In the solution structure, these residues remain in close proximity (~6 Å); however, the chemical shifts of the Cβ-atoms from these residues suggest that the cysteine side chains are in a reduced state. In addition, these two cysteine residues are not conserved and are not likely required for the folding of the protein (7). The crystal structure of MAL^{TIR} has been used in a number of attempts to model the interactions involving this adaptor during signaling (7, 37–41); our work suggests that this structure may not be the signaling-competent form and questions the validity of the findings of these modeling studies. Our work now provides a more appropriate template structure for modeling approaches and interaction studies.

Our data point to C91 as being the most reactive cysteine in MAL and available for posttranslational modification. Indeed, we identified that MAL can be glutathionylated on this residue. MAL was basally glutathionylated in murine BMDMs, LPS transiently increased MAL glutathionylation, and the glutathionylation returned to basal levels after 60 min. Mutagenesis of C91 to alanine confirms this residue as the site of glutathionylation. Mutagenesis of the neighboring amino acid H92 also abrogated glutathionylation. MAL^{C91A} or MAL^{H92P} were unable to signal to NF-κB when overexpressed and acted as dominant-negative mutants of TLR4 signaling and could not reconstitute MAL-deficient cells. Interestingly, MAL^{C91A} showed only minor dominant-negative effects against TLR2. Previous reports suggest MAL is not required by TLR2 (42), which may explain the failure of MAL^{C91A} to exert a strong dominant-negative effect on TLR2. Finally, immunoprecipitation showed that the interaction with MyD88 of MAL^{C91A} or MAL^{H92P} was reduced, and both mutants failed to undergo degradation in response to IRAK4 overexpression. In the cell, glutathionylation of MAL on C91 might therefore be critical for MAL to signal via the Myddosome and IRAK4. As the modified residue is close to the BB loop, the modification could influence the conformation of this functionally important flexible loop.

Redox regulation of proteins is a rapidly evolving field. Increasing evidence suggests that during TLR-mediated immune activation, the cytosolic environment becomes more oxidizing. This can lead to the modification of cysteine residues on cytosolic proteins, most commonly to their oxidation by hydrogen peroxide (H_2O_2) species produced by NADPH (43), or by glutathionylation (44). Glutathionylation is emerging as an important posttranslational modification in a number of proteins including NF-κB (45). The

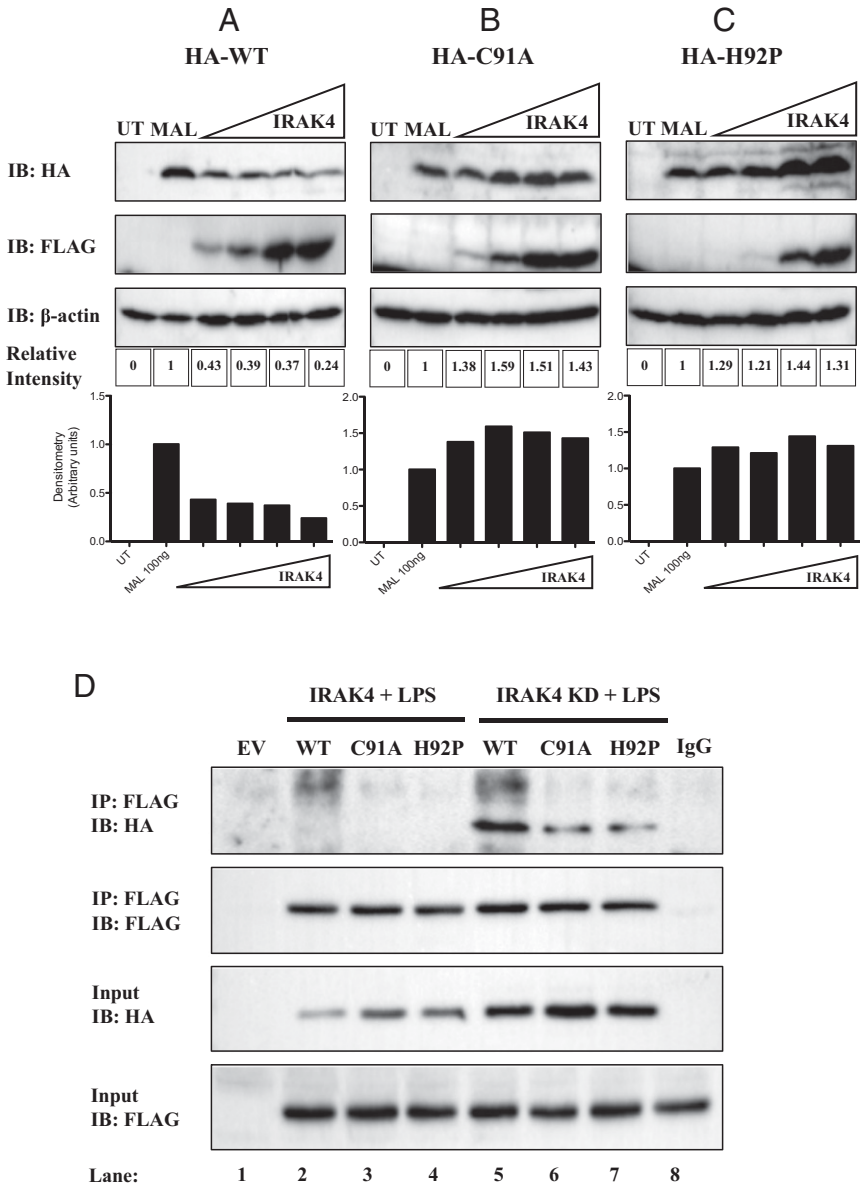

Fig. 6. IRAK4 cannot degrade or interact with C91A and H92P MAL mutants. HEK293T cells were transfected with FLAG-IRAK4, (*A*) wild-type MAL, (*B*) MAL^{C91A}, (*C*) MAL^{H92P}, or mock-transfected. In each transfection, the total concentration of plasmid DNA was kept constant by addition of relevant EV control. Posttransfection (24 h), the cells were lysed in 50 μL 5× sample-loading buffer. Cell lysates were analyzed by SDS/PAGE. Proteins were detected by immunoblot using anti-HA, anti-FLAG, and anti-β-actin antibodies. Densitometry was performed using ImageLab 5.0 software using β-actin as a loading control. (*D*) MTC cells were transfected with wild-type MAL, MAL^{C91A}, MAL^{H92P}, FLAG-IRAK4, kinase-dead FLAG-IRAK4 (IRAK4-KD), or EV. In each transfection, the total concentration of plasmid DNA was kept constant by addition of relevant EV control. Posttransfection (24 h), the cells were lysed in low-stringency lysis buffer. Fifty μL of lysate was kept for analysis, while the remaining lysate was added to protein A/G beads coated with 1 μg of anti-FLAG antibody or 1 μg mouse-IgG control antibody for 2 h rotating at 4 °C. Samples were washed three times in 1 mL low-stringency lysis buffer and dried A/G beads were resuspended in 50 μL sample-loading buffer. Whole-cell lysates and immunoprecipitated samples were analyzed by SDS/PAGE. Proteins were detected by immunoblot using anti-HA and anti-FLAG antibodies. The results shown are representative of three independent experiments.

glutathione transferase GSTO1-1 has been associated with the glutathionylation of cysteines in proteins in the TLR4 pathway, resulting in an on/off switch (46, 47). The precise target of GSTO1-1 in TLR4 signaling is unclear; however, the available evidence suggests that it regulates proteins early in the TLR4 signaling cascade, which could involve the cytosolic TIR domain of TLR4, MAL, or MyD88 (48). MyD88 has also been shown to be redox-regulated, with H_2O_2 treatment resulting in modification of MyD88 thiols (49). Glutathionylation of the redox enzyme glutathione transferase pi (GSTP) on cysteines 47 and 101 has been previously reported to alter its monomeric structure (50). Monomeric GSTP can associate with Jun N-terminal kinase (JNK) in resting cells, and dissociates from JNK under oxidative stress conditions, including H_2O_2 treatment, possibly by glutathionylation (51). We now contribute an example of glutathionylation of C91 in MAL, which appears to promote MyD88 and IRAK4 interaction. We identified glutathionylation of MAL as a positive regulatory mechanism in TLR4 activation, promoting Myddosome assembly for NF-κB activation.

Experimental Procedures

Biological Reagents, Mice, and Cell Culture. HEK293T cells were obtained from the Centre for Applied Microbiology and Research, Wiltshire, UK. MTCs and HEK293-TLR2 cells were purchased from Invivogen. All experiments were

carried out with prior ethical approval from the Trinity College Dublin Animal Research Ethics Committee (HPRA licence AE19136). C57BL/6 mice were killed using CO_2; bone marrow was extracted and differentiated using L929 media for 6 d into primary macrophages. All cell lines and primary cells were maintained in Dulbecco's modified Eagle's medium (DMEM) supplemented with 10% FCS, 1% penicillin/streptomycin, and maintained at 37 °C in a humidified atmosphere of 5% CO_2. The HA-tagged MAL plasmid has been described previously (15), and site-directed mutagenesis of this plasmid was performed to obtain HA-tagged MAL mutants using QuikChange II Mutagenesis Kit (Agilent Technologies). These plasmids were used for mammalian cell transfections. Anti-TIRAP (D6M9Z), Anti-IκBα (44D4), and Anti-Myc (2276S) antibodies were purchased from Cell Signaling Technology. Anti-HA.11 antibody was purchased from Biolegend (MMS-101R). Anti-HA (H3663), anti-FLAG (F3165), and anti-β-actin antibody (Clone AC-74) were purchased from Sigma. Anti-GSH antibody was obtained from ViroGen (101-A-100). Protein A/G beads (sc-2003) and Mouse IgG (sc-2025) were purchased from Santa Cruz Biotechnology. Rabbit IgG was obtained from Millipore (2455657). GeneJuice was purchased from Novagen (70967). LPS from *E. coli* serotype EH100 was obtained from Enzo Life Sciences (ALX-581-010). Neon transfection kit was purchased from Bio-sciences (MPK10096). Pam3Csk4 (tlrl-pms), Blasticidin (anti-bl-1), Normocin (anti-nr-2), and Hygromycin B Gold (anti-hg-1) were obtained from Invivogen. All other reagents were obtained from Sigma unless otherwise stated.

Coimmunoprecipitation Studies. HA-tagged MAL (3 μg) with 4 μg HA-tagged empty vector (EV) and 7 μg MAL mutants were coexpressed in HEK293T or MTC cells in 10-cm dishes. Cells were seeded at 2.5×10^5 cells per mL 24 h before transfection with GeneJuice per manufacturer's instructions. Once 70% confluent, cells were washed with PBS and lysed in 700 μL low-stringency lysis buffer (50 mM Hepes pH 7.5, 100 mM NaCl, 1 mM EDTA, 10% glycerol, 0.5% Nonident P-40). Supernatants were removed and agitated for 10 min by occasional vortexing. Supernatants were pelleted at 4 °C; 50 μL of each supernatant was retained to analyze expression of input. Supernatant was then added to relevant precoupled antibody on A/G beads. Samples were incubated for 2 h rotating at 4 °C. Following incubation, the beads were washed three times with wash buffer and boiled in sample-loading buffer before being subjected to SDS/PAGE. For glutathione immunoprecipitations, 50 mM *N*-ethylmaleimide was added to the low-stringency lysis buffer and treated as above. After washing beads three times, sample-loading buffer without DTT was added and gently heated at 50 °C for 10 min to aid elution off beads. For endogenous immunoprecipitations, BMDMs were seeded at 1×10^6 cells per mL in 10-cm dishes and treated with the same method as glutathione immunoprecipitations.

Reporter Assays. HEK293T, MTC, and HEK-TLR2 cells were seeded at 2×10^5 cells per mL The following day, cells were cotransfected with 20 ng NF-κB reporter plasmid and 50 ng of each respective MAL plasmid or EV using GeneJuice. In each experiment, 60 ng TK Renilla plasmid was transfected to normalize for transfection efficiency and cell death. After 24 h, reporter activity was assessed as previously described (52). Data are expressed as the mean relative light intensity folded over control pooled for three separate experiments with SEM.

Electroporation Assay. The Neon transfection system (100 μL tip) was used for transfection. MAL-deficient iBMDMs were harvested and resuspended to a density of 1.1×10^6 cells per mL in DMEM. Cells were washed once to remove media and resuspended in 110 μL of Buffer R. Resuspended cell suspension (100 μL) was electroporated at 1,680 V for 20 ms with one pulse for optimal transfection with minimal cell death. Immediately after, electroporation cells were placed in 900 μL DMEM without antibiotics in a 12-well plate and left to adhere overnight. Cells were washed with PBS and treated with LPS for indicated times. SDS/PAGE was carried out as listed above. Densitometry was calculated using ImageLab 5.0 software (Bio-Rad).

Expression in *E. coli* and Purification of MAL^{TIR} and Its Cysteine Mutants. BL-21, SHuffle (New England Biolabs) or Origami (Merck Millipore) *E. coli* cells were transformed by heat-shock with the pMCSG7 vector (53) encoding wild-type MAL^{TIR} (residues 79–221) or its mutants C89A, C91A, C116A, C134A, C142A, C157A, and C174A. The cells were then grown in 50-mL starter cultures of Luria's broth (LB) with 100 mg/L of ampicillin overnight at 37 °C. Cells were centrifuged at 800 × *g* and washed in M9 salts. One mL of starter culture was added to each flask containing 500 mL autoinduction media (54), with ^{15}N-labeled ammonium chloride added for the expression of ^{15}N-labeled protein (55), and grown while shaking at 37 °C until the optical density (OD) of each flask reached an absorbance of 0.8 at the wavelength of 600 nm. Once the OD was reached, the temperature was reduced to 20 °C for overnight protein expression. The cells were then lysed by sonication, and the protein was purified using nickel-affinity chromatography. Tobacco etch virus protease was added to the protein for an overnight incubation at 4 °C to cleave the 6-histidine tag from the protein. The protein was further purified by reeluting over the nickel-affinity column, followed by size-exclusion chromatography with a Superdex 75 gel-filtration column (GE Healthcare 26/600 S75) into a buffer consisting of 20 mM Tris·HCl (pH 8.6) with 200 mM NaCl.

Expression and Purification of ^{15}N and ^{13}C-Labeled $MAL^{TIRC116A}$. The plasmid coding for the C116A mutant of MAL^{TIR} ($MAL^{TIRC116A}$) was transformed into *E. coli* BL-21 cells by heat-shock, and grown overnight in a starter culture of LB in the presence of 100 mg/L ampicillin while shaking at 37 °C. The protein was then expressed in the same media while shaking at 37 °C until the cells reached an OD of 0.7 at the wavelength of 600 nm. The sample was centrifuged at 800 × *g*, washed in M9 salts, and resuspended in minimal M9 media containing ^{13}C glucose and ^{15}N ammonium chloride until the cell density reached an OD of 0.8 at the wavelength of 600 nm. The temperature was then reduced to 20 °C and the cells were induced with 1 mM isopropyl-1-thiogalactopyrano-side for overnight expression. The protein was purified as described above.

Structural Analysis by NMR. Double- and triple-resonance NMR experiments, including 2D ^1H-^{15}N-heteronuclear single quantum correlation (HSQC), 3D CbCacoNH, HbHacoNH, HNCaCb, HNCa, HNcoCA, HNCo, HNCa, HCcH, HCCh, ^{13}C-HSQC-NOESY (separate spectra for the aliphatic and aromatic regions), and ^{15}N-HSQC-NOESY (mixing time of 90 ms for all NOESY spectra), were conducted using ∼300 μM protein concentration, and 5-mm Shigemi tubes at 291 K on a 900-MHz Bruker Avance-III spectrometer equipped with a cryogenically cooled probe. All 3D experiments, excluding the NOESY spectra, were acquired using nonuniform sampling and processed using maximum entropy reconstruction as previously described (29, 56, 57). The ^1H, ^{15}N, and ^{13}C atom frequencies were assigned to the protein using the CCPNMR software (58), followed by backbone torsion-angle prediction calculations based on chemical shifts using TALOS+ (59) and NOE calculations using CYANA 3.0 (60). The structure has been deposited in the Protein Data Bank (PDB ID code 2NDH).

The ^1H and ^{15}N chemical shifts of purified ^{15}N-labeled MAL^{TIR} cysteine mutants were measured by ^1H-^{15}N-HSQC using a 900-MHz NMR spectrometer and analyzed with the CCPNMR software (58). The chemical shifts of each mutant were compared with the wild-type protein.

To compare the effect of pH on the structure, the ^{15}N-labeled $MAL^{TIRC116A}$ was divided and buffer-exchanged into three buffers, each made of 10 mM Hepes and 50 mM salt, at pH 7.5, 8.0, or 8.6. The chemical shifts of ^1H and ^{15}N were measured at each pH value and analyzed using the CCPNMR software (58).

NMR datasets were compared against each other using the Euclidean method for distance measurements, following the frequency assignment of ^1H and ^{15}N atoms in each ^1H-^{15}N-HSQC experiment using the CCPNMR software (58). Individual residues were compared by d^2, where $d^2(p_1, p_2) = (H_1 - H_2)^2 + (N_1 - N_2)^2$. Overall comparison between datasets was calculated using rmsd, where $\text{rmsd} = \sqrt{1/n \sum d^2(p_1, p_2)}$.

Determination of Redox Shifts of Cysteines in Wild-Type MAL^{TIR}. Stock solutions of GSH and GSSG were made in 10 mM Hepes buffer and adjusted to pH 7.5. Nitrogen was bubbled through both solutions to remove oxygen. A ^1H spectrum of each stock was measured using a 900-MHz magnet and analyzed with the TopSpin 3.2 (Bruker) software to confirm whether the stock-solution redox species were indeed reduced or oxidized. Purified ^{15}N-labeled wild-type MAL^{TIR} in 10 mM Hepes (pH 7.5) buffer was added to five different buffers containing varying ratios of GSH:GSSG that equate to specific electrochemical potentials (GSH only, −225 mV, −198.67 mV, −189.77 mV, and GSSG only). Electrochemical potential was calculated using the Nernst equation $E^o = E^o_{GSH/GSSG} - (RT/nF)\ \ln K_{eq}$, where $E^o_{GSH/GSSG}$ is the standard potential of glutathione at pH 7.5 (−240 mV) (61), R is the universal gas constant (8.314 $J\ K^{-1} \cdot m^{-1}$), T is the absolute temperature, *n* is the number of electrons transferred, *F* is the Faraday constant (9.648×10^4 C mol^{-1}), and K_{eq} is the equilibrium constant ($[GSH]^2/GSSG$). A ^1H-^{15}N-HSQC was completed for each of the redox conditions at 298 K, using a 900-MHz NMR spectrometer, to determine the chemical shifts and intensity of the resonances from each residue. To correct for non-redox-related contributions to intensity changes (e.g., salt concentrations, etc.), the intensities were normalized to the average of a set of signals (15 peaks) from residues that were distal to any cysteine residues and neither overlapped with other peaks nor were strongly perturbed by the titration.

Ellman's Assay. Wild-type MAL^{TIR} was purified from three types of *E. coli* cells (BL-21, SHuffle, and Origami), each with different cytosolic redox environments. The protein sample from BL-21 expression was split into three conditions: with the addition of 10 mM reducing agent 1,4-DTT, with the addition of 0.03 mM hydrogen peroxide, and with no addition. Ellman's reagent (dithiobisnitrobenzoic acid) was added to each of the five conditions before measuring the optical density at 412 nm using a spectrophotometer [NanoDrop, Thermo Scientific]. Calculations were performed based on the proportion of oxidized thiols, which correlated with the color intensity of the solution. The percent of reduced thiols in solution was used to calculate to the nearest number of reduced cysteine residues on MAL^{TIR}.

Mass Spectrometric Analysis of MAL Oxidized Using Glutathione. Purified wild-type MAL^{TIR} from *E. coli* BL-21 cells was buffer-exchanged into either 10 mM Hepes (pH 7.5) or 20 mM Tris (pH 8.6). Five mM GSSG was then added to each solution, while keeping another without glutathione for control. These samples were incubated at room temperature for 1 h before subjecting each to a trypsin digest. Samples were separated using reversed-phase chromatography on a Shimadzu Prominence nanoLC system. Using a flow rate of 30 μl/min, samples were desalted on an Agilent C18 trap (0.3 × 5 mm, 5 μm) for 3 min, followed by separation on a Vydac Everest C18 (300 A, 5 μm, 150 mm × 150 μm) column at a flow rate of 1 μl/min. A gradient of 10–60% buffer B over 30 min where buffer A = 1% ACN/0.1% Formic acid (FA) and buffer B = 80% ACN/0.1% FA was used to separate peptides. Eluted peptides were directly analyzed on a TripleTof 5600 instrument (ABSciex) using a Nanospray III interface. Gas and voltage settings were adjusted as required. An MS TOF scan across *m/z* 350–1800 was performed for 0.5 s followed by information-dependent acquisition of up to 20 peptides across *m/z* 40–1800 (0.05 s per spectra). Data were converted to mgf format and searched in MASCOT accessed via the Australian Proteomics Computational Facility. Data were searched in the SwissProt database, searching all species, with trypsin as enzyme, two miscleavages, MS tolerance of 50 ppm, MS/MS tolerance of 0.1 Da. Oxidation (Met, variable) and carbamidomethylation (Cys, fixed) modifications were also included.

Intact Mass. Intact masses were analyzed using purified wild-type MAL^{TIR} from *E. coli* BL-21 cells and directly measured on TripleTOF 5600 (Sciex) and Orbitrap Elite (Thermo) mass spectrometers. The presence of disulfide bonds was detected by comparing the measured mass of the protein to the theoretically calculated mass. The number of disulfide bonds in MAL^{TIR} was calculated using the theoretical mass of reduced MAL^{TIR}, which corresponded to 16,006 Da and 16,017 Da, for monoisotopic and average masses, respectively.

ACKNOWLEDGMENTS. We thank Professor Paul Hertzog for his contributions to troubleshooting electroporation parameters of iBMDMs. The Queensland NMR Network is acknowledged for providing access to the 900-MHz spectrometer. This work was funded by Science Foundation Ireland (12/IA/1531 to L.A.J.O.) and the National Health and Medical Research Council (NHMRC Grants 1003326, 1107804, and 1071659 to B.K.). B.K. is an NHMRC Principal Research Fellow (1003325 and 1110971). M.M. is supported by an Australian Research Council Future Fellowship (FT10100925).

1. Yamamoto M, et al. (2002) Essential role for TIRAP in activation of the signalling cascade shared by TLR2 and TLR4. *Nature* 420:324–329.
2. Horng T, Barton GM, Flavell RA, Medzhitov R (2002) The adaptor molecule TIRAP provides signalling specificity for Toll-like receptors. *Nature* 420:329–333.
3. Fitzgerald KA, et al. (2001) Mal (MyD88-adapter-like) is required for Toll-like receptor-4 signal transduction. *Nature* 413:78–83.
4. Bonham KS, et al. (2014) A promiscuous lipid-binding protein diversifies the subcellular sites of toll-like receptor signal transduction. *Cell* 156:705–716.
5. Motshwene PG, et al. (2009) An oligomeric signaling platform formed by the Toll-like receptor signal transducers MyD88 and IRAK-4. *J Biol Chem* 284:25404–25411.
6. Lin SC, Lo YC, Wu H (2010) Helical assembly in the MyD88-IRAK4-IRAK2 complex in TLR/IL-1R signalling. *Nature* 465:885–890.
7. Valkov E, et al. (2011) Crystal structure of Toll-like receptor adaptor MAL/TIRAP reveals the molecular basis for signal transduction and disease protection. *Proc Natl Acad Sci USA* 108:14879–14884.
8. Lin Z, Lu J, Zhou W, Shen Y (2012) Structural insights into TIR domain specificity of the bridging adaptor Mal in TLR4 signaling. *PLoS One* 7:e34202.
9. Snyder GA, et al. (2014) Crystal structures of the Toll/Interleukin-1 receptor (TIR) domains from the Brucella protein TcpB and host adaptor TIRAP reveal mechanisms of molecular mimicry. *J Biol Chem* 289:669–679.
10. Woo JR, Kim S, Shoelson SE, Park SY (2012) X-ray crystallographic structure of TIR-domain from the human TIR-domain containing adaptor protein/MyD88-adaptor-like protein (TIRAP/MAL). *Bull Korean Chem Soc* 33:3091–3094.
11. Ohnishi H, et al. (2009) Structural basis for the multiple interactions of the MyD88 TIR domain in TLR4 signaling. *Proc Natl Acad Sci USA* 106:10260–10265.
12. Khan JA, Brint EK, O'Neill LA, Tong L (2004) Crystal structure of the Toll/interleukin-1 receptor domain of human IL-1RAPL. *J Biol Chem* 279:31664–31670.
13. Xu Y, et al. (2000) Structural basis for signal transduction by the Toll/interleukin-1 receptor domains. *Nature* 408:111–115.
14. Nyman T, et al. (2008) The crystal structure of the human toll-like receptor 10 cytoplasmic domain reveals a putative signaling dimer. *J Biol Chem* 283:11861–11865.
15. Dunne A, Ejdeback M, Ludidi PL, O'Neill LA, Gay NJ (2003) Structural complementarity of Toll/interleukin-1 receptor domains in Toll-like receptors and the adaptors Mal and MyD88. *J Biol Chem* 278:41443–41451.
16. Li C, Zienkiewicz J, Hawiger J (2005) Interactive sites in the MyD88 Toll/interleukin (IL) 1 receptor domain responsible for coupling to the IL1beta signaling pathway. *J Biol Chem* 280:26152–26159.
17. Jiang Z, et al. (2006) Details of Toll-like receptor:adapter interaction revealed by germ-line mutagenesis. *Proc Natl Acad Sci USA* 103:10961–10966.
18. Dunne A, et al. (2010) IRAK1 and IRAK4 promote phosphorylation, ubiquitination, and degradation of MyD88 adaptor-like (Mal). *J Biol Chem* 285:18276–18282.
19. Gray P, et al. (2006) MyD88 adapter-like (Mal) is phosphorylated by Bruton's tyrosine kinase during TLR2 and TLR4 signal transduction. *J Biol Chem* 281:10489–10495.
20. Ulrichts P, et al. (2010) Caspase-1 targets the TLR adaptor Mal at a crucial TIR-domain interaction site. *J Cell Sci* 123:256–265.
21. Mansell A, et al. (2006) Suppressor of cytokine signaling 1 negatively regulates Toll-like receptor signaling by mediating Mal degradation. *Nat Immunol* 7:148–155.
22. Zhao X, et al. (2017) Membrane targeting of TIRAP is negatively regulated by phosphorylation in its phosphoinositide-binding motif. *Sci Rep* 7:43043.
23. Morris D, et al. (2013) Glutathione and infection. *Biochim Biophys Acta* 1830:3329–3349.
24. Xie Y, Kole S, Precht P, Pazin MJ, Bernier M (2009) S-glutathionylation impairs signal transducer and activator of transcription 3 activation and signaling. *Endocrinology* 150:1122–1131.
25. Meissner F, Molawi K, Zychlinsky A (2008) Superoxide dismutase 1 regulates caspase-1 and endotoxic shock. *Nat Immunol* 9:866–872.
26. Mailloux RJ, et al. (2011) Glutathionylation acts as a control switch for uncoupling proteins UCP2 and UCP3. *J Biol Chem* 286:21865–21875.
27. Watanabe Y, et al. (2016) Glutathione adducts induced by ischemia and deletion of glutaredoxin-1 stabilize HIF-1α and improve limb revascularization. *Proc Natl Acad Sci USA* 113:6011–6016.
28. Lobstein J, et al. (2012) SHuffle, a novel Escherichia coli protein expression strain capable of correctly folding disulfide bonded proteins in its cytoplasm. *Microb Cell Fact* 11:56.
29. Miljenović T, Jia X, Lavrencic P, Kobe B, Mobli M (2017) A non-uniform sampling approach enables studies of dilute and unstable proteins. *J Biomol NMR* 68:119–127.
30. Ve T, Williams SJ, Kobe B (2015) Structure and function of Toll/interleukin-1 receptor/resistance protein (TIR) domains. *Apoptosis* 20:250–261.
31. Schafer FQ, Buettner GR (2001) Redox environment of the cell as viewed through the redox state of the glutathione disulfide/glutathione couple. *Free Radic Biol Med* 30:1191–1212.
32. Mullen L, Hanschmann EM, Lillig CH, Herzenberg LA, Ghezzi P (2015) Cysteine oxidation targets peroxiredoxins 1 and 2 for exosomal release through a novel mechanism of redox-dependent secretion. *Mol Med* 21:98–108.
33. Dalle-Donne I, et al. (2008) Molecular mechanisms and potential clinical significance of S-glutathionylation. *Antioxid Redox Signal* 10:445–473.
34. Toshchakov VU, Basu S, Fenton MJ, Vogel SN (2005) Differential involvement of BB loops of toll-IL-1 resistance (TIR) domain-containing adapter proteins in TLR4- versus TLR2-mediated signal transduction. *J Immunol* 175:494–500.
35. Stack J, Bowie AG (2012) Poxviral protein A46 antagonizes Toll-like receptor 4 signaling by targeting BB loop motifs in Toll-IL-1 receptor adaptor proteins to disrupt receptor:adaptor interactions. *J Biol Chem* 287:22672–22682.
36. Waschütza G, et al. (1996) Engineered disulfide bonds in recombinant human interferon-gamma: The impact of the N-terminal helix A and the AB-loop on protein stability. *Protein Eng* 9:905–912.
37. Vyncke L, et al. (2016) Reconstructing the TIR side of the Myddosome: A paradigm for TIR-TIR Interactions. *Structure* 24:437–447.
38. Paracha RZ, et al. (2014) Structural evaluation of BTK and PKCδ mediated phosphorylation of MAL at positions Tyr86 and Tyr106. *Comput Biol Chem* 51:22–35.
39. Guven-Maiorov E, et al. (2015) The architecture of the TIR domain signalosome in the Toll-like receptor-4 signaling pathway. *Sci Rep* 5:13128.
40. Guven-Maiorov E, Keskin O, Gursoy A, Nussinov R (2015) A structural view of negative regulation of the Toll-like receptor-mediated inflammatory pathway. *Biophys J* 109:1214–1226.
41. Naro C, Sette C (2016) Dissecting a hub for immune response: Modeling the structure of MyD88. *Structure* 24:349–351.
42. Kenny EF, et al. (2009) MyD88 adaptor-like is not essential for TLR2 signaling and inhibits signaling by TLR3. *J Immunol* 183:3642–3651.
43. Ngkelo A, Meja K, Yeadon M, Adcock I, Kirkham PA (2012) LPS induced inflammatory responses in human peripheral blood mononuclear cells is mediated through NOX4 and Giα dependent PI-3kinase signalling. *J Inflamm (Lond)* 9:1.
44. Reynaert NL, et al. (2006) Dynamic redox control of NF-kappaB through glutaredoxin-regulated S-glutathionylation of inhibitory kappaB kinase beta. *Proc Natl Acad Sci USA* 103:13086–13091.
45. Liao BC, Hsieh CW, Lin YC, Wung BS (2010) The glutaredoxin/glutathione system modulates NF-kappaB activity by glutathionylation of p65 in cinnamaldehyde-treated endothelial cells. *Toxicol Sci* 116:151–163.

46. Menon D, Board PG (2013) A role for glutathione transferase Omega 1 (GSTO1-1) in the glutathionylation cycle. *J Biol Chem* 288:25769–25779.
47. Menon D, Coll R, O'Neill LA, Board PG (2014) Glutathione transferase omega 1 is required for the lipopolysaccharide-stimulated induction of NADPH oxidase 1 and the production of reactive oxygen species in macrophages. *Free Radic Biol Med* 73: 318–327.
48. Menon D, Coll R, O'Neill LA, Board PG (2015) GSTO1-1 modulates metabolism in macrophages activated through the LPS and TLR4 pathway. *J Cell Sci* 128:1982–1990.
49. Stottmeier B, Dick TP (2016) Redox sensitivity of the MyD88 immune signaling adapter. *Free Radic Biol Med* 101:93–101.
50. Tew KD, et al. (2011) The role of glutathione S-transferase P in signaling pathways and S-glutathionylation in cancer. *Free Radic Biol Med* 51:299–313.
51. Adler V, et al. (1999) Regulation of JNK signaling by GSTp. *EMBO J* 18:1321–1334.
52. Jefferies CA, et al. (2003) Bruton's tyrosine kinase is a Toll/interleukin-1 receptor domain-binding protein that participates in nuclear factor kappaB activation by Toll-like receptor 4. *J Biol Chem* 278:26258–26264.
53. Eschenfeldt WH, Lucy S, Millard CS, Joachimiak A, Mark ID (2009) A family of LIC vectors for high-throughput cloning and purification of proteins. *Methods Mol Biol* 498:105–115.
54. Studier FW (2005) Protein production by auto-induction in high density shaking cultures. *Protein Expr Purif* 41:207–234.
55. Tyler RC, et al. (2005) Auto-induction medium for the production of [U-15N]- and [U-13C, U-15N]-labeled proteins for NMR screening and structure determination. *Protein Expr Purif* 40:268–278.
56. Mobli M (2015) Reducing seed dependent variability of non-uniformly sampled multidimensional NMR data. *J Magn Reson* 256:60–69.
57. Mobli M, Maciejewski MW, Gryk MR, Hoch JC (2007) An automated tool for maximum entropy reconstruction of biomolecular NMR spectra. *Nat Methods* 4:467–468.
58. Vranken WF, et al. (2005) The CCPN data model for NMR spectroscopy: Development of a software pipeline. *Proteins* 59:687–696.
59. Shen Y, Delaglio F, Cornilescu G, Bax A (2009) TALOS+: A hybrid method for predicting protein backbone torsion angles from NMR chemical shifts. *J Biomol NMR* 44: 213–223.
60. Güntert P, Mumenthaler C, Wüthrich K (1997) Torsion angle dynamics for NMR structure calculation with the new program DYANA. *J Mol Biol* 273:283–298.
61. Gilbert HF (1995) Thiol/disulfide exchange equilibria and disulfide bond stability. *Methods Enzymol* 251:8–28.

Supporting Information

Hughes et al. 10.1073/pnas.1701868114

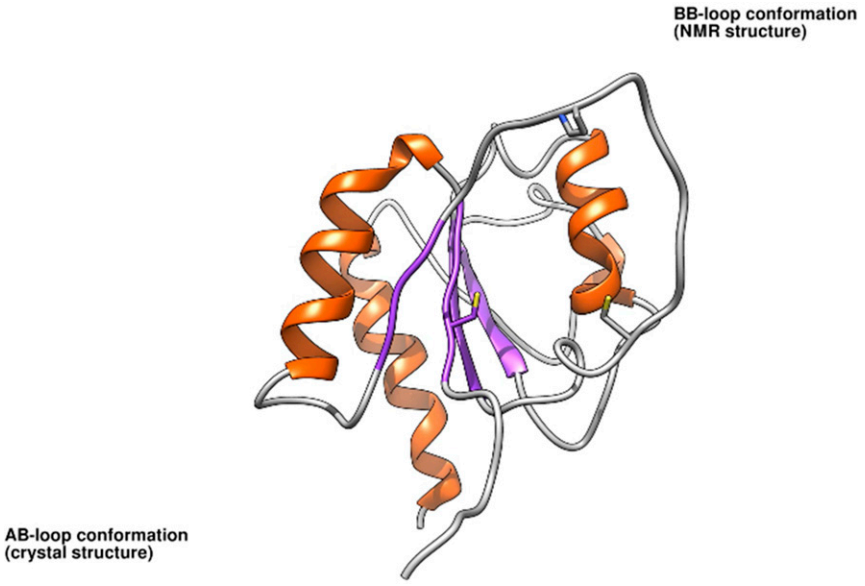

Movie S1. Morphing movie illustrating the transition between the crystal structure of MAL^{TIR} and the solution structure of $MAL^{TIRC116A}$. The structures are shown in cartoon representation, with the side chains of C89, C134, and P125 highlighted in stick representation. The movie was generated using UCSF Chimera (1).

Movie S1

Other Supporting Information Files

SI Appendix (PDF)

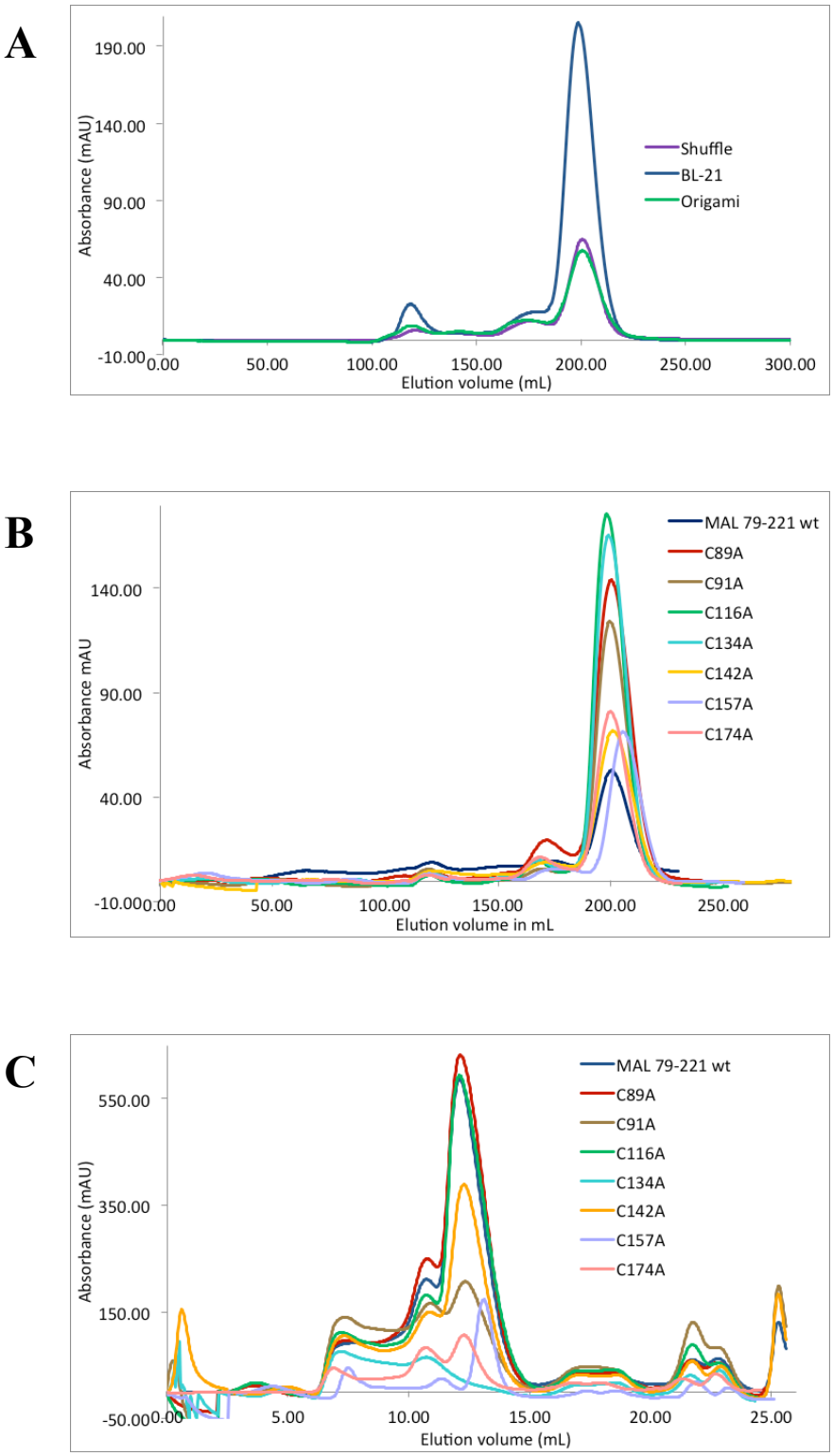

SI Appendix, Fig. S1. Size-exclusion chromatography of MAL^{TIR} and its cysteine mutants in different *E. coli* strains. (A) Size-exclusion chromatography of MAL^{TIR} produced in three different *E. coli* cell types. (B) Size-exclusion chromatography of MAL^{TIR} and single-cysteine mutants produced in BL21 *E. coli* cells. (C) Size-exclusion chromatography of MAL^{TIR} and single-cysteine mutants produced in SHuffle *E. coli* cells. Each protein was eluted from a Superdex 75 26/600 (A, B) or Superdex 75 10/300 (C) (GE Healthcare) columns in a buffer consisting of 20 mM Tris (pH 8.6) with 200 mM NaCl.

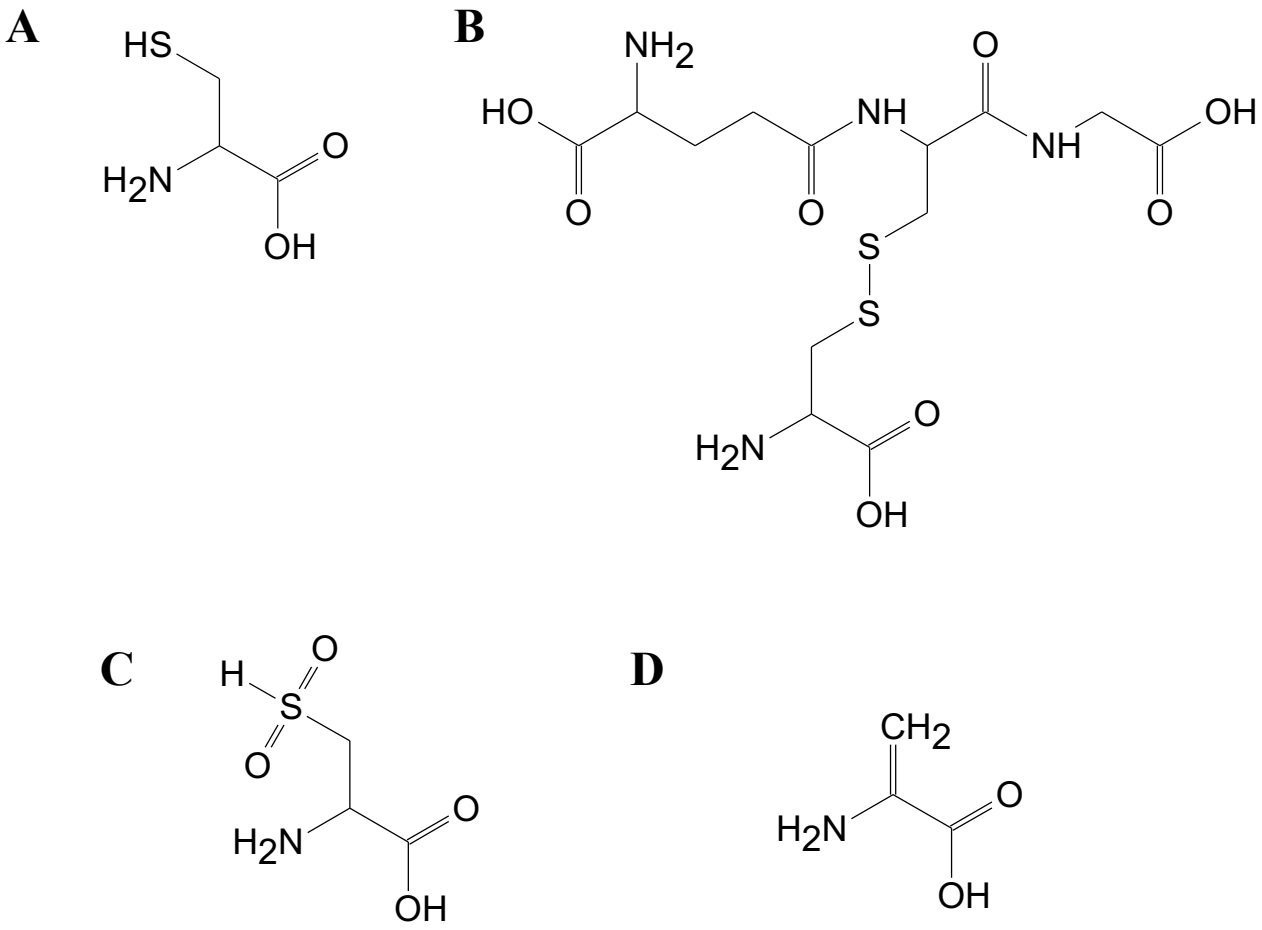

SI Appendix, Fig. S2. Structure of the amino-acid L-cysteine (A), and its modifications *S*-glutathionylation (B), dioxidation (C) and dehydroalanine (D).

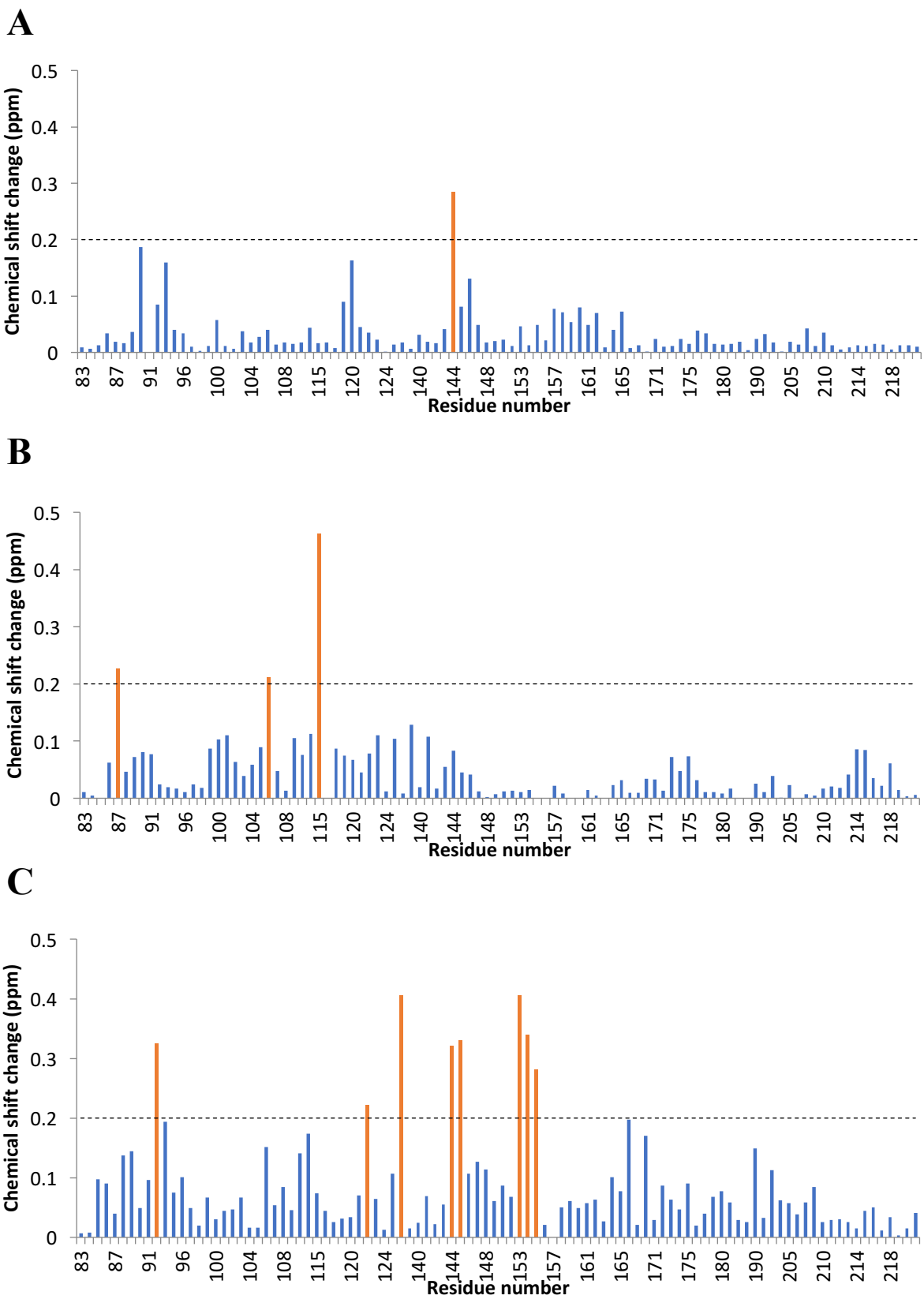

SI Appendix, Fig. S3. Comparison of chemical shifts between the (A) C91A, (B) C116A and (C) C157A mutants and the wild-type MAL^{TIR} protein. The following residues were not assigned in at least one of the spectra and were therefore excluded from the analysis: 94, 110-112, 119, 125-128, 131-136, 128,139, 149, 155, 169-170, 177, 181, 183-185, 188-189, 192-198, 201-203, 207.

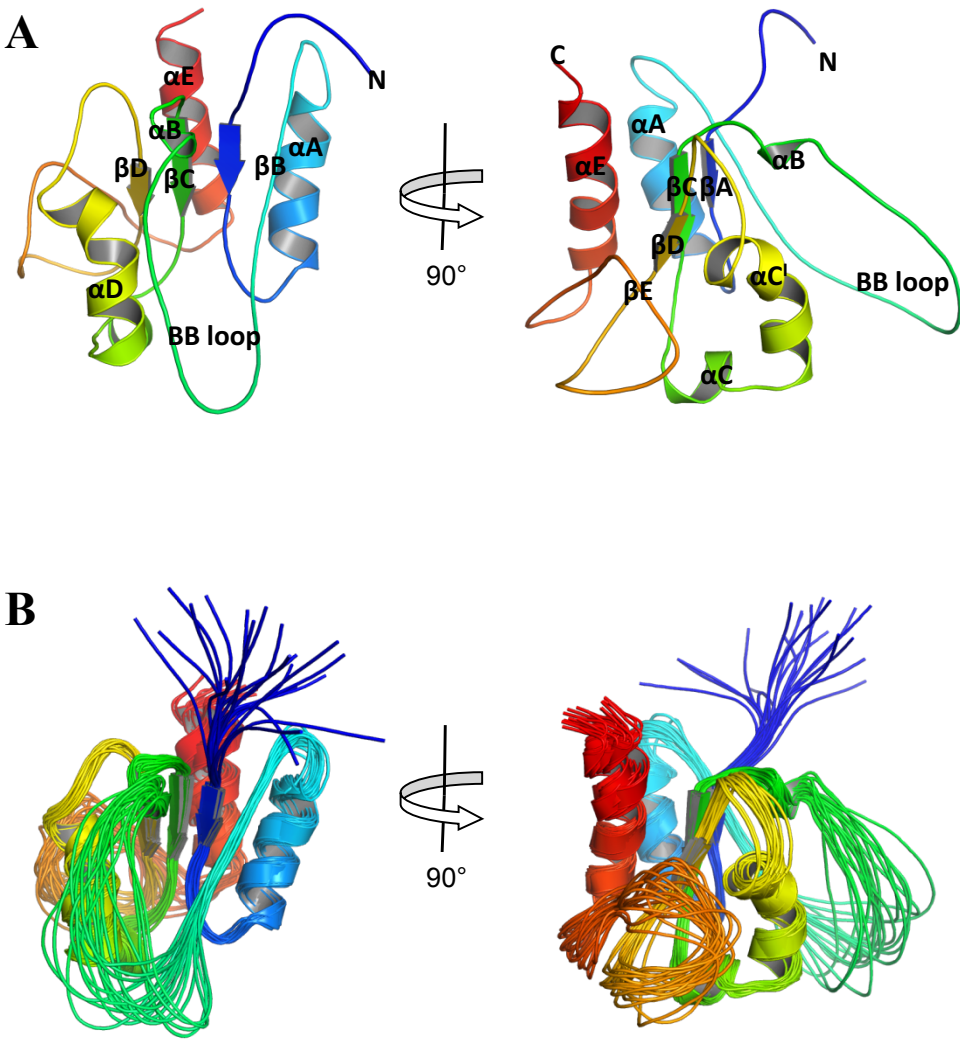

SI Appendix, Fig. S4. (A) NMR solution structure of human MAL^{TIRC116A}. The views are related by a rotation of 90° around the y-axis. (B) Top-twenty lowest-energy models, showing the inherent flexibility of the BB-loop in green. The views are related by a rotation of 90° around the y-axis.

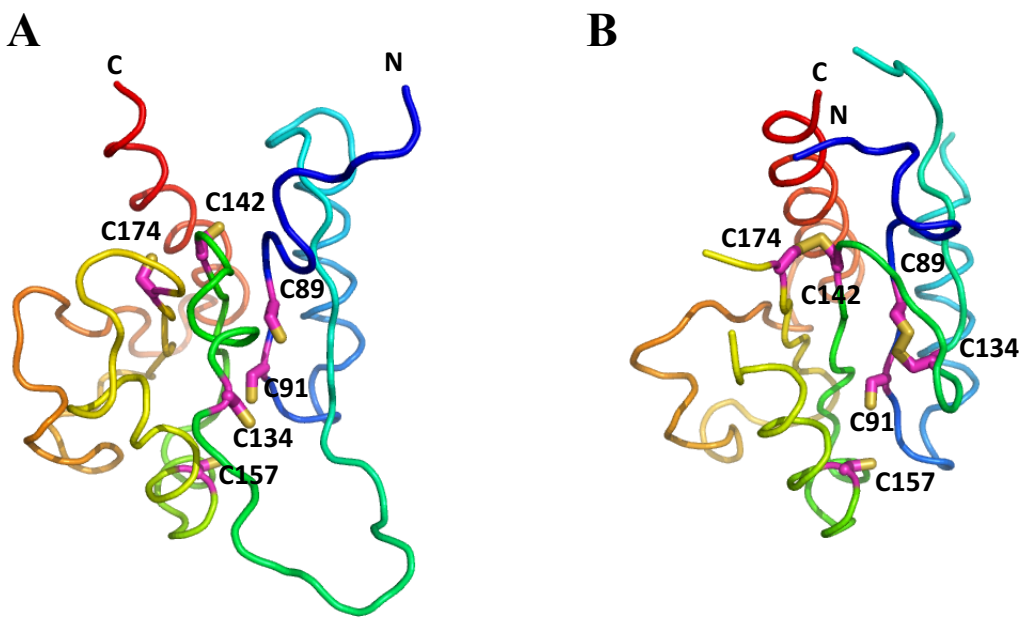

SI Appendix, Fig. S5. (A) NMR solution structure of human $MAL^{TIRC116A}$ (in ribbon representation, colored continuously from N [blue] to C-terminus [red]), highlighting the side-chains of the cysteine residues (in stick representation, with sulfurs in yellow and carbons in magenta). **(**B) Crystal structure of human MAL^{TIR}, shown as in A.

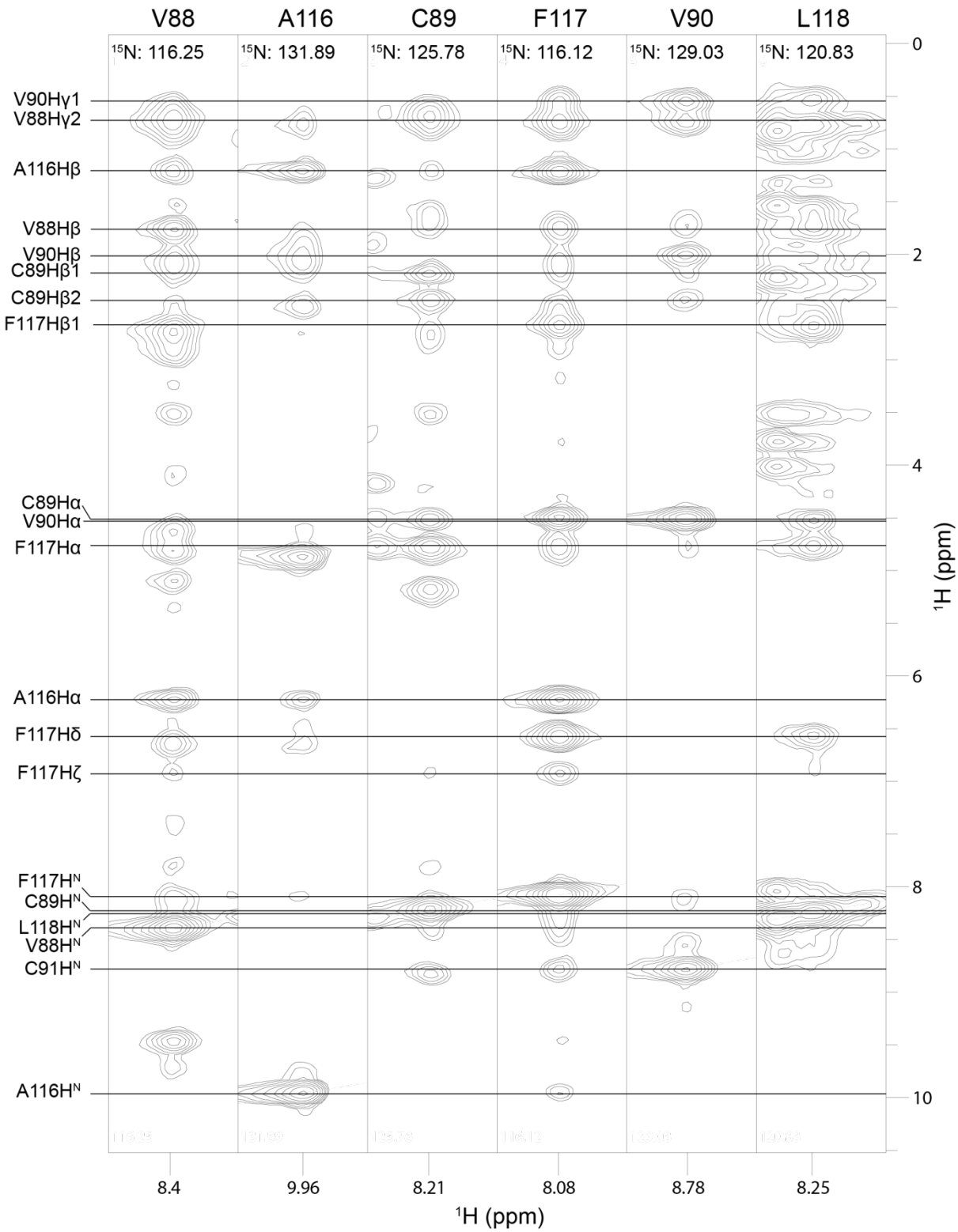

SI Appendix, Fig. S6. ^{15}N-NOESY strips from MAL^{TIRC116A} exhibiting short to medium-ranged NOE cross-peaks between residues situated in the βA strand (V88, C89, V90) and the βB strand (A116, F117, L118). The large number of atoms detected between the residues indicates that these residues are in close proximity to one another.

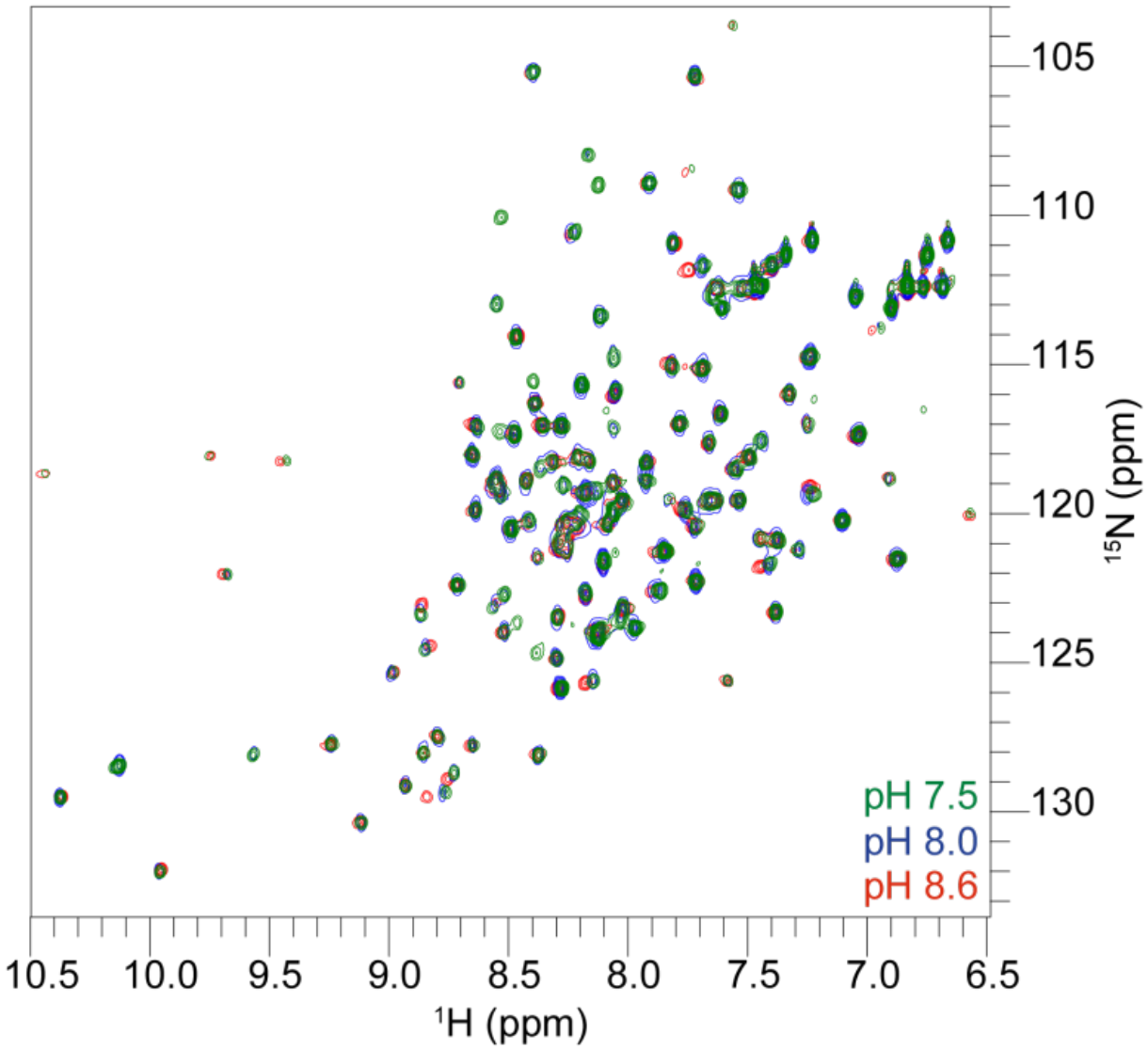

SI Appendix, Fig. S7. Overlay of ^{1}H-^{15}N-HSQC spectra of $MAL^{TIRC116A}$ at pH 7.5 (green), 8.0 (blue) and 8.6 (red).

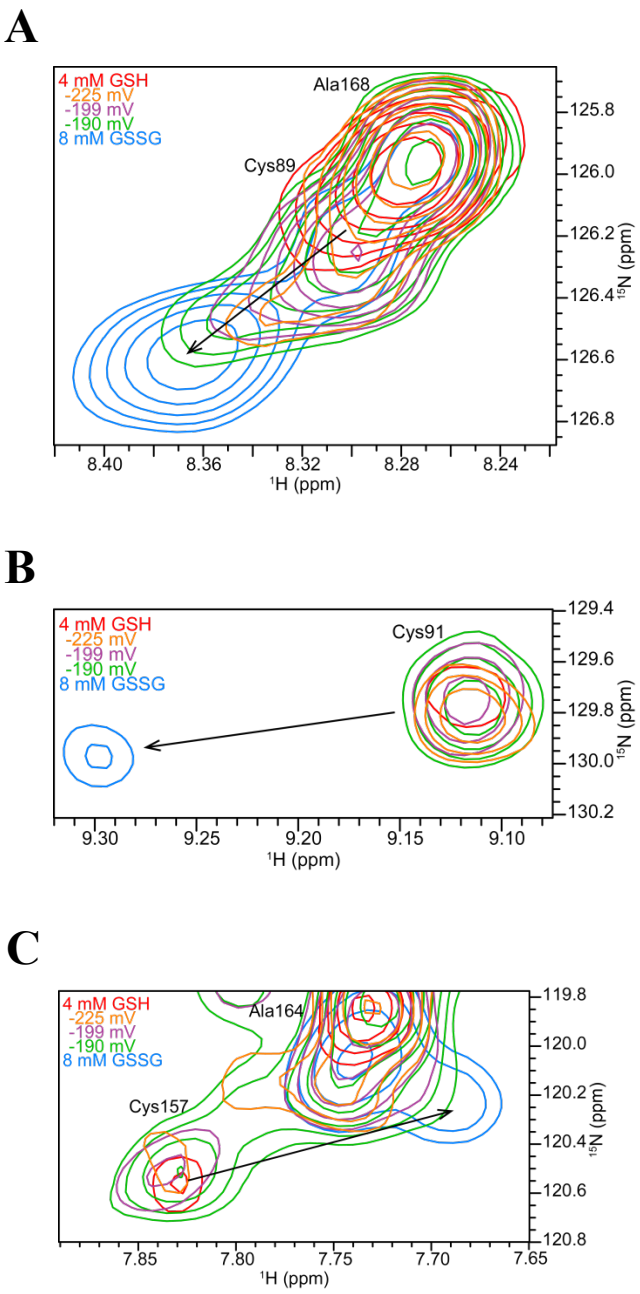

SI Appendix, Fig. S8. Cysteine residues C89 (A), C91 (B) and C157 (C) show ^{1}H and ^{15}N shifts following exposure to increasingly oxidising conditions.

Movie Still S1. Still image from Movie S1 illustrating the transition between the crystal structure of MAL^{TIR} and the solution structure of $MAL^{TIRC116A}$ (left to right). The structures are shown in cartoon representation, with the side-chains of C89, C134 and P125 highlighted in stick representation. The movie was generated using UCSF Chimera [1].

Table S1. Redox state of cysteine residues in MAL^{TIR} produced in different cell types or exposed to redox reagents, as determined by the Ellman's assay.

Wild-type MAL^{TIR} growth condition	**Reduced**	**Oxidized**	**% Reduced**
BL-21 purified with 10 mM DTT	7	0	100
BL-21	6	1	90
SHuffle	4	3	57
Origami	4	3	53
H_2O_2 (0.03 mM)	0	7	0

Table S2. Number of reduced and oxidised cysteine residues in MAL^{TIR} and its mutants produced in SHuffle *E. coli* cells.

MAL mutant	**Oxidised cysteines**	**Reduced cysteines**
wild-type	3	4
C89A	3	3
C91A	5	1
C116A	3	3
C134A	-	-
C142A	2	4
C157A	3-4	2-3
C174A	3	3

Table S3. Modifications detected using mass spectrometry, following the addition of oxidized glutathione.

Cysteine residue	**Tris pH 8.6**	**Hepes pH 7.5**
89	Dehydroalanine	Dioxidation
91	Glutathionylation, dioxidation	Glutathionylation, dehydroalanine
116	Glutathionylation	Glutathionylation
134	Dehydroalanine	Glutathionylation, dehydroalanine
142	Glutathionylation, dioxidation	Glutathionylation, dioxidation
157	Glutathionylation	Glutathionylation
174	Glutathionylation	Glutathionylation

Table S4. RMSD values of ^{1}H and ^{15}N chemical shifts for cysteine-to-alanine mutants of MAL^{TIR} compared to the wild-type protein.

Cysteine mutant	**RMSD (ppm)**
C89A	0.036
C91A	0.054
C116A	0.075
C134A	0.028
C142A	0.047
C157A	0.120
C174A	0.062

Table S5. Pairwise changes of ^{1}H and ^{15}N chemical shifts between wild-type MAL^{TIR} and the cysteine-to-alanine mutants.

Residue number	C89A/WT	C91A/WT	C116A/WT	C134A/WT	C142A/WT	C157A/WT	C174A/WT
83	0.00624	0.01300	0.01400	0.01200	0.01300	0.00956	0.02200
84	0.02100	0.00840	0.00536	0.00901	0.00273	0.00833	0.04900
85	0.15200	0.01700	0.00000	0.00000	0.06800	0.12700	0.23600
86	0.08100	0.03900	0.07400	0.09200	0.10600	0.10100	0.02600
87	0.06600	0.02300	0.27400	0.00930	0.01500	0.05600	0.02100
88	0.01200	0.02100	0.05000	0.01700	0.15000	0.19000	0.04200
89		0.05000	0.09700	0.03400	0.01100	0.20400	0.14100
90	0.17900	0.23000	0.10200	0.08500	0.02300	0.05100	0.03400
91	0.03700	0.27200	0.10600	0.01100	0.01900	0.11400	0.01200
92	0.07100	0.10800	0.03600	0.00362	0.04500	0.33600	0.04700
93	0.02900	0.19500	0.24000	0.00665	0.01000	0.25800	0.04700
94							
95	0.00424	0.04700	0.02300	0.01300	0.01400	0.10600	0.00961
96	0.03100	0.04800	0.01100	0.02700	0.01800	0.12700	0.01500
97	0.01100	0.01300	0.03500	0.00840	0.01800	0.06800	0.01700
98	0.01600	0.00324	0.02600	0.01200	0.01400	0.02300	0.01400
99	0.02500	0.01400	0.09300	0.02100	0.01700	0.07700	0.01100
100	0.01900	0.07000	0.12700	0.03100	0.01200	0.03000	0.00883
101	0.02200	0.01500	0.14700	0.00730	0.03600	0.06300	0.01900
102	0.01300	0.00713	0.08900	0.00956	0.09100	0.06200	0.01400
103	0.00765	0.04100	0.05000	0.01400	0.03000	0.08500	0.01800
104	0.03800	0.02500	0.08300	0.08400	0.11400	0.02200	0.03000
105	0.01100	0.03900	0.12400	0.01300	0.01600	0.02300	0.01700
106	0.00306	0.05300	0.27900	0.08100	0.00435	0.16100	0.01600
107	0.03800	0.01600	0.04900	0.01900	0.03700	0.07500	0.03700
108	0.01400	0.02100	0.01800	0.02200	0.02000	0.11700	0.00932
109	0.01600	0.02100	0.14400	0.02200	0.02500	0.04800	0.00857
110							
111							

112							
113	0.02000	0.02000	0.08700	0.01800	0.00966	0.03600	0.02500
114	0.05100	0.05700	0.13600	0.02800	0.09400	0.19900	0.13400
115	0.01200	0.02100	0.65400	0.01300	0.03300	0.10400	0.04700
116							
117	0.11000	0.10000	0.11300	0.01700	0.01700	0.02800	0.27000
118	0.08200	0.11100	0.08200	0.00947	0.12900	0.03900	0.11300
119							
120	0.16400	0.22400	0.09100	0.12300	0.15700	0.04700	0.04600
121	0.11800	0.04500	0.05000	0.10900	0.01800	0.09800	0.06200
122	0.05600	0.04400	0.09600	0.07200	0.14000	0.25200	0.05800
123	0.02000	0.02700	0.14600	0.01700	0.01100	0.08400	0.07000
124	0.01000	0.00126	0.01600	0.00870	0.05500	0.01700	0.00500
125							
126							
127							
128							
129	0.01800	0.01900	0.11000	0.03300	0.05500	0.14400	0.02100
130	0.03800	0.01700	0.01100	0.05400	0.01400	0.08900	0.06800
131							
132							
133							
134							
135							
136							
137	0.00984	0.00781	0.14200	0.01100	0.03600	0.02200	0.02800
138							
139							
140	0.03600	0.03700	0.02700	0.03600	0.03200	0.02700	0.03500
141	0.10900	0.02100	0.12300	0.06800	0.21100	0.08200	0.00650

142	0.05100	0.02300	0.02000	0.05000	0.31000	0.03000	0.12200
143	0.09600	0.05600	0.06300	0.06000	0.18400	0.07300	0.13300
144	0.07700	0.33900	0.11400	0.08600	0.04000	0.43300	0.19200
145	0.03300	0.11200	0.04700	0.02600	0.11100	0.18400	0.09300
146	0.02400	0.16100	0.05400	0.01100	0.01400	0.15000	0.01500
147	0.00172	0.06900	0.01600	0.01500	0.02300	0.17700	0.00284
148	0.01800	0.02500	0.00238	0.00982	0.02200	0.16100	0.00000
149							
150	0.02400	0.02500	0.00860	0.02000	0.02200	0.07400	0.01000
151	0.01300	0.03000	0.01600	0.01200	0.02600	0.12300	0.00000
152	0.01600	0.01600	0.02000	0.00872	0.01900	0.09300	0.00196
153	0.00875	0.06500	0.01500	0.02200	0.01400	0.41600	0.00747
154	0.02600	0.01400	0.01300	0.00311	0.01600	0.36200	0.00115
155							
156	0.01400	0.23000	0.00000	0.00000	0.01900	0.02100	0.01400
157	0.02500	0.08900	0.02500	0.00980	0.01400		0.01200
158	0.02500	0.08300	0.01100	0.02400	0.04600	0.06500	0.01400
159	0.09300	0.07100	0.00000	0.00000	0.13200	0.08300	0.13800
160	0.03200	0.11300	0.00000	0.00717	0.01500	0.06900	0.04900
161	0.02000	0.06500	0.01700	0.03700	0.02800	0.08000	0.00307
162	0.00931	0.07400	0.00587	0.02200	0.03100	0.08200	0.04400
163	0.01000	0.00930	0.00000	0.02400	0.01000	0.03200	0.06500
164	0.02000	0.04500	0.03000	0.04000	0.03500	0.11100	0.11800
165	0.02400	0.09600	0.04400	0.02100	0.03000	0.10900	0.13700
166	0.02900	0.11000	0.00972	0.03300	0.00992	0.26100	0.07500
167	0.03400	0.01800	0.01400	0.05100	0.04100	0.02800	0.05100
168	0.02300	0.00222	0.04100	0.04400	0.07500	0.21200	0.09000
169							
170							
171	0.02900	0.03300	0.04000	0.05300	0.03300	0.04100	0.08900

172	0.01100	0.01000	0.01300	0.05300	0.05700	0.09900	0.02500
173	0.02400	0.01600	0.08200	0.00484	0.10900	0.08800	0.53300
174	0.03500	0.02500	0.06700	0.01600	0.11500	0.04900	
175	0.05400	0.02300	0.10300	0.01700	0.05700	0.12700	0.09600
176	0.04900	0.05200	0.03300	0.01100	0.02500	0.02500	0.09900
177							
178	0.01700	0.03800	0.01200	0.00233	0.05700	0.05400	0.02300
179	0.01700	0.02000	0.01200	0.01100	0.00732	0.09600	0.04500
180	0.01400	0.01900	0.01100	0.02000	0.06253	0.09600	0.01100
181							
182	0.01800	0.02200	0.02300	0.01500	0.01400	0.07700	0.01900
183							
184							
185							
186	0.01300	0.02100	0.00000	0.00000	0.01200	0.04100	0.01800
187	0.00000	0.00504	0.00000	0.00000	0.00757	0.03500	0.10500
188							
189							
190	0.01100	0.03000	0.02500	0.00950	0.00317	0.20000	0.04800
191	0.01200	0.04600	0.01500	0.01600	0.01600	0.03700	0.00169
192							
193							
194							
195							
196							
197							
198							
199	0.00392	0.02400	0.04600	0.01200	0.01100	0.15300	0.02400
200	0.00844	0.00202	0.00250	0.01100	0.02400	0.07700	0.01400
201							

202							
203							
204	0.00972	0.00824	0.02300	0.01300	0.01500	0.01000	0.00807
205	0.01300	0.02700	0.03000	0.01100	0.02200	0.08000	0.02000
206	0.00000	0.02000	0.00000	0.00000	0.00779	0.05500	0.01400
207							
208	0.05100	0.04700	0.01000	0.05000	0.00821	0.07500	0.03400
209	0.01100	0.01600	0.00689	0.01200	0.05500	0.11500	0.08400
210	0.01600	0.04600	0.01900	0.01900	0.04700	0.03500	0.02400
211	0.02100	0.01700	0.03000	0.01500	0.02200	0.04200	0.00775
212	0.00677	0.00652	0.02200	0.01100	0.05000	0.03100	0.05500
213	0.03000	0.01300	0.05200	0.01100	0.01200	0.03300	0.12300
214	0.04900	0.01700	0.11600	0.04100	0.03600	0.01800	0.00652
215	0.01300	0.01600	0.09700	0.01300	0.02100	0.05100	0.01800
216	0.00443	0.02000	0.05000	0.01400	0.03300	0.06400	0.05500
217	0.01500	0.01900	0.02900	0.01000	0.03000	0.01500	0.02500
218	0.03800	0.00506	0.06500	0.00923	0.06500	0.04300	0.02800
219	0.00783	0.01600	0.02100	0.01300	0.02300	0.00563	0.00707
220	0.01300	0.01700	0.00323	0.02000	0.01500	0.02200	0.01000
221	0.01300	0.01400	0.00776	0.00930	0.02100	0.04800	0.01600

Table S6. NMR structure statistics[a] for MAL^{TIRC116A}

Experimental restraints[b]		
	Inter-proton distance restraints	
	Intra-residue	362
	Sequential	422
	Medium-range (i–j < 5)	317
	Long-range (i–j > 5)	262
	Dihedral-angle restraints	216
	Total number of restraints per residue	11.12
Mean RMSD of the 20-structure ensemble (Å)[c]		
	Backbone atoms (residues 85–120, 134–179 & 204–220)	0.94 ± 0.17
	All heavy atoms (residues 85–120, 134–179 & 204–220)	1.28 ± 0.14
Stereochemical quality[d]		
	Residues in most favoured Ramachandran region (%)	78.0
	Ramachandran outliers (%)	0 ± 0

[a]All statistics are given as mean ± SD.
[b]Only structurally relevant restraints, as defined by CYANA, are included.
[c]Mean RMSD calculated over the entire ensemble of 20 structures.
[d]As reported by CYANA [2].

Table S7. RMSD (ppm) comparison between the ^{1}H and ^{15}N chemical shifts of MAL^{TIR} nuclei at pH 8.0 and 8.6 compared to 7.5.

pH	**7.5**
8.0	0.006
8.6	0.017

SI Appendix References:

1. Pettersen, E.F., et al., *UCSF Chimera--a visualization system for exploratory research and analysis.* J Comput Chem, 2004. **25**(13): p. 1605-12.

2. Vranken, W.F., et al., *The CCPN data model for NMR spectroscopy: development of a software pipeline.* Proteins, 2005. **59**(4): p. 687-96.

DOI: 10.1111/imr.12608

INVITED REVIEW

WILEY Immunological Reviews

Metabolic regulation of NLRP3

Mark M. Hughes | Luke A.J. O'Neill

School of Biochemistry and Immunology, Trinity Biomedical Sciences Institute, Trinity College Dublin, Dublin, Ireland

Correspondence
Mark M. Hughes, School of Biochemistry and Immunology, Trinity Biomedical Sciences Institute, Trinity College Dublin, Dublin, Ireland.
Email: mhughes4@tcd.ie

Funding information
Science Foundation Ireland

Summary

A shift in our understanding of macrophage biology has come about as a result of recent discoveries in the area of metabolic reprogramming of macrophages. The NLRP3 inflammasome drives the activation of caspase-1, leading to the production of IL-1β, IL-18, and a type of cell death termed pyroptosis. The NLRP3 inflammasome has been shown to sense metabolites such as palmitate, uric acid, and cholesterol crystals and is inhibited by ketone bodies produced during metabolic flux. The NLRP3 inflammasome has also been shown to be regulated by mitochondrial reactive oxygen species and components of glycolysis, such as Hexokinase. Here, we review these findings and discuss their importance for inflammation and furthermore discuss potential therapeutic benefits of targeting NLRP3.

KEYWORDS

glycolysis, inflammasome, inflammation, Krebs cycle, metabolism, NLRP3

1 | INTRODUCTION

Inflammation has long been identified as the driving factor of many chronic inflammatory conditions and autoimmunity, including atherosclerosis,[1] type 2 diabetes,[2] ageing,[3] obesity,[4] and rheumatoid arthritis (RA).[5] Macrophages of the innate immune system have been extensively examined in inflammatory phenotypes to elucidate the molecular mechanism of chronic low-grade inflammation. In recent years, metabolism has come to the forefront in macrophage biology, underpinning key inflammatory processes required for pathogen clearance. Macrophages sense and respond to foreign milieu in the extracellular environment through pattern recognition receptors (PRRs), such as the Toll-like receptor (TLR) superfamily. Once activated, TLRs drive assembly of inflammasomes, multimeric molecular signaling platforms. The NLRP3 (NLR family, pyrin domain containing 3) inflammasome is a multi-component assembly of adapter and effector proteins highly expressed in myeloid cells, consisting of NLRP3, adapter protein apoptosis-related speck-like protein (ASC), and caspase-1[6] (Figure 1).

The discovery of the NLRP3 inflammasome in 2002 by Jürg Tschopp[7] identified the mechanism of IL-1β and IL-18 cleavage. In this seminal study, they identified the components of the inflammasome in a cell free system and further linked NLRP3 to the autoimmune disease Muckle-Wells syndrome.[8]

NLRP3 has been known to exert a role in metabolism, as NLRP3-deficient mice are hypersensitive to insulin when given a high-fat diet,[9] and furthermore insulin sensitivity is increased in obese type 2 diabetic patients who undergo calorie restriction and exercise due to decreased levels of NLRP3.[10]

Of importance, a disparity exists between murine and human inflammasome activation. Murine inflammasomes require a 2-step activation, requiring a "priming" signal via NF-κB activation to generate caspase-1, pro-IL-1β, and pro-IL-18 via TLRs. The second driving signal in NLRP3 inflammasome activation is sensing of damage-associated molecular patterns (DAMPs), such as extracellular ATP, the pore-forming ionophore nigericin, and crystalline substances. In contrast, human monocytes circumvent the requirement for DAMP recognition, and drive NLRP3 inflammasome activation through an alternate TLR4-dependant mechanism.[11]

NLRP3 can also promote a form of cell death termed pyroptosis. NLRP3 assembly primes caspase-1 auto-catalytic activation, driving the recently described "non-canonical inflammasome" cleavage of the pore-forming Gasdermin D protein, driving pyroptosis.[12,13] Owing to the complexity of inflammasome sensing and regulation, NLRP3 can be considered an intracellular safeguard to

This article is part of a series of reviews covering The IL-1 cytokine and receptor family appearing in Volume 281 of *Immunological Reviews*.

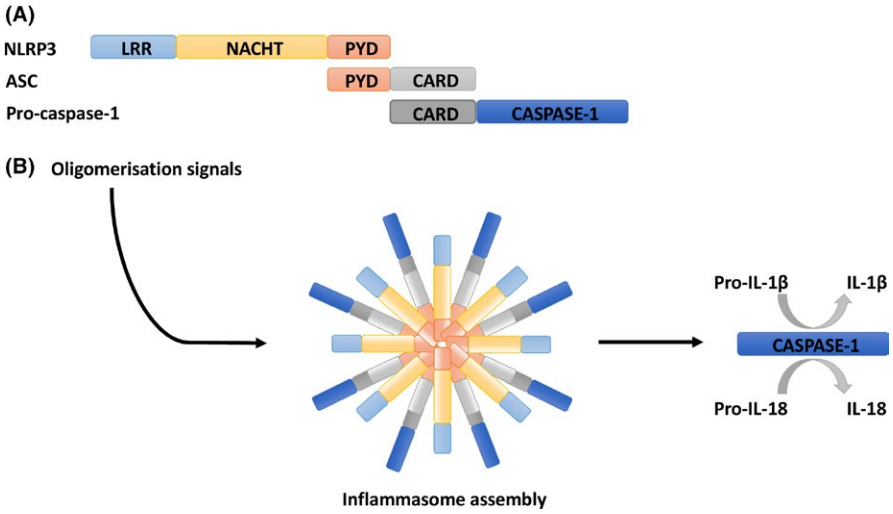

FIGURE 1 Assembly of the NLRP3 inflammasome. A, Individual components of NLRP3 inflammasome. NLRP3 interacts with adapter ASC through homologous PYD domain interactions. The CARD domain of ASC then allows recruitment of Caspase-1 through homologous CARD domain interactions. B, Oligomeric NLRP3 inflammasome activation promotes caspase-1 activation and maturation of the inflammatory cytokines pro-IL-1β and pro-IL-18 into mature IL-1β and IL-18

sense and limit altered metabolite production. How NLRP3 regulates homeostasis in healthy individuals however, remains to be fully elucidated.

Recent studies have now identified a role for metabolites in the regulation and activation of the NLRP3 inflammasome. In this review, we will summarize recent findings that identify new components and regulators of the NLRP3 inflammasome. We will highlight the dynamic interface between NLRP3 and immunometabolism, how these novel NLRP3 regulators impact on the cytokine IL-1β, and furthermore how specific targeting of NLRP3 during metabolic reprogramming and chronic inflammatory conditions could provide therapeutic benefits.

2 | REDOX SENSING IN NLRP3 ACTIVATION

The energy demands of our cells are in constant flux, depending on molecular oxygen to supply the Krebs cycle for generation of ATP to maintain homeostasis under normoxic conditions. Macrophage activation rewires the metabolic demands of macrophages, generating reactive oxygen species (ROS) as a microbicidal mechanism to remove invading pathogens. The most abundant ROS producers are the complexes of the electron transport chain, or via the NADPH oxidase enzymes.[14] Utilization of ROS however, does have setbacks. Cysteine residues are highly prone to oxidation and as such, must be regulated to prevent proteasomal degradation during metabolic reprogramming.[15] Indeed, glutathione (GSH) protects the cell from overproduction of ROS and has been attributed to regulate various macrophage functions.[16] In addition to acting as an antioxidant, GSH can post-translationally modify proteins, and we have recently identified a positive role for glutathionylation in TLR signaling adapter MyD88-adapter-like (MAL) activation.[17] Here, we will discuss novel regulators of NLRP3 (Table 1) and potential mechanisms of NLRP3 regulation.

Glutathionylation has been linked to negative regulation of caspases. Both caspase-1 and caspase-3 are negatively regulated by GSH, limiting their proteolytic capabilities.[18,19] Glutathionylation of NLRP3 has recently been identified in macrophages co-treated with LPS and curcumin, an anti-inflammatory compound.[20] Interestingly, the deglutathionylation of NLRP3 was associated with increased interaction of glutathionylated caspase-1, suggesting the NLRP3 inflammasome assembles in tandem with enzymatically inhibited caspase-1, possibly to prevent activation of the NLRP3 inflammasome. This finding warrants further research, as GSH may itself limit inflammasome activation. Oxidative stress could thereby induce NLRP3 activation, triggering deglutathionylation of caspase-1 to promote IL-1β processing.

Recent evidence has identified a new component of the inflammasome, NEK7, a serine-threonine kinase previously associated with mitosis.[21] Mice deficient in NEK7 could not form competent NLRP3 inflammasomes in vivo. NEK7 bound to the LRR of NLRP3, dependent on generation of mitochondrial ROS. This finding presents NEK7 as a potential ROS-sensing inflammasome stimulus, which may detect increasing ROS levels to trigger inflammasome assembly. It would be interesting to elucidate if ROS generated from mitochondrial-independent sources could also act as a NEK7 trigger, or if NEK7 is exclusively sensing mitochondrial ROS. Concurrently, NEK7 was also identified by He et al[22] to drive NLRP3 activation, and further attributed NEK7 activation to potassium (K^+) efflux, suggesting NEK7 acts as both an ion and ROS sensor. The efflux of cytosolic K^+ is a known trigger for NLRP3 inflammasome activation,[23] and furthermore the chloride intracellular channel (CLIC) proteins CLIC1 and CLIC4 have been shown to impact on *Il1β* transcription and NLRP3 inflammasome activation.[24] CLICs have been shown to be activated downstream of K^+ efflux and ROS. Mitochondrial ROS has been shown to drive translocation of CLICs to the plasma membrane where they cause chloride efflux. The chloride efflux was then shown to drive NEK7-NLRP3 activation.[25] This study therefore provides a new insight into ROS as a driver of NLRP3. Interestingly, a known activating NLRP3 variant in cryopyrin-associated periodic syndrome (CAPS)-associated macrophages, R258W, also required NEK7 for chronic activation, independent of K^+ efflux.[22]

TABLE 1 Novel regulators of NLRP3 activation

Component	Function in cell	Effect on NLRP3	References
Glutathione	Regulates oxidative stress and post-translationally modifies cysteines	Deglutathionylation of NLRP3 promotes interaction with Caspase-1	20
NEK7	Serine/threonine kinase involved in mitosis	Binds LRR of NLRP3 dependent on K^+ efflux and mitochondrial ROS	21,22
CLIC1/4	Drive Cl^- efflux and maintains intracellular pH	Mitochondrial ROS promotes CLIC translocation, driving Cl^- efflux for NEK7-NLRP3 activation	24,25
AIM2 inflammasome	Senses bacterial and viral dsDNA	Triggers K^+ efflux for NLRP3 activation	26
Tristetraprolin	Binds to AU-rich elements in 3′-UTRs	Represses human NLRP3 translation via binding to the 3′-UTR	27
Ugonin U	A natural flavonoid from *Helminthostachys zeylanica*	Drives mitochondrial ROS generation and Ca_2^+ release via PLC, activating NLRP3	30
UCP2	A mitochondrial uncoupler protein promoting mitochondrial proton leak	UCP2 deficiency limits fatty acid synthesis, decreasing NLRP3 transcription and activation	31
NOX4	Oxygen sensing and superoxide anion generation	NOX4 deficiency reduces CPT1A levels, limiting NLRP3 activation	32
GB111-NH_2	Small molecule agonist of NLRP3	Drives mitochondrial ROS through inhibition of GAPDH and α-enolase triggering NLRP3 activation	34
mTORC1	Regulates redox sensing and protein synthesis	Inhibition of mTORC1 suppresses NLRP3 activation	35
N-acetylglucosamine	Glucose-derived peptidoglycan in Gram-positive bacterial cell walls	Promotes hexokinase dissociation from mitochondria-activating NLRP3	39
β-hydroxybutyrate	Ketone body produced during starvation	Inhibits NLRP3 inflammasome activation via targeting K^+ efflux	52
Bile acids	Amphipathic detergents which promote nutrient absorption	Bind the TGR5 receptor, activating PKA via cAMP, promoting NLRP3 phosphorylation and ubiquitination	58
IL-10	Anti-inflammatory cytokine	IL-10 deficiency promotes NLRP3 activation due to accumulation of damaged mitochondria	78

Recently, a new non-canonical activator of NLRP3 has been described, the AIM2 inflammasome itself. Using the intracellular pathogen *Legionella pneumophila*, Cunha et al[26] identified the AIM2 inflammasome triggered caspase-1 and caspase-11-mediated pore formation, promoting K^+ efflux to trigger NLRP3 activation, adding further complexity to NLRP3 regulation.

Mechanisms to regulate NLRP3 post-transcriptionally have also been described. Tristetraprolin (TTP), an RNA-binding protein, binds to the 3′-untranslated region (UTR) of NLRP3 in human macrophages, repressing NLRP3 expression. Knockdown of TTP increased NLRP3 activation, but not AIM2 or NRLC4 activation, and subsequently increased caspase-1 activation and IL-1β cleavage.[27] Regulation of NLRP3 by TTP may also be impacted by levels of ROS produced by the metabolic shift in macrophages upon PAMP recognition. TTP contains redox-reactive cysteines which, when oxidized, result in inhibition of TTP RNA-binding capacity.[28] Thus, TTP oxidation may act as a feedback mechanism, linking increased ROS levels produced during metabolic reprogramming to rapid NLRP3 transcription.

Ugonin U, a natural flavonoid derived from *Helminthostachys zeylanica* has been shown to drive superoxide generation via the activity of phospholipase C (PLC).[29] In human monocytes, Ugonin U stimulated NLRP3 activation by triggering mitochondrial ROS generation. Ugonin U-mediated activation of PLC was found to trigger release of intracellular calcium (Ca^{2+}), and negative targeting of Ca^{2+} release inhibited the inflammatory effects of Ugonin U.[30] Furthermore, scavenging of mitochondrial ROS by the tool compound MitoTEMPO limited the effects of Ugonin U, firmly placing mitochondrial ROS as a determinant in NLRP3 inflammasome activation.

Lipid metabolism has also been linked to NLRP3. Moon et al identified a role for the uncoupling protein-2 (UCP2) in NLRP3 activation. UCP2-deficient mice were found to have overall improved survival in sepsis models, concomitant with impaired fatty acid synthesis, and decreased IL-1β and IL-18 levels. UCP2 was identified as a driver of fatty acid synthase (FASN), a key enzyme involved in fatty acid synthesis. UCP2-deficient mice had reduced lipid synthesis, concomitant with decreased NLRP3-mediated caspase-1 activation. Inhibition of FASN by chemical inhibitors also suppressed NLRP3 activation and *NLRP3* and *IL1β* transcription, linking fatty acid synthesis as a key driver of both inflammatory gene transcription and NLRP3 activation.[31] In a separate and somewhat contradicting study, Moon et al also identified the ROS producer NADPH Oxidase 4 (NOX4), an enzyme involved in superoxide anion formation, as an NLRP3 activator through fatty acid oxidation. NOX4-deficient mice had reduced levels of the mitochondrial fatty acid oxidation enzyme carnitine palmitoyltransferase 1A (CPT1A), resulting in decreased NLRP3 inflammasome activation, with no effect on NLRC4 or AIM2 inflammasomes. Inhibition of fatty acid oxidation by the drug etoxomir also limited NLRP3 activation, identifying another prominent role of an altered oxidative environment

inducing NLRP3 activation.[32] Production of ROS is crucial as a microbicidal mechanism, however the consequences of producing an oxidative environment lie firmly on antioxidant capacity, the lack of which can damage cell machinery, driving inflammation through mechanisms which can activate the NLRP3 inflammasome.

3 | GLYCOLYSIS AND NLRP3

As mentioned above, activation of TLRs will alter metabolism in macrophages causing a shift to aerobic glycolysis. Inhibition of glycolysis by a glucose analog, 2-deoxyglucose, was shown to suppress LPS-induced IL-1β mRNA production in macrophages, with a strong increase in the Krebs cycle intermediate succinate.[33] Enzymes involved in metabolism and metabolic intermediates have since been identified to have an impact on NLRP3 activation and ROS production (Table 2). Limiting glucose uptake can trigger glycolytic stress, decreasing the amount of reducing equivalents required for homeostasis. Indeed, a compound termed GB111-NH_2, induces NLRP3 inflammasome formation by inhibiting glycolytic enzymes GAPDH and α-enolase, impairing NADH production and driving mitochondrial ROS production.[34] This provides a curious contradiction. Inhibition of glycolysis with 2-deoxyglucose appears to block induction of IL-1β mRNA, whereas targeting of GAPDH and α-enolase increases NLRP3 activation and IL-1β secretion. The biological significance of this is not clear but warrants further investigation (Figure 2).

3.1 | mTORC1 and hexokinase

Energy metabolism is under constant surveillance by redox/nutrient sensor mammalian target of rapamycin complex I (mTORC1) to regulate protein synthesis. However, unlike the study with GB111-NH_2, mTORC1-mediated glycolysis was shown to drive NLRP3 inflammasome activation. Inhibiting mTORC1 by torin1, a selective mTOR inhibitor, suppressed NLRP3 activation both in vitro and in vivo.[35] Furthermore, deficiency of Raptor, an mTORC1-binding partner, suppressed caspase-1 activation and glycolysis during NLRP3 inflammasome activation, with mTORC2 deficiency having no effect observed on NLRP3 activation. Hexokinase-1, the first enzyme in glycolysis which converts glucose to glucose-6-phosphate, provided a mechanistic link between mTORC1 and NLRP3 activation, as depletion of glucose in the media of respiring macrophages blocked caspase-1 activation during NLRP3 inflammasome activation. Interestingly, Hexokinase-1 knockdown also suppressed NLRP3 activation by extracellular ATP, linking energy sensing and active glycolysis as prerequisites for NLRP3 inflammasome activation.[35] Inhibition of

TABLE 2 Metabolic components regulate NLRP3

Metabolic component	Function in cell	Role of NLRP3	References
Glucose	Drives glycolysis	*High glucose* NLRP3 transcription TXNIP-mediated NLRP3 activation via TRPM2-p47 phox interaction	82,83
Hexokinase	Converts glucose to G6P	Acts as PRR for N-acetylglucosamine NLRP3 activation	39
Aldolase	Converts F1,6-BP to G3P	NLRP3-activated caspase-1 cleavage of aldolase	50
GAPDH	Converts G3P to 1,3BPG	NLRP3-activated caspase-1 cleavage of GAPDH Cleavage results in sarcopenia	49
PGK1	Converts 1,3BPG to 3PG	Higher levels of PGK1 in NLRP3 conditionally active myeloid cells	84
Enolase	Converts 2-PG to PEP	Inhibited by GB111-NH_2 Impairs NADH production Drives inflammasome formation	34
Pyruvate kinase	Converts PEP to pyruvate	Modulates EIF2AK2 phosphorylation EIF2AK2 binds to NLRP3 PKM2 inhibition blocks NLRP3 activity	42
Citrate synthase	Adds acetyl CoA to oxaloacetate	Bacterial citrate synthase drives NLRP3 activation Excess citrate drives NLRP3 activation	69
Aconitase	Converts citrate to isocitrate	*S. typhimurium*-depleted aconitase induces NLRP3 activation	69
Isocitrate dehydrogenase	Converts isocitrate to α-ketoglutarate	*S. typhimurium*-depleted isocitrate dehydrogenase induces NLRP3 activation	69
Succinate	Converted to fumarate in Krebs cycle	Hypoxia-induced succinate accumulation activates NLRP3 in rheumatoid arthritis	64
Itaconate	SDH inhibition	Dimethyl itaconate blocks NLRP3 inflammasome activation	85
Fumarate	Converted to malate in Krebs cycle	Dimethyl fumarate inhibits NLRP3 activation in colitis	65
NAPDH	Product of pentose phosphate pathway	Reduced expression of NLRP3, ASC, caspase-1, and IL-1β	86

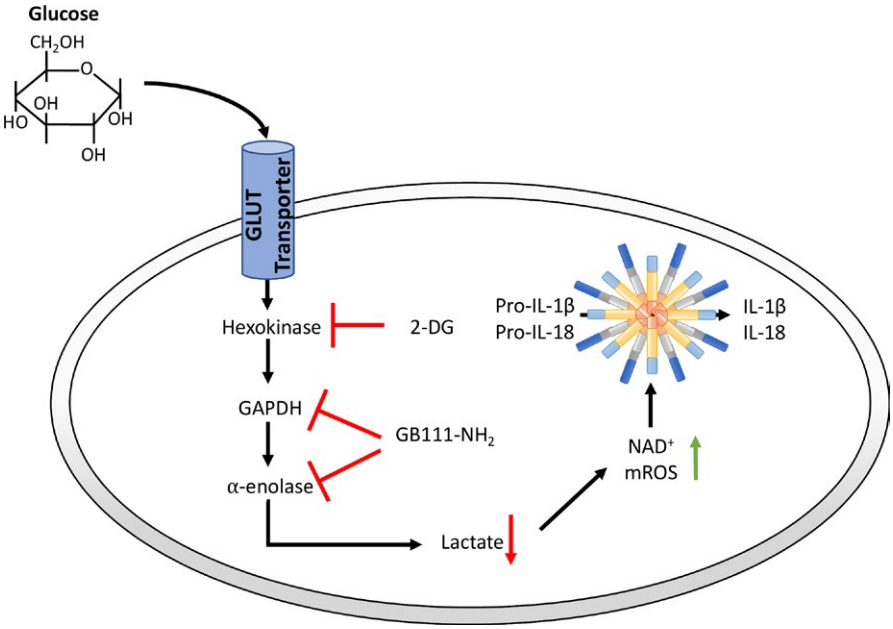

FIGURE 2 Impact of altered glycolysis on NLRP3 activation. Extracellular glucose is transported into cells via specific GLUT transporters. Glucose is sequentially converted to pyruvate through a series of glycolytic enzymes. A glucose analog, 2-deoxyglucose, cannot be utilized as a substrate by hexokinase and blocks glycolysis. The small molecule inhibitor GB111-NH_2 inhibits the enzymatic functions of GAPDH and α-enolase, resulting in decreased lactate and a disrupted NAD^+/NADH ratio, promoting mitochondrial ROS production and NLRP3 inflammasome activation

glycolysis by 2-deoxyglucose however, also triggers a decrease in intracellular ATP levels, which is sensed by NLRP3 and triggers inflammasome activation. 2-deoxyglucose dose-dependently decreased intracellular ATP, with concomitant increase in IL-1β secretion.[36] One possible explanation to this ATP and 2-deoxyglucose paradox may be due to imbalanced energy sensing as a trigger for inflammasome activation. Under resting conditions, hexokinase is tethered to the mitochondria via Akt activity.[37] Hexokinase may also play a role in ATP depletion-mediated NLRP3 activation, as Akt activity decreases during ATP starvation,[38] which may promote untethering of hexokinase from the mitochondria, without need for signal 2 to drive NLRP3 activation.

A more recent study has identified hexokinase as an intracellular PRR for N-acetylglucosamine, a glucose-derivative peptidoglycan utilized by Gram-positive bacterial cell walls. Sensing of N-acetylglucosamine by hexokinase was sufficient to induce dissociation of hexokinase from mitochondria, promoting NLRP3 inflammasome activation.[39] 2-deoxyglucose may therefore indirectly promote hexokinase mitochondrial dissociation to drive NLRP3 activation in the absence of intracellular ATP. In contrast to classical NLRP3 activators such as ATP, N-acetylglucosamine was not found to trigger pyroptosis, emphasizing a physiological role for NLRP3 to mount an effective host defense mechanism.

3.2 | PKM2

Pyruvate kinase M2 (PKM2), the last enzyme in glycolysis which converts phosphoenolpyruvate to pyruvate, induces Warburg metabolism through binding to the hypoxia-inducible factor 1α (HIF1α) in LPS-treated macrophages,[40] translocating to the nucleus and binding to the IL-1β promoter, driving inflammation.[41] PKM2 can be pharmacologically induced into a tetrameric form, which limits Warburg metabolism and promotes OXPHOS.

A role for PKM2 in NLRP3 activation in macrophages has been described. Knockdown of PKM2 or enzymatic inhibition by shikonin limits IL-1β cleavage in both NLRP3 and AIM2 inflammasomes. Conditional knockout of PKM2 in myeloid cells also blocks NLRP3 activation in vivo.[42] Interestingly, lactate promotes phosphorylation of the transcription factor EIF2AK2, in a PKM2-dependent manner, driving IL-1β maturation possibly through phosphorylated EIF2AK2 interacting with NLRP3 inflammasome.

3.3 | NLRP3, impaired glucose tolerance and aging

NLRP3 deficiency in mice was found to limit age-associated inflammation. Chronic caspase-1 activation is also associated with aging in neurodegenerative conditions.[43] Recent evidence has identified NLRP3 as a regulator of age-related neurodegeneration, concomitant with errors in metabolism. NLRP3-deficient mice present with decreased age-associated caspase-1 activation. Impaired glucose tolerance is also linked to errors in metabolism. Aged control mice were found to have impaired glucose tolerance, whereas NLRP3-deficient mice were more glucose tolerant, providing further evidence that NLRP3 activity impacts on metabolic processes.[44] IL-1β is known to orchestrate impaired glucose tolerance in an NLRP3-dependent manner,[45] however IL-1 receptor (IL-1R) deficiency did not increase glucose tolerance, indicating an NLRP3-caspase-1 axis independent of IL-1β activity in impaired glucose tolerance.

A novel small molecule inhibitor of NLRP3, termed MCC950, which displays high potency toward NLRP3 inhibition and can reverse the inflammatory phenotypes associated with Muckle-Wells syndrome and a mouse model of CAPS.[46] MCC950 contains an active sulfonylurea group which is proposed to inhibit NLRP3. Sulfonylureas are also used clinically to promote insulin secretion in patients with type 2 diabetes to reverse impaired glucose tolerance, however these treatments are

eventually futile due to progressive death of β-cells in the pancreas from IL-1β.[47] Recently, a secretagogue with dual insulin secretory and NLRP3 inhibitory properties has been reported. With similar efficacy to MCC950, 6 sulfonylurea secretagogues exhibited nanomolar potency in NLRP3 inhibition while also effectively stimulating insulin secretion from a murine pancreatic cell line,[48] holding promise as a therapeutic treatment for diabetic symptoms.

Recent evidence supports NLRP3 activity as detrimental mediator of sarcopenia. While no evidence was found for NLRP3 activity in an inflammatory setting, NLRP3-mediated caspase-1 activation promotes Glyceraldehyde 3-phosphate dehydrogenase (GAPDH) proteolysis, resulting in decreased glycolytic potential as a mechanism of decreased skeletal muscle in aging,[49] further limiting glucose metabolism in the aging process. Caspase-1 activation has also been linked to cleavage of other glycolytic enzymes in muscle tissue.[50] Targeting age-associated NLRP3 activity may therefore hold therapeutic benefit to limit over-activation of NLRP3 during aging and the alterations in glucose metabolism that occur with aging.

4 | LIPID METABOLISM AND NLRP3 FUNCTION

Fatty acids such as palmitate have been shown to activate NLRP3.[51] This may be one reason why obesity drives inflammation. More recently, the ketone body β-hydroxybutyrate (BHB) has been shown to suppress the activation of the NLRP3 inflammasome when stimulated with urate crystals, lipotoxic lipids, and ATP in macrophages (Figure 3). Ketone bodies are made from free fatty acids during starvation. BHB was shown to specifically target the NLRP3 inflammasome. BHB had no impact on canonical caspase-1 activation from AIM2 and NLRC4 inflammasomes, nor the non-canonical caspase-11 inflammasome.[52] BHB targeted K^+ efflux, resulting in reduced ASC oligomerization and reduced NLRP3 inflammasome stability. BHB or a ketogenic diet, which would drive BHB levels endogenously, also attenuated NLRP3-mediated caspase-1 activation and pro-IL-1β processing in in vivo mouse models of Muckle-Wells syndrome, urate crystal-induced peritonitis, and familial cold auto-inflammatory syndrome.[52] A ketone diet was also shown to upregulate antioxidant pathways and limit ROS generation thereby limiting NLRP3-mediated inflammation.[53] A potential role for BHB as an anti-depressant in neuronal inflammation has also been recently identified. In rat models of stress-induced neuronal inflammation, BHB attenuated hippocampal IL-1β production and reduced anxiety- and depression-related phenotypes.[54] BHB acting as an anti-inflammatory with causal anti-depressant effects further emphasizes a therapeutic role for potential BHB therapies.

Interestingly, a ketogenic diet has been reported to alleviate gout-induced inflammation, (which is driven by uric acid, a produce of purine metabolism), without impacting on bacterial clearance during infection. BHB blocked both mouse and human gout in neutrophils and macrophages. BHB plays a dual role by limiting the priming and assembly of NLRP3 in neutrophils, as BHB decreased phosphorylation of NF-κB, decreasing inflammasome assembly components.[55] Overall, there may be a balance between fatty acids as activators and ketone bodies as inhibitors of NLRP3, with obesity promoting and starvation limiting inflammation via its effects on NLRP3.

Recent data have further emphasized the link between NLRP3 and obesity. NLRP3-deficient mice are resistant to diet-induced metabolic syndrome symptoms and nephropathy, further highlighting a connection between inflammasome activation and lipid metabolism.[56]

Cholesterol catabolism results in the production of amphipathic bile acids, which function as detergents to promote intestinal nutrient absorption and homeostasis.[57] A new role for bile acids in the regulation of the NLRP3 inflammasome has been described. Bile acids specifically target NLRP3 and inhibit inflammasome activation through a TGR5-cAMP-PKA axis.[58] TGR5 activation by bile acids triggered NLRP3 ubiquitination via PKA-mediated phosphorylation of Ser291 on NLRP3 (Figure 4). Bile acids also suppressed LPS-induced septic shock in vivo. In tandem with other studies targeting NLRP3 in type

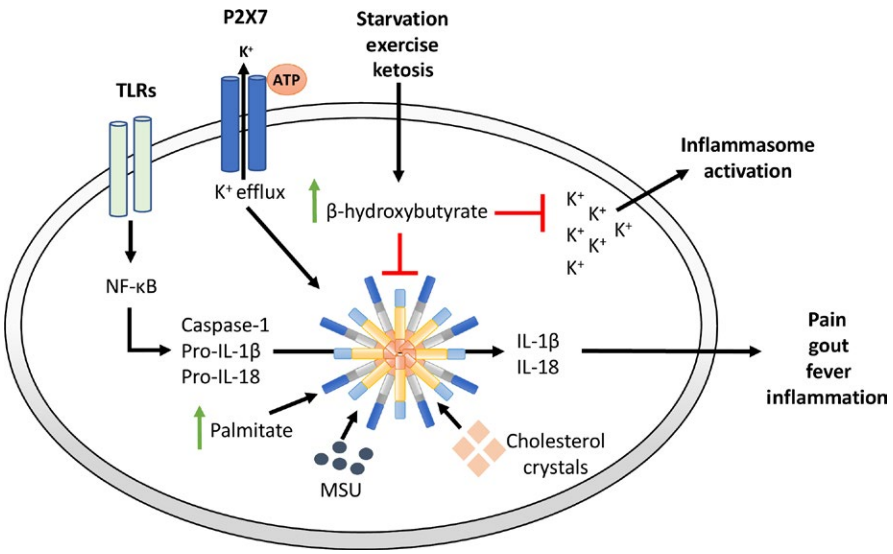

FIGURE 3 Dietary metabolites regulate NLRP3 activation via K+ efflux. TLRs drive the transcription of NLRP3 inflammasome components via NF-κB nuclear translocation and promote NLRP3 inflammasome assembly. Extracellular ATP, sensed by the P2X7 receptor, and MSU crystals trigger NLRP3 inflammasome activation. The ketone body β-hydroxybutyrate produced during starvation periods limits NLRP3 inflammasome activation, blocking ATP and MSU-mediated pro-IL-1β and pro-IL-18 processing. β-hydroxybutyrate targeted K^+ efflux, decreasing ASC oligomerization with NLRP3

2 diabetes, a high-fat diet model which induces NLRP3-dependent insulin resistance and type 2 diabetes was abolished with bile acid treatment.

Finally, another fatty acid-derived lipid, prostaglandin E_2 (PGE_2), has been identified to regulate NLRP3-mediated IL-1β maturation endogenously. In human macrophages, PGE_2 inhibits NLRP3 activation through the EP4 receptor, increasing intracellular cAMP levels.[59] In a more recent study in murine macrophages, PGE_2 has been identified to promote pro-IL-1β processing. PGE_2 can signal through the EP2 receptor, and ablation of the EP2 receptor decreases IL-1β maturation in an NLRP3-dependent manner.[60] Furthermore, in primary human monocytes, PGE_2 was shown to boost processing of pro-IL-1β by NLRP3. The role of PGE_2-mediated PKA activation on NLRP3 activity however, is not fully elucidated. It would be interesting to examine the effects of PGE_2-mediated PKA activation on potential phosphorylation of NLRP3 as seen with bile acids. Overall, the evidence suggests that PGE_2 will limit NLRP3 and this may be part of its anti-inflammatory tissue protective effects.

5 | MITOCHONDRIAL REPROGRAMMING AND NLRP3

The Krebs cycle has garnered much excitement in the field of immunology in recent years as Krebs cycle intermediates directly impact on cytokine production, including the production of pro-IL-1β through succinate accumulation,[33] targeting of complex I of the mitochondrial electron transport chain to boost IL-10,[61] and targeting complex II to prevent succinate oxidation, limiting ROS-induced pro-IL-1β.[62] (Figure 5). Oxidized mitochondrial DNA itself acts as a second signal to drive NLRP3 inflammasome activation.[63] Succinate has been a focus, being shown to stabilize HIF1α to promote NLRP3 activation.[64] Such activation of NLRP3 exacerbated tissue damage and promoted inflammation, indicating a possible prominent role of NLRP3 hyperactivation specifically in the context of joint inflammation in RA. Under normoxic conditions, succinate dehydrogenase converts succinate to fumarate, another Krebs cycle intermediate. A role for fumarate in NLRP3 regulation has also been described. Dimethyl fumarate (DMF) limits NLRP3 activation in a model of Dextran sulfate sodium (DSS) colitis. Administration of DMF prevented intestinal shortening, promoting weight gain comparable to control levels. Furthermore, DMF reduced both production and activation of NLRP3.[65] Further work is required to examine the role of fumarate in inflammatory signaling. It is intriguing that succinate and fumarate can have profound inflammatory and anti-inflammatory activities, respectively.

Salmonella typhimurium infection is sensed by the NLRC4 inflammasome through recognition of flagellin,[66] triggering inflammasome activation via phosphorylation of NLRC4,[67] with delayed activation of NLRP3,[68] suggesting a mechanism of NLRP3 evasion. Indeed, upon infection *S. typhimurium* downregulates flagellin expression to avoid NLRC4 entirely. During infection with *S. typhimurium*, the bacteria's own Krebs cycle enzymes aconitase, isocitrate lyase, and isocitrate dehydrogenase have been shown to inhibit NLRP3 activation. *S. typhimurium* deficient in these enzymes induced NLRP3 activation rapidly in macrophages.[69] Aconitase-deficient *S. typhimurium* were unable to drive acute systemic virulence and failed to persist in chronic infection. Each mutant was identified to require a ROS signal to drive NLRP3 activation, as mice overexpressing a mitochondrial-located human catalase, which degrades mitochondrial hydrogen peroxide thereby limiting ROS, failed to induce NLRP3 activation upon *S. typhimurium* infection. However, mitochondrial ROS is not the only inducible source of ROS. Macrophages infected with the protozoan parasite *Leishmania amazonensis* also trigger NLRP3 inflammasome activation via ROS induced by the professional ROS generator NADPH oxidase,[70] as NADPH oxidase inhibition prolonged *L. amazonensis* infection, adding further complexity into the source of ROS and disease outcomes.

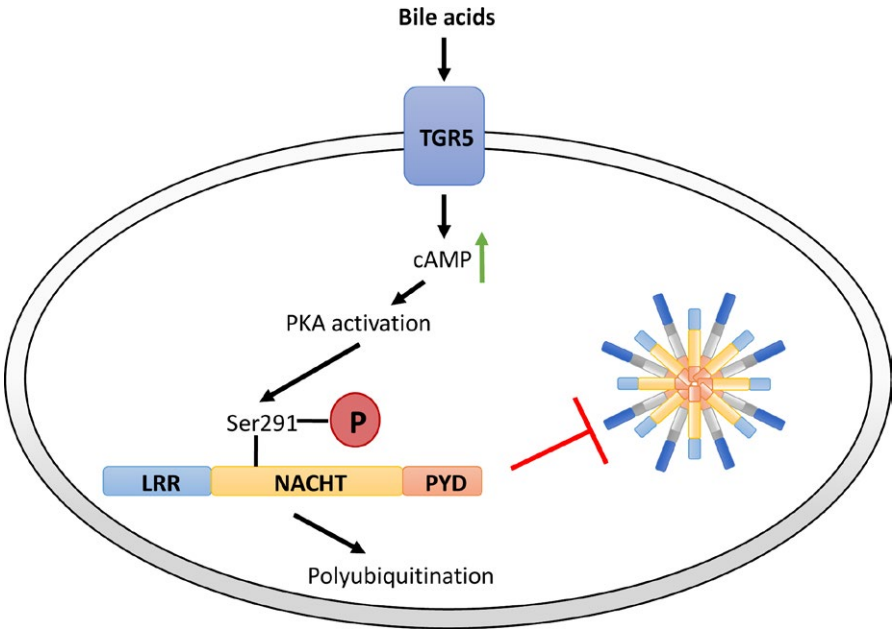

FIGURE 4 Bile acids promote NLRP3 phosphorylation and degradation. Bile acids produced from cholesterol catabolism are sensed by the TGR5 receptor, increasing intracellular cAMP levels, mediating PKA activation. PKA phosphorylates NLRP3 in the NACHT domain on Ser291. Phosphorylation of NLRP3 on Ser291 promotes K48 and K63-linked polyubiquitination and NLRP3 degradation, limiting NLRP3 inflammasome activation

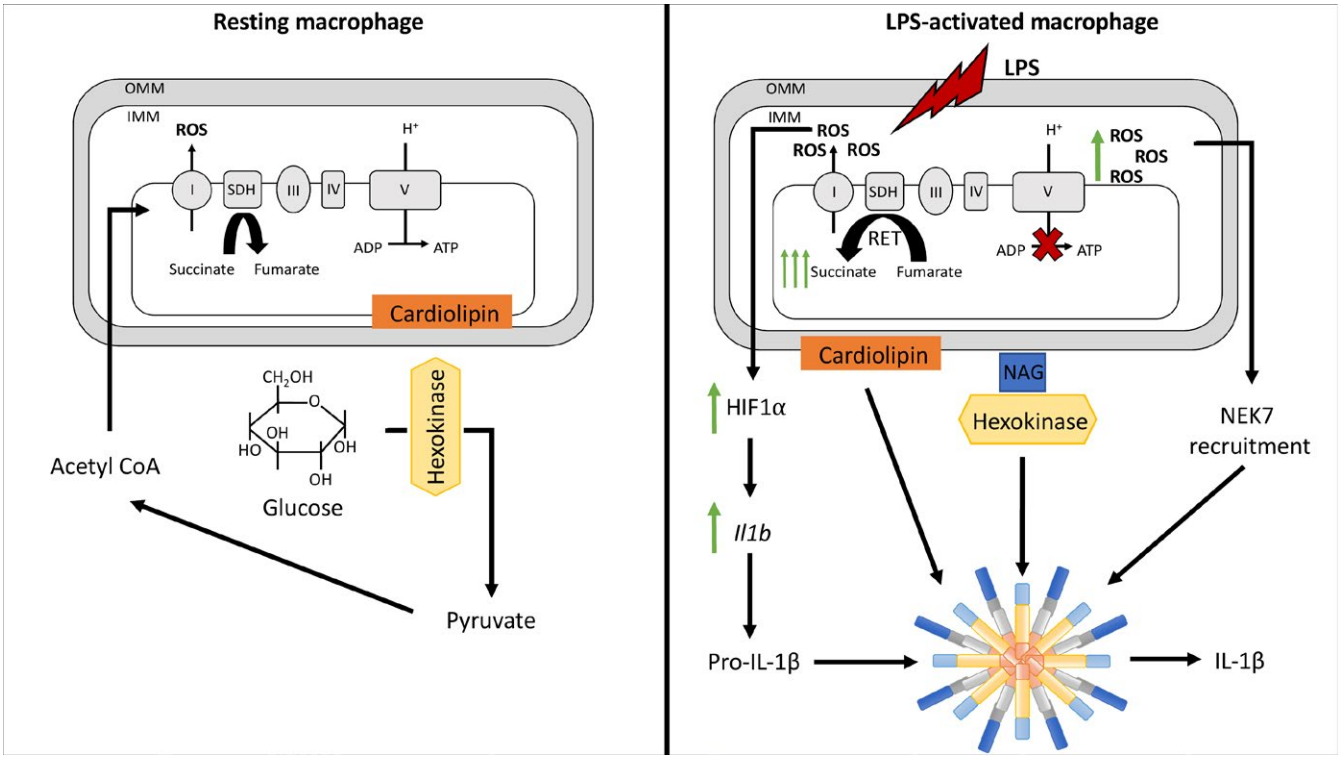

FIGURE 5 Altered mitochondrial dynamics impact NLRP3 activation. Under resting conditions (left), macrophages utilize glucose via glycolysis to produce pyruvate in the cytosol. Pyruvate undergoes a series of decarboxylation reactions to form Acetyl CoA, which is used as fuel to drive the Krebs cycle and ATP production. Hexokinase remains tethered to the mitochondrial membrane and cardiolipin is retained in the inner mitochondrial membrane. LPS-activated macrophages (right), undergo metabolic reprogramming, promoting succinate oxidation by succinate dehydrogenase, generating ROS which promotes HIF1α stability and transcription of IL-1β mRNA. Damaged mitochondria also transport cardiolipin to the outer mitochondrial membrane, which triggers NLRP3 activation. *N*-acetylglucosamine sensing promotes hexokinase untethering and drives NLRP3 activation. Increased levels of mitochondrial ROS (mROS) also drive recruitment of NEK7 to activate the NLRP3 inflammasome

Conflicting evidence arises when mitochondrial ROS is considered an NLRP3 inflammasome stimulus. Some researchers identify ROS as a regulatory signal,[71,72] whereas others indicate ROS itself as a weak signal to drive inflammasome activation and instead stems from mitochondrial dysfunction, triggering cardiolipin interaction with NLRP3 due to translocation from the inner to outer mitochondrial membrane, independent of ROS (Figure 5).[73] Proximity of NLRP3 to mitochondria is also considered a determinant in inflammasome activation. The mitochondrial antiviral signaling protein MAVS has been shown to directly interact with NLRP3 and promote its oligomerization, which may facilitate ROS activation by mitochondrial localization.[74] Activation of caspase-1 by both NLRP3 and AIM2 inflammasomes has been identified to promote mitochondrial damage and limit mitophagy through cleavage of Parkin, increasing the levels of intracellular ROS, which may in turn act as a positive feedback mechanism to promote inflammasome activation and pyroptosis.[75]

Mitochondrial-derived ROS can also drive NLRP3-mediated lysosome damage through permeabilization, as NLRP3-deficient mice retain lysosomal integrity. This mechanism is also attributed to the effects of adding exogenous K^+ and scavenging of mitochondrial-derived ROS, limiting NLRP3 activation.[76]

Imiquimod, a TLR7 agonist, and a structurally related compound termed CL097 drive K^+-independent NLRP3 activation by targeting ROS produced by the quinone oxidoreductase NQO2 and complex I of the electron transport chain.[77] Inhibition of both components trigger ROS and cysteine oxidation. Interestingly, addition of exogenous cell-permeable antioxidants, such as glutathione ethyl ester, blocked imiquimod and CL097-mediated NLRP3 activation. This evidence provides another strong link between mitochondrial ROS and NLRP3 activation. NLRP3 itself however was not suggested to act as the sensor of such ROS. Instead, as mentioned above, NEK7 was proposed to sense ROS, as NEK7-deficient dendritic cells failed to drive IL-1β processing in response to imiquimod or CL097 in an NLRP3-dependent manner.

In parallel to the role of mTORC1 in NLRP3 activation discussed earlier, the anti-inflammatory cytokine IL-10 has been shown to resist metabolic reprogramming of macrophages, specifically limiting glucose uptake by glucose receptor GLUT1 and glycolytic flux to sustain OXPHOS, through induction of an mTOR inhibitor, DDIT4.[78] IL-10 limited the aberrant effects of damaged mitochondria in NLRP3 signaling by promoting mitophagy, as IL-10-deficient mice accumulate damaged mitochondria, driving NLRP3 activation and pro-IL-1β processing. Overall, there is clearly a damaging association between

NLRP3 chronic activation and mitochondrial dysregulation. Loss of anti-inflammatory signaling further promotes such dysregulation, and may underlie many pathological associations linked with chronic NLRP3 activation.

6 | CONCLUSIONS AND FUTURE PERSPECTIVES

In this review, we have presented recent evidence to support a role for metabolic reprogramming in NLRP3 activation and dysregulation. The discovery of an altered metabolism in activated macrophages and associated metabolic components which can drive inflammation hold much promise in unraveling a bioenergetics-independent role of metabolism in host survival. It is important to consider metabolic rewiring as an evolutionarily advantageous mechanism to provide rapid ATP production and cytokine production to limit pathogenicity, however it is this innate ability to reprogram macrophages that also leads to chronic inflammation. Metabolic syndromes, such as obesity, and chronic low-grade inflammatory stimuli promote aberrant NLRP3 activation and lead to pathologies. Age-associated inflammation may also alter NLRP3 activation, predisposing NLRP3 to endogenous metabolites and nutrients which trigger IL-1β cleavage.

Metabolic regulators, such as β-hydroxybutyrate, act as endogenous regulators of general inflammation. Ketone bodies as a fuel source to limit inflammation have promising therapeutic benefits, however we must consider the risk of ketoacidosis, which can result in long-term damage to organs. Oral ketone esters have successfully increased BHB levels in humans, and could therefore be an effective route to alleviate inflammation in chronic inflammatory conditions such as gout and obesity,[79,80] where NLRP3 dysregulation triggers chronic inflammation. It will be interesting to see the development of potential new ketone body derivatives which may dampen inflammation without driving ketoacidosis.

Mitochondrial dynamics are essential for regulating many processes aside from ATP production, including apoptosis and nutrient sensing.[81] Mitochondrial dynamics are now attributed to inflammatory disorders coupled to decreased Krebs cycle activity in activated macrophages. Krebs cycle metabolites acting as DAMPs for NLRP3 activation is an exciting prospect as a novel regulator of mitochondrial dysregulation, however such findings require further elucidation as this could also pose unwanted inflammation if dysregulated. We must however bear in mind that NLRP3 can be activated by metabolism-independent mechanisms.

Further unraveling the role of glycolysis, OXPHOS, mitochondrial dynamics and lipid metabolism on inflammasome activation has the potential to lead to novel therapeutics to limit inflammation-related pathologies.

ACKNOWLEDGEMENTS

This work was funded by Science Foundation Ireland (12/IA/1531). The authors declare no financial or commercial conflict of interest.

CONFLICT OF INTEREST

The authors declare no conflict of interest.

ORCID

Mark M. Hughes http://orcid.org/0000-0003-0851-9563

Luke A.J. O'Neill http://orcid.org/0000-0002-4333-2748

REFERENCES

1. Chavez-Sanchez L, Espinosa-Luna JE, Chavez-Rueda K, et al. Innate immune system cells in atherosclerosis. *Arch Med Res*. 2014;45:1-14. https://doi.org/10.1016/j.arcmed.2013.11.007.
2. Lee J. Adipose tissue macrophages in the development of obesity-induced inflammation, insulin resistance and type 2 diabetes. *Arch Pharm Res*. 2013;36:208-222. https://doi.org/10.1007/s12272-013-0023-8.
3. Minciullo PL, Catalano A, Mandraffino G, et al. Inflammaging and anti-inflammaging: the role of cytokines in extreme longevity. *Arch Immunol Ther Exp (Warsz)*. 2016;64:111-126. https://doi.org/10.1007/s00005-015-0377-3.
4. Johnson AR, Milner JJ, Makowski L. The inflammation highway: metabolism accelerates inflammatory traffic in obesity. *Immunol Rev*. 2012;249:218-238. https://doi.org/10.1111/j.1600-065X.2012.01151.x.
5. Chimenti MS, Triggianese P, Conigliaro P, et al. The interplay between inflammation and metabolism in rheumatoid arthritis. *Cell Death Dis*. 2015;6:e1887. https://doi.org/10.1038/cddis.2015.246.
6. Lu A, Magupalli VG, Ruan J, et al. Unified polymerization mechanism for the assembly of ASC-dependent inflammasomes. *Cell*. 2014;156:1193-1206. https://doi.org/10.1016/j.cell.2014.02.008.
7. Martinon F, Burns K, Tschopp J. The inflammasome: a molecular platform triggering activation of inflammatory caspases and processing of proIL-beta. *Mol Cell*. 2002;10:417-426.
8. Agostini L, Martinon F, Burns K, et al. NALP3 forms an IL-1beta-processing inflammasome with increased activity in Muckle-Wells autoinflammatory disorder. *Immunity*. 2004;20:319-325.
9. Zhou R, Tardivel A, Thorens B, et al. Thioredoxin-interacting protein links oxidative stress to inflammasome activation. *Nat Immunol*. 2010;11:136-140. https://doi.org/10.1038/ni.1831.
10. Vandanmagsar B, Youm YH, Ravussin A, et al. The NLRP3 inflammasome instigates obesity-induced inflammation and insulin resistance. *Nat Med*. 2011;17:179-188. https://doi.org/10.1038/nm.2279.
11. Gaidt MM, Ebert TS, Chauhan D, et al. Human monocytes engage an alternative inflammasome pathway. *Immunity*. 2016;44:833-846. https://doi.org/10.1016/j.immuni.2016.01.012.
12. Kayagaki N, Warming S, Lamkanfi M, et al. Non-canonical inflammasome activation targets caspase-11. *Nature*. 2011;479:117-121. https://doi.org/10.1038/nature10558.
13. Kayagaki N, Stowe IB, Lee BL, et al. Caspase-11 cleaves gasdermin D for non-canonical inflammasome signalling. *Nature*. 2015;526:666-671. https://doi.org/10.1038/nature15541.
14. Holmstrom KM, Finkel T. Cellular mechanisms and physiological consequences of redox-dependent signalling. *Nat Rev Mol Cell Biol*. 2014;15:411-421. https://doi.org/10.1038/nrm3801.
15. Garcia-Santamarina S, Boronat S, Hidalgo E. Reversible cysteine oxidation in hydrogen peroxide sensing and signal transduction. *Biochemistry*. 2014;53:2560-2580. https://doi.org/10.1021/bi401700f.
16. Hughes MM, McGettrick AF, O'Neill LA. Glutathione and glutathione transferase omega 1 as key posttranslational regulators in macrophages. *Microbiol Spectr*. 2017;5:789-801. https://doi.org/10.1128/microbiolspec.MCHD-0044-2016.

17. Hughes MM, Lavrencic P, Coll RC, et al. Solution structure of the TLR adaptor MAL/TIRAP reveals an intact BB loop and supports MAL Cys91 glutathionylation for signaling. *Proc Natl Acad Sci U S A*. 2017;114:E6480-6489. https://doi.org/10.1073/pnas.1701868114.
18. Meissner F, Molawi K, Zychlinsky A. Superoxide dismutase 1 regulates caspase-1 and endotoxic shock. *Nat Immunol*. 2008;9:866-872. https://doi.org/10.1038/ni.1633.
19. Huang Z, Pinto JT, Deng H, et al. Inhibition of caspase-3 activity and activation by protein glutathionylation. *Biochem Pharmacol*. 2008;75:2234-2244. https://doi.org/10.1016/j.bcp.2008.02.026.
20. Guglielmo A, Sabra A, Elbery M, et al. A mechanistic insight into curcumin modulation of the IL-1beta secretion and NLRP3 S-glutathionylation induced by needle-like cationic cellulose nanocrystals in myeloid cells. *Chem Biol Interact*. 2017;274:1-12. https://doi.org/10.1016/j.cbi.2017.06.028.
21. Shi H, Wang Y, Li X, et al. NLRP3 activation and mitosis are mutually exclusive events coordinated by NEK7, a new inflammasome component. *Nat Immunol*. 2016;17:250-258. https://doi.org/10.1038/ni.3333.
22. He Y, Zeng MY, Yang D, et al. NEK7 is an essential mediator of NLRP3 activation downstream of potassium efflux. *Nature*. 2016;530:354-357. https://doi.org/10.1038/nature16959.
23. Munoz-Planillo R, Kuffa P, Martinez-Colon G, et al. K(+) efflux is the common trigger of NLRP3 inflammasome activation by bacterial toxins and particulate matter. *Immunity*. 2013;38:1142-1153. https://doi.org/10.1016/j.immuni.2013.05.016.
24. Domingo-Fernandez R, Coll RC, Kearney J, et al. The intracellular chloride channel proteins CLIC1 and CLIC4 induce IL-1beta transcription and activate the NLRP3 inflammasome. *J Biol Chem*. 2017;292:12077-12087. https://doi.org/10.1074/jbc.M117.797126.
25. Tang T, Lang X, Xu C, et al. CLICs-dependent chloride efflux is an essential and proximal upstream event for NLRP3 inflammasome activation. *Nat Commun*. 2017;8:202. https://doi.org/10.1038/s41467-017-00227-x.
26. Cunha LD, Silva ALN, Ribeiro JM, et al. AIM2 engages active but unprocessed caspase-1 to induce noncanonical activation of the NLRP3 inflammasome. *Cell Rep*. 2017;20:794-805. https://doi.org/10.1016/j.celrep.2017.06.086.
27. Haneklaus M, O'Neil JD, Clark AR, et al. The RNA-binding protein Tristetraprolin (TTP) is a critical negative regulator of the NLRP3 inflammasome. *J Biol Chem*. 2017;292:6869-6881. https://doi.org/10.1074/jbc.M116.772947.
28. Lee SJ, Michel SL. Cysteine oxidation enhanced by iron in tristetraprolin, a zinc finger peptide. *Inorg Chem*. 2010;49:1211-1219. https://doi.org/10.1021/ic9024298.
29. Chen CY, Liaw CC, Chen YH, et al. A novel immunomodulatory effect of ugonin U in human neutrophils via stimulation of phospholipase C. *Free Radic Biol Med*. 2014;72:222-231. https://doi.org/10.1016/j.freeradbiomed.2014.04.018.
30. Chen CY, Yang CH, Tsai YF, et al. Ugonin U stimulates NLRP3 inflammasome activation and enhances inflammasome-mediated pathogen clearance. *Redox Biol*. 2017;11:263-274. https://doi.org/10.1016/j.redox.2016.12.018.
31. Moon JS, Lee S, Park MA, et al. UCP2-induced fatty acid synthase promotes NLRP3 inflammasome activation during sepsis. *J Clin Invest*. 2015;125:665-680. https://doi.org/10.1172/jci78253.
32. Moon JS, Nakahira K, Chung KP, et al. NOX4-dependent fatty acid oxidation promotes NLRP3 inflammasome activation in macrophages. *Nat Med*. 2016;22:1002-1012. https://doi.org/10.1038/nm.4153.
33. Tannahill GM, Curtis AM, Adamik J, et al. Succinate is an inflammatory signal that induces IL-1beta through HIF-1alpha. *Nature*. 2013;496:238-242. https://doi.org/10.1038/nature11986.
34. Sanman LE, Qian Y, Eisele NA, et al. Disruption of glycolytic flux is a signal for inflammasome signaling and pyroptotic cell death. *Elife*. 2016;5:e13663. https://doi.org/10.7554/eLife.13663.
35. Moon JS, Hisata S, Park MA, et al. mTORC1-induced HK1-dependent glycolysis regulates NLRP3 inflammasome activation. *Cell Rep*. 2015;12:102-115. https://doi.org/10.1016/j.celrep.2015.05.046.
36. Nomura J, So A, Tamura M, et al. Intracellular ATP decrease mediates NLRP3 inflammasome activation upon nigericin and crystal stimulation. *J Immunol*. 2015;195:5718-5724. https://doi.org/10.4049/jimmunol.1402512.
37. Majewski N, Nogueira V, Bhaskar P, et al. Hexokinase-mitochondria interaction mediated by Akt is required to inhibit apoptosis in the presence or absence of Bax and Bak. *Mol Cell*. 2004;16:819-830. https://doi.org/10.1016/j.molcel.2004.11.014.
38. Hahn-Windgassen A, Nogueira V, Chen CC, et al. Akt activates the mammalian target of rapamycin by regulating cellular ATP level and AMPK activity. *J Biol Chem*. 2005;280:32081-32089. https://doi.org/10.1074/jbc.M502876200.
39. Wolf AJ, Reyes CN, Liang W, et al. Hexokinase is an innate immune receptor for the detection of bacterial peptidoglycan. *Cell*. 2016;166:624-636. https://doi.org/10.1016/j.cell.2016.05.076.
40. Luo W, Hu H, Chang R, et al. Pyruvate kinase M2 is a PHD3-stimulated coactivator for hypoxia-inducible factor 1. *Cell*. 2011;145:732-744. https://doi.org/10.1016/j.cell.2011.03.054.
41. Palsson-McDermott EM, Curtis AM, Goel G, et al. Pyruvate kinase M2 regulates Hif-1alpha activity and IL-1beta induction and is a critical determinant of the warburg effect in LPS-activated macrophages. *Cell Metab*. 2015;21:65-80. https://doi.org/10.1016/j.cmet.2014.12.005.
42. Xie M, Yu Y, Kang R, et al. PKM2-dependent glycolysis promotes NLRP3 and AIM2 inflammasome activation. *Nat Commun*. 2016;7:13280. https://doi.org/10.1038/ncomms13280.
43. Pasinelli P. Caspase-1 and -3 are sequentially activated in motor neuron death. *Proc Natl Acad Sci U S A*. 2000;97:13901-13906.
44. Youm YH, Grant RW, McCabe LR, et al. Canonical Nlrp3 inflammasome links systemic low-grade inflammation to functional decline in aging. *Cell Metab*. 2013;18:519-532. https://doi.org/10.1016/j.cmet.2013.09.010.
45. Stienstra R, van Diepen JA, Tack CJ, et al. Inflammasome is a central player in the induction of obesity and insulin resistance. *Proc Natl Acad Sci U S A*. 2011;108:15324-15329. https://doi.org/10.1073/pnas.1100255108.
46. Coll RC, Robertson AA, Chae JJ, et al. A small-molecule inhibitor of the NLRP3 inflammasome for the treatment of inflammatory diseases. *Nat Med*. 2015;21:248-255. https://doi.org/10.1038/nm.3806.
47. Dinarello CA, Donath MY, Mandrup-Poulsen T. Role of IL-1beta in type 2 diabetes. *Curr Opin Endocrinol Diabetes Obes*. 2010;17:314-321. https://doi.org/10.1097/MED.0b013e32833bf6dc.
48. Hill JR, Coll RC, Sue N, et al. Sulfonylureas as concomitant insulin secretagogues and NLRP3 inflammasome inhibitors. *ChemMedChem*. 2017;12:1449-1457. https://doi.org/10.1002/cmdc.201700270.
49. McBride MJ, Foley KP, D'Souza DM, et al. The NLRP3 inflammasome contributes to sarcopenia and lower muscle glycolytic potential in old mice. *Am J Physiol Endocrinol Metab*. 2017;313:E222-e232. https://doi.org/10.1152/ajpendo.00060.2017.
50. Shao W, Yeretssian G, Doiron K, et al. The caspase-1 digestome identifies the glycolysis pathway as a target during infection and septic shock. *J Biol Chem*. 2007;282:36321-36329. https://doi.org/10.1074/jbc.M708182200.
51. Wen H, Gris D, Lei Y, et al. Fatty acid-induced NLRP3-ASC inflammasome activation interferes with insulin signaling. *Nat Immunol*. 2011;12:408-415. https://doi.org/10.1038/ni.2022.
52. Youm YH, Nguyen KY, Grant RW, et al. The ketone metabolite beta-hydroxybutyrate blocks NLRP3 inflammasome-mediated inflammatory disease. *Nat Med*. 2015;21:263-269. https://doi.org/10.1038/nm.3804.
53. Kong G, Huang Z, Ji W, et al. The ketone metabolite beta-hydroxybutyrate attenuates oxidative stress in spinal cord injury by suppression of class I histone deacetylases. *J Neurotrauma*. 2017;34:2645-2655. https://doi.org/10.1089/neu.2017.5192.

54. Yamanashi T, Iwata M, Kamiya N, et al. Beta-hydroxybutyrate, an endogenic NLRP3 inflammasome inhibitor, attenuates stress-induced behavioral and inflammatory responses. *Sci Rep*. 2017;7:7677. https://doi.org/10.1038/s41598-017-08055-1.
55. Goldberg EL, Asher JL, Molony RD, et al. beta-Hydroxybutyrate deactivates neutrophil NLRP3 inflammasome to relieve gout flares. *Cell Rep*. 2017;18:2077-2087. https://doi.org/10.1016/j.celrep.2017.02.004.
56. Bakker PJ, Butter LM, Kors L, et al. Nlrp3 is a key modulator of diet-induced nephropathy and renal cholesterol accumulation. *Kidney Int*. 2014;85:1112-1122. https://doi.org/10.1038/ki.2013.503.
57. Chiang JY. Regulation of bile acid synthesis: pathways, nuclear receptors, and mechanisms. *J Hepatol*. 2004;40:539-551. https://doi.org/10.1016/j.jhep.2003.11.006.
58. Guo C, Xie S, Chi Z, et al. Bile acids control inflammation and metabolic disorder through inhibition of NLRP3 inflammasome. *Immunity*. 2016;45:944. https://doi.org/10.1016/j.immuni.2016.10.009.
59. Sokolowska M, Chen LY, Liu Y, et al. Prostaglandin E2 inhibits NLRP3 inflammasome activation through EP4 receptor and intracellular cyclic AMP in human macrophages. *J Immunol*. 2015;194:5472-5487. https://doi.org/10.4049/jimmunol.1401343.
60. Zaslona Z, Palsson-McDermott EM, Menon D, et al. The induction of Pro-IL-1beta by lipopolysaccharide requires endogenous prostaglandin E2 production. *J Immunol*. 2017;198:3558-3564. https://doi.org/10.4049/jimmunol.1602072.
61. Kelly B, Tannahill GM, Murphy MP, et al. Metformin inhibits the production of reactive oxygen species from NADH: ubiquinone oxidoreductase to limit induction of interleukin-1beta (IL-1beta) and boosts interleukin-10 (IL-10) in lipopolysaccharide (LPS)-activated macrophages. *J Biol Chem*. 2015;290:20348-20359. https://doi.org/10.1074/jbc.M115.662114.
62. Mills EL, Kelly B, Logan A, et al. Succinate dehydrogenase supports metabolic repurposing of mitochondria to drive inflammatory macrophages. *Cell*. 2016;167:457-470. https://doi.org/10.1016/j.cell.2016.08.064.
63. Shimada K, Crother TR, Karlin J, et al. Oxidized mitochondrial DNA activates the NLRP3 inflammasome during apoptosis. *Immunity*. 2012;36:401-414. https://doi.org/10.1016/j.immuni.2012.01.009.
64. Li Y, Zheng JY, Liu JQ, et al. Succinate/NLRP3 inflammasome induces synovial fibroblast activation: therapeutical effects of clematichinenoside AR on arthritis. *Front Immunol*. 2016;7:532. https://doi.org/10.3389/fimmu.2016.00532.
65. Liu X, Zhou W, Zhang X, et al. Dimethyl fumarate ameliorates dextran sulfate sodium-induced murine experimental colitis by activating Nrf2 and suppressing NLRP3 inflammasome activation. *Biochem Pharmacol*. 2016;112:37-49. https://doi.org/10.1016/j.bcp.2016.05.002.
66. Zhao Y, Yang J, Shi J, et al. The NLRC4 inflammasome receptors for bacterial flagellin and type III secretion apparatus. *Nature*. 2011;477:596-600. https://doi.org/10.1038/nature10510.
67. Matusiak M, Van Opdenbosch N, Vande Walle L, et al. Flagellin-induced NLRC4 phosphorylation primes the inflammasome for activation by NAIP5. *Proc Natl Acad Sci U S A*. 2015;112:1541-1546. https://doi.org/10.1073/pnas.1417945112.
68. Broz P, Newton K, Lamkanfi M, et al. Redundant roles for inflammasome receptors NLRP3 and NLRC4 in host defense against Salmonella. *J Exp Med*. 2010;207:1745-1755. https://doi.org/10.1084/jem.20100257.
69. Wynosky-Dolfi MA, Snyder AG, Philip NH, et al. Oxidative metabolism enables Salmonella evasion of the NLRP3 inflammasome. *J Exp Med*. 2014;211:653-668. https://doi.org/10.1084/jem.20130627.
70. Lima-Junior DS, Mineo TWP, Calich VLG, et al. Dectin-1 activation during *Leishmania amazonensis* phagocytosis prompts Syk-dependent reactive oxygen species production to trigger inflammasome assembly and restriction of parasite replication. *J Immunol*. 2017;199:2055-2068. https://doi.org/10.4049/jimmunol.1700258.
71. Dostert C, Petrilli V, Van Bruggen R, et al. Innate immune activation through Nalp3 inflammasome sensing of asbestos and silica. *Science*. 2008;320:674-677. https://doi.org/10.1126/science.1156995.
72. Zhou R, Yazdi AS, Menu P, et al. A role for mitochondria in NLRP3 inflammasome activation. *Nature*. 2011;469:221-225. https://doi.org/10.1038/nature09663.
73. Iyer SS, He Q, Janczy JR, et al. Mitochondrial cardiolipin is required for Nlrp3 inflammasome activation. *Immunity*. 2013;39:311-323. https://doi.org/10.1016/j.immuni.2013.08.001.
74. Park S, Juliana C, Hong S, et al. The mitochondrial antiviral protein MAVS associates with NLRP3 and regulates its inflammasome activity. *J Immunol*. 2013;191:4358-4366. https://doi.org/10.4049/jimmunol.1301170.
75. Yu J, Nagasu H, Murakami T, et al. Inflammasome activation leads to Caspase-1-dependent mitochondrial damage and block of mitophagy. *Proc Natl Acad Sci U S A*. 2014;111:15514-15519. https://doi.org/10.1073/pnas.1414859111.
76. Heid ME, Keyel PA, Kamga C, et al. Mitochondrial reactive oxygen species induces NLRP3-dependent lysosomal damage and inflammasome activation. *J Immunol*. 2013;191:5230-5238. https://doi.org/10.4049/jimmunol.1301490.
77. Gross CJ, Mishra R, Schneider KS, et al. K+ efflux-independent NLRP3 inflammasome activation by small molecules targeting mitochondria. *Immunity*. 2016;45:761-773. https://doi.org/10.1016/j.immuni.2016.08.010.
78. Ip WKE, Hoshi N, Shouval DS, et al. Anti-inflammatory effect of IL-10 mediated by metabolic reprogramming of macrophages. *Science*. 2017;356:513-519. https://doi.org/10.1126/science.aal3535.
79. Clarke K, Tchabanenko K, Pawlosky R, et al. Kinetics, safety and tolerability of (R)-3-hydroxybutyl (R)-3-hydroxybutyrate in healthy adult subjects. *Regul Toxicol Pharmacol*. 2012;63:401-408. https://doi.org/10.1016/j.yrtph.2012.04.008.
80. Kemper MF, Srivastava S, Todd King M, et al. An ester of beta-hydroxybutyrate regulates cholesterol biosynthesis in rats and a cholesterol biomarker in humans. *Lipids*. 2015;50:1185-1193. https://doi.org/10.1007/s11745-015-4085-x.
81. Nunnari J, Suomalainen A. Mitochondria: in sickness and in health. *Cell*. 2012;148:1145-1159. https://doi.org/10.1016/j.cell.2012.02.035.
82. Feng H, Gu J, Gou F, et al. High glucose and lipopolysaccharide prime NLRP3 Inflammasome via ROS/TXNIP pathway in mesangial cells. *J Diabetes Res*. 2016. https://doi.org/10.1155/2016/6973175
83. Tseng HH, Vong CT, Kwan YW, et al. TRPM2 regulates TXNIP-mediated NLRP3 inflammasome activation via interaction with p47 phox under high glucose in human monocytic cells. *Sci Rep*. 2016;6. https://doi.org/10.1038/srep35016
84. Wang C, Xu CX, Alippe Y, et al. Chronic inflammation triggered by the NLRP3 inflammasome in myeloid cells promotes growth plate dysplasia by mesenchymal cells. *Sci Rep*. 2017;7:4880. https://doi.org/10.1038/s41598-017-05033-5
85. Lampropoulou V, Sergushichev A, Bambouskova M, et al. Itaconate links inhibition of succinate dehydrogenase with macrophage metabolic remodeling and regulation of inflammation. *Cell Metab*. 2016;24:158-166. https://doi.org/10.1016/j.cmet.2016.06.004
86. Qin YY, Li M, Feng X, et al. Combined NADPH and the NOX inhibitor apocynin provides greater anti-inflammatory and neuroprotective effects in a mouse model of stroke. *Free Radic Biol Med*. 2017;104:333-345. https://doi.org/10.1016/j.freeradbiomed.2017.01.034

How to cite this article: Hughes MM, O'Neill LAJ. Metabolic regulation of NLRP3. *Immunol Rev*. 2017;281:1–11. https://doi.org/10.1111/imr.12608

Microbiology Spectrum
American Society for Microbiology Press

Glutathione and Glutathione Transferase Omega 1 as Key Posttranslational Regulators in Macrophages

MARK M. HUGHES,[1] ANNE F. MCGETTRICK,[1] and LUKE A. J. O'NEILL[1]

[1]School of Biochemistry and Immunology, Trinity Biomedical Science Institute, Trinity College Dublin, Dublin 2, Ireland

ABSTRACT Macrophage activation during phagocytosis or by pattern recognition receptors, such as Toll-like receptor 4, leads to the accumulation of reactive oxygen species (ROS). ROS act as a microbicidal defense mechanism, promoting clearance of infection, allowing for resolution of inflammation. Overproduction of ROS, however, overwhelms our cellular antioxidant defense system, promoting oxidation of protein machinery, leading to macrophage dysregulation and pathophysiology of chronic inflammatory conditions, such as atherosclerosis. Here we will describe the role of the antioxidant tripeptide glutathione (GSH). Until recently, the binding of GSH, termed glutathionylation, was only considered to maintain the integrity of cellular components, limiting the damaging effects of an aberrant oxidative environment. GSH can, however, have positive and negative regulatory effects on protein function in macrophages. GSH regulates protein secretion, driving tumor necrosis factor α release, hypoxia-inducible factor-1α stability, STAT3 phosphorylation, and caspase-1 activation in macrophages. GSH also plays a role in host defense against *Listeria monocytogenes*, modifying the key virulence protein PrfA in infected macrophages. We will also discuss glutathione transferase omega 1, a deglutathionylating enzyme recently shown to play a role in many aspects of macrophage activity, including metabolism, NF-κB activation, and cell survival pathways. Glutathionylation is emerging as a key regulatory event in macrophage biology that might be susceptible to therapeutic targeting.

INTRODUCTION

The cytoplasm of an activated macrophage is a dangerous place due to the accumulation of reactive oxygen species (ROS), which can perturb cytoplasmic oxidative balance. Macrophage activation through monocyte recruitment in tissues occurs in a highly regulated manner upon detection of microbial pathogen-associated molecular patterns (PAMPs), such as the Gram-negative bacterial cell wall component lipopolysaccharide (LPS), stimulating ROS production. ROS can be generated from many cellular processes, either directly or as a result of incomplete reduction of free radicals (1). One of the main sources of ROS is the NADPH oxidase (NOX), a specialized transmembrane protein complex that generates superoxide (O_2^-), which has been implicated in several inflammatory diseases (2). The generation of ROS can also stem from the mitochondrial electron transport chain, due to insufficient reduction of superoxide anions. Another source is the inducible form of nitric oxide synthase 2 (iNOS). iNOS produces nitric oxide from L-arginine and is known to play key roles in macrophage function (3, 4).

While ROS have benefits, acting as endogenous signaling molecules (5), activated macrophages produce high levels of ROS, which can go unregulated under

Received: 26 July 2016, **Accepted:** 23 November 2016, **Published:** 20 January 2017

Editor: Siamon Gordon, Oxford University, Oxford, United Kingdom

Citation: Hughes MM, McGettrick AF, O'Neill LAJ. 2017. Glutathione and glutathione transferase omega 1 as key posttranslational regulators in macrophages. *Microbiol Spectrum* 5(1):MCHD-0044-2016. doi:10.1128/microbiolspec.MCHD-0044-2016.

Correspondence: Luke A. J. O'Neill, laoneill@tcd.ie

inflammatory conditions, indiscriminately targeting redox-sensitive protein machinery. Glutathione (γ-L-glutamyl-L-cysteinyl-glycine; GSH) is the fundamental nonprotein tripeptide redox agent that detoxifies ROS. Composed of the amino acids glutamate, cysteine, and glycine, GSH is utilized within the cell to maintain redox homeostasis (6). Overproduction of ROS can target the thiol group (-SH) of cysteine amino acids on proteins. GSH can prevent oxidation of proteins via formation of mixed disulfides (-SSG) to redox-sensitive cysteine amino acids in proteins (7). Cells contain a variety of redox enzymes, such as glutathione transferases and glutaredoxins, which utilize GSH to detoxify ROS and maintain protein integrity. GSH is predominantly found in the thiol-reduced form, reaching intracellular concentrations of up to 10 mM (8), and the ratio of reduced GSH to oxidized GSH (termed GSSG) can be used as a measure of cellular oxidative imbalance (9). GSH may, however, not be limited to antioxidant defense, with posttranslational modifications placing GSH as both a positive and negative regulator of protein function. Here we will discuss emerging themes in the field of GSH biology, notably the enzymatic addition or removal of GSH to proteins, which modifies their function. Glutathionylation is emerging as a key process in macrophage activation, targeting proteins such as caspase-1, hypoxia-inducible factor-1α (HIF1α), and STAT3. Here we will discuss this process and its regulation during macrophage activation.

GSH AS AN ANTIOXIDANT

GSH is ubiquitously expressed in all cell types and tissues. Aside from cellular detoxification, GSH is also a source of readily accessible cysteine, a rate-limiting amino acid for many cellular processes, including GSH synthesis. The amino acid cysteine is also crucial for maintaining protein tertiary structure via disulfide bond formation (10, 11) and is highly redox sensitive. Due to the presence of a thiol group, cysteine is readily oxidized to cystine, a cysteine dimer, and can subsequently generate ROS. Excessive ROS can promote the formation of thiol intermediates on cysteines, termed sulfenic acid, sulfinic acid, and sulfonic acid in proteins (12). Overoxidation of cysteine residues to sulfonic acid is irreversible and promotes proteasomal degradation. GSH can reverse the formation of sulfenic and sulfinic acid in conjunction with reductase (sulfenic) or sulfiredoxin (sulfinic) enzymes, resulting in regeneration of native protein structure and generation of nontoxic intermediates as a by-product, such as H_2O. High levels of GSH may thereby have a dual role in acting as a cysteine storage pool for physiological use as well as oxidative defense.

GSH is synthesized in a two-step enzymatic process requiring ATP investment at each step to generate GSH from the amino acids glutamate, cysteine, and glycine (Fig. 1). Upon exposure to oxidative stress inducers such as O_2^- or hydrogen peroxide (H_2O_2), GSH scavenges ROS and forms GSSG, which can be recycled in the cytoplasm back to reduced GSH by glutathione reductase (13). One of the main sources of endogenous ROS is mitochondria. Although the sizes of mitochondria are modest (ranging from 0.5 to 3 μm), they contain a concentrated level of GSH, comprising roughly 10 to 15% of cellular GSH (14), that can buffer ROS production. Mitochondria are metabolic powerhouses that not only promote ATP production through oxidative phosphorylation (OXPHOS), but also have been recently reported to regulate the proinflammatory status of macrophages when challenged with Toll-like receptor (TLR) agonists, such as LPS, via the tricarboxylic acid cycle component succinate (15, 16). Due to the critical nature of OXPHOS, the pathway is tightly regulated, and GSH has been shown to play a role in OXPHOS regulation. Complex V, otherwise known as ATP synthase, and succinyl-coenzyme A transferase are both negatively regulated by glutathionylation (17). The main purpose of OXPHOS is to produce ATP via cofactors such as NADH, which donate their energy-rich electrons into the complex assembly chain. This process, however, is not perfect, with some electrons donated directly to O_2, resulting in superoxide anion generation that can lead to pathophysiological conditions if unregulated (18). GSH conjugates to these superoxide anions to help protect mitochondrial integrity. It is likely that GSH controls ROS generated by succinate, which drives ROS production by complex I in LPS-activated macrophages (16). Utilization of molecular oxygen to generate ATP can also produce free radicals, leading to lipid peroxidation and generation of a harmful by-product, 4-hydroxynonenal (4-HNE) (19). GSH can therefore prevent formation 4-HNE by preventing ROS accumulation (Fig. 2). While lipid peroxidation is not uncommon, GSH in this context is crucial for redox homeostasis, as high levels of 4-HNE (up to 20 μM) have been shown to inhibit NF-κB signaling (20) and promote caspase-3 activation via Akt inhibition to promote apoptosis (21). Damaged mitochondria are known to undergo autophagy (22), or deliberate breakdown of cellular components and organelles to generate basic components for new synthesis pathway intermediates.

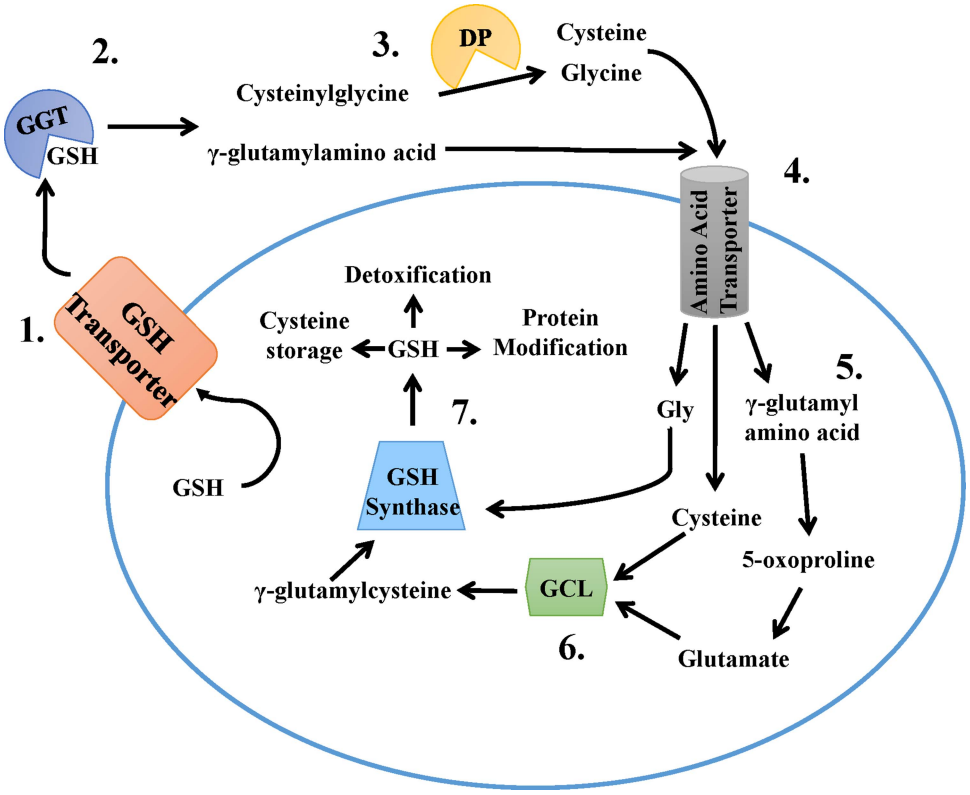

FIGURE 1 GSH synthesis pathway in mammalian cells. GSH is exported from the cell to the extracellular environment via a glutathione transporter (1). Extracellular GSH is targeted by γ-glutamylpeptidase (GGT), transferring the γ-glutamyl component of GSH to an amino acid, forming γ-glutamylamino acid and cysteinylglycine (2). Cysteinylglycine is further cleaved by dipeptidase (DP) into the amino acids cysteine and glycine (3). γ-glutamylamino acid, cysteine, and glycine reenter the cell via an amino acid transporter (4). Release of the amino acid component of γ-glutamylamino acid forms 5-oxoproline, which is further converted to glutamate in an ATP-dependent process (5). Newly formed glutamate and cysteine are ligated into γ-glutamylcysteine via glutamate cysteine ligase (GCL) in an ATP-dependent process (6). γ-Glutamylcysteine and glycine are ligated via GSH synthase to re-form GSH (7).

Recent evidence has identified that the immunosuppressive mycotoxin patulin induces depletion of GSH, inhibiting TLRs in macrophages and enhancing mitophagy in a p62-dependent manner (23), further emphasizing the critical role of GSH in maintaining mitochondrial integrity.

GSH REGULATES PROTEIN ACTIVITY IN MACROPHAGES

Within the past decade, studies have revealed a role for GSH in posttranslational modification of proteins. This reversible modification regulates some of the best-characterized enzymes and pathways. The ability of GSH to bind to a cysteine residue can be influenced by the neighboring amino acids (24). Positively charged amino acids, such as histidine, lysine, and arginine, can directly influence the probability of GSH binding. Cysteines are more susceptible to oxidation by ROS due to positively charged amino acids lowering their thiol pK_a, which deprotonates cysteines, promoting glutathionylation (25). A recent study has used a Web-based software program called GSHSite to rank potentially glutathionylated proteins in mouse macrophages based on conserved cysteine amino acids, positively charged flanking amino acids, and the ability of GSH to access cysteines in folded proteins (26). Using this approach, two known glutathionylated proteins, thioredoxin (TRX) and protein tyrosine phosphatase 1b, were correctly identified as glutathionylated proteins. Proteomic approaches to quantify cellular glutathionylation can also be employed using mass spectrometry

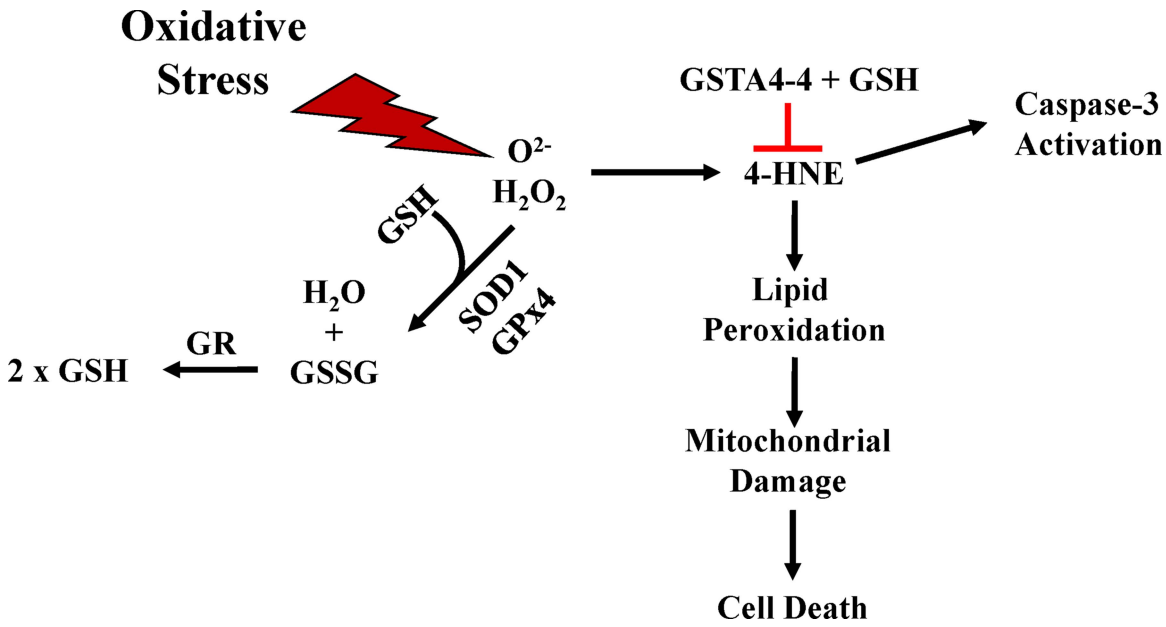

FIGURE 2 Cellular roles of GSH. Oxidative stress can be induced by many exogenous factors, including LPS, or endogenously by the mitochondrial electron transport chain. ROS can build up within the cell, in the form of O_2^- and H_2O_2, which damages organelles and results in 4-HNE production. 4-HNE can promote lipid peroxidation and caspase-3 activation. The redox enzyme GSTA4-4 can target 4-HNE, utilizing GSH to prevent lipid peroxidation and maintain homeostasis. O_2^- and H_2O_2 can be reduced via redox enzymes SOD1 and glutathione peroxidase 4 (GPx4), respectively. Both enzymes utilize GSH to remove ROS, forming glutathione disulfide (GSSG). GSSG can then be reduced to GSH by glutathione reductase (GR).

(MS) (27). Su et al. were able to quantify 690 mouse macrophage proteins that were susceptible to glutathionylation when Raw 264.7 cells were pretreated with the oxidant diamide, and 290 proteins that were glutathionylated in response to hydrogen peroxide treatment. Similarly, Ullevig et al. identified >130 glutathionylated proteins in THP-1 monocytic cells treated with hydrogen peroxide to induce metabolic stress (28). While MS can identify glutathionylated proteins, methodologies differ in sample preparation, which may account for the differences in reported glutathionylation targets. As a result, glutathionylation can also be confirmed by Western blotting conditions, using nonreducing SDS-PAGE and an anti-GSH antibody. These studies have highlighted a number of proteins in macrophages as potential GSH targets, which may alter their function; however, GSH concentration can also impact macrophage function.

Research by Yang et al. has discovered that GSH regulates CD36 activity (29). CD36 is critical for oxidized low-density lipoprotein (oxLDL) clearance, a process that can go awry in atherosclerosis and promote foam cell generation. Macrophages treated with buthionine sulfoximine (BSO), a compound that inhibits GSH synthesis, resulting in decreased intracellular GSH levels, had increased ROS production and CD36 levels. This increased oxLDL uptake, driving foam cell generation. Importantly, the addition of antioxidants such as *N*-acetylcysteine and antioxidant enzymes catalase or superoxide dismutase 1 (SOD1) to peritoneal macrophages inhibited the effects of BSO on CD36 protein levels, preventing oxLDL uptake. GSH therefore displays antiatherogenic properties and regulates the levels of CD36 within macrophages to limit oxLDL uptake.

In related research, Vasamsetti et al. found that monocyte-to-macrophage differentiation in atherosclerotic plaque formation was dependent on GSH levels (30). Treatment of monocytes with the antioxidant resveratrol dose-dependently inhibited phorbol myristate acetate (PMA)-induced monocyte-to-macrophage differentiation. BSO-mediated GSH depletion was found to induce monocyte differentiation and promote inflammation, while resveratrol and BSO cotreatment prevented monocyte-to-macrophage transition, restoring GSH levels. Maintaining high GSH levels within monocytes is therefore protective in preventing monocyte differentiation in atherosclerotic plaques and maintaining

lower CD36 levels, thereby preventing foam cell generation. Examination of the redox status of the cell has yielded a number of proteins in macrophages that are regulated by glutathionylation, which will now be discussed.

GLUTATHIONYLATED PRDX2 IS SECRETED FROM MACROPHAGES AND DRIVES TNF-α RELEASE

Using a redox proteomics MS approach, LPS-treated macrophages were found to secrete glutathionylated proteins from the cytoplasm. LPS treatment promoted oxidation of proteins due to increased ROS production, which were subsequently glutathionylated (31). Of particular note, the enzyme peroxiredoxin-2 (PRDX2), involved in hydrogen peroxide regulation, was secreted in the glutathionylated form and was identified to act as an inflammatory mediator, promoting tumor necrosis factor α (TNF-α) release. LPS did not induce PRDX2 expression; rather, it promoted oxidation of PRDX2 from the mainly reduced cytosolic form, promoting glutathionylation of PRDX2, which could drive TNF-α. Similarly, recombinant PRDX2 was found to drive TNF-α production. The identification of a redox enzyme with cytokine-like properties has resulted in the coining of the term "redoxkine." Furthermore, the redox enzyme TRX1, a substrate for PRDX2, was also found to be glutathionylated and secreted. PRDX2 uses reduced TRX1 as an electron donor for hydrogen peroxide reduction. TRX1 is an oxidoreductase enzyme and can target proteins due to its thiol-disulfide exchange properties and has been found to have immunomodulatory effects. Indeed, TRX1 has been shown to regulate lymphocyte response to HIV-1 entry into lymphocytes by controlling CD4 membrane localization (32). Many cytokine receptors can be activated by disulfide bond-mediated dimerization, including the interleukin-3 (IL-3), IL-5, and granulocyte-macrophage colony-stimulating factor receptors (33). The enzymatic activity of both PRDX2 and TRX1 could therefore initiate the dimerization of cytokine receptors and promote inflammation. The glutathionylation and secretion of PRDX2 and TRX1 by activated macrophages thereby identifies a new danger signal whereby redoxkines could alter extracellular receptor complexes, further driving inflammatory responses.

GSH NEGATIVELY REGULATES CASPASE-1 ACTIVATION

The cytokine IL-1β is a central proinflammatory cytokine (34), whose overproduction can give rise to a range of diseases, including autoinflammatory diseases such as Muckle-Wells syndrome, as well as common diseases such as gout. Upon exposure to PAMPs, such as LPS, IL-1β transcription is induced by the transcription factor NF-κB to produce pro-IL-1β, also known as "signal 1." Pro-IL-1β must be cleaved to elicit an inflammatory phenotype. PAMP or danger-associated molecular pattern recognition stimulates the formation of a multicomponent complex termed the "inflammasome," which processes pro-IL-1β and pro-IL-18 into bioactive IL-1β and IL-18 via proteolytic cleavage by caspase-1, termed "signal 2" (35, 36). Several inflammasomes have been identified. Nucleotide-binding domain leucine-rich repeat-containing receptors (NLRs) are critical components. A feature common to NLRs is a central nucleotide-binding (NACHT) domain and C-terminal leucine-rich repeat (LRR) domain. The NLRs can further contain an N-terminal pyrin domain (PYD) and a caspase recruitment domain (CARD). NLR family members, such as NLRP3, form inflammasomes with apoptosis-associated speck-like protein containing a CARD (ASC) and procaspase-1 (37). The NLRP3 inflammasome is the most-studied inflammasome and has been shown to be activated by mitochondrial ROS (38, 39). GSH has been shown to play a regulatory role in this process. Upstream of caspase-1, GSH has been found to limit inflammasome activation. In a model of dextran sulfate sodium-induced murine colitis, which mimics inflammatory bowel disease, pretreatment of mice with dimethyl fumarate (DMF) dose-dependently reduced inflammatory bowel disease progression and weight loss. The mechanism of DMF protection was attributed to increased GSH levels and activity of the antioxidant enzyme NRF2, which transcribes a host of antioxidant genes, subsequently dampening mitochondrial ROS levels. NRF2 has also been shown to upregulate GCLc, the catalytic subunit of the rate-limiting enzyme in GSH synthesis, further driving GSH levels (40). DMF was found to decrease activation of the NLRP3 inflammasome, subsequently limiting caspase-1 activity (41). Aside from ROS disruption, research by Meissner et al. has reported that glutathionylation of caspase-1 on cysteine 362 and 397 directly inhibits its activity (Fig. 3). They have shown that SOD1, an enzyme that converts O_2^- into O_2 and H_2O_2, regulates the activity of caspase-1 and subsequent endotoxic shock response, with no effect on mitogen-activated protein kinase or NF-κB signaling (42). SOD1-deficient macrophages had higher levels of O_2^-, affecting the cellular redox environment, causing oxidation and glutathionylation of caspase-1 on Cys362 and Cys397. Overexpres-

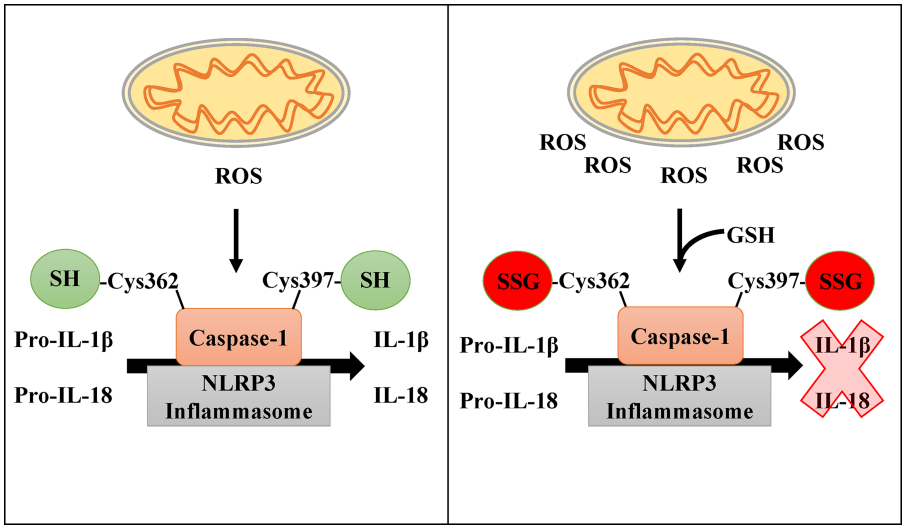

FIGURE 3 GSH-dependent inhibition of caspase-1 activity. (Left) Production of ROS from mitochondria drives NLRP3 inflammasome activation, producing mature IL-1β and IL-18 via caspase-1 activity. (Right) Over time, ROS accumulation leads to GSH binding to Cys362 and Cys397 on caspase-1, inhibiting caspase-1 catalytic activity. Oxidizing agents, such as superoxide and hydrogen peroxide, can induce glutathionylation of caspase-1, preventing cleavage of pro-IL-1β and pro-IL-18.

sion of caspase-1-containing cysteine-to-serine mutants (C362S, C397S) yielded a higher production of IL-1β compared to wild-type caspase-1, due to GSH being unable to glutathionylate and inhibit caspase-1. When caspase-1-containing C362S or C397S was transfected into caspase-1-deficient macrophages, both mutants were overactive under normoxic or oxygen-rich conditions promoting IL-1β production. Conversely, when subjected to hypoxia, neither mutant of caspase-1 could increase IL-1β processing, indicating that Cys362 and Cys397 are redox sensitive and potential glutathionylation targets when oxidized to limit caspase-1 activation. Finally, SOD1-deficient mice were shown to be more resistant to LPS-induced sepsis when compared to both caspase-1-deficient and wild-type mice. Serum cytokine analyses identified that SOD1-deficient mice had decreased IL-1β and IL-18 compared to wild-type mice. The ratio of GSH/GSSG is commonly used as a measure of oxidative imbalance (43). SOD1-deficient mice challenged with 3-h *Escherichia coli* infection and 30-min ATP, which drives inflammasome activation, were found to have >10-fold-higher GSSG levels compared to wild-type mice. SOD1-deficient mice, therefore, have a higher oxidative burden, which would result in oxidation and glutathionylation of caspase-1. GSH is therefore a negative regulator of caspase-1 activity both *in vitro* and *in vivo*. This presents something of a paradox. ROS are a positive signal for NLRP3 and yet inhibit caspase-1 by glutathionylation. It is possible that this is a matter of timing, whereby ROS will initially activate NLRP3 but then later limit caspase-1 by glutathionylation. This implicates GSH in the regulation of inflammation by ROS.

GSH STABILIZES HIF1α PROTEIN

Watanabe et al. have found that the transcription factor HIF1α is redox regulated by GSH in a mouse model of ischemia (44). GSH was shown to promote stability of HIF1α protein. Furthermore, the cell-permeable oxidizing agent oxidized GSH (GSSG-ethyl ester) was shown to increase HIF1α levels. Deletion of the deglutathionylating enzyme glutaredoxin-1 (Glrx) improved ischemic revascularization. *In vivo* analyses of Glrx deletion discovered that blood flow recovery after ischemic hind limb revascularization was significantly improved, concomitant with increased levels of vascular endothelial growth factor A (VEGF-A) and HIF1α. The deletion of Glrx is thereby highly advantageous during ischemic tissue recovery, as its absence will promote GSH binding, subsequently stabilizing HIF1α and thereby increasing angiogenesis and revascularization. To further implicate GSH as a modulator of HIF1α, MS identified that cysteine 520 (or cysteine 533 in mice) was bound to a GSH adduct on HIF1α. Functional mutation of cysteine 520 to serine (C520S) yielded decreased HIF1α

stability (Fig. 4). These data clearly identify GSH as a positive regulator of HIF1α activity that may play a vital role in angiogenesis in response to ischemic tissue damage. Since HIF1α is also required for a number of macrophage responses (45, 46), GSH may positively regulate the expression of these genes via stabilization of HIF1α.

GSH IMPAIRS STAT3 PHOSPHORYLATION

Since its discovery as a potential oncogene, STAT3 has been the subject of intense research. STAT3 is activated by multiple macrophage-activating cytokines, including IL-6. Glutathionylation was shown to negatively regulate STAT3. Initial studies by Xie et al. identified that STAT3 could be glutathionylated when treated with diamide, which induces oxidative stress (47). Such treatment was found to decrease IL-6-dependent STAT3 signaling, along with decreased tyrosine phosphorylation and nuclear accumulation (Fig. 5). Further research by Butturini et al. identified the redox-sensitive cysteine residues in STAT3, cysteines 328 and 542, which directly impair phosphorylation when glutathionylated (48). Cotreatment with diamide and reduced GSH was found to induce glutathionylation of STAT3. Furthermore, STAT3 phosphorylation by JAK2 was abrogated with diamide and GSH treatment, indicating that GSH inhibits phosphorylation of STAT3. Functional mutagenesis of the key cysteine amino acids to serine (C328S, C542S) prevented STAT3 from being glutathionylated when pretreated with diamide. Further work is required to verify the downstream consequences of this negative regulatory event on STAT3, considering it plays a vital role in many essential pathways, from autophagy to oncogenesis.

FIGURE 4 HIF1α protein is stabilized by glutathionylation. MS revealed two redox-sensitive cysteines that undergo glutathionylation, Cys520 in humans or Cys533 in mice. Ischemia-reperfusion of Glrx-deficient mice showed improved hind limb revascularization and increased HIF1α levels. HIF1α stability was increased due to deficiency of Glrx, increasing expression of VEGF-A and blood flow recovery.

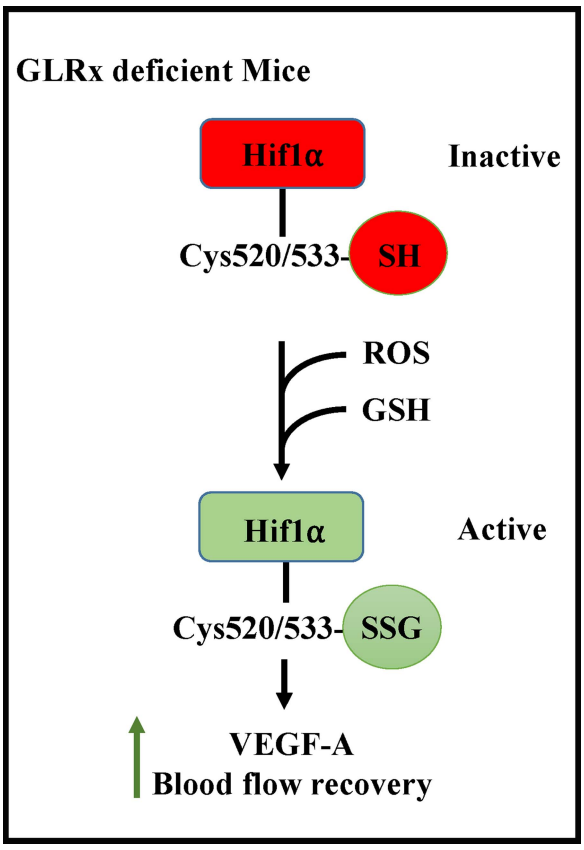

GSH PROMOTES VIRULENCE GENE EXPRESSION DURING MACROPHAGE INFECTION WITH *LISTERIA MONOCYTOGENES*

GSH has been found to aid the activation of the master transcription factor of *Listeria monocytogenes*, PrfA, via allosteric regulation. *L. monocytogenes* is a Gram-positive intracellular pathogen that infects macrophages, and the success of its survival is entirely dependent on PrfA activation, as PrfA-deficient strains are avirulent (49). *L. monocytogenes* is one of the few Gram-positive strains of bacteria to produce GSH, as most other strains utilize other low-molecular-weight thiols, such as bacillithiol and mycothiol (50, 51). Reniere et al. have shown that the bifunctional *L. monocytogenes* glutathione synthase (gshF), a multidomain protein capable of synthesizing GSH without GCL, is critical for the survival of *L. monocytogenes* in macrophages (52). GSH was shown to react with PrfA. Mutation of key cysteines in PrfA (C38A, C144A, C205A, and C229A) decreased its ability to induce ActA, which is responsible for actin-based motility, limiting pathogenicity. GSH allosterically regulates PrfA, acting as a cofactor, as gshF-deficient strains are avirulent. In this instance, GSH acts as a cofactor to upregulate virulence genes in *L. monocytogenes* during macrophage infection (Fig. 6).

CONTROLLING GLUTATHIONYLATION IN MACROPHAGES: GSTO1-1

Our understanding of how glutathionylation is controlled in macrophages has also improved recently. A particular focus has been the enzyme glutathione

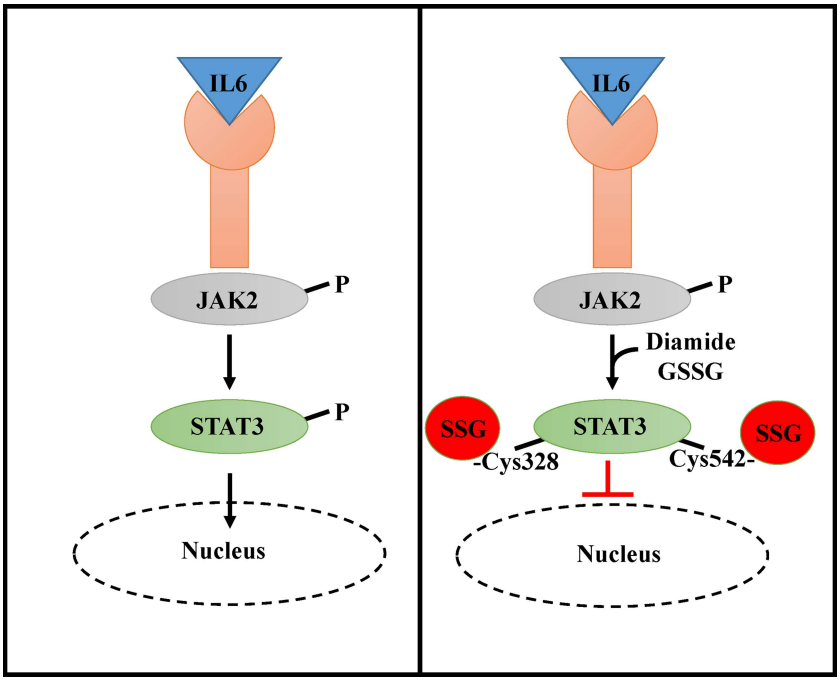

FIGURE 5 Glutathionylation of STAT3 prevents STAT3 phosphorylation and nuclear translocation. Activation of the IL-6 receptor by the cytokine IL-6 drives phosphorylation of JAK2. JAK2 subsequently phosphorylates STAT3, promoting nuclear translocation for upregulation of STAT3-dependent gene transcription. The oxidant diamide induces glutathionylation of two redox-sensitive cysteines on STAT3, Cys328 and Cys542, preventing JAK2-dependent STAT3 phosphorylation and nuclear translocation.

transferase omega 1 (GSTO1-1). Glutathione transferases (previously termed glutathione *S*-transferases; GSTs) have come to the forefront in recent years as phase II detoxification enzymes that play a critical role in the regulation of cellular responses. Seven classes of GSTs have been identified, each class containing up to several isoforms that are involved in GSH conjugation reactions (53). As a broad family of GSH-conjugating enzymes, GST diversity can be viewed as evolutionarily advantageous. GSTO1-1 stands out from this family due to an atypical cysteine amino acid active site, which allows GSTO1-1 to carry out different enzymatic reactions, including thioltransferase activity. GSTO1-1 appears to play a part in multiple processes in macrophages, including antioxidant defense, enhanced glycolysis, xenobiotic detoxification, ROS production, and GSH cycling and cell survival crosstalk, which will be discussed later. Staining for GSTO1-1 by immunohistochemistry has revealed that the expression of GSTO1-1 is widespread in different tissues, but notably in macrophages (54). GSTO1-1 was detected in macrophages in the skin and lung but not in endothelial cells, lymphocytes, or smooth muscle cells in these tissues.

In response to LPS and interferon gamma (IFN-γ), macrophages can differentiate into a proinflammatory, M1 or M(LPS IFN-γ) macrophage, or alternatively they can be activated by the cytokine IL-4 into a resolving anti-inflammatory macrophage, termed M2 or M(IL–4) (55). The need to clarify specific subsets of genes upregulated by these stimuli can thereby aid as potential biomarkers for macrophage populations in disease states. A recent screen comparing undifferentiated human and mouse macrophages with IL-4-differentiated macrophages both *ex vivo* and *in vitro* revealed novel IL-4-controlled gene subsets. The authors identified transglutaminase 2 as a novel M2 marker that is consistently induced in both human and mouse macrophages with IL-4 treatment (56). Interestingly, the authors found that GSTO1-1 was also consistently detected within their analyses as a signature gene in both human and mouse IL-4-treated macrophages. GSTO1-1 could therefore become a potential biomarker for M2 macrophage populations. This represents somewhat of a paradox, as GSTO1-1 has been found to play roles in response to proinflammatory stimuli. GSTO1-1 has, however, been reported to play a role in the glutathionylation cycle (57), and endogenous IL-4 has been shown to drive GSH synthesis in a mouse model of liver injury through glutamate cysteine ligase enzymatic activity (58). In this manner, IL-4 signaling may increase

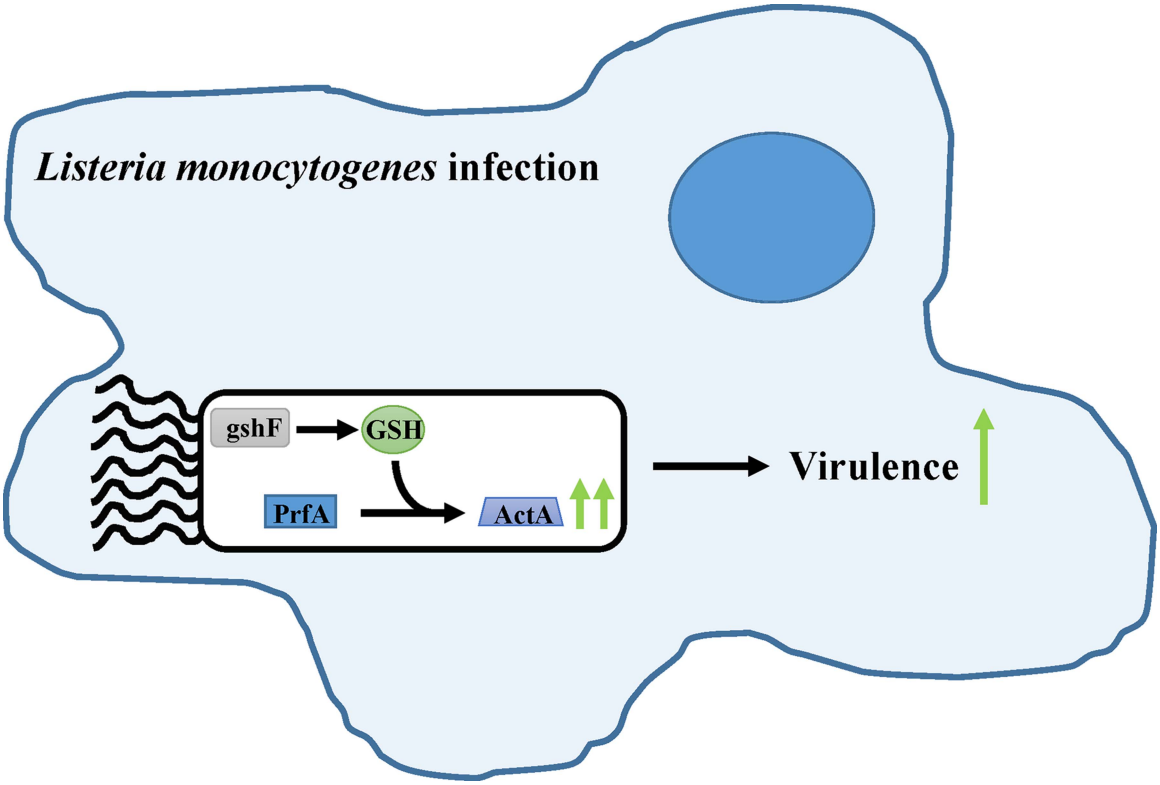

FIGURE 6 GSH acts as a cofactor to promote virulence gene expression by *L. monocytogenes*. Macrophage infection by *L. monocytogenes* is dependent on the master virulence gene transcription factor PrfA. PrfA transcribes ActA, an actin-mobility protein that promotes virulence success of *L. monocytogenes*. *L. monocytogenes* synthesizes its own GSH with the enzyme gshF. PrfA is only active when GSH binds as a cofactor, an event essential for virulence.

GSTO1-1 levels; however, further examination into the role of GSTO1-1 in IL-4 signaling is required.

GSTO1-1 AND NF-κB TRANSLOCATION

NF-κB, one of the most widely characterized transcription factors that upregulates a plethora of inflammatory genes, has been shown to require GSTO1-1 for nuclear translocation in macrophages. NF-κB has previously been reported as a redox-sensitive protein. Oxidation of Cys38 in the p65 subunit of NF-κB and Cys62 in the p50 subunit will prevent DNA binding (59). Menon et al., examining the effect of GSTO1-1 deficiency via knockdown approaches in macrophages, discovered that the absence of GSTO1-1 prevented nuclear translocation of NF-κB upon LPS stimulation (60). This indicates that NF-κB may require GSTO1-1 for dissociation from IκBα, possibly by deglutathionylation. This would place GSTO1-1 as a potential downstream effector of TLR4 signaling. Components of the TLR4 signaling pathway are possibly deglutathionylated by GSTO1-1, allowing them to become active, which would promote NF-κB activation.

GSTO1-1 AS AN AUTOPHAGY GATEKEEPER

GSTO1-1 has recently been reported to play a key role in cell survival following treatment of macrophages with aflatoxin B_1 (AFB_1), a mycotoxin considered to be the most potent carcinogen found in contaminated food, with powerful immunosuppressive effects (61). GSTO1-1 has previously been linked to apoptosis regulation, preventing apoptosis via the activity of Jun N-terminal protein kinase 1 (JNK1) (62). Interestingly, Paul et al. have identified a cytoprotective role for GSTO1-1 in AFB_1-treated macrophages. A 6-h treatment of AFB_1 was reported to induce an elevation in ROS levels from mitochondria, resulting in loss of mitochondrial membrane potential and subsequent JNK-mediated caspase-dependent cell death (63). GSTO1-1 was identified as the causative link between autophagy and apoptosis, as small interfering RNA-mediated knockdown of

GSTO1-1 mimicked 6-h AFB_1 treatment results, promoting apoptosis. Taken together, these data indicate that GSTO1-1 plays a role in cell survival via autophagy induction by agents such as AFB_1. Increased ROS and NF-κB activity was found to promote mitochondrial fission in hepatocellular carcinoma, enhancing autophagy and preventing apoptosis (64). GSTO1-1-mediated NF-κB translocation may thereby promote autophagy and could therefore be exploited by cancer cells. Further studies will be required to verify the role of GSTO1-1 in autophagy induction and if other xenobiotics could induce similar autophagy-related cell responses.

GSTO1-1 AND METABOLIC REPROGRAMMING IN MACROPHAGES

GSTO1-1 has been implicated in multiple responses induced by LPS in macrophages, notably induction of the ROS generator NOX1, enhanced mitochondrial ROS production by succinate, and enhanced glycolysis. The knockdown of GSTO1-1 in macrophages decreased expression of NOX1 after LPS stimulation. NOX1 is one of the main producers of ROS, along with mitochondria, and similar results were obtained utilizing the GSTO1-1 inhibitor ML175. The authors suggested that GSTO1-1 acts upstream of NOX1 on the TLR4 pathway (65), and further studies published by the same authors identified a critical role for GSTO1-1 in the modulation of macrophage metabolism via LPS. Indeed, LPS activation will skew the phenotype of macrophages toward a proglycolytic environment (66); however, this switch is significantly attenuated in GSTO1-1-deficient cells. In addition to the effect on NOX1, GSTO1-1-deficient cells did not increase mitochondrial ROS generation with LPS treatment, compared to a significant ROS enhancement in control cells, implicating GSTO1-1 in mitochondrial ROS production. Succinate accumulates in LPS-treated macrophages, which stabilizes HIF1α to promote IL-1β levels (15). The buildup of succinate and citrate was abolished in GSTO1-1-deficient cells, concomitant with decreased HIF1α production (67). These data clearly place GSTO1-1 as a key modulator of LPS responsiveness within macrophages. It is possible that GSTO1-1 regulates a key component of TLR4 signaling, which might impact deglutathionylation of adaptor proteins. This identifies GSTO1-1 as a key regulator of LPS responsiveness in macrophage activation (Fig. 7).

CONCLUDING REMARKS

Glutathionylation of proteins is emerging as a key posttranslational regulator in macrophages, with target proteins including HIF1α, STAT3, and caspase-1. A unifying aspect here is ROS, which promote glutathionylation, with HIF1α being stabilized and STAT3 and caspase-1 being inhibited. Additional proteins are likely to be identified in the so-called glutathionylome, with further complexities being revealed as to how ROS affect macrophage function. The GSH flux has also been found to affect monocyte-to-macrophage differentia-

FIGURE 7 GSTO1-1 regulates macrophage responses to cellular processes. GSTO1-1 protects macrophages from AFB_1-induced apoptosis. GSTO1-1 is also essential for LPS action in macrophages, including translocation of NF-κB to the nucleus, increased glycolysis, elevated TCA cycle intermediate succinate levels, NOX-1 activation, and subsequent ROS induction. GSTO1-1 is therefore likely to regulate components in the TLR4 signaling pathway.

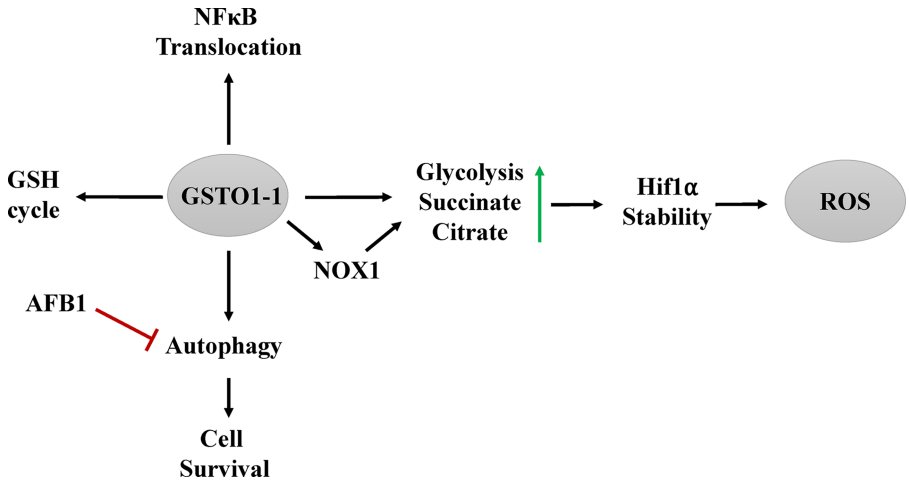

tion, being detrimental in atherosclerosis. GSTO1-1 has emerged as a potential regulator of these events, being highly expressed in macrophages and acting on LPS signaling. Several studies have linked GSTO1-1 to neurological disorders such as Alzheimer's disease and Parkinson's disease (68, 69). Further work on glutathionylation and GSTO1-1 in macrophages may lead to a greater understanding of these and possibly other inflammatory diseases.

ACKNOWLEDGMENTS

This work was funded by Science Foundation Ireland. The authors declare no financial or commercial conflict of interest.

REFERENCES

1. Panth N, Paudel KR, Parajuli K. 2016. Reactive oxygen species: a key hallmark of cardiovascular disease. *Adv Med* **2016:**9152732. doi:10.1155/2016/9152732.

2. Gimenez M, Schickling BM, Lopes LR, Miller FJ, Jr. 2016. Nox1 in cardiovascular diseases: regulation and pathophysiology. *Clin Sci (Lond)* **130:**151–165.

3. Zhang G, Li X, Sheng C, Chen X, Chen Y, Zhu D, Gao P. 2016. Macrophages activate iNOS signaling in adventitial fibroblasts and contribute to adventitia fibrosis. *Nitric Oxide* **61:**20–28.

4. Dey P, Panga V, Raghunathan S. 2016. A cytokine signalling network for the regulation of inducible nitric oxide synthase expression in rheumatoid arthritis. *PLoS One* **11:**e0161306. doi:10.1371/journal.pone.0161306.

5. Sandalio LM, Rodríguez-Serrano M, Romero-Puertas MC, del Río LA. 2013. Role of peroxisomes as a source of reactive oxygen species (ROS) signaling molecules. *Subcell Biochem* **69:**231–255.

6. Morris D, Khurasany M, Nguyen T, Kim J, Guilford F, Mehta R, Gray D, Saviola B, Venketaraman V. 2013. Glutathione and infection. *Biochim Biophys Acta* **1830:**3329–3349.

7. Alanazi AM, Mostafa GA, Al-Badr AA. 2015. Glutathione. *Profiles Drug Subst Excip Relat Methodol* **40:**43–158.

8. Montero D, Tachibana C, Rahr Winther J, Appenzeller-Herzog C. 2013. Intracellular glutathione pools are heterogeneously concentrated. *Redox Biol* **1:**508–513.

9. Zhou Y, Harrison DE, Love-Myers K, Chen Y, Grider A, Wickwire K, Burgess JR, Stochelski MA, Pazdro R. 2014. Genetic analysis of tissue glutathione concentrations and redox balance. *Free Radic Biol Med* **71:**157–164.

10. Perlman JH, Wang W, Nussenzveig DR, Gershengorn MC. 1995. A disulfide bond between conserved extracellular cysteines in the thyrotropin-releasing hormone receptor is critical for binding. *J Biol Chem* **270:**24682–24685.

11. Patil NA, Tailhades J, Hughes RA, Separovic F, Wade JD, Hossain MA. 2015. Cellular disulfide bond formation in bioactive peptides and proteins. *Int J Mol Sci* **16:**1791–1805.

12. Paulech J, Liddy KA, Engholm-Keller K, White MY, Cordwell SJ. 2015. Global analysis of myocardial peptides containing cysteines with irreversible sulfinic and sulfonic acid post-translational modifications. *Mol Cell Proteomics* **14:**609–620.

13. Lu SC. 2013. Glutathione synthesis. *Biochim Biophys Acta* **1830:**3143–3153.

14. Marí M, Morales A, Colell A, García-Ruiz C, Fernández-Checa JC. 2009. Mitochondrial glutathione, a key survival antioxidant. *Antioxid Redox Signal* **11:**2685–2700.

15. Tannahill GM, Curtis AM, Adamik J, Palsson-McDermott EM, McGettrick AF, Goel G, Frezza C, Bernard NJ, Kelly B, Foley NH, Zheng L, Gardet A, Tong Z, Jany SS, Corr SC, Haneklaus M, Caffrey BE, Pierce K, Walmsley S, Beasley FC, Cummins E, Nizet V, Whyte M, Taylor CT, Lin H, Masters SL, Gottlieb E, Kelly VP, Clish C, Auron PE, Xavier RJ, O'Neill LA. 2013. Succinate is an inflammatory signal that induces IL-1β through HIF-1α. *Nature* **496:**238–242.

16. Mills EL, Kelly B, Logan A, Costa AS, Varma M, Bryant CE, Tourlomousis P, Däbritz JH, Gottlieb E, Latorre I, Corr SC, McManus G, Ryan D, Jacobs HT, Szibor M, Xavier RJ, Braun T, Frezza C, Murphy MP, O'Neill LA. 2016. Succinate dehydrogenase supports metabolic repurposing of mitochondria to drive inflammatory macrophages. *Cell* **167:**457–470.e13. doi:10.1016/j.cell.2016.08.064.

17. Garcia J, Han D, Sancheti H, Yap LP, Kaplowitz N, Cadenas E. 2010. Regulation of mitochondrial glutathione redox status and protein glutathionylation by respiratory substrates. *J Biol Chem* **285:**39646–39654.

18. Gao L, Laude K, Cai H. 2008. Mitochondrial pathophysiology, reactive oxygen species, and cardiovascular diseases. *Vet Clin North Am Small Anim Pract* **38:**137–155, vi.

19. Zhong H, Yin H. 2015. Role of lipid peroxidation derived 4-hydroxynonenal (4-HNE) in cancer: focusing on mitochondria. *Redox Biol* **4:**193–199.

20. Dou X, Li S, Wang Z, Gu D, Shen C, Yao T, Song Z. 2012. Inhibition of NF-κB activation by 4-hydroxynonenal contributes to liver injury in a mouse model of alcoholic liver disease. *Am J Pathol* **181:**1702–1710.

21. Ji GR, Yu NC, Xue X, Li ZG. 2014. 4-Hydroxy-2-nonenal induces apoptosis by inhibiting AKT signaling in human osteosarcoma cells. *ScientificWorldJournal* **2014:**873525. doi:10.1155/2014/873525.

22. Youle RJ, Narendra DP. 2011. Mechanisms of mitophagy. *Nat Rev Mol Cell Biol* **12:**9–14.

23. Tsai WT, Lo YC, Wu MS, Li CY, Kuo YP, Lai YH, Tsai Y, Chen KC, Chuang TH, Yao CH, Lee JC, Hsu LC, Hsu JT, Yu GY. 2016. Mycotoxin patulin suppresses innate immune responses by mitochondrial dysfunction and p62/sequestosome-1-dependent mitophagy. *J Biol Chem* **291:**19299–19311.

24. Grek CL, Zhang J, Manevich Y, Townsend DM, Tew KD. 2013. Causes and consequences of cysteine *S*-glutathionylation. *J Biol Chem* **288:**26497–26504.

25. Forman HJ, Fukuto JM, Torres M. 2004. Redox signaling: thiol chemistry defines which reactive oxygen and nitrogen species can act as second messengers. *Am J Physiol Cell Physiol* **287:**C246–C256.

26. Chen YJ, Lu CT, Huang KY, Wu HY, Chen YJ, Lee TY. 2015. GSHSite: exploiting an iteratively statistical method to identify S-glutathionylation sites with substrate specificity. *PLoS One* **10:**e0118752. doi:10.1371/journal.pone.0118752.

27. Su D, Gaffrey MJ, Guo J, Hatchell KE, Chu RK, Clauss TR, Aldrich JT, Wu S, Purvine S, Camp DG, Smith RD, Thrall BD, Qian WJ. 2014. Proteomic identification and quantification of S-glutathionylation in mouse macrophages using resin-assisted enrichment and isobaric labeling. *Free Radic Biol Med* **67:**460–470.

28. Ullevig SL, Kim HS, Short JD, Tavakoli S, Weintraub ST, Downs K, Asmis R. 2016. Protein *S*-glutathionylation mediates macrophage responses to metabolic cues from the extracellular environment. *Antioxid Redox Signal* **25:**836–851.

29. Yang X, Yao H, Chen Y, Sun L, Li Y, Ma X, Duan S, Li X, Xiang R, Han J, Duan Y. 2015. Inhibition of glutathione production induces macrophage CD36 expression and enhances cellular-oxidized low density lipoprotein (oxLDL) uptake. *J Biol Chem* **290:**21788–21799.

30. Vasamsetti SB, Karnewar S, Gopoju R, Gollavilli PN, Narra SR, Kumar JM, Kotamraju S. 2016. Resveratrol attenuates monocyte-to-macrophage differentiation and associated inflammation via modulation of intracellular GSH homeostasis: relevance in atherosclerosis. *Free Radic Biol Med* **96:**392–405.

31. Salzano S, Checconi P, Hanschmann EM, Lillig CH, Bowler LD, Chan P, Vaudry D, Mengozzi M, Coppo L, Sacre S, Atkuri KR, Sahaf B, Herzenberg LA, Herzenberg LA, Mullen L, Ghezzi P. 2014. Linkage

of inflammation and oxidative stress via release of glutathionylated peroxiredoxin-2, which acts as a danger signal. *Proc Natl Acad Sci U S A* **111:**12157–12162.

32. Moolla N, Killick M, Papathanasopoulos M, Capovilla A. 2016. Thioredoxin (Trx1) regulates CD4 membrane domain localization and is required for efficient CD4-dependent HIV-1 entry. *Biochim Biophys Acta* **1860:**1854–1863.

33. Stomski FC, Woodcock JM, Zacharakis B, Bagley CJ, Sun Q, Lopez AF. 1998. Identification of a Cys motif in the common β chain of the interleukin 3, granulocyte-macrophage colony-stimulating factor, and interleukin 5 receptors essential for disulfide-linked receptor heterodimerization and activation of all three receptors. *J Biol Chem* **273:**1192–1199.

34. McGettrick AF, O'Neill LA. 2013. NLRP3 and IL-1β in macrophages as critical regulators of metabolic diseases. *Diabetes Obes Metab* **15**(Suppl 3)**:**19–25.

35. Li P, Allen H, Banerjee S, Franklin S, Herzog L, Johnston C, McDowell J, Paskind M, Rodman L, Salfeld J, Towne E, Tracey D, Wardwell S, Wei FY, Wong W, Kamen R, Seshadri T. 1995. Mice deficient in IL-1β-converting enzyme are defective in production of mature IL-1β and resistant to endotoxic shock. *Cell* **80:**401–411.

36. Kuida K, Lippke JA, Ku G, Harding MW, Livingston DJ, Su MS, Flavell RA. 1995. Altered cytokine export and apoptosis in mice deficient in interleukin-1 beta converting enzyme. *Science* **267:**2000–2003.

37. Haneklaus M, O'Neill LA, Coll RC. 2013. Modulatory mechanisms controlling the NLRP3 inflammasome in inflammation: recent developments. *Curr Opin Immunol* **25:**40–45.

38. Kim SR, Kim DI, Kim SH, Lee H, Lee KS, Cho SH, Lee YC. 2014. NLRP3 inflammasome activation by mitochondrial ROS in bronchial epithelial cells is required for allergic inflammation. *Cell Death Dis* **5:** e1498. doi:10.1038/cddis.2014.460.

39. Ren JD, Wu XB, Jiang R, Hao DP, Liu Y. 2016. Molecular hydrogen inhibits lipopolysaccharide-triggered NLRP3 inflammasome activation in macrophages by targeting the mitochondrial reactive oxygen species. *Biochim Biophys Acta* **1863:**50–55.

40. Kim AD, Zhang R, Kang KA, You HJ, Hyun JW. 2011. Increased glutathione synthesis following Nrf2 activation by vanadyl sulfate in human Chang liver cells. *Int J Mol Sci* **12:**8878–8894.

41. Liu X, Zhou W, Zhang X, Lu P, Du Q, Tao L, Ding Y, Wang Y, Hu R. 2016. Dimethyl fumarate ameliorates dextran sulfate sodium-induced murine experimental colitis by activating Nrf2 and suppressing NLRP3 inflammasome activation. *Biochem Pharmacol* **112:**37–49.

42. Meissner F, Molawi K, Zychlinsky A. 2008. Superoxide dismutase 1 regulates caspase-1 and endotoxic shock. *Nat Immunol* **9:**866–872.

43. Schafer FQ, Buettner GR. 2001. Redox environment of the cell as viewed through the redox state of the glutathione disulfide/glutathione couple. *Free Radic Biol Med* **30:**1191–1212.

44. Watanabe Y, Murdoch CE, Sano S, Ido Y, Bachschmid MM, Cohen RA, Matsui R. 2016. Glutathione adducts induced by ischemia and deletion of glutaredoxin-1 stabilize HIF-1α and improve limb revascularization. *Proc Natl Acad Sci U S A* **113:**6011–6016.

45. Cramer T, Yamanishi Y, Clausen BE, Förster I, Pawlinski R, Mackman N, Haase VH, Jaenisch R, Corr M, Nizet V, Firestein GS, Gerber HP, Ferrara N, Johnson RS. 2003. HIF-1α is essential for myeloid cell-mediated inflammation. *Cell* **112:**645–657.

46. Cheng SC, Quintin J, Cramer RA, Shepardson KM, Saeed S, Kumar V, Giamarellos-Bourboulis EJ, Martens JH, Rao NA, Aghajanirefah A, Manjeri GR, Li Y, Ifrim DC, Arts RJ, van der Veer BM, Deen PM, Logie C, O'Neill LA, Willems P, van de Veerdonk FL, van der Meer JW, Ng A, Joosten LA, Wijmenga C, Stunnenberg HG, Xavier RJ, Netea MG. 2014. mTOR- and HIF-1α-mediated aerobic glycolysis as metabolic basis for trained immunity. *Science* **345:**1250684. doi:10.1126/science.1250684.

47. Xie Y, Kole S, Precht P, Pazin MJ, Bernier M. 2009. *S*-Glutathionylation impairs signal transducer and activator of transcription 3 activation and signaling. *Endocrinology* **150:**1122–1131.

48. Butturini E, Darra E, Chiavegato G, Cellini B, Cozzolino F, Monti M, Pucci P, Dell'Orco D, Mariotto S. 2014. S-Glutathionylation at Cys328 and Cys542 impairs STAT3 phosphorylation. *ACS Chem Biol* **9:**1885–1893.

49. Chakraborty T, Leimeister-Wächter M, Domann E, Hartl M, Goebel W, Nichterlein T, Notermans S. 1992. Coordinate regulation of virulence genes in *Listeria monocytogenes* requires the product of the *prfA* gene. *J Bacteriol* **174:**568–574.

50. Perera VR, Newton GL, Parnell JM, Komives EA, Pogliano K. 2014. Purification and characterization of the *Staphylococcus aureus* bacillithiol transferase BstA. *Biochim Biophys Acta* **1840:**2851–2861.

51. Liu Y, Yang X, Yin Y, Lin J, Chen C, Pan J, Si M, Shen X. 2016. Mycothiol protects *Corynebacterium glutamicum* against acid stress via maintaining intracellular pH homeostasis, scavenging ROS, and *S*-mycothiolating MetE. *J Gen Appl Microbiol* **62:**144–153.

52. Reniere ML, Whiteley AT, Hamilton KL, John SM, Lauer P, Brennan RG, Portnoy DA. 2015. Glutathione activates virulence gene expression of an intracellular pathogen. *Nature* **517:**170–173.

53. Board PG, Menon D. 2013. Glutathione transferases, regulators of cellular metabolism and physiology. *Biochim Biophys Acta* **1830:**3267–3288.

54. Yin ZL, Dahlstrom JE, Le Couteur DG, Board PG. 2001. Immunohistochemistry of omega class glutathione S-transferase in human tissues. *J Histochem Cytochem* **49:**983–987.

55. Murray PJ, Allen JE, Biswas SK, Fisher EA, Gilroy DW, Goerdt S, Gordon S, Hamilton JA, Ivashkiv LB, Lawrence T, Locati M, Mantovani A, Martinez FO, Mege JL, Mosser DM, Natoli G, Saeij JP, Schultze JL, Shirey KA, Sica A, Suttles J, Udalova I, van Ginderachter JA, Vogel SN, Wynn TA. 2014. Macrophage activation and polarization: nomenclature and experimental guidelines. *Immunity* **41:**14–20.

56. Martinez FO, Helming L, Milde R, Varin A, Melgert BN, Draijer C, Thomas B, Fabbri M, Crawshaw A, Ho LP, Ten Hacken NH, Cobos Jiménez V, Kootstra NA, Hamann J, Greaves DR, Locati M, Mantovani A, Gordon S. 2013. Genetic programs expressed in resting and IL-4 alternatively activated mouse and human macrophages: similarities and differences. *Blood* **121:**e57–e69. doi:10.1182/blood-2012-06-436212.

57. Menon D, Board PG. 2013. A role for glutathione transferase Omega 1 (GSTO1-1) in the glutathionylation cycle. *J Biol Chem* **288:**25769–25779.

58. Ryan PM, Bourdi M, Korrapati MC, Proctor WR, Vasquez RA, Yee SB, Quinn TD, Chakraborty M, Pohl LR. 2012. Endogenous interleukin-4 regulates glutathione synthesis following acetaminophen-induced liver injury in mice. *Chem Res Toxicol* **25:**83–93.

59. Toledano MB, Leonard WJ. 1991. Modulation of transcription factor NF-κB binding activity by oxidation-reduction *in vitro*. *Proc Natl Acad Sci U S A* **88:**4328–4332.

60. Menon D, Coll R, O'Neill LA, Board PG. 2014. Glutathione transferase omega 1 is required for the lipopolysaccharide-stimulated induction of NADPH oxidase 1 and the production of reactive oxygen species in macrophages. *Free Radic Biol Med* **73:**318–327.

61. Meissonnier GM, Pinton P, Laffitte J, Cossalter AM, Gong YY, Wild CP, Bertin G, Galtier P, Oswald IP. 2008. Immunotoxicity of aflatoxin B1: impairment of the cell-mediated response to vaccine antigen and modulation of cytokine expression. *Toxicol Appl Pharmacol* **231:** 142–149.

62. Piaggi S, Raggi C, Corti A, Pitzalis E, Mascherpa MC, Saviozzi M, Pompella A, Casini AF. 2010. Glutathione transferase omega 1-1 (GSTO1-1) plays an anti-apoptotic role in cell resistance to cisplatin toxicity. *Carcinogenesis* **31:**804–811.

63. Paul S, Jakhar R, Bhardwaj M, Kang SC. 2015. Glutathione-S-transferase omega 1 (GSTO1-1) acts as mediator of signaling pathways involved in aflatoxin B1-induced apoptosis-autophagy crosstalk in macrophages. *Free Radic Biol Med* **89:**1218–1230.

64. Huang Q, Zhan L, Cao H, Li J, Lyu Y, Guo X, Zhang J, Ji L, Ren T, An J, Liu B, Nie Y, Xing J. 2016. Increased mitochondrial fission promotes autophagy and hepatocellular carcinoma cell survival through the ROS-modulated coordinated regulation of the NFKB and TP53 pathways. *Autophagy* **12:**999–1014.

65. Menon D, Coll R, O'Neill LA, Board PG. 2014. Glutathione transferase omega 1 is required for the lipopolysaccharide-stimulated induction of NADPH oxidase 1 and the production of reactive oxygen species in macrophages. *Free Radic Biol Med* **73:**318–327.

66. Palsson-McDermott EM, Curtis AM, Goel G, Lauterbach MA, Sheedy FJ, Gleeson LE, van den Bosch MW, Quinn SR, Domingo-Fernandez R, Johnston DG, Jiang JK, Israelsen WJ, Keane J, Thomas C, Clish C, Vander Heiden M, Xavier RJ, O'Neill LA. 2015. Pyruvate kinase M2 regulates Hif-1α activity and IL-1β induction and is a critical determinant of the Warburg effect in LPS-activated macrophages. *Cell Metab* **21:**65–80.

67. Menon D, Coll R, O'Neill LA, Board PG. 2015. GSTO1-1 modulates metabolism in macrophages activated through the LPS and TLR4 pathway. *J Cell Sci* **128:**1982–1990.

68. Li YJ, Oliveira SA, Xu P, Martin ER, Stenger JE, Scherzer CR, Hauser MA, Scott WK, Small GW, Nance MA, Watts RL, Hubble JP, Koller WC, Pahwa R, Stern MB, Hiner BC, Jankovic J, Goetz CG, Mastaglia F, Middleton LT, Roses AD, Saunders AM, Schmechel DE, Gullans SR, Haines JL, Gilbert JR, Vance JM, Pericak-Vance MA, Hulette C, Welsh-Bohmer KA. 2003. Glutathione *S*-transferase omega-1 modifies age-at-onset of Alzheimer disease and Parkinson disease. *Hum Mol Genet* **12:**3259–3267.

69. Li YJ, Scott WK, Zhang L, Lin PI, Oliveira SA, Skelly T, Doraiswamy MP, Welsh-Bohmer KA, Martin ER, Haines JL, Pericak-Vance MA, Vance JM. 2006. Revealing the role of glutathione *S*-transferase omega in age-at-onset of Alzheimer and Parkinson diseases. *Neurobiol Aging* **27:**1087–1093.

LETTER

doi:10.1038/nature25986

Itaconate is an anti-inflammatory metabolite that activates Nrf2 via alkylation of KEAP1

Evanna L. Mills[1,2,3,4]*, Dylan G. Ryan[1]*, Hiran A. Prag[5], Dina Dikovskaya[6], Deepthi Menon[1], Zbigniew Zaslona[1], Mark P. Jedrychowski[2,3], Ana S. H. Costa[7], Maureen Higgins[6], Emily Hams[8], John Szpyt[3], Marah C. Runtsch[1], Martin S. King[5], Joanna F. McGouran[9], Roman Fischer[10], Benedikt M. Kessler[10], Anne F. McGettrick[1], Mark M. Hughes[1], Richard G. Carroll[1,4], Lee M. Booty[4,5], Elena V. Knatko[6], Paul J. Meakin[11], Michael L. J. Ashford[11], Louise K. Modis[4], Gino Brunori[12], Daniel C. Sévin[13], Padraic G. Fallon[8], Stuart T. Caldwell[14], Edmund R. S. Kunji[5], Edward T. Chouchani[2,3], Christian Frezza[7], Albena T. Dinkova-Kostova[6,15], Richard C. Hartley[14], Michael P. Murphy[5]§ & Luke A. O'Neill[1,4]§

The endogenous metabolite itaconate has recently emerged as a regulator of macrophage function, but its precise mechanism of action remains poorly understood[1–3]. Here we show that itaconate is required for the activation of the anti-inflammatory transcription factor Nrf2 (also known as NFE2L2) by lipopolysaccharide in mouse and human macrophages. We find that itaconate directly modifies proteins via alkylation of cysteine residues. Itaconate alkylates cysteine residues 151, 257, 288, 273 and 297 on the protein KEAP1, enabling Nrf2 to increase the expression of downstream genes with anti-oxidant and anti-inflammatory capacities. The activation of Nrf2 is required for the anti-inflammatory action of itaconate. We describe the use of a new cell-permeable itaconate derivative, 4-octyl itaconate, which is protective against lipopolysaccharide-induced lethality *in vivo* and decreases cytokine production. We show that type I interferons boost the expression of *Irg1* (also known as *Acod1*) and itaconate production. Furthermore, we find that itaconate production limits the type I interferon response, indicating a negative feedback loop that involves interferons and itaconate. Our findings demonstrate that itaconate is a crucial anti-inflammatory metabolite that acts via Nrf2 to limit inflammation and modulate type I interferons.

Macrophages have a key role in innate immunity. They respond rapidly to pathogens and subsequently promote an anti-inflammatory phenotype to limit damage and promote tissue repair. The factors driving these changes are incompletely understood. Itaconate, a metabolite synthesized by the enzyme encoded by *Irg1*[1], is increased in lipopolysaccharide (LPS)-activated macrophages[2] and has been suggested to limit inflammation by inhibiting succinate dehydrogenase (SDH), a crucial pro-inflammatory regulator[4]; however, the details remain unclear.

Itaconate was the most abundant metabolite in LPS-treated human macrophages (Fig. 1a) and reached 5 mM in mouse bone marrow-derived macrophages (BMDMs) after LPS stimulation (Fig. 1b, c). Itaconate can disrupt SDH activity, but is less potent than the classic SDH inhibitor malonate (Extended Data Fig. 1), suggesting that it may exert its anti-inflammatory effects via additional mechanisms.

Itaconate contains an electrophilic α,β-unsaturated carboxylic acid that could potentially alkylate protein cysteine residues by a Michael addition to form a 2,3-dicarboxypropyl adduct. An attractive candidate protein that undergoes cysteine alkylation is KEAP1, a central player in the anti-oxidant response (Fig. 1d). KEAP1 normally associates with and promotes the degradation of Nrf2, but alkylation of crucial KEAP1 cysteine residues allows newly synthesized Nrf2 to accumulate, migrate to the nucleus and activate a transcriptional anti-oxidant and anti-inflammatory program[5]. We therefore examined KEAP1 and Nrf2 as targets of itaconate.

The cell-permeable itaconate derivative dimethyl itaconate (DMI)[3] boosted levels of Nrf2 protein, expression of downstream target genes, including *Hmox1*, and glutathione (GSH) (Extended Data Fig. 2a–d). However, the lack of a negative charge on the conjugated ester group in DMI increases its reactivity towards Michael addition, making it a far superior Nrf2 activator than itaconate akin to the potent Nrf2 activator dimethylfumarate (DMF)[6]. DMI is rapidly degraded within cells without releasing itaconate[7], hence is unlikely to mimic endogenous itaconate. Even so, these data indicate that Nrf2 activation is anti-inflammatory[8] (Extended Data Fig. 2e, f).

To overcome the limitations of DMI, we synthesized 4-octyl itaconate (OI), a cell-permeable itaconate derivative (Extended Data Fig. 3a). Itaconate and OI had similar thiol reactivity that was far lower than that of DMI (Extended Data Fig. 3b, c, f), making it a suitable cell-permeable itaconate surrogate. Furthermore, OI was hydrolysed to itaconate by esterases in mouse myoblast C2C12 cells (Extended Data Fig. 3d) and LPS-activated mouse macrophages (Extended Data Fig. 3e). OI boosted Nrf2 levels (Fig. 1e, compare lane 5 to lane 1) and enhanced LPS-induced Nrf2 stabilization (Fig. 1e, compare lane 6 to lane 2), and increased the expression of downstream target genes[9], including the anti-inflammatory protein HMOX1[10] (Fig. 1f, g). We used a quantitative NAD(P)H:quinone oxidoreductase-1 (NQO1) inducer bioassay[11,12], to assess the potency of Nrf2 activation by the CD value (concentration required to double the specific enzyme activity) for NQO1, the prototypical Nrf2 target gene. OI (CD value of 2 μM), was more potent than the clinically used Nrf2 activator DMF (CD value of 6.5 μM) (Fig. 1h, Extended Data Fig. 3f). OI stimulated synthesis of the key anti-oxidant GSH (Extended Data Fig. 3g–i). OI also boosted canonical activation of Nrf2 by the pro-oxidant hydrogen peroxide (H_2O_2) (Extended Data Fig. 3j, k). Importantly, the related octyl esters 4-octyl 2-methylsuccinate and octyl succinate, which are not Michael acceptors, had no effect on Nrf2 activity, confirming the requirement

[1]School of Biochemistry and Immunology, Trinity Biomedical Sciences Institute, Trinity College Dublin, Dublin, Ireland. [2]Department of Cancer Biology, Dana-Farber Cancer Institute, Harvard Medical School, Boston, Massachusetts 02115, USA. [3]Department of Cell Biology, Harvard Medical School, Boston, Massachusetts 02115, USA. [4]GlaxoSmithKline, Gunnelswood Road, Stevenage, Hertfordshire, UK. [5]MRC Mitochondrial Biology Unit, University of Cambridge, Cambridge CB2 0XY, UK. [6]Jacqui Wood Cancer Centre, Division of Cancer Research, School of Medicine, University of Dundee, Dundee DD1 9SY, UK. [7]MRC Cancer Unit, University of Cambridge, Hutchison/MRC Research Centre, Box 197, Cambridge Biomedical Campus, Cambridge CB2 0XZ, UK. [8]School of Medicine, Trinity Biomedical Sciences Institute, Trinity College Dublin, Dublin, Ireland. [9]School of Chemistry, Trinity Biomedical Sciences Institute, Trinity College Dublin, Dublin, Ireland. [10]Nuffield Department of Medicine, Target Discovery Institute, University of Oxford, Oxford OX3 7FZ, UK. [11]Division of Molecular and Clinical Medicine, School of Medicine, University of Dundee, Dundee DD1 9SY, UK. [12]GlaxoSmithKline, Park Road, Ware, Hertfordshire, UK. [13]Cellzome, GlaxoSmithKline R&D, Heidelberg, Germany. [14]WestCHEM School of Chemistry, University of Glasgow, Glasgow G12 8QQ, UK. [15]Department of Pharmacology and Molecular Sciences, Johns Hopkins University School of Medicine, Baltimore, Maryland 21205, USA.
*These authors contributed equally to this work.
§These authors jointly supervised this work.

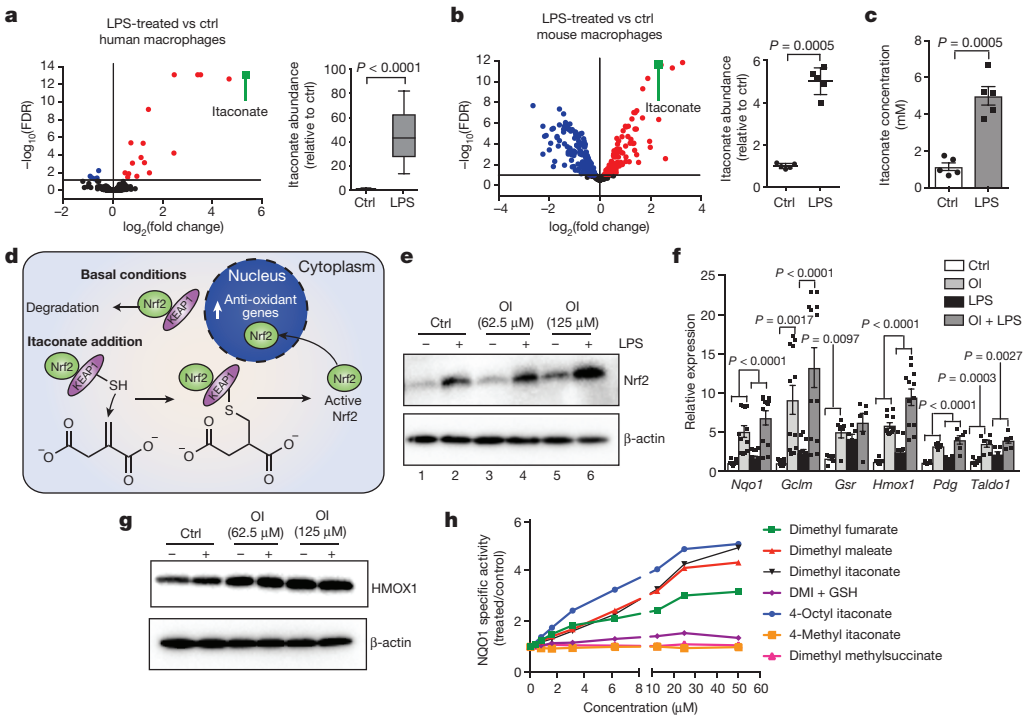

Figure 1 | Itaconate activates Nrf2. **a**–**c**, Metabolite levels and itaconate abundance in control (ctrl) versus LPS-induced (**a**, $n = 12$, 4 h; **b**, **c**, $n = 5$, 24 h) human (**a**) and mouse (**b**, **c**) macrophages. Red and blue dots represent metabolites significantly up- and downregulated by LPS, respectively. FDR, false discovery rate. **d**, Reactivity of itaconate with KEAP1 thiol group. **e**, **g**, LPS-induced Nrf2 (**e**, 24 h) and HMOX1 (**g**, 6 h) after treatment with OI as indicated. **f**, Nrf2 target gene expression in mouse macrophages with or without LPS (6 h) and OI (*Nqo1*, *Gclm*, *Hmox1*, $n = 12$; *Gsr*, *Pgd*, *Taldo1*, $n = 6$). **h**, NQO1 activity in mouse Hepa1c1c7 cells treated as indicated (48 h, $n = 8$). Data are mean ± s.e.m. *P* values calculated using one-way or two-tailed Student's *t*-test for paired comparisons. Blots are representative of three independent experiments. In the box plots, line shows mean. For gel source data, see Supplementary Fig. 1.

for the itaconate moiety (Extended Data Fig. 3l). Dimethyl malonate, a potent SDH inhibitor[4], did not activate Nrf2 (Extended Data Fig. 3m), confirming that Nrf2 activation by OI is independent of SDH inhibition.

Itaconate is generated by IRG1 in the mitochondrial matrix and must cross the mitochondrial inner membrane to act on Nrf2 in the cytosol. Itaconate is structurally similar to malate, which is transported across the mitochondrial inner membrane by the dicarboxylate, citrate and oxoglutarate carriers. All three carriers transported itaconate, whereas other tested carriers could not (Fig. 2a and Extended Data Fig. 4), suggesting that LPS-induced itaconate is generated in the mitochondrial matrix and is then exported to the cytosol to activate Nrf2.

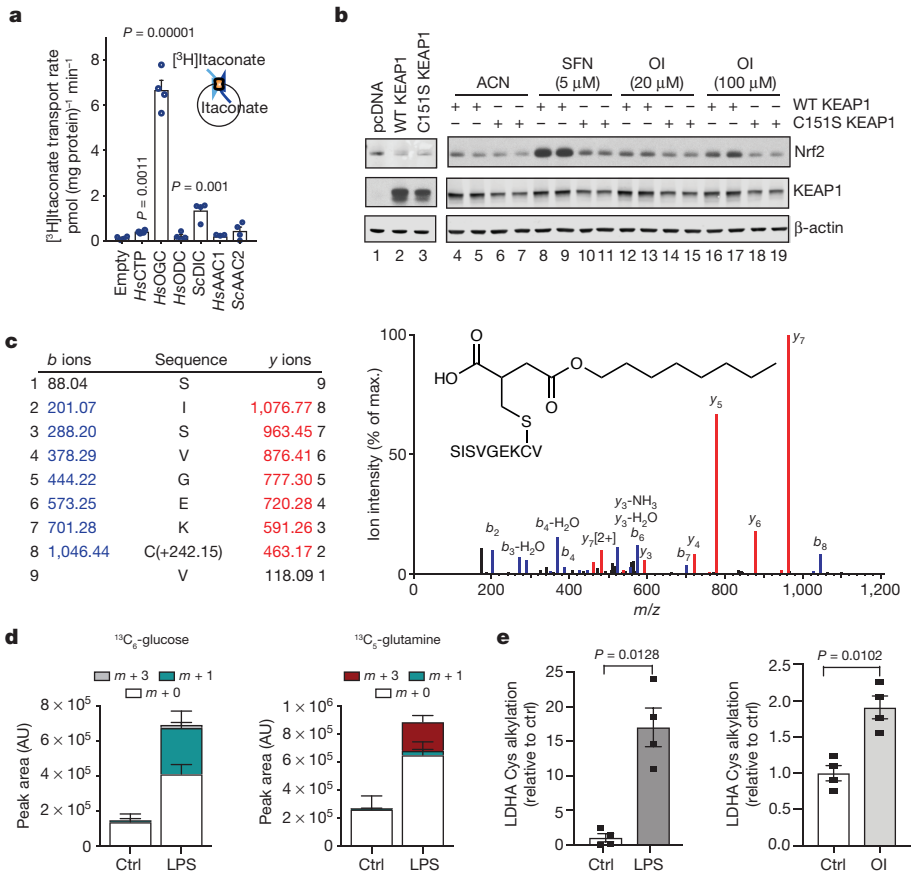

Figure 2 | Itaconate alkylates cysteines. **a**, Itaconate transport by the indicated carriers ($n = 4$). *Hs*AAC1, *Homo sapiens* ADP/ATP carrier; *Hs*CTP, *H. sapiens* citrate carrier; *Hs*ODC, *H. sapiens* oxodicarboxylate carrier; *Hs*OGC, *H. sapiens* 2-oxoglutarate carrier; *Sc*AAC2, *Saccharomyces cerevisiae* ADP/ATP carrier; *Sc*DIC, *S. cerevisiae* dicarboxylate carrier. **b**, Nrf2 and KEAP1 protein after co-transfection with Nrf2–V5, and the wild-type (WT) or Cys151Ser mutant KEAP1. **c**, Tandem mass spectrometry spectrum of Cys151-containing KEAP1 peptide after OI treatment. **d**, Metabolite ($^{13}C_6$-glucose (left), $^{13}C_5$-glutamine (right)) tracing to itaconate-cysteine adduct with or without LPS (24 h, $n = 5$). AU, arbitrary units. **e**, LDHA Cys84 alkylation plus LPS (24 h) or OI (250 μM, 4 h) ($n = 4$). Data are mean ± s.e.m. (in **d**, **e**) or s.d. (in **a**). *P* values calculated using one-way ANOVA for multiple comparisons or two-tailed Student's *t*-test for paired comparisons. Blots are representative of three independent experiments. For gel source data, see Supplementary Fig. 1.

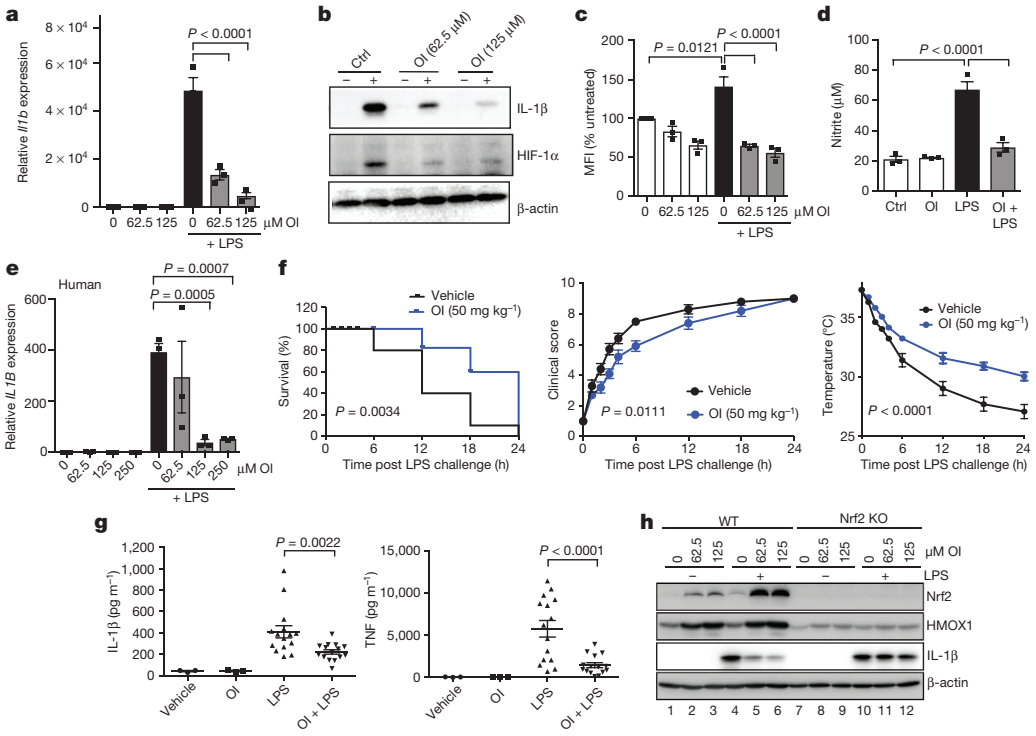

Figure 3 | OI limits IL-1β in an Nrf2-dependent manner and protects against LPS lethality. a–d, LPS (24 h) induced *Il1b* mRNA (**a**, $n = 3$), IL-1β and HIF-1α protein (**b**), ROS production (**c**, $n = 3$; measured as the percentage change in mean fluorescent intensity (MFI) relative to untreated control) and nitrite production (**d**, $n = 3$) ± OI. **e**, *IL1B* mRNA in human PBMCs treated as in **a–d** ($n = 3$). **f**, Survival (left), clinical score (middle) and body temperature (right) measurements in mice ($n = 10$) injected intraperitoneally with OI (50 mg kg^{-1}, 2 h) and LPS (15 mg kg^{-1}). **g**, Serum IL-1β and TNF levels from mice injected intraperitoneally with OI (50 mg kg^{-1}, 2 h) and/or LPS (2.5 mg kg^{-1}, 2 h, $n = 3$ vehicle, OI; $n = 15$ LPS, OI plus LPS). **h**, Nrf2, HMOX1 and IL-1β protein in wild-type and Nrf2 knockout (KO) mouse BMDMs treated with LPS (6 h) and OI as indicated. Data are mean ± s.e.m. *P* values calculated using one-way ANOVA. Blots are representative of three independent experiments. For gel source data, see Supplementary Fig. 1.

Our hypothesis is that itaconate activates Nrf2 by alkylation of KEAP1 cysteine residue(s)[13–15], similar to the modification of cysteines by fumarate (Extended Data Fig. 5a). Cysteine 151 (Cys151) is a principal sensor on KEAP1 for sulforaphane[16] and DMF[17]. OI stabilized V5-tagged Nrf2 (Nrf2–V5) in COS1 cells co-expressing wild-type KEAP1 but not a Cys151Ser mutant, similarly to sulforaphane (Fig. 2b, compare lanes 16 and 17 to lanes 18 and 19). To analyse KEAP1 alkylation directly, we overexpressed Myc-DDK-tagged KEAP1 in human HEK293T cells and treated the cells with OI. Tandem mass spectrometry of immunoprecipitated KEAP1 revealed that for the KEAP1 peptide (144–152), which contains Cys 151, OI treatment increased its mass by 242.15 Da, consistent with alkylation by OI (Fig. 2c). OI also modified other known KEAP1 regulatory cysteine residues (Cys257, Cys288 and Cys273) (Extended Data Fig. 5b–d, Extended Data Table 1a). Furthermore, itaconate-cysteine adducts, derived in part from glucose and glutamine (Fig. 2d and Extended Data Fig. 6), were detected in LPS-treated macrophages. These data suggest that itaconate activates Nrf2 by alkylating KEAP1 cysteine residues. We further explored cysteine alkylation induced by itaconate using an untargeted mass spectrometry approach in macrophages treated with OI, or with LPS, which increases itaconate levels. We identified several proteins that contain alkylated cysteine residues (Extended Data Table 1b, c). Notably LDHA, which has a crucial role in the regulation of glycolysis, was alkylated in OI- and LPS-treated macrophages (Fig. 2e and Extended Data Fig. 5e, f). This modification, here defined as 2,3-dicarboxypropylation, generates a stable thioether. As there are no known pathways for the removal of such post-translational modifications, modified proteins are probably degraded, suggesting that this modification will have profound effects on macrophage function.

We next assessed whether itaconate activation of Nrf2 could be anti-inflammatory. OI, used at concentrations that did not affect cellular viability, decreased LPS-induced *Il1b* mRNA, pro-IL-1β, HIF-1α and IL-10 protein levels, and decreased the extracellular acidification rate, yet had no effect on NF-κB activity or TNF (also known as TNFα) levels (Fig. 3a, b and Extended Data Fig. 7a–f). OI also decreased *Il1b* mRNA in BMDMs treated with the TLR2 and TLR3 ligands, Pam3CSK and polyinosinic:polycytidylic acid (poly(I:C)), respectively (Extended Data Fig. 7g). Levels of LPS-induced reactive oxygen species (ROS), nitrite and inducible nitric oxide synthase (iNOS) were limited by OI (Fig. 3c, d and Extended Data Fig. 7h, i). These effects are likely to be a consequence of ROS detoxification after Nrf2 induction by OI. IL-1β and TNF were decreased by OI in human peripheral blood mononuclear cell (PBMCs) (Fig. 3e, Extended Data Fig. 7j). OI also counteracted the pro-inflammatory response to LPS *in vivo*. OI, which activated Nrf2 (Extended Data Fig. 7k), prolonged survival, decreased clinical score and improved body temperature regulation, and decreased IL-1β and TNF levels but not IL-10 in an LPS model of sepsis (Fig. 3f, g and Extended Data Fig. 7l).

OI induction of HMOX1 was blocked in Nrf2-deficient macrophages (Fig. 3h (compare lanes 2 and 3 to lanes 8 and 9) and Extended Data Fig. 8a, d) or when Nrf2 was silenced (Extended Data Fig. 8a, d (compare lanes 7 and 8 to lanes 11 and 12)). Without Nrf2, the decrease in LPS-induced IL-1β with OI was significantly impaired (Fig. 3h (compare lane 6 to lane 12), Extended Data Fig. 8b–f (compare lanes 6 and 8 to 10 and 12 in c, d)). Furthermore, two Nrf2 activators, diethyl maleate and 15-deoxy-Δ12,14-prostaglandin J2 decreased LPS-induced IL-1β, IL-10, nitric oxide synthase (NOS2) and nitrite (Extended Data Fig. 8g–k). Thus, itaconate activates an anti-inflammatory program through Nrf2.

We next investigated how switching from a pro- to an anti-inflammatory state might affect itaconate production from aconitate by IRG1.

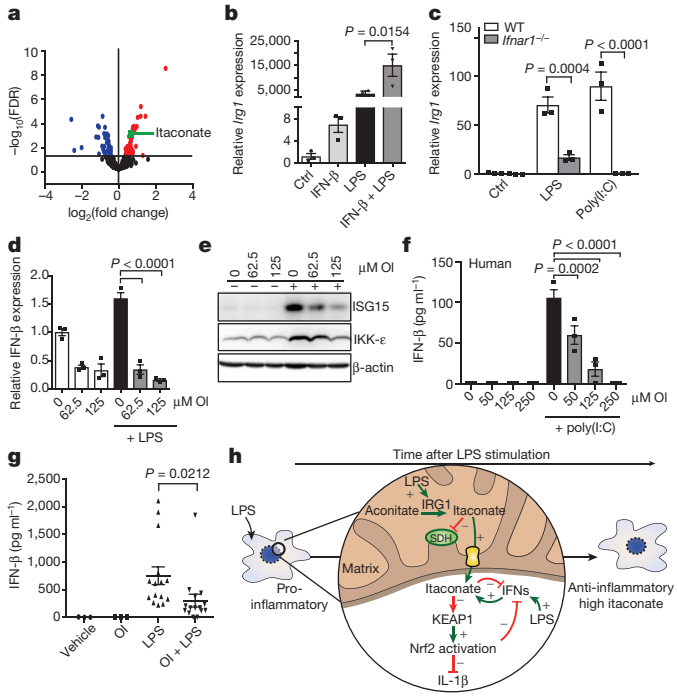

Figure 4 | A feedback loop exists between itaconate and IFN-β. **a**, Metabolite levels in control versus IFN-β-treated (1,000 U ml^{-1}; 27 h; $n = 5$) mouse macrophages. **b**, LPS-induced (24 h) *Irg1* expression ± IFN-β (1,000 U ml^{-1}; $n = 3$). **c**, *Irg1* expression in wild-type and IFN receptor-deficient (*Ifnar1*$^{-/-}$) BMDMs plus LPS or poly(I:C) (40 μg ml^{-1}) for 24 h ($n = 3$). **d**, IFN-β ($n = 3$) expression plus LPS (24 h) and OI as indicated. **e**, ISG15 and IKK-ε expression after treatment with LPS (24 h) and OI. **f**, IFN-β protein expression in PBMCs treated with poly(I:C) (20 μg ml^{-1}; 24 h) and OI ($n = 3$) as indicated. **g**, Serum IFN-β levels from mice injected intraperitoneally with OI (50 mg kg^{-1}, 2 h) with or without LPS (2.5 mg kg^{-1}; 2 h) ($n = 3$ vehicle, OI; $n = 15$ LPS, OI and LPS). **h**, The anti-inflammatory role of itaconate. Data are mean ± s.e.m. *P* values calculated using one-way ANOVA. Blots are representative of three independent experiments. Data in **f** are representative from one of two human donors. For gel source data, see Supplementary Fig. 1.

By modelling gene networks that control *Irg1* expression, the IFN response factor IRF1 was identified as a regulator[18]. We show here that itaconate levels are increased after IFN-β treatment (Fig. 4a), in agreement with others[19]. Levels of citrate and aconitate, the substrate for Irg1, were reduced by IFN-β as was the downstream metabolite α-ketoglutarate (Extended Data Fig. 9a). These data are consistent with an increase in aconitate conversion to itaconate rather than α-ketoglutarate. IFN-β enhanced basal and LPS-induced *Irg1* expression (Fig. 4b). LPS- and poly(I:C)-induced *Irg1* expression in BMDMs lacking type I IFN receptor was decreased (Fig. 4c), indicating that autocrine IFN facilitates IRG1 induction. OI limited the IFN response, decreasing the expression of IFN-β, IKK-ε, ISG20 and ISG15 protein, IFN-β production in poly(I:C)-treated PBMCs and LPS-induced IFN-β production *in vivo* (Fig. 4d–g and Extended Data Fig. 9b, c). IFN-β enhanced both the mRNA and protein expression of IL-10, with or without the addition LPS (Extended Data Fig. 9d), suggesting that the decrease in IL-10 after OI treatment is due to reduced type I IFN production[20]. Nrf2 knockout or knockdown attenuated the reduction of ISG20 expression by OI, whereas the Nrf2 activators diethyl maleate and 15-deoxy-Δ12,14-prostaglandin J2 reduced ISG20 expression (Extended Data Fig. 9e–g). This agrees with increased expression of IRF3-regulated genes in LPS-treated Nrf2-deficient mice[21].

These data suggest the operation of a negative-feedback loop: itaconate is generated in response to LPS, in part through type I IFNs, and promotes an anti-inflammatory program by Nrf2 activation (Fig. 4h), as well as SDH inhibition[3,22]. This limits further inflammatory gene expression and its own production by downregulating the IFN response. This helps to explain why Nrf2-deficient mice are more sensitive to septic shock[21], even though under certain circumstances these mice are protected from inflammation[23]. Our identification of itaconate as an inflammatory regulator, that directly modifies proteins through a newly identified post-translational modification, unveils therapeutic opportunities to use itaconate or OI to treat inflammatory diseases[24]. Furthermore, an intriguing link was recently made[25] from itaconate to vitamin B_{12}, and this warrants further investigation in the context of inflammation and immunity. Further understanding the role of itaconate as an anti-inflammatory metabolite and regulator of type I IFNs is likely to yield new insights into the pathogenesis of inflammatory diseases.

Online Content Methods, along with any additional Extended Data display items and Source Data, are available in the online version of the paper; references unique to these sections appear only in the online paper.

Received 28 July 2017; accepted 9 February 2018.
Published online 28 March 2018.

1. Michelucci, A. *et al.* Immune-responsive gene 1 protein links metabolism to immunity by catalyzing itaconic acid production. *Proc. Natl Acad. Sci. USA* **110,** 7820–7825 (2013).
2. Strelko, C. L. *et al.* Itaconic acid is a mammalian metabolite induced during macrophage activation. *J. Am. Chem. Soc.* **133,** 16386–16389 (2011).
3. Lampropoulou, V. *et al.* Itaconate links inhibition of succinate dehydrogenase with macrophage metabolic remodeling and regulation of inflammation. *Cell Metab.* **24,** 158–166 (2016).
4. Mills, E. L. *et al.* Succinate dehydrogenase supports metabolic repurposing of mitochondria to drive inflammatory macrophages. *Cell* **167,** 457–470 (2016).
5. Hayes, J. D. & Dinkova-Kostova, A. T. The Nrf2 regulatory network provides an interface between redox and intermediary metabolism. *Trends Biochem. Sci.* **39,** 199–218 (2014).
6. Brennan, M. S. *et al.* Dimethyl fumarate and monoethyl fumarate exhibit differential effects on KEAP1, NRF2 activation, and glutathione depletion *in vitro*. *PLoS One* **10,** e0120254 (2015).
7. ElAzzouny, M. *et al.* Dimethyl itaconate is not metabolized into itaconate intracellularly. *J. Biol. Chem.* **292,** 4766–4769 (2017).
8. Kobayashi, E. H. *et al.* Nrf2 suppresses macrophage inflammatory response by blocking proinflammatory cytokine transcription. *Nat. Commun.* **7,** 11624 (2016).
9. Lee, J. M., Calkins, M. J., Chan, K., Kan, Y. W. & Johnson, J. A. Identification of the NF-E2-related factor-2-dependent genes conferring protection against oxidative stress in primary cortical astrocytes using oligonucleotide microarray analysis. *J. Biol. Chem.* **278,** 12029–12038 (2003).
10. Piantadosi, C. A. *et al.* Heme oxygenase-1 couples activation of mitochondrial biogenesis to anti-inflammatory cytokine expression. *J. Biol. Chem.* **286,** 16374–16385 (2011).
11. Prochaska, H. J. & Santamaria, A. B. Direct measurement of NAD(P)H:quinone reductase from cells cultured in microtiter wells: a screening assay for anticarcinogenic enzyme inducers. *Anal. Biochem.* **169,** 328–336 (1988).
12. Fahey, J. W., Dinkova-Kostova, A. T., Stephenson, K. K. & Talalay, P. The "Prochaska" microtiter plate bioassay for inducers of NQO1. *Methods Enzymol.* **382,** 243–258 (2004).
13. Dinkova-Kostova, A. T. *et al.* Direct evidence that sulfhydryl groups of Keap1 are the sensors regulating induction of phase 2 enzymes that protect against carcinogens and oxidants. *Proc. Natl Acad. Sci. USA* **99,** 11908–11913 (2002).
14. McMahon, M., Lamont, D. J., Beattie, K. A. & Hayes, J. D. Keap1 perceives stress via three sensors for the endogenous signaling molecules nitric oxide, zinc, and alkenals. *Proc. Natl Acad. Sci. USA* **107,** 18838–18843 (2010).
15. Dinkova-Kostova, A. T., Kostov, R. V. & Canning, P. Keap1, the cysteine-based mammalian intracellular sensor for electrophiles and oxidants. *Arch. Biochem. Biophys.* **617,** 84–93 (2017).
16. Zhang, D. D. & Hannink, M. Distinct cysteine residues in Keap1 are required for Keap1-dependent ubiquitination of Nrf2 and for stabilization of Nrf2 by chemopreventive agents and oxidative stress. *Mol. Cell. Biol.* **23,** 8137–8151 (2003).
17. Linker, R. A. *et al.* Fumaric acid esters exert neuroprotective effects in neuroinflammation via activation of the Nrf2 antioxidant pathway. *Brain* **134,** 678–692 (2011).
18. Tallam, A. *et al.* Gene regulatory network inference of immunoresponsive gene 1 (*IRG1*) identifies interferon regulatory factor 1 (*IRF1*) as its transcriptional regulator in mammalian macrophages. *PLoS One* **11,** e0149050 (2016).
19. Naujoks, J. *et al.* IFNs modify the proteome of legionella-containing vacuoles and restrict infection via IRG1-derived itaconic acid. *PLoS Pathog.* **12,** e1005408 (2016).
20. Guarda, G. *et al.* Type I interferon inhibits interleukin-1 production and inflammasome activation. *Immunity* **34,** 213–223 (2011).

21. Thimmulappa, R. K. *et al.* Nrf2 is a critical regulator of the innate immune response and survival during experimental sepsis. *J. Clin. Invest.* **116,** 984–995 (2006).
22. Cordes, T. *et al.* Immunoresponsive gene 1 and itaconate inhibit succinate dehydrogenase to modulate intracellular succinate levels. *J. Biol. Chem.* **291,** 14274–14284 (2016).
23. Freigang, S. *et al.* Nrf2 is essential for cholesterol crystal-induced inflammasome activation and exacerbation of atherosclerosis. *Eur. J. Immunol.* **41,** 2040–2051 (2011).
24. Dinarello, C. A. Interleukin-1 in the pathogenesis and treatment of inflammatory diseases. *Blood* **117,** 3720–3732 (2011).
25. Shen, H. *et al.* The human knockout gene CLYBL connects itaconate to vitamin B_{12}. *Cell* **171,** 771–782 (2017).

Supplementary Information is available in the online version of the paper.

Acknowledgements We thank M. McMahon and J. D. Hayes for plasmids, and Cancer Research UK (C20953/A18644) and the BBSRC (BB/L01923X/1) for financial support for ATDK. This work was supported by a Wellcome Trust Investigator award to R.C.H. (110158/Z/15/Z), a grant to M.P.M. from the Medical Research Council UK (MC_U105663142), a Wellcome Trust Investigator award to MPM (110159/Z/15/Z), and a grant to E.R.S.K. and M.S.K. from the Medical Research Council UK (MC_U105663139). B.M.K. and R.F. are supported by the Kennedy Trust Fund. We acknowledge Metabolon for their assistance with the metabolic work and analysis. The O'Neill laboratory acknowledges the following grant support: European Research Council (ECFP7-ERC-MICROINNATE), Science Foundation Ireland Investigator Award (SFI 12/IA/1531), GlaxoSmithKline Visiting Scientist Programme and The Wellcome Trust (oneill-wellcometrust-metabolic, grant number 205455). E.T.C. is supported by the Claudia Adams Barr Program.

Author Contributions E.L.M. and D.G.R. designed and performed experiments and analysed the data. E.L.M. wrote the manuscript with assistance from all other authors. D.M., M.M.H., M.C.R. and A.F.M. performed *in vitro* experiments using OI. R.G.C., D.C.S., A.S.H.C. and C.F. assisted with the metabolomics analysis. Z.Z., P.G.F. and E.H. assisted with the *in vivo* mouse LPS trials. S.T.C. and R.C.H. were responsible for the design and synthesis of octyl esters. H.A.P., E.R.S.K., M.S.K. and L.M.B. assessed the effect of OI and itaconate on mitochondrial parameters and itaconate transport. D.D., M.H. and A.T.D.-K. performed the NQO1 assay and KEAP1 wild-type and Cys151Ser mutant experiments. J.F.M., R.F., B.M.K., E.T.C., M.P.J. and J.S. assisted with mass spectrometry experiments. L.K.M. and G.B. provided guidance and advice. E.V.K., P.J.M. and M.L.J.A. assisted with experiments in Nrf2-deficient mice. L.A.O'N. conceived ideas and oversaw the research programme. M.P.M. provided advice, reagents and oversaw a portion of the work.

Author Information Reprints and permissions information is available at www.nature.com/reprints. The authors declare no competing interests. Readers are welcome to comment on the online version of the paper. Publisher's note: Springer Nature remains neutral with regard to jurisdictional claims in published maps and institutional affiliations. Correspondence and requests for materials should be addressed to L.A.O'N. (laoneill@tcd.ie).

Reviewer Information *Nature* thanks N. S. Chandel, R. Rossignol, S. Werner and the other anonymous reviewer(s) for their contribution to the peer review of this work.

METHODS

Isolation of human PBMCs. Human PBMCs were isolated from human blood using Lymphoprep (Axis-Shield). Whole blood (30 ml) was layered on 20 ml lymphoprep and spun for 20 min at 2,000 r.p.m. with no brake on. The PBMCs were isolated from the middle layer. PBMCs were maintained in RPMI supplemented with 10% (v/v) FCS, 2 mM L-glutamine, and 1% penicillin/streptomycin solution.

Generation of human macrophages. Blood was layered on Histopaque and centrifuged at 800*g* for 20 min, acceleration 9, and deceleration at 4. The PBMC layer was isolated and the macrophages were sorted using magnetic-activated cell sorting (MACS) CD14 beads. Cells were plated at 0.5×10^6 cells ml^{-1} in media containing M-CSF (100 ng ml^{-1}) and maintained at 37 °C, 5% CO_2 for 5 days, to allow differentiation into macrophages. For further details, see Supplementary Methods.

Generation and treatment of BMDMs. Mice were euthanized in a CO_2 chamber and death was confirmed by cervical dislocation. Bone marrow cells were extracted from the leg bones and differentiated in DMEM (containing 10% fetal calf serum, 1% penicillin/streptomycin and 20% L929 supernatant) for 6 days, at which time they were counted and replated for experiments. Unless stated, 5×10^6 BMDMs per millilitre were used in *in vitro* experiments. Unless stated, the LPS concentration used was 100 ng ml^{-1}, the DMI and OI concentration was 125 μM, and in experiments where pre-treatments occurred before LPS stimulation this was for 3 h.

Synthesis of itaconate compounds. For details on synthesis and characterization of chemical compounds, see Supplementary Methods.

Metabolomic analysis with Metabolon. Macrophages were plated at 2×10^6 per well in 6-well plates and treated as required. BMDMs $n = 5$, human macrophages $n = 12$. Analysis was performed by Metabolon. For further details, see Supplementary Methods.

Metabolite measurements for absolute succinate and itaconate quantification and metabolite tracing. Cells were treated as desired. For tracing studies, immediately before LPS stimulation, the media was removed and replaced with DMEM media (1 ml) containing U-^{13}C-glucose (4.5 g l^{-1}) or U-^{13}C-glutamine (584 mg ml^{-1}) deplete of ^{12}C- glucose or ^{12}C-glutamine. Samples were extracted in methanol/acetonitrile/water, 50:30:20 (v/v/v) (1 ml per 1×10^6 cells) and agitated for 15 min at 4 °C in a Thermomixer and then incubated at −20 °C for 1 h. Samples were centrifuged at maximum speed for 10 min at 4 °C. The supernatant was transferred into a new tube and centrifuged again at maximum speed for 10 min at 4 °C. The supernatant was transferred autosampler vials. Liquid chromatograph–mass spectrometry (LC–MS) analysis was performed using a Q Exactive mass spectrometer coupled to a Dionex U3000 UHPLC system (Thermo). For further details, see Supplementary Methods.

Western blotting. Protein samples from cultured cells were prepared by direct lysis of cells in 5× Laemmli sample buffer, followed by heating at 95 °C for 5 min. For spleen samples, 30 mg of spleen was homogenized in RIPA buffer using the Qiagen TissueLyserII system. The resulting homogenate was centrifuged at 14,000 r.p.m. for 10 min at 4 °C, and supernatants were used for SDS–PAGE. Protein samples were resolved on 8% or 12% SDS–PAGE gels and were then transferred onto polyvinylidene difluoride (PVDF) membrane using either a wet or semi-dry transfer system. Membranes were blocked in 5% (w/v) dried milk in TBS-Tween (TBST) for at least 1 h at room temperature. Membranes were incubated with primary antibody, followed by the appropriate horseradish peroxidase-conjugated secondary antibody. They were developed using LumiGLO enhanced chemiluminescent (ECL) substrate (Cell Signalling). Bands were visualized using the GelDoc system (Biorad).

Quantitative PCR. Total RNA was isolated using the RNeasy Plus Mini kit (Qiagen) and quantified using a Nanodrop 2000 UV-visible spectrophotometer. cDNA was prepared using 20–100 ng μl^{-1} total RNA by a reverse transcription PCR (RT–PCR) using a high capacity cDNA reverse transcription kit (Applied Biosystems), according to the manufacturer's instructions. Quantitative PCR (qPCR) was performed on cDNA using SYBR Green probes. qPCR was performed on a 7900 HT Fast Real-Time PCR System (Applied Biosystems) using Kapa fast master mix high ROX (Kapa Biosystems, for SYBR probes) or 2× PCR fast master mix (Applied Biosystems, for Taqman probes). For SYBR primer pair sequences, see Supplementary Methods. Fold changes in expression were calculated by the $\Delta\Delta C_t$ method using mouse *Rps18* as an endogenous control for mRNA expression. All fold changes are expressed normalized to the untreated control.

NQO1 bioassay. Inducer potency was quantified by use of the NQO1 bioassay in Hepa1c1c7 mouse hepatoma cells[11,12]. Cells (10^4 per well of a 96-well plate) were grown for 24 h and exposed ($n = 8$) to serial dilutions of compounds for 48 h before lysis. NQO1 enzyme activity was quantified in cell lysates using menadione as a substrate. Protein concentrations were determined in aliquots from the same cell lysates by the bicinchoninic acid (BCA) assay (Thermo Scientific). The CD value was used as a measure of inducer potency. For assays examining the effect of GSH on inducer potency, 50 μM of each compound was incubated with 1 mM GSH in the cell culture medium at 37 °C for 30 min before treatment.

Preparation of rat liver mitochondria. Female Wistar rats aged between 10 and 12 weeks (Charles River) were culled by stunning and cervical dislocation before the liver being excised and stored in ice-cold buffer (STE buffer; 250 mM sucrose, 5 mM Tris-Cl, 1 mM EGTA (pH 7.4 at 4 °C)). Rat liver mitochondria were isolated by homogenization and differential centrifugation at 4 °C in STE buffer[26]. In brief, minced tissue was homogenized in STE buffer before centrifugation (1,000*g*, 3 min, 4 °C) and centrifuging the resulting supernatant (10,000*g*, 10 min, 4 °C). The mitochondrial pellet was resuspended in fresh STE before centrifuging (10,000*g*, 10 min, 4 °C). The resulting pellet was resuspended in STE and assayed for protein concentration via BCA assay (Thermo Scientific) against a BSA standard curve.

Preparation of bovine heart mitochondrial membranes. Bovine heart mitochondria were isolated by differential centrifugation in 250 mM sucrose, 10 mM Tris-Cl, 0.2 mM EDTA (pH 7.8 at 4 °C). To prepare membranes, bovine heart mitochondria were blended with MilliQ water at 4 °C before adding KCl to a final concentration of 150 mM and blending until homogenous. The suspension was centrifuged (13,500*g*, 40 min, 4 °C) and the pellet was resuspended in re-suspension buffer (20 mM Tris-Cl, 1 mM EDTA, 10% glycerol, pH 7.55 at 4 °C) before homogenization and assaying for protein by BCA assay (Thermo Scientific)[27].

Measuring complex II and III activity. Bovine heart mitochondrial membranes (80 μg protein per ml) were incubated in 50 mM potassium phosphate buffer (50 mM potassium phosphate, 1 mM EDTA, pH 7.4, 4 °C) supplemented with 3 mM KCN, 4 μM rotenone and succinate. In a 96-well microplate, inhibitor or vehicle control and membrane incubation were plated and incubated for 10 min at 30 °C. Alternatively, where indicated, itaconate was incubated with membranes and removed by twice centrifuging membranes and resuspending in non-itaconate containing buffer, before plating with 1 mM succinate. Oxidized cytochrome-*c* was added before measuring the respiratory chain activity by assessing the reduction of cytochrome-*c* spectrophotometrically at 550 nm at 20 s intervals for 5 min at 30 °C. Final concentrations were 10 μg protein per well bovine heart membranes and 30 μM ferricytochrome *c*.

Measuring rat liver mitochondrial respiration. Respiration of rat liver mitochondria was assessed with an Oxygraph-2K (OROBOROS instruments high resolution respirometry). Rat liver mitochondria (0.5 mg mitochondrial protein per ml) were added to KCl buffer (pH 7.2, 37 °C) and respiration assessed in the presence of 4 μg ml^{-1} rotenone, 1 mM succinate, 1 μM FCCP and inhibitors or buffer control.

Assessing itaconate ester reactivity with glutathione. GSH (1 or 5 mM) and 5 mM itaconate esters or vehicle control were incubated in KCl buffer (pH 7.2 or 8) at 37 °C for 2 h, where indicated, 10 μg recombinant GST was added to the incubation. The reaction was stopped by acidification with 5% sulfosalicylic acid before assessing glutathione content by the GSH recycling assay as described previously[28].

Itaconate transport assays. Itaconate transport by mitochondrial carriers was assessed as described previously[29]. For further details see Supplementary Methods.

Cell uptake of itaconate. C2C12 mouse myoblasts were plated at 300,000 cells per well in a 6-well plate in complete growth medium and adhered overnight in a humidified 5% CO_2, 37 °C incubator. The following day, media was replaced with serum-free DMEM containing itaconate esters and cells were treated for 30 min at 37 °C. Cells were extracted as described above (method for succinate quantification), with MS internal standard (100 pmol) added and stored at −80 °C before LC–MS/MS analysis. For further details, see Supplementary Methods.

LC–MS/MS analysis was performed using an LCMS-8060 mass spectrometer (Shimadzu) with a Nexera X2 UHPLC system (Shimadzu). For further details, see Supplementary Methods.

KEAP1 cysteine target validation. COS1 cells (2.5×10^5 per well) in 6-well plates were co-transfected (Lipofectamine 2000) with 0.8 μg of Nrf2-V5 and 1.6 μg of wild-type or Cys151S mutant KEAP1[14], or 1.6 μg of pcDNA. Cells were grown for 21 h then treated with 20 or 100 μM OI, 5 μM sulforaphane or 0.1% acetonitrile (vehicle) for 3 h. Cell were washed in PBS and lysed in 200 μl of SDS-lysis buffer (50 mM Tris-HCl, pH 6.8, 2% (w/v) sodium dodecyl sulfate (SDS) and 10% (v/v) glycerol). Lysates were sonicated (20 s at 30% amplitude using Vibra-Cell ultrasonic processor, Sonic) and boiled (3 min), and dithiothreitol (DTT) and Bromophenol blue were added up to 0.1 M and 0.02% (w/v) final concentrations, respectively. Proteins (10 μg) were resolved on a gradient (4–12%) NuPAGE SDS gel, transferred onto nitrocellulose membranes, and immunoblotted with anti-KEAP1 (rat monoclonal, Merk Millipore, clone 144), anti-Nrf2 (rabbit monoclonal, CST), and anti-β-actin (mouse monoclonal, Sigma) antibodies. Horseradish peroxidase (HRP)- or IRDye-labelled secondary antibodies were used interchangeably, followed by either ECL detection or scanning using Odyssey imager (Li-COR).

ELISA. Cytokine concentrations in cell supernatants were measured using ELISA Duoset kits for mouse IL-10 and TNF and human IFN-β and IL-1β, according to the manufacturer's instructions. Cytokine concentrations in serum samples isolated from whole blood were measured using Quantikine ELISA kits for mouse or human IL-1β, IFN-β, IL-10 and TNF. Duoset and Quantikine kits were from R&D Systems. Optical density values were measured at a wavelength of 450 nm, using a FLUOstar Optima plate reader (BMG Labtech). Concentrations were calculated using a four-parameter fit curve.

FACS analysis of ROS. BMDMs were seeded at 0.5×10^6 cells per ml and treated as normal. Then 2 h before staining, 100% ethanol was added to the dead cell control well. Thirty minutes before the end of the stimulation, CellROX (5 μM) was added directly into the cell culture medium. Supernatants of cells that were to be stained with Aqua Live/Dead were removed, and an Aqua Live/Dead dilution (1 ml; 1:1,000 in PBS) was added to each well. Cells were incubated in tinfoil at 37 °C for 30 min. Cells were washed with PSB, scraped in PBS (0.5 ml), and transferred to polypropylene FACS tubes. Samples were analysed using a DAKO CyAn flow cytometer, and data was analysed using FlowJo software. MFI was quantified as a measure of cellular ROS production.

Nitric oxide assay. Nitric oxide concentrations in cell supernatants were measured using Greiss reagent assay kit from Thermo Fischer Scientific according to the manufacturer's instructions. Optical density values were measured at a wavelength of 548 nm, using a SoftMax Pro plate reader. Concentrations were calculated using a linear standard curve.

GSH/GSSG measurements. BMDMs were plated at 0.1×10^6 cells per ml in opaque 96-well plates. Cells were pre-treated with OI (125 μM) for 2 h and then stimulated with hydrogen peroxide (100 μM) for 24 h. After 24 h, cell media was removed and the reduced glutathione to oxidized glutathione (GSH/GSSG) ratio was quantified using MyBio GSH/GSSG-Glo Assay (V6611) as per manufacturer's instructions. Luminescence was quantified using a FLUOstar Optima plate reader.

LDH assay. Cells were plated at 0.5×10^6 cells per ml in white 24-well plates (500 μl per well) and treated as required. Cytotoxicity, as determined by LDH release, was assayed using CytoTox96 Non-radioactive Cytotoxicity Assay kit (Promega) according to the manufacturer's instructions.

Seahorse analysis of lactate production. Cells were plated at 0.2×10^6 cells per well of a 24-well Seahorse plate. Cells were treated and stimulated as normal. A utility plate containing calibrant solution (1 ml per well) was placed in a CO_2-free incubator at 37 °C overnight. The next day, media was removed from cells and replaced with glucose-supplemented XF assay buffer (500 μl per well) was placed in a CO_2-free incubator for at least 0.5 h. Compounds (glucose, oligomycin and 2-deoxy-D-glucose (2DG); 70 μl) were added to the appropriate port of the injector plate. This plate together with the utility plate was run on the Seahorse for calibration. Once complete, the utility plate was replaced with the cell culture plate and run on the Seahorse XF-24.

Endotoxin-induced model of sepsis. For cytokine measurements, mice were treated intraperitoneally with OI (50 mg kg^{-1}) in 40% cyclodextrin in PBS or vehicle control for 2 h before stimulation with LPS (Sigma; 2.5 mg kg^{-1}) intraperitoneally for 2 h. Mice were euthanized in a CO_2 chamber, blood samples were collected and serum was isolated. Cytokines were measured using R&D ELISA kits according to manufacturer's protocol. For temperature recording, mice ($n = 10$ per group) were treated intraperitoneally with OI (50 mg kg^{-1}) in 40% cyclodextrin in PBS or vehicle control for 2 h before stimulation with LPS (5 mg kg^{-1}) and monitored for temperature at 1, 2, 3, 4, 6, 12, 18 and 24 h after LPS treatment. Temperature was monitored using subcutaneously implanted temperature transponder chips (Bio Medic Data Systems; IPTT 300) which were injected between the shoulder blades 48 h before experiment. At defined times, body temperature was measured by scanning the transponder with a corresponding BMDS Smart Probe. Animals were additionally monitored for clinical signs of endotoxic shock, based on temperature change, body condition, physical condition and unprovoked behaviour, with a combined score of 9 indicating the humane end point for the experiment.

siRNA transfection of BMDMs. Cells were plated at 1×10^6 cells per ml in 12-well plates overnight. On the day of transfection, the media was replaced with 500 μl DMEM without penicillin/streptomycin or FBS. For each target gene, two Eppendorfs were prepared. Optimem (250 μl per well) was added to each tube. RNAimax (add 5 μl per well) was added to one set of tubes and short interfering siRNA (siRNA; 50 nM per well) was added to the second set of tubes. The tube containing the siRNA was added to the tube with RNAimax, mixed well by pipetting and incubated for 15 min. The mix (500 μl) was added to each well. Twenty-four hours after transfection, cells were treated as required.

Analysis of KEAP1 modification by OI. Human embryonic kidney cells (HEK293T cells) were transfected with a pCMV6-KEAP1 vector (Myc-DDK-tagged mouse KEAP1) (OriGene). C2C12, Hepa1c1c7 cells and COS1 cells were from American Type Culture Collection (ATCC). The L929 cells are from Sigma (85011425). HEK293T cells were obtained from the Centre for Applied Microbiology and Research. Cell lines have not been tested for mycoplasma contamination. Twenty-four hours after transfection, cells were treated with OI (500 μM) or vehicle control (PBS) for 4 h. Tagged KEAP1 was immunoprecipitated using an anti-Flag antibody (Sigma) and protein A/G beads (Santa Cruz). After immunoprecipitation, bound KEAP1 was eluted off the beads using Flag peptide (500 μl; 200 μg ml^{-1}) (Sigma) diluted in 1× TBS pH 7.4. The samples were then concentrated and the Flag peptide was removed using 10K centrifugation filter columns (Merck). The concentrated samples were then divided in half for downstream processing. One-half of each sample was diluted 1:2 with 5× SDS sample buffer and separated using SDS–PAGE (Bio-Rad). Overexpressed KEAP1 was detected using Coomassie blue staining and the corresponding bands were excised from the gel and subjected to in-gel digest as described. In brief, the gel slices were cut into smaller pieces (1–2 mm^3) before reduction with DTT (10 mM) and alkylation with iodoacetamide (50 mM). Half of the gel slices from each sample were then subjected to a trypsin (2 μg) digest, the other half were digested with elastase (1 μg) overnight at 37 °C. Similarly, the remaining sample concentrates (in solution) were reduced with DTT and alkylated with iodoacetamide, before precipitation of the protein via the methanol–chloroform extraction method. The protein pellet was re-suspended in urea (6 M), which was then diluted to <1 M urea with ultrapure H_2O. The samples were then digested with trypsin (2 μg) overnight at 37 °C. Digested protein samples were analysed in an Orbitrap Fusion Lumos coupled to a UPLC ultimate 3000 RSLCnano System (both Thermo Fisher). For further details, see Supplementary Methods.

Assessment of cysteine alkylation by itaconate using Iodo-TMT. After treatment, cells were lysed in HEPES pH 7.5, EDTA, glycerol and NP40. 2 mM TCEP and 50 mM NEM were added in a buffer containing 50 mM HEPES, 2% SDS, 125 mM NaCl, pH 7.2, and samples were incubated for 60 min at 37 °C in the dark to reduce and alkylate all unmodified protein cysteine residues. 20% (v/v) TCA was added to stabilize thiols and incubated overnight at 4 °C and then pelleted for 10 min at 4,000*g* at 4 °C. The pellet was washed three times with cold methanol (2 ml) and then resuspended in 2 ml 8 M urea containing 50 mM HEPES, pH 8.5. Protein concentrations were measured by BCA assay (Thermo Scientific) before protease digestion. Protein lysates were diluted to 4 M urea and digested with LysC (Wako) in a 1:100 enzyme:protein ratio and trypsin (Promega) at a final 1:200 enzyme:protein ratio for 4 h at 37 °C. Protein extracts were diluted further to a 2.0 M urea and LysC (Wako) at 1:100 enzyme:protein ratio and trypsin (Promega) at a final 1:200 enzyme:protein ratio were added again and incubated overnight at 37 °C. Protein extracts were diluted further to a 1.0 M urea concentration, and trypsin (Promega) was added to a final 1:200 enzyme:protein ratio for 6 h at 37 °C. Digests were acidified with 250 μl of 25% acetic acid to a pH value of ~2, and subjected to C18 solid-phase extraction (50 mg Sep-Pak, Waters). Excess TMT label (6–7 M) was added to each digest for 30 min at room temperature (repeated twice). The reaction was quenched using 4 μl 5% hydroxylamine. Samples were subjected to an additional C18 solid-phase extraction (50 mg Sep-Pak). For LC–MS/MS parameters, data processing and MS2 spectra assignment, TMT reporter ion intensities and quantitative data analysis, see Supplementary Methods.

Reagents. For a complete list of reagents, see Supplementary Methods.

Mouse strains. Wild-type C57BL/6 mice were from Harlan UK and Harlan Netherlands. Animals were maintained under specific pathogen-free conditions in line with Irish and European Union regulations. Experiments were approved by local ethical review and were carried out under the authority of Ireland's project license. All animal studies performed in GSK were ethically reviewed and carried out in accordance with Animals (Scientific Procedures) Act 1986 and the GSK Policy on the Care, Welfare and Treatment of Animals. Nrf2-deficient mice and their wild-type counterparts, both on the C57BL/6 genetic background (used for isolation of BMDM cells), were bred and maintained in the Medical School Resource Unit of the University of Dundee.

Statistical analysis. Data were expressed as mean ± s.e.m. and *P* values were calculated using two-tailed Student's *t*-test for pairwise comparison of variables, one-way ANOVA for multiple comparison of variables, and two-way ANOVA involving two independent variables. A Sidak's multiple comparisons test was used. A confidence interval of 95% was used for all statistical tests. Sample sizes were determined on the basis of previous experiments using similar methodologies. For all experiments, all stated replicates are biological replicates. For *in vivo* studies, mice were randomly assigned to treatment groups. For mass spectrometry analyses, samples were processed in random order and experimenters were blinded to experimental conditions.

Data availability. Full scans for all western blots are provided in Supplementary Fig 1. Source Data for all mouse experiments have been provided. All other data are available from the corresponding author on reasonable request.

26. Chappell, J. B. & Hansford, R. V. A. *Subcellular Components: Preparation and Fractionation* 2nd edn (Butterworth, 1972).
27. Bridges, H. R., Mohammed, K., Harbour, M. E. & Hirst, J. Subunit NDUFV3 is present in two distinct isoforms in mammalian complex I. *Biochim. Biophys. Acta* **1858,** 197–207 (2017).
28. Akerboom, T. P. & Sies, H. Assay of glutathione, glutathione disulfide, and glutathione mixed disulfides in biological samples. *Methods Enzymol.* **77,** 373–382 (1981).
29. Booty, L. M. *et al.* The mitochondrial dicarboxylate and 2-oxoglutarate carriers do not transport glutathione. *FEBS Lett.* **589,** 621–628 (2015).

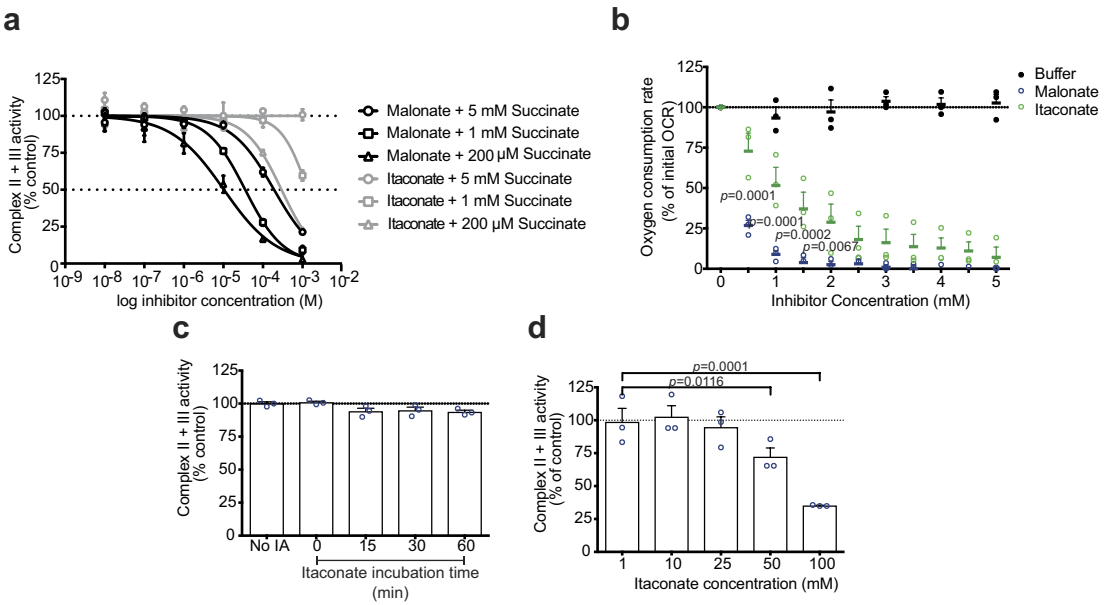

Extended Data Figure 1 | The effect of itaconate on complex II activity. a, Complex II and III activity in bovine heart mitochondrial membranes incubated with succinate plus malonate or itaconate ($n = 3$ independent experiments). **b**, Effect of malonate or itaconate on the oxygen consumption rate (OCR) of rat liver mitochondria in the presence of succinate (1 mM) and FCCP (1 μM; $n = 3$ independent experiments). **c**, **d**, Complex II and III activity in bovine heart mitochondrial membranes incubated with itaconate (IA; 1 mM unless indicated), with subsequent removal and addition of succinate (1 mM; $n = 3$ independent experiments) (see Methods for further details). Data are mean ± s.e.m. *P* values calculated using one or two-way ANOVA.

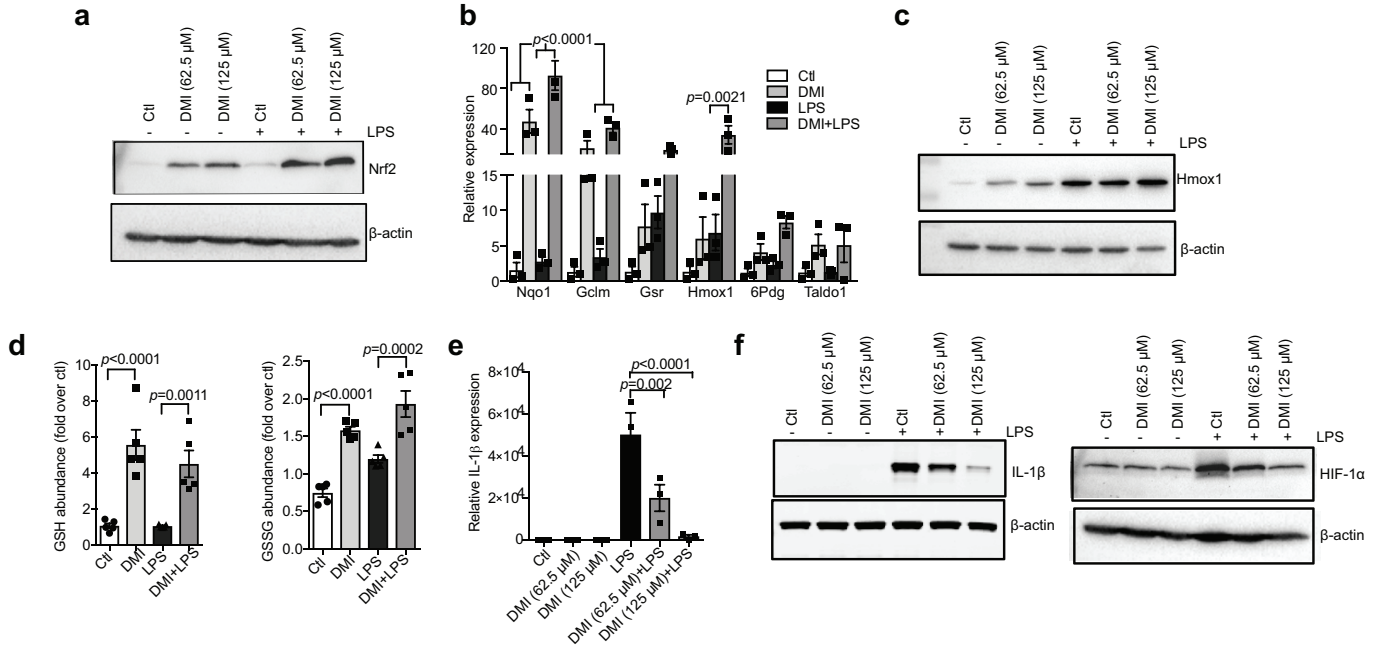

Extended Data Figure 2 | DMI activates Nrf2 and limits cytokine production. a, **c**, LPS (100 ng ml^{-1})-induced Nrf2 (**a**, 24 h) and HMOX1 (**c**, 6 h) protein expression with or without the itaconate derivative DMI. **b**, Nrf2-dependent mRNA expression after treatment with LPS (6 h) and DMI where indicated ($n = 3$). **d**, Reduced glutathione (GSH) and oxidized glutathione (GSSG) levels after treatment with LPS and DMI ($n = 5$). **e**, **f**, LPS (24 h)-induced *Il1b* mRNA (**e**), IL-1β and HIF-1α protein (**f**) expression in mouse macrophages with or without DMI ($n = 3$). Data are mean ± s.e.m. *P* values calculated using one-way ANOVA. Blots are representative of three independent experiments. For gel source data, see Supplementary Fig. 1.

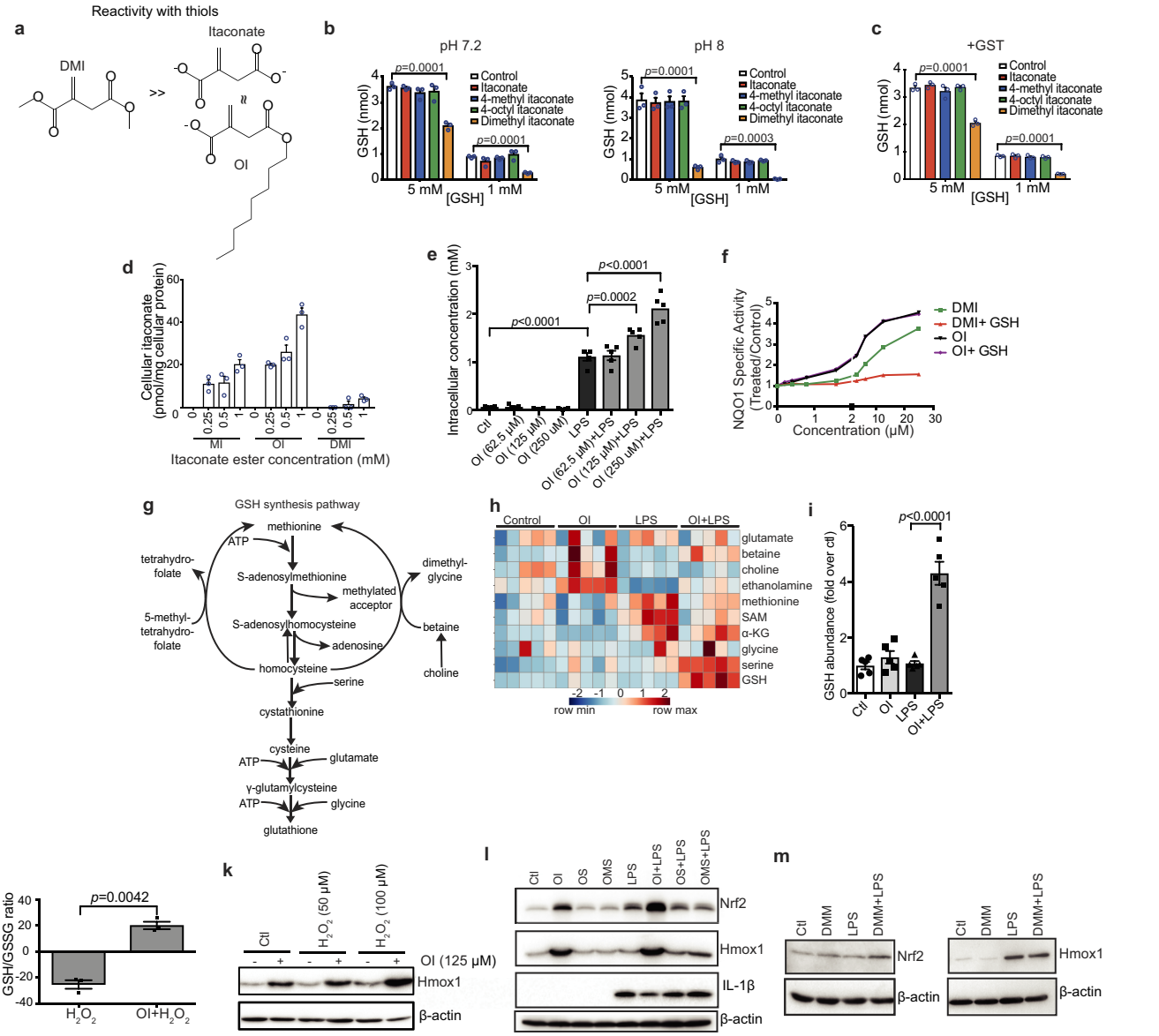

Extended Data Figure 3 | OI is the best tool to assess itaconate-dependent Nrf2 activity. a, Reactivity of DMI, itaconate and OI with thiols. **b**, **c**, Itaconate ester reactivity with GSH and glutathione-*S*-transferase (GST) as detailed in the Methods ($n = 3$). **d**, Itaconate levels in mouse C2C12 cells plus itaconate esters ($n = 3$). MI, 4-methyl itaconate. **e**, **i**, Itaconate (**e**) or GSH (**i**) levels plus LPS (6 h) and OI as indicated ($n = 5$). **f**, NQO1 activity in mouse Hepa1c1c7 cells treated with DMI or OI (48 h) and GSH ($n = 8$). **g**, **h**, Metabolic intermediates in GSH synthesis (**h**, average of five biological replicates). **i**, GSH levels after treatment with LPS (6 h) and/or OI ($n = 5$). **j**, GSH/GSSG ratio after treatment with OI (2 h) and H_2O_2 (100 μM, 24 h; $n = 3$) as indicated. **k**, HMOX1 protein levels after treatment with OI and/or H_2O_2 (24 h). **l**, Nrf2, HMOX1 and IL-1β protein levels in BMDMs pre-treated with OI, 4-octyl 2-methylsuccinate (OMS) or octyl succinate (OS), all 125 μM for 3 h with or without LPS (6 h). **m**, LPS-induced Nrf2 (24 h) and HMOX1 (6 h) protein expression with or without dimethyl malonate (DMM). Data are mean ± s.e.m. *P* values calculated using one- or two-way ANOVA. Blots are representative of three independent experiments. For gel source data, see Supplementary Fig. 1.

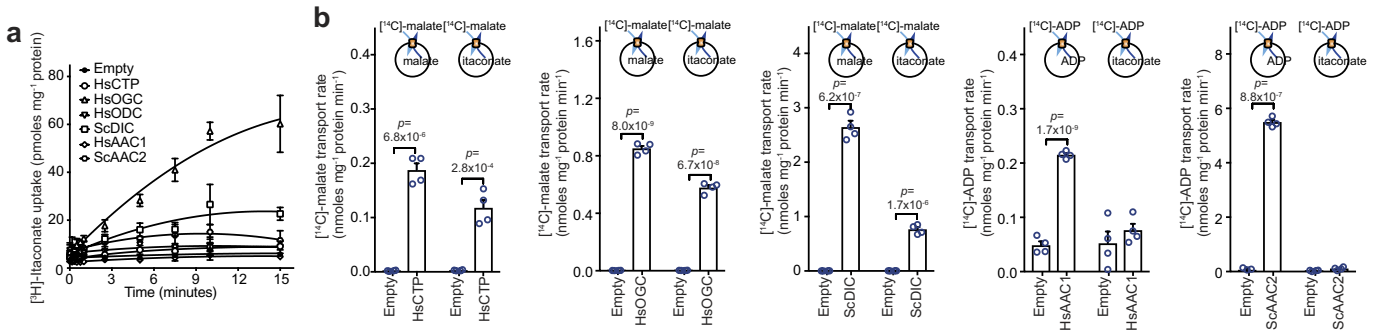

Extended Data Figure 4 | Itaconate is transported by the mitochondrial oxoglutarate, dicarboxylate and citrate carriers. a, Itaconate uptake into vesicles of *Lactococcus lactis* membranes expressing the indicated carriers loaded with itaconate (1 mM), and transport initiated by the addition of [^{3}H]itaconate (1 μM). **b**, Initial transport rates of each carrier with either canonical substrate (homo-exchange) or canonical substrate/itaconate (hetero-exchange). $n = 4$ independent experiments; data are mean ± s.d. *P* values calculated using two-tailed Student's *t*-test.

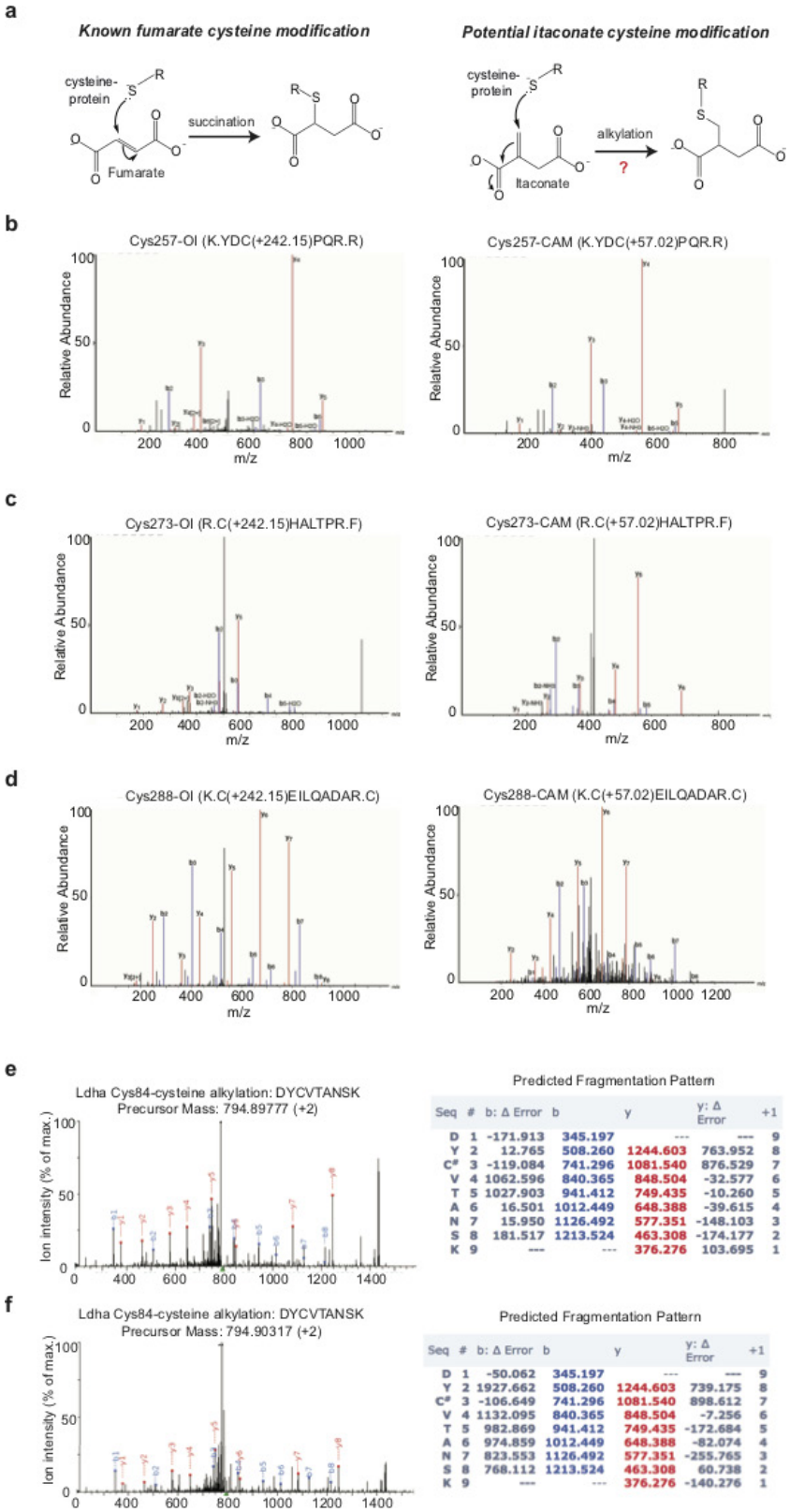

Extended Data Figure 5 | KEAP1 is alkylated by OI on major redox sensing cysteine residues. a, Modification of cysteine by fumarate or itaconate. Tandem mass spectrometry spectrum of KEAP1 Cys257 (**b**), Cys257 (**c**) and Cys288 (**d**) peptides, indicating alkylation of these sites after OI treatment (left) but not in the corresponding carbamidomethylated (CAM) peptides (right). **e**, **f**, LDHA Cys84 alkylation after treatment with LPS (**e**, 24 h) or OI (**f**, 250 μM, 4 h) ($n = 4$). Detected N- and C-terminal fragment ions of both peptides are assigned in the spectrum and depicted as follows: *b*: N-terminal fragment ion; *y*: C-terminal fragment ion; asterisk: fragment ion minus NH_3; 0 or asterisk: fragment ion minus H_2O; and 2+: doubly charged fragment ion. Representative of one independent experiment.

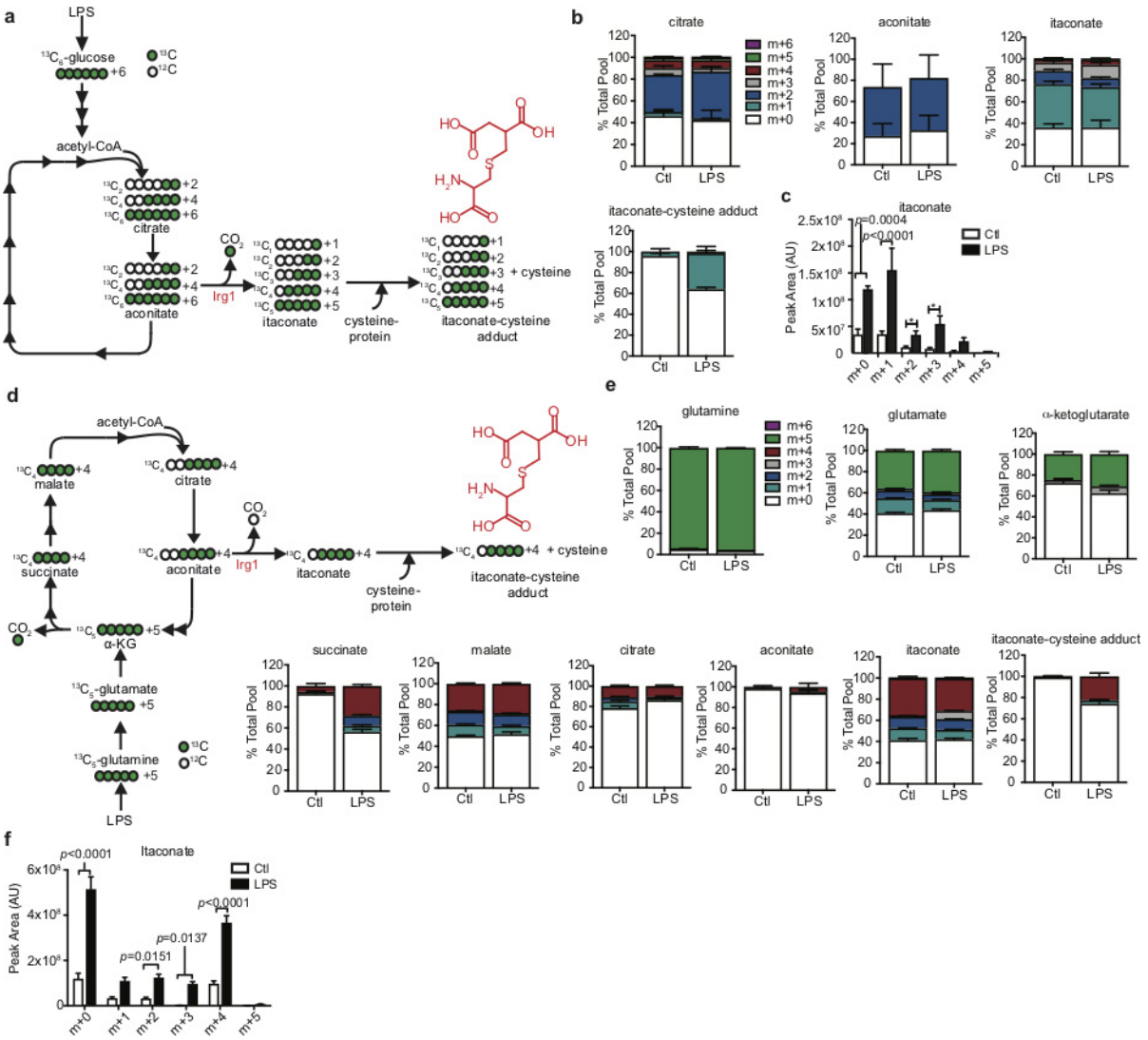

Extended Data Figure 6 | Identification of an itaconate-cysteine adduct. **a**–**e**, $^{13}C_6$-glucose (**a**–**c**) or $^{13}C_5$-glutamine (**d**, **e**) labelling experiment tracking itaconate-cysteine adduct formation in BMDMs treated with LPS ($n = 5$; 24 h). Data in **b** and **e** are expressed as the percentage isotopologue of the total pool. Data in **c** and **f** represent changes in the total pool after LPS treatment. Data are mean ± s.e.m., for five replicates. *P* values calculated using two-way ANOVA.

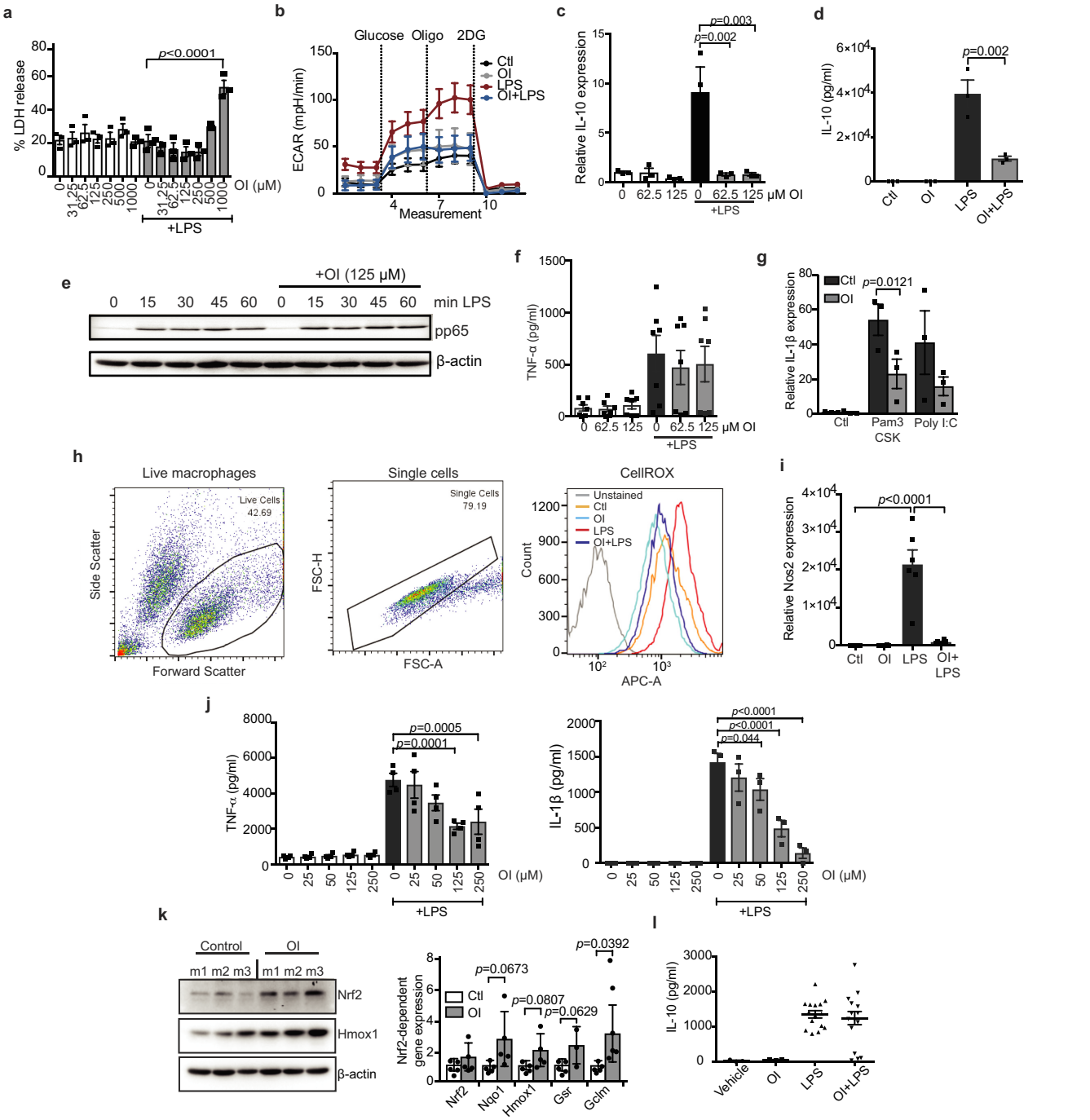

Extended Data Figure 7 | OI decreases LPS-induced cytokine production, extracellular acidification rate, ROS and nitric oxide. **a**, Percentage cytotoxicity (LDH release) in BMDMs after treatment with LPS and OI as indicated ($n = 3$). **b**, LPS-induced extracellular acidification rate (ECAR) after treatment with OI and/or LPS as indicated, analysed on the Seahorse XF-24 in BMDMs (trace representative of three independent experiments). **c**, **d**, LPS-induced *Il10* mRNA (**c**, 4 h) and protein (**d**, 24 h) and TNF protein (**f**; $n = 7$) after OI treatment as indicated ($n = 3$). **e**, Phosphorylated p65 (pp65) protein levels (a measure of NF-κB activity) after treatment with LPS and OI as indicated. **h**, Representative gating strategy for FACS analysis of ROS production in cells as treated in **d** (image representative of three independent experiments). **i**, LPS-induced NOS2 expression ($n = 6$), with or without OI treatment. **j**, LPS-induced TNF ($n = 4$) and IL-1β ($n = 3$) protein levels after OI treatment in PBMCs. **k**, Nrf2 and HMOX1 protein levels or Nrf2-dependent gene expression ($n = 5$) in peritoneal macrophages from mice (m) injected intraperitoneally with OI (50 mg kg^{-1}, 6 h) or vehicle control. **l**, Serum IL-10 from mice injected intraperitoneally with vehicle control or OI (50 mg kg^{-1}, 2 h) and LPS (2.5 mg kg^{-1}, 2 h, $n = 3$ vehicle, OI; $n = 15$ LPS, OI plus LPS). Data are mean ± s.e.m. *P* values calculated using one-way ANOVA. Blots are representative of three independent experiments. For gel source data, see Supplementary Fig. 1.

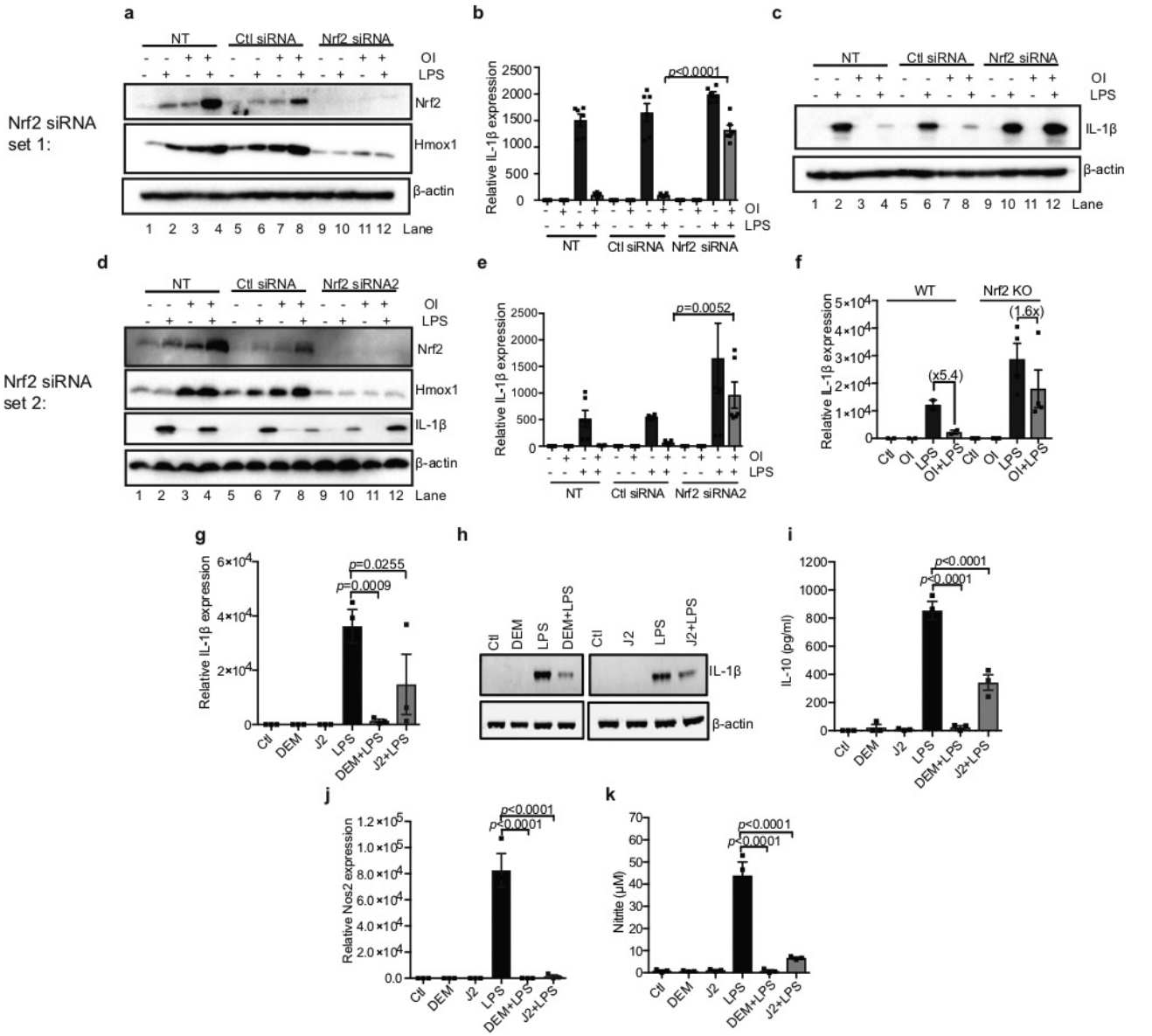

Extended Data Figure 8 | The effects of OI on cytokine production are Nrf2-dependent. a–e, Nrf2, HMOX1 and IL-1β protein levels (**a**, **c**, **d**) and *Il1b* mRNA expression (**b**, **e**) in mouse BMDMs transfected with two different *Nrf2* siRNAs (50 nM) compared with a non-silencing scrambled control siRNA plus LPS (6 h; **a**–**c**, **e**; 24 h; **d**) and/or OI ($n = 6$). NT, non-transfected. **f**, *Il1b* mRNA expression in wild-type and Nrf2-knockout BMDMs treated with LPS (24 h; WT $n = 2$, Nrf2 KO $n = 4$) and/or OI. **g**–**k**, *Il1b* (**g**) and *Nos2* (**j**) mRNA, and IL-1β (**h**), IL-10 (**i**), TNF and nitrite (**k**) production with or without LPS (24 h), diethyl maleate (DEM; 100 μM) or 15-deoxy-Δ12,14-prostaglandin J2 (J2; 5 μM) pre-treatment for 3 h ($n = 3$). Data are mean ± s.e.m. *P* values calculated using one-way ANOVA. Blots are representative of three independent experiments. For gel source data, see Supplementary Fig. 1.

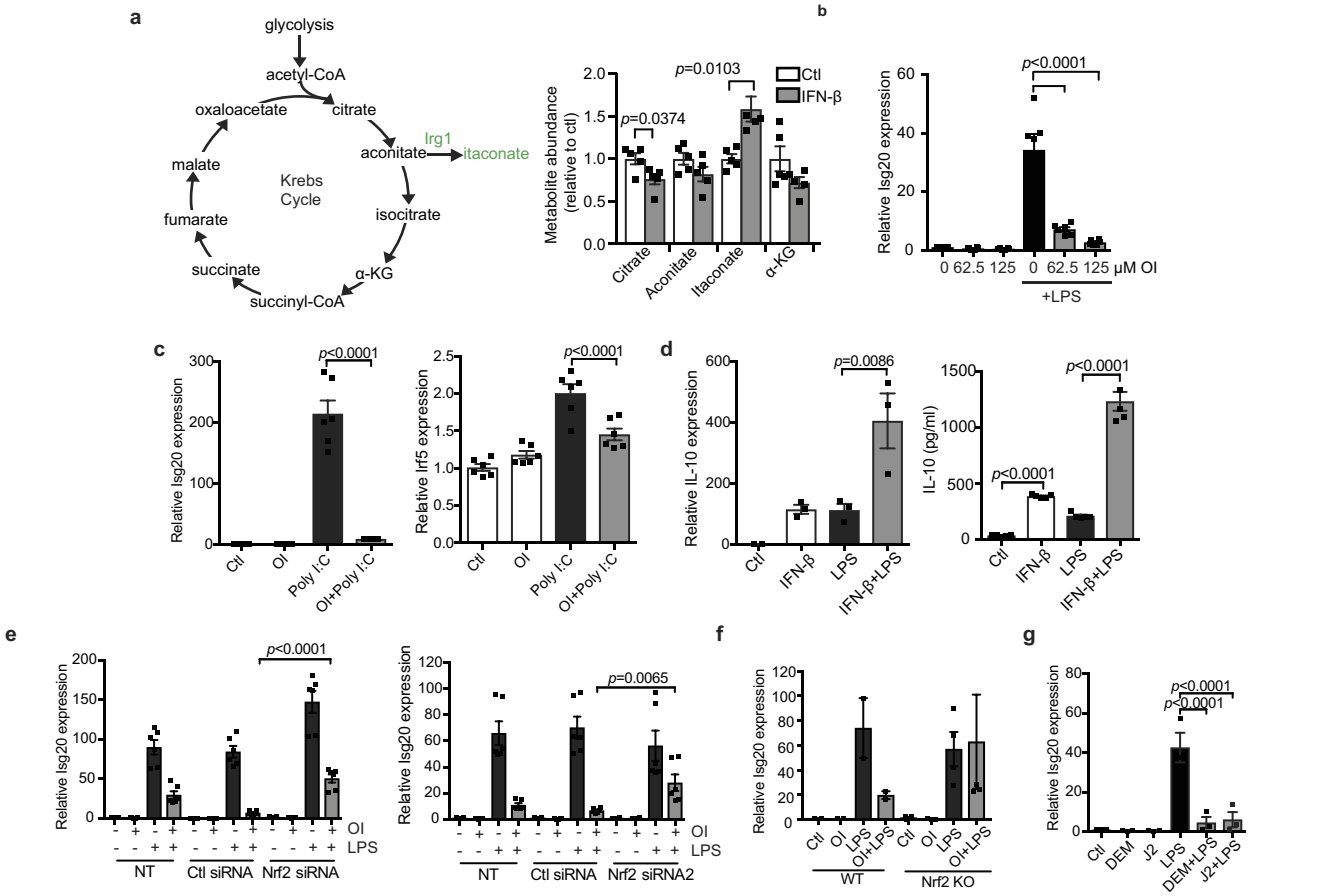

Extended Data Figure 9 | An Nrf2-dependent feedback loop exists between itaconate and IFN-β. a, Metabolite levels after treatment with IFN-β (1,000 U ml^{-1}; 27 h; $n = 5$). **b**, **c**, *Isg20* and *Irf5* mRNA expression in BMDMs treated with LPS (**b**) or poly(I:C) (**c**, 40 μg ml^{-1}; 24 h) and/or OI ($n = 6$). **d**, *Il10* mRNA ($n = 3$) and IL-10 protein ($n = 5$) expression after treatment with LPS for 4 h (left) or 24 h (right) and/or IFN-β treatment (1,000 U ml^{-1}) for 3 h. **e**, *Isg20* expression in BMDMs transfected with two different *Nrf2* siRNAs (50 nM) compared with non-silencing control plus LPS (6 h) and/or OI ($n = 6$). **f**, *Isg20* mRNA expression in wild-type ($n = 2$) and Nrf2-knockout ($n = 4$) BMDMs plus LPS (6 h) and/or OI. **g**, *Isg20* mRNA expression after pre-treatment with LPS (24 h) and/or diethyl maleate (100 μM) or 15-deoxy-Δ12,14-prostaglandin J2 (5 μM) for 3 h ($n = 3$). Data are mean ± s.e.m. *P* values calculated using one-way ANOVA.

Extended Data Table 1 | Mass spectrometry analysis of itaconate-induced cysteine alkylation

a

4-OI Residue	Peptide Amino Acid Position	Peptide Sequence	-10logP	Enzyme	Digest Type
Cys23	22-31	S.KC(+242.15)PEGAGDAV.M	31.47	Elastase	In Gel
Cys151	144-152	A.SISVGEKC(+242.15)V.L	44.11	Elastase	In Gel
	146-152	I.SVGEKC(+242.15)V.L	30.95		
	144-153	A.SISVGEKC(+242.15)VL.H	30.25		
	145-152	S.ISVGEKC(+242.15)V.L	29.32		
Cys257	254-260	V.KYDC(+242.15)PQR.R	35.44	Elastase	In Gel
	255-260	K.YDC(+242.15)PQR.R	40.13	Trypsin	In Gel
	255-260	K.YDC(+242.15)PQR.R	41.08	Trypsin	In Solution
Cys273	273-279	R.C(+242.15)HALTPR.F	35.93	Trypsin	In Gel
	273-279	R.C(+242.15)HALTPR.F	38.65	Trypsin	In Solution
Cys288	282-293	L.QTQLQKC(+242.15)EILQA.D	41.70	Elastase	In Gel
	282-290	L.QTQLQKC(+242.15)EI.L	36.70		
	284-293	T.QLQKC(+242.15)EILQA.D	33.47		
	280-296	R.FLQTQLQKC(+242.15)EILQADAR.C	55.81	Trypsin	In Gel
	288-296	K.C(+242.15)EILQADAR.C	50.84		
	288-296	K.C(+242.15)EILQADAR.C	48.80	Trypsin	In Solution
Cys297	294-304	A.DARC(+242.15)KDYLVQI.F	37.15	Elastase	In Gel
K615	602-615	R.SGVGVAVTMEPCRK(+242.15).Q	37.59	Trypsin	In Gel
	602-615	R.SGVGVAVTM(+15.99)EPCRK(+242.15).Q	36.40		

b

Protein	Alkylated residue	Peptide amino acid position	Peptide sequence	X score	Ppm
Plsl	Cys111	97-123	KEGIC(+4.98)AIGGTSEQSSVGTQHSYSEEEK	5.998	-2.22
Acon	Cys385	378-395	VGLIGSC(+4.98)TNSSYEDMGR	4.212	4.17
Ldha	Cys84	82-90	DYC(4.98)VTANSK	3.474	-2.91
Anxa1	Cys189	186-204	GDRC(4.98)QDLSVNQDLADTDAR	3.514	-0.48
Ifi5b	Cys317	310-320	QMIEVPNC(+4.98)ITR	2.412	-4.16
Ipyr2	Cys156, 157	153-171	STDC(4.98)C(+4.98)GDNDPIDVCEIGSK	4.664	22.60
Ef2	Cys41	33-42	STLTDSLVC(+4.98)K	3.677	-1.41
Thio	Cys73	73-81	C(+4.98)MPTFQFYK	2.422	-2.22

c

Protein	Alkylated residue	Peptide amino acid position	Peptide sequence	X score	Ppm
Gilt	Cys69	61-73	VSLYYESLC(+4.98)GACR	4.677	3.40
Fgd6	Cys1004	9996-1005	NVALLDEQC(+4.98)K	3.759	-7.98
Olfr644	Cys306	305-313	FC(+4.98)KILLGNK	3.155	-2.10
Ldha	Cys84	82-90	DYC(+4.98)VTANSK	2.832	3.88
Padi6	Cys553	553-558	C(+4.98)ISLNR	2.446	-18.58
Ubr4	Cys4241	4237-4244	LIASC(+4.98)HWK	2.421	-7.45
Hmox2	Cys314	314-323	C(+4.98)PFYAAQPDK	2.279	2.89
Lhpp	Cys113	112-118	FC(+4.98)TNESQK	2.169	-11.64

a, Cysteine/lysine residue(s) in KEAP1 modified by OI as determined by tandem mass spectrometry. **b**, Cysteine residues modified by itaconate in BMDMs treated with LPS identified using tandem mass spectrometry. **c**, Cysteine residues modified by itaconate in BMDMs treated with OI identified using tandem mass spectrometry.

nature research

Corresponding author(s): Luke O'Neill

☐ Initial submission ☐ Revised version ☒ Final submission

Life Sciences Reporting Summary

Nature Research wishes to improve the reproducibility of the work that we publish. This form is intended for publication with all accepted life science papers and provides structure for consistency and transparency in reporting. Every life science submission will use this form; some list items might not apply to an individual manuscript, but all fields must be completed for clarity.

For further information on the points included in this form, see Reporting Life Sciences Research. For further information on Nature Research policies, including our data availability policy, see Authors & Referees and the Editorial Policy Checklist.

Experimental design

1. Sample size

Describe how sample size was determined.

We have used at least 3 biological replicates for each experiment. This is designed to account for biological variability taking into account that the majority of experiments were performed in murine macrophages from inbred mice. See statistical analyses section of methods for full details.

2. Data exclusions

Describe any data exclusions.

Any exclusions from in vitro data were deemed outliers in GraphPad Prism. From the LPS in vivo cytokine data one LPS-treated sample has been removed as it appears that I did stimulate in response to LPS, most like an injection error.

3. Replication

Describe whether the experimental findings were reliably reproduced.

The in vivo trial required some optimization with various doses of compound as this was the first time it had been used in vivo. In vitro experiments were highly reproducible. All experimental findings were reproduced as biological replicates at the value stated in figure legends, unless otherwise indicated.

4. Randomization

Describe how samples/organisms/participants were allocated into experimental groups.

See statistical analyses section of methods. For in vivo studies, mice were randomly assigned to treatment groups. For MS analyses, samples were processed in random order and experimenters were blinded to experimental conditions.

5. Blinding

Describe whether the investigators were blinded to group allocation during data collection and/or analysis.

The in vivo trials were blinded. For MS analyses, samples were processed in random order and experimenters were blinded to experimental conditions.

Note: all studies involving animals and/or human research participants must disclose whether blinding and randomization were used.

6. Statistical parameters

For all figures and tables that use statistical methods, confirm that the following items are present in relevant figure legends (or in the Methods section if additional space is needed).

n/a	Confirmed
☐	☒ The exact sample size (*n*) for each experimental group/condition, given as a discrete number and unit of measurement (animals, litters, cultures, etc.)
☐	☒ A description of how samples were collected, noting whether measurements were taken from distinct samples or whether the same sample was measured repeatedly
☐	☒ A statement indicating how many times each experiment was replicated
☐	☒ The statistical test(s) used and whether they are one- or two-sided (note: only common tests should be described solely by name; more complex techniques should be described in the Methods section)
☐	☒ A description of any assumptions or corrections, such as an adjustment for multiple comparisons
☐	☒ The test results (e.g. *P* values) given as exact values whenever possible and with confidence intervals noted
☐	☒ A clear description of statistics including central tendency (e.g. median, mean) and variation (e.g. standard deviation, interquartile range)
☐	☒ Clearly defined error bars

See the web collection on statistics for biologists for further resources and guidance.

Software

Policy information about availability of computer code

7. Software

Describe the software used to analyze the data in this study.	Flowjo was used to flow cytometry analysis. Metabolite spectra were analysed using XCalibur Qual Browser and XCalibur Quan Browser software (Thermo Scientific). Labsolutions software (Shimadzu) was used to assess itaconate uptake. SoftMax Pro software was used for ELISAs. MS data was analysed with PEAKS Studio 8 (Bioinformatics Solutions). GraphPad Prism was used for all graphing and statistical tests.

For manuscripts utilizing custom algorithms or software that are central to the paper but not yet described in the published literature, software must be made available to editors and reviewers upon request. We strongly encourage code deposition in a community repository (e.g. GitHub). *Nature Methods* guidance for providing algorithms and software for publication provides further information on this topic.

Materials and reagents

Policy information about availability of materials

8. Materials availability

Indicate whether there are restrictions on availability of unique materials or if these materials are only available for distribution by a for-profit company.	4-octyl itaconate is available from the authors.

9. Antibodies

Describe the antibodies used and how they were validated for use in the system under study (i.e. assay and species).	Antibodies used were goat anti-mouse IL-1β (R&D Systems, AF401-NA), mouse anti-β-actin (Sigma-Aldrich, AC-74), rabbit anti-HIF-1α (Novus, NB100-449), rabbit anti-phospho-pIRF3 (Cell Signalling Technology, 4947) rabbit anti-total IRF3 (Cell Signalling Technology, 4302), rabbit anti-phospho-pTBK1 (Cell Signalling Technology, 5483) rabbit anti-total TBK1 (Cell Signalling Technology, 3013), rabbit anti-IKKε (Cell Signalling Technology, 3416), Nrf2 (Cell Signalling Technology, 12721), Hmox1 (Enzo Life Sciences, ADI-SPA-896-D), Ass1 (Abcam, SAB5300141). Secondary horseradish peroxidase-conjugated anti-mouse IgG, anti-rabbit IgG and anti-goat IgG were from Jackson ImmunoResearch Inc.

10. Eukaryotic cell lines

a. State the source of each eukaryotic cell line used.

C2C12, Hepa1c1c7 cells and COS1 cells were from American Type Culture Collection (ATCC). The L929 cells are from Sigma, cat no is 85011425.HEK293T cells were obtained from the Centre for Applied Microbiology and Research, Wiltshire, UK.

b. Describe the method of cell line authentication used.

No authentication was used

c. Report whether the cell lines were tested for mycoplasma contamination.

They were not tested.

d. If any of the cell lines used are listed in the database of commonly misidentified cell lines maintained by ICLAC, provide a scientific rationale for their use.

No commonly misidentified cell lines were used

Animals and human research participants

Policy information about studies involving animals; when reporting animal research, follow the ARRIVE guidelines

11. Description of research animals

Provide details on animals and/or animal-derived materials used in the study.

8 week old, C57BL/6JOlaHsd female mice were purchased from Envigo UK. The rats were 10-12 week old female Wistar Rats from Charles River Laboratories, Strain Code:003. Nrf2-deficient mice and their wild type counterparts, both on the C57Bl/6 genetic background (used for isolation of BMDM cells) were bred and maintained in the Medical School Resource Unit of the University of Dundee.

Policy information about studies involving human research participants

12. Description of human research participants

Describe the covariate-relevant population characteristics of the human research participants.

The blood was from anonymous donors so I do not have this information.

nature research

Corresponding author(s): Luke O'Neill

☐ Initial submission ☐ Revised version ☒ Final submission

Flow Cytometry Reporting Summary

Form fields will expand as needed. Please do not leave fields blank.

Data presentation

For all flow cytometry data, confirm that:

☒ 1. The axis labels state the marker and fluorochrome used (e.g. CD4-FITC).

☒ 2. The axis scales are clearly visible. Include numbers along axes only for bottom left plot of group (a 'group' is an analysis of identical markers).

☒ 3. All plots are contour plots with outliers or pseudocolor plots.

☒ 4. A numerical value for number of cells or percentage (with statistics) is provided.

Methodological details

5. Describe the sample preparation.	Murine bone marrow derived macrophages
6. Identify the instrument used for data collection.	Dako CyAn flow cytometer
7. Describe the software used to collect and analyze the flow cytometry data.	FlowJo
8. Describe the abundance of the relevant cell populations within post-sort fractions.	This was pure in vitro prepared bone marrow derived macrophages
9. Describe the gating strategy used.	Cells were gated first on side-scatter (area) versus forward scatter (area) (Population; P1; to determine the macrophage population) Then on forward-scatter (height) versus forward scatter (area) (P2; to eliminate doublets) Then on side-scater (area) versus pacific blue (to eliminate dead cells) Finally on counts versus APC (as a meaure of CellROX staining).

Tick this box to confirm that a figure exemplifying the gating strategy is provided in the Supplementary Information. ☒

Article

Immunity

A Common Variant in the Adaptor Mal Regulates Interferon Gamma Signaling

Graphical Abstract

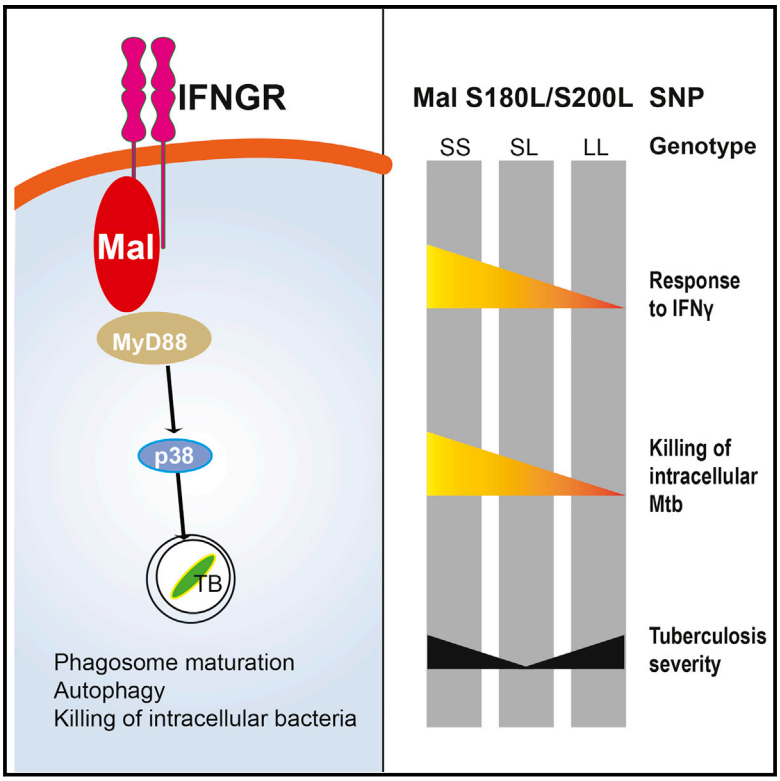

Authors

Clíona Ní Cheallaigh, Frederick J. Sheedy, James Harris, ..., Luke A.J. O'Neill, Ed C. Lavelle, Joseph Keane

Correspondence

nicheacm@tcd.ie (C.N.C.), lavellee@tcd.ie (E.C.L.)

In Brief

Mal (encoded by *TIRAP*) is a signaling adaptor in the TLR pathway. Ní Cheallaigh and colleagues demonstrate an additional role for Mal in IFN-γ signaling and find that it is required to kill intracellular *M. tuberculosis*. The common human Mal S180L polymorphism attenuates IFN-γ signaling and impairs responses to tuberculosis infection.

Highlights

- Mal has a TLR-independent role in IFNGR signaling
- IFNGR signaling via Mal leads to p38 phosphorylation, autophagy, and killing of TB
- The S180L mutation attenuates responses to IFN-γ stimulation
- S180L mutations impair in vitro and in vivo responses to TB

Ní Cheallaigh et al., 2016, Immunity *44*, 368–379
February 16, 2016
http://dx.doi.org/10.1016/j.immuni.2016.01.019

CellPress

A Common Variant in the Adaptor Mal Regulates Interferon Gamma Signaling

Clíona Ní Cheallaigh,[1,2,*] Frederick J. Sheedy,[1] James Harris,[3] Natalia Muñoz-Wolf,[2] Jinhee Lee,[4] Kim West,[4] Eva Palsson McDermott,[5] Alicia Smyth,[6] Laura E. Gleeson,[1] Michelle Coleman,[1] Nuria Martinez,[4] Claire H.A. Hearnden,[2] Graham A. Tynan,[2] Elizabeth C. Carroll,[2] Sarah A. Jones,[3] Sinéad C. Corr,[5] Nicholas J. Bernard,[5] Mark M. Hughes,[5] Sarah E. Corcoran,[5] Mary O'Sullivan,[1] Ciara M. Fallon,[1] Hardy Kornfeld,[4] Douglas Golenbock,[4] Stephen V. Gordon,[6] Luke A.J. O'Neill,[5] Ed C. Lavelle,[2,7,8,*] and Joseph Keane[1,8]

[1]Department of Clinical Medicine, Institute of Molecular Medicine, Trinity College Dublin and St. James's Hospital, D08 W9RT, Dublin, Ireland
[2]Adjuvant Research Group, School of Biochemistry & Immunology, Trinity Biomedical Sciences Institute, Trinity College Dublin, D02 PN40, Dublin, Ireland
[3]Centre for Inflammatory Diseases, Southern Clinical School, Monash University Faculty of Medicine, Nursing and Health Sciences, Clayton, Victoria 3168, Australia
[4]Department of Medicine, University of Massachusetts Medical School, Worcester, MA 01655, USA
[5]Inflammation Research Group, School of Biochemistry & Immunology, Trinity Biomedical Sciences Institute, Trinity College Dublin, D02 PN40, Dublin, Ireland
[6]UCD Schools of Veterinary Medicine, Medicine and Medical Science, and Biomolecular and Biomedical Science, and UCD Conway Institute, University College Dublin, Belfield, Dublin 4, Ireland
[7]Advanced Materials and BioEngineering Research (AMBER), Centre for Research on Adaptive Nanostructures and Nanodevices (CRANN), Trinity College, D02 PN40, Dublin, Ireland
[8]Co-senior author
*Correspondence: nicheacm@tcd.ie (C.N.C.), lavellee@tcd.ie (E.C.L.)
http://dx.doi.org/10.1016/j.immuni.2016.01.019

SUMMARY

Humans that are heterozygous for the common S180L polymorphism in the Toll-like receptor (TLR) adaptor Mal (encoded by *TIRAP*) are protected from a number of infectious diseases, including tuberculosis (TB), whereas those homozygous for the allele are at increased risk. The reason for this difference in susceptibility is not clear. We report that Mal has a TLR-independent role in interferon-gamma (IFN-γ) receptor signaling. Mal-dependent IFN-γ receptor (IFNGR) signaling led to mitogen-activated protein kinase (MAPK) p38 phosphorylation and autophagy. IFN-γ signaling via Mal was required for phagosome maturation and killing of intracellular *Mycobacterium tuberculosis* (*Mtb*). The S180L polymorphism, and its murine equivalent S200L, reduced the affinity of Mal for the IFNGR, thereby compromising IFNGR signaling in macrophages and impairing responses to TB. Our findings highlight a role for Mal outside the TLR system and imply that genetic variation in *TIRAP* may be linked to other IFN-γ-related diseases including autoimmunity and cancer.

INTRODUCTION

Genetic variation in proteins involved in innate immunity, particularly Toll-like receptors (TLRs) and their signaling adaptor proteins, has been proposed to account for variation in susceptibility to infectious pathogens. MyD88 adaptor-like (Mal), encoded by the gene Toll-interleukin 1 receptor (TIR) domain-containing adaptor protein (*TIRAP*), was initially described as a signaling adaptor protein leading to nuclear factor kappa-light-chain-enhancer of activated B cells (NF-κB) activation downstream of TLR4 (Fitzgerald et al., 2001; Horng et al., 2001) and TLR2 (Horng et al., 2002; Yamamoto et al., 2002). A role for Mal as a "bridging adaptor" has since been established with Mal recruited to the plasma membrane, where it facilitates myeloid differentiation primary response gene 88 (MyD88) delivery to activated TLRs to initiate signal transduction in a structure called the Myddosome (Bonham et al., 2014; Kagan and Medzhitov, 2006). Mal has also been reported to function as a signaling adaptor for endosomal TLR signaling (Bonham et al., 2014).

Two non-synonymous single nucleotide polymorphisms (SNPs) in *TIRAP* with functional consequences have been identified, D96N and S180L. The S180L SNP is common in Indian and European (approximately 15%–20% carrying the L allele and 2%–3% being homozygous for the L allele) populations (Ferwerda et al., 2009) and results in alteration of a potential binding site near D96, leading to steric occlusion (Valkov et al., 2011). S180L has been associated with altered susceptibility to a number of infectious diseases including severe sepsis, severe pneumococcal disease, *Haemophilus influenzae,* and malaria (Ferwerda et al., 2009; Khor et al., 2007; Ladhani et al., 2010). An association has been reported between the S180L *TIRAP* polymorphism and TB susceptibility with heterozygotes for the mutation showing protection from disease and homozygotes showing increased susceptibility (Capparelli et al., 2013; Castiblanco et al., 2008; Khor et al., 2007; Selvaraj et al., 2010), although other studies have failed to replicate these findings (Dissanayeke et al., 2009; Nejentsev et al., 2008). A recent meta-analysis of the data confirms the association (Liu et al., 2014). The mechanism underlying the effect of the S180L SNP has not yet been elucidated.

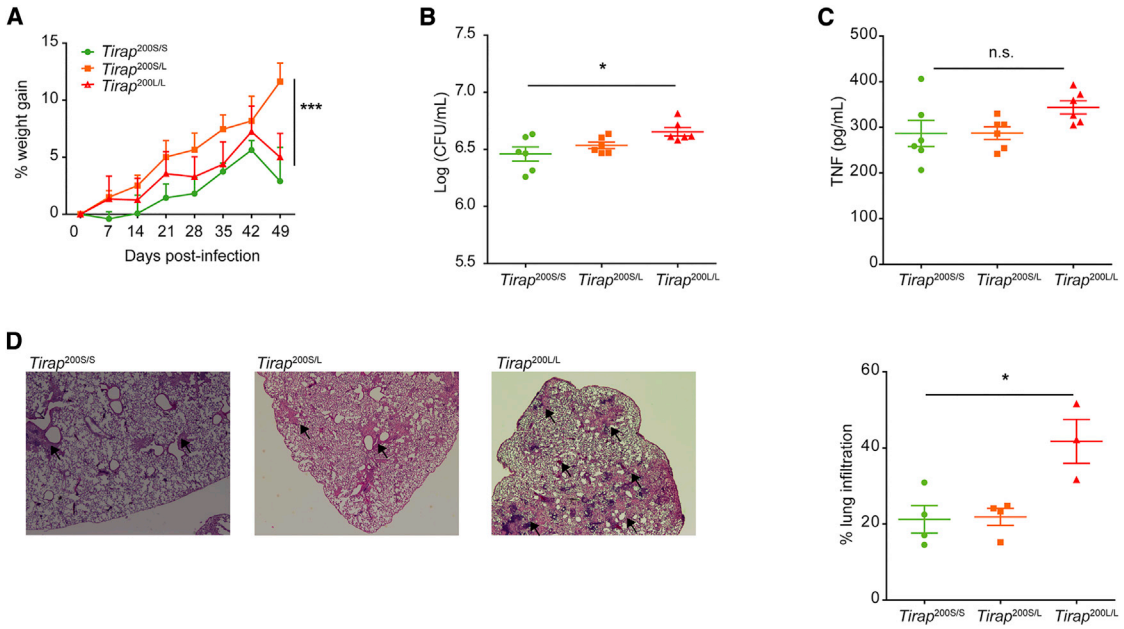

Figure 1. Mice Homozygous for *Mal* S200L, the Equivalent of *Mal* S180L, Develop More Severe Lung Inflammation in Response to In Vivo Infection with *Mycobacterium tuberculosis*

Age- and sex-matched WT (Mal$^{200S/S}$), heterozygote (Mal$^{200S/L}$), and homozygote (Mal$^{200L/L}$) mice were infected with 500 cfu of *Mycobacterium tuberculosis* (*Mtb*) H37Rv by aerosol.

(A) Weights of eight mice in each group were measured weekly.

(B) Mice were sacrificed at 8 weeks post-infection, and lung homogenates from five or six mice per group were plated for measurement of bacterial burden.

(C) TNF-α in lung homogenates from five or six mice per group was measured by ELISA.

(D) Lungs from three to four mice per group were fixed in formalin, stained with haemotoxylin and eosin, and area of inflammation assessed by microscopy with representative images and quantifications are shown. All data are means ± SD. A two-way ANOVA was used to analyze data in (A). A one-way ANOVA (non-parametric, Kruskal-Wallis) was used to analyze data in (B)–(D). *$p < 0.05$, ***$p < 0.001$) for all experiments.

Macrophages are key phagocytic cells that can eliminate or harbor intracellular bacteria, such as *Mtb* and also play a key role in secreting cytokines, which polarize subsequent adaptive immunity to a beneficial T helper 1 (Th1) or deleterious Th2 type response. Macrophages carry out a number of key antimicrobial functions including autophagy and phagosomal maturation, which if successful can kill intracellular mycobacteria (Deretic et al., 2006; Harris et al., 2009). IFN-γ plays a critical role in promoting antimicrobial functions. It activates macrophages, leading to production of nitric oxide (NO) and reactive oxygen species (ROS), phagosomal maturation, autophagy, and bactericidal activity (Gutierrez et al., 2004; MacMicking, 2012; Matsuzawa et al., 2014). Individuals with partial or complete defects in the IFN-γ signaling pathway have increased susceptibility to *Mtb*, as well as to other mycobacterial species (Bogunovic et al., 2012; Filipe-Santos et al., 2006).

In this study, we report that the murine equivalent of S180L, S200L, replicated human findings with homozygotes displaying increased severity of tuberculous disease. In vitro, the S200L mutation resulted in impaired phagosome maturation and killing of *Mtb*. We demonstrate that, unlike S180L, S200L did not affect TLR signaling. The impaired TB immunity seen with S200L was due to its effect on a Mal-dependent, TLR-independent, IFNGR signaling pathway. Mal-dependent responses to IFN-γ included p38 MAPK phosphorylation, autophagy, and phagosomal maturation, but not the canonical signal transducer and activator of transcription-1 (STAT-1) phosphorylation pathway. The S180L polymorphism reduced the affinity of Mal for the IFNGR, thereby compromising human macrophage responses to IFN-γ. This Mal-dependent IFNGR signaling pathway, modulated by the S180L mutation, might affect susceptibility to infectious diseases, inflammatory diseases, and cancer.

RESULTS

The S200L Mutation Is Associated with Increased Severity of TB Disease in Vivo

Mice with the equivalent of the human S180L mutation in *TIRAP* (*Tirap* 200L) were generated to provide an in vivo model of *Mtb* infection (Figure S1). Wild-type (SS), heterozygote (SL), and homozygote (LL) mice were infected with a high dose of *Mtb* H37Rv (a laboratory strain of virulent *Mtb)* via aerosol and weighed weekly. SL mice were protected against weight loss (Figure 1A). Mice were sacrificed at 8 weeks post-infection and lung lysates were analyzed. LL mice showed increased severity of TB disease, with an increase in bacterial burden (Figure 1B), despite similar levels of lung tumor necrosis factor alpha (TNF-α) production (Figure 1C). Most markedly however, we observed increased lung inflammation in LL mice (Figure 1D) compared to SL and SS mice. This correlates with the protection for heterozygotes and the increased susceptibility seen in homozygotes

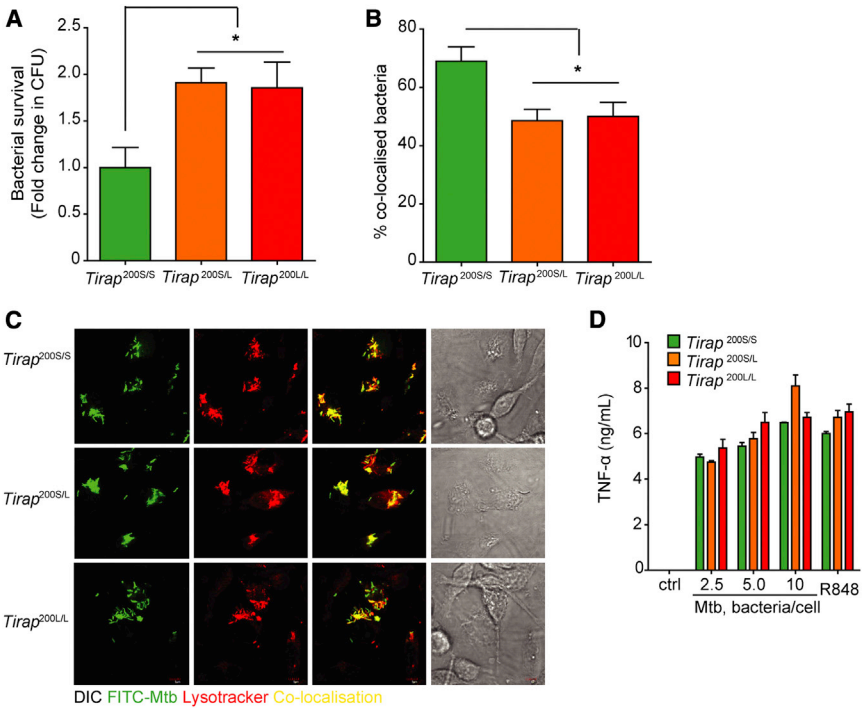

Figure 2. The S200L Mutation Impairs Macrophage Phagosome Maturation and Killing of Intracellular *Mtb*

(A) Primary BMM were infected with *Mtb* H37Rv and lysed at 72 hr. Serial dilutions of lysates were plated out to determine bacterial numbers.

(B and C) Cells were infected with FITC-stained *Mtb* H37Rv for 2 hr, fixed and stained with Lysotracker (LT, Life Technologies DND-99), and co-localization of *Mtb* with LT^+ phagolysosomes was assessed by confocal microscopy and quantified in (B) with representative images in (C).

(D) Primary BMM were infected overnight with *Mtb* H37Rv and supernatants analyzed for TNF-α production by ELISA. All experiments show mean ± SD pooled from three separate experiments with macrophages from one mouse per group in each experiment *$p < 0.05$ (one-way ANOVA used to analyze all experiments).

for the mutation in human studies. The phenotype of TB infection seen with the S200L mutation in mice replicated the human phenotype with S180L.

S200L Affects Macrophage Function Independently of Cytokine Production

Mycobacterial survival in macrophages is an in vitro read-out of macrophage function (Watson et al., 2012). Macrophages from mice with the S200L mutation displayed a defect in killing of intracellular mycobacteria (Figure 2A). Macrophages from mice with the S200L mutation displayed a defect in phagosome maturation, corresponding with the defect seen in bactericidal activity (Figures 2B and 2C). Unlike *Tirap*$^{-/-}$ macrophages described later, the S200L macrophages displayed no impairment in production of these cytokines (Figures 2D and S2A), indicating that the defect seen in mycobactericidal activity was not due to an impairment of cytokine production. In addition, S200L homozygote macrophages, unlike *Tirap*$^{-/-}$ macrophages, did not exhibit attenuated cytokine responses to TLR2 and TLR4 ligands (Figures S2B and S2C), indicating that S200L did not affect TLR2 or TLR4 signaling.

Mal and MyD88, but Not TLRs 2 and 4, Are Required for Macrophage Killing of Virulent Mtb

We proceeded to assess whether Mal-deficient macrophages showed a similar in vitro phenotype to S200L macrophages in response to *Mtb* infection. Immortalized and primary murine bone marrow macrophages were used, as well as *TIRAP*-silenced THP-1 cells. In contrast to our observations in S200L macrophages (Figure 2D), we observed that production of the key anti-mycobacterial cytokine TNF-α in response to *Mtb* was greatly reduced in Mal-deficient cells (Figures 3A–3C). Production of IL-1α, IL-1β, IL-6, and IL-12p40, but not IL-27 or IL-10, was also impaired in the absence of Mal (Figures S3A and S3B, with confirmation of *TIRAP silencing* in Figure S3C). Mal-deficient macrophages (Figures 3D and 3E and S3D) showed a marked inability to kill intracellular *Mtb*, similar to that seen in the S200L macrophages. We also assessed the role of TLRs 2 and 4 in our model. *Tlr2*$^{-/-}$, *Tlr2/4* double knockout (*dko*) and *Myd88*$^{-/-}$ macrophages replicated the defect in pro-inflammatory cytokine production seen in Mal deficient cells. *Tlr4*$^{-/-}$ macrophages showed a smaller, but still significant, impairment in cytokine responses (Figures 3F and 3G and S3E and S3F). Notably, whereas *Myd88*$^{-/-}$ macrophages replicated the defect in bactericidal activity seen in *Tirap*$^{-/-}$ cells, *Tlr2*$^{-/-}$, *Tlr4*$^{-/-}$, and *Tlr2/4 dko* murine macrophages and THP-1 macrophages treated with an anti-TLR2 antibody did not show a similar defect despite impairments in cytokine induction (Figures 3H and 3I and S3G). Consistent with our findings is a previous report of unimpaired bactericidal activity of *Tlr2/4/9* triple knockout macrophages and impaired restriction of *Mtb* growth by *Myd88*$^{-/-}$ macrophages (Hölscher et al., 2008). These data indicated that Mal and MyD88 had a function in killing of *Mtb*, and that this was distinct from the known role of Mal downstream of TLRs 2 and 4. This defect in mycobactericidal activity seen in the absence of Mal, but not in the absence of TLRs 2 and 4, was not due to defects in cytokine production.

Mal Is Required for Autophagy and IFN-γ Induced Phagosome Maturation

We sought to identify Mal-dependent but TLR-independent macrophage effector mechanisms. Autophagy provides a mechanism of killing and removing intracellular pathogens and contributes to a number of critical host immune responses to *Mtb* (Ní Cheallaigh et al., 2011). To determine whether *Mtb*-induced autophagic flux was impaired in the absence of Mal, we infected primary macrophages with *Mtb* in the presence or absence of bafilomycin, which blocks autophagosome fusion with lysosomes and thereby completion of autophagy and breakdown

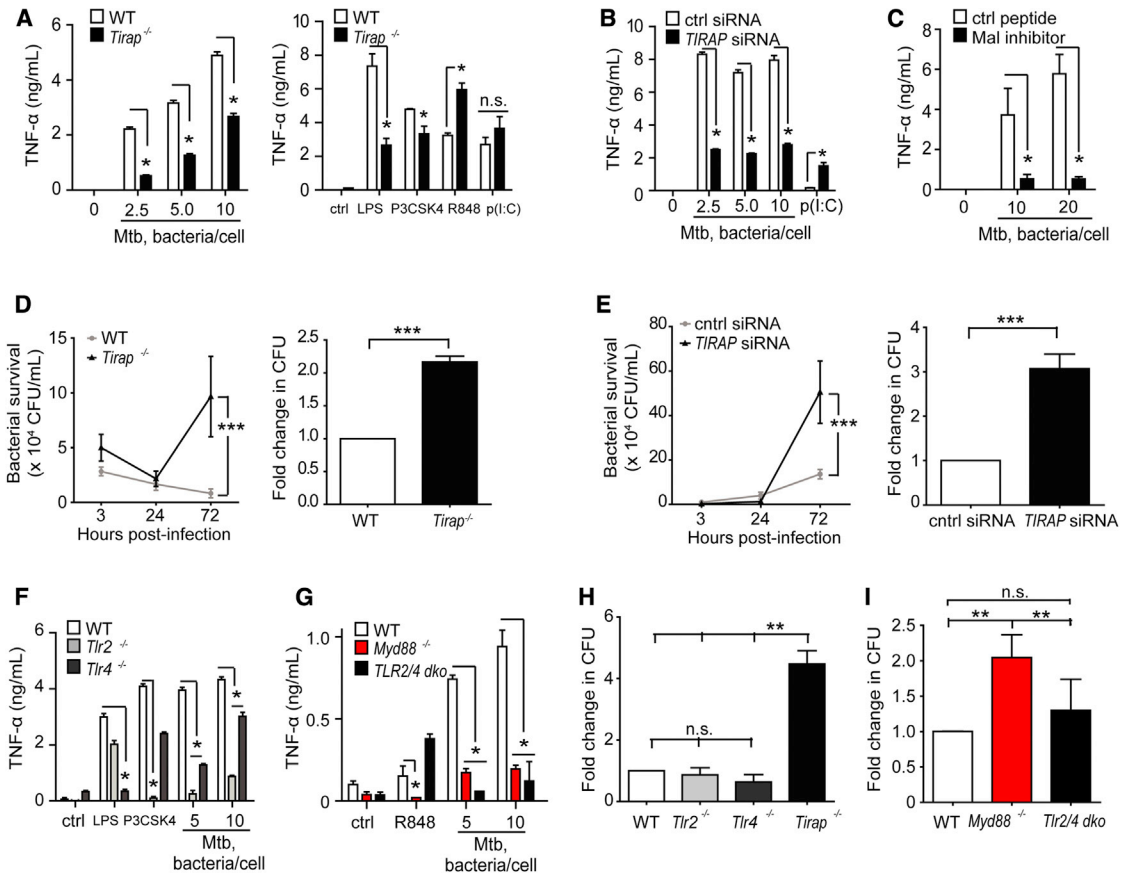

Figure 3. Mal and MyD88, but Not TLR2 or TLR4, Are Required for Macrophage Killing of Virulent *Mycobacterium tuberculosis*

(A) TNF-α secretion by murine wild-type (WT) and *Tirap*$^{-/-}$ immortalized bone marrow-derived macrophages (iBMM) (1 × 10^6/ml) infected with *Mtb* H37Rv (left panel) or treated with the indicated TLR ligands (right panel), was measured in supernatants collected after 20 hr stimulation and analyzed by ELISA.

(B) Cytokine secretion by PMA-differentiated THP-1 (5 × 10^5/ml) cells transfected with siRNA against Mal or scrambled control in response to infection with *Mtb* H37Rv (20 hr) was measured by ELISA.

(C) ELISA of TNF-α secretion by PMA-differentiated THP-1 cells (5 × 10^5/ml) treated with a Mal inhibitor peptide (TIRAP inhibitory peptide, Calbiochem, 613571) before infection with *Mtb* H37Rv (20 hr).

(D) WT and *Tirap*$^{-/-}$ iBMM were infected with *Mtb* H37Rv at a multiplicity of infection of 10 bacteria/cell and lysed at 3, 24, and 72 hr. Serial dilutions of lysates were plated out to determine bacterial numbers. Left panels show data representative of at least three separate experiments, right panels are mean ± SD pooled from bacterial counts at 72 hr from three separate experiments.

(E) PMA-differentiated THP-1 cells transfected with siRNA against *TIRAP* (Dharmacon/Thermoscientific) or scrambled control siRNA, were infected with *Mtb* H37Rv and bacterial numbers determined as above. Left panel shows data representative of at least three separate experiments, and right panel is mean ± SD pooled from three separate experiments.

(F and G) TNF-α secretion by iBMM (1 × 10^6/ml) infected with *Mtb* H37Rv (20 hr) was measured by ELISA.

(H and I) iBMM were infected with *Mtb* H37Rv and bacterial numbers determined as above. Data are means ± SD of data pooled from three separate experiments.

*p < 0.05 (Mann-Whitney) for all experiments.

of autophagosomes (Yamamoto et al., 1998). *Mtb*-induced autophagic flux was reduced in the absence of Mal (Figure 4A-B). When autophagy was impaired in macrophages using knockdown of the key effector proteins ATG7 or BECLIN-1 by siRNA, a similar defect in bactericidal activity and phagosomal maturation to that seen in Mal-deficient cells was observed (Figures S4A–S4C).

We assessed whether Mal was required for phagosomal maturation by pretreating macrophages with IFN-γ or RPMI control and infecting the macrophages with FITC-labeled live *Mtb*. We identified phagolysosomes using anti-CD63 antibody or LysoTracker Red and assessed co-localization of bacteria and phagolysosomes. IFN-γ pre-treatment increased co-localization of bacteria and phagolysosomes in WT, but not in *Tirap*$^{-/-}$ macrophages (Figures 4C and 4D [LysoTracker] and Figures 4E and 4F [CD63]) a trend which persisted up to 24 hr post IFN-γ treatment (Figure S4D). Similar results were obtained in differentiated THP-1 cells treated with siRNA against Mal and stained with LysoTracker or the mature endolysosomal marker LAMP-1 (Figures 4G and S4E). Notably, IFN-γ did increase phagosomal maturation in *Tlr2/4* dko, but not *Myd88*$^{-/-}$ macrophages (Figure 4H). Thus, Mal and MyD88, but not TLRs 2 and 4, were required for IFN-γ-induced phagosome maturation.

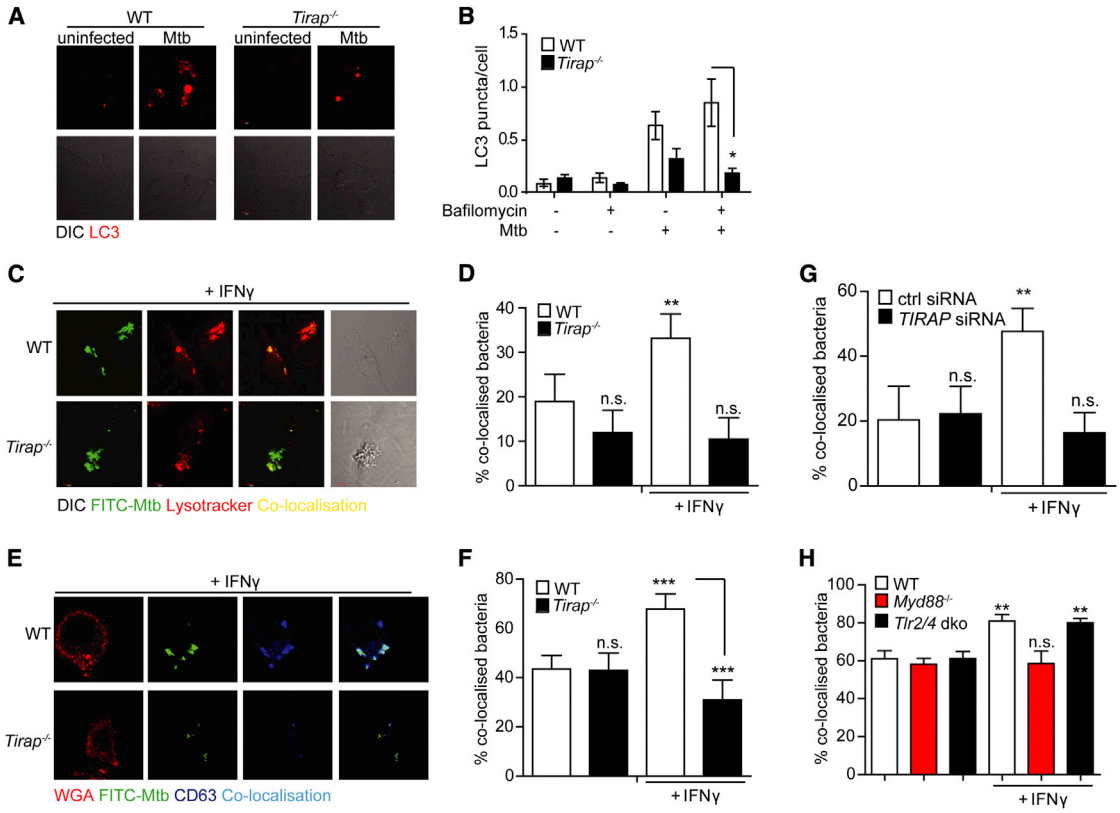

Figure 4. Mal Regulates IFN-γ Induced Maturation of *Mtb* Containing Phagosomes Independently of TLR2 and TLR4

(A and B) Primary WT and *Tirap*$^{-/-}$ bone-marrow-derived macrophages (BMM) were stimulated for 16 hr with *Mtb* in the presence or absence of bafilomycin. Cells were stained with anti-LC3 antibody (Invitrogen L10352) (representative images in (A) and LC3^{+} puncta per cell quantified by confocal microscopy (B).

(C–F) WT and *Tirap*$^{-/-}$ iBMM were stimulated overnight with rmIFN-γ (20 ng/ml) prior to infection with FITC-labeled *Mtb* H37Rv. Cells were stained with Lysotracker (LT) (C and D) and co-localization of *Mtb* with LT^{+} phagolysosomes was assessed by confocal microscopy, (representative images in C, quantified in D). Alternatively, cells were stained with anti-CD63 antibody (Santa Cruz, H-193) (E and F) and co-localization of *Mtb* with CD63-positive phagolysosomes was assessed by confocal microscopy, (representative images in E, quantified in F).

(G) THP-1 cells were transfected with siRNA against *TIRAP* or scrambled control prior to differentiation with PMA. Cells were stimulated overnight with recombinant human (rh)IFN-γ (20 ng/ml) prior to infection with FITC-labeled *Mtb* H37Rv and stained with LT. Co-localization of *Mtb* with LT^{+} phagolysosomes was quantified by confocal microscopy.

(H) iBMM were infected with FITC-labeled *Mtb* H37Rv and stained with LT. Co-localization of *Mtb* with LT^{+} phagolysosomes was quantified by confocal microscopy. Data shown are mean ± SD from a single experiment representative of three separate experiments are shown for (B) and mean ± SD of data pooled from three separate experiments for all other experiments (D, F–H). *$p < 0.05$ (Mann-Whitney) for all experiments.

Mal and MyD88, but Not TLRs 2 and 4, Are Required for Interferon-Inducible Protein 10 Production, p38 Phosphorylation, and Autophagy in Response to IFN-γ

Given our findings of impaired IFN-γ induced phagosomal maturation in the absence of Mal and MyD88 but not TLRs 2 and 4, we hypothesized that the Mal-dependent but TLR-independent pathway required for killing of intracellular *Mtb* might be explained by Mal participating in MyD88-dependent IFNGR signaling. Previously, normal STAT-1 phosphorylation but impaired IFN-inducible protein 10 (IP-10) secretion was reported in MyD88-deficient macrophages (Sun and Ding, 2006). We identified a profound defect in IFN-γ-induced IP-10 secretion in *Tirap*$^{-/-}$ and Myd88$^{-/-}$ macrophages, but not in *Tlr2/4* dko macrophages or *Tram*$^{-/-}$ macrophages (Figure 5A and S5A). IP-10 secretion was also reduced in *TIRAP*-silenced THP-1 cells (Figure S5B). IFN-γ-induced STAT-1 phosphorylation remained intact in Mal-deficient cells (Figure S5C). We observed a reduction in *Cxcl10/Ip10* mRNA and *Tnfa* mRNA in *Tirap*$^{-/-}$ macrophages after IFN-γ treatment—a trend not observed for the STAT-1 target gene, *Nos2*, or for *Arg1* mRNA (Figure S5D).

P3 mitogen-activated protein kinases (MAPK) are a class of MAPK that respond to stress stimuli including cytokines and are involved in apoptosis and autophagy. An IFNγ-induced p38 MAPK signaling pathway, which culminates in autophagy and killing of intracellular bacteria, was recently reported (Matsuzawa et al., 2014). We hypothesized that Mal might be required for this pathway. P38 MAPK was phosphorylated in response to IFN-γ, peaking at 4 hr post-treatment (Figures 5B, top panel), and this was impaired in *Tirap*$^{-/-}$ macrophages (Figure 5B, bottom panel and S5E). IFN-γ induced autophagy, but not starvation-induced autophagy, was reduced in *Tirap*$^{-/-}$ macrophages, (Figures 5C and S6A and S6B). These data demonstrate that Mal was required for IFN-γ induced P38 MAPK phosphorylation, autophagy and IP-10 secretion.

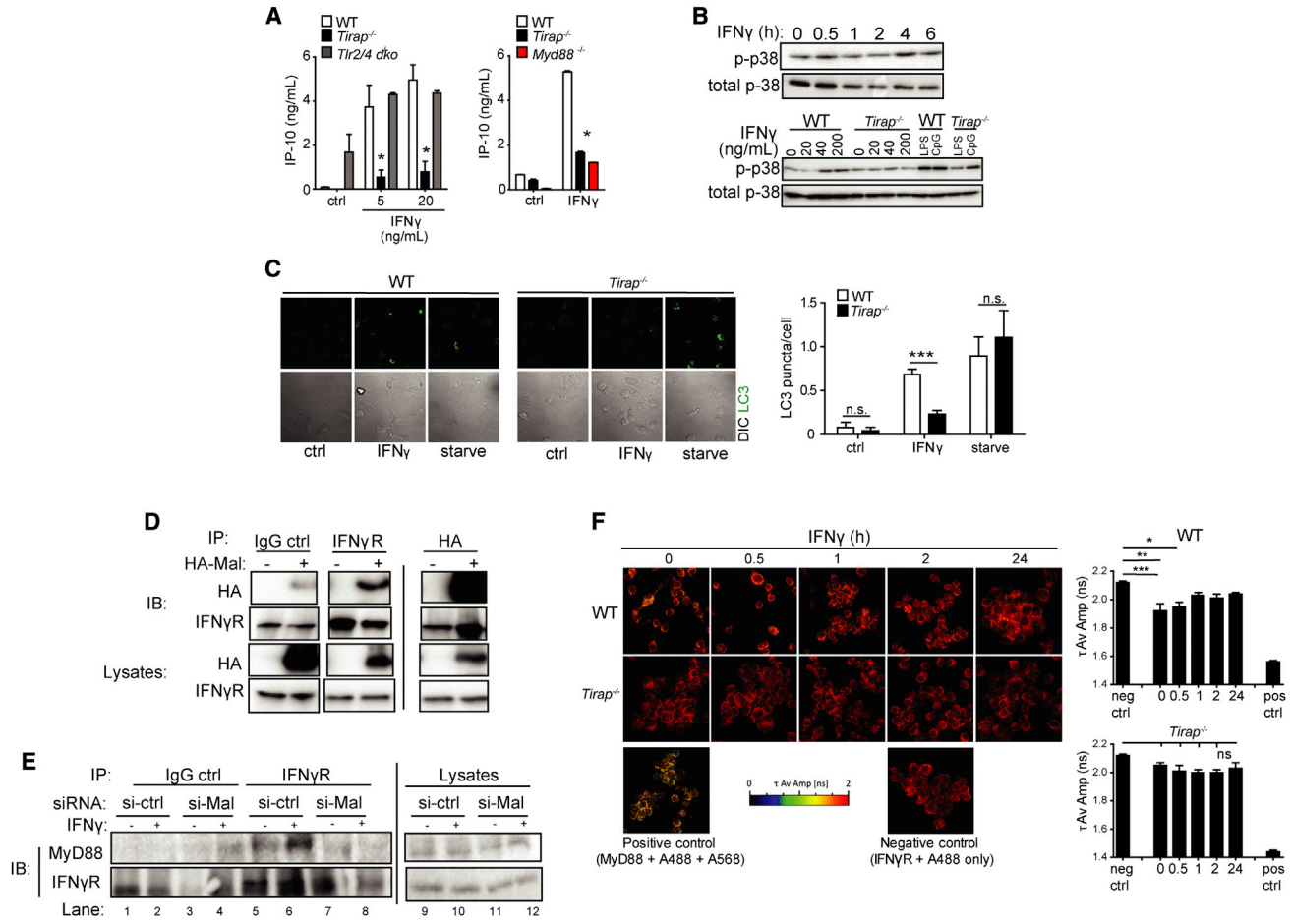

Figure 5. Mal Associates with the IFN-γR and Is Required for IFN-γ Induced p38 Phosphorylation and Autophagy

(A) iBMM were treated with rmIFN-γ for 20 hr and secretion of IP-10 was measured by ELISA. Data are means ± SD from a single experiment representative of three separate experiments *p < 0.05, (Mann-Whitney).

(B) Primary BMM were treated for the indicated times (0–6 hr) at 20 ng/mL (top panel) and for 4 hr with rmIFN-γ at the indicated concentrations (0–100 ng/mL, bottom panel) alongside LPS or R848 (10 min). Lysates were prepared and analyzed for phosphorylation of p38 MAP-kinase by immunoblotting with anti-p-p38 antibody (Cell Signaling, 9211). Blots were stripped and re-probed for total p38 (bottom panels). Data shown are representative of three separate experiments.

(C) Primary BMM were stimulated for 16 hr with rmIFN-γ (20 ng/ml) and bafilomycin (100nM) or for 2 hr with starvation medium. Cells were stained with anti-LC3 antibody and LC3 puncta per cell were quantified with confocal microscopy. Data are means ± SD from a single experiment representative of three separate experiments, *p < 0.05, (Mann-Whitney).

(D) HEK293 cells were transfected with HA-tagged Mal and immunoprecipitation was performed with antibodies to HA (Sigma, H6908) and interferon gamma receptor (Santa Cruz, sc-700), along with a control non-specific rabbit IgG, on cell lysates as indicated. Lysates were then blotted with anti-HA antibody. Data shown are representative of three independent experiments.

(E) RAW264.7 cells were transfected with the indicated siRNAs (50 nM) for 72 hr prior to treatment with IFN-γ (100 ng/ml, 10 min) and immunoprecipitation was performed with antibodies to IFN-γR1 or an IgG control on cell lysates as indicated. IP-samples were then analyzed for MyD88 expression by immunoblotting with anti-MyD88 (Millipore, 16527) (top panel) alongside IFN-γR1 expression (bottom panels). Data shown are representative of three independent experiments.

(F) iBMM were treated with IFN-γ (10 ng/ml) for 0–24 hr. Cells were fixed and stained with antibodies against MyD88 and IFNGR2 followed by fluorescent secondary antibodies (Alexa Fluor 568 and Alexa Fluor 488). Changes in the amplitude weighted average lifetime (τ Av Amp) of the donor (A488) due to proximity with the acceptor (A568) were measured. A decrease in τ Av Amp indicates interaction between the molecules and is quantified on right. *p < 0.05, **p < 0.01, ***p < 0.005; one-way ANOVA.

Mal Interacts Directly with the IFNGR

We hypothesized that Mal might act as a bridging adaptor for MyD88 and the IFNGR. Immunoprecipitation of endogenous IFNGR resulted in co-immunoprecipitation of overexpressed Mal (Figure 5D, left panel). This interaction required full-length Mal, as a mutant construct consisting solely of the TIR domain did not immunoprecipitate with the IFNGR (Figure S7A). Immunoprecipitation of full-length overexpressed HA-Mal resulted in co-immunoprecipitation of IFNGR, confirming that Mal can bind IFNGR directly (Figure 5D, right panel). Mal did not precipitate with other proteins including Beclin-1 and BCL-2 (Figure S7B).

We then hypothesized that if Mal functions as a bridging adaptor between MyD88 and the IFNGR, then the previously

reported interaction between MyD88 and the IFNGR (Sun and Ding, 2006) would be reduced in the absence of Mal. We observed increased recruitment of MyD88 to IFNGR in IFNγ-treated control cells (Figure 5E, lanes 5/6); however, in *TIRAP*-silenced or Mal-deficient cells (knockdown shown in Figure S7C) this interaction was reduced to background levels (Figure 5E, lanes 7/8 and Figure S7D).

We then confirmed this finding using fluorescence lifetime imaging microscopy-fluorescence resonance energy transfer (FLIM FRET) technology. FRET occurred between IFNGR and MyD88, indicating that they are interacting basally and for up to 0.5 hr post IFN-γ treatment (Figure 5F) in WT cells. This steady-state interaction between MyD88 and IFNGR was disrupted after initial signal transduction. In *Tirap*$^{-/-}$ cells, there was no evidence of such a basal interaction, a pattern not altered by subsequent IFN-γ treatment. These data demonstrated that Mal bound to IFNGR and was required for the interaction between MyD88 and IFNGR.

Interferon Gamma Is Required for Autophagy and Phagosome Maturation in Response to Mtb

Our data had established that Mal is required for an IFN-γ signaling pathway, culminating in p38 MAPK phosphorylation and autophagy. We hypothesized that the observed defect in autophagy and killing of intracellular *Mtb* was due to the defect in the IFN-γ induced p38 MAPK phosphorylation pathway. However, we observed the deficits in autophagy and killing in a monoculture of macrophages in the absence of exogenous IFN-γ. We therefore hypothesized that macrophages secrete small quantities of IFN-γ that are functionally relevant in our model. Immortalized and primary macrophages and differentiated THP-1 cells produced small but detectable amounts of IFN-γ when infected with *Mtb* (Figures S8A–S8C). IFN-γ production was reduced in *Tirap*$^{-/-}$ immortalized bone-marrow-derived macrophages (iBMM) (Figure S8A)—this may be due to impaired TLR2 and/or TLR4 signaling or impaired IFN-γ signaling, because IFN-γ can upregulate its own production in a positive feedback loop. We also observed IFN-γ production by immortalized and primary macrophages using intracellular staining and flow cytometry (Figures S8D–S8F). Macrophages produced a considerable amount of IFN-γ if allowed to recover from LPS tolerization and restimulated for 4 hr (Figures S8E–S8G). Although our data show that *Mtb* can induce IFN-γ production by macrophages, the levels produced are extremely low compared to those produced by T cells or NK cells. We therefore sought to assess whether the low levels of IFN-γ present in our macrophage cultures were functionally signficant for our key endpoints. Macrophages treated with a blocking antibody against IFN-γ (Figures S9A and S9B) and *Ifng*$^{-/-}$ macrophages (Figures S9C and S9D) showed reduced maturation of *Mtb* containing phagosomes. In the case of *Ifng*$^{-/-}$ macrophages, maturation was restored by adding exogenous IFN-γ (Figure S9D). *Ifng*$^{-/-}$ macrophages also showed reduced autophagy in response to *Mtb* (Figures S9E and S9F). Finally, *Ifng*$^{-/-}$ macrophages showed a defect in bactericidal activity as assessed by intracellular bacterial burden at 72 hr, similar to that seen in *Tirap*$^{-/-}$ macrophages (Figure S9G). These data demonstrated that macrophages secrete small but functionally relevant amounts of IFN-γ.

The S200L/S180L Mal Mutation Reduces IFN-γ Signaling

Given the new role identified for Mal in IFN-γ signaling, we then proceeded to look at the effect of the S200L polymorphism on TLR2, TLR4, and IFN-γ signaling in macrophages. As noted above, the S200L mutation did not affect secretion of the pro-inflammatory cytokine TNF-α in response to the TLR2 ligands Malp-2 and Pam_3CysK_4 or the TLR4 ligand LPS (Figures S2A–S2C) or *Tnfa* mRNA levels in response to TLR2 and TLR4 ligands (Figure 6B). However, macrophages from LL mice and, to a lesser extent, SL mice, showed a decreased IP-10 response to IFN-γ stimulation (Figures 6A and 6C), indicating that carriage of the 200L allele in mice, impairs IFN-γ, but not TLR, responses.

We then sought to determine the effect of the S180L mutation in human macrophages. We derived macrophages from peripheral blood monocytes (MDMs) from donors genotyped using allelic discrimination. MDMs were stimulated with TLR ligands and TNF-α secretion was measured by ELISA. We observed decreased responses to TLR2 and TLR4 ligands in human MDMs (Figure 6E). We observed a decrease in IFN-γ-driven IP-10 secretion in MDMs from individuals who were homozygous for the S180L mutation (Figure 6D). We proceeded to assess whether the S180L mutation altered the affinity of Mal for the IFNGR. Using site-directed mutagenesis, we synthesized HA-tagged human Mal with the S180L mutation (180L). S180L variant human Mal shows decreased affinity for the IFNGR relative to HA-tagged wild-type Mal (Figure 6F). The S180L mutation reduces the affinity of Mal for the IFNGR and reduces IP-10 secretion in response to IFN- γ stimulation.

DISCUSSION

Here we show that the murine equivalent of the S180L mutation in Mal, Mal S200L, replicated the phenotype previously reported from humans with the S180L polymorphism: it conferred protection from tuberculous disease on heterozygotes for the mutation and increased susceptibility on homozygotes. In vitro, Mal S200L impaired phagosome maturation and killing of intracellular mycobacteria. However, unlike S180L, S200L did not affect TLR signaling. We demonstrated a mechanism for these observations: the S200L polymorphism affected a TLR-independent, Mal-dependent, IFNGR signaling pathway. Mal-dependent IFNGR signaling was required for p38 phosphorylation, autophagy, phagosome maturation, and killing of intracellular mycobacteria. This IFNGR signaling pathway was attenuated by the human mutation S180L. This offers an explanation for how the common S180L mutation affects host innate immune responses to *Mtb.* The fact that this common polymorphism attenuates IFNGR signaling might have relevance for host susceptibility to a number of IFN-γ-related conditions including autoimmunity and cancers.

A number of publications regarding the effect of the S180L SNP on infectious disease susceptibility in humans have reported a heterozygote advantage with increased susceptibility seen in homozygotes (Capparelli et al., 2013; Castiblanco et al., 2008; Khor et al., 2007; Selvaraj et al., 2010). A murine model using the equivalent of the S180L mutation, S200L,

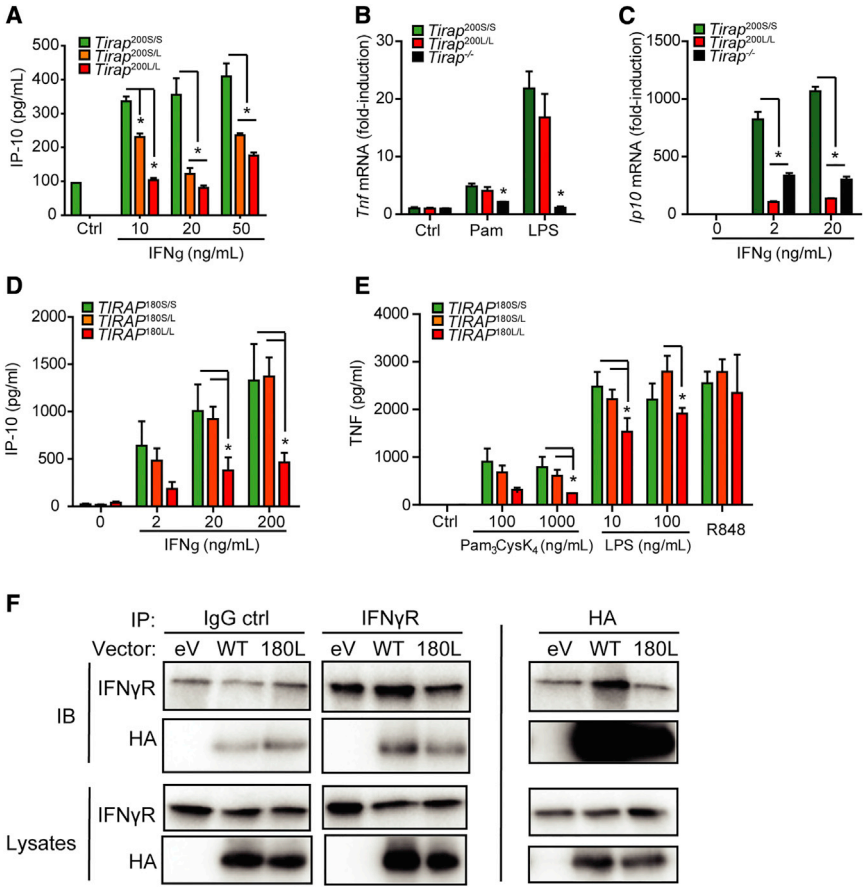

Figure 6. The S180L/S200L Mutation Reduces Affinity for IFNγR1 and Impairs Responses to IFN-γ

(A) IP-10 secretion by primary murine BMM stimulated for 20 hr with rmIFN-γ and supernatants analyzed by ELISA, mean ± SD pooled from three separate experiments with macrophages from one mouse per group in each experiment.

(B and C) *Tnfa* and *Ip-10* mRNA levels from iBMM stimulated for 4 hr with Pam_3Cys_4K (100 μg/mL), LPS (100 ng/ml) or rmIFN-γ at the concentrations indicated.

(D and E) Monocyte-derived macrophages from human volunteers genotyped for the S180L SNP (n = 12 for *TIRAP* 180S/S, n = 12 for *TIRAP* 180S/L, and n = 4 for *TIRAP* 180L/L) were stimulated with rhIFN-γ (D) or TLR ligands (E) for 16 hr. Supernatants were analyzed for IP-10 production (D) or TNF (E) by ELISA. Mean ± SD shown in graph, analyzed using two-way ANOVA.

(F) HEK293 cells were transfected with HA-tagged wild-type, HA-tagged S180L variant Mal, or HA-tagged empty vector and an immunoprecipitation was performed with antibodies to HA and IFNGR1 on cell lysates as indicated prior to Western blotting.

replicated these findings, with heterozygotes protected from weight loss (a cardinal clinical feature of human tuberculosis) and homozygotes displaying increased bacterial burden and lung inflammation.

In vitro, macrophages from mice carrying the L allele displayed impaired phagosome maturation and killing of *Mtb* but did not show evidence of impaired cytokine production. In contrast, macrophages from TLR-deficient mice displayed impaired cytokine production but preserved phagosome maturation and killing of *Mtb.* Mal-deficient macrophages displayed impairment of cytokine production in addition to the phenotype seen in the S180L macrophages of impaired phagosome maturation and killing.

These findings led us to search for a TLR-independent function for Mal. We show here a TLR2- and TLR4-independent role for Mal in the IFNGR signaling pathway. Mal bound to the IFNGR and MyD88 and acted as a bridging adaptor between these proteins. Mal was required for IP-10 production in response to IFN-γ and for a pathway involving p38 MAPK phosphorylation, culminating in autophagy and killing of intracellular bacteria. Autophagy is a key means of killing intracellular bacteria, including *Mtb*, and also plays a role in regulation of cytokine secretion (Ní Cheallaigh et al., 2011; Peral de Castro et al., 2012). IFN-γ-induced phagosome maturation is dependent on Beclin-1 and might indeed be autophagy-dependent (Harris et al., 2007). The defect in autophagy seen in the absence of Mal-dependent IFNGR signaling provides an explanation for why Mal and MyD88, but not TLRs 2 and 4, are required for macrophage killing of *Mtb.*

IFN-γ is a canonical macrophage activator and is known to play a critical role in immune responses to *Mtb* (Bogunovic et al., 2012; Cooper et al., 1993; Filipe-Santos et al., 2006; Flesch and Kaufmann, 1991; Flynn et al., 1993). IFN-γ is secreted in large quantities by activated Th1 cells (Mosmann and Coffman, 1989), activated $CD8^+$ cytotoxic cells (Sad et al., 1995), and NK cells (Perussia, 1991). However, our model for bactericidal activity and autophagy consisted of a monoculture of macrophages. There are numerous reports of macrophages secreting IFN-γ (Darwich et al., 2009; Di Marzio et al., 1994; Fenton et al., 1997; Fultz et al., 1993), albeit in limited quantities, although some authors have highlighted the possible effect of contaminating cells in producing IFN-γ (Schleicher et al., 2005). The increased proportion of IFN-γ producing cells in macrophages pre-stimulated with LPS and then "recovered" (O'Carroll et al., 2014) provides compelling evidence that macrophages can produce IFN-γ given appropriate stimuli.

We show here that the murine immortalized and primary macrophages used in our *Mtb* infection model secreted small but functionally decisive quantities of IFN-γ in response to infection with *Mtb* and that Mal played a critical role in macrophage responses to *Mtb*, which are IFN-γ dependent.

Given our identification of a role for Mal in IFNGR signaling and its established role in TLR2 and TLR4 signaling, we examined the effect of the S180L polymorphism and the murine equivalent of the S180L polymorphism, S200L, on these pathways. We show that responses to IFN-γ are reduced in human cells with the 180L variant. Human 180L variant Mal showed a reduced affinity for the IFNGR. Cells from mice with the equivalent mutation also showed impairment in IFNGR signaling.

Human S180L reduced responses to TLR2 and TLR4 ligands, consistent with the known role of Mal as a signaling adaptor protein downstream of TLRs 2 and 4, and with published data on the role of TLR2 as a pattern-recognition receptor involved in pro-inflammatory cytokine production by *Mtb*-infected macrophages. Previously published data have shown that Mal is not required for responses to high doses of TLR2 ligands (Kenny et al., 2009); however, we hypothesize that the doses of *Mtb* used in this study correspond to the lower doses of TLR2 ligands for which Mal is required. Our findings that S180L reduced responses to TLR 2 and 4 ligands are consistent with a previous report using L-variant Mal transfected into murine MEFs (Khor et al., 2007) and with a recent study where PBMCs from individuals with the Mal S180L allele were stimulated with heat-killed *Mtb* (Capparelli et al., 2013). In contrast, another publication reported no difference between TLR2 and TLR4 signaling in vitro in PBMCs from individuals with the SS and SL genotypes but did show an increase in response to low doses of TLR2 ligand in PBMCs from a single individual with the LL genotype (Ferwerda et al., 2009). This finding might have been caused by the presence of polymorphisms in MyD88 which interact with the Mal SNP (Capparelli et al., 2013).

Macrophages from mice homozygous for the S200L mutation, the murine equivalent of S180L, did not show an impairment in TLR signaling but did show an impairment in IFN-γ signaling. Murine Mal differs from human Mal in that it has 20 more amino acids at the N terminus. Mutations in Mal might selectively impair certain signaling pathways only, as demonstrated by a recent report on a form of Mal with an altered lipid binding domain, which selectively impaired responses to the TLR9 ligand CpG but not the TLR4 ligand LPS (Bonham et al., 2014).

Importantly, the selective impairment of IFN-γ but not TLR signaling in S200L macrophages meant that the reduced phagosomal maturation and bacterial killing in macrophages with the L allele and the increased bacterial burden and increased inflammatory response seen in homozygote S200L mice could be the result of aberrant IFN-γ signaling associated with the S180L SNP rather than the result of impairment in TLR signaling. The increased inflammation seen in the homozygote mutant mice might reflect the increase in bacterial burden in the homozygote mice or might reflect a loss of IFN-γ-mediated regulation of neutrophil recruitment and inflammation (Mishra et al., 2013; Nandi and Behar, 2011). The increase in bacterial burden and inflammation is not as marked as the defect seen in mice entirely deficient in IFN-γ (Cooper et al., 1993; Flynn et al., 1993), but could be consistent with a partial defect in IFN-γ signaling.

Macrophage in vitro assays and assessment of bacterial burden and inflammation following infection demonstrated a disadvantage for homozygote mutants, whereas serial weights demonstrated increased severity of disease in both WT and mutant homozygote individuals. A number of publications on the S180L SNP and TB susceptibility in humans have reported a heterozygote advantage and/or increased susceptibility in mutant homozygotes. A heterozygote advantage in vivo has also been reported for a SNP in leukotriene A4 hydrolase (LTA4), with impaired in vitro responses seen in homozygotes for the mutation. This effect has been attributed to the effect of the SNP on mitochondrial reactive oxygen species production and cell necrosis (Roca and Ramakrishnan, 2013). As we face an era of drug-resistant tuberculosis, improved understanding of common mutations, which affect inflammatory responses to pathogens such as Mal S180L, might guide us to improved use of immunomodulatory treatment. Tobin and colleagues have highlighted the potential of using LTA4H host genotypes to guide choice of treatment for tuberculosis: individuals with tuberculous meningitis with a LTA4 genotype associated with an excessive inflammatory response benefited from adjunctive immunomodulatory steroid treatment, whereas this was harmful in those with a LTA4 genotype associated with an inadequate inflammatory response (Tobin et al., 2012). It is tempting to speculate that the Mal S180L genotype could be used to inform treatment decisions in a similar manner.

The S180L SNP in Mal has been reported to be associated with altered susceptibility to not only mycobacterial disease, but also to other infectious diseases including pneumococcal disease, malaria, and Chaga's disease. IFN-γ signaling also plays an important role in immune responses to these pathogens. Hitherto, the association of systemic lupus erythematosus (SLE) with S180L has been unexplained. TLR2 and TLR4 are not thought to play an important role in SLE (Kim et al., 2009), although TLR 9 has been implicated (Yang et al., 2012). Our data suggest that the increased susceptibility to SLE associated with S180L might be due to defects in the Mal-dependent IFN-γ signaling pathway rather than alterations in TLR2 and 4 signaling (Pollard et al., 2013).

Indeed, IFN-γ has a critical role in immunity, including promoting differentiation of macrophages to a classically activated phenotype (Martinez and Gordon, 2014). IFN-γ plays a role across a spectrum of non-infectious diseases including atherogenesis, autoimmune diseases such as chronic atopic dermatitis, and cancer (Feingold, 2014; Ikeda et al., 2002; Schroecksnadel et al., 2006). Given the frequency of the Mal S180L SNP, it might be fruitful to assess whether the Mal-dependent IFN-γ signaling pathway plays a role in these diseases.

EXPERIMENTAL PROCEDURES

Cell Lines and Culture

Primary bone-marrow-derived macrophages were derived from the femurs of *Tirap*$^{-/-}$, *Ifng*$^{-/-}$, and WT mice and differentiated for 7 days with medium containing MCSF. THP-1 cells (ATCC) were transfected with siRNA against Mal (Dharmacon) and scrambled control prior to being differentiated into macrophage-like cells with phorbol myristate acetate (100 nmol/L).

Assessment of Bacterial Growth

Macrophages were grown at 1 × 10^5 cells/ml in 12-well plates in antibiotic-free RPMI supplemented with 10% fetal calf serum. A suspension of *Mtb* H37Rv was prepared as described in Supplemental Experimental Procedures, and macrophages were infected with *Mtb* at a MOI of 10 bacteria/macrophage. Extracellular bacteria were washed off at 3 hr post-infection. Cells were lysed at the indicated time points and bacteria were harvested and colonies were counted approximately 21 days later.

Phagosome Maturation Assays

Mtb H37Rv was labeled with FITC (1 mg/ml, Sigma). Bacteria were incubated with cells for 1 hr prior to the addition of LysoTracker Red DND-99 (Invitrogen) (100 nmol/L) for 1 hr prior to fixation. Alternatively, cells were fixed, permeabilized, and with anti-CD63 /LAMP-3 (Santa Cruz Biotechnology) (1 μg/mL) followed by secondary antibody. Images were recorded on an Olympus FluoView 1000 and a Zeiss LSM 510 laser scanning confocal microscope.

Autophagy Analysis

Autophagosome formation was measured by LC3 punctate staining using LC3 antibody (Invitrogen). Autophagic flux was inhibited using either bafilomycin (100mM) or a combination of E64d and pepstatin.

Cytokine Measurements

Cytokine measurements were performed in supernatants using commercial ELISA kits.

Co-Immunoprecipitation

HEK293 cells were incubated for 24 hr with DNA encoding various proteins in the presence of Genejuice. Immunoprecipitation was initiated by incubation of lysates for 2 hr with protein A/G sepharose beads (Amersham) plus control antibodies. Precleared lysates were then incubated at 4°C for at least 2 hr with various antibodies and protein G beads (Amersham) prior to separation by SDS- PAGE and visualization with an enhanced chemiluminescence system (Li-Cor).

Plasmids

HA-Mal has been previously described (Valkov et al., 2011). Site-directed mutagensis was carried out to generate HA-tagged S180L variant Mal which was amplified using Miniprep (QIAGEN). The sequences of both HA-Mal and HA-S180L Mal were confirmed by seqencing (Eurofins).

Fluorescence Lifetime Imaging Microscopy-Fluorescence Resonance Energy Transfer

Macrophages were stained with primary antibodies against IFNGR2 (MyBioSource) and MyD88 (Abcam) and secondary antibodies Alexa Fluor A488 (donor) and A568 (acceptor) antibodies. An Olympus FV1000 microscope equipped with a PicoHarp300 FLIM extension and a 485 nm pulsed laser diode from PicoQuant was used to record FLIM data.

Genotyping

Mal genotype was determined on DNA extracted from buccal swabs (Isohelix, Cell Product). Genotyping of the Mal S180L and polymorphism was performed using the TaqMan Allelic Discrimination System (PE Biosystems).

FACS Analysis

Immortalized macrophages were stimulated, fixed, and stained with anti-pSTAT1 (Y701) antibody conjugated to AlexaFluor 488 before analysis on a BD FACSCanto II analyzer. For analysis of intracellular IFN-γ production, macrophages were infected Mtb H37Rv and then incubated with Brefeldin A. Cells were permeabilized and stained with an anti-mouse IFN-γ antibody (BD) or isotype control.

Mice

Mal S200L heterozygote and homozygote mice (C57BL/6 background) were generated as described in Figure S1. S200L mice were generated with C57BL/6 embryonic stem cells and C57BL/6 blastocysts. Mice were age and sex matched. Mice were infected with Mtb via aerosol (Martens et al., 2012) at approximately 8 weeks of age.

Bacterial Load

At 8 weeks, mice were sacrificed. Lung homogenates from six mice were plated to measure bacterial burden.

Lung Histology

Lungs were inflated, fixed, and stained (H&E). Lung surface area of inflammation was measured with a Nikon Eclipse E400. Percent total lung area involved with inflammation was calculated by dividing the cumulative area of inflammation by the total lung surface area examined for each lung studied.

Lung Cytokine Expression

Lung lysates were assayed for TNF-α by ELISA (R&D Systems).

Statistical Analysis

A one-way ANOVA was performed to assess for statistically significant difference of the means between groups. Chi-square analysis was used to assess statistically significant proportions of co-localization between groups. p values < 0.05 were considered significant. Error bars represent SD of the mean.

SUPPLEMENTAL INFORMATION

Supplemental Information includes six figures and Supplemental Experimental Procedures and can be found with this article online at http://dx.doi.org/10.1016/j.immuni.2016.01.019.

AUTHOR CONTRIBUTIONS

Conceptualization: C.N.C., F.J.S., J.H., N.M.-W., S.V.G., L.A.J.O.N., E.C.L., and J.K.; Methodology: C.N.C., F.J.S., J.H., J.L., N.M.-W., E.P.M., M.M.H., S.A.J., and S.V.G.; Investigation: C.N.C., F.J.S., J.H., N.M.-W., J.L., K.W., E.P.M., A.S., L.E.G., M.C., N.M., C.H.A.H., G.A.T., E.C.C., S.A.J., M.M.H., S.C.C., M.O.S., and C.M.F.; Formal Analysis: C.N.C., F.J.S., J.H., N.M.-W., and S.A.J.; Resources: S.C.C., N.J.B., D.G., H.K., S.V.G., and L.A.J.O.N.; Writing – Original Draft: C.N.C.; Writing – Review & Editing: C.N.C., F.J.S., J.H., H.K., E.C.L., and J.K.; Funding Acquisition: C.N.C., L.A.J.O.N., E.C.L., and J.K.; Supervision: H.K., S.V.G., L.A.J.O.N., E.C.L., and J.K. F.J.S. and J.H. contributed equally to this work.

ACKNOWLEDGMENTS

Supported in part by Health Research Board Ireland by grant NSAFP 2009/2 (C.N.C.), CSA/2004/7 and CSA/2012/16 (J.K.), The Royal City of Dublin Hospital Trust (J.K.), NIH grant HL081149 (H.K.), Wellcome Trust PhD award 102395/Z/13/Z (A.S.), Science Foundation Ireland Investigator Awards 08/IN.1/B2038 (S.G.) and 12/IA/1421 (E.C.L.), and the Science Foundation Ireland Strategic Research Cluster 07/SRC/B1144 (E.C.L.).

Received: August 26, 2014
Revised: April 20, 2015
Accepted: November 6, 2015
Published: February 16, 2016

REFERENCES

Bogunovic, D., Byun, M., Durfee, L.A., Abhyankar, A., Sanal, O., Mansouri, D., Salem, S., Radovanovic, I., Grant, A.V., Adimi, P., et al. (2012). Mycobacterial disease and impaired IFN-γ immunity in humans with inherited ISG15 deficiency. Science *337*, 1684–1688.

Bonham, K.S., Orzalli, M.H., Hayashi, K., Wolf, A.I., Glanemann, C., Weninger, W., Iwasaki, A., Knipe, D.M., and Kagan, J.C. (2014). A promiscuous lipid-binding protein diversifies the subcellular sites of toll-like receptor signal transduction. Cell *156*, 705–716.

Capparelli, R., De Chiara, F., Di Matteo, A., Medaglia, C., and Iannelli, D. (2013). The MyD88 rs6853 and TIRAP rs8177374 polymorphic sites are associated with resistance to human pulmonary tuberculosis. Genes Immun. *14*, 504–511.

Castiblanco, J., Varela, D.-C., Castaño-Rodríguez, N., Rojas-Villarraga, A., Hincapié, M.-E., and Anaya, J.-M. (2008). TIRAP (MAL) S180L polymorphism is a common protective factor against developing tuberculosis and systemic lupus erythematosus. Infect. Genet. Evol. *8*, 541–544.

Cooper, A.M., Dalton, D.K., Stewart, T.A., Griffin, J.P., Russell, D.G., and Orme, I.M. (1993). Disseminated tuberculosis in interferon gamma gene-disrupted mice. J. Exp. Med. *178*, 2243–2247.

Darwich, L., Coma, G., Peña, R., Bellido, R., Blanco, E.J., Este, J.A., Borras, F.E., Clotet, B., Ruiz, L., Rosell, A., et al. (2009). Secretion of interferon-gamma by human macrophages demonstrated at the single-cell level after costimulation with interleukin (IL)-12 plus IL-18. Immunology *126*, 386–393.

Deretic, V., Singh, S., Master, S., Harris, J., Roberts, E., Kyei, G., Davis, A., de Haro, S., Naylor, J., Lee, H.H., and Vergne, I. (2006). Mycobacterium tuberculosis inhibition of phagolysosome biogenesis and autophagy as a host defence mechanism. Cell. Microbiol. *8*, 719–727.

Di Marzio, P., Puddu, P., Conti, L., Belardelli, F., and Gessani, S. (1994). Interferon gamma upregulates its own gene expression in mouse peritoneal macrophages. J. Exp. Med. *179*, 1731–1736.

Dissanayeke, S.R., Levin, S., Pienaar, S., Wood, K., Eley, B., Beatty, D., Henderson, H., Anderson, S., and Levin, M. (2009). Polymorphic variation in TIRAP is not associated with susceptibility to childhood TB but may determine susceptibility to TBM in some ethnic groups. PLoS ONE *4*, e6698.

Feingold, K.R. (2014). The adverse effect of IFN gamma on stratum corneum structure and function in psoriasis and atopic dermatitis. J. Invest. Dermatol. *134*, 597–600.

Fenton, M.J., Vermeulen, M.W., Kim, S., Burdick, M., Strieter, R.M., and Kornfeld, H. (1997). Induction of gamma interferon production in human alveolar macrophages by Mycobacterium tuberculosis. Infect. Immun. *65*, 5149–5156.

Ferwerda, B., Alonso, S., Banahan, K., McCall, M.B., Giamarellos-Bourboulis, E.J., Ramakers, B.P., Mouktaroudi, M., Fain, P.R., Izagirre, N., Syafruddin, D., et al. (2009). Functional and genetic evidence that the Mal/TIRAP allele variant 180L has been selected by providing protection against septic shock. Proc. Natl. Acad. Sci. USA *106*, 10272–10277.

Filipe-Santos, O., Bustamante, J., Chapgier, A., Vogt, G., de Beaucoudrey, L., Feinberg, J., Jouanguy, E., Boisson-Dupuis, S., Fieschi, C., Picard, C., and Casanova, J.L. (2006). Inborn errors of IL-12/23- and IFN-gamma-mediated immunity: molecular, cellular, and clinical features. Semin. Immunol. *18*, 347–361.

Fitzgerald, K.A., Palsson-McDermott, E.M., Bowie, A.G., Jefferies, C.A., Mansell, A.S., Brady, G., Brint, E., Dunne, A., Gray, P., Harte, M.T., et al. (2001). Mal (MyD88-adapter-like) is required for Toll-like receptor-4 signal transduction. Nature *413*, 78–83.

Flesch, I.E., and Kaufmann, S.H. (1991). Mechanisms involved in mycobacterial growth inhibition by gamma interferon-activated bone marrow macrophages: role of reactive nitrogen intermediates. Infect. Immun. *59*, 3213–3218.

Flynn, J.L., Chan, J., Triebold, K.J., Dalton, D.K., Stewart, T.A., and Bloom, B.R. (1993). An essential role for interferon gamma in resistance to Mycobacterium tuberculosis infection. J. Exp. Med. *178*, 2249–2254.

Fultz, M.J., Barber, S.A., Dieffenbach, C.W., and Vogel, S.N. (1993). Induction of IFN-gamma in macrophages by lipopolysaccharide. Int. Immunol. *5*, 1383–1392.

Gutierrez, M.G., Master, S.S., Singh, S.B., Taylor, G.A., Colombo, M.I., and Deretic, V. (2004). Autophagy is a defense mechanism inhibiting BCG and Mycobacterium tuberculosis survival in infected macrophages. Cell *119*, 753–766.

Harris, J., De Haro, S.A., Master, S.S., Keane, J., Roberts, E.A., Delgado, M., and Deretic, V. (2007). T helper 2 cytokines inhibit autophagic control of intracellular Mycobacterium tuberculosis. Immunity *27*, 505–517.

Harris, J., Hope, J.C., and Lavelle, E.C. (2009). Autophagy and the immune response to TB. Transbound. Emerg. Dis. *56*, 248–254.

Hölscher, C., Reiling, N., Schaible, U.E., Hölscher, A., Bathmann, C., Korbel, D., Lenz, I., Sonntag, T., Kröger, S., Akira, S., et al. (2008). Containment of aerogenic Mycobacterium tuberculosis infection in mice does not require MyD88 adaptor function for TLR2, -4 and -9. Eur. J. Immunol. *38*, 680–694.

Horng, T., Barton, G.M., and Medzhitov, R. (2001). TIRAP: an adapter molecule in the Toll signaling pathway. Nat. Immunol. *2*, 835–841.

Horng, T., Barton, G.M., Flavell, R.A., and Medzhitov, R. (2002). The adaptor molecule TIRAP provides signalling specificity for Toll-like receptors. Nature *420*, 329–333.

Ikeda, H., Old, L.J., and Schreiber, R.D. (2002). The roles of IFN γ in protection against tumor development and cancer immunoediting. Cytokine Growth Factor Rev. *13*, 95–109.

Kagan, J.C., and Medzhitov, R. (2006). Phosphoinositide-mediated adaptor recruitment controls Toll-like receptor signaling. Cell *125*, 943–955.

Kenny, E.F., Talbot, S., Gong, M., Golenbock, D.T., Bryant, C.E., and O'Neill, L.A. (2009). MyD88 adaptor-like is not essential for TLR2 signaling and inhibits signaling by TLR3. J. Immunol. *183*, 3642–3651.

Khor, C.C., Chapman, S.J., Vannberg, F.O., Dunne, A., Murphy, C., Ling, E.Y., Frodsham, A.J., Walley, A.J., Kyrieleis, O., Khan, A., et al. (2007). A Mal functional variant is associated with protection against invasive pneumococcal disease, bacteremia, malaria and tuberculosis. Nat. Genet. *39*, 523–528.

Kim, W.U., Sreih, A., and Bucala, R. (2009). Toll-like receptors in systemic lupus erythematosus; prospects for therapeutic intervention. Autoimmun. Rev. *8*, 204–208.

Ladhani, S.N., Davila, S., Hibberd, M.L., Heath, P.T., Ramsay, M.E., Slack, M.P., Pollard, A.J., and Booy, R. (2010). Association between single-nucleotide polymorphisms in Mal/TIRAP and interleukin-10 genes and susceptibility to invasive haemophilus influenzae serotype b infection in immunized children. Clin. Infect. Dis. *51*, 761–767.

Liu, Q., Li, W., Li, D., Feng, Y., and Tao, C. (2014). TIRAP C539T Polymorphism Contributes to Tuberculosis Susceptibility: Evidence from a Meta-Analysis. Infect Genet Evol.

MacMicking, J.D. (2012). Interferon-inducible effector mechanisms in cell-autonomous immunity. Nat. Rev. Immunol. *12*, 367–382.

Martens, G.W., Vallerskog, T., and Kornfeld, H. (2012). Hypercholesterolemic LDL receptor-deficient mice mount a neutrophilic response to tuberculosis despite the timely expression of protective immunity. J. Leukoc. Biol. *91*, 849–857.

Martinez, F.O., and Gordon, S. (2014). The M1 and M2 paradigm of macrophage activation: time for reassessment. F1000Prime Rep. *6*, 13.

Matsuzawa, T., Fujiwara, E., and Washi, Y. (2014). Autophagy activation by interferon-γ via the p38 mitogen-activated protein kinase signalling pathway is involved in macrophage bactericidal activity. Immunology *141*, 61–69.

Mishra, B.B., Rathinam, V.A., Martens, G.W., Martinot, A.J., Kornfeld, H., Fitzgerald, K.A., and Sassetti, C.M. (2013). Nitric oxide controls the immunopathology of tuberculosis by inhibiting NLRP3 inflammasome-dependent processing of IL-1β. Nat. Immunol. *14*, 52–60.

Mosmann, T.R., and Coffman, R.L. (1989). TH1 and TH2 cells: different patterns of lymphokine secretion lead to different functional properties. Annu. Rev. Immunol. *7*, 145–173.

Nandi, B., and Behar, S.M. (2011). Regulation of neutrophils by interferon-γ limits lung inflammation during tuberculosis infection. J. Exp. Med. *208*, 2251–2262.

Nejentsev, S., Thye, T., Szeszko, J.S., Stevens, H., Balabanova, Y., Chinbuah, A.M., Hibberd, M., van de Vosse, E., Alisjahbana, B., van Crevel, R., et al. (2008). Analysis of association of the TIRAP (MAL) S180L variant and tuberculosis in three populations. Nat. Genet. *40*, 261–262, author reply 262–263.

Ní Cheallaigh, C., Keane, J., Lavelle, E.C., Hope, J.C., and Harris, J. (2011). Autophagy in the immune response to tuberculosis: clinical perspectives. Clin. Exp. Immunol. *164*, 291–300.

O'Carroll, C., Fagan, A., Shanahan, F., and Carmody, R.J. (2014). Identification of a unique hybrid macrophage-polarization state following recovery from lipopolysaccharide tolerance. J. Immunol. *192*, 427–436.

Peral de Castro, C., Jones, S.A., Ní Cheallaigh, C., Hearnden, C.A., Williams, L., Winter, J., Lavelle, E.C., Mills, K.H.G., and Harris, J. (2012). Autophagy regulates IL-23 secretion and innate T cell responses through effects on IL-1 secretion. J. Immunol. *189*, 4144–4153.

Perussia, B. (1991). Lymphokine-activated killer cells, natural killer cells and cytokines. Curr. Opin. Immunol. *3*, 49–55.

Pollard, K.M., Cauvi, D.M., Toomey, C.B., Morris, K.V., and Kono, D.H. (2013). Interferon-γ and systemic autoimmunity. Discov. Med. *16*, 123–131.

Roca, F.J., and Ramakrishnan, L. (2013). TNF dually mediates resistance and susceptibility to mycobacteria via mitochondrial reactive oxygen species. Cell *153*, 521–534.

Sad, S., Marcotte, R., and Mosmann, T.R. (1995). Cytokine-induced differentiation of precursor mouse CD8+ T cells into cytotoxic CD8+ T cells secreting Th1 or Th2 cytokines. Immunity *2*, 271–279.

Schleicher, U., Hesse, A., and Bogdan, C. (2005). Minute numbers of contaminant CD8+ T cells or CD11b+CD11c+ NK cells are the source of IFN-gamma in

IL-12/IL-18-stimulated mouse macrophage populations. Blood *105*, 1319–1328.

Schroecksnadel, K., Frick, B., Winkler, C., and Fuchs, D. (2006). Crucial role of interferon-gamma and stimulated macrophages in cardiovascular disease. Curr. Vasc. Pharmacol. *4*, 205–213.

Selvaraj, P., Harishankar, M., Singh, B., Jawahar, M.S., and Banurekha, V.V. (2010). Toll-like receptor and TIRAP gene polymorphisms in pulmonary tuberculosis patients of South India. Tuberculosis (Edinb.) *90*, 306–310.

Sun, D., and Ding, A. (2006). MyD88-mediated stabilization of interferon-gamma-induced cytokine and chemokine mRNA. Nat. Immunol. *7*, 375–381.

Tobin, D.M., Roca, F.J., Oh, S.F., McFarland, R., Vickery, T.W., Ray, J.P., Ko, D.C., Zou, Y., Bang, N.D., Chau, T.T., et al. (2012). Host genotype-specific therapies can optimize the inflammatory response to mycobacterial infections. Cell *148*, 434–446.

Valkov, E., Stamp, A., Dimaio, F., Baker, D., Verstak, B., Roversi, P., Kellie, S., Sweet, M.J., Mansell, A., Gay, N.J., et al. (2011). Crystal structure of Toll-like receptor adaptor MAL/TIRAP reveals the molecular basis for signal transduction and disease protection. Proc. Natl. Acad. Sci. USA *108*, 14879–14884.

Watson, R.O., Manzanillo, P.S., and Cox, J.S. (2012). Extracellular M. tuberculosis DNA targets bacteria for autophagy by activating the host DNA-sensing pathway. Cell *150*, 803–815.

Yamamoto, A., Tagawa, Y., Yoshimori, T., Moriyama, Y., Masaki, R., and Tashiro, Y. (1998). Bafilomycin A1 prevents maturation of autophagic vacuoles by inhibiting fusion between autophagosomes and lysosomes in rat hepatoma cell line, H-4-II-E cells. Cell Struct. Funct. *23*, 33–42.

Yamamoto, M., Sato, S., Hemmi, H., Sanjo, H., Uematsu, S., Kaisho, T., Hoshino, K., Takeuchi, O., Kobayashi, M., Fujita, T., et al. (2002). Essential role for TIRAP in activation of the signalling cascade shared by TLR2 and TLR4. Nature *420*, 324–329.

Yang, Z., Liang, Y., Qin, B., Li, C., and Zhong, R. (2012). TLR9 polymorphisms and systemic lupus erythematosus risk in Asians: a meta-analysis study. Cytokine *57*, 282–289.